

# Reactive Ionic Liquids



By

Rachel Elizabeth Whiteside, MSci

Presented to the School of Chemistry and Chemical Engineering

The Queen's University of Belfast

in fulfilment

of the requirements

for the degree of

Doctor of Philosophy

Queen's University of Belfast

July 2018

## Contents

1	General Introduction.....	11
1.1	Abstract .....	11
1.2	Ionic liquids- a historical approach.....	14
1.3	Ionic liquids in modern chemistry.....	16
1.4	Reactive ionic liquids.....	18
1.4.1	Inorganic synthesis in Ionic liquids .....	19
1.4.2	Dissolution in ionic liquids.....	21
1.5	Project Aims.....	23
2	Alkali metal solvation in ionic liquids .....	24
2.1	Introduction .....	24
2.1.1	Current solvents for alkali metal solvation .....	24
2.1.2	The solvated electrons phenomenon.....	30
2.1.3	Alkali metals in ionic liquids.....	33
2.1.4	Flash photolysis techniques in ionic liquids .....	35
2.1.5	Significance and application.....	38
2.1.6	Inorganic synthesis and single electron reductions.....	39
2.2	Results and discussion .....	42
2.2.1	Design and synthesis of the amine functionalised ionic liquid .....	42
2.2.2	Alkali metal solvation.....	46
2.2.3	Spectroscopic analysis.....	47
2.2.4	Proof of concept: non-reactive ionic liquids .....	61
2.2.5	Computational modelling.....	62
2.2.6	Development of aliphatic analogues.....	69
2.2.7	Crown ether interactions and alkali metal solvation .....	71
2.2.8	Reactions with elemental lead.....	80
2.2.9	Silver nitrate reduction tests.....	82
2.2.10	Birch Reduction Tests.....	82
2.2.11	Chemical reduction tests.....	83

2.3	Conclusions .....	85
2.4	Future work.....	86
2.5	Experimental methods .....	86
2.5.1	Materials .....	86
2.5.2	Nuclear magnetic resonance spectroscopy .....	87
2.5.3	Electron paramagnetic resonance spectroscopy .....	87
2.5.4	UV/Vis spectroscopy .....	88
2.5.5	Atomic adsorption spectroscopy.....	88
2.5.6	Synthesis of ionic liquids .....	88
2.5.7	Crown ether experiments .....	96
2.5.8	Chemical reduction experiments .....	97
2.5.9	Computational experiments.....	97
2.5.10	Single Crystal Analysis.....	98
3	<i>p-tert</i> -Butylcalix-[4]-arene solvation in basic ionic liquids and a study of basic anion-ionic liquid interactions with phenolic compounds .....	103
3.1	Introduction .....	103
3.1.1	Discovery of <i>p-tert</i> -butylcalix-[4]-arenes .....	103
3.1.2	Significance of <i>p-tert</i> -butylcalix-[4]-arenes in modern chemistry .....	106
3.1.3	Physical properties of <i>p-tert</i> -butylcalix-[4]-arenes and their influence on lower rim functionalisation methods.....	111
3.1.4	Acetate anion containing ionic liquids.....	118
3.1.5	Methyl carbonate anion ionic liquids.....	119
3.2	Results and Discussion .....	121
3.2.1	Screening of ionic liquids .....	121
3.2.2	Behaviour of <i>p-tert</i> -butylcalix-[4]-arenes in [P <sub>66614</sub> ][OAc] ionic liquids 125	
3.2.3	Comparative systems.....	139
3.2.4	Interactions of <i>p-tert</i> -butylcalix-[4]-arenes and guanidine bases .....	152
3.2.5	Behaviour of <i>p-tert</i> -butylcalix-[4]-arenes in methyl carbonate ionic liquids	159

3.2.6	Selective mono-alkylations of <i>p-tert</i> -butylcalix-[4]-arenes using ammonium calixarate salts .....	166
3.3	Conclusions .....	173
3.4	Future work.....	174
3.5	Experimental methods .....	175
3.5.1	Materials .....	175
3.5.2	Nuclear magnetic resonance spectroscopy .....	176
3.5.3	UV/Vis spectrometry .....	176
3.5.4	Densimetry.....	177
3.5.5	Thermogravimetric Analysis, TGA .....	177
3.5.6	Mass spectrometry.....	177
3.5.7	Infrared spectroscopy.....	177
3.5.8	Synthesis of <i>p-tert</i> -butylcalix-[4]-arate salts .....	178
3.5.9	Synthesis of mono-alkylated <i>tert</i> -butylcalix-4-arenes .....	179
3.5.10	Single Crystal Analysis.....	183
4	Liquid coordination complexes of group 13 chlorometallates .....	186
4.1	Introduction .....	186
4.1.1	Group 13 chlorometallates in molecular solvents.....	186
4.1.2	Group 13 chlorometallate molten salts/ ionic liquids .....	187
4.1.3	Group 13 chlorometallate liquid coordination complexes .....	193
4.1.4	Experimental techniques for speciation elucidation.....	198
4.2	Results and Discussion .....	210
4.2.1	Chlorogallate liquid coordination complexes.....	210
4.2.2	Chloroindate liquid coordination complexes.....	241
4.3	Conclusions .....	255
4.4	Future Work .....	256
4.5	Experimental methods .....	256
4.5.1	Synthesis of donor ligands and liquid coordination complexes.....	257
4.5.2	Raman and IR spectroscopy .....	257



4.5.3	Extended X-ray Fine Structure spectroscopy.....	258
4.5.4	Viscosimetry .....	258
4.5.5	Densitometry .....	258
4.5.6	Conductivity .....	259
4.5.7	Nuclear magnetic resonance spectroscopy .....	259
4.5.8	Powder X-ray diffraction .....	262
5	Liquid coordination complexes of chlorocuprates.....	263
5.1	Introduction .....	263
5.1.1	Chlorocuprates in classical molecular solvents and ionic liquids. ....	263
5.1.2	Chlorocuprate liquid coordination complexes .....	269
5.2	Results and Discussion .....	273
5.2.1	Chlorocuprate liquid coordination complexes .....	273
5.2.2	Copper (I) chloride – trioctylphosphine liquid coordination complexes and chalcogenide interactions .....	311
5.2.3	Copper (II) chloride – trioctylphosphine liquid coordination complexes and chalcogenide interactions .....	317
5.2.4	Liquid coordination complexes as precursors for semiconductor materials .....	324
5.3	Conclusions .....	341
5.4	Future work.....	342
5.5	Experimental Methods .....	344
5.5.1	Synthesis of donor ligands and liquid coordination complexes.....	344
5.5.2	Raman and IR spectroscopy .....	345
5.5.3	Extended X-ray Fine Structure spectroscopy.....	345
5.5.4	High-Energy Resolution Fluorescence Detected XANES.....	346
5.5.5	Nuclear magnetic resonance spectroscopy .....	346
5.5.6	Chalcogenide solvation experiments .....	347
5.5.7	Synthesis of binary and ternary semiconductor materials .....	348
6	Conclusions .....	350
7	References .....	354

8	Appendix.....	381
8.1	Table of Figures.....	381
8.2	Table of Tables.....	394
8.3	Alkali metal solvation in ionic liquids.....	398
8.3.1	Nuclear Magnetic resonance spectroscopy.....	398
8.4	<i>p-tert</i> -Butylcalix-[4]-arene solvation in basic ionic liquids.....	404
8.4.1	Nuclear magnetic resonance spectroscopic data.....	404
8.4.2	Thermogravimetric analysis.....	421
8.5	Liquid coordination complexes of chlorometallates and donor ligands.....	424
8.5.1	Acronyms.....	424
8.5.2	Density Data for chlorogallate and chloroindate liquid coordination complexes.....	424
8.5.3	Viscosity data for chlorogallate and chloroindate liquid coordination complexes.....	430
8.5.4	Nuclear magnetic resonance spectroscopic data for chlorogallate and chloroindate liquid coordination complexes.....	432
8.5.5	Infrared spectroscopic data for chlorogallate and chloroindate liquid coordination complexes.....	439
8.5.6	Extended X-ray fine structure spectroscopy-Chlorogallate systems.....	444
8.5.7	Extended X-ray fine structure spectroscopy-Chlorocuprate systems.....	452
8.5.8	Nuclear magnetic resonance spectroscopic data for chlorocuprate systems.....	454
8.5.9	Powder X-ray diffraction data.....	454

## Publications

Rachel E. Whiteside, H. Q. Nimal Gunaratne, Ryan Kavanagh, Jorge Kohanoff, Kenneth Seddon, Peter Nockemann, Alkali Metal Solvation in Ionic Liquids. *Chem. commun.*, 2018, **Manuscript in preparation.**

Rachel E. Whiteside, H. Q. Nimal Gunaratne, Aline F. V. Muzio, Peter Nockemann, Selective Monoalkylation of *p-tert*-butylcalix-4-arene in a Methyl Carbonate Ionic Liquids, *Chem. commun.*, 2018, **Manuscript submitted.**

Rachel E. Whiteside, James M. Hogg, Iuliia Mikulska, Sofia Diaz-Moreno, Gary A. Leeke, Peter Nockemann and Małgorzata Swadźba-Kwaśny\*, Liquid Coordination Complexes of Copper(I) Chloride and Trioctylphosphine, *Inorg. Chem.*, 2018, **Manuscript submitted.**

Rachel E. Whiteside, James M. Hogg, Fergal Coleman, Janine Richter, Christopher Hardacre, Peter Nockemann, John D. Holbrey, Sofia Diaz-Moreno, Gianantonio Cibin, Shu Hayama, Małgorzata Swadźba-Kwaśny\*, *Liquid coordination complexes of Group 13 chlorometallates and trioctylphosphine chalcogenides: speciation and physico-chemical properties*, *Inorg. Chem.*, 2018, **Manuscript in preparation.**

## Other publications

Alexander Wolff, Thomas Doert, Jens Hunger, Martin Kaiser, Julia Pallmann, Romy Reinhold, Sivathemehan Yogendra, Lars Giebeler, Jörg Sichelschmidt, Walter Schnelle, Rachel E. Whiteside, H. Q. Nimal Gunaratne, Peter Nockemann, Jan J. Weigand, Eike Brunner, Michael Ruck\*, Low-temperature tailoring of copper-deficient  $\text{Cu}_{3-x}\text{P}$  – electric properties, phase transitions and performance in Li ion batteries, *Chem. mater.*, 2018. **Manuscript submitted.**

Oldamur Hollóczy, \* Alexander Wolff, Julia Pallmann, Rachel E. Whiteside, Jennifer Hartley, Matthias A. Grasser, Peter Nockemann, Eike Brunner, Thomas Doert, Michael Ruck, Spontaneous Substitutions on Phosphorus Trihalides in Imidazolium Halide Ionic Liquids: A Grotthuss Diffusion of Anions?, *Inorganic Chem*, 2018, **Manuscript in preparation.**

## **Declaration**

## Acknowledgements

I firstly wish to thank my family and friends for their constant support and belief in me when I didn't believe in myself. Without their constant support this thesis simply wouldn't exist. A specific thanks to my parents (Paul and Heather), Matthew Whiteside, James Hogg and Pia McAleenan.

Secondly, I wish to thank my supervisor Peter Nockemann for his valuable comments, encouragement and support throughout this project. Further thanks for his encouragement, patience and assistance in learning new techniques such as single crystal diffraction. And a thanks to the Nockemann group for their constant support and friendship; Eadaoin McCourt, Robert Boyd, Ena Bradley, Donnacha Brolly and Ciaran Carroll. These thanks extend to all those in office 03.404; Lucy Brown, Josh McCann, Eoghain O'Hara, Sophie Tyrrell, and Fergal Coleman.

Thirdly, I wish to thank Nimal Gunaratne for his constant support, knowledge and assistance in all of my experimental ventures. Further thanks to Gosia Swadzba-Kwasny for her guidance with the LCC projects and throughout all EXAFS experiments and data analysis.

A further thanks to the Diamond Light source, Sofia Diaz-Moreno, Giannantonio Cibin, Stephen Parry and Iuliia Mikulska for their assistance in EXAFS and HERFD-XANES experiments and data analysis. Many thanks to BESSY II KMC-2 beamline for their assistance in collaborative projects with TU Dresden. I wish to again thank my supervisor for allowing for external collaborations with TU Dresden Ruck group with specific thanks to Alexander Wolff, Julia Pallmann and Mathias Grasser the PhD students and now friends on the project.

Many thanks to all of the masters, exchange and summer students who were placed under my guidance throughout this project; Aline Muzio (calixarene project), Janine Richter (Ga/In LCCs) and Martin Vacik (semiconductor synthesis).

Many thanks to the late Kenneth Seddon; his valuable comments and development of the QUILL research centre has been an invaluable source of knowledge, support and equipment for not just myself but a wealth of students past, present and future. Further thanks to QUILL for the opportunity to present this work on multiple occasions at biannual meeting to industrial sponsors. Specific thanks to Roland Kalb of Proionic for his assistance in the calixarene project. A thanks to all QUILL and

CCE staff and students who have helped in any capacity throughout my time here (Natalia Plechkova, Geetha Srinivasan, Deborah Poland)

Further thanks to those involved in the postgraduate process within the school of chemistry for support, organisation of submission and annual progress reviews; Stuart James, Karen Moore, and Julie McConnell. Further thanks to Cristina Lagunas and John Holbrey for valuable comments within annual progress reviews.

I wish to extend my thanks to all ASEP and QUILL technical staff for assistance and support in a variety of analytical techniques. Specific thanks to Richard Murphy (NMR), Samuel Moore (AAS) and Conor McGrann (MS).

Thanks to the Department for the Economy for funding this project.

# 1 General Introduction

## 1.1 Abstract

The main aim of this work is the utilisation of the often coined 'designer capabilities' of ionic liquids to improve current synthetic methods within both inorganic and organic chemistry. The term 'reactive ionic liquids' refers to the ones where the liquids are integral to the reaction process to which they have been applied. This can be both as a catalyst, reagent or as a solvent to which dissolution of a reagent is not available in conventional solvents. This project aimed to investigate three new types of ionic liquids for three specific applications to demonstrate the true designer properties of these solvents.

The first application that was aimed for was an ionic liquid to dissolve alkali metals at room temperature and above. This goal was achieved *via* an aminopyridinium cation that provided a primary amine functionality to mimic ammonia, along with an aromatic functionality to stabilise the solvated electrons formed upon solvation. This solvation mechanism has been studied extensively with a variety of spectroscopic techniques, comparative studies and computational techniques. Applications to single electron reductions have been studied.

The second application was based upon *p*-*tert*-butylcalix-[4]-arenes, TBCs, which are well-known for their useful derivatives in sensors and extraction applications. However, they are often subject to unselective and poor yielding functionalisation reactions along with the initial calixarene motif's poor solubility in many organic solvents. Basic anion-containing ionic liquids were deemed to be a suitable alternative to conventional methods that utilise conventional solvents, alkyl halides and inorganic bases that often result in a mixture of alkylation products. Methyl carbonate-anion ionic liquids were found to be effective in mono-deprotonating TBC and consequently forming calixarate salts, which can be successfully mono-alkylated in high yield.

The final application is based on the inorganic synthesis of semiconductor species. This study utilised liquid coordination complexes, LCCs as new generation ionic liquids composed of a halometallate and donor ligand in which cationic, anionic and neutral complexes are formed in equilibria and exhibit ionic liquid-like properties in regards to their low volatility. These LCCs have been studied extensively *via* a variety of spectroscopic techniques including multinuclear NMR, IR, Raman and EXAFS spectroscopy to elucidate their speciation. They have also been shown to be

good candidates for binary and tertiary semiconductor synthesis *via* conventional heating methods in ampoule conditions. Furthermore, the effect of temperature on the LCC speciation has been found to cause a huge variation in the position of equilibrium present as determined by variable temperature NMR spectroscopy.

Along with studying the applications of ionic liquids, this work has led to the development of new methodologies for speciation determination within EXAFS techniques. Using plots of R-factors as a function of total coordination number and relative bond ratios, local minima can determine the total coordination number of the centre under investigation and the relative molar ratio of each bonding species.



### **Sodium solvation**

Can ionic liquids replace ammonia?  
Can a new single electron reduction method be developed in ionic liquids?

### **Functionalisation of calixarenes**

Can ionic liquids work as both an intrinsic base to initiate functionalisation and as a more effective solvent than conventional organic solvents?

# **Reactive Ionic Liquids**

Ionic liquids which are integral to the reaction process to which they have been applied. This can be both as a catalyst, reagent or as a solvent to which dissolution of a reagent is not available in conventional solvents.

### **Synthesis of semiconductor materials**

Can LCCs work as both an intrinsic precursor and a capping agent to form binary and tertiary semiconductor materials?

Can speciation in LCCs be further elucidated to gain greater control of particle size, shape and morphology?

## 1.2 Ionic liquids- a historical approach

Ionic liquids were first reported in 1914 by Walden and co-workers who cited molten salts with melting points below 100 °C, specifically ethylammonium nitrate, [N<sub>2000</sub>][NO<sub>3</sub>]. The commonly accepted definition of an ionic liquid is a liquid that consists of ions and is liquid below 100 °C. The reasoning behind this arbitrary temperature as the melting point threshold is to distinguish these compounds as separate from conventional molten salts which are often very high in melting point.

Since this initial report ionic liquids remained somewhat dormant for several years with the progression of the molten salts community being rapid in the late 1960s; ionic liquids only came into the spotlight in the late 1990s with their wide range of properties and scope being realised throughout the chemistry community.<sup>1</sup>

A typical ionic liquid is comprised of a bulky organic cation such as imidazolium, phosphonium and ammonium *etc.* and a variety of anions such as halides, triflates, methyl sulphates, nitrates, tetrafluoroborates, chlorometallates *etc.* (Figure 1-1) The combination of the various cations and anions can dramatically change the properties exhibited by the ionic liquid in regards to melting point, Lewis acidity/basicity, viscosity, density and hydrophobicity/philicity.

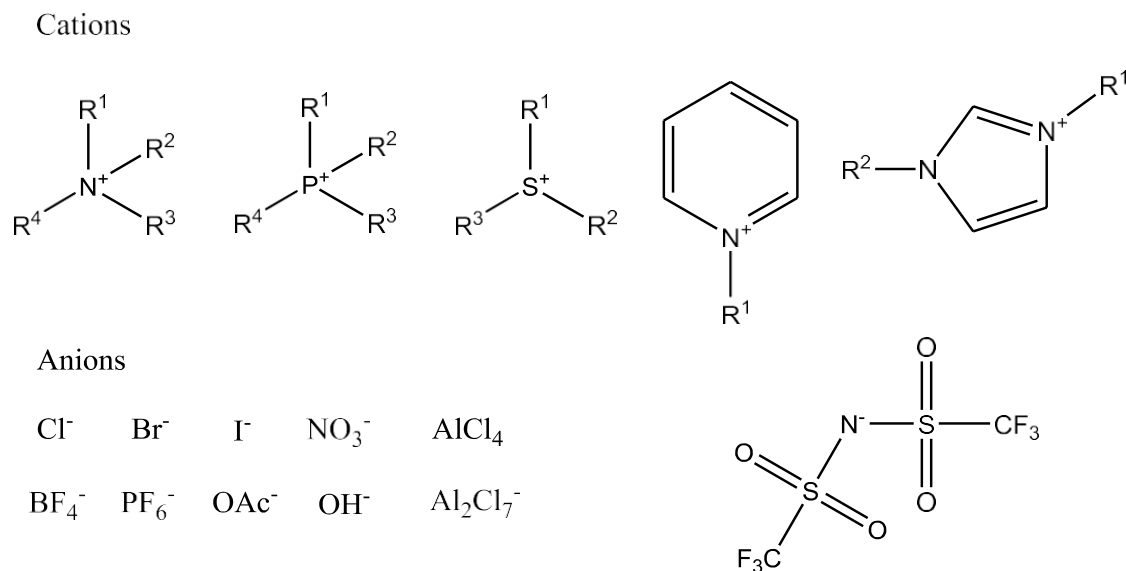
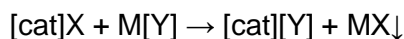


**Figure 1-1**-Structures of some common cations and anions found in ionic liquids.

Conventional ionic liquids are synthesised *via* a general procedure that involves an alkylation of an amine, phosphine, alkylimidazole *etc.* to result in a position of positive charge and dependent on the desired anion and alkylating agent (usually an alkyl halide or dialkyl sulphate), a metathesis reaction can be carried out. This

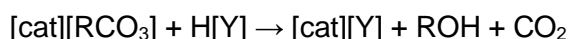
reaction involves the addition of a metal salt of the desired cation such as M[OTf], M[NTf<sub>2</sub>] and M [SCN] where M = Li, Na, Ag, K and the consequent precipitation of the metal halide salt that forms due to metathesis (Equation 1-1).

Equation 1-1



More recently a new methodology termed the CBILs method uses acid base chemistry to provide a cleaner and more atom efficient method of synthesising ionic liquids.<sup>2,3</sup> This method requires the base ionic liquid to have a methyl carbonate anion that can be easily formed *via* alkylation of the cation starting material with dimethyl carbonate. The methyl carbonate anion upon the addition of a Lewis acid results in the decomposition of the methyl carbonate anion to form carbon dioxide and methanol. As a result of this, the conjugate base of the Lewis acid added is formed and is anion of the ionic liquid (Equation 1-2.)

Equation 1-2



Synthesis of chlorometallates and their transition metal chloride anions simply require controlled addition of the metal chloride to the cation halide salt often resulting in a exotherm hence slow addition is required to prevent localised heating and thermal decomposition. There is a great variation in the anions achieved with metal chlorides and determination. What has currently been observed within literature is well documented in a review by Estager *et. al.*<sup>4</sup>

Historical strategies to ionic liquids and their application as a solvent surrounded two main approaches; homogeneity of the reactants and the separation of the resultant products. Being non-volatile, the separation of the organic products from the IL is simple *via* vacuum distillation. Improving the homogeneity of reaction mixtures can improve the rate of reaction and yields observed. The formation of two phase systems such as that observed in the BASIL process is another beneficial aspect of ionic liquids. In these processes, acidic impurities, HCl are removed from the diethoxyphenylphosphine product using methylimidazole to form methylimidazolium chloride, which then causes a phase separation.<sup>5</sup>

### 1.3 Ionic liquids in modern chemistry

Conventional ionic liquids that are now “off the shelf” in nature due to a now well-established industry with companies such as Proionic, Io-Li-Tech and Solvay; all providing a vast array of cations and anions. However, it is notable that task-specific ionic liquids are less available, with ILs commonly sold for their solvent properties alone hence the ‘designer’ solvent capabilities of ILs are not commercially utilised.

Along with solvent properties the second most utilised ionic liquids within industrial processes are those with catalytic properties; most commonly in Lewis acid or Lewis base-driven catalytic processes. For example, chloroaluminate anion ionic liquids have been used in many catalytic processes including Friedel-Crafts, Ziegler-Natta catalysis and alkylation reactions.<sup>6–8</sup> Moving forwards, alternative Lewis acidic and Lewis basic ILs were sought to be more air and water stable.

The chemical stability of ionic liquids is often disputed with the initial purity often hard to determine and to achieve above a *puriss* quality as conventional distillation methods *etc.* are not available. Obtaining clean and colourless ionic liquids is difficult and requires significant purification of starting materials and resultant product. Although high purity is achievable *via* purification methods such as alumina treatment and charcoal treatment studied by Driesen and co-workers for optical studies.<sup>9</sup> Purification to ‘ultra-pure’ standard *i.e.* > 99 % is laborious and results in significant losses of IL.

The chemical stability as mentioned is often under dispute; an in depth review by Gao and co-workers highlights issues with the long term thermal stability that is less than previously reported.<sup>10,11</sup> In regards to the chemical stability, imidazolium cations are the most widely reported; under basic conditions can be deprotonated at the C2 position to generate reactive nucleophiles. Furthermore, in the presence of acetic anhydride or ethyl formate acylation can occur in the C2 position.<sup>12</sup> Phosphonium cations have also been noted to decompose *via* ylide formation and S<sub>N</sub>2 elimination.<sup>13</sup> Ammonium cations have been found to degrade *via* Hoffman elimination in basic conditions especially in the presence of [OH]<sup>–</sup> anions.<sup>14</sup>

With recent ionic liquid developments there has been a push towards greener cations and anions with no halides present specifically, fluorides *i.e.* a move away from triflates and bistriflamide. Other fluorine containing anions such as tetrafluoroborates, [BF<sub>4</sub>]<sup>–</sup> and hexafluorophosphate,<sup>15</sup> [PF<sub>6</sub>]<sup>–</sup> have issues with hydrolysis<sup>16</sup> and thermal decomposition in which highly corrosive HF is formed.

<sup>17</sup>Ohno and co-workers have pioneered the use of amino acids as ionic liquid anion precursors with great success.<sup>18,19</sup> Other green alternative anions include the use of acetate, tetrazole and methyl carbonate anions that consist of solely carbon, nitrogen and oxygen.

Coleman and co-workers sought to find alternative boron containing cations; termed borenium ionic liquids they consist of a borenium cation that is formed *via* chloride extraction from the neutral adduct of BCl<sub>3</sub> and pyridines with AlCl<sub>3</sub> as shown in Figure 1-2.<sup>20</sup> These ILs have been found to exhibit super Lewis acidity exceeding that of chloroaluminate ionic liquids due to it containing both a Lewis acidic cation and anion.

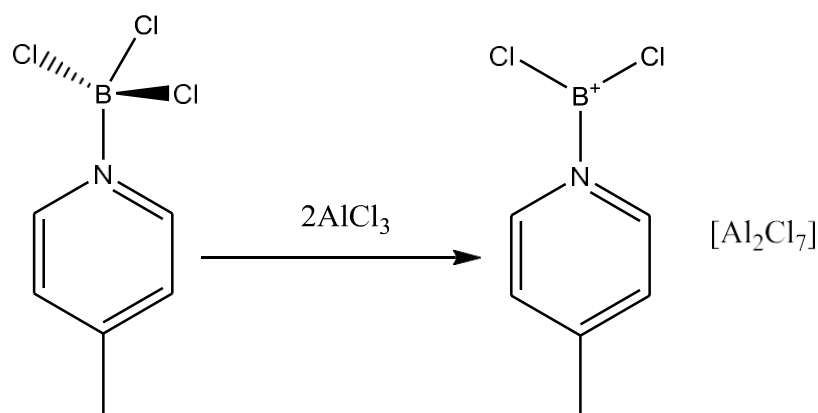


**Figure 1-2**-Formation of borenium ionic liquids.

In regards to cation stability, the main driving force in this development is the electrochemical stability of the cation; previous studies in the molten salts field were driven by applications to battery electrolytes and the most apparent issue was the electrochemical limits of the cation. Azepanium ionic liquids are one of the most recent developments for electrochemical applications with an electrochemical window of up to 6.5 V.<sup>21</sup> More recently, there has been a drive towards the next generation of ionic liquids consisting of low-melting coordination complexes that aim to provide cheaper, cleaner and less synthetically demanding ILs. There are two main groups of these new ionic liquids; deep eutectic solvents and liquid coordination complexes.

Liquid coordination complexes as will be discussed in great detail in chapter 3 and 4 are liquids consisting of low-melting coordination complexes, LCCs are comprised of a metal halide salt and a donor ligand to which ionic and neutral species form and remain in equilibria.<sup>22</sup> Deep eutectic solvents are formed by a mixture of two or three components that due to hydrogen bonding interactions form a eutectic a specific

molar ratio at which the melting point is lower than all components.<sup>23,24</sup> Abbot and co-workers characterised DES containing ammonium salts with the general formula  $[R^1R^2R^3R^4N^+][X^-] \cdot Y$  into 3 types:<sup>25</sup>

Type I:  $MCl_x$ ,  $M = Zn, Sn, Fe, Al, Ga$ .

Type II:  $Y = MCl_x \cdot yH_2O$ ,  $M = Cr, Co, Cu, Ni, Fe$ .

Type III:  $Y = R^5Z$ ,  $Z = CONH_2, COOH, OH$ .

DES have been used within a multitude of applications including catalysis,<sup>26</sup> metal extraction,<sup>27</sup> desulphurisation of fuels<sup>28</sup> and biomimetic studies.<sup>29</sup> DES exhibit many ionic liquid properties such as low vapour pressure, liquids below 100 °C *etc.*, however, although their low costs make them attractive to previous ionic liquids, the thermal stability of many DES is poor.

## 1.4 Reactive ionic liquids

Reactive ionic liquids within this work are ionic liquids in which they are integral to the reaction process to which they have been applied. This can be both as a catalyst, reagent or as a solvent to which dissolution of a reagent is not available in conventional solvents.

Task specific ionic liquids, TSILs were first termed by Davis and are ILs which incorporate functional groups designed to impart to them particular properties or reactivities.<sup>30</sup> One of the first of such examples was the incorporation of the antifungal drug miconazole in 1998 as an imidazolium-like cation to which it can be utilised as a drug or gelation agent.<sup>31</sup> Similarly ionic liquids have been used to incorporate multiple herbicides,<sup>32</sup> antibiotics,<sup>33</sup> and anti-viral drugs.<sup>34</sup> Davis termed the TSILs as having the components of an IL solvent, but components that manifest specific types of interactions with dissolved substrates. It should be highlighted that TSILs are also termed functionalised ionic liquids.

More recent and notable examples of task specific/reactive ionic liquids include the use of ionic liquids as a fragrance delivery method. Gunaratne and co-workers utilised aldehyde functionalised pyridinium cations to form hemiacetals with alcohol functionalised fragrance molecules.<sup>35</sup> The hemiacetals formed acted as a catch and release mechanism for the attached fragrances such that in the contact with water the hemiacetal cleaves, releasing the fragrance molecule as demonstrated in Figure 1-3.

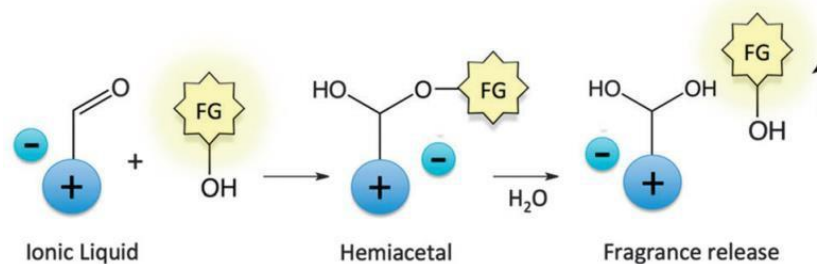


**Figure 1-3-**TSIL for fragrance delivery by Gunaratne and co-workers.<sup>35</sup>

Task specific ionic liquids have also been utilised in a multitude of organic reactions; a review by Salunkhe and co-workers provides an in-depth look at the vast array of catalytic TSILs available.<sup>36</sup> Examples of such TSILs are altered in functionality for Lewis acid and Lewis basic catalysis, stabilisation of nanoparticles / inorganic catalysis in homo- and heterogeneous catalysis.

#### 1.4.1 Inorganic synthesis in Ionic liquids

A review by Feldmann and co-workers highlighted that many current inorganic syntheses require low boiling liquids such as ammonia, sulphur dioxide, conventional organic solvents and water.<sup>37</sup> The thermodynamic threshold of many inorganic reactions requires a high energy input that is most readily achieved *via* heating, however, as a consequence the safety, handling and containment of such low-boiling solvents becomes hazardous and difficult. The use of an ionic liquid does not circumvent all of the issues with conventional solvents as the stability at high temperature is often not as great as would be suspected, however, ILs have provided some interesting compounds often provide counter anions or cations to inorganic clusters. Examples of inorganic clusters formed include Zintl phase anions,<sup>38</sup> clathrates,<sup>39</sup> polychalcogenides<sup>40</sup> and polyhalides.<sup>41</sup>

Lanthanide and actinide chemistry has also been of great significant in regards to the use of ionic liquids; Binnemans<sup>42</sup> was the first to complete a detailed review of lanthanide and actinide chemistry in ionic liquids; more recently Mudring and co-workers completed a review.<sup>43</sup> A key aspect of this research field is the dissolution of rare earth elements *via* carboxylic acid functionalised cations such as betainium cations.<sup>44</sup> A second key aspect of this research field is the formation of cations and anions that are centred on a rare earth element. Key examples include uranyl oxides that can form both cationic and anionic species such as the anionic triacetato complex  $[\text{UO}_2(\text{CH}_3\text{COO})_3]^-$ , and the cationic crown ether complex  $[\text{UO}_2(18\text{-crown-6})]^{2+}$  in imidazolium and pyrrolidinium bistriflamide ionic liquids.<sup>45</sup>

Dehnen and co-workers have largely focused on the formation of crystalline chalcogenides; forming a multitude of crystalline polychalcogenides. Conventional ionothermal methods have been described by Dehnen and co-workers in Figure 1-4. The ionic liquids used within this field tend to be what would be deemed to be inert/bystander ionic liquids such that they are simple imidazolium cations and non-coordinating bistriflamides in a majority of cases hence they do not appear to have an apparent purpose.<sup>46</sup>

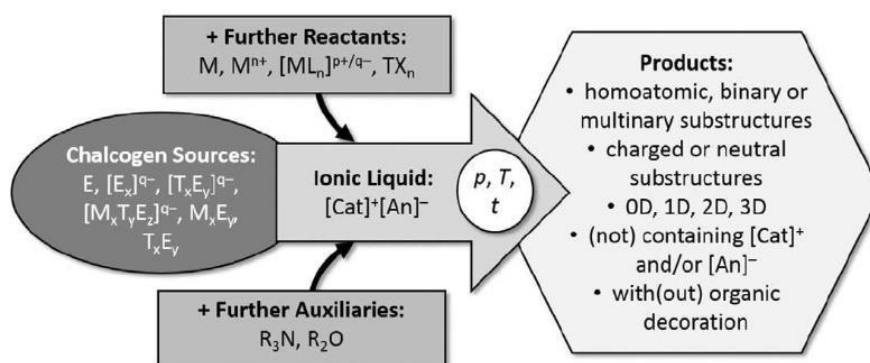


**Figure 1-4**-Figure by Dehnen and co-workers describing the general synthetic approach for the formation of crystalline chalcogen compounds in ionic liquids, outlining all the parameters that can be varied. The auxiliaries do not necessarily need to be part of the desired products; they instead help to trigger network formation or destruction. In most known cases known,  $E = Se$ .  $[Cat]^+ =$  cation,  $[An]^- =$  anion.<sup>46</sup>

However, the templating effect has been widely observed in ionothermal synthesis; Morris and has reviewed several studies the impact of ionic liquid size and asymmetry on the morphology and topology of zeolites, metal organic frame works and coordination polymers.<sup>47</sup> It is found that ILs can act as directing agents causing one morphology to be preferred over another, which is not normally accessible in hydro- or solvothermal methods.

Ruck and co-workers, who also carried out a significant number of studies in regards to the reduction in reaction temperatures in ionothermal syntheses of compounds containing group 15 and 16 elements.<sup>48</sup> Ruck cited a long list of benefits to ionothermal methods in comparison to comparative solvothermal and solid state methodologies including;

- (1) Ionic liquids appear to enhance stability of ionic reaction intermediates.
- (2) The very high solubility of main group elements (e.g., Bi, Te, Sb, Se, Ga, In) and their halide salts allow reactions to occur under mild conditions.
- (3) Synproportionation as well as redox reactions can be easily carried out in IL for polycations synthesis.



Ionothermal syntheses have not been limited to Main group and rare earth elements with transition metals have also featured heavily. Examples of zinc containing semiconductors,<sup>49</sup> iridium nanoparticles in imidazolium ILs,<sup>50</sup> and a large number of transition metal complexes have been reported.<sup>51</sup> Finally, a study by Puga and co-workers surrounded the incorporation of boron clusters as ionic liquid anions. Examples of the cluster anions formed and the counter cations are shown in Figure 1-5.<sup>52</sup> Synthesised *via* metathesis of the ammonium salts of the boron clusters e.g.  $[\text{NHMe}_3][\text{C}_2\text{B}_9\text{H}_{12}]$  with  $[\text{C}_n\text{mim}]\text{Cl}$  to form  $[\text{C}_n\text{mim}][\text{C}_2\text{B}_9\text{H}_{12}]$ .

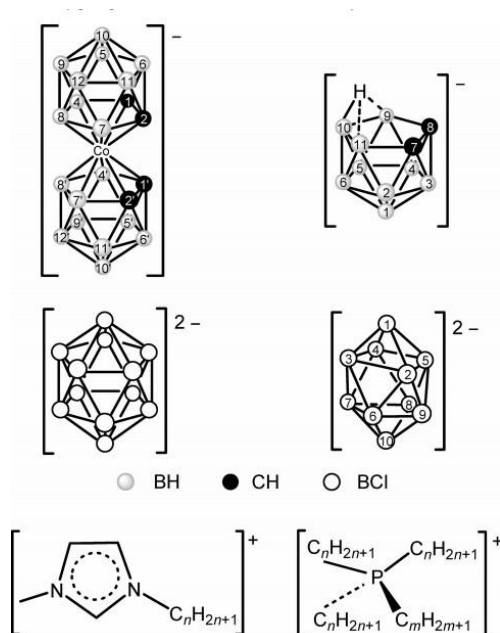


**Figure 1-5**-Boron cluster anions synthesised by Puga and co-workers.<sup>52</sup>

### 1.4.2 Dissolution in ionic liquids

Ionic liquids have been well reported for their unusual and exciting solvation abilities. In general ionic liquids have a relatively low polarity and are effective for solvation of more organic substrates especially in cases of non-coordinating anions. However, the polarity of the ionic liquid and its solvation properties cannot be seen as a one-box-fits all with infinite combinations available; the tuning of solvation properties is one of the attractive qualities of ILs. Here, a selection of notable substrates and their dissolution within ionic liquids.

One of the first substrates that were celebrated for its solubility in ionic liquids was cellulose; being a covalently bonded glucose polymer it is often difficult to dissolve. Holbrey and co-workers found that  $[\text{C}_2\text{mim}][\text{Cl}]$  was an effective non-derivatising

solvent for cellulose with scope for revolutionising the cellulose processing methodologies.<sup>53</sup> More recently the solvation mechanism has been confirmed to be due to the basic nature of the anion hence acetate anion-containing ionic liquids are now preferred with next generation ionic liquids comprising of guanidine bases and  $\text{sCO}_2$  have been found to be effective alternatives.<sup>54,55</sup>

Carbon dioxide is another substrate of great interest; specifically, termed carbon capture it is of vast importance in regards to carbon reduction and climate change reversal strategies. Davis and co-workers demonstrated that an amine functionalised imidazolium cation can work cooperatively with another of the cations forming an amide linkage and ammonium group as shown in Figure 1-6.

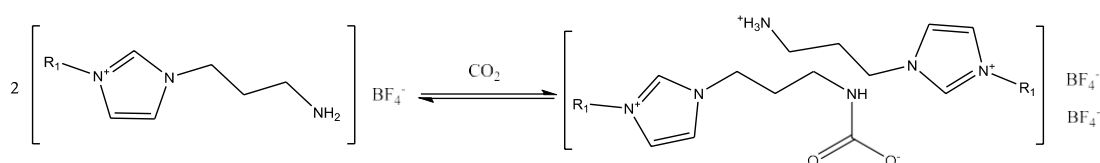


**Figure 1-6**-Carbon capture by amine functionalised imidazolium cations.<sup>56</sup>

Anion functionality has also been utilised in carbon capture with Dai and co-workers demonstrating how super-base derived protic ionic liquids *i.e.* imidazolate and phenolate anions can capture  $\text{CO}_2$  as shown in Figure 1-7.

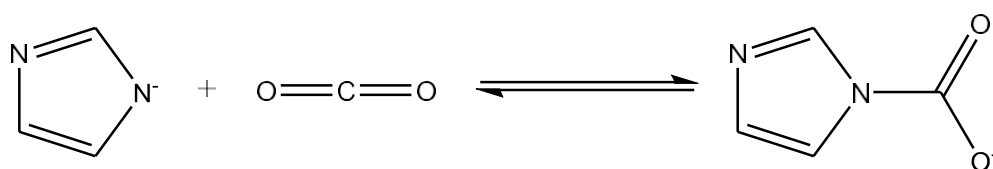


**Figure 1-7**-Carbon capture by imazolate anions by Dai and co-workers.<sup>57</sup>

As discussed, the significance of ionic liquids in inorganic synthesis is partially due to their ability to dissolve often insoluble inorganic compounds without aqueous solvent. One such example of note is the dissolution of metal oxides in betainium functionalised ionic liquids by Nockemann and co-workers. The metal oxides successfully dissolved include actinides such as uranyl(VI) oxide, rare-earth metals such as neodymium(III) oxide, transition metals such as zinc(II) oxide, iron(III) oxide, and precious metal oxides such as palladium(II) oxide.<sup>58</sup> This dissolution of metal oxides in betainium ionic liquids has allowed for the synthesis of novel polynuclear metal complexes.<sup>59</sup>

Reverting to a more biological application ionic liquids have also been found to be an interesting solvent for proteins and consequently enzymes. This is of significant

importance in regards to bio catalysis. A review by Gorke and co-workers highlighted the importance of the polarity of the ionic liquid and its possible inhibition of enzymatic processes.<sup>60</sup>

Metal extraction is another field of task specific ionic liquids such that ionic liquids manipulate coordination affinities of desired metals to extract them from aqueous solutions. A review by Dai and co-workers indicates the vast array of ionic liquid motifs available to be used; both cation and anionic functionalities have been utilised with amide, crown ether, alkyl phosphonates and cryptand like functionalities common.<sup>61</sup>

## 1.5 Project Aims

The overall aim of this PhD is to find new ionic liquids tailored towards a specific application whether it is in within organic or inorganic synthesis. There are three main applications of ionic liquids studies within this work;

- (1) Dissolution of alkali metals- Can ionic liquids replace highly volatile solvents such as ammonia to provide a safer alternative that can be used at ambient temperature and higher?
- (2) Dissolution of *p-tert*-butylcalix-[4]-arene - Can basic ionic liquids be used to dissolve these large molecular cages and assist in the initiation of functionalisation reactions? Historically these reactions require inorganic bases to initiate alkylation reactions. Can an ionic liquid replace inorganic bases and enhance the solubility of the calixarene starting material?
- (3) Gain greater understanding of group 13 liquid coordination complexes using multiple spectroscopic techniques including multinuclear NMR, Raman, EXAFS and XANES spectroscopy. Can LCCs be used for the synthesis of binary and tertiary semiconductor compounds?

## 2 Alkali metal solvation in ionic liquids

*The Challenge:*

*Can an ionic liquid be designed, synthesised and used to dissolve alkali metals?*

### 2.1 Introduction

For many years ammonia has been vital in many synthetic processes across both organic and inorganic chemistry. With a specific focus in inorganic chemistry it is apparent that the use of liquid ammonia in the formation of metal anionic cluster has been vital but not without difficulty. Looking at Zintl anions as a specific example, the initial fusion step followed by the solvation in anhydrous ammonia is successful, but the air sensitive nature of the cluster formed and the low boiling point of liquid ammonia leads to difficulties in handling, isolating and storage of these compounds.

From a different perspective, there has been little to no work on the solvation of alkali metals into ionic liquids. Ionic liquids themselves being biased towards solvating organic materials, this overall aim to solvate alkali metals requires tact and essentially analogues of previously successful solvents e.g. ammonia and ethylenediamine. It should then be noted that the solvation of alkali metals is not a simple task but a solvation method in which solvated electrons are generated. The solvated electrons could be considered as “small anions” and have the ability to act as a reducing agent in both inorganic and organic reactions, leading into many possible applications ranging from solid state chemistry to organic synthesis.

The starting hypothesis of the project was to design an amine functionalised ionic liquid that successfully dissolves alkali metals and which would stabilise the resultant formation of solvated electrons. These could then in turn be utilised to form anionic metal clusters. It was also aimed to fully study the formation of these electrons and apply them to some simple reduction and radical controlled reactions such as Birch reductions, radical polymerisation and single electron reductions *etc.*

#### 2.1.1 Current solvents for alkali metal solvation

Currently, there are a limited number of solvents for alkali metal solvation that do not result in an explosive reaction. The reaction between water and elemental sodium and potassium has been well documented throughout literature and is observed in almost every secondary school chemistry class. Its explosive nature is a result of an almost too successful reactive solvation as shown in Figure 2-1.

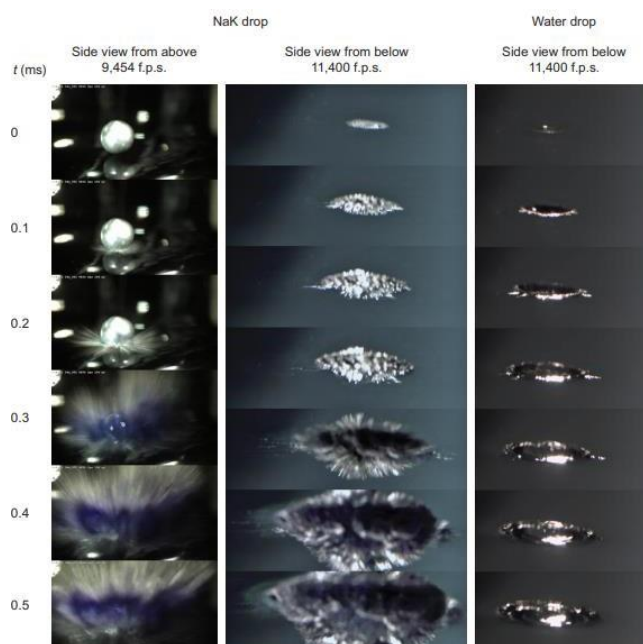
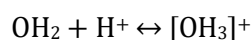
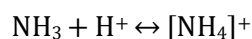


**Figure 2-1**-Reproduced from Mason *et al.* High-speed camera images of a Na/K alloy drop versus a water drop impacting on water.<sup>62</sup>

Ammonia is the most prominent solvent for alkali metal solvation; ammonia itself comprises of many similarities to water. Liquid ammonia itself is a very interesting compound, both as a solvent and a reactant; exhibiting similar behaviour to water in terms of it being a somewhat polar protic solvent, exhibiting significant hydrogen bonding it also demonstrates several unusual solvation trends that in many cases are not exploited by the general chemistry community due to handling issues of the anhydrous form.

Firstly, looking at the similarities of ammonia and water it is seen that they both exhibit a relatively high polarity with dipole moments of 1.42 D and 1.85 D respectively, and trigonal pyramid and bent geometries. Both solvents are the anomalies of their respective group hydrides in regards to their high boiling and melting points. In terms of acting as a protic solvent, they form essentially oxygen and nitrogen analogues in the same conditions *e.g.* the formation of ammonium and hydronium ions as shown in Equation 2-1.

**Equation 2-1**



Similarly, in the auto-ionisations of the solvents as shown below in Equation 2-2.

#### Equation 2-2



Hydrogen bonding is also a property that can be compared between ammonia and water; the N-H bond is significantly stronger than the O-H bond and as a consequence the solvation properties of the compounds are very different. The increased stability in turn reduces the reactivity of ammonia with solute species compared to water. Solvation within ammonia or as it is usually referred to “ammonation” and is again analogous with water and the solvation of ionic species, the lone pair from the nitrogen and its high electronegativity causing a charge distribution cause the interactions between the ionic compound to be disrupted due to the greater forces of interaction with ammonia in comparison to the lattice energy of the solute.

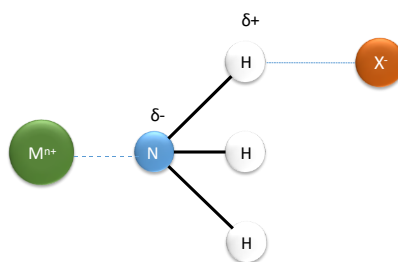
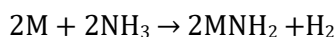


**Figure 2-2-**Predicted coordination within ammonia and metal salt solutions.

Ammonolysis is again analogous with hydrolysis with a hexaamine first sphere coordination surrounding the metal cation. With the solvation of the alkali metal resulting in the release of solvated electron the electrical conductivity of ammonia is also of great interest. It is reported, that the conductivity trends and curves of solutes in ammonia are similar to those observed in aqueous systems. It should however, be noted that permeability of electrolytes/ inorganic salts in ammonia is lower due to the lower dissociation constants.<sup>63</sup>

Within alkali metal solvation in ammonia the main difference between it and water is lack of reaction in the latter. The alkali metal-ammonia solutions are described as metastable and decompose slowly in anhydrous conditions to form the alkali metal amide as per Equation 2-3. The presence of other metals, specifically iron, can act as catalyst to this decomposition with many organic chemists utilising a rusty nail in Birch reductions.

### Equation 2-3



Birch reductions were first reported in 1944 by Arthur Birch who cited the first reported the reductions of various naphthalene compounds. Since, there has been a push towards safer and less volatile alternatives to Birch reductions. One such methodology developed by Dye and co-workers uses silica encapsulated sodium and potassium amalgams that upon curing at 150 °C form air-stable free flowing powders.<sup>64</sup> Differences in the curing process result in different ‘stages’ of materials being formed with stage 0 able to reduce biphenyl to its radical anion; stage I powders reduce naphthalene (0.043 V) and phenanthroline (0.142 V), and stage II powders reduce pyrene (0.529 V) and anthracene (0.642 V) to their radical anions. The variation in reduction abilities of the differing powders is mirrored in their stabilities in air with stage 0 requiring glovebox conditions and stage II being stable in air.<sup>65,66</sup> Since this discovery, the commercial interest has been significant with it being sold as the commercial product SiGNa for both organic synthetic reductions and fuel cell applications.

Methylamine is an alternative to ammonia however sodium is termed ‘very slightly soluble in methylamine and lithium also forms only a very dilute blue solution’ hence it is not as effective as it’s ammonia analogue.<sup>67</sup> Dye and co-workers later citing that lithium is soluble in methyl amine up to 20 mol% hence predicting the presence of the tetra coordinated cation,  $[Li(CH_3NH_2)_4]^+$ .<sup>68</sup> Furthermore, it was found to form an electride complex that is distinguishable from it bronze-like appearance. Electrides are classically defined as ionic compounds in which an electron is the anion.

Ethylenediamine, *en*, is a robust solvent that has been shown to be successfully dissolves rubidium potassium, sodium and lithium. Windwer and Sundheim studied the conductivity, electron spin resonance spectra, and optical absorption spectra of such solutions after observing that the as mentioned elements were soluble in ethylenediamine.<sup>69</sup> Dye and co-workers later confirmed the conductance and solubility’s of the alkali metals in *en* stating that the solubility of caesium, lithium and rubidium was comparable to that observed in ammonia.<sup>70</sup> However, sodium was found to be markedly less soluble in ethylenediamine compared to ammonia with suggestions that this is due to the difference in dielectric constant/polarity of *en* compared to ammonia. Methylamine and ethylamine are also solvents which can solvate an alkali metal but to a lesser extent than ammonia or ethylenediamine.

Hexamethylphosphoramide, HMPA is another polar solvent that has been reported for alkali metal solvation. First reported by Normont and co-workers, HMPA was found to dissolve sodium, potassium and lithium in comparable concentrations to ammonia, ethylenediamine and methyl amine.<sup>71</sup> Randles and co-workers studies the behaviours of the HMPA-Alkali metal solutions in greater detail with conductance density and emission experiments.<sup>72,73</sup> HMPA differs significantly in structure from the simple amines discussed such that it a phosphoramidate in which a central P=O is bbouns to three NMe<sub>2</sub> groups to afford a tetrahedral geometry.

Within conventional organic solvents such as THF and diethyl ether; Dye and co-workers reported that solvation of alkali metals could be achieved with the assistance of cyclohexyl-18-crown-6 to form deep blue solutions that if kept cool (-78 °C) remained stable for several days, but at room temperature remained stable for 5-10 minutes.<sup>74</sup> The development of other cyclic ethers were pioneered by Noble prize winners Lehn<sup>75</sup>, Cram<sup>76</sup> and Pedersen<sup>77</sup>.

Alkali metal anions are also a consideration; forming at high concentrations alkali metal anions, called alkalides or electrides can formed at high concentrations.<sup>78</sup> Initially these were discovered after irregular and un-assignable bands in the NIR spectra, that were later found to be due to sodium borosilicate within glassware in which K<sup>+</sup> and Li<sup>+</sup> exchanged. The diamagnetic Na<sup>-</sup>, K<sup>-</sup> and Cs<sup>-</sup> species were initially suspected by many, however, the sodium anion was conclusively confirmed by Dye and co-workers in 1974 *via* <sup>23</sup>Na NMR spectroscopy, in which a peak at -63 ppm was assigned to be Na<sup>-</sup> anion as shown in Figure 2-3.<sup>79</sup>



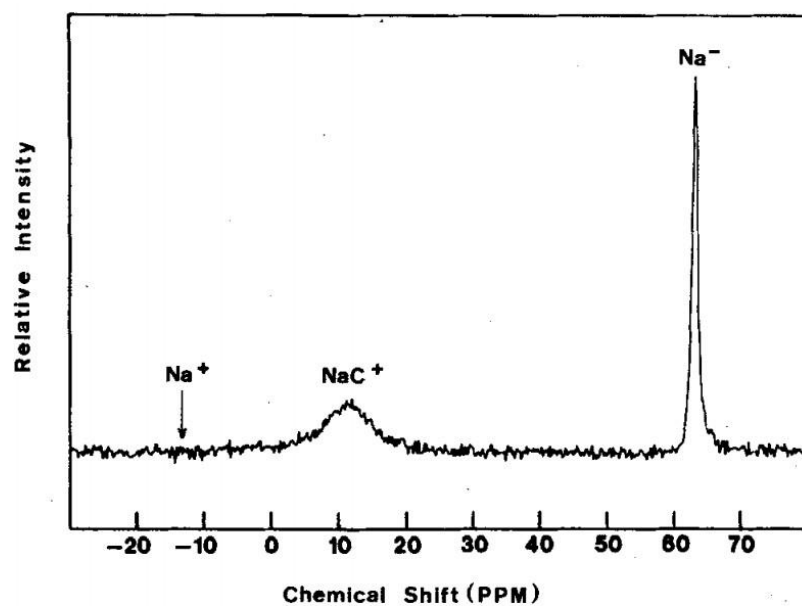


**Figure 2-3-** $^{23}\text{Na}$  NMR spectra achieved by Dye and co-workers of 2, 2, 2 crypt and sodium in ethylenediamine.<sup>79</sup>

The crystal structure was soon determined after this confirmation of the  $\text{Na}^-$  anion, as shown in Figure 2-4 by Tehan and Dye.<sup>80</sup> This structure confirmed that the cation species was enclosed by the complex ligand and the anionic species remained uncomplexed.

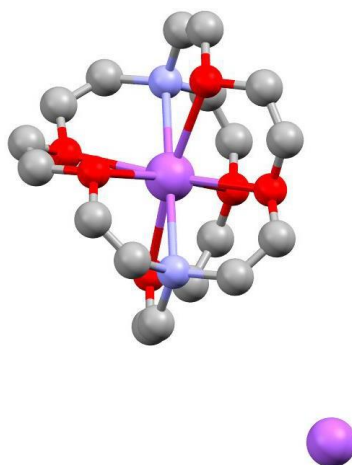


**Figure 2-4-**Single crystal diffraction determined structure of  $[2, 2, 2\text{-cryptandNa}^+][\text{Na}^-]$  by Dye and co-workers.<sup>80</sup>

Since this discovery multiple other complex ligands have been used including azo-crowns in which the oxygens of the [2,2,2-crypt] are replaced with nitrogens.<sup>81</sup>

### 2.1.2 The solvated electrons phenomenon

Humphry Davy was the first to pioneer the solvation of alkali metals such as sodium and potassium in the 19<sup>th</sup> century. Initially forming amalgams of alkali metals with potash and forming peroxo species, he discovered the solvation of potassium species in gaseous ammonia and observed a blue colour.<sup>82</sup> Continuing on from this it was Hannay and Hogarth in 1879 repeated the experiments of Davy with great success.<sup>83</sup>

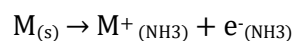
Significant work by Gibson and Argo confirmed the blue colour using UV/Vis spectroscopy; they carried out significant modelling of the properties of the electrons in ammonia solutions using electromotive force measurements conducted by Kraus. They postulated that the blue colour observed could be due to unionised metal atoms, solvated electrons or unsolvated electrons.<sup>84,85</sup> This was later confirmed to be due to solvated electrons. Charles Kraus, aforementioned, was heavily involved in the development and understanding of solvated electrons, with his main focus on the electrochemistry of sodium-ammonia-metal solutions.

Solvated electrons are a phenomenon that are most commonly observed upon the solvation of alkali metals in ammonia. Often identified by the vivid blue colour that is observed, solvated electrons are formed *via* the solvation of the alkali metal to form a metastable solution. The solvated electron itself is a strong and effective reductant within many organic and inorganic reactions. The solution formed exhibits some very interesting and useful properties including:

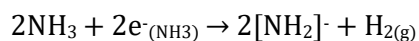
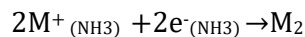
- Paramagnetism (dilute solutions only)
- Magnetic susceptibility that corresponds directly to the release of a single electron per metal atom.
- An increase in volume. This increase in volume is greater than the sum of the solute and solvent due to the charge radius/cavity of the solvated electron corresponding to 300-400 pm
- Conductivity that is directly related to the concentration of the metal species in ammonia with an initial decrease in conductivity followed by an increase that corresponds to the formation of an 'expanded metal'. Minimum molar conductivity observed at approximately 0.05 mol dm<sup>-3</sup>.

The formation and decomposition of solvated electrons can be described in Equation 2-4 and Equation 2-5.

**Equation 2-4-** Formation of solvated electrons in ammonia.



**Equation 2-5-** Decomposition of solvated electrons in ammonia.



As discussed, the ratio of ammonia to alkali metal has a significant impact upon the solution formed *i.e.* saturated solutions. High concentrations promote recombination between the metal species and the solvated electrons, hence decomposing the meta-stable solution. Reactions with ammonia itself to form sodium amide as shown above is one of the most significant methods of decomposition and is utilised with the Birch Reduction.<sup>86,87</sup>

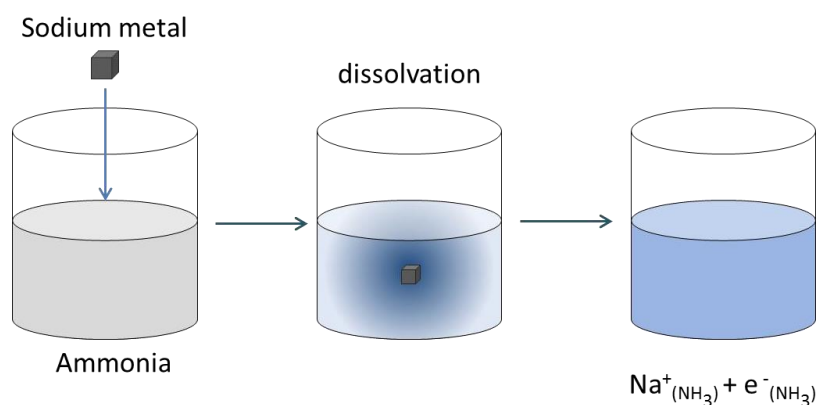


**Figure 2-5-** Solvation of sodium in liquid ammonia.

The ‘suspension’ of solvated electrons is often described as an outer-sphere electron transfer process in which the electron transfer occurs with a very weak electronic interaction between the reactants in the transition states. Within organic reactions, outer-sphere electron transfer is described as ‘non-bonded’ electron transfer. Including ammonia, there are several solvents that have reported observations of solvated electrons, for example methylamine and ethylamine.

Within recent commentary solvated electrons at specific concentrations are known as electrides, which, have been seen as them themselves acting as the anion species within ionic mixtures. This slight alteration in perspective is due to the behaviour exhibited by electrides, in that they act identically to chloride and

hydroxide anions in that they are neither localised to a specific cation nor are delocalised as if they are within a metal, but instead sit in the same sites as  $\text{Cl}^-$  and  $\text{OH}^-$ .

Due to the air sensitivity, low temperatures required and somewhat instability of solvated electrons there are limited applications within general benchtop chemistry, however; reactions that employ alkali metal and ammonia are very much worth investigating in further detail. The use of cryptand/crown ether during the formation of an electride can prevent the recombination of the cation and electride. It is reported that the cationic alkali metals lie as a sandwich between two crypts. All in all, the utilisation of solvated electrons is entirely dependent on the reaction timeframe, the stability of the electrides, in respect to the time frame and the solvent used *i.e.* a non-reducible solvent is critical.<sup>88</sup>

Molten expanded metals or ammoniated metal ion are held together by electrons. These expanded metals are no longer blue like the dilute ammonia-metal solutions but are bronze-like in appearance that is often likened to the molten metal itself. Unlike the diluted solvated electron solutions these expanded metals do not contain sufficient ammonia molecules to fully dissolve the metal; these solutions are believed to be formed at concentrations  $<1\text{M}$ . In these cases, the decreasing paramagnetism/ magnetic susceptibility can be explained by the dominance in the formation of the neutral and non-conducting species  $(\text{M}^+_{(\text{NH}_3)})(\text{e}^-_{(\text{NH}_3)})$ . Referring back to the decrease in paramagnetism seen upon moving from dilute to saturated solutions, these are due to the formation of the neutral, non-conducting but diamagnetic species  $(\text{M}^+_{(\text{NH}_3)})_2(\text{e}^-_{(\text{NH}_3)})$ .<sup>89</sup> As discussed, the solvated electron is most commonly utilised in the Birch reduction in which the formation of sodium/solvated electron combination is vital in the reduction of benzene to form 1, 4-cyclohexadienes.

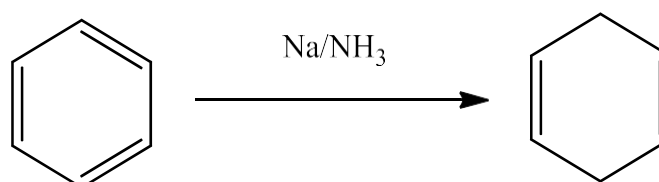


**Figure 2-6**-Birch reduction of benzene.

Relevantly, solvated electrons are also majorly credited with the discovery and synthesis of Zintl anions in that the simplified synthetic method involves the solvation of stoichiometric amounts of an alkali metal and p-element in ammonia

during which solvated electrons act as the reducing agent to form anion metal clusters.

With the Birch reaction being one of the most common uses of solvated electrons, previous study carried out by Greenfield and Schindewolf in part looked into the effects of a [2,2,2]-cryptand compound into the activity of birch reductions.<sup>90</sup> They found that the addition of alkali cation complexing cryptands such as C<sub>211</sub> to Li solutions, C<sub>221</sub> to Na solutions or C<sub>222</sub> to K solutions cause a significant decrease in reaction rate. This is, however, believed to be due to the utilisation of the alkali metal cation within the reaction mechanism with suggestion that it is specifically *via* the formation of ion pairs or complexes with reacting species. This suggestion is further supported by the increase in reaction rate *via* the addition of alkali metal halides.

Relating this to the use of solvated electrons in the decrease in reaction rate by cryptand compound is not seen as a significant worry in terms of reaction rate due to the suspected role of the alkali metal cation within Zintl phase synthesis being only that of a stabilising cation. Reported analytical methods include optical and conductivity techniques, magnetic resonance, expansion volumes or surface tension measurements. The most significant methods include UV/Vis spectroscopy, chronoamperometry (this can analyse the stability solvated electrons) and magnetic susceptibility.<sup>91</sup> Using these methods, the stability and essentially the lifetime of the solvated electrons in solution can be quantified, however, this is not without extensive understanding of the solvation mechanism.

Quantum theory is commonly used to describe the motion of small particles in space using the Schrödinger equation. A solvated electron itself is not a particle in free space or a one-dimensional box but should be termed a spherical particle in a spherical box; the box in question being the solvent cage. The solvent cage itself acts as a box by forming a potential wall. The spherical boundaries have high potential barriers which can only be overcome by a significant increase in the particles energy or *via* tunnelling, a quantum mechanical phenomenon linked to thin 'walls' *i.e.* the high potential barrier is very thin and quick drops to zero. Regardless, it is the description of these boundaries that outwardly relate to the colour observed along with the energy of the solvated electron.

### 2.1.3 Alkali metals in ionic liquids

Currently, there are no known reports of solvated electrons from ammonia/sodium methods within ionic liquids, however, the interesting electrochemical properties and

many reactions that involve electron transfer that occur within ionic liquids give rise to significant possibilities of solvated electrons being feasible. The feasibility of this can be further increased *via* the use of ammonium and amine functionalised ILs. On the other hand, the usually high viscosity of ionic liquids lends itself to limiting the diffusive recombination processes of the solvated electrons.

Alkali metal salts have been utilised in conjunction with chloroaluminates in respect to molten salts and chlorometallate ionic liquids for battery applications. Osteryoung and co-workers carried out extensive studies on  $\text{AlCl}_3$ -NaCl melts, finding species such as  $\text{NaAlCl}_4$  and  $\text{NaAl}_2\text{Cl}_7$ .<sup>92</sup> Later, moving towards more ambient temperatures chloroaluminate ionic liquids such as 1-ethyl-3-methylimidazolium chloroaluminate with NaCl. The benefits of NaCl addition are for buffering of the solutions; NaCl is observed to drive the solution to neutrality hence limiting the effects of the latent acidity of the solutions in an often metallically contained system.<sup>93</sup>

More recently, a movement away from lithium ion batteries has sought to utilise sodium as an alternative and more abundant ion. Wu and co-workers in a similar methodology to the previous chloroaluminate work simply added the  $\text{NaBF}_4$  salt to  $[\text{C}_2\text{mim}][\text{BF}_4]$  noting the common anion. It was found, that electrochemical windows *ca.* 4 V could be achieved.<sup>94</sup> The sodium is acting as a charge carrier and electrolyte in the low conductivity ionic liquid.

Chelate ionic liquids utilising small amino ethers and alkali metal salts such as lithium bistriflamide have recently become of interest in the electrochemistry field. Li and co-workers were the first to coin the term 'chelate ionic liquids' and as shown in Figure 2-7, these species are similar in structure to the alkalides in that the cationic species is stabilised by a ligand species in which bonding occurs *via* nitrogen and oxygen donors.

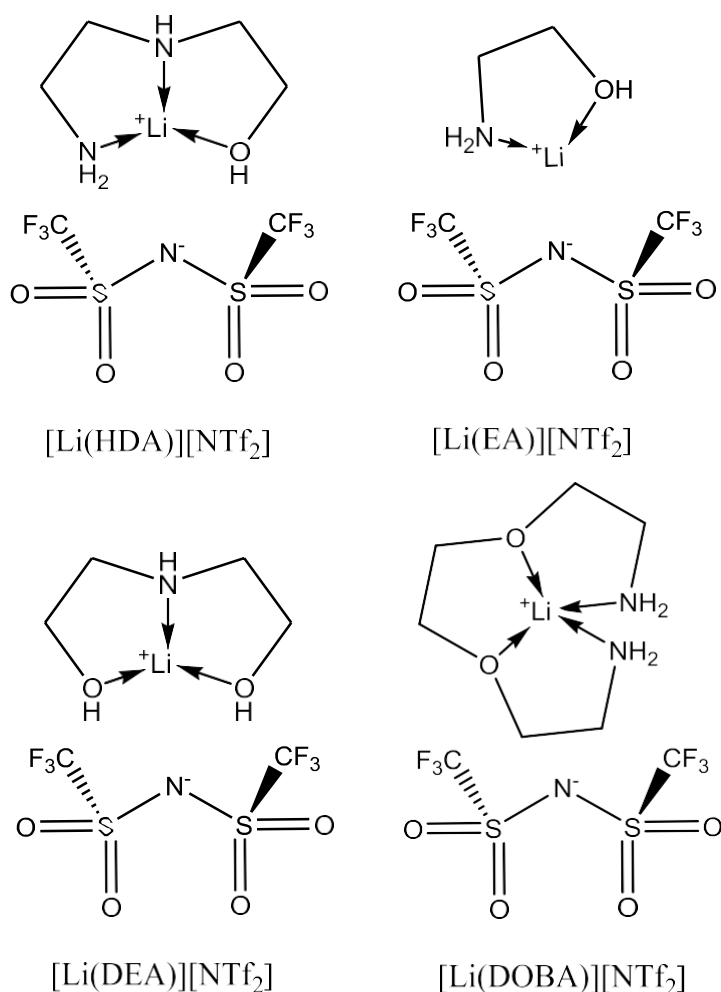


**Figure 2-7**-Lithium bistriflamide chelate ionic liquids by Li and co-workers.<sup>95</sup>

#### 2.1.4 Flash photolysis techniques in ionic liquids

The use of flash photolysis is a very common technique in investigating the charge transfer effects within solutions, however, the somewhat slow dynamic response of the 'ionised' IL to the formation of the dry electron / pre-solvated electron affects the consequent rate and yield of solvated electrons.<sup>96</sup> Flash photolysis in summary is a technique in which a flash lamp or laser exposes a sample to a specific wavelength of light causing excitation and expulsion of an electron. The expelled electron and its behaviour, relaxation and recombination is subsequently monitored *via* UV/Vis spectroscopy or Near-Infrared Spectroscopy.

A study by Wishart *et al.* looked into the formation and stability of dry solvated electrons *i.e.* dry electrons formed *via* flash photolysis in methyltributylammonium bis(trifluoromethylsulfonyl)imide,  $[\text{N}_{4441}][\text{NTf}_2]$ . It should be noted that this method of solvated electron formation follows the process of ionising the IL to form  $e_{\text{hot}}$  followed by thermodynamic equilibration to give  $e_{\text{th}}$  which then becomes  $e_{\text{solv}}$ . This

difference should always be noted as it is aimed to not expect a 'wet' solvated electron synthesis to affect the IL/solvent. In relation to this Wishart *et al.* noted the differences in the UV/Vis absorption spectra of solvated electrons in different solutions. Table 2-1 below shows that polar solvents such as water have higher energy solvated electrons than the non-polar IL and simple alkyl amines *etc.*

**Table 2-1-** Solvent dependent absorption spectrum of solvated electrons<sup>97–100</sup>

Solvent	Solvated electron absorption spectrum/ nm
R <sub>4</sub> NNTf <sub>2</sub>	1410
H <sub>2</sub> O	715
Alcohols	580-820
NH <sub>3</sub>	1850
Simple alkylamines	1900-1950
Ethylenediamine	1360
1,3-propanediamine	1500
Acetonitrile	1450
[C <sub>4</sub> mpyr][NTf <sub>2</sub> ]	1100

It should, however, be noted that the energies seen in the IL and ethylenediamine are very close and indicate that they may be comparable with that required for Zintl phase formation. This study again noted issues regarding the viscosity of the IL affecting diffusion-controlled reactions. Continuing on from the studies surrounding the formation and behaviour of dry electron in ILs, calculations and observations using UV/Vis spectroscopy found that the dry electrons do not lie localised to the positive cation but instead the localisation is dependent on the HOMO/LUMO gaps and alignment of the LUMO of the cation and anions within the IL. Firstly, comparing the localisation of solvated electrons over [C<sub>1</sub>mim][Cl] and [C<sub>1</sub>mim][NO<sub>2</sub>] carries greatly with the former localising mainly over the aromatic cation and the latter over the anion species. The reason for this is believed to be due to the alignment of electronic levels within the IL. As shown in Figure 2-8 the HOMO of the IL is predominantly associated with the anion; this is also the case for the LUMO, except in that of [C<sub>1</sub>mim][Cl]. It is this subtle difference in energy levels that explains the difference in electron localisation within what are in fact very similar solutions.



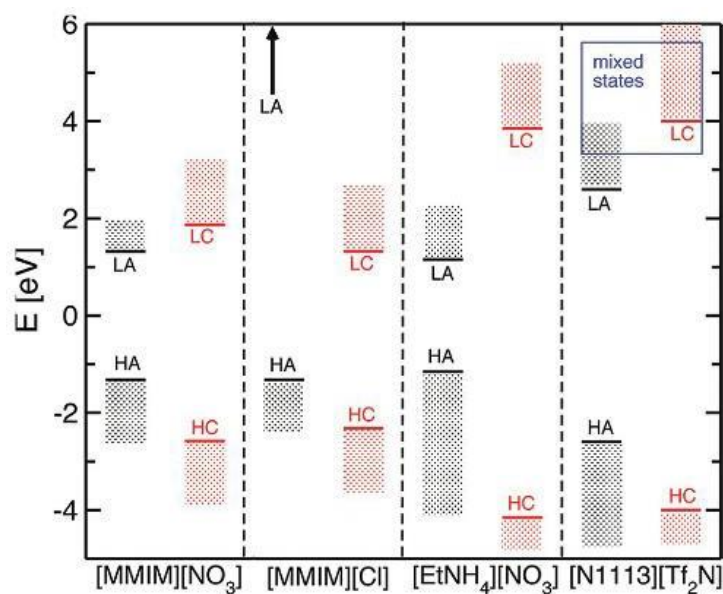


**Figure 2-8-** HOMOs and LUMOs of cations and anions in four ILs. LA/LC and HA/HC denote anion and cation energy levels.<sup>101,102</sup>

However, to give some insight into the electron rate constant properties of some ionic liquids with specific focus on diffusion rate Neta *et al.* carried out a study into the electron transfer reaction of butylpyridinium radicals, pyridine radicals and primary alcohols.<sup>100,103</sup> Using flash photolysis, dry solvated electron was formed and the relative durosemiquinone optical absorption at 440 nm and in relation to the flash photolysis the dose per pulse was determined by thiocyanate dosimetry.

The ionic liquids studied included N-butylpyridinium tetrafluoroborate ([C<sub>4</sub>Py][BF<sub>4</sub>]) and methyltributylammonium bistriflamide, [N<sub>4441</sub>][NTf<sub>2</sub>]) with the main reaction being monitored being that of the butylpyridine radical and the durosemiquinone species due to the neutral state of a single species before and afters.

Using previously reported electrochemically derived redox couples of the reactions, they found that solvent polarity has a significant impact upon charge transfer reactions. With solvent of low polarity such as hexane slowing reactions and solvents of high polarity such as water assisting in charge transfer. Relating this to ionic liquids; with them generally having a lower polarity than that of water but it can be postulated that ILs exhibit similar behaviour to ethanol and acetonitrile.

It has also been reported that the change in rate of charge transfer reactions is due to the change in solvation energies and the diffusion constants. With Ionic liquids being generally more viscous it can be predicted that this could be an issue, however, the polarity of the IL will favour the formation of the charged species. However, the example test reaction discussed with [N<sub>4441</sub>][NTf<sub>2</sub>], found an increase

in rate despite the increased viscosity hence causing several studies to suggest that the liquid viscosity does not describe the diffusion of the reactants within the IL. This variation was not small but in the range of a factor of 5-10, however, the size of the cation and the length of the aliphatic chains increase the rate constant further.<sup>103</sup>

### 2.1.5 Significance and application

The significance of the generation of solvated electrons in a non-volatile ionic liquid is generally unknown; as of yet, there are no reports of a chemically induced solvated electron in ionic liquids. Currently, the greatest similarity within the IL field is in flash photolytic techniques such that the dry electron originates from the ionic liquid itself

Within the ionic liquids community, the stability of ILs to radiation is of great interest for application to nuclear waste processing and containment. Examples of ionic liquid applications in which radiation exposure is inevitable include metal extraction,<sup>42,104</sup> nuclear waste processing,<sup>105</sup> and coal mining.<sup>106</sup> Solvated electrons can be seen to have similar properties to beta radiation,  $\beta^-$  in that they are both a classification of ionising radiation composed of an energetic electron. Multiple studies have taken place investigating the stability of various ILs in radiative conditions.

Nagarajan and co-workers studied the effects of gamma radiation on a multitude of ionic liquids, finding that in a majority of cases decomposition occurred with radiative products lowering the viscosity of the ILs as a function of their radiation dose and causing colourisation of the ionic liquid.<sup>107</sup> Wishart and co-workers have carried out extensive studies on the both the cation and anion stability in radiated ionic liquids. Studies surrounding sulphonyl imide anions,<sup>108</sup> imidazolium cations,<sup>109</sup> bistriflamide anions,<sup>109</sup> halide anions,<sup>110</sup> and guanidinium cations<sup>111</sup> to name but a few. Degradation occurs in all cases with EPR spectroscopy the main methodology used to monitor the formation of radical decomposition products. Other studies by Wren and co-workers have utilised other spectroscopic techniques such as UV/Vis, Raman and infrared along with conductivity and viscosity measurements.<sup>112</sup> As of yet, no truly stable ionic liquids have been observed using flash photolytic or *via* an external radiative source.

Single electron reductions are the initiators of many polymerisation reactions. Radical polymerisations can be initiated using a variety of radical compounds that are formed *via* thermal driven homolytic cleavage, photolysis,<sup>113,114</sup> inorganic redox,

<sup>115</sup> and ionising radiation.<sup>116</sup> Ionic liquids, specifically transition metal-containing ILs in terms of radical polymerisations have been demonstrated to be effective solvents for polymerisation product extraction and have indicated that control can be induced.<sup>117</sup> An alkali metal- IL alternative will give the benefits of an ionic liquid without the inherent toxicity of transition metal catalysts.

### 2.1.6 Inorganic synthesis and single electron reductions

Single electron reductions are evident throughout inorganic chemistry; the reduction of many elements within metal complexes, clusters and even bulk materials is of great importance. The desired reduced state of many complexes and materials is sought due to useful electrochemical and catalytic applications.

An interesting example of single electron reduction within lanthanide and actinide chemistry is demonstrated by Arnold, Love and co-workers in which a novel uranyl oxide complexes in which an actinide species can bind in close proximity to the uranyl species allowing for uranyl-4f interactions a single electron transfer to occur as shown in Figure 2-9.<sup>118</sup>

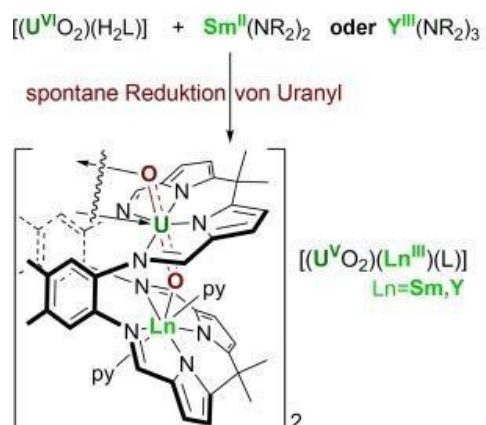


**Figure 2-9-** Single electron reduction of U(VI) to U(V) via lanthanide coordination  $Ln = Sm(II)$  or  $Y(III)$ .<sup>118</sup>

Within transition metal chemistry, Limberg and co-workers noted the use of  $KC_8$  a potassium graphite material to reduce a nickel(II) halide complex to a novel dinickel (I) dinitrogen complex and shown in Figure 2-10.<sup>119</sup> These species have been successfully shown to activate  $N_2$  and similar structures  $O_2$  molecules.<sup>120</sup>

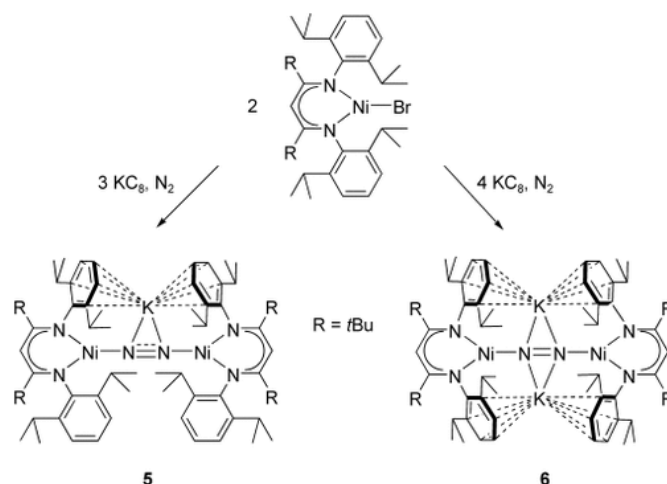


**Figure 2-10-** Reduction of  $[\text{LNiBr}]$  by  $\text{KC}_8$  in a nitrogen atmosphere. ( $\text{L}=[\text{HC}(\text{CRNC}_6\text{H}_3-(\text{iPr})_2)_2]^-$ )<sup>119</sup>

The alkali metal is crucial in the bonding and activation of these neutral gaseous molecules; an extensive review by Gannon and Holland highlights the role of the alkali metals in the coordination and activation of transition metal catalysts.<sup>121</sup> Application of these activation complexes is mainly focused around the Haber-Bosch process and ammonia production.

Metal clusters are naturally one of the first aspects of inorganic chemistry that comes to mind upon the utilisation of reductions in their syntheses. A detailed review by Morse in 1986 highlighted the vast array of transition metal clusters already discovered and in the 30 years since this field has expanded exponentially.<sup>122</sup> The term metal clusters encompass multiple types of cluster including atomic clusters, molecular clusters, intermetallic clusters *etc.* Reduction of preformed clusters and transition metal salts for example with alkali metals can provide an effective pathway to controlled oxidation state clusters.<sup>123</sup>

Zintl phase or Zintl anions are a class of inorganic intermetallic clusters of group 1-2 elements and group 13-16 elements. In Zintl phases the group 1-2 metal acts as a reducing agent to form the anionic cluster of the group 13-16 elements. One of the most common classic Zintl clusters is the  $\text{Na}_4\text{Pb}_9$  cluster; first discovered by Eduard Zintl in 1931 in which a stoichiometric melt of lead and sodium was dissolved in liquid anhydrous ammonia and the cluster crystallised as dark black crystals.<sup>124</sup>

Since their initial discovery there have been multiple combinations and sizes of clusters formed including  $[\text{Sb}_7]^{3-}$ ,  $[\text{Sn}_9]^{4-}$ ,  $[\text{Ge}_9]^{4-}$  and  $[\text{Si}_9]^{4-}$  most commonly with sodium and potassium counter ions. In order to achieve more stable and higher quality crystalline materials, Corbett and co-workers incorporated cryptand compounds into Zintl synthesis to give 'naked' anions.<sup>125</sup> The applications of Zintl

phases is vast including fundamental studies bridging the gap from atom to nanoclusters, catalysis and thermoelectric devices.<sup>126</sup>

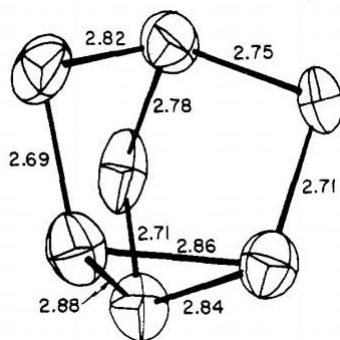
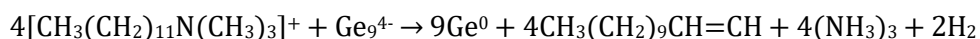


**Figure 2-11-** Anionic structure of [Na-(crypt)]<sub>3</sub>[Sb<sub>7</sub>] synthesised and determined by Corbett and co-workers.<sup>125</sup>

An in-depth review inorganic synthesis in ionic liquids by Claus Feldmann and co-workers highlights the vast array of inorganic transformations that can occur.<sup>37</sup> Focussing specifically on reducing conditions, it is evident that there is not a conventional one size fits all approach like would be undertaken in organic transformations such that a library of reagent and conditions can be used. Instead, only specific examples are evident within the literature with three main areas which have been highlighted below- IL driven reduction, redox species added, and simply as a product stabiliser.

Guest-free germanium clathrates have been successfully formed by Guloy and co-workers *via* the soft oxidation of Na<sub>4</sub>Ge<sub>9</sub> in dodecyltrimethylammonium chloride ([N<sub>11112</sub>][AlCl<sub>4</sub>]).<sup>127</sup> The quaternary ammonium is heated to 300 °C initiating a Hoffman elimination reaction and the oxidation of the germanium cluster following Equation 2-6 with larger germanium clusters of various sizes formed up to Na<sub>24</sub>Ge<sub>136</sub>.

#### Equation 2-6



Hughbanks *et. al.* demonstrated a redox reaction between ferrocenium tetrafluoroborates and Li<sub>2</sub>Zr<sub>6</sub>MnCl<sub>15</sub> type compounds in chloroaluminate ionic liquids to form zirconium halide clusters.<sup>128</sup> Although the synthesis is driven by oxidation of the zirconium centre and reduction of the iron species, which is not a component of the final product, however, the ionic liquid imidazolium cation does stabilise the zirconium halide clusters

Similarly, Ruck and co-workers utilised a redox reaction in which Bi(0) and Bi(III) are mixed within 1-butyl-3-methylimidazolium chloroaluminate ionic liquids.<sup>129</sup> The final bismuth cluster co-crystallise with the tetrachloroaluminate anions to form Bi<sub>5</sub>[AlCl<sub>4</sub>]<sub>3</sub>.

## 2.2 Results and discussion

The overarching aim of this project is the design, synthesis and application of a new ionic liquid for sodium solvation. The design inspiration of this ionic liquid is solvents that are currently very effective at alkali metal solvation such as ammonia and ethylenediamine, hence the primary functionality of the IL will be a primary amine. However, learning from ammonia systems, it is well documented that the main intrinsic decomposition pathway is *via* proton abstraction and sodium amide formation. To combat this primary amine functionality will be on the cation in which the protons can remain acidic for solvated electron formation but tightly associated to the core cation. The anionic species will be tasked with stabilising and coordinating to the sodium cation hence stable anions with available oxygens for coordination will be sought.

Furthermore, upon discovery of a successful amine-functionalised ionic liquid the mechanism of solvation will be studied in great detail using a variety of spectroscopic and computational techniques.

### 2.2.1 Design and synthesis of the amine functionalised ionic liquid

The first class of amine-functionalised ionic liquids investigated were aminopyridinium ILs, ultimately aliphatic amino-functionalised ionic liquids were preferred, as the possibility of reduction would be diminished compared to aromatic group containing ionic liquids, however, the acidity of the protons on the amine functionality is desired to be analogous to the coordinated NH<sub>3</sub>·Na system to stabilise the solvated electron without decomposition. The structure of the aminopyridinium motif is shown in Figure 2-12, along with the ionic liquid form. The positive charge on N, in the ionic liquid form, would increase the acidity of amino hydrogens providing a beneficial effect in interacting with electrons

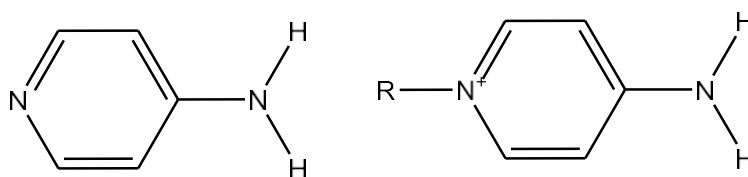


**Figure 2-12-** Structure of 4-aminopyridine and 1-alkyl-4-aminopyridinium ionic liquid cation.

The simplicity in which these ionic liquids can be synthesised and sourced is also a very important factors; and it is this that initially lead to the functionalised pyridinium ILs which are formed by a simple alkylation reaction with an alkyl halide and 4-aminopyridine followed by an anion exchange. Within literature, there are erroneous reports of the alkylation occurring on the 4-amino functionality, however, corroboration of NMR, mass spectroscopy and single crystal analysis has since disproved this and has confirmed that alkylation occurs solely on the 1-N position.<sup>130</sup> It is believed that the positive charge localised on the pyridyl ring increases the reduction potential from what are normally very reducible pyridinium compounds to levels that allow our ionic liquid cation to remain stable upon the solvation of sodium etc. If a carbon linker was placed between the *para*-amino functionality and the pyridyl ring, it would be expected that the system would break down due to the reduction potential of the aromatic species being lowered to the range of the solvated electron.

4-Aminopyridine, an isomer of nicotamide, is formed by the decarbonylation of pyridine-4-carboxamide *via* the Hofmann rearrangement which utilises sodium hypobromite and results in a carbon dioxide by-product. Alkylation of 4-aminopyridine does not require the use of any protecting groups due to the resonance within the ring that essentially deactivates the primary amine at the *para* position whilst increasing the electron density on the nitrogen within the pyridyl ring leaving it more open for attack as shown in Figure 2-13.

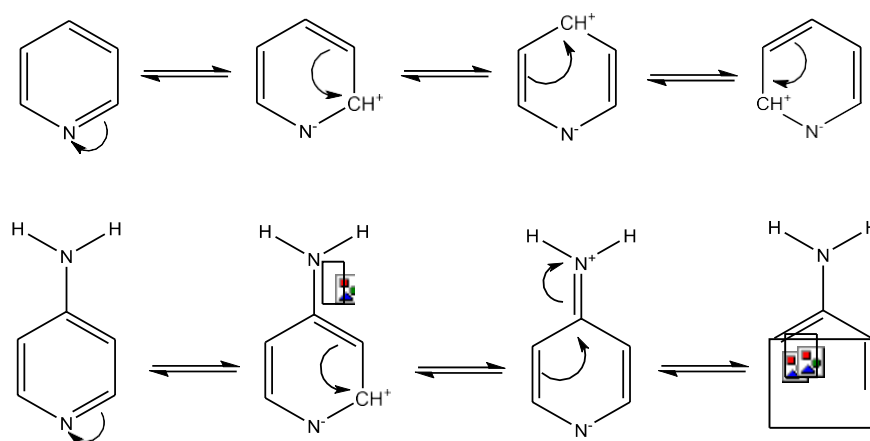


**Figure 2-13**-Resonance within amino substituted pyridine molecules.

The resonance of the 4-aminopyridine directs the alkylating agent to the nitrogen within the ring and away from the primary amine at the *meta* position. This is instantly a very efficient synthesis of an ionic liquid, bypassing any need for protecting groups as shown in Figure 2-14. Currently, only alkyl bromide and iodides

for alkylation have been used in these alkylation reactions but it is predicted that chloride and dialkyl sulphates will be equally effective. To further improve the synthesis, acetone is used as a solvent; both starting materials exhibit moderate solubility within acetone, whilst the salt product has very low to no solubility hence precipitating out of solution. The work-up is simple with only a filtration under vacuum and a single wash with acetone required. To form the bistriflamide salt, a simple metathesis reaction is carried out by simply dissolving both the cation salt and lithium bistriflamide in water, mix and extract the ionic liquid with dichloromethane.

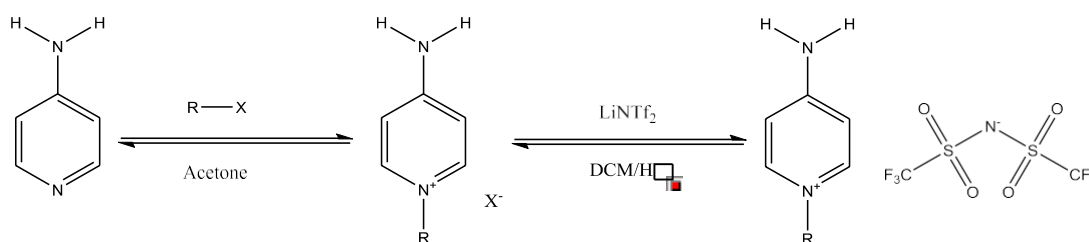


**Figure 2-14**-Synthesis of 4-aminopyridinium ionic liquids.

These simple 4-aminopyridine-based ionic liquids are very efficient to synthesise with high yields and little to no purification processes required. 1-pentyl-4-aminopyridinium bistriflamide was successfully crystallised and the structure was measured and elucidated as shown in Figure 2-15.

Notably, there is alternating hydrogen bonding between the protons on the functionalised amines and the nitrogen and sulfonyl oxygens on the bistriflamide anions. Also note the only protons that hydrogen bond with the anion are *via* the amine functionality. Within the bromide form of a similar cation 1-butyl-4-aminopyridinium bromide, the protons in the 2 and 4 positions contribute to the hydrogen bonding with the anion as shown in Figure 2-17.

The bromide anion lies 3.401 Å from the primary amine functionality with long range  $\pi$  stacking between the pyridinium rings (7.789 Å) and intercalating acetone molecules (3.659 Å).



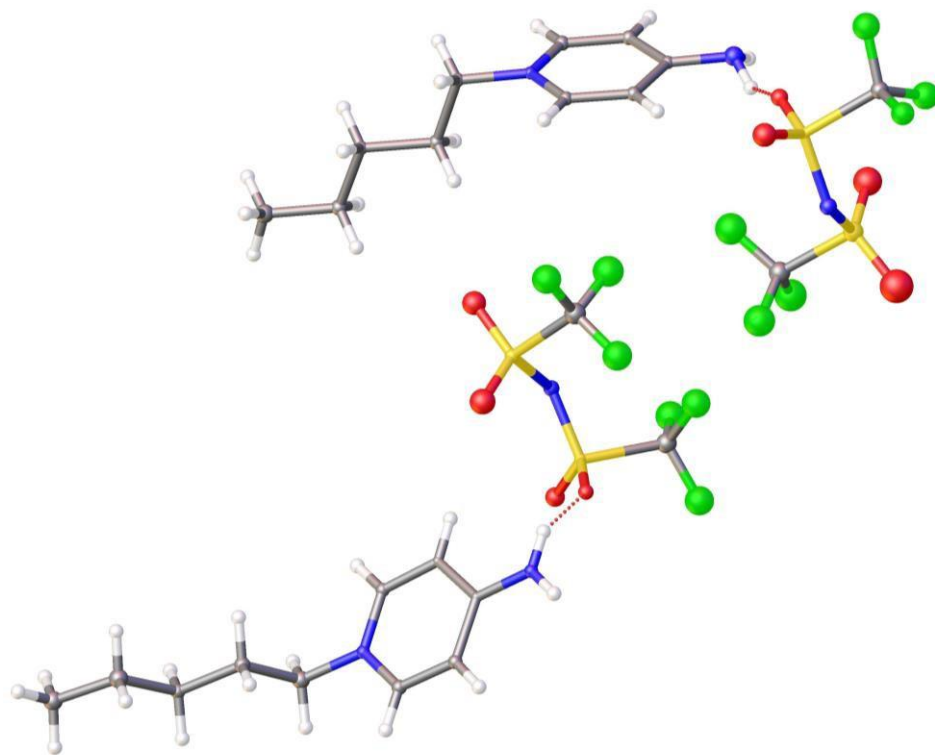


**Figure 2-15-** Single crystal diffraction determined structure of 1-pentyl-4-aminopyridinium bistriflamide.

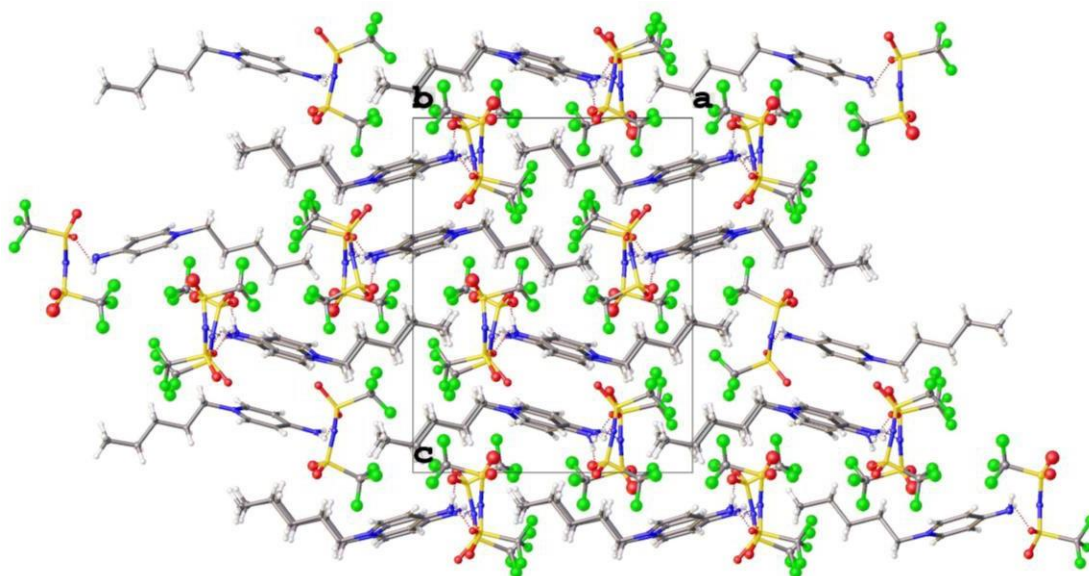


**Figure 2-16-** Single crystal diffraction determined structure and packing of 1-pentyl-4-aminopyridinium bistriflamide.

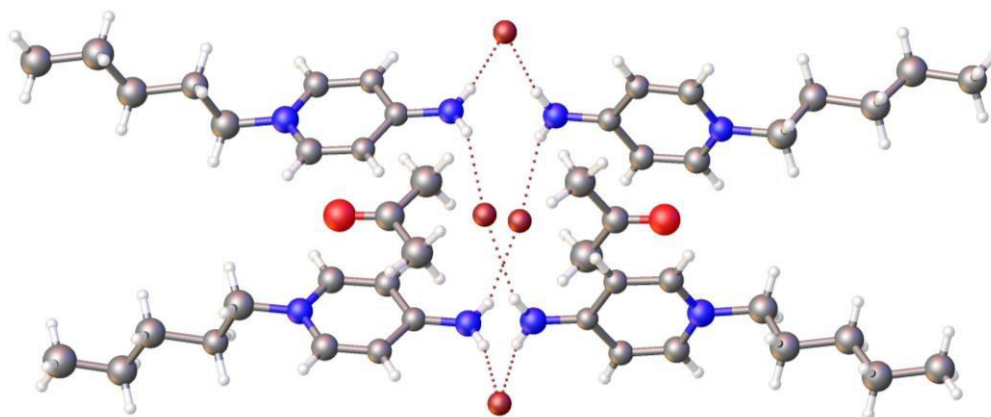


**Figure 2-17-**Structure of 1-butyl-4-aminopyridinium bromide as determined by single crystal diffraction.

## 2.2.2 Alkali metal solvation

Simplicity is key. When initially planning the experiments it was expected that the use of crypts, crown ethers and even anhydrous ammonia would be necessary to assist in the sodium solvation as demonstrated by Fässler and co-workers.<sup>131</sup> Despite this, initial tests with the neat 1-pentyl-4-aminopyridinium bistriflamide were found to be very successful with a visible solvation and very little effort required. It was found that mass transport is the most limiting factor in the solvation process. To overcome this, an adapted method from initial tests is utilised in which the metallic sodium is placed in the IL and heated to initiate melting and dispersion. Our most effective method requires the application of heat to the IL and sodium metal separately to 95 °C (the melting point of sodium) and the sodium is then added to the IL and agitate the solution as shown in Figure 2-18.

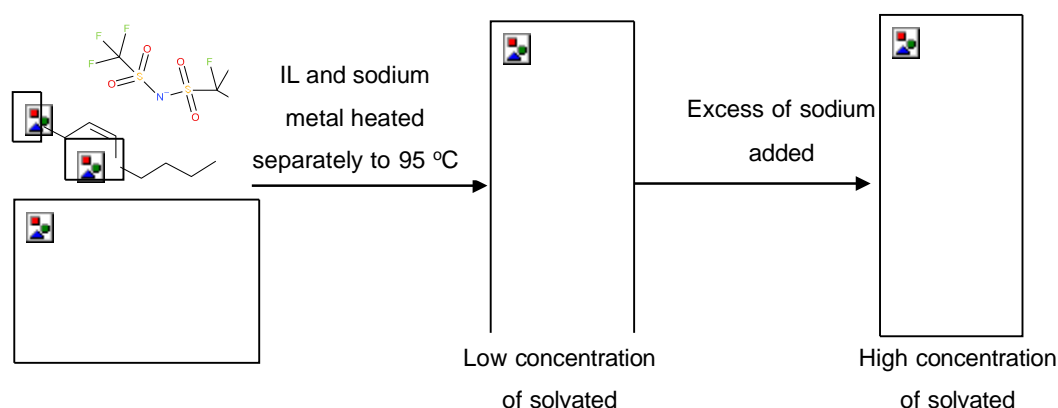


**Figure 2-18-** Formation of solvated electrons in 1-butyl-4-aminopyridinium bistriflamide.

Upon addition of molten sodium to the ionic liquid, solvation is immediately visible with deep blue streaks that are reminiscent to those observed in sodium ammonia

systems which then disperse across the bulk solution and increase in depth as the concentration increases. Currently, it is believed that the electrons formed are sensitive to oxygen and moisture similarly to those within conventional solvents due to this solvation is carried out within under glovebox or Schlenk conditions.

One of the most profound characteristics of this methodology is the temperature at which it is carried out at. Previously all sodium solvation in anhydrous ammonia consequently required very low temperatures, below 240 K. This increase in operating temperature may lead to an extensive number of organic and inorganic reactions which are now feasible. Similarly, the addition of potassium metal also resulted in the formation of a deep blue solution, however; it appeared to form more sluggishly than the sodium metal system.

### 2.2.3 Spectroscopic analysis

Elucidation of the sodium's solvation mechanism in the 1-alkyl-4-aminopyridinium bistriflamide is vital in determining possible uses of such solvation in the future specifically, in regards to the formation of solvated electrons and single electron reductions.

#### 2.2.3.1 UV/Vis spectroscopic analysis

The vivid colour of the 1-pentyl-4-aminopyridinium bistriflamide lends itself to UV/Vis spectroscopy, however, as shown in Figure 2-19, even at what are deemed to be somewhat low concentrations, a deep colour is observed. Using a 1 mm quartz cuvette, the absorbance is above 1 as shown in Figure 2-20 and Figure 2-21.

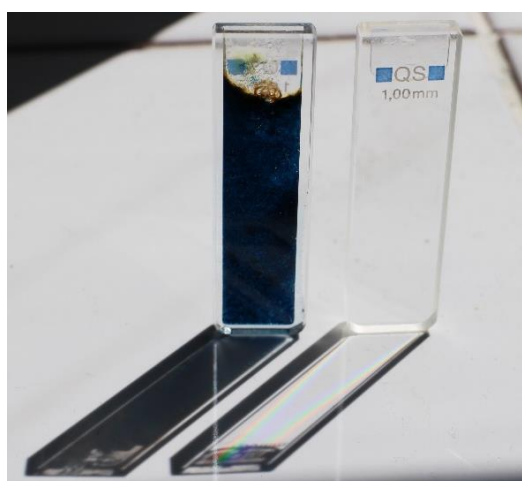


**Figure 2-19-** Image of 1 mm UV quartz cells containing sodium dissolved in 1-pentyl-4-aminopyridinium bistriflamide (left) and the neat ionic liquid (right).

For the peak at approximately 600 nm, several indentations are observed. The spectra have been repeated several times and the indentations have been noted repeatedly. These bands on the peak are due to vibrionic interactions of the electron to a specific aspect of the ionic liquid *i.e.* the aspect that stabilises the electron and in turn forms the cage in which the electron sits. There have been many quantum mechanical estimations on the origin of the couplings observed within many solvents and it is seen that they arise from a dipole induced electron trap even within diethyl ether which is largely regarded as a non-polar solvent. It should also be noted that further modes of the solvent induced cage can be observed further along the spectra towards the IR region; however, these bands are often broad and less predominant.<sup>132</sup>

Significant work by Gibson and Argo confirmed the blue colour of sodium -ammonia solutions using UV/Vis spectroscopy; they carried out significant modelling of the properties of the electrons in 'ammono' solutions using electromotive force measurements conducted by Kraus and co-workers.<sup>84,85</sup> Work by Mason *et al.* describes the formation of hydroxides upon the controlled reaction of sodium potassium alloys in water. No hydroxyl stretches are observed between 3480 and 3620  $\text{cm}^{-1}$ , and at around 900  $\text{cm}^{-1}$ .<sup>133</sup>

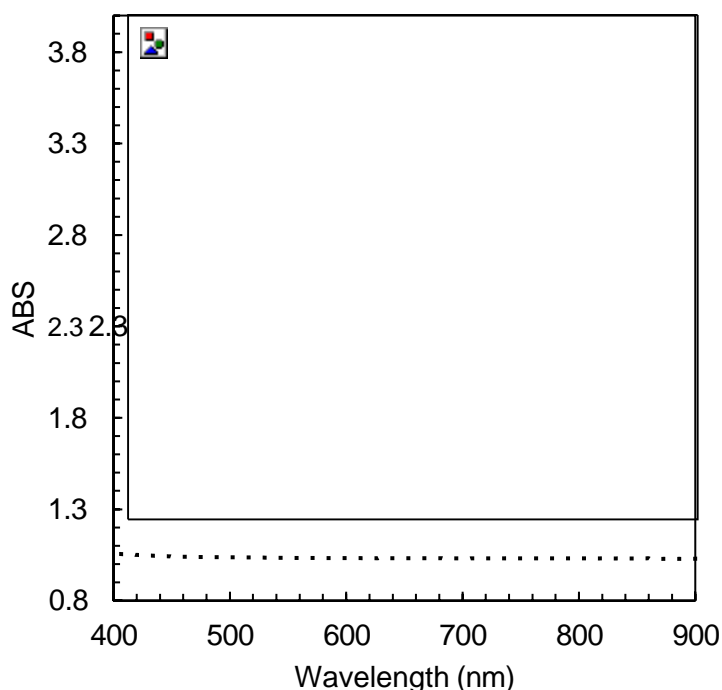


**Figure 2-20-** UV/Vis-NIR Spectra of 1-pentyl-4-aminopyridinium bistriflamide with sodium (blue) and the neat IL (dashed).

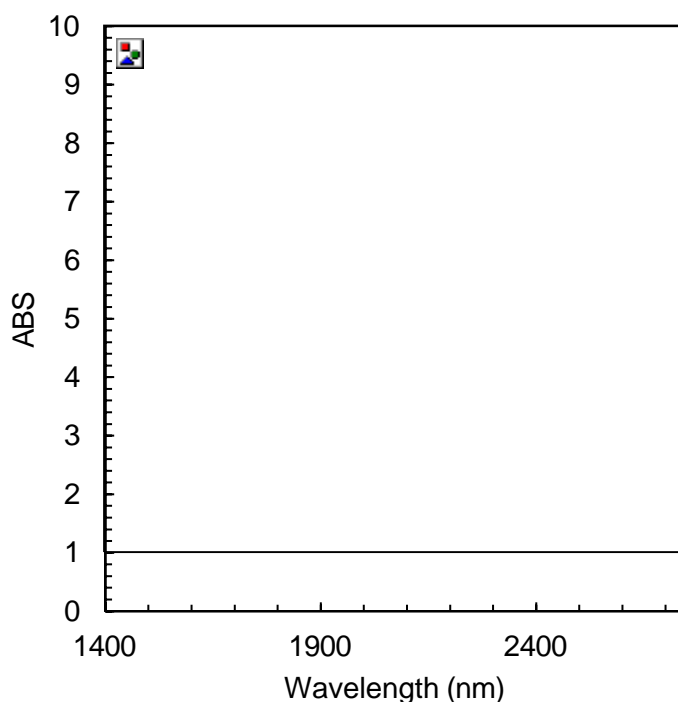


**Figure 2-21**-UV/Vis-NIR Spectra of 1-pentyl-4-aminopyridinium bistriflamide with sodium (blue) and the neat IL (dashed).

### 2.2.3.2 Nuclear magnetic resonance spectroscopy

Nuclear magnetic resonance is a useful tool in the elucidation of stability and solvation structure of metals in solution. Multinuclear NMR spectroscopy allows for different aspects and perspective of the ionic liquid before, during and after solvation of the sodium metal has occurred.

#### 2.2.3.2.1 Ionic liquid stability analysis

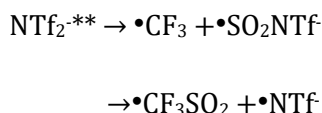
Conventional proton  $^1\text{H}$ , fluorine  $^{19}\text{F}$  and carbon  $^{13}\text{C}$  NMR of the 1-pentyl-4-aminopyridinium bistriflamide allow for the stability of the ionic liquid to be monitored before and after solvation occurs. For this to occur, the solution must be quenched; using a methodology that will also be used to undergo atomic adsorption spectroscopic methods. Bistriflamidic acid in deionised water is added to the IL-sodium solution, which is known to not contain any residual sodium pieces. Dichloromethane is then added and the IL moves into the organic layer. Small samples are taken from the organic layer until a flame test is observed to be negative for sodium with increasing amount of the aqueous acid added to facilitate this exchange. The aqueous layer is then appropriately diluted for atomic adsorption analysis and the organic layer is concentrated under vacuum to recover the IL.

The recovered IL is a colourless solid upon drying under vacuum (75 °C, 24 hours). The before and after solvation samples were dissolved in  $d^3$ -CD<sub>3</sub>CN and analysed with <sup>1</sup>H, <sup>13</sup>C and <sup>19</sup>F NMR spectroscopy.

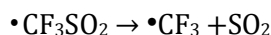
As shown in Figure 2-22 the <sup>1</sup>H NMR spectra show little difference in the before and after solvation samples. There is slight shift in the NH<sub>2</sub> peak of ca. 6.4 ppm, however, the most evident thing that should be taken from these spectra is the lack of apparent reduction products. The spectra were a result of 128 scans, hence giving good resolution and consequently small amounts of reduction products should be apparent.

As shown in Figure 2-23, the <sup>19</sup>F NMR spectra the peak remains as a singlet at -80.13 ppm. Decomposition of the bistriflamide anion was a concern due to previous observations by Wishart *et al.* studying the effects of radiation on common anions, however, no corrosion of glassware was observed hence no HF is believed to have been evolved. Under flash photolysis techniques it is suggested that homolytic cleavage of the bistriflamide anion occurs in the C-S and O-S bonds as per Equation 2-7. The •CF<sub>3</sub>SO<sub>2</sub> radical formed is unstable and further cleaves to form •CF<sub>3</sub> and SO<sub>2</sub> and per Equation 2-8.<sup>134</sup> These decomposition pathways have been *via* flash photolysis and exposure to gamma radiation.

Equation 2-7



Equation 2-8



In regards to the behaviour of ionic liquids in the sole presence of beta radiations there are few studies; often a combination of alpha, beta and gamma radiation used in combination. Radiolytic products have not been detected in the <sup>19</sup>F NMR spectra. Within the <sup>19</sup>F NMR the CF<sub>3</sub><sup>-</sup> group, in general, is expected to lie within -50 - -90 ppm; no changes in shift are observed indicating no reaction products of the •CF<sub>3</sub> radical are formed.

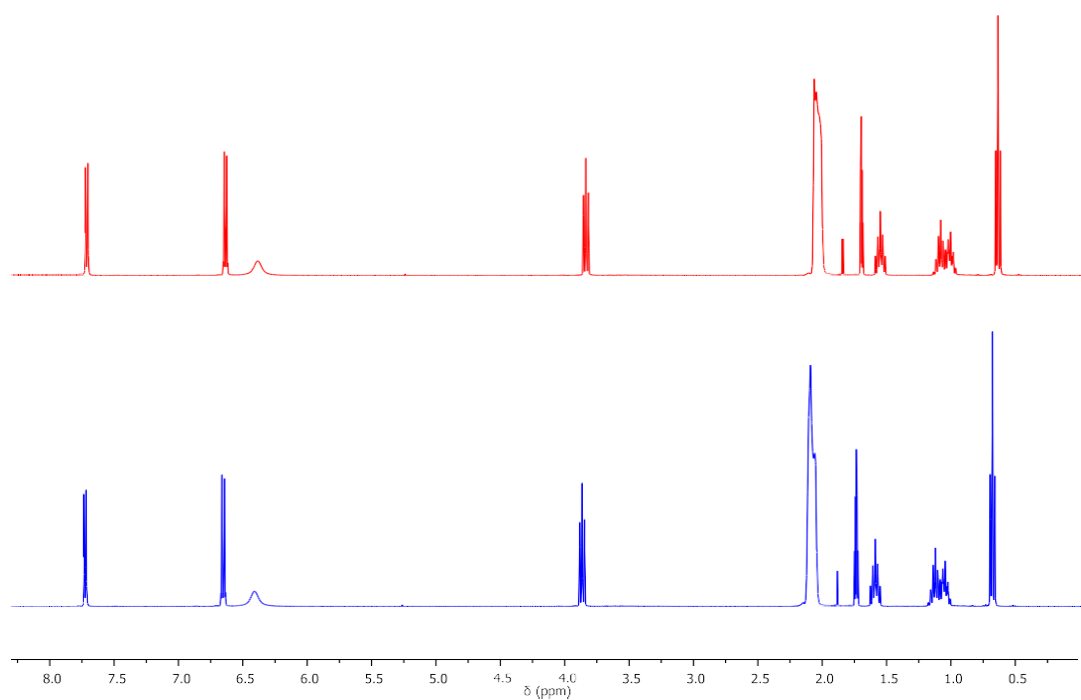


**Figure 2-22**  $^1\text{H}$  NMR spectra of 1-pentyl-4-aminopyridinium bistriflamide before (red) and after (blue) sodium solvation and quenching.

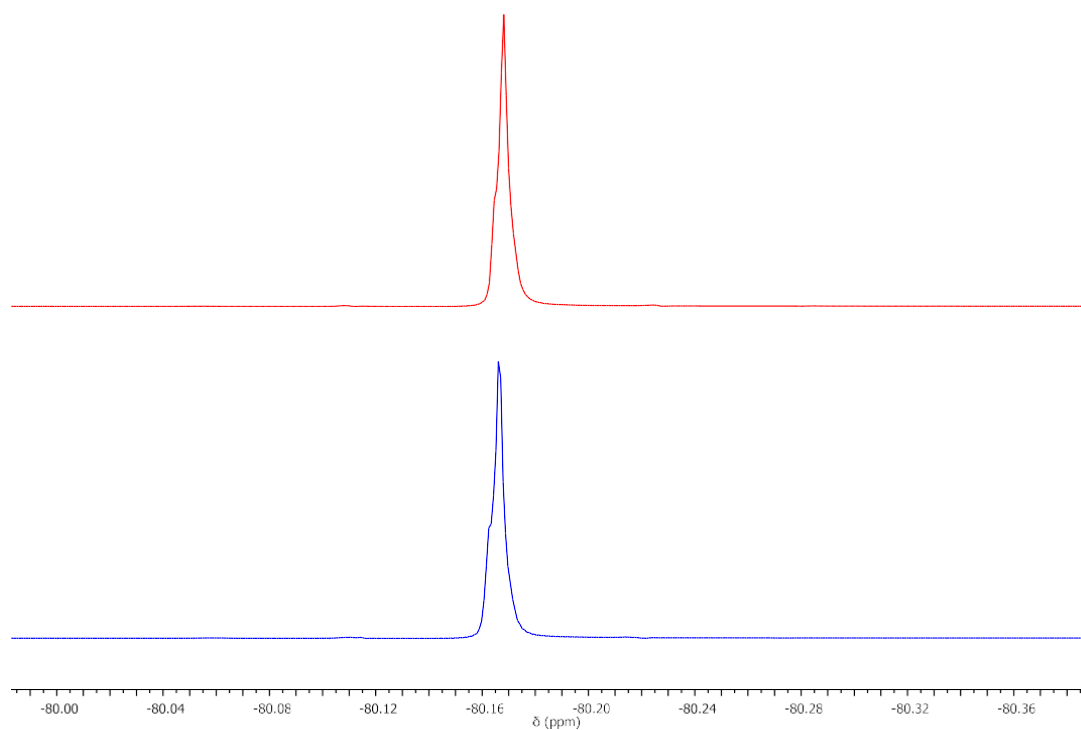


**Figure 2-23**  $^{19}\text{F}$  NMR spectra of 1-pentyl-4-aminopyridinium bistriflamide before (red) and after (blue) sodium solvation and quenching.

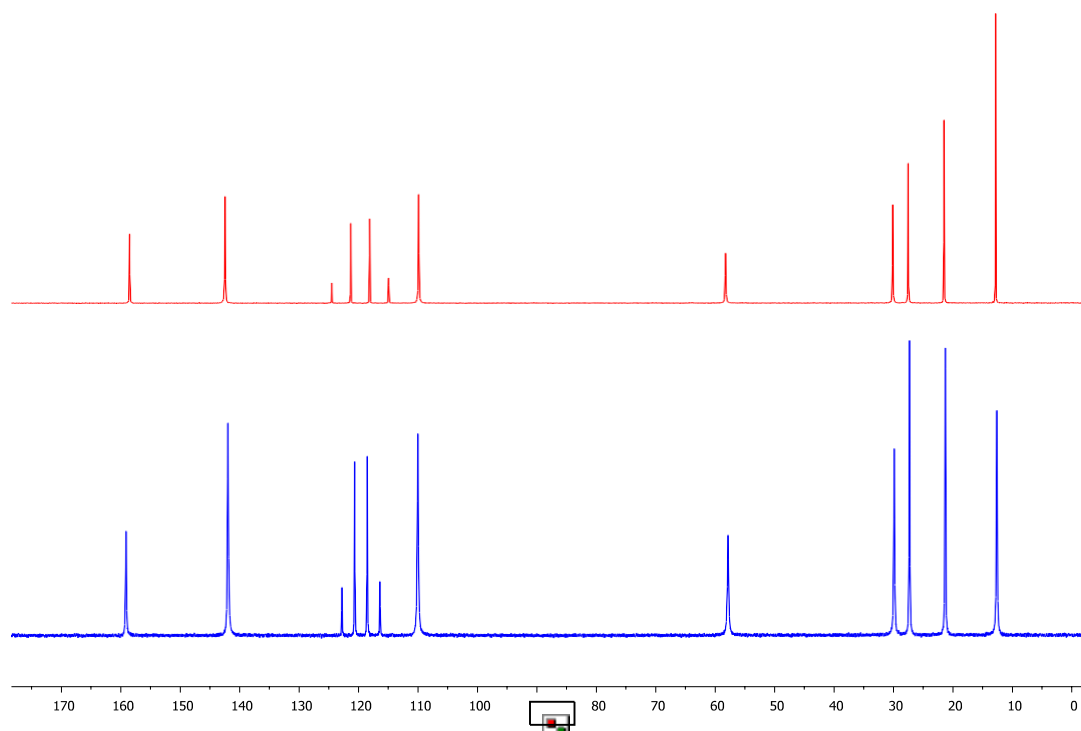


**Figure 2-24-** $^{13}\text{C}$  NMR spectra of 1-pentyl-4-aminopyridinium bistriflamide before (red) and after (blue) sodium solvation and quenching.

Finally,  $^{13}\text{C}$  NMR spectra as shown in Figure 2-24 again show that the ionic liquid is stable in terms of the cation and anion. Peaks referring to the cation appear at near identical chemical shifts with only a slight variation in peak height. In regards to the anion, a quartet assigned to the  $\text{CF}_3$  group of the bistriflamide anion remains at 121 ppm, however, the coupling constants change from 16.26 MHz to 11.62 MHz.

Multinuclear NMR spectroscopy has determined that the ionic liquid is stable after solvation of sodium metal. Minimal changes in the NMR analysis have been observed.

#### **2.2.3.2.2 Sodium NMR spectroscopy**

Previous spectra by Dye and co-workers investigating [2, 2, 2]-cryptand and sodium found that three differing sodium environments could be observed;  $\text{Na}^+$ ,  $[\text{Na-2,2,2-cryptand}]^+$  and  $\text{Na}^-$  at ca. -11 ppm, 10 ppm and 62 ppm respectively. The active blue solution of 1-pentyl-4-aminopyridinium bistriflamide and sodium metal was prepared under glovebox conditions and placed in an NMR tube with a 0.1 M NaCl  $\text{D}_2\text{O}$  capillary. The  $^{23}\text{Na}$  spectra were recorded on a 600 MHz Bruker Avance spectrometer. As shown in Figure 2-25 the reference peak at 0 ppm referring to the NaCl  $\text{D}_2\text{O}$  solution is prominent. A broad peak was observed at -11.49 ppm and assigned to the solvated sodium in the solution.  $^{23}\text{Na}$  NMR and the  $^{23}\text{Na}$  atom is



quadrupolar such that the nuclear spin is 3/2. Quadrupolar nuclei respond greatly to changes in symmetry; one of the most simplistic examples of this is the  $^{23}\text{Na}$  NMR spectra of NaCl vs NaOH in  $\text{D}_2\text{O}$ . NaCl in aqueous solution have differing hydrated structures. NaCl results in an octahedral  $[\text{Na}(\text{H}_2\text{O})_6]$  hence giving rise to a narrow single peak at 0 ppm. NaOH, however, in aqueous solution can form multiple hydrated forms of differing symmetry hence giving rise to a broader peak.<sup>135</sup>

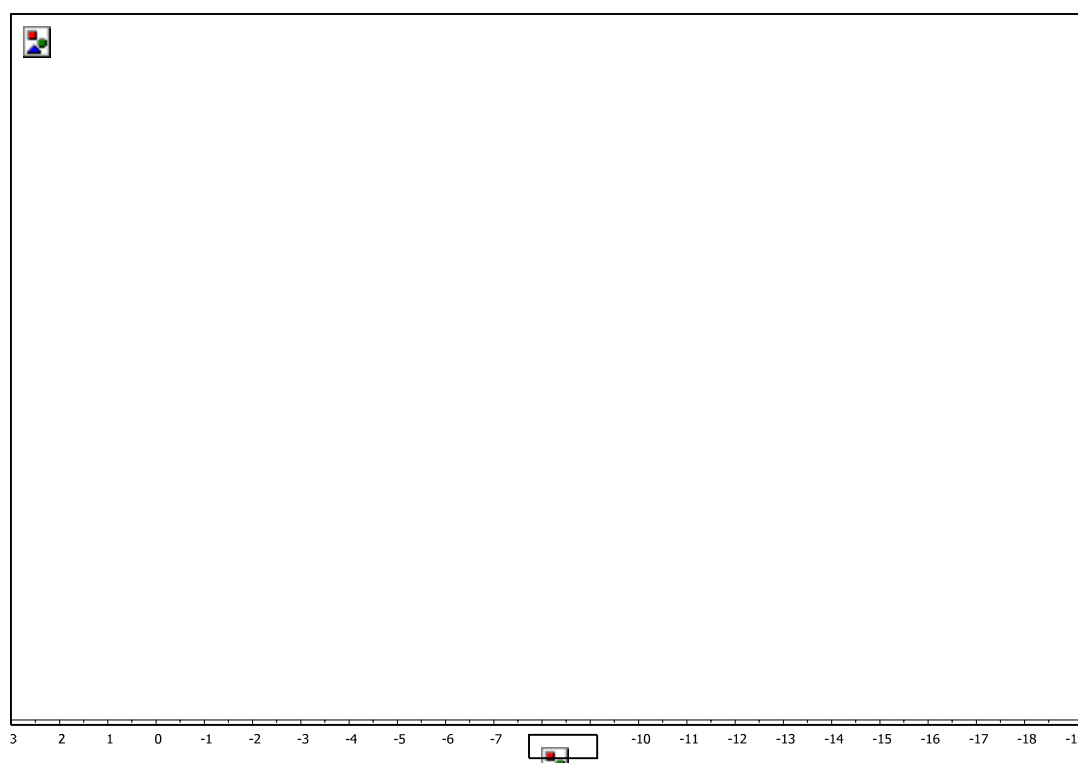


**Figure 2-25**  $^{23}\text{Na}$  NMR spectrum of 1-pentyl-4-aminopyridinium bistriflamide.

In the 1-pentyl-4-aminopyridinium bistriflamide and sodium metal solution NMR spectra demonstrates a broad peak at -11.49 ppm. This corresponds well to that observed by Dye and co-workers for  $\text{Na}^+$  unbound by the cryptand. In the IL it is suspected that the bistriflamide anion coordinates to the sodium cation forming a *pseudo*-octahedral, anionic  $[\text{Na}(\text{NTf}_2)_3]^{2-}$  coordination as shown in Figure 2-26 hence explaining the broadness of the peak observed.

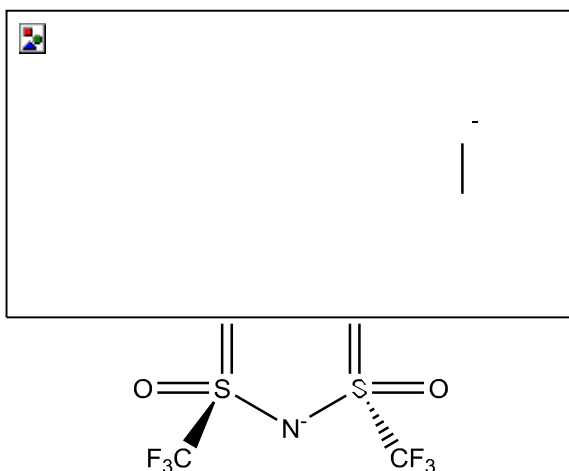


**Figure 2-26**-Suspected coordination of sodium as a  $[\text{Na}(\text{NTf}_2)_3]^{2-}$  anion in 1-pentyl-4-aminopyridinium bistriflamide.

Finally, no NaOH peaks were observed hence it can be confirmed that no water impurities have assisted in the solvation of the sodium metal in the ionic liquid.

#### 2.2.3.2.3 Paramagnetism and NMR

In this work, a previously reported NMR method for measuring the paramagnetic sensitivity of inorganic species, the so-called Evan's method, was adapted.<sup>136</sup> Developed in 1959, Evan's method requires use of co-axial NMR tubes in which, and the insert contains a deuterated solvent, and in some cases a standard whilst the tube contains a paramagnetic species in the same solvent.

#### Equation 2-9

$$\chi_{\text{mass}} = 3\Delta f / 4\pi f m + \chi_o + \chi_o(d_o - d_s)/m$$

$\chi_{\text{mass}}$  = Mass susceptibility in  $\text{cm}^3 \text{g}^{-1}$

$\Delta f$  = Observed change in frequency, Hz

$f$  = Spectrometer frequency, Hz

$m$  = Concentration of paramagnetic substance,  $\text{g cm}^{-3}$

$\chi_o$  = Mass susceptibility of solvent,  $\text{cm}^3 \text{g}^{-1}$

$d_o$  = Density of solvent,  $\text{g cm}^{-3}$

$d_s$  = Density of solution in  $\text{g cm}^{-3}$

As paramagnetism is induced by the sodium solvation, the changes in density *etc.*, are not overly quantifiable due to the unstable nature of the solution, hence Evan's method will simply show the presence of paramagnetic influence on the IL.

The only deuterated solvent at our disposal for this study was  $d_6$ -benzene as most conventional chlorinated solvent may result in the release of chlorine gas and

alternatives such as methanol and deuterium oxide, which are not suitable as they will react with any sodium and solvated electrons present.

The influence of paramagnetism within the NMR study can take two forms, contact and pseudo-contact. Evan's method utilises *pseudo*-contact in which the paramagnetic influence is *via* the influence of the bulk material. Whereas within our systems our ionic liquid will experience the majority of the paramagnetic influence, hence it will be this IL proton NMR that will be monitored. It was difficult to see any shift in the solvent reference peak due to the significant broadening observed, hence Evan's method cannot be fully adopted, however, broadening is observed and downfield shift each of which indicates the presence of a paramagnetic shift.

It was observed with 1-pentyl-4-aminopyridinium bistriflamide that throughout the  $^1\text{H}$ ,  $^{13}\text{C}$  and  $^{19}\text{F}$  NMRs carried out peak broadening was observed as shown in Figure 2-27. The proton NMR was most evident with the shift observed majorly within the amine and aromatic region, hence indicating the paramagnetic species may lay bias to this paramagnetic source. The 'active' solution shown in Figure 2-27 is of a relatively low concentration solution; to further confirm that this broadening is due to the sodium induced solvated electrons formed a high concentration solution was formed. Much darker and almost black in appearance the  $^1\text{H}$  NMR spectrum as shown in Figure 2-28 is ineligible suggesting a greater paramagnetic influence.

Reverting back to the low concentration solutions, carbon  $^{13}\text{C}$  NMR analysis remains narrow in nature whereas the  $^{19}\text{F}$  fluorine NMR spectra, as shown in Figure 2-29 exhibited broadening that suggested a second peak environment may be present. As discussed, the sodium  $^{23}\text{Na}$  NMR analysis suggested an  $[\text{Na}(\text{NTf}_2)_x]^{(1-x)}$  complex may be present hence this may be the source of this new peak at -79.5 ppm.

This study has confirmed that a paramagnetic source is present upon sodium solvation in the ionic liquid; solvated electrons are well reported for their paramagnetic properties hence further supporting the first observation of suspected solvated electrons in an ionic liquid.

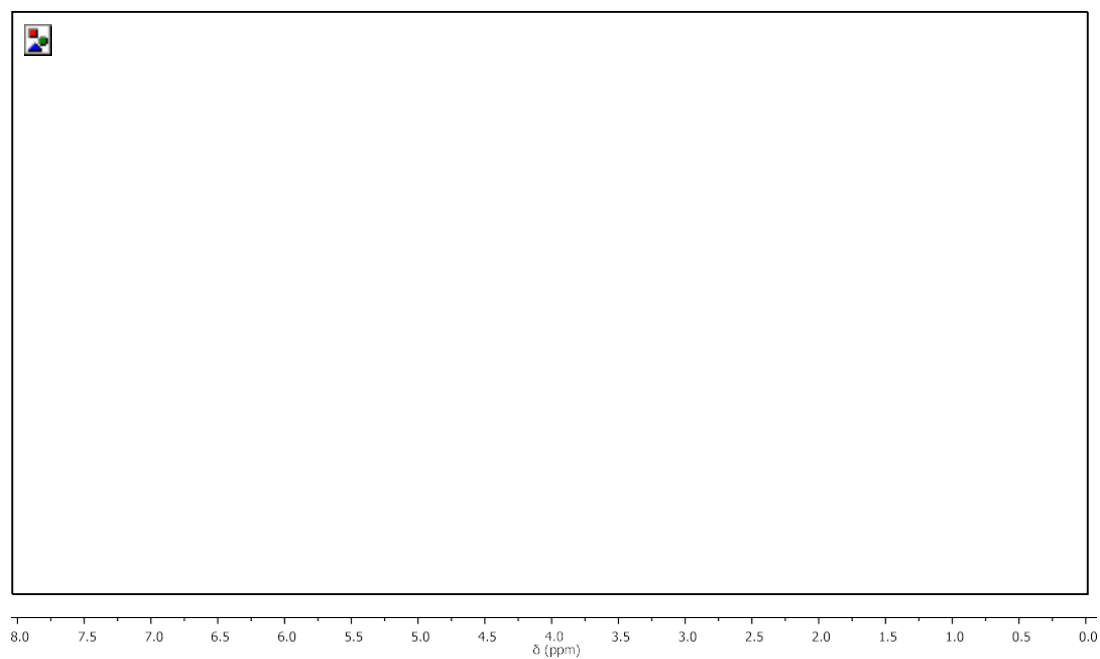


**Figure 2-27-** Evan's method of 'low concentration' sodium in 1-pentyl-4-aminopyridinium bistriflamide.  $^1\text{H}$  NMR spectra before (red) and after solvation of sodium (blue).

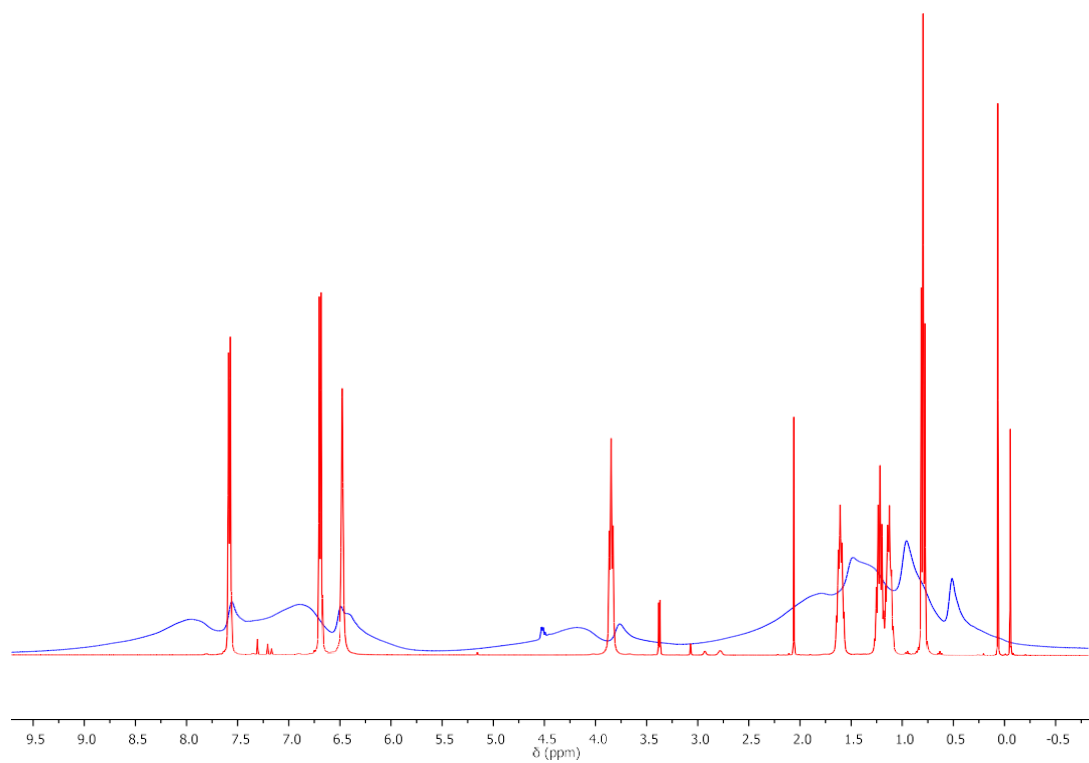


**Figure 2-28-** Evan's method of 'high concentration' sodium in 1-pentyl-4-aminopyridinium bistriflamide.  $^1\text{H}$  NMR spectra before (red) and after solvation of sodium (blue).

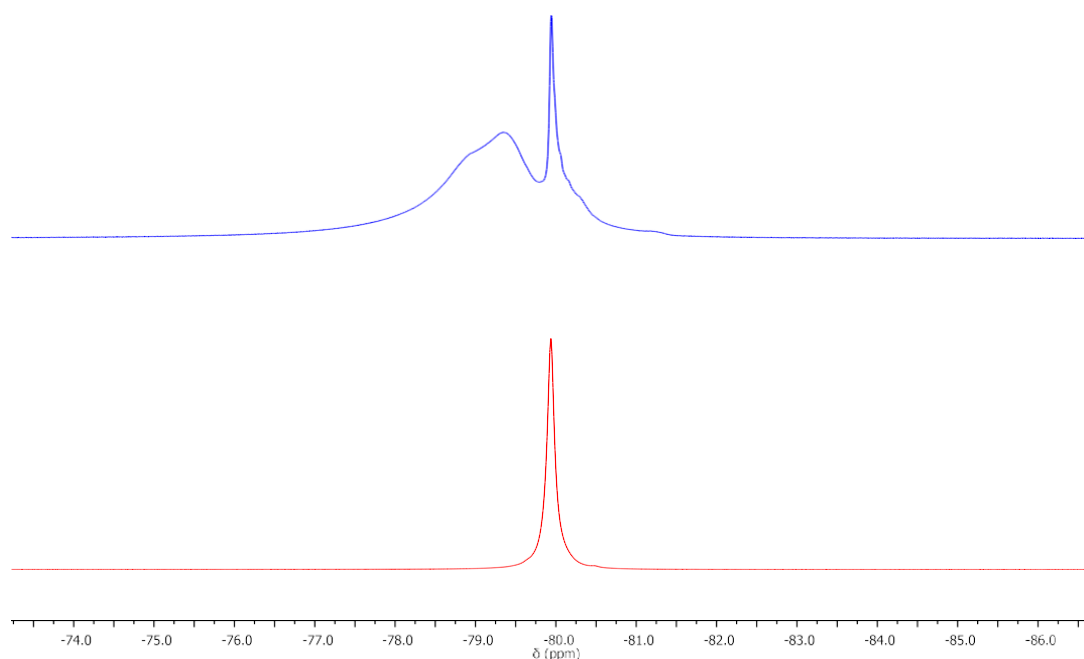


**Figure 2-29-** Evan's method of 'low concentration' sodium in 1-pentyl-4-aminopyridinium bistriflamide.  $^{19}\text{F}$  NMR spectra before (red) and after solvation of sodium (blue).

### 2.2.3.3 Electron paramagnetic spectroscopy

Electron paramagnetic resonance or EPR spectroscopy, as it is more commonly termed, is essentially an electron analogue of NMR.<sup>137</sup> Within EPR it is electron spin,  $m_s$  that gives rise to peaks; when placed in a magnetic field of strength  $B_0$ , the unpaired electron's magnetic moment aligned either with or against the field. This change in alignment requires a specific energy,  $B$  and it is this which is detected *via* microwave irradiation as per Equation 2-10.

**Equation 2-10**

$$E = m_s g_e \mu_B B_0$$

$$h\nu = m_s g_e \mu_B B_0$$

where  $\mu_B$  is a Bohr magneton which is, a constant describing the spin angular momentum of an unpaired electron and  $g_e$  is the Landé  $g$  factor. The  $g$ -factor is very important to us when proving the presence of our solvated electrons. EPR is not only for the detection of solvated electrons but it will give an indication of where the electron is *via* hyperfine splitting patterns *i.e.*  $2MI+1$ . Firstly, the  $g$ -factor will give us an indication of where the electron is sitting; the  $g$ -factor of a free electron in a vacuum and in liquid ammonia is well reported as 2.0023 and 2.0012 respectively.

<sup>138</sup> The g-factor is a value which describes both the spin and angular momentum of an electron; usually each element will have a set g-factor that relates to the degenerate electrons of spin half. Utilising EPR it was planned to investigate two aspects of the system, firstly it was aimed to match or reach the g-factor that is commonly associated with a free electron in a vacuum and secondly it was wished that no radical decomposition products would be observed. Finally, it was wished to detect a signal overall a cold finger was used to hold our sample of the 1-butyl-4-aminopyridinium bistriflamide sample and to cool to 77 K using liquid nitrogen.

Previous EPR measurements carried out by V. I. Feldman and co-workers investigating the generation of a hot/excess electron *via* laser flash photolysis in 1-butyl-1-methylpyrrolidinium bistriflamide. The irradiated sample was found to have a unique splitting pattern within the EPR spectra and this was believed to be due to the formation of alkyl radicals from the organic cations decomposition, however, they did observe a sharp signal at approximately  $g = 2.004$ . It was found that by irradiating the sample further with UV light *i.e.* bleaching the sample  $>600\text{ nm}$ , the sharp signal decreased significantly, with the singlet signal eventually disappearing. By looking at the differences in the signal with respect to the signal before and after photo bleaching they could extract out the signal and believe it to be due to a physically trapped excess electron.<sup>139</sup>

This work also noted the sensitivity of EPR and that the results obtained are similar to the solvated electrons found in non-polar solvents such as ethers *etc.* where electrons in polar media give rise to peaks broader than 2 mT. It should be noted that the g value calculated in this work is rather high with the g-value of free electrons expected to be 2.0023 or below, however, the authors believe this slight increase is due to the asymmetry that may occur within the cavities of the IL that the electron will lie. As shown in Figure 2-30 and Figure 2-31, the spectra obtained showed a single peak relating to the system and a peak at below 180 G which is well reported to be due to the  $>1200\text{ ppm}$   $\text{Fe}_2\text{O}_3$  impurities within the glass of the NMR tubes. One of the first characteristics observed is the absence of any decomposition products and that only one EPR-active species is present. If there are decomposition products present they are at a very low concentration. Secondly, the g-factor of our singlet solution peak is 2.001, and this is within the range of a free electron in vacuum and liquid ammonia. However, as always, caution should be taken as the g-factor for elemental sodium is 2.002. Comparing this to the previously mentioned radiation induced radical decomposition where EPR spectra were found

to have very clear splitting in the spectra indicating decomposition. No decomposition of the pyridinium cation or anion was observed.

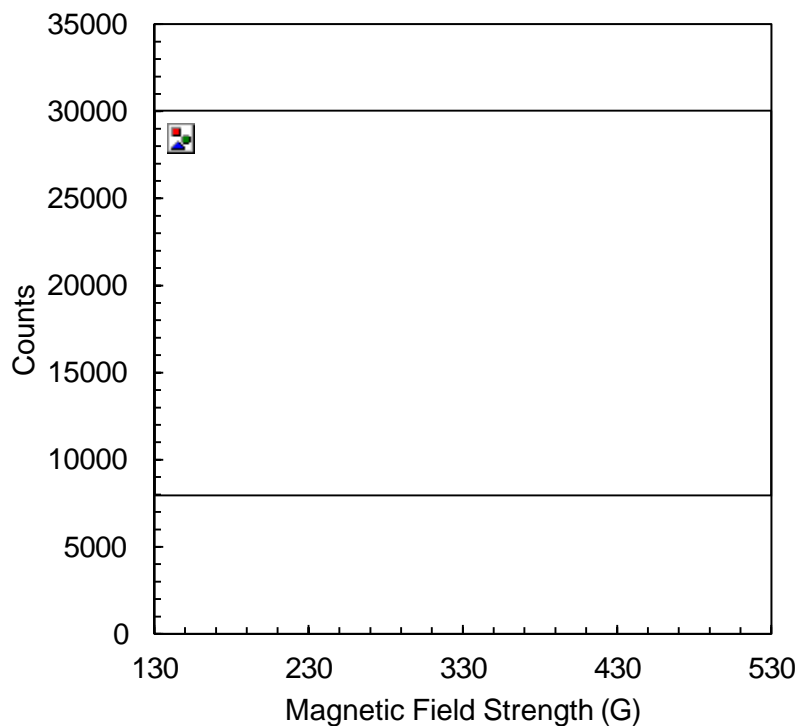


**Figure 2-30-** EPR spectra of elemental sodium dissolved in 1-pentyl-4-aminopyridinium bistriflamide.

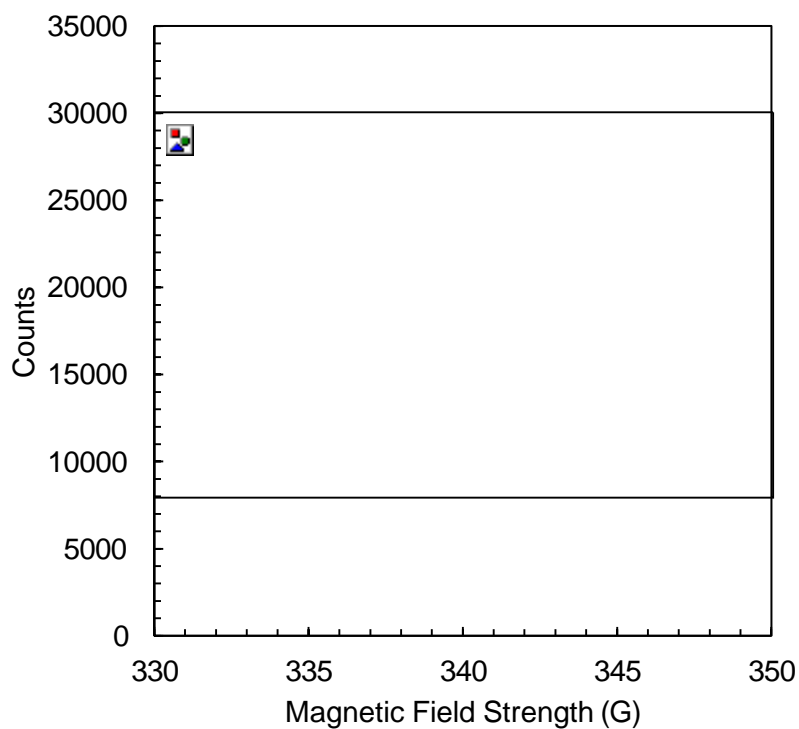


**Figure 2-31-** EPR spectra of elemental sodium dissolved in 1-pentyl-4-aminopyridinium bistriflamide.

#### 2.2.3.4 Atomic absorption spectroscopy

Atomic adsorption spectroscopy, AAS is a quantitative technique that utilises an element's intrinsic emission to both identify and quantify the element in solution. This methodology was first refined by Herschel who catalogued the colours observed in the alcohol flame from salts of sodium, potassium, calcium, strontium, lithium, barium, copper, and iron as shown in Figure 2-32. Later studies in greater detail by Bunsen and Kirchoff refining the identification of spectral lines the birth of atomic adsorption spectroscopy was found.<sup>140</sup>

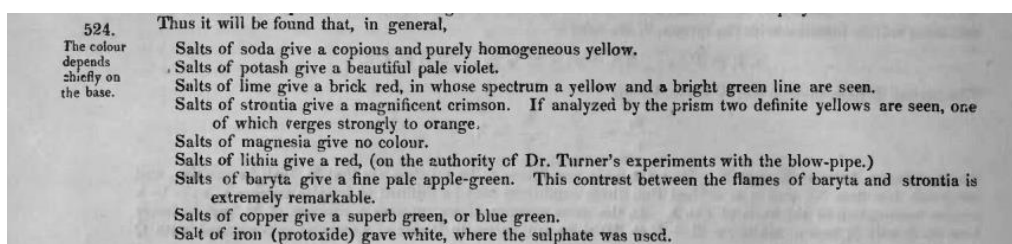


**Figure 2-32**—Except from the Treatises of Sound and Light, Encyclopaedia Metropolitana, 1848 by Sir, J. F. W. Herschel.<sup>141</sup>

Janssen and Guoy were the main driving force being the introduction of quantitative analysis *via* AAS and the practicalities of such measurements.<sup>142</sup> Hence today AAS is a robust and widely used technique not just within chemistry but within a variety fields and is relatively inexpensive compared to ICP analyses. Flame AAS techniques today require all species to be within an aqueous solvent and it must be below 2 ppm in concentration to be within the detector limit. Each measurement gives five readings which are averaged and a standard deviation calculated.

Bistriflamidic acid in deionised water is added to the IL-sodium solution which is known to not contain any residual sodium pieces. Dichloromethane is then added, and the IL moves into the organic layer. Small samples are taken from the organic layer until a flame test is observed to be negative for sodium with increasing amount of the aqueous acid added to facilitate this exchange. The aqueous layer is then appropriately diluted for analysis and the organic layer is concentrated under vacuum to recover the IL.

Studying 1-pentyl-4-aminopyridinium bistriflamide, a saturated solution was formed and allowed to stir for 1 hour. Whilst still molten, stirring was stopped and excess sodium metal separated from solution. A sample of the blue IL was then extracted and prepared using the methods described. It was found that 22.9 mg Na / g IL had been dissolved which equates to 0.443 mol Na / mol IL. Comparing this to sodium and ammonia solutions there are several considerations that must be made. Firstly,



within conventional lithium and ammonia solutions as shown in Figure 2-33 the concentration and the colour observed are linked.

The low concentration species at *ca.* <5 MPM have a predominantly blue colour whereas higher concentrations at *ca.* >8 MPM have a bronze-like appearance. Initially, this bronze-like appearance was believed to be due to electride formation, however, Zurek and co-workers found it can also be due to various complexes listed in Figure 2-33. It is postulated that the IL behaves in an analogously to ammonia such that the IL stabilises the electron *via* the cation, however, unlike ammonia systems the sodium cation will be stabilised by the bistriflamide anion *via* the sulphonyl oxygens.

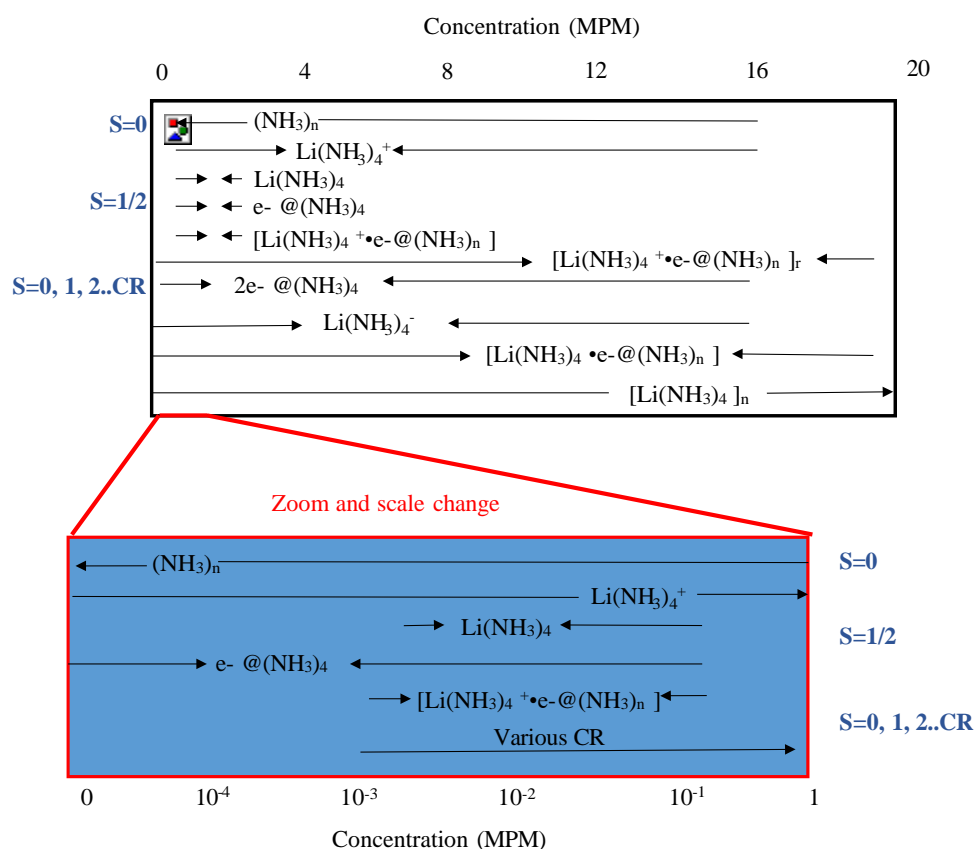


**Figure 2-33**-The species which are present in lithium–ammonia solutions, as derived from a combination of the theoretical work done by Zurek *et al.* and experimental information.<sup>143</sup>

## 2.2.4 Proof of concept: non-reactive ionic liquids

As aforementioned, the amine functionality along with a stabilisation mechanism is key to successful alkali metal solvation. The first ‘non-reactive’ ionic liquid tested was similar to the 1-alkyl-4-aminopyridinium cation; however, the primary amine functionality is inhibited with two methyl groups as shown in Figure 2-34 by blocking

its functionality, it was explored whether the conjugation of the ionic liquid cation alone could dissolve an alkali metal. Using an identical solvation procedure, both sodium and potassium metals were tested with the tertiary amine bistriflamide salt and no solvation was observed with the alkali metal remaining intact and no colour changes occurring. This indicates the necessity of having N-H's for solvating metals.

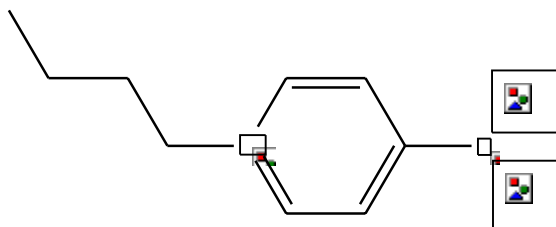


**Figure 2-34-**1-Butyl-4-(dimethyl)aminopyridinium cation.

The second 'non-reactive' ionic liquid tested was 1-butylpyrrolidinium bistriflamide,  $[C_4Py][NTf_2]$  *i.e.* an aromatic cation with no primary amine functionality; upon addition of sodium and heating no solvation was observed with the sodium metal remaining as molten globules.

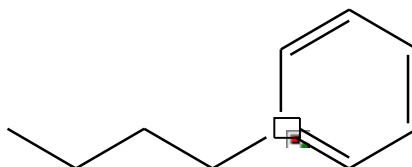


**Figure 2-35-** 1-Butylpyridinium cation

## 2.2.5 Computational modelling

Computations chemistry can help elude the structure of complex system in which spectroscopic techniques can only hint at what is occurring in solution. The ability to locate the position of the suspected solvated electron and the resultant sodium cation would allow a greater interpretation of the experimental data. The initial goals of the computation study were to determine the effects of sodium in an ionic liquid; 1-pentyl-4-aminopyridinium bistriflamide as a blue phase, which was observed to form upon mixing with sodium metal.

Using density functional theory, DFT and specifically PBE (Perdew–Burke–Ernzerhof exchange energy) the quantum mechanical derived ground state from first principles can be studies in condensed matter. PBE is a plane wave basis set much like the more commonly found B3LYP. Three simulations were complete to help in the elucidation of this solvation mechanism at PBE level of theory. The three simulations are listed below:

- (1) Relaxation of the neutral geometry of the IL taken from single crystal experimental data
- (2) Pending the results of step 1, the relaxed geometry had an additional excess electron added to the simulation cell to test where a solvated electron would be located in the IL. This was probed through single-point energy and relaxation calculations.
- (3) Taking the relaxed cell from step 1, a sodium atom was added into the centre of the simulation cell. This way, the sodium atom is in close proximity to both the “positive” and “negative” components of the ionic liquid. The resultant spin from the unpaired electron that comes from the sodium atom could then be probed through single-point energy and relaxation calculations.

Subsequently, all 3 simulations were repeated at an enhanced level of theory, PBE0. As PBE0 is a hybrid functional, it incorporates elements of exact Hartree-Fock exchange into the approximation of the exchange-correlation terms of the calculation in order to provide increased accuracy of results. The results for the PBE level calculations on the IL are shown in Figure 2-36 where relaxed with an excess electron and in Figure 2-37 for the IL relaxed in the presence of a sodium atom. In both environments the excess spin is located on the 4-aminopyridinium conjugated ring specifically on the 1-N and 4-C positions for the excess electron environment and additionally on the 2-N position in the presence of a sodium atom. Furthermore, the excess spin in the presence of a sodium atom lies on the nearest ionic liquid cations.

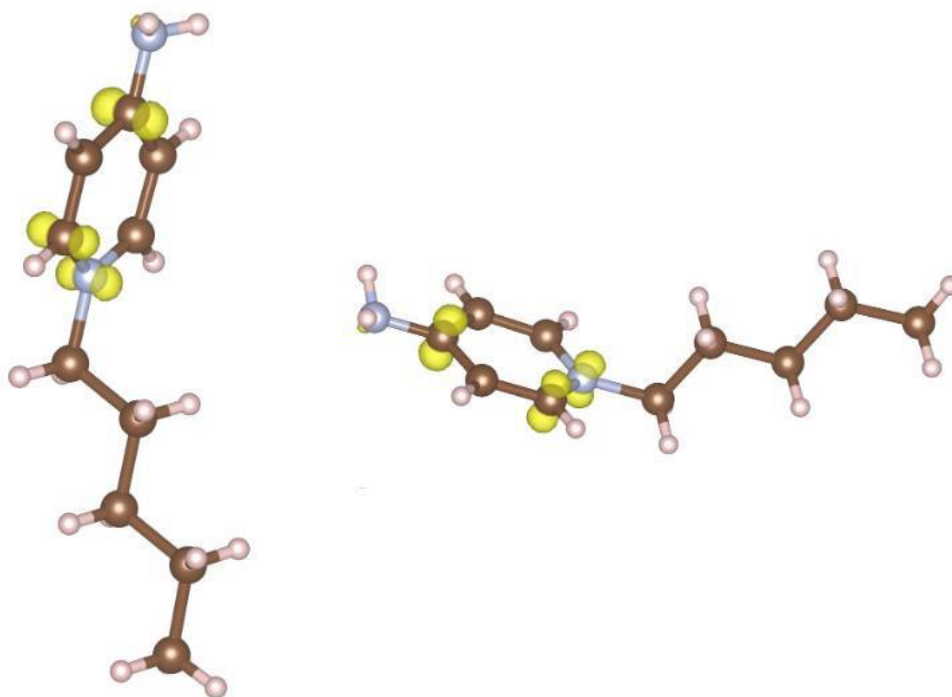


**Figure 2-36-** 1-pentyl-4-aminopyridine cation with an excess electron at the PBE level. The left image presents a top-down view, while the right is a side-on view. Positive spin density is denoted in yellow, while negative spin is blue. Isosurfaces are drawn at  $0.02 \text{ e}/\text{\AA}^3$ .

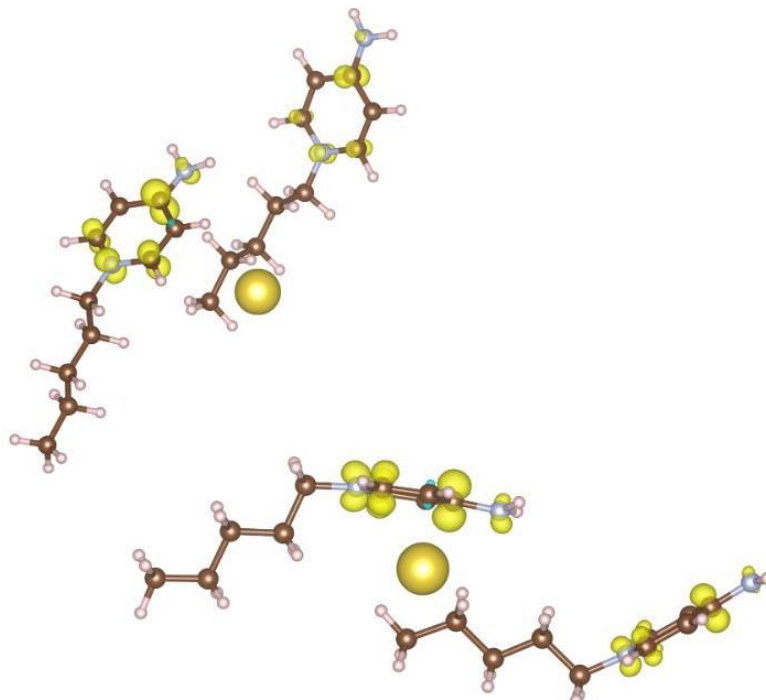


**Figure 2-37-** 1-pentyl-4-aminopyridine cation with a sodium atom present at the PBE level. The left image presents a top-down view, while the right is a side-on view. Positive spin density is denoted in yellow, while negative spin is blue. Isosurfaces are drawn at  $0.02 \text{ e}/\text{\AA}^3$ .

Using a high-level theory, PBE0, the results are relatively similar such that in both the excess electron and sodium-containing ionic liquid environments; the spin is found on the ring of the IL cation. It should be noted by referring to the location of the spin it is determined that this is the HOMO energy level of the IL system. As PBE0 is a hybrid functional, it is possible for PBE0 to "collapse" the electron down into the lowest energy states, unlike PBE, which is more likely to distribute the electron around the sample as a way to reduce the energy as much as possible. The results from the PBE0 calculations are shown in Figure 2-38 and Figure 2-39, for the excess electron and the sodium-containing IL respectively. A lower isocontour ( $0.005 \text{ e}/\text{\AA}^3$  instead of  $0.02 \text{ e}/\text{\AA}^3$ ) for the excess electron, as shown in Figure 2-40.

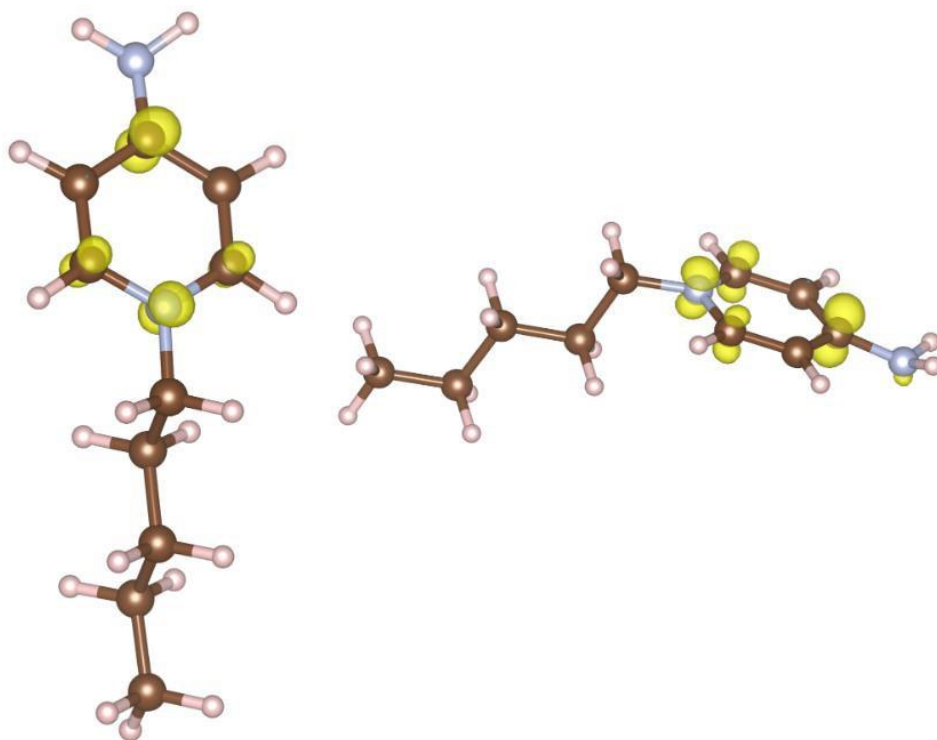


**Figure 2-38**-1-pentyl-4-aminopyridine cation with an excess electron at the PBE0 level. The left image presents a top-down view, while the right is a side-on view. Positive spin density is denoted in yellow, while negative spin is blue. Isosurfaces are drawn at  $0.02 \text{ e}/\text{\AA}^3$ .

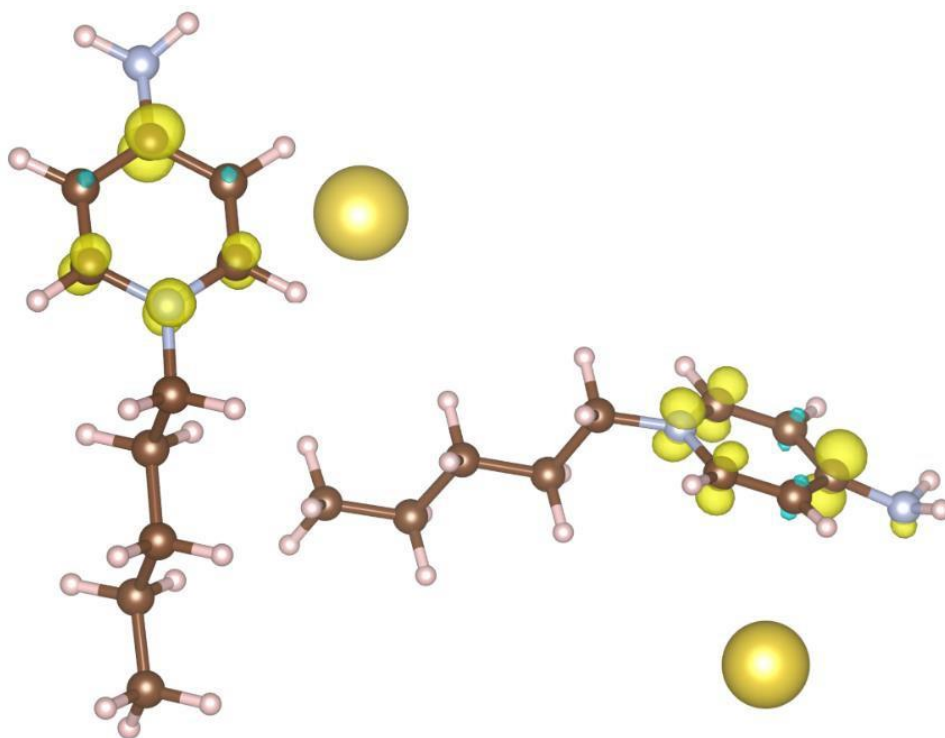


**Figure 2-39**-1-pentyl-4-aminopyridine cation with a sodium atom present at the PBE0 level. The left image presents a top-down view, while the right is a side-on view. Positive spin density is denoted in yellow, while negative spin is blue. Isosurfaces are drawn at  $0.02 \text{ e}/\text{\AA}^3$ .

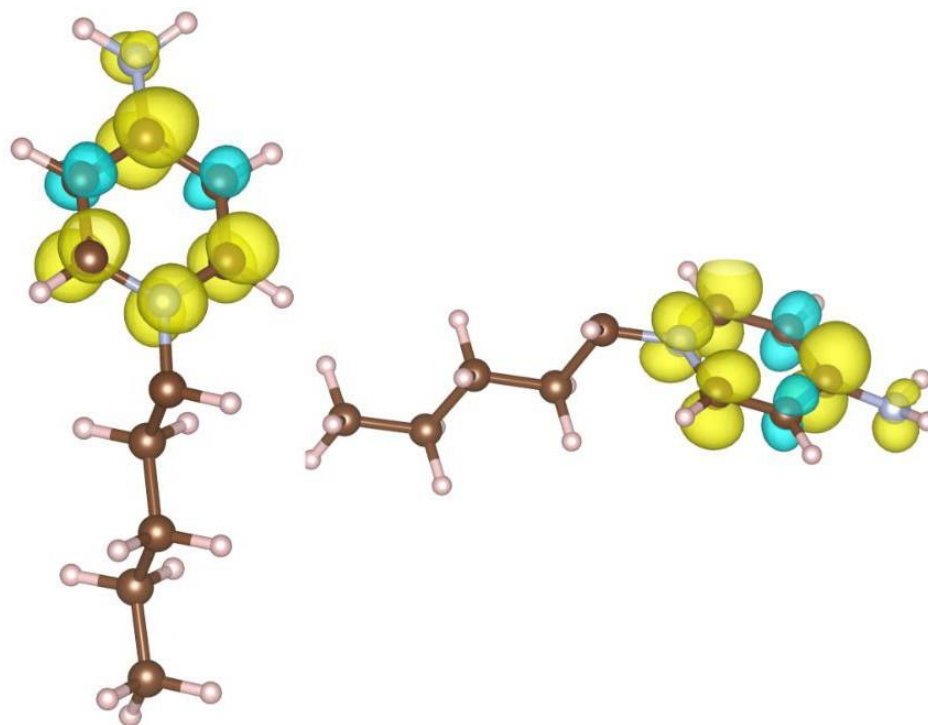


**Figure 2-40**-cation with an excess electron at the PBE0 level. The left image presents a top-down view, while the right is a side-on view. Positive spin density is denoted in yellow, while negative spin is blue. Isosurfaces are drawn at  $0.005 \text{ e}/\text{\AA}^3$ .

The predicted density of states or PDOS as it is more commonly referred to can indicate the presence of an unpaired electron in the system. PDOS of the neutral IL is shown in Figure 2-41, in the presence of an excess electron in Figure 2-42 and in the presence of a sodium atom in Figure 2-43. From the previous calculations it is observed that the electron is located in the conjugated aromatic ring; as electrons are a spin-active species PDOS can locate it in the system. In the neutral IL the spin lies across the whole system as no excess spin is located, hence the body of the IL is a somewhat degenerate species.

Upon the addition of an excess electron or a sodium atom the first noticeable change in the PDOS data is that the symmetry across the x-axis is no longer present. This indicates that the additional electron that locates on the organic ring will alter the exchange-correlation effects of the ring. A slight magnetic behaviour is to be expected as a result of this shift between the positive and negative axis due to the unpaired electron. This correlates with what has been observed within the NMR and EPR spectroscopic studies such that a broadening and an unpaired electron has been observed respectively.

In the excess electron ionic liquid environment, Figure 2-42, additional states are present in the spin-up channel at 3.5 eV that come from the localisation of the excess electron in the outermost p-orbitals of the carbon and nitrogen of the organic ring. A similar effect can be seen in the IL and sodium atom environment, Figure 2-43, where additional states, present also in the spin-up channel at 3.5 eV, correspond to carbon, nitrogen and sodium. This suggests that the unpaired electron of the sodium is delocalised along the organic ring, as seen in the earlier figures, but a small amount of spin still remains on the sodium suggesting the electron is not completely removed from the sodium atom. The data presented above, combined with experimental findings, suggest that the unpaired electron of sodium will delocalise and behave like a solvated electron in the presence of the IL.

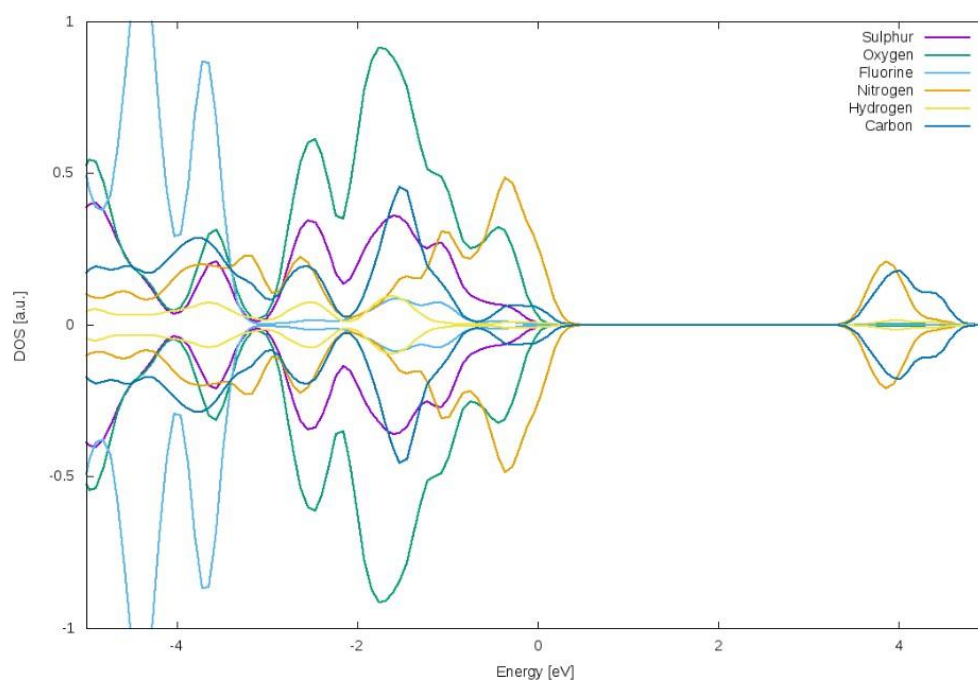


**Figure 2-41**-PDOS of the neutral structure at the PBE level. The positive axis and negative x-axis denote the spin-up and spin-down channels respectively.

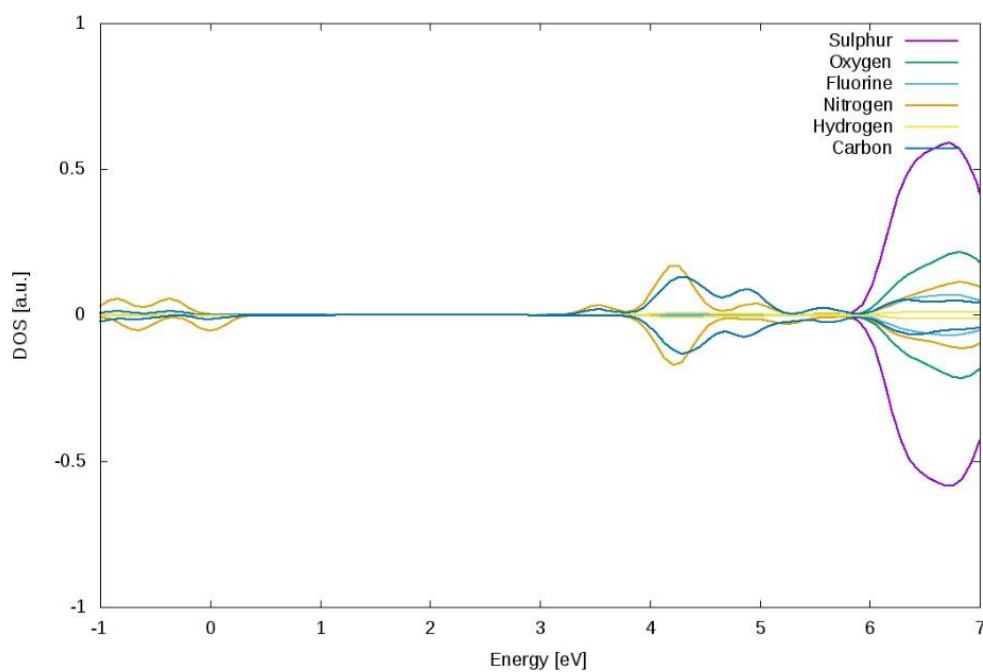


**Figure 2-42**-PDOS of IL containing an excess electron at the PBE0 level. The positive axis and negative x-axis denote the spin-up and spin-down channels respectively.



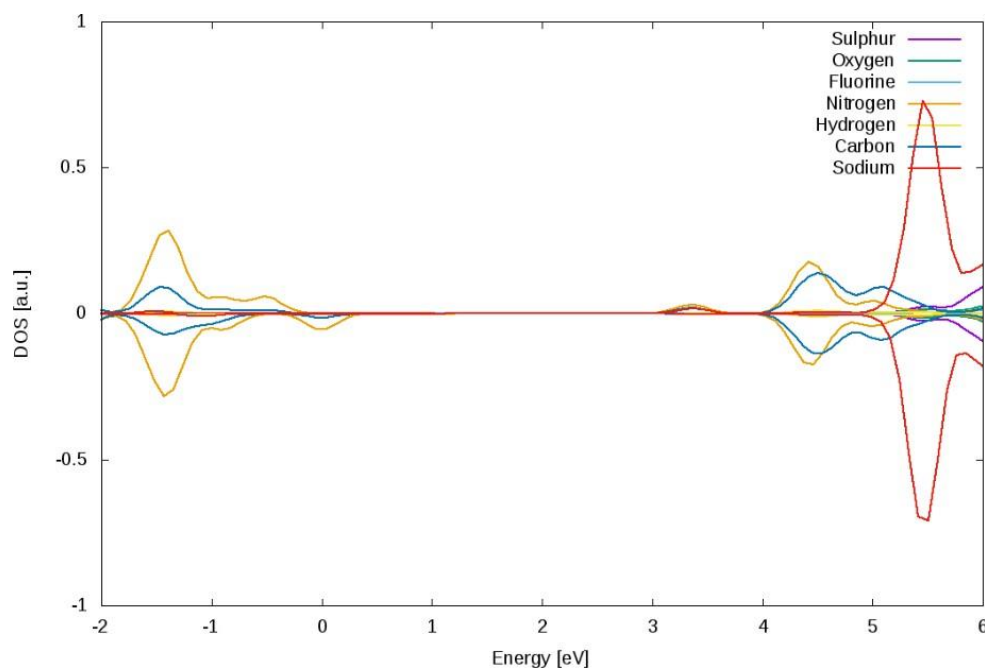


**Figure 2-43**-PDOS of IL containing a sodium atom at the PBE0 level. The positive axis and negative x-axis denote the spin-up and spin-down channels respectively.

## 2.2.6 Development of aliphatic analogues

As initially discussed, the aromaticity of the first amine functionality is determined to stabilise/accept the solvated electron, hence driving the alkali metal solvation. However, within any aromatic system, reduction is possible; so, in order to investigate the necessity of this aromaticity an aliphatic analogue was sought after for comparison.

### 2.2.6.1 Synthesis of aliphatic amine functionalised ionic liquids

The target cation, as shown in Figure 2-44, was inspired by the simple ethylenediamine motif, however, synthesis of such a species was not as simple as initially thought. Starting from N,N'-dimethylethylenediamine a protecting group must be employed on the primary amine functionality. There are multiple amine-protecting groups available; however, phthalic anhydride was selected for its primary amine selectivity and simple water by-product upon reaction as shown in Figure 2-45.

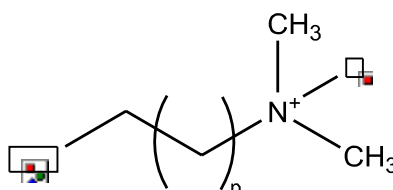


**Figure 2-44**-Target aliphatic cation for alkali metal solvation.

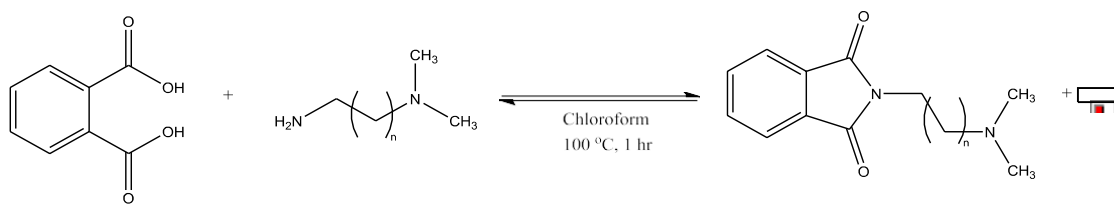


**Figure 2-45-**Phthalic anhydride protection of N,N'-dimethylethylenediamine.

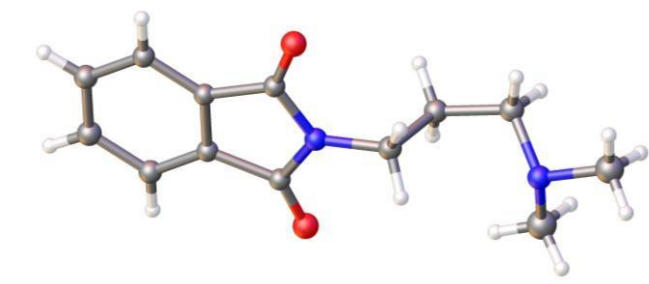


**Figure 2-46-** Single crystal diffraction determined structure of phthalic anhydride protected N,N'-dimethylethylenediamine.

The mono-protected diamine is then alkylated with an iodoalkane (C<sub>1</sub>-C<sub>6</sub>) in the minimum amount of acetone solvent, as shown in Figure 2-47 that then both forms and precipitates the protected salt product. The de-protection step as shown in Figure 2-48 was initially very successful with precipitation of white foam like by-product however; complete separation of the product and by-product is difficult and requires multiple filtrations throughout the reaction. Upon collection of the final de-protected product, the yield is low due to the multiple separations as discussed.

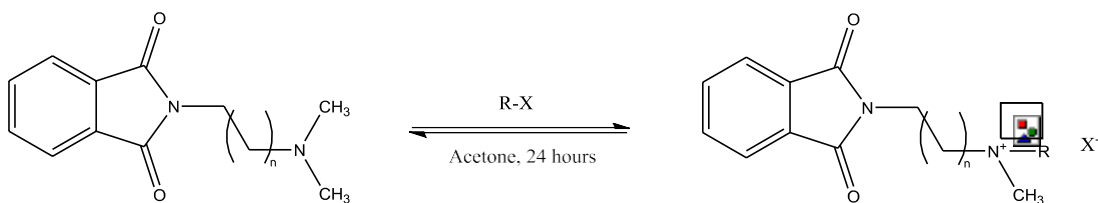


**Figure 2-47-**Alkylation of Phthalic anhydride protected N,N'-dimethylethylenediamine.

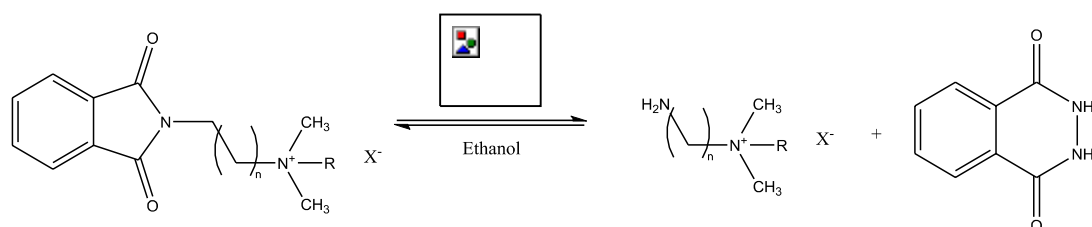


**Figure 2-48-**Deprotection of Alkylated Phthalic anhydride protected N,N'-dimethylethylenediamine.

The de-protected halide salt of the desired cation is then mixed with Li[NTf<sub>2</sub>]; commonly this results in a phase separation with the bistriflamide anion, which is well known for its hydrophobicity. However, this was not observed within this metathesis; instead, a homogenous water soluble ionic liquid was present hence this conventional method was unsuccessful and even with use of multiple organic extractants such as dichloromethane the ionic liquid remained within the water layer.

The most effective method of separation was found to comprise of the initial formation of a saturated solution of Li[NTf<sub>2</sub>] in water and addition of the IL halide salt and mixing. The solution is then evaporated to dryness and placed in to dry acetonitrile consequently precipitating the lithium halide salt; however, the product continues to have phthalic anhydride impurities that subsequent washes with organic solvents fail to remove.

#### **2.2.6.2 Testing of aliphatic amine functionalised ionic liquids**

Due to the low yielding synthesis of the aliphatic amine functionalised ionic liquid only an observational test could be carried out. In an identical procedure to that employed on the 1-alkyl-4-aminopyridinium bistriflamide system. Upon the addition of molten sodium, no blue colour was observed. The molten sodium appeared as smooth surfaced globules that appear to have no interaction with the ionic liquid. No solvation was observed upon the surface of the sodium metal. It is noteworthy that the cations with amino-pendants, shown in figure. 2-44, would have less acidic N-Hs compared to aminopyridinium cations.

18-crown-6 was added to the solution in an attempt to promote solvation of the sodium metal, however, no solvation was observed. This may partially be due to the amine and crown ether interacting as will be discussed in 2.2.7.

#### **2.2.7 Crown ether interactions and alkali metal solvation**

Crown ethers have previously been utilised for synthesis of Zintl anions by Fässler *et al.* following the procedure listed below:<sup>[15]</sup>

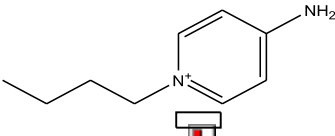
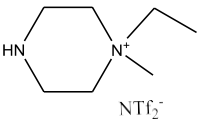
- (1) Crown ether is melted at 40 °C and potassium metal added.
- (2) Deep blue solution formed over several hours.
- (3) Elemental lead added to form a deep green solution.
- (4) Ethylenediamine used to extract products which crystallised after several weeks

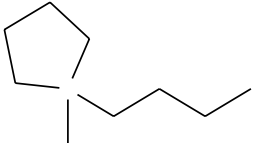
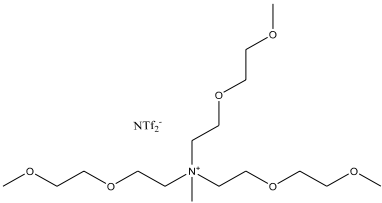
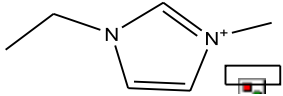
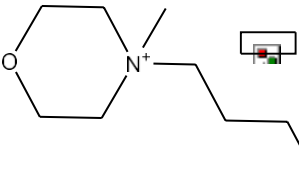
This vivid blue colour observed by Fässler and co-workers although not explicitly termed to be a solution of solvated electrons, heavily indicates that potassium metal dissolved. Utilising this as a method of reduction, it was seen as a good screening technique for this work's IL stability to solvated electrons. The general methodology was as follows:

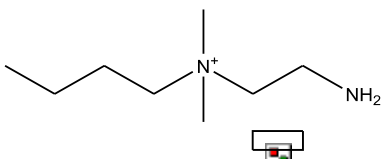
- (1) Crown ether is melted at 40 °C and potassium metal added.
- (2) Deep blue solution formed over several hours.
- (3) Dry ionic liquid is added under a flow of nitrogen
- (4) Observations made
- (5) Sample of IL is extracted, quenched and monitored by NMR spectroscopy

A variety of ionic liquids were screened for stability after exposure to 18-crown-6 and potassium solutions; upon addition to the blue solutions, in all cases the colour disappeared and samples were taken; NMR analysis showed that decomposition of all of the ionic liquids tested except 1-pentyl-4-aminopyridinium bistriflamide. A detailed description of observations and NMR analysis is listed in Table 2-2.

**Table 2-2-**Reduction screening experiments with 18-crown-6 and elemental potassium.

Ionic Liquid	Solution components	Observations
<p>1-butyl-4-aminopyridinium bistriflamide</p> 	<p>18-crown-6 = 0.56 g Potassium= 70.8 mg IL= 0.25 g</p>	<p>Potassium and 18-crown-6 heated and stirred at 52 °C forming a deep blue solution. IL added and blue colour disappears immediately. NMR <sup>1</sup>H analysis showed IL is intact. Single crystal extracted KNTf<sub>2</sub>·18-crown-6 complex.</p>
<p>1-ethyl-1-methylpiperazinium bistriflamide</p> 	<p>18-crown-6 = 0.50 g Potassium= 54.6 mg IL= 0.12 g</p>	<p>Potassium and 18-crown-6 heated and stirred at 52 °C forming a deep blue solution. IL added and the solution becomes white then yellow and eventually black. NMR <sup>1</sup>H and <sup>19</sup>F analysis showed IL is no longer intact.</p>

<p>1-Butyl-1-methylpyrrolidinium bistriflamide</p> 	<p>18-crown-6 = 0.50 g Potassium = 85 mg IL = 0.31 g</p>	<p>Potassium and 18-crown-6 heated and stirred at 72 °C forming a deep blue solution. IL added and the blue colour disappeared immediately then forming a yellow paste. NMR <math>^1\text{H}</math> and <math>^{19}\text{F}</math> analysis showed IL is no longer intact.</p>
<p>1-methyl-1-tri(diethyleneglycol)ammonium bistriflamide</p> 	<p>18-crown-6 = 0.50 g Potassium = 94 mg IL = 0.30 g</p>	<p>Potassium and 18-crown-6 heated and stirred at 72 °C forming a deep blue solution. IL added and the blue colour disappeared immediately then forming an orange-yellow paste. NMR <math>^1\text{H}</math> and <math>^{19}\text{F}</math> analysis showed IL is no longer intact. Crystals extracted and found to be hydrated <math>\text{KNTf}_2 \cdot 18\text{-crown-6}</math> complex.</p>
<p>1-Butyl-3-methylimidazolium bistriflamide</p> 	<p>18-crown-6 = 0.50 g Potassium = 84 mg IL = 0.54 g</p>	<p>Potassium and 18-crown-6 heated and stirred at 72 °C forming a deep blue solution. IL added and the blue colour disappeared immediately then forming dark black solution. NMR <math>^1\text{H}</math> and <math>^{19}\text{F}</math> analysis showed IL is no longer intact.</p>
<p>Trihexyltetradecylphosphonium bistriflamide [P<sub>66614</sub>][NTf<sub>2</sub>]</p>	<p>18-crown-6 = 0.50 g Potassium = 43 mg IL = 0.305 g</p>	<p>Potassium and 18-crown-6 heated and stirred at 52 °C forming a deep blue solution. IL added and the blue colour disappeared immediately then forming dark solution. NMR <math>^1\text{H}</math> and <math>^{19}\text{F}</math> analysis showed IL is no longer intact. Crystals extracted from NMR tube and found to be hydrated <math>\text{KNTf}_2 \cdot 18\text{-crown-6}</math> complex.</p>
<p>1-Butyl-1-methylmorpholinium bistriflamide</p> 	<p>18-crown-6 = 0.77 g Potassium = 43 mg IL = 0.49 g</p>	<p>Potassium and 18-crown-6 heated and stirred at 52 °C forming a deep blue solution. IL added and the blue colour disappeared immediately then forming dark solution. NMR <math>^1\text{H}</math> and <math>^{19}\text{F}</math> analysis showed IL is no longer intact.</p>

<p>N,N'-dimethylbutyl(2-aminoethyl)ammonium bistriflamide</p> 	<p>18-crown-6= 0.50 g Potassium= 33.7 mg IL= 0.14 g</p>	<p>Potassium and 18-crown-6 heated and stirred at 52 °C forming a deep blue solution. IL added and the blue colour disappeared immediately. NMR <sup>1</sup>H and <sup>19</sup>F analysis showed IL is no longer intact.</p>
---	---	--

The hydrated KNTf<sub>2</sub>·18-crown-6 complex structure is shown in Figure 2-49. The potassium atom is bound in an 18-crown-6 cavity with two water molecules in the plane perpendicular to the crown ether forming an overall octahedral geometry. Above the crown ether potassium motif, a second crown ether molecule is present and hydrogen bonded to the mentioned coordinating water molecules on the potassium cation. The bistriflamide anion acts as a bystander with little interaction to the cationic complex. The central potassium as mentioned is bound to two water molecules with bond distances of 2.699 Å and 2.723 Å. The central potassium, cation is also bound to the 18-crown-6 with bond distances ranging from 2.776 Å - 2.856 Å from the central cation to the etheryl oxygens. The neighbouring 18-crown-6 lies at its closest point 4.415 Å from the potassium cation.

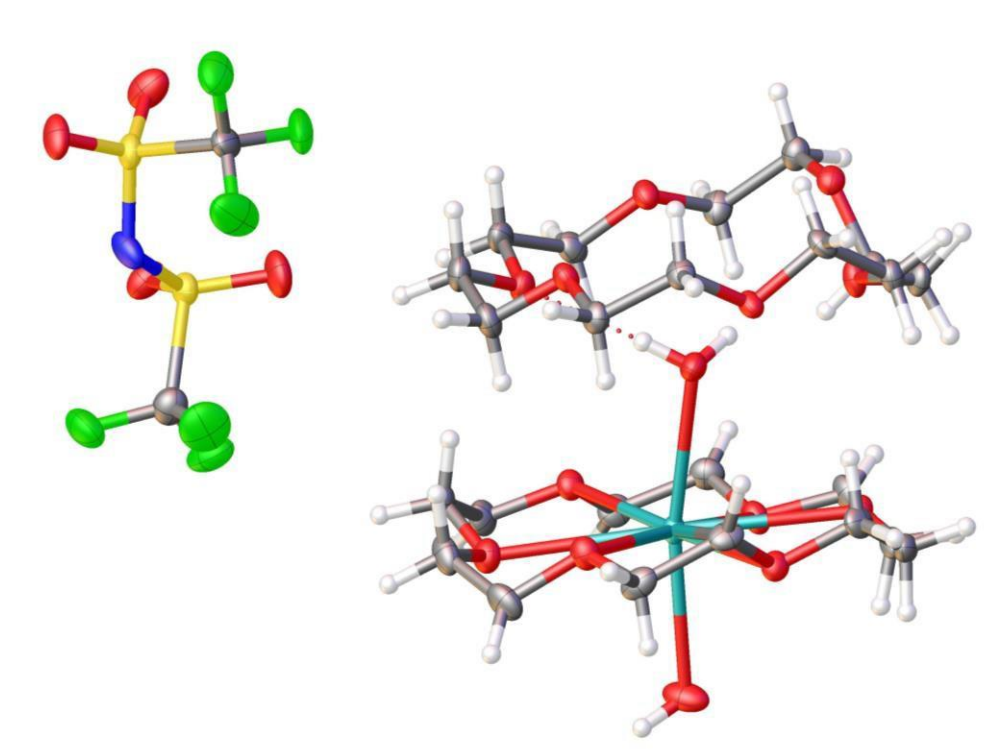


**Figure 2-49**-Single crystal diffraction determined structure hydrated KNTf<sub>2</sub>· 18-crown-6 complex.

A similar cationic motif has been reported previously in literature; Nasri *et. al.* reported a cation iron porphyrin that crystallised with the  $[K(C_{12}H_{24}O_6)(H_2O)_2]^+$  cation and trifluoromethanesulphonate.<sup>144</sup> The somewhat surprising disappearance of the solvated electrons with the addition of 1-butyl-4-aminopyridinium bistriflamide lead too many questions regarding the decomposition of solvated electrons with the addition of an ionic liquid that is suspected to form solvated electrons.

A combination of addition methods was studied and some interesting results were found as shown in Figure 2-50. Test 1, a repetition of the screening study and the same outcome was observed in that upon addition of the IL to the potassium -18-crown-6 solutions the blue colour disappeared. Test 2 was an inversion of test 1 with the IL-potassium solution formed and the 18-crown-6 added; again, the blue colour disappeared. Finally, in test 3 the crown ether and ionic liquid were pre-mixed and potassium added resulting in no solvation occurring. This peculiar result raised many questions regarding the solvation mechanism and stability of the solvated electrons and interactions that each solvent was have with one another.

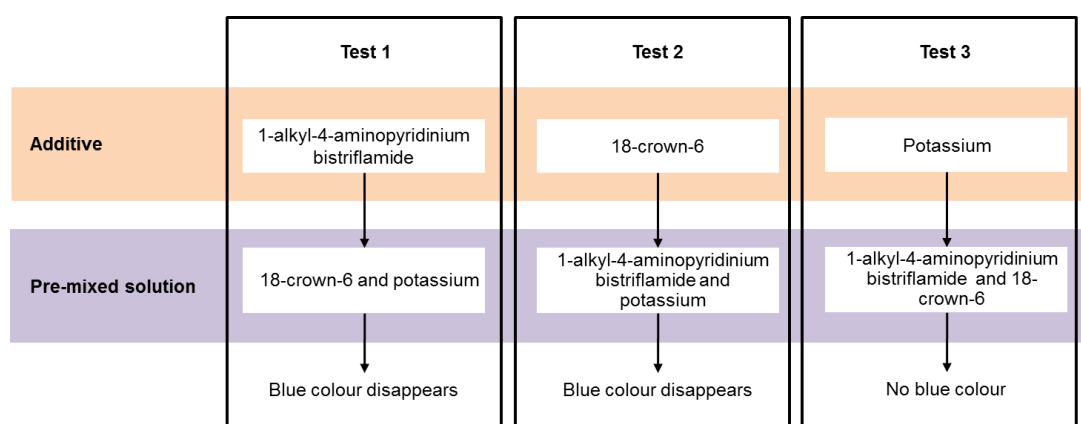


**Figure 2-50**-Addition combinations of 1-pentyl-4-aminopyridinium bistriflamide and potassium-18-crown-6 solutions.

In the solid state, it was found that the neat IL's primary amine functionality interacts with the oxygens on the bistriflamide anion. Can the amine interact with the etheryl oxygens in the crown ether? Crystals extracted from the combination addition study found exactly this. As shown in Figure 2-51 and Figure 2-52, the amine functionality and C1 carbon on the alkyl chain strongly interacts with the crown ether, hence any drive for solvation of the alkali metal is inhibited.

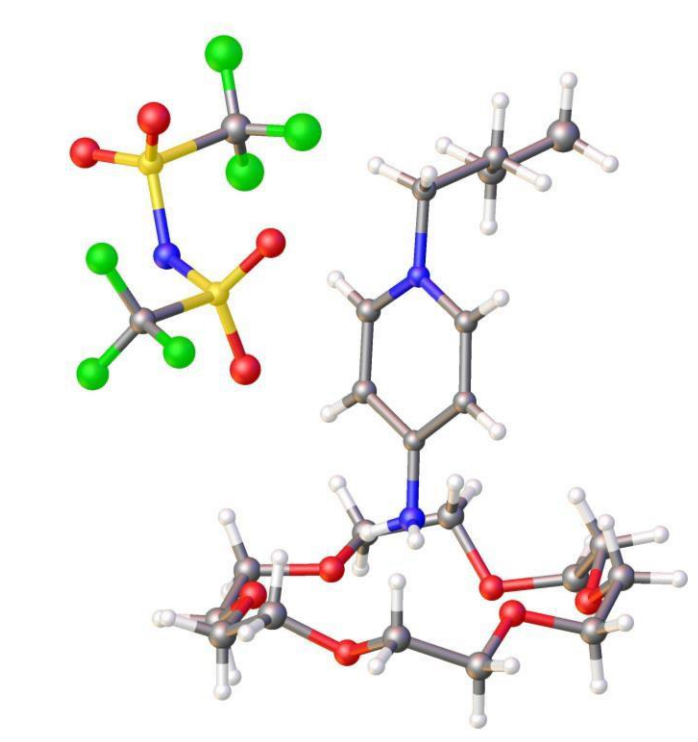


**Figure 2-51-** Single crystal diffraction determined structure of 1-butyl-4-aminopyridinium bistriflamide and 18-crown-6.

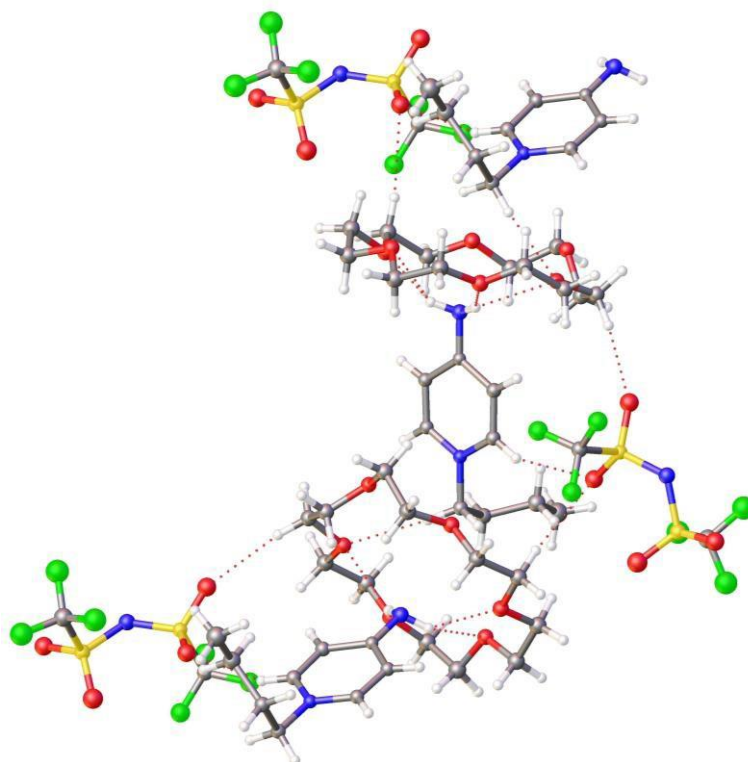


**Figure 2-52-** Single crystal diffraction determined structure of 1-butyl-4-aminopyridinium bistriflamide and 18-crown-6.



Looking further at the packing of the structure it is observed that each crown ether molecule interacts with a 4-amino functionality of a cation and the CH<sub>2</sub> on the C1 position of the alkyl chain of another position. The 4- position primary amine lies at its closest point 2.047 Å from the etheryl oxygen. Furthermore, the C1 position of the alkyl chain lays 2.704 Å from the 18-crown-6.

A screening experiment of similar motifs to the 1-alkyl-4-aminopyridinium ionic liquid was added to the 18-crown-6 and crystals were grown to probe possible interactions. As shown in Figure 2-53 and, Figure 2-54 and Figure 2-55, it was found for the 2- and 4- aminopyridine that the *meta* and *para* amine functionalities interact directly with etheryl groups of the 18-crown-6. Per 18-crown-6 molecule two molecules of the aminopyridine cluster above and below the planar cyclic crown ether in both 2- and 4- amine positions. The variation in amine position on the ring alters the orientation between the crown ethers in packing; in the 2-aminopyridine structure (Figure 2-53) the crown ethers orientate in perpendicular rows, whereas in the 4-aminopyridine structure (Figure 2-55) the crown ethers orientate in parallel layers.

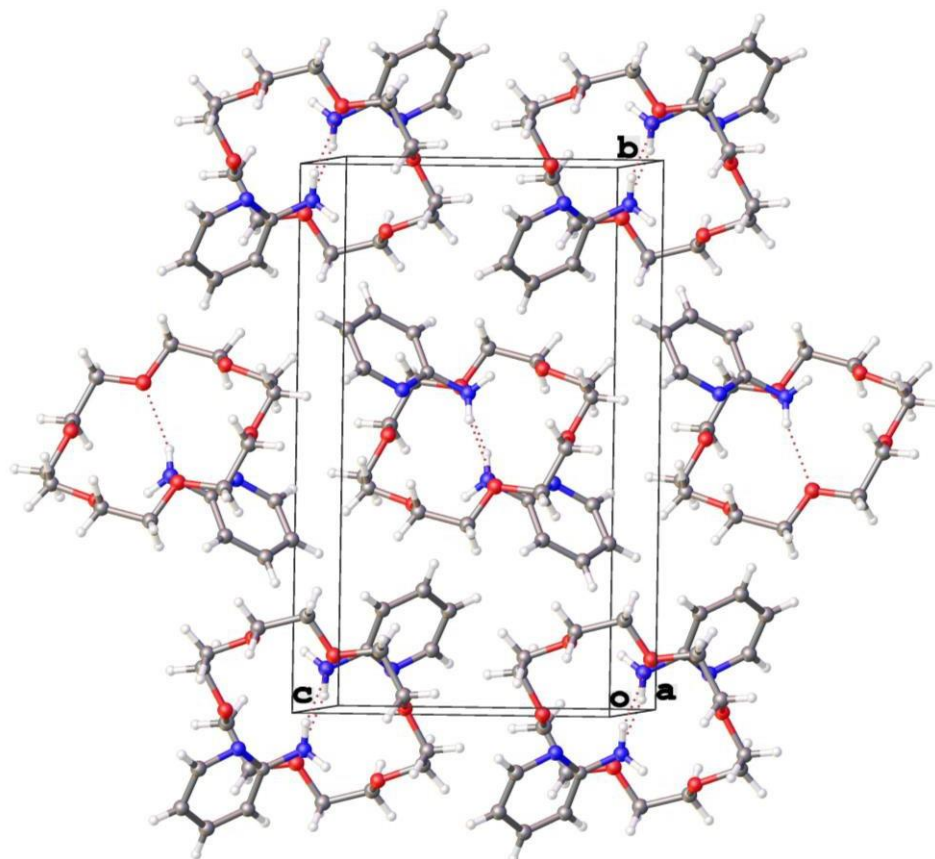


**Figure 2-53**-Single crystal determined structure of 2-aminopyridine and 18-crown-6.

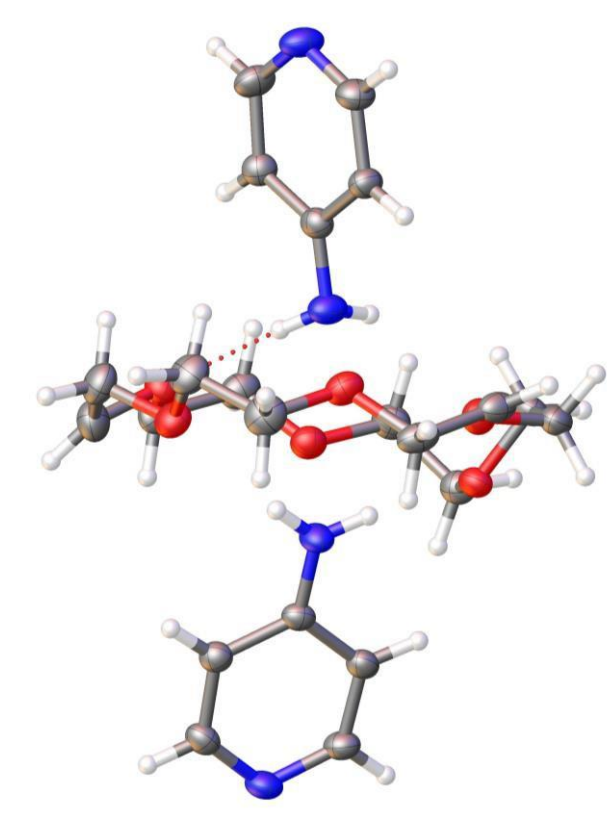


**Figure 2-54-** Single crystal determined structure of 4-aminopyridine and 18-crown-6.

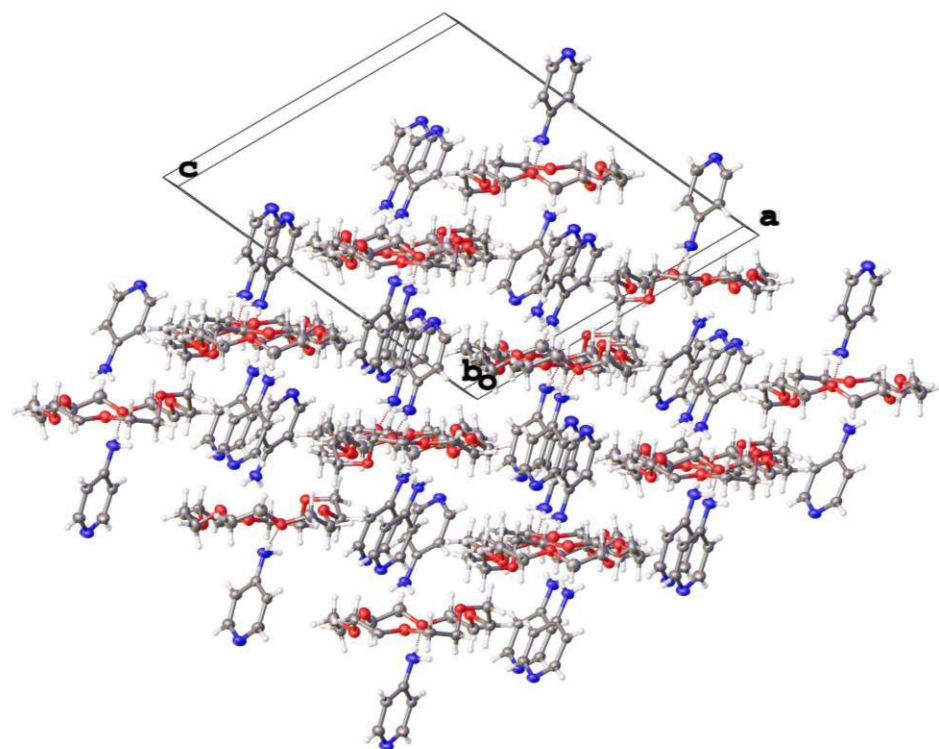


**Figure 2-55-** Single crystal determined structure of 4-aminopyridine and 18-crown-6.

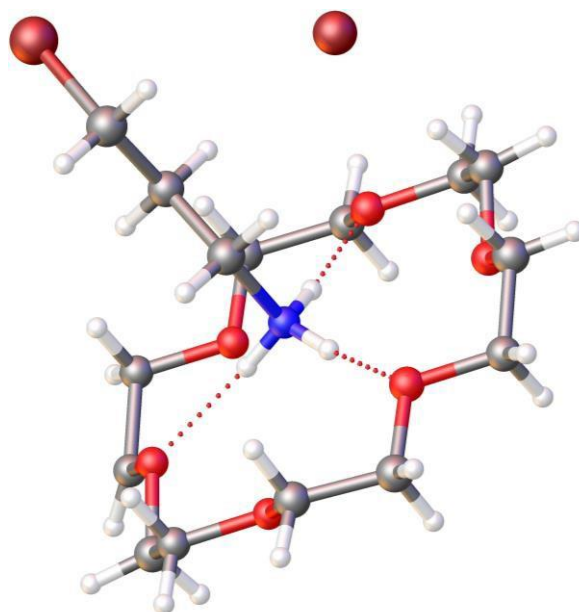


**Figure 2-56-** Single crystal determined structure of 18-crown-6 of bromopropylamine hydrobromide.

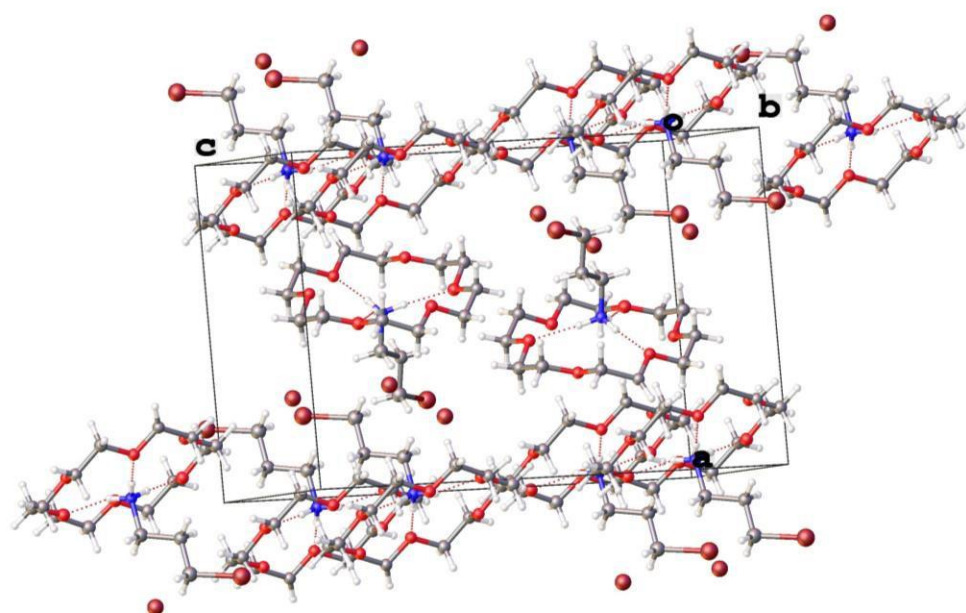


**Figure 2-57-** Single crystal determined structure of 18-crown-6 of 4-bromopropylamine hydrobromide.

The final substrate study investigates the interaction of a zwitterionic compound, 4-bromopropylamine hydrobromide and with 18-crown-6. The zwitterion nature of this compound means that the primary amine functionality is protonated and as a result the hydrogen bonding interaction of the amine protons and the oxygens of the crown ether are greater. As listed in Table 2-3, the hydrogen bonding interactions of the

zwitterionic compound is greater than the neutral aminopyridine molecules; the ionic liquid lies in the midpoint of the neutral and ionic substrates highlighting the induced acidity of the 4-amino functionality once the pyridyl ring is quarternised.

**Table 2-3-** Hydrogen bonding distance in the amine-18-crown-6 interaction study.

Substrate	Shortest hydrogen bonding distance (Å)
4-aminopyridine	2.168
2-aminopyridine	2.191
4-bromopropylamine hydrobromide	1.948
1-butyl-4-aminopyridinium bistriflamide	2.047

## 2.2.8 Reactions with elemental lead

Taking a more classical approach to Zintl phase synthesis an ampoule reaction was utilised for lead-based reductions. One of the first reported Zintl phases was  $\text{Na}_4\text{Pb}_9$ . Utilising a classical method, elemental sodium, and elemental lead and 1-pentyl-4-aminopyridinium bistriflamide was sealed in a glass ampoule under vacuum and heated for 2 weeks at 110 °C and slowly cooled. As shown in Figure 2-58 the resultant reaction mixture was a blue / black paste. Upon opening the ampoule, colourless block-type crystals were collected and measured on the single crystal diffractometer and were identified as sodium bistriflamide.

Previous reports of crystal structures of this compound by Matsumoto and co-workers found that each sodium atom is coordinated to 6 oxygen atoms and one nitrogen atom as shown in Figure 2-59.<sup>145</sup> Within the sodium bistriflamide crystals obtained in the lead reduction experiment, these were found to be merohedral twins but resulted in an identical structure to that reported by Matsumoto and co-workers.

The discovery of sodium bistriflamide in the ampoule reaction indicates an oxidative process has occurred such that the sodium atom has oxidised from  $\text{Na}(0)$  to  $\text{Na}(I)$ . Throughout this study it has been believed that the cation is the acceptor of the solvated electrons that form as consequence of the sodium solvation; the sodium cation, however, has not been as simple to identify the movement and resultant state. Computational studies were unable to account for the expected movement and coordination of the sodium atom hence the identification of this structure is vital. The coordination of the Na cation to the oxygen species corresponds the  $^{23}\text{Na}$  NMR spectra collected preciously that is similar in chemical shift to [2,2,2]-cryptand complexed  $\text{Na}^+$ .

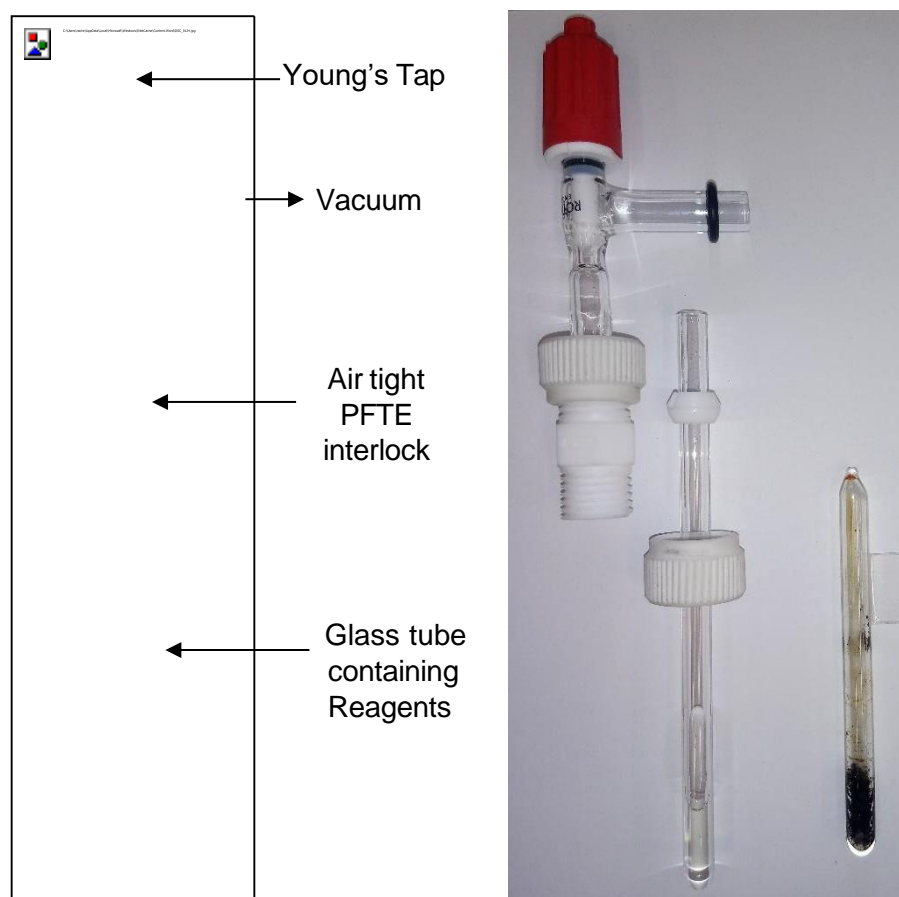


**Figure 2-58**-Apparatus used in sodium-IL and lead reduction experiments. Right apparatus before sodium and lead addition and left sealed ampoule after reaction.

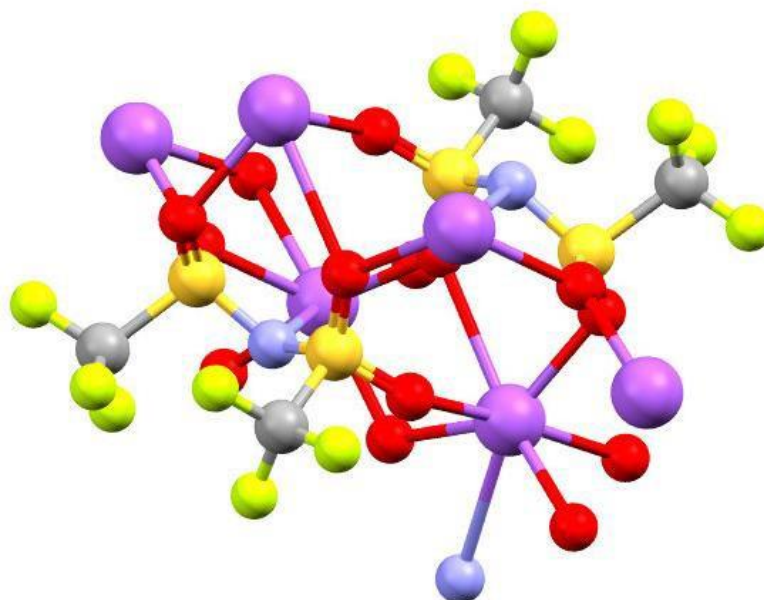


**Figure 2-59**-Previously reported structure for sodium bistriflamide by Matsumoto and co-workers<sup>145</sup>

Unfortunately, no other species were collected from the reaction mixture hence the outcome of the reaction in regards to the lead and cation of the IL is unknown. It is

suspected that analogously to the lead anions seen in Zintl phases the anion is stabilised by ammonia or as in this case it would be stabilised by the amine functionality of the IL cation. In future further investigations with greater control in regards to cooling *etc.* this aspect would be further investigated.

### 2.2.9 Silver nitrate reduction tests

An experiment investigating the reduction of Ag(I) to Ag(0) was carried out. Firstly a control experiment with the 18-crown-6 (0.50 g) and potassium metal added to form a deep blue solution to which silver nitrate was added. A brown precipitate formed instantly and is believed to be Ag(0). The experiment was then repeated with 1-pentyl-4-amnopyridine and elemental potassium; the blue solution that formed had AgNO<sub>3</sub> added. Upon addition of the AgNO<sub>3</sub>, the blue colour disappeared and a brown precipitate formed in a near identical method to the crown ether control experiment. As a final control, the silver nitrate was added to the ionic liquid and 18-crown-6 without the addition of potassium metal; the solutions dissolved the silver nitrate and precipitation of a brown solid only occurred after several hours of stirring, hence confirming that the immediate precipitation in the previous solutions occurred due to the reducing ability of the alkali metal solvated.

### 2.2.10 Birch Reduction Tests

As discussed in 2.1.2, Birch reductions are one of the most popular applications of solvated electrons in general chemistry. Birch reductions are single electron reductions most commonly of aromatic species in which solvated electrons attack the aromatic ring to form a radical species as shown in Figure 2-60. The radical species then attacks a proton source (most commonly an alcohol) to form the reduced product.

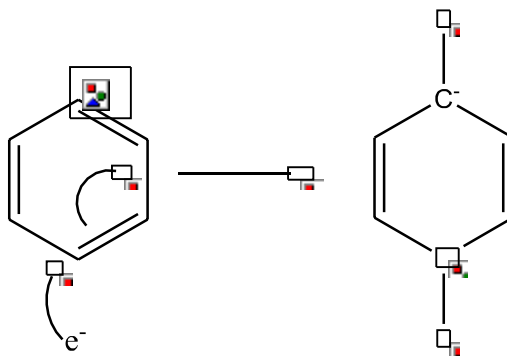


Figure 2-60-Radical formation in Birch reductions of benzene.

1-pentyl-4-aminopyridinium bistriflamide and sodium metal were melted together generating a deep blue solution (ca. 4 g); to this solution benzene was added to the contained and the reaction vessel closed. Upon addition of the benzene, a slight decolourisation of the blue solution occurred. The benzene-IL mixture was allowed to stir for 1 hour; a sample of the reaction mixture was then taken, and ethanol added to the sample as a proton source. A portion of water was added to quench the solution completely and then a portion of diethyl ether was added to the mixture to extract possible reaction products. The ether was then passed through a silica plug to remove water impurities and the sample was directly measured for NMR without rotary evaporation.  $^1\text{H}$  NMR analysis showed no reduction had occurred.

The reason behind this failure to reduce the benzene substrate may be due to coordination of the sodium cation. Conventional Birch reductions occur more sluggishly in the presence of cryptand compounds. A computational study by Rzepa and co-workers found that the sodium cation interacts and complexes to the anionic intermediate, hence directing one single reduction product over the other.<sup>146</sup> The complex is comprised of  $[\text{Na}(\text{NH}_3)_3]^+$  cation that coordinates to the cyclohexadiene anion radical hence being crucial in the transition step and stabilisation of the radical before the addition of the proton source.

### 2.2.11 Chemical reduction tests

Further confirmation of the stability of the 1-alkyl-4-aminopyridinium bistriflamide was sought hence a series of conventional chemical reduction reactions were completed on the IL. If reduction occurs, it would be expected that multiple partial and full reduction products would be achieved as shown in Figure 2-61. The first of such reaction conditions utilised simple sodium borohydride in methanol for 72 hours. After 72 hours the reaction mixture was neutralised and the residual salt was removed with water.  $^1\text{H}$  NMR analysis of the final product as shown in Figure 2-62 indicates that no reduction has occurred.

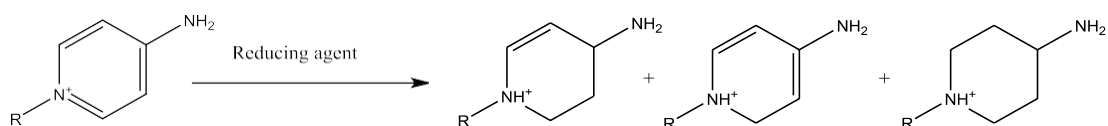
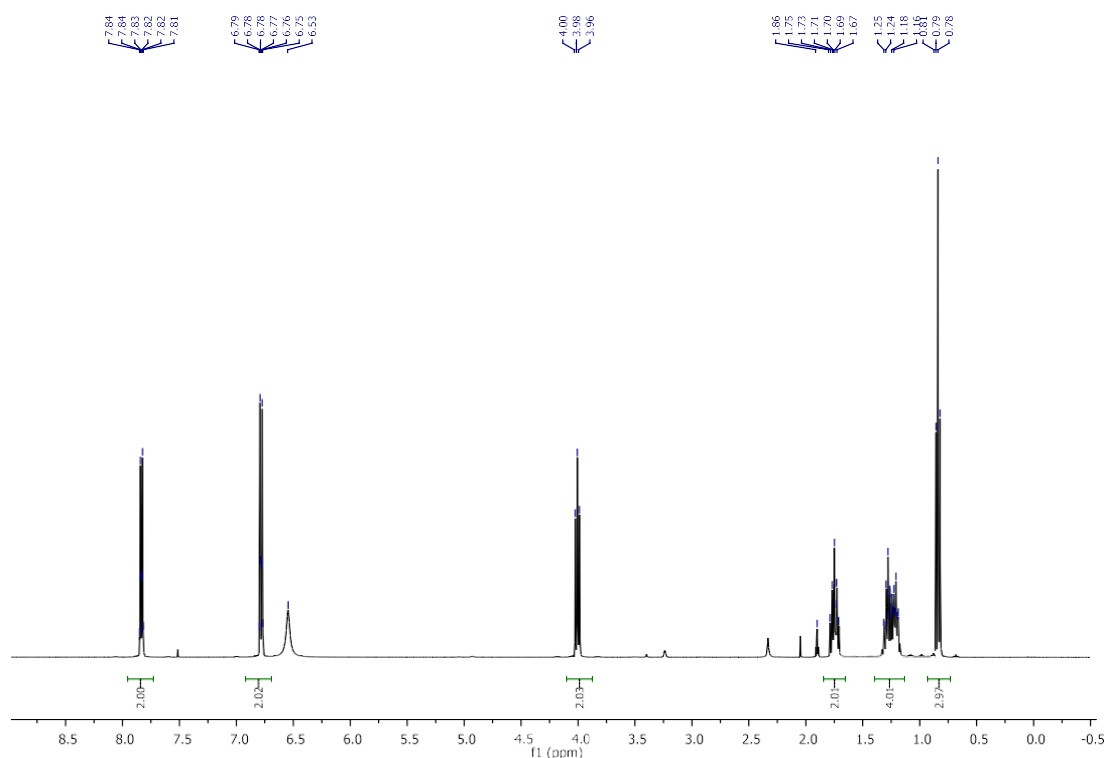


**Figure 2-61**-Reduction products of 1-alkyl-4-aminopyridinium bistriflamide.

To confirm that the methodology is robust the reaction was repeated with 1-butylpyridinium bistriflamide instead of the amine-functionalised IL. As shown in

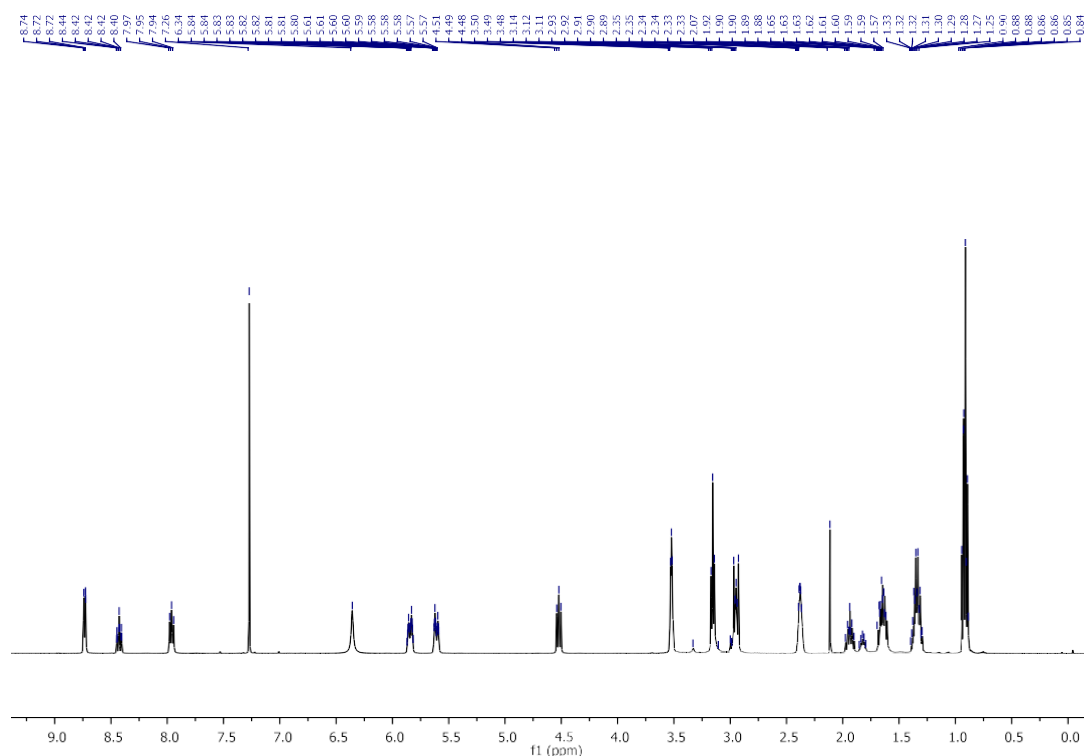


Figure 2-63 reduction occurs forming multiple partial and full reduction products. Again referring back to the 1-alkyl-4-aminopyridinium bistriflamide, a more durable reduction method was used; sodium borohydride in carboxylic media was applied to the IL in THF and was left to stir at room temperature for 48 hours.<sup>147</sup> Once again, after work-up no apparent reduction was observed *via* NMR analysis. The reaction was further repeated but under reflux conditions (65 °C) and again no reduction was observed.



**Figure 2-62**-<sup>1</sup>H NMR of 1-pentyl-4-aminopyridinium bistriflamide after undergoing a conventional NaBH<sub>4</sub> reduction reaction in methanol for 3 days. (*d*<sub>3</sub>-acetonitrile).





**Figure 2-63**  $^1\text{H}$  NMR of 1-butylpyridinium bistriflamide after undergoing a conventional  $\text{NaBH}_4$  reduction reaction in methanol for 3 days. ( $d$ -chloroform).

## 2.3 Conclusions

In this study a primary amine-functionalised ionic liquid has been designed synthesised and successfully applied to alkali metal solvation with a specific focus on sodium. The solvation mechanism has been studied *via* multinuclear NMR, UV/Vis, and infrared spectroscopy; along with a systematic computational study. Each analysis suggests the formation of solvated electrons as a consequence of alkali metal solvation; with the formation of a deep blue colour and induced paramagnetism observed. Furthermore, the IL was found to be stable after solvation and quenching, hence being a reusable IL.

A series of reduction studies were completed, investigating the behaviour of the ionic liquid in reducing conditions such as crown ethers and alkali metals and classical sodium borohydride reductions with the IL found to be stable in all environments tested. Studies investigating the use of crown ethers found that the amine functionality interacts that strongly with the etheryl oxygens of the crown, hence they cannot be used in conjunction with the IL for solvation.

The IL has been applied to both inorganic and organic reductions with mixed success; organic Birch reductions were attempted with benzene; however, no reduction was observed. This failure to reduce benzene is believed to be due to the

unavailability of the sodium cation to stabilise the transition state. In regards to inorganic reductions, silver nitrate tests found that the silver was reduced from Ag(I) to Ag(0). In a more controlled reaction with elemental lead an oxidation product of sodium bistriflamide was successfully isolated, although the reduction product was not isolated or determined the presence of a Na(I) species indicates an electron is lost and solvation has occurred. Furthermore, it confirmed the suggestion from  $^{23}\text{Na}$  NMR analysis that the Na(I) coordinates with the bistriflamide anion.

## 2.4 Future work

In future, there is significant scope in monitoring the stability of this IL under radiative and flash photolytic techniques. Within sodium and potassium solvation experiments the ionic liquid has been found to be stable, hence making it a prime candidate for these studies with further scope for atomistic simulations to further confirm the behaviour of the sodium cation formed.

In regards to application of this new method of sodium solvation to reduction chemistry it would be sought to repeat the Zintl-type reduction reactions with a variety of elements including lead, tin, antimony and chalcogenides in an attempt to replicate the anionic clusters formed by Ruck and co-workers.<sup>40</sup> Using more controlled cooling methods and post reaction treatment with liquid ammonia or ethylene diamine may allow for extraction and growth of the suspected cluster products formed.

Further to this, the addition of organic solvents/reagent such as ethene, butene *etc.* is of merit for application to polymerisations and other radical initiated reactions.

## 2.5 Experimental methods

### 2.5.1 Materials

4-aminopyridine, 2-aminopyridine, iodoethane, bromobutane, iodopentane, iodoheptane were obtained from Alfa Aesar in 99 % purity. N,N'-dimethylethylamine, N,N'-dimethylpropylamine, phthalic anhydride and deuterated solvents were acquired from Sigma Aldrich. Lithium bistriflamide was obtained from 3M PURITY

All solvents were acquired from Honeywell at 99.9 % purity.

## 2.5.2 Nuclear magnetic resonance spectroscopy

Multinuclear NMR was used throughout this body of work. All NMR spectra were recorded on either a Bruker Advance DPX 400 MHz, or a Bruker Advance DPX 600 MHz spectrometer. The frequencies of the measurements are summarised below in **Table 4-21**. Samples which were liquid at room temperature were recorded using DMSO capillaries as an external deuterium lock to prevent the solvent affecting the equilibria present in the sample.

**Table 2-4-** Summary of the frequency of measurements used for each spectrometer.

Nuclei	Bruker Advance DPX 400 Frequency of Measurement (MHz)	Bruker Advance DPX 600 Frequency of Measurement (MHz)
$^1\text{H}$	400	600
$^{13}\text{C}$	75	150
$^{23}\text{Na}$	-	
$^{19}\text{F}$	282	-

Active Sodium/IL solutions were placed in a NMR tube under glovebox conditions along with a capillary containing NaCl (0.01 M) in deuterium oxide. All  $^{23}\text{Na}$  spectra were recorded on a Bruker Ascend 600 MHz NMR spectrometer.

**Evans Method:** Co-axial NMR tubes were utilized; the insert containing d6-benzene and tetramethylsilane. Electron solutions are generated as described in section 5.2 The external tube is initially filled with a non- activated IL a small amount of tetramethylsilane and the proton NMR is measured. The solvated electron containing the IL is then placed in the external tube with a small amount of tetramethylsilane and a second proton NMR is measured. The spectra are aligned using the TMS peak and the IL peaks are compared.

## 2.5.3 Electron paramagnetic resonance spectroscopy

All EPR measurements were carried out under the supervision of Dr Grace Morgan and Dr Anthony Fitzpatrick, University College Dublin. Generated electron/IL solutions were placed in a NMR tube under glove bag conditions. The sample was cooled to 77 K using liquid nitrogen. EPR data was collected using a Magnettech mS200 X-band EPR working at 9.381 GHz with magnetic field centred at 300 mT and a field sweep of 400 mT. Modulation amplitude of 0.5 mT was used in conjunction with a microwave power of 0.1 mW and a gain of 10.

## 2.5.4 UV/Vis spectroscopy

All spectra were measured on an Aligent Technologies Cary 60 UV/Vis spectrometer with a total range of 190 to 1100 nm using a 0.5 mm quartz cuvette sample holder.

## 2.5.5 Atomic adsorption spectroscopy

Standards- Prepared by QUB analytical services ASEP. 1 ppm and 2 ppm sodium chloride solutions in deionized water.

Sample Preparation- Sodium /IL solutions were prepared as described. To the samples ( $\approx 1$  g) a portion of dichloromethane (15 mL) and deionized water (15 mL) was added and solution shaken thoroughly. The solution was then acidified with Bistriflamidic acid and again was shaken thoroughly. The aqueous layer was then extracted and diluted appropriately to an estimated concentration below 2 ppm.

Measurements were carried out on a Perkin Elmer Analyst 100 atomic adsorption spectrometer; calibrated before use 5 measurements were taken per sample and averaged.

## 2.5.6 Synthesis of ionic liquids

### 2.5.6.1 Synthesis of aminopyridinium ionic liquids

#### 2.5.6.1.1 Synthesis of 1-alkyl-4-aminopyridinium halide

**General method:** 4-aminopyridine (5.31 mmol) was dissolved in the minimum amount of acetone (7.95 mL). To this solution, bromoalkane (5.37 mmol) was added dropwise to form a colourless solution. The reaction mixture was placed in a reaction tube, sealed and allowed to stir at 40°C overnight. The white precipitate formed was collected under vacuum filtration and was rinsed with a small amount of acetone (3 mL). The white powder collected and dried under vacuum. (80 °C, 24 hours)

**1-Butyl-4-aminopyridinium bromide:** White powder, 1.09 g, 4.72 mmol, 88.8%

$^1\text{H}$  NMR (300 MHz,  $\text{D}_2\text{O}$ )  $\delta$  7.99 (d,  $J$  = 6.3 Hz, 2H, Ar-H), 6.85 (d,  $J$  = 6.3 Hz, 2H, Ar-H), 4.13 (t,  $J$  = 7.2 Hz, 2H, ARN- $\text{CH}_2$ ), 1.90 – 1.67 (m, 2H, - $\text{CH}_2$ -), 1.30 (dq,  $J$  = 14.5, 7.3 Hz, 2H, - $\text{CH}_2$ - $\text{CH}_3$ ), 0.91 (t,  $J$  = 7.4 Hz, 3H,  $\text{CH}_3$ ).

**1-Ethyl-4-aminopyridinium bromide:** white powder, 0.577 g, 2.84 mmol, 53.4 %

$^1\text{H}$  NMR (300 MHz,  $\text{D}_2\text{O}$ )  $\delta$  8.00 (d,  $J$  = 5.7 Hz, 2H, Ar-H), 6.84 (d,  $J$  = 5.7 Hz, 2H, Ar-H), 4.16 (q,  $J$  = 7.3 Hz, 2H, Py- $\text{CH}_2$ ), 1.45 (t,  $J$  = 7.3 Hz, 3H,  $\text{CH}_3$ ).

**1-Pentyl-4-aminopyridinium bromide:** 4-aminopyridine (17.54 g, 187 mmol) was dissolved in the minimum amount of acetone (500 mL). To this solution, bromopentane (28.75 g, 190 mmol) was added dropwise to form a colourless solution. The reaction mixture was placed in a reaction tube, sealed and allowed to stir at 40 °C for 4 days. The white precipitate formed was collected under vacuum filtration and was rinsed with a small amount of acetone (50 mL). The white powder (38.6 g, 157 mmol, 84.2%) collected and dried under vacuum (80 °C, 24 hours)

$^1\text{H}$  NMR (300 MHz,  $\text{D}_2\text{O}$ )  $\delta$  7.94 (d,  $J$  = 6.6 Hz, 2H, Ar-H), 6.80 (d,  $J$  = 6.6 Hz, 2H, Ar-H), 4.08 (t,  $J$  = 7.0 Hz, 2H, ARN- $\text{CH}_2$ ), 1.91 – 1.66 (m, 2H, - $\text{CH}_2$ -), 1.25 (dd,  $J$  = 16.1, 9.2 Hz, 4H, - $\text{CH}_2$ -), 0.82 (t,  $J$  = 6.8 Hz, 3H,  $\text{CH}_3$ )

**1-Hexyl-4-aminopyridinium iodide:** 4-aminopyridine (5.0 g, 53 mmol) was dissolved in the minimum amount of acetone (500 mL). To this solution, iodoheptane (11.24 g, 53 mmol) was added dropwise to form a colourless solution. The reaction mixture was placed in a reaction tube, sealed and allowed to stir at 40 °C for 2 days. The white precipitate formed was collected under vacuum filtration and was rinsed with a small amount of acetone (25 mL). The white powder (15.9 g, 51.9 mmol, 98 %) collected and dried under vacuum (80 °C, 24 hours)

$^1\text{H}$  NMR (300 MHz, MeOD)  $\delta$  8.05 (d,  $J$  = 7.4 Hz, 2H, Ar-H), 6.78 (d,  $J$  = 7.4 Hz, 2H, Ar-H), 4.08 (t,  $J$  = 7.4 Hz, 2H, ARN- $\text{CH}_2$ ), 3.47 – 3.06 (m, 2H, - $\text{CH}_2$ -), 1.92 – 1.68 (m, 2H, 2H), 1.28 (m, 6H, - $\text{CH}_2$ -), 0.86 (t,  $J$  = 6.4 Hz, 3H,  $\text{CH}_3$ ).

**1-Hexyl-N, N-dimethyl-pyridin-1-ium-4-amine iodide:** 4-Dimethylaminopyridine (5.0 g, 40.9 mmol) was dissolved in the minimum amount of acetone (150 mL). To this solution iodoheptane (8.11 g, 40.9 mmol) was added dropwise to form a colourless solution. The reaction mixture was placed in a reaction tube, sealed and allowed to stir at 40 °C for 2 days. The precipitate formed was collected under vacuum filtration and was rinsed with a small amount of acetone (15 mL). The white powder (12.1 g, 37.8 mmol, 92.4 %) collected and dried under vacuum (80 °C, 24 hours)

$^1\text{H}$  NMR (300 MHz,  $\text{CDCl}_3$ )  $\delta$  9.92 (d,  $J$  = 7.3 Hz, 2H, Ar-H), 8.52 (d,  $J$  = 7.2 Hz, 2H, Ar-H), 5.80 (t,  $J$  = 7.2 Hz, 2H, Py- $\text{CH}_2$ ), 5.04 – 4.80 (m, 6H,  $\text{N}(\text{CH}_3)_2$ ), 3.49 – 3.23 (m, 4H), 2.80 (d,  $J$  = 2.8 Hz, 4H, Py-R- $\text{CH}_2$ -R), 2.34 (t,  $J$  = 6.0 Hz, 3H, Py-R- $\text{CH}_3$ ).

#### 2.5.6.1.2 Synthesis of 1-alkyl-4-aminopyridinium bistriflamide

**1-Butyl-4-aminopyridinium bistriflamide:** 1-butyl-4-aminopyridinium bromide (1.09 g, 4.70 mmol) was dissolved in the minimum amount of deionized water (10.3 mL). Lithium bistriflamide (1.347 g, 4.72 mmol) was dissolved in the minimum amount of deionized water (8.0 mL). The two solutions were mixed and a white solid instantly formed in an emulsion. Dichloromethane (50 mL) was added to the emulsion dissolving the white solid. The organic layer was extracted and concentrated using a rotary evaporator to form a colourless viscous liquid that crystallised upon sitting to form white needle like crystals. The white crystals (1.80 g, 4.17 mmol, 88.7%) collected dried under vacuum (80 °C, 24 hours)

<sup>1</sup>H NMR (300 MHz, Acetone)  $\delta$  8.17 (d,  $J$  = 7.3 Hz, 2H, Ar-H), 6.95 (d,  $J$  = 7.3 Hz, 2H, Ar-H), 4.20 (t,  $J$  = 7.3 Hz, 2H, Ar-H), 1.78 (dt,  $J$  = 15.1, 7.5 Hz, 2H, ARN-CH<sub>2</sub>), 1.26 (dq,  $J$  = 14.8, 7.4 Hz, 2H, -CH<sub>2</sub>-), 0.82 (t,  $J$  = 7.4 Hz, 3H-CH<sub>3</sub>).

<sup>13</sup>C NMR (75 MHz, Acetone)  $\delta$  206.66 (s), 144.45 (s), 111.42 (s), 59.28 (s), 33.96 (s), 30.25 (dp,  $J$  = 38.7, 19.3 Hz), 20.33 (s), 14.12 (s).

<sup>19</sup>F NMR (282 MHz, Acetone)  $\delta$  -80.23 (ms)

**1-Ethyl-4-aminopyridinium bistriflamide:** 1-ethyl-4-aminopyridinium bromide (0.576 g, 2.84 mmol) was dissolved in the minimum amount of deionized water (1 mL). Lithium bistriflamide (0.544 g, 2.87 mmol) was dissolved in the minimum amount of deionized water (6.7 mL). The two solutions were mixed and a white solid instantly formed in an emulsion. Dichloromethane (50 mL) was added to the emulsion dissolving the white solid. The organic layer was extracted and concentrated using a rotary evaporator to form a colourless viscous liquid that crystallised upon sitting to form white needle like crystals. The white crystals (0.72 g, 1.71 mmol, 62.9 %) collected and dried under vacuum (80 °C, 24 hours)

<sup>1</sup>H NMR (300 MHz, Acetone)  $\delta$  8.14 (d,  $J$  = 7.4 Hz, 2H, Ar-H), 6.91 (d,  $J$  = 7.5 Hz, 2H, Ar-H), 4.21 (q,  $J$  = 7.3 Hz, 2H, Py-CH<sub>2</sub>), 1.39 (t,  $J$  = 7.3 Hz, 3H, CH<sub>3</sub>).

<sup>13</sup>C NMR (75 MHz, Acetone)  $\delta$  206.84 (s), 160.50 (s), 144.14 (s), 111.50 (s), 55.36 (s), 54.75 (s), 31.62 – 29.30 (m), 16.80 (s).

<sup>19</sup>F NMR (282 MHz, Acetone)  $\delta$  -79.68. (s).

**1-Pentyl-4-aminopyridinium bistriflamide:** 1-Pentyl-4-aminopyridinium bromide (38.6 g, 157 mmol) was dissolved in the minimum amount of deionized water (200

mL). Lithium bistriflamide (45.4 g, 158 mmol) was dissolved in the minimum amount of deionized water (100 mL). The two solutions were mixed and a white solid instantly formed in an emulsion. Dichloromethane (350 mL) was added to the emulsion dissolving the white solid. The organic layer was extracted twice and concentrated using a rotary evaporator to form a colourless viscous liquid that crystallised upon sitting to form white waxy solid. The white solid (52.57 g, 118 mmol, 75.2 %) collected were consequently analysed using NMR.

$^1\text{H}$  NMR (400 MHz,  $\text{C}_6\text{D}_6$ )  $\delta$  7.57 (d,  $J$  = 7.1 Hz, 2H, Ar-H), 6.68 (d,  $J$  = 7.3 Hz, 2H, Ar-H), 6.46 (s, 2H,  $\text{NH}_2$ ), 3.81 (t,  $J$  = 7.3 Hz, 2H, Py- $\text{CH}_2$ ), 1.70 – 1.38 (m, 2H, Py- $\text{CH}_2\text{CH}_2$ ), 1.30 – 0.96 (m, 4H, Py-R- $\text{CH}_2\text{CH}_2\text{-CH}_3$ ), 0.73 (t,  $J$  = 7.2 Hz, 3H,  $\text{CH}_3$ ).

$^{13}\text{C}$  NMR (101 MHz, Acetone)  $\delta$  206.84, 158.63, 142.33, 124.48, 121.29, 118.11, 114.92, 109.93, 58.23, 30.18, 27.59, 21.57, 12.90.

$^{19}\text{F}$  NMR (282 MHz,  $\text{CDCl}_3$ )  $\delta$  -80.21 (s).

**1-Hexyl-4-aminopyridinium bistriflamide:** 1-Hexyl-4-aminopyridinium bromide (15.0 g, 49 mmol) was dissolved in the minimum amount of deionized water (150 mL). Lithium bistriflamide (15.0 g, 51 mmol) was dissolved in the minimum amount of deionized water (100 mL). The two solutions were mixed and a white solid instantly formed in an emulsion. Dichloromethane (350 mL) was added to the emulsion dissolving the white solid. The organic layer was extracted twice and concentrated using a rotary evaporator to form a colourless viscous liquid that crystallised upon sitting to form white waxy solid. The white crystalline solid (21.2 g, 41.9 mmol, 82.15%) collected was consequently analysed using NMR.

$^1\text{H}$  NMR (300 MHz,  $\text{CDCl}_3$ )  $\delta$  7.80 (d,  $J$  = 6.9 Hz, 2H, Ar-H), 6.94 (d,  $J$  = 6.9 Hz, 2H, Ar-H), 6.51 (s, 2H,  $\text{NH}_2$ ), 4.07 (t,  $J$  = 7.3 Hz, 2H, Py- $\text{CH}_2\text{-R}$ ), 1.82 (m, 2H, Py-R- $\text{CH}_2\text{-CH}_3$ ), 1.30 (m, 6H, Py-R- $\text{CH}_2\text{-CH}_3$ ), 0.88 (t,  $J$  = 6.0 Hz, 3H,  $\text{CH}_3$ ).

$^{13}\text{C}$  NMR (75 MHz,  $\text{CDCl}_3$ )  $\delta$  207.23, 158.93, 142.38, 111.23, 77.85, 77.43, 77.00, 59.29, 53.83, 31.40, 31.33, 31.26, 26.02, 22.69, 14.20.

$^{19}\text{F}$  NMR (282 MHz,  $\text{CDCl}_3$ )  $\delta$  -79.63 (s).

#### 2.5.6.2 Synthesis of Simple Diamine Based Ionic Liquids

A summary of the synthetic method is shown in Figure 2-64

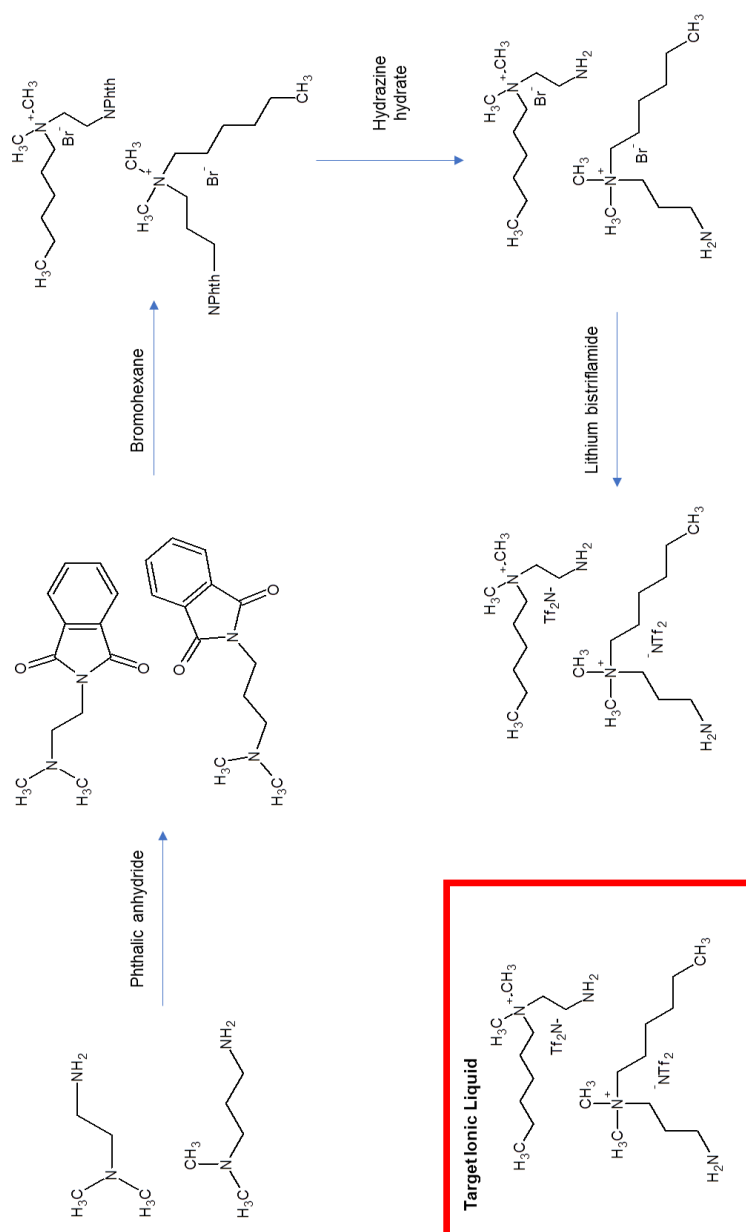


**Figure 2-64-** Synthesis of simple diamine based ionic liquids.

### 2.5.6.3 Protection of the primary amine functionality

**2-[3-(Dimethylamino)ethyl]isoindoline-1,3-dione:** 3-Dimethylaminoethylamine (10 g, 113.4 mmol) was added to a suspension of phthalic anhydride (18.99 g, 128 mmol) in chloroform (200 ml) to form a colourless solution and was refluxed for 24 hours. The originally colourless solution became yellow and was rinsed twice with a saturated solution of sodium hydrogen carbonate (200 mL) followed by deionized water (200 mL). The washed organic layer was then dried with anhydrous magnesium sulphate and concentrated using a rotary evaporator to form yellow oil (21.8 g, 99.1 mmol, 88.1 %).



$^1\text{H}$  NMR (400 MHz,  $\text{CDCl}_3$ )  $\delta$  7.71 (ddd,  $J$  = 50.9, 5.3, 3.1 Hz, 4H, Ar-H), 3.75 (t,  $J$  = 6.6 Hz, 2H, PANH-CH<sub>2</sub>-R-N(CH<sub>3</sub>)<sub>2</sub>), 2.53 (t,  $J$  = 6.6 Hz, 2H, CH<sub>2</sub>-N(CH<sub>3</sub>)<sub>2</sub>), 2.23 (s, 6H, N(CH<sub>3</sub>)<sub>2</sub>).

$^{13}\text{C}$  NMR (101 MHz,  $\text{CDCl}_3$ )  $\delta$  168.18, 133.65, 132.04, 123.01, 77.28, 77.16, 76.96, 76.64, 56.97, 45.35, 35.82.

**2-[3-(Dimethylamino)propyl]isoindoline-1,3-dione:** 3-Dimethylaminopropylamine (15 g, 146.8 mmol) was added to a suspension of phthalic anhydride (24.45 g, 165 mmol) in chloroform (300 ml) to form a colourless solution and was refluxed for 24 hours. The originally colourless solution became yellow and was rinsed twice with a saturated solution of sodium hydrogen carbonate (200 mL) followed by deionized water (200 mL). The washed organic layer was then dried with anhydrous magnesium sulphate and concentrated using a rotary evaporator to form a yellow oil (33.65 g, 144.2 mmol, 98.7 %.)

$^1\text{H}$  NMR (400 MHz,  $\text{CDCl}_3$ )  $\delta$  7.77 – 7.60 (m, 2H, Ar-H), 7.61 – 7.49 (m, 2H, Ar-H), 3.69 – 3.48 (m, 2H, PANH-CH<sub>2</sub>-R-N(CH<sub>3</sub>)<sub>2</sub>), 2.19 (dd,  $J$  = 12.9, 5.9 Hz, 2H, R-CH<sub>2</sub>-R-N(CH<sub>3</sub>)<sub>2</sub>), 2.03 (s, 6H, N(CH<sub>3</sub>)<sub>2</sub>), 1.76 – 1.60 (m, 2H, CH<sub>2</sub>-N(CH<sub>3</sub>)<sub>2</sub>).

#### 2.5.6.4 Alkylation of the Non-Protected Tertiary Amine

**3-(1,3-Dioxoisoindolin-2-yl)propyl-trimethyl-ammonium iodide:** 2-[3-(Dimethylamino) propyl]isoindoline-1,3-dione (8.5 g, 36.5 mmol) diluted with acetone (19 mL) was cooled with ice. To the solution iodomethane (7.79 g, 54.9 mmol) was added dropwise and the solution and a precipitate was formed immediately; the mixture was allowed to increase to room temperature and a second portion of acetone (19 mL) was added to facilitate stirring. The reaction was left to stir for 1 hour. The white suspension formed was filtered under vacuum, rinsed with acetone and the light yellow solid product collected. The solid was dried in a 60 °C oven for 2 hours resulting in a dry powdery yellow solid (13.12 g, 350.6 mmol, 96.1 %.)

$^1\text{H}$  NMR (300 MHz,  $\text{D}_2\text{O}$ )  $\delta$  9.18 – 8.84 (m, 4H, Ar-H), 4.96 (t,  $J$  = 6.6 Hz, 2H, PAN-CH<sub>2</sub>-R-N(CH<sub>3</sub>)<sub>3</sub>), 4.64 – 4.53 (m, 2H, PAN-R-CH<sub>2</sub>--N(CH<sub>3</sub>)<sub>3</sub>), 4.28 (s, 9H, N(CH<sub>3</sub>)<sub>3</sub>), 3.47 – 3.26 (m, 2H, R-CH<sub>2</sub>-R).

**3-(1,3-Dioxoisoindolin-2-yl)propyl-dimethyl-propyl-ammonium bromide:** 2-[3-(Dimethylamino) propyl]isoindoline-1,3-dione (3.00 g, 12.9 mmol) diluted with acetone (6.5 mL) was cooled with ice. To the solution 1-bromopropane (1.59 g, 12.9 mmol) was added dropwise and the solution was allowed to increase to room temperature where it was left to stir for 16 hours. The white suspension formed was

filtered under vacuum, rinsed with acetone and the white solid product collected (1.15 g, 3.23 mmol, 25.1 %.)

$^1\text{H}$  NMR (300 MHz,  $\text{D}_2\text{O}$ )  $\delta$  7.89 – 7.62 (m, 4H, Ar-H), 3.79 – 3.63 (m, 2H, R-CH<sub>2</sub>-R), 3.33 (ddd,  $J$  = 12.6, 9.5, 4.4 Hz, 2H, R-CH<sub>2</sub>-R), 2.97 (s, 6H, N(CH<sub>3</sub>)<sub>2</sub>), 0.80 (t,  $J$  = 7.0 Hz, 3H, CH<sub>3</sub>).

**3-(1,3-Dioxoisindolin-2-yl)propyl-dimethyl-butyl-ammonium bromide:** -[3-(Dimethylamino) propyl]isoindoline-1,3-dione (28.18 g, 121.1 mmol) diluted with acetone (50 mL) was cooled with ice. To the solution 1-bromobutane (16.74 g, 122.3 mmol) was added dropwise and the solution was allowed to increase to room temperature where it was left to stir for 92 hours. The white suspension formed was filtered under vacuum, rinsed with acetone and the white solid product collected. (26.0 g, 58.14%)

$^1\text{H}$  NMR (400 MHz, DMSO)  $\delta$  8.02 – 7.80 (m, 4H, Ar-H), 4.07 – 3.95 (m, 2H, R-CH<sub>2</sub>-R), 3.62 – 3.50 (m, 2H, R-CH<sub>2</sub>-R), 3.12 (s, 6H, N(CH<sub>3</sub>)<sub>2</sub>), 1.77 – 1.64 (m, 2H, R-CH<sub>2</sub>-R), 1.40 – 1.19 (m, 4H, R-CH<sub>2</sub>-R), 0.90 (t,  $J$  = 7.2 Hz, 3H, CH<sub>3</sub>).

$^{13}\text{C}$  NMR (101 MHz, DMSO)  $\delta$  167.47, 134.65, 131.61, 123.26, 63.32, 59.28, 50.35, 40.15, 39.94, 39.73, 39.52, 39.31, 39.10, 38.89, 31.03, 27.77, 21.59, 21.33, 13.66.

**3-(1,3-Dioxoisindolin-2-yl)ethyl-dimethyl-pentyl-ammonium iodide:** 2-[3-(Dimethylamino) ethyl]isoindoline-1,3-dione (8.44 g, 386 mmol) diluted with acetone (25 mL) was cooled with ice. To the solution 1-bromohexane (7.74 g, 389.9 mmol) was added dropwise and the solution was allowed to increase to room temperature where it was left to stir for 4 days. The white suspension formed was filtered under vacuum, rinsed with acetone and the white solid product collected (6.87 g, 165 mmol, 42.8 %.)

$^1\text{H}$  NMR (300 MHz,  $\text{D}_2\text{O}$ )  $\delta$  8.17 – 7.38 (m, 4H, Ar-H), 4.06 (t,  $J$  = 6.6 Hz, 2H, PAN-CH<sub>2</sub>-CH<sub>2</sub>-N(CH<sub>3</sub>)<sub>2</sub>R<sup>2</sup>), 3.55 (t,  $J$  = 6.9 Hz, 2H, R<sup>1</sup>N-CH<sub>2</sub>-R<sup>2</sup>), 3.31 (t,  $J$  = 8.1 Hz, 2H, PANH-CH<sub>2</sub>-CH<sub>2</sub>-N(CH<sub>3</sub>)<sub>2</sub>R<sup>2</sup>), 3.11 (s, 6H, N(CH<sub>3</sub>)<sub>2</sub>), 1.79 – 1.60 (m, 2H, R<sup>1</sup>N-CH<sub>2</sub>-R), 1.23 (t, 3H, R<sup>1</sup>N-CH<sub>3</sub>), 0.84 – 0.67 (m, 2H, R<sup>1</sup>N-CH<sub>2</sub>-R).

**3-(1,3-Dioxoisindolin-2-yl)propyl-dimethyl-hexyl-ammonium bromide:** -[3-(Dimethylamino) propyl]isoindoline-1,3-dione (3.00 g, 12.9 mmol) diluted with acetone (6.5 mL) was cooled with ice. To the solution 1-bromooctane (2.129 g, 12.9 mmol) was added dropwise and the solution was allowed to increase to room temperature where it was left to stir for 92 hours. The white suspension formed was

filtered under vacuum, rinsed with acetone and the white solid product collected.  
(3.113 g, 7.83 mmol, 60.7 %)

$^1\text{H}$  NMR (400 MHz,  $\text{D}_2\text{O}$ )  $\delta$  7.95 – 7.76 (m, 4H, Ar-H), 3.79 (t,  $J$  = 6.6 Hz, 2H, PAH- $\text{CH}_2$ ), 3.43 – 3.32 (m, 2H, PAN- $\text{CH}_2\text{-CH}_2\text{-R}$ ), 3.32 – 3.23 (m, 2H), 3.05 (s, 6H,  $\text{N}(\text{CH}_3)_2\text{RR}$ ), 2.22 – 2.08 (m, 2H, R- $\text{CH}_2\text{-R}$ ), 1.73 – 1.59 (m, 2H, R- $\text{CH}_2\text{-R}$ ), 1.34 – 1.15 (m, 6H, R- $\text{CH}_2\text{-R}$ ), 0.83 (dd,  $J$  = 9.8, 4.4 Hz, 3H,  $\text{CH}_3$ ).

**3-(1,3-Dioxoisindolin-2-yl)propyl-dimethyl-octyl-ammonium bromide:** 2-[3-(Dimethylamino) propyl]isoindoline-1,3-dione (3.00 g, 12.9 mmol) diluted with acetone (6.5 mL) was cooled with ice. To the solution 1-bromooctane (2.49 g, 12.9 mmol) was added dropwise and the solution was allowed to increase to room temperature where it was left to stir for 16 hours. The white suspension formed was filtered under vacuum, rinsed with acetone and the white solid product collected (1.85 g, 5.2 mmol, 40.4 %.)

$^1\text{H}$  NMR (300 MHz,  $\text{D}_2\text{O}$ )  $\delta$  7.92 – 7.59 (m, 4H, Ar-H), 3.70 (t,  $J$  = 6.5 Hz, 2H, PAN- $\text{CH}_2\text{-R}$ ), 3.37 – 3.26 (m, 2H, PAN- $\text{CH}_2\text{-CH}_2\text{-R}$ ), 3.23 – 3.09 (m, 8H, R- $\text{CH}_2\text{-R}$ ), 2.97 (s, 6H,  $\text{N}(\text{CH}_3)_2\text{RR}$ ), 2.07 (dt,  $J$  = 13.1, 6.6 Hz, 2H, R- $\text{CH}_2\text{-R}$ ), 1.67 (tt,  $J$  = 14.9, 7.4 Hz, 2H,  $-\text{CH}_2\text{-CH}_3$ ), 0.96 – 0.83 (m, 3H,  $\text{CH}_3$ ).

#### 2.5.6.5 Deprotection of the Primary Amine

3-(1,3-dioxoisindolin-2-yl)propyl-trialkyl-ammonium iodide (13.3 mmol) was dissolved in absolute ethanol (200 mL). To the solution hydrazine hydrate (40 mmol 98%) was added dropwise. The reaction mixture was heated to 60 °C and was left to stir for 16 hours. A large amount of white gelatinous solid was formed and the reaction mixture was cooled in an ice bath for 1 hour. The solid was then collected by filtration under gravity and rinsed with absolute ethanol (200 mL). The filtrate was concentrated under vacuum to form a white solid.

**2-Aminopropyl(trimethyl)ammonium iodide:** (2.08 g, 8.53 mmol, 64 %, crude product.)  $^1\text{H}$  NMR (300 MHz,  $\text{D}_2\text{O}$ )  $\delta$  3.64 (dd,  $J$  = 14.0, 7.0 Hz, 2H, EtOH), 3.44 – 3.31 (m, 2H, N- $\text{CH}_2$ ), 3.13 (s, 9H,  $\text{N}(\text{CH}_3)_3$ ), 2.81 (t,  $J$  = 7.0 Hz, 4H, N-R- $\text{CH}_2\text{-CH}_3$ ), 2.05 – 1.92 (m, 4H, N-R- $\text{CH}_2\text{-CH}_3$ ), 1.17 (t,  $J$  = 7.0 Hz, 5H, EtOH).

**2-Aminopropyl(dimethyl)butylammonium bromide:** (1.53 g, 6.79 mmol, 51 % crude)  $^1\text{H}$  NMR (400 MHz,  $\text{CDCl}_3$ )  $\delta$  8.16 (dd,  $J$  = 5.9, 3.3 Hz, 0.25 H, phthalic anhydride impurity), 7.72 (dd,  $J$  = 6.0, 3.3 Hz, 0.25 H, phthalic anhydride impurity), 3.79 – 3.66 (m, 2H, N-R- $\text{CH}_2\text{-CH}_3$ ), 3.57 – 3.45 (m, 2H, N-R- $\text{CH}_2\text{-CH}_2\text{-R}$ ), 3.38 (s, 6H,  $\text{N}(\text{CH}_3)_2$ ), 3.26 (t,  $J$  = 6.5 Hz, 2H, N-R- $\text{CH}_2\text{-R-NH}_2$ ), 3.10 (m, 3H, N-R- $\text{CH}_2\text{-CH}_2\text{-}$

R), 1.72 (dd,  $J = 16.1, 8.0$  Hz, 2H, N-R-CH<sub>2</sub>-NH<sub>2</sub>), 1.39 – 1.14 (m, 6H, N-R-CH<sub>2</sub>-R), 0.87 (t,  $J = 7.0$  Hz, 3H, N-R-CH<sub>3</sub>).

**2-Aminopropyl(dimethyl)pentylammonium iodide:** (4.14 g, 14.77 mmol, 39.9 % crude, larger scale reaction) <sup>1</sup>H NMR (400 MHz, CDCl<sub>3</sub>)  $\delta$  3.73 (dt,  $J = 14.1, 6.8$  Hz, 2H, N-CH<sub>2</sub>-R-NH<sub>2</sub>), 3.61 – 3.48 (m, 2H, N-CH<sub>2</sub>-R), 3.40 (d,  $J = 14.0$  Hz, 6H N-R-CH<sub>2</sub>-R), 3.28 (t,  $J = 6.4$  Hz, 2H, N-R-CH<sub>2</sub>-R), 1.45 – 1.30 (m, 4H, N-R-CH<sub>2</sub>-R), 1.24 (t,  $J = 7.0$  Hz, 1H, N-R-CH<sub>2</sub>-NH<sub>2</sub>), 0.92 (t,  $J = 6.9$  Hz, 3H, N-R-CH<sub>3</sub>).

#### 2.5.6.6 Anion Exchange

General method: Deprotected amine IL (14.4 mmol) was mixed with lithium bistriflamide (14.5 mmol) with the minimum amount of water and DCM (1:1) mixture) and allowed to stir for 2 hours. The mixture was then concentrated to dryness on the rotary evaporator. The mixture was then placed in to dry acetonitrile (distilled) and the Lil precipitated as a fine white powder. The mixture was then added to a glass centrifuge tube and the precipitate collected at the bottom of the vessel. The liquor was decanted and then rotavapped to dryness. The resultant product was again dropped into dry acetonitrile for a further 3 times to remove residual Lil. The final product was dried under high vacuum for 24 hours at 65 °C.

**2-Aminopropyl(dimethyl)pentylammonium bistriflamide:** (2.1 g, 4.78 mmol, 33.2 %) <sup>1</sup>H NMR (400 MHz, Acetone)  $\delta$  4.62 – 4.51 (m, 4H, N-R-CH<sub>2</sub>-R), 4.38 – 4.27 (m, 2H, N-R-CH<sub>2</sub>-R), 4.21 – 4.02 (m, 6H, -R-CH<sub>2</sub>-NH<sub>2</sub>), 2.82 – 2.77 (m, 2H, N-R-CH<sub>2</sub>-R), 2.77 – 2.61 (m, 4H), 2.22 – 2.04 (m, H, N-R-CH<sub>2</sub>-NH<sub>2</sub>), 1.67 (dd,  $J = 9.0, 5.1$  Hz, 3H, N-R-CH<sub>3</sub>).

<sup>19</sup>F NMR (376 MHz, Acetone)  $\delta$  -79.57 (s).

#### 2.5.7 Crown ether experiments

18-crown-6 (ca. 0.5 g) was weighed into cold finger apparatus and heated to 60 °C under a flow of dry N<sub>2</sub> gas. A freshly cut piece of potassium metal (75 mg) was added to the molten crown ether and stirred until a homogenous blue solution was formed. The ionic liquid under test was then added and observations made. After one hour a sample of the reaction mixture was taken (ensuring that it was not blue in colour or containing elemental potassium) and was added to deuterated chloroform. NMR spectroscopic analysis was then carried out.

## 2.5.8 Chemical reduction experiments

### ***Sodium borohydride reductions***

1-pentyl-4-aminopyridinium bistriflamide (0.5 g, 0.001 mol) was added to a premixed solution of sodium borohydride (0.05 g 0.0013 mol) in methanol (3 mL). Upon addition a small amount of fizzing was observed and the solution was stirred at room temperature for 3 days remaining colourless throughout. The reaction mixture was neutralised with hydrochloric acid and ionic liquid/reduction products were extracted into chloroform. The chloroform layer was then concentrated to form a colourless viscous liquid, which later solidified to form a crystalline solid.

### ***Sodium borohydride and acetic acid reductions***

1-pentyl-4-aminopyridinium bistriflamide (0.25 g, 0.00059 mol) was dissolved in tetrahydrofuran (2 mL). Sodium borohydride (0.045 g 0.0012 mol) and acetic acid (0.288 g, 0.0048 mol) were premixed and then added dropwise to the IL-THF solution. Upon addition a small amount of fizzing was observed and the solution was stirred at room temperature for 3 days remaining colourless throughout. The reaction mixture was neutralised with sodium hydroxide and ionic liquid/reduction products were extracted into chloroform. The chloroform layer was then concentrated to form a colourless viscous liquid which later solidified to form a crystalline solid.

1-pentyl-4-aminopyridinium bistriflamide (0.25 g, 0.00059 mol) was dissolved in tetrahydrofuran (2 mL). Sodium borohydride (0.045 g 0.0012 mol) and acetic acid (0.288 g, 0.0048 mol) were premixed and then added dropwise to the IL-THF solution. Upon addition a small amount of fizzing was observed, and the solution was placed under reflux for 24 hours remaining colourless throughout. The reaction mixture was neutralised with sodium hydroxide and ionic liquid/reduction products were extracted into chloroform. The chloroform layer was then concentrated to form a colourless viscous liquid which later solidified to form a crystalline solid.

## 2.5.9 Computational experiments

Calculations were completed under the supervision of Ryan Kavanagh and Jorge Kohanoff, School of maths and Physics, Queen's University Belfast.

Calculations were performed under periodic boundary conditions, using the Quickstep module of the CP2K program package.<sup>148</sup> The electronic structure was

modelled with the BLYP functional<sup>149</sup> enhanced by the MOLOPT-DZVP basis set.<sup>150</sup> The PBE and PBE0 hybrid functional were utilised.<sup>151</sup>

#### **2.5.10 Single Crystal Analysis**

Data was collected using an Aligent SuperNova, Dual, Cu, EosS2 diffractometer. The crystals were kept at 100(2) K during data collection. Using Olex<sup>2</sup>,<sup>152</sup> the structures were solved with the ShelXT,<sup>153</sup> ShelXS<sup>154</sup> and Superflip<sup>155</sup> structure solution programs using intrinsic phasing and refined with the ShelXL refinement package using least squares minimization. Non-hydrogen atom positions were fully refined using anisotropic thermal parameters and the hydrogen atoms were initially located at idealized positions and then refined using riding coordinates.

**Table 2-5-** Single crystal data for amine and 18-crown-6 interactions.

	2-aminopyridine and 18-crown-6		4-aminopyridine and 18-crown-6	
Bond precision:	C-C = 7.5714 Å	Wavelength=1.54184	C-C = 0.0031 Å	Wavelength=1.54184
Cell:	a=8(44) b=16(8) c=9(12)		a=14.7994(10) b=10.7854(6) c=16.7203(11)	
	alpha=90 beta=103.8999(19) gamma =90		alpha=90 beta=114.422(8) gamma=90	
Temperature:	115 K		115 K	
	Calculated	Reported	Calculated	Reported
Volume	1118(**)	1200(**)	2430.1(3)	2430.0(3)
Space group	P 21/c	P 21/c	P 21/c	P 21/c
Sum formula	C22 H36 N4 O6	C22 H36 N4 O6	C22 H36 N4 O6	C22 H36 N4 O6
Mr	452.55	452.55	452.55	452.55
Dx, g cm <sup>-3</sup>	1	1.252	1.237	1.237
Z	2	2	4	4
μ (mm <sup>-1</sup> )	0.808	0.753	0.744	0.744
F000	488	488	976	976
F000'	489.55		979.09	
(h, k, l) <sub>max</sub>	9,19,11	10,19,11	18,13,20	18,13,20
N <sub>ref</sub>	2197	2343	4842	4699

**Table 2-6**-Single crystal data for amine and 18-crown-6 interactions.

	4-bromopropylamine hydrobromide and 18-crown-6		1-pentyl-4-aminopyridinium bistriflamide and 18-crown-6	
Bond precision:	C-C = 0.0140 Å	$\lambda=1.54184$	C-C = 0.0093 Å	$\lambda = 1.54184$
Cell:	A = 12.8153(4) b = 8.6514(3) c = 19.6050(7)		a = 9.2448(2) b = 16.6930(4) c = 20.8657(6)	
	$\alpha = 90 \beta = 91.146(3) \gamma = 90$		$\alpha = 90 \beta = 101.439(3) \gamma = 90$	
Temperature:	115 K		115 K	
	Calculated	Reported	Calculated	Reported
Volume	2173.18(13)	2173.18(13)	3156.11(14)	3156.13(14)
Space group	P 21/n	P 21/n	P 21/n	P 21/n
Sum formula	C15 H33 Br2 N O6	C15 H33 Br2 N O6	C23 H39 F6 N3 O10 S2	C23 H39 F6 N3 O10 S2
Mr	483.22	483.24	695.69	695.69
Dx, g cm <sup>-3</sup>	1.477	1.477	1.464	1.464
Z	4	4	4	4
$\mu$ (mm <sup>-1</sup> )	4.964	4.964	2.355	2.355
F000	992	992	1456	1456
F000'	988.9		1464.25	
(h, k, l) <sub>max</sub>	15,10,24	15,10,24	11,20,25	11,20,25
Nref	4341	4292	6301	6247



**Table 2-7**-Single crystal data for 1-alkyl-4-aminopyridinium ionic liquids.

	1-butyl-4-aminopyridinium bromide		1-pentyl-4-aminopyridinium bistriflamide	
Bond precision:	C-C = 9.6389 Å	$\lambda = 1.54184$	C-C = 0.0119 Å	$\lambda = 1.54184$
Cell:	a = 14(92) b = 14(16) c = 14(8)		a = 13.5561(1) b = 16.0626(2) c = 17.1823(2)	
	$\alpha = 90^\circ \beta = 90^\circ \gamma = 90^\circ$		$\alpha = 90^\circ \beta = 90^\circ \gamma = 91^\circ$	
Temperature:	115 K		115 K	
	Calculated	Reported	Calculated	Reported
Volume	2761(3)	2761(2)	3741.38(7)	3741.38(7)
Space group	P -1	P -1	P 21 21 21	P 21 21 21
Sum formula	C23 H40 Br2 N4 O	C23 H40 Br2 N4 O	C12 H17 F6 N3 O4 S2	C12 H17 F6 N3 O4 S2
Mr	548.39	548.41	445.41	445.4
Dx, g cm <sup>-3</sup>	1.319	1.319	1.582	1.581
Z	4	4	8	8
$\mu$ (mm <sup>-1</sup> )	3.891	3.867	3.368	3.368
F000	1136	1136	1824	1824
F000'	1132.78		1836.66	
(h, k, l) <sub>max</sub>	17,17,17	17,17,16	16,19,21	16,19,21
Nref	10902	7007	7426[ 4134]	7371

**Table 2-8-** Single crystal data for 2-[3-(Dimethylamino)propyl]isoindoline-1,3-dione.

	2-[3-(Dimethylamino)propyl]isoindoline-1,3-dione	
Bond precision:	C-C = 0.0015 Å	$\lambda = 1.54184$
Cell:	a = 14.35(14) b = 5.58(8) c = 15.24(16)	
	$\alpha = 90$ $\beta = 92.053(1)$ $\gamma = 90$	
Temperature:	100 K	
	Calculated	Reported
Volume	1221.21(2)	1221.21(2)
Space group	P 21/c	P 21/c
Sum formula	C13 H16 N2 O2	C13 H16 N2 O2
Mr	232.28	232.28
Dx, g cm <sup>-3</sup>	1.263	1.263
Z	4	4
$\mu$ (mm <sup>-1</sup> )	0.699	0.699
F000	496	496
F000'	497.49	
(h, k, l) <sub>max</sub>	17,7,18	17,6,18
Nref	2411	2393
Tmin,Tmax		0.848,1.000

### 3 *p*-*tert*-Butylcalix-[4]-arene solvation in basic ionic liquids and a study of basic anion-ionic liquid interactions with phenolic compounds

*The Challenge:*

*Can ionic liquids provide an effective alternative to molecular solvents for *p*-*tert*-butylcalix-[4]-arenes?*

*If successful, can the *p*-*tert*-butylcalix-[4]-arene be utilised in a meaningful manner with a specific focus on functionalisation for current applications?*

#### 3.1 Introduction

##### 3.1.1 Discovery of *p*-*tert*-butylcalix-[4]-arenes

*p*-*tert*-butylcalix-[4]-arene, TBC is often described as a molecular basket; the tetrameric cyclic structure affords a cone-shaped motif reminiscent of a calyx; a Greek cup like cavity or structure as shown in Figure 3-1. Chemically, they are metacyclophanes which are classically defined as benzene rings connected by an aliphatic bridge at the 1,3-positions of the ring.<sup>156</sup> Synthesised and characterised by condensation of *p*-*tert*-butylphenol and formaldehyde by Zinke and Ziegler in 1948; they were often referred to as insoluble, high melting solids.<sup>157</sup> However, this was not the first report of such a condensation; Bæyer in 1872 reported the condensation of benzaldehyde and pyrogallol and the resultant product being referred to as a red/brown 'resorcinous tar'.<sup>158</sup> Upon recrystallisation and neutralisation with HCl a crystalline colourless product was achieved that corresponds to a 1:1 phenol-aldehyde composition; this product is now believed to be the 'neutralisation' product as will be discussed.

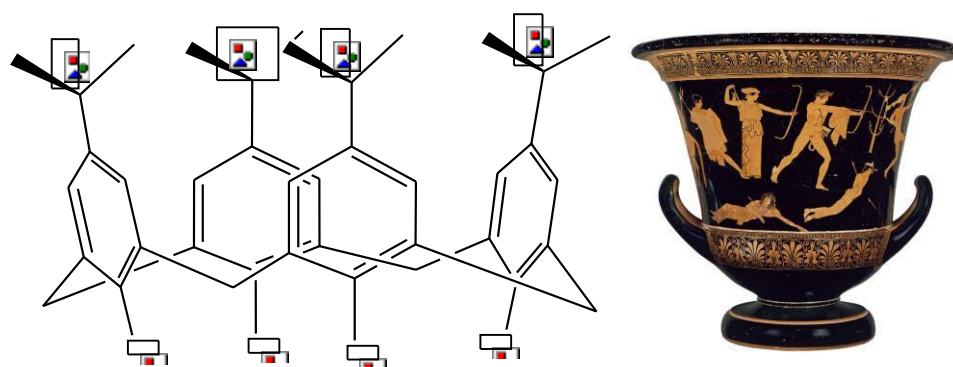
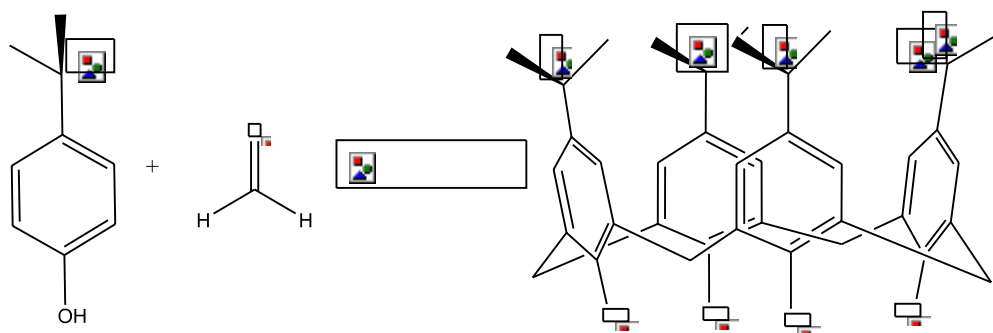


Figure 3-1-Structure of *tert*-butylcalix-[4]-arene and a Krater calyx<sup>159</sup>

Similarly, Bakelite, an early commercial plastic is formed *via* a similar methodology in such that the resin is formed by a condensation reaction by Leo Baekland in 1907; furthermore, he also investigated the aforementioned pyrogallol and formaldehyde condensations. Upon investigating, the phenol and formaldehyde reactions he observed that the resultant product was a “hard gum in excess of phenol” which upon further purification is the thermosetting commercial plastic Bakelite.<sup>160,161</sup>

Zinke carried out a significant number of studies regarding the synthesis of TBC; often investigating the utilisation of different synthetic procedures *via* variations in temperature, neutralisations and suspensions within unconventional solvents such as linseed oil.<sup>157,162–165</sup> *Via* these variations in synthetic procedures Zinke focused on the products obtained from each specifically on their appearance, melting points and elemental analysis. One such product was described as “platelets decomposing above 300 °C and having such limited solubility in organic solvents that a molecular-weight determination was not possible” an indication of the difficulty that such a reaction could entail with regards to product determination without modern techniques such as NMR, CHNS, mass spectrometry *etc.* One method utilising 3,5-dichlor-2-oxy-benzylalcohol, with base and formaldehyde afforded a crystalline product with what was believed to be consisting of 8 phenol–aldehyde units with a reported molecular weight *ca.* 1725 g/mol.<sup>162</sup>

Commonly, multiple products are achieved ranging from *p-tert*-butylcalix-[4]-arene to *p-tert*-butylcalix-[20]-arene as determined by reverse phase HPLC; with the most common isomers formed being  $n \leq 8$ .<sup>166</sup> Cornforth *et al.* were the first to have reported the use of a counter current chromatographic technique utilising Craig’s apparatus with ethanol and ligroin (C<sub>7</sub>-C<sub>8</sub> hydrocarbons) monitored *via* UV/Vis spectroscopy.<sup>167,168</sup> A more recently developed technique utilises sCO<sub>2</sub> supercritical fluid chromatography showing good separation of calix-[4]-arenes of similar compositions.<sup>169</sup> Water soluble TBC’s can be separated by capillary zone electrophoresis; however, this methodology is only suitable for small-scale purifications.<sup>170,171</sup>



**Figure 3-2-** Condensation reaction of *p*-*tert*-butylphenol and formaldehyde.

The condensation reaction itself is often base or acid catalysed; with regards to base catalysts such as sodium hydroxide NaOH the concentration can have a huge impact on the yield and product composition achieved with higher concentrations favouring larger hexamers and lower concentrations favouring tetramers.<sup>165</sup> Furthermore, the cation used in the inorganic base can have an effect; however, it is not a conventional trend in that as you move from  $\text{Li}^+$  to  $\text{Cs}^+$  there is no overarching trend; instead, there is a moderately low yield over all with moderate bases such as NaOH and KOH showing the highest yield of cyclic tetramers, 48-54 %. In all cases, the yield of the tetramer decreased at higher concentration and the hexamer became prevalent.

The key to the success of most syntheses' is reported to be due to the 'neutralisation step' in which the formaldehyde, base catalyst and *p*-*tert*-butylphenol are pre-mixed at 110-120 °C affording a yellow solid. The solid, once collected is dissolved in chloroform and neutralised with aqueous HCl. Once dried, the solid is termed 'truly' neutral and is utilised to continue the reaction *via* the use of a further amount of base catalyst.<sup>165</sup>

Methodology by Hayes and Hunter utilise a HCl acid catalyst with the linear tetramer of the *p*-methylphenol to form "novolak" which is more commonly known as a *p*-methylcalix-[4]-arene *via* an intramolecular condensation reaction. The linear tetramer is prepared from 3-bromo-2:2'-dihydroxy-5,5'-dimethyldiphenylmethane and an intermolecular nucleophilic substitution with another identical molecule.<sup>172</sup> A modification of this method was discussed by Bohmer *et al.*, in which two differing units undergo the cyclisation step to form asymmetric modifications.<sup>173</sup>

Munch *et al.* pioneered a single step methodology that incorporates the reflux of *p*-*tert*-butylphenol and formaldehyde in Xylene with concentrated aqueous base. This method was found to form products similar to those reported by Zinke. This method is commonly referred to as the Petrolite process.<sup>161,165</sup> With regards to modern

developments, there is little deviation from the classical methodologies; each utilising an acid or base catalyst; the main focus of synthetic developments has been in regards to functionalised calixarenes.

Sartori *et al.* utilised acid catalysts such as  $\text{BF}_3 \cdot \text{Et}_2\text{O}$  to form modified TBC structures with benzyl groups attached to the –CH– 1, 3-benzyl linkers of the TBC.<sup>174,175</sup> Such reactions were found to be specifically effective in forming calixarenes of greater unit numbers  $n = 6, 7, 8$  etc. Other notable acid catalysts used include  $\text{AlCl}_3$ <sup>(175)</sup>,  $\text{TiCl}_4$ <sup>(176)</sup>, and  $\text{SnCl}_4$ <sup>(176)</sup>.

Since the synthesis of the basic calixarene motif there has also been a huge interest in the solubility and functionalisation of the simple calix motif. There are two evident aspects to this functionalisation; the first being the enhancement of solubility *via* the attachment of somewhat polar species to either the lower or upper rim utilising a variety of organic reactions including esterification, sulphonation and Claisen rearrangements to name but a few.<sup>177–180</sup> The second aspect of functionalisation focuses on the utilisation of the calixarene *via* the addition of a ligated species to assist in application to separations, host-guest complexes and enhancement of rare earth luminescence.<sup>181,182</sup>

### 3.1.2 Significance of *p*-*tert*-butylcalix-[4]-arenes in modern chemistry

In regards to previous work encompassing *p*-*tert*-butylcalix-[4]-arenes and the discipline of ionic liquids the reports are majorly focused upon metal extraction in which the favourable physical and chemical properties of ILs can be utilised to form both a solvent and extraction component simultaneously.<sup>183</sup> Often the calixarene extractants utilised incorporate a variety of functionalities and the backbone of the ionic liquid for example the incorporation of the imidazolium or pyridinium motif which in turn has complexing abilities as well as forming a point of ionicity.<sup>184,185</sup> However, it is only within the last 30 years that the integration of ionic liquid and TBC motif has been utilised. Integration of the IL functionality enhances selectivity and ion selectivity of the extractants and also allows for liquefaction of the calixarene motif. Furthermore, the lower rim and cone motif can be secured in place hence forming a firm special cavity for complexation to occur.

The *p*-*tert*-butylcalix-[4]-arene motif has prevalence within a variety of sensor applications; an example of such has been demonstrated by Gupta *et al.* in that the TBC motif, is utilised within an electroactive membrane as a binding species for  $\text{Pb}^{2+}$

in the range of  $1.1 \times 10^{-5}$  -  $1.0 \times 10^{-1}$  M as monitored by potentiometric techniques for application to monitoring of lead waste in water supplies.<sup>13</sup>

Most commonly, the TBC motif is functionalised to include a receptor such as that demonstrated by Grigg *et al.* in which a bipyridyl, bpy is attached to the lower rim of the TBC *via* an ether functionalised phenolic group on the lower rim as shown in Figure 3-3.<sup>186</sup> This bpy group then acts as an ligand for metal anions such as  $\text{Ru}^{2+}$  that when bound to the motif the luminescence of the cation is quenched *via* a pH induced photoinduced intramolecular electron transfer due to stabilisation of the charges species by each other in the 1 and 3, phenolic positions of the TBC. Noting the 2, 4-positions remain as free phenolic groups to allow for the pH control of the luminescence. There is a somewhat stabilisation of the luminescence of the  $\text{Ru}^{2+}$  when dual functionalisation of the TBC as shown in Figure 3-3 that is pH dependent as the pH increases the deprotonation of the 2' and 4' positions result in quenching of the luminescence. Single functionalised forms are found to be readily quenched *via* the phenolic proton in the 3' position forming quenching phenolate anions.

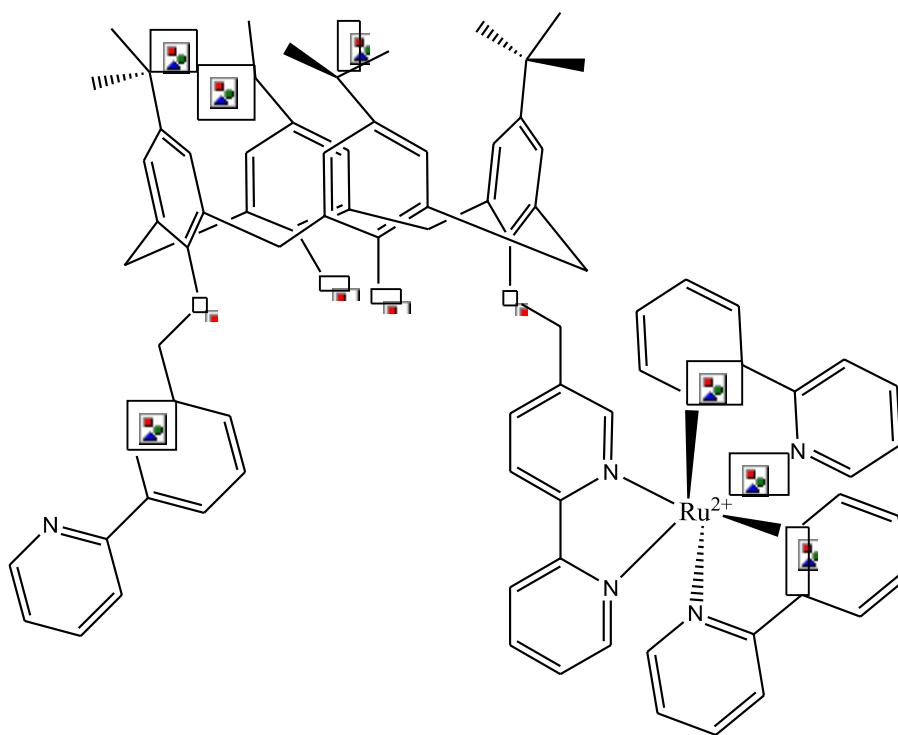


**Figure 3-3**-bipyridyl functionalised tert-butylcalix-[4]-arene by Grigg *et al.*<sup>186</sup>

Utilisation of TBC as a chromogenic centre is prevalent throughout literature; it should be noted that there are significantly more examples in non *tert*-butyl examples and this is believed to be due to the enhanced solubility of such compounds.<sup>187–189</sup>

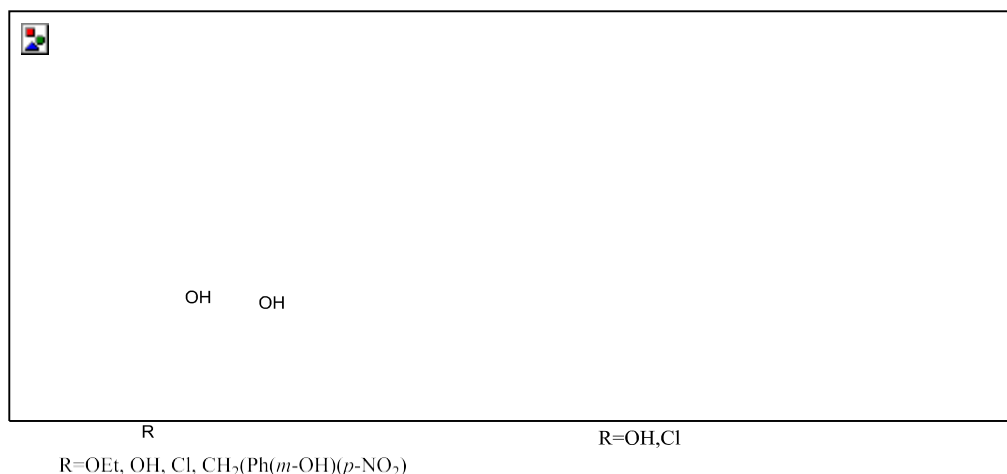


**Figure 3-4**-Examples of TBC motifs for chromogenic studies used by Diamond *et al.*<sup>190</sup>

The utilisation of TBCs as chromophores and chromogenic centres has been of great interest to Diamond *et al.*<sup>190</sup> Observing bathochromic shift upon complexation of  $Na^+$  and  $Li^+$  to TBC motifs shown in Figure 3-4 they demonstrated that the binding of the metal cation and the consequent deprotonation of the phenol ring is crucial in providing a response *i.e.* a spectral change in the UV/vis spectrum.<sup>190,191</sup> Upon the addition of the  $Na^+$  and  $Li^+$  cation in basic solution (morpholine) to the motifs described in Figure 3-4, no response is observed hence supporting the theory that the deprotonation as a consequence of binding is critical in forming a response. Furthermore later studies with nitrophenol residues of the Diamond TBC motifs have shown a single phenolic deprotonation is required for a response to be detected with further deprotonations having a hypochromic affect.<sup>190,191</sup> This has been demonstrated with *t*-Bu,  $NO_2$  and octyldecyl alkyl substituents in the upper rim.

Liu *et al.* have also focused on the binding of alkali metals such a  $Li^+$ ,  $Na^+$ ,  $K^+$  and  $Cs^+$  utilising azo benzylidene type ligands on the 2' and 4' positions of the lower rim as shown in Figure 3-5. The azobenzylidene ligands bind to the alkali metal cations *via* the  $CH=N$  and the 2-hydroxyl group on the benzene ring encapsulating the cation. The binding of such compounds causes the chromophore of the modified TBC to shift from the colour of the solution changed distinctly from yellow ( $\lambda_{max} = 379$  nm) to red ( $\lambda_{max} = 480$  nm) upon complexation with  $Na^+$ . This bathochromic shift from yellow to red is believe to be due to the binding to the alkali metal cation, specifically well with  $Na^+$  cations via the size-fit of the cation in the TBC-Ligand 3D cavity and the binding to not just the ligand species but also the ionisable phenolic protons depending on conditions.



Similarly to what was observed by Grigg *et al.*, pH and the phenolic protons that are un-functionalised can cause a hypsochromic shift- of 376 to 352 nm at pH = 1 with or without Na<sup>+</sup> cations present due to the protonation of the azo group. Furthermore, the aforementioned bathochromic shifts are increased in basic conditions due to the formation of phenolate anions and increased complexation/electrostatic binding between species. From these examples it is seen that not just the ligands but the remaining phenolic protons that can be integral to the functionality along with the rigidity or lack thereof of the TBC basket structure *i.e.* scope for  $\pi$ -metal interactions as reported by Kim *et al.*<sup>192</sup>

Binding with a variety of azo, phosphinoyl, thiol and Schiff base ligands have been demonstrated with a number of other elements including but not exclusively UO<sub>2</sub><sup>2+</sup><sup>(193)</sup>, Nd<sup>3+</sup><sup>(194,195)</sup>, VO<sup>2+</sup><sup>(195,196)</sup>, Fe<sup>3+</sup><sup>(195,197)</sup>, Ni<sup>2+</sup><sup>(195,198)</sup>, Mo<sup>3+</sup><sup>(199)</sup>, W<sup>3+</sup><sup>(199)</sup>, Cu<sup>2+</sup><sup>(195,198)</sup>, Cr<sub>2</sub>O<sub>7</sub><sup>2-</sup><sup>(200)</sup>, Ag<sup>+</sup><sup>(201)</sup> and Zn<sup>2+</sup><sup>(195,198,202)</sup>. Naturally, as TBC motifs have been shown to bind with a variety of species with a significant bias towards the use of amide and crown etheryl functionalities of the lower rim there have been several studies into the utilisation of *p*-*tert*-butylcalix-[4]-arenes within extraction and separation chemistry.<sup>203–206</sup>

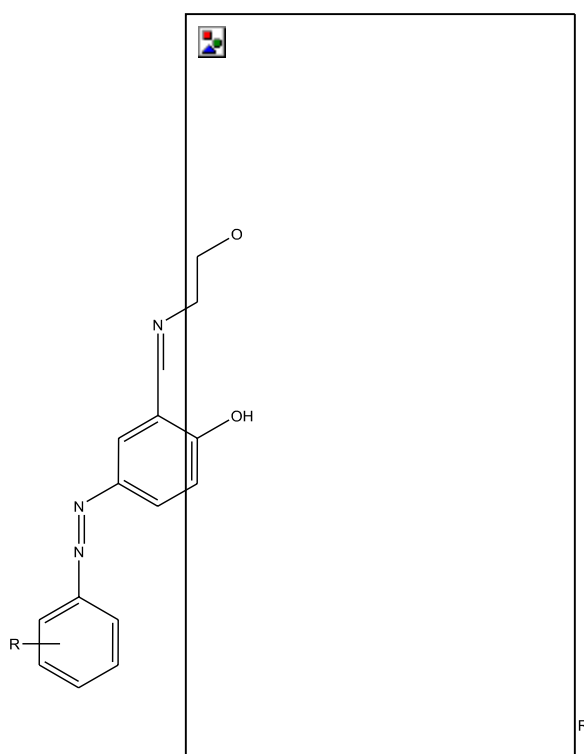


**Figure 3-5**-TBC functionalised by Liu *et al.* for alkali metal complexation.<sup>207</sup>

Binding with the alkali metals and consequent extraction has been of great interest, since initial studies by Cho and Chang reporting binding and extraction with

ethoxycarbonylmethyl derivatives; calix-[4]-arene for  $\text{Na}^+$ , calix-[6]-arene for  $\text{Cs}^+$ , and calix-[8]-arene for  $\text{K}^+$  in chloroform and water mixtures of the metal picrate salts.<sup>208</sup> There is also scope for selectivity between the alkali metal and alkali earth metal cations as demonstrated by Bozkurt *et al.* with the picrate salts showing that  $\text{Cs}^+/\text{Sr}^{2+}$  and  $\text{Na}^+$  can be selectively extracted, and further research by Casnati *et al.* found that by tuning of the calix-crown lower rim modification, selectivity of  $\text{K}^+$  can exceed that of valinomycin.<sup>209,210</sup>

Other such examples have been altered with aliphatic and acyclic amines such as isobutylamine, morpholine and piperazine hence altering the basicity of the ligand etheryl groups on the TBC and the steric of the lower rim cavities. Furthermore, the use of the amine functionalities allow for a pH switching mechanism to be induced hence blocking the binding of the alkali metals *via* the non-functionalised phenolic groups and allowing softer, larger cations such as  $\text{Pb}^{2+}$ ,  $\text{Hg}^{2+}$  and  $\text{Cd}^{2+}$  to be preferentially bound to the modified.<sup>211</sup>

One of the first integrations of the TBC motif into an ionic liquid was completed by Jin and Shreeve in 2004 that utilised the previous successes of the crown ether and cavitand type TBC extractants and integrated them into a di-imidazolium cation as shown in Figure 3-6.<sup>212</sup>

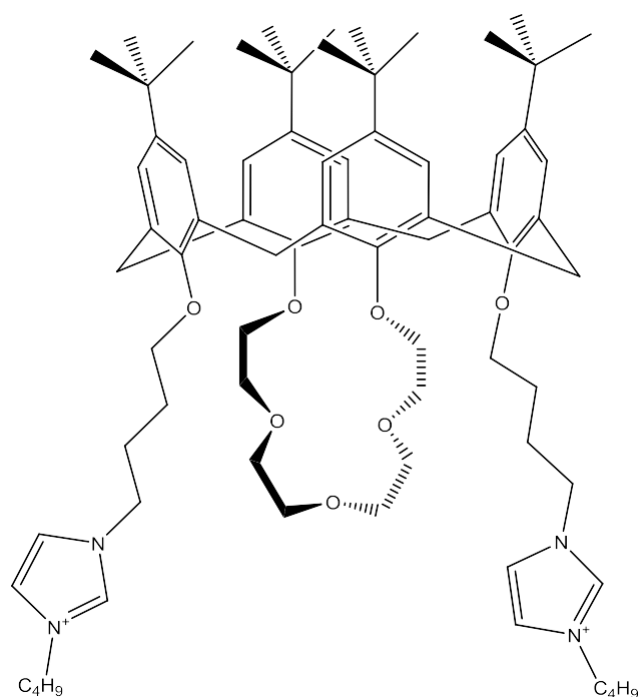


**Figure 3-6-** *p-tert*-butylcalix-[4]-arene-dialkylimidazolium cations by Shreeve and Jin.<sup>212</sup>

Thio-TBC derivatives have also been prepared by Kalchenko *et al.* such that the thio functionality is located in the 1,3-benzyl linker and the IL functionality is located on

the lower rim, similarly to what is described in Figure 3-6 with examples of imidazolium and pyridinium functionality.<sup>213</sup> Other examples utilising terpyridines along with the thio and crown etheresque modifications have been synthesised by Muravev *et al.* and demonstrated to bind to a series of lanthanides and alkali metals cooperatively.<sup>214</sup>

Rare earth elements have also been extracted using TBC motifs modified with a diglycolamide ligand and tetrazole linker on the lower rim. Such structures have been demonstrated by Arrachart and Pellet-Rostaing *et al.* to be a new platform for urban mining based lanthanide extraction from Nd/Fe/B/Dy magnets.<sup>215</sup> It is demonstrated that extraction efficiency changes along the lanthanide series with selectivity towards Yb<sup>3+</sup> in comparison to La<sup>3+</sup> and Eu<sup>3+</sup>.

Along with extraction techniques these TBC-ILs have been utilised as synthetic reagents in regard to the preparation of gold clusters as shown in Figure 3-7. TBC-IL with integrated N-heterocyclic carbenes or phosphines have been demonstrated to form Au<sup>+</sup> precursor complexes with the carbon and phosphine, respectively, which upon treatment with a reducing agent such as NaBH<sub>4</sub> clusters are formed of differing sizes dependant on the precursors conformation, steric and stabilisation properties.<sup>216,217</sup>

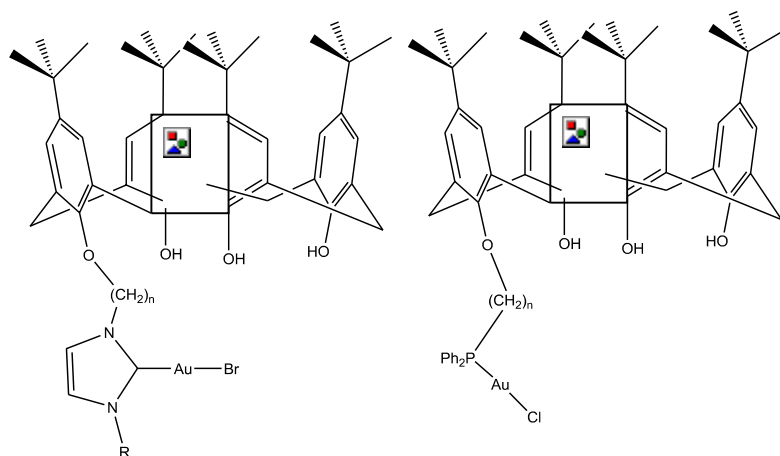


**Figure 3-7**-Synthetic precursors to gold nanoclusters from TBC-ILs.

### 3.1.3 Physical properties of *p*-*tert*-butylcalix-[4]-arenes and their influence on lower rim functionalisation methods

As aforementioned the *p*-*tert*-butylcalix-[4]-arenes were initially referred to as insoluble high melting solids. The reported melting point for *p*-*tert*-butylcalix-[4]-arene is 342-344 °C, in comparison the melting point of elemental lead is 327.12

°C.<sup>171</sup> These high melting points of the non-functionalised *p*-*tert*-butylcalix-[4]-arenes govern that most if not all reactions of TBC must be *via* conventional wet-chemistry methods. Furthermore, the functionalised TBC's also exhibit these high melting points for example, *p*-*tert*-butylcalix-[4]-arene tetramethyl ester = 226-228 °C, *p*-*tert*-butylcalix-[4]-arene tetrabenzyl ester = 230-231 °C, *p*-*tert*-butylcalix-[4]-arene tetraacetate = 383-386 °C and *p*-*tert*-butylcalix-[4]-arene trimethylsilyl ester = 411-412 °C. The solubility of TBC in most organic solvents is low; there are no reports within literature data on exact values.<sup>218</sup>

Within aqueous solutions the solubility is near negligible at ambient conditions and at higher temperatures (433-473 K) and pressures (5 MPa) it is equated to be 1800 to 3600 times lower than that of anthracene.<sup>219</sup>

### 3.1.3.1 Esterification of the lower rim

Esterification reactions of TBC require use of an acyl chloride and an acid or base catalyst proceeding to form the ester of the lower rim phenolic protons as shown in Figure 3-8. Methods analysed by No and Koo found that esterification using acyl chlorides with either an acid or base catalyst resulted in a tetra-acyl ester products.<sup>220</sup> The use of NaH, a base catalyst, resulted in the cone conformer product to be preferentially formed, whereas utilisation of an acid catalyst, acetic and hydride/*p*-toluenesulphonic acid resulted in different product orientations.<sup>221</sup>



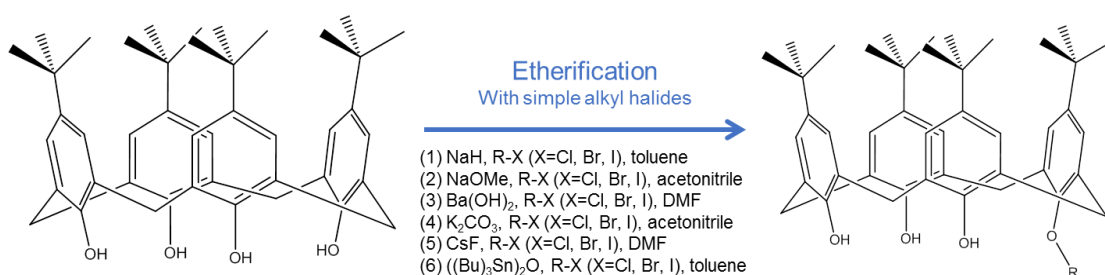
**Figure 3-8**—Esterification of *p*-*tert*-butylcalix-[4]-arenes with acyl chloride via 4 different methodologies.<sup>220,222</sup>

It is evident that a majority of not all esterification reactions results in the formation of multiple esterification products and in multiple conformers.<sup>223,224</sup>

### 3.1.3.2 Etherification of the lower rim with simple alkyl halides

The etherification of TBC is one of the most studied synthetic methods; however, it is still not without its drawbacks. It is difficult to achieve a single desired product instead a of resultant mixture of mono-, di-, tri- and tetra-alkylated products hence lowering the isolated yield and laborious separation procedures. This low solubility is

undesirable with many synthetic techniques and it is often facilitated *via* the addition of a strong inorganic base/salt such as Na[OMe], K[OAc], NaH, Cs[CO<sub>3</sub>] or CsF, which in each case carry their own issues regarding safety, solubility and the extent of the TBC deprotonation.<sup>181,225–227</sup> The solubility of the starting material (TBC) itself also determines the sluggishness of reactions where, especially, utilisation of weaker bases afford a greater mix of di-, tri- and tetra- ethers hence requiring elaborate separation techniques. Peculiarly, Na[OMe] in acetonitrile has shown to be an effective method of monoalkylation producing a yield of approximately 75 % demonstrated by Shu *et al.* which contravenes the idea that use of stronger bases should result in a greater proportion of multiple alkylations.<sup>226</sup>

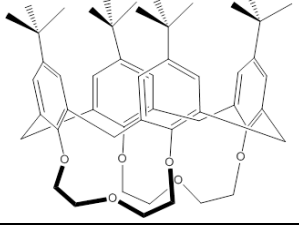
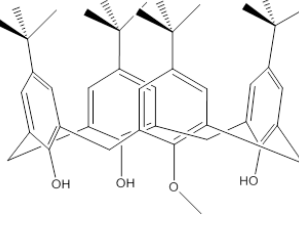
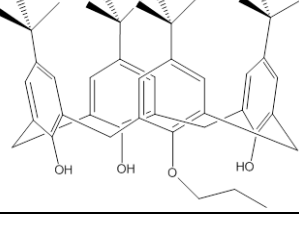
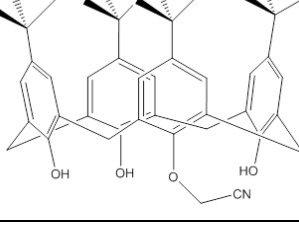
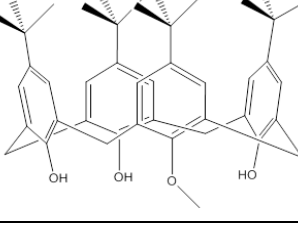


**Figure 3-9**-Etherification of *p*-*tert*-butylcalix-[4]-arenes with simple alkyl halides *via* 6 different methodologies.<sup>226,228–231</sup>

As shown in Figure 3-9 the procedure generally requires a base and alkyl halide in an organic solvent; the temperatures in which these procedures are carried out can be varied however most are under reflux for several hours forming a mixture of products. Further details on the yields and products achieved *via* these methods is summarised in Table 3-1. Iwanoto *et al.* found that method (1) in Figure 3-9 was optimal for mono-alkylations; gaining a maximum isolated yield of 67 % with benzylbromide.<sup>232</sup> Further comparison of yields of mono-alkylated products *via* methods (4) and (5) as shown in Figure 3-9 have been investigated by Groenen *et al.* with the greatest yield obtained *via* method (4) with Me-X of 67 %.<sup>229</sup> This formation of di-, tri- and tetra-alkylated products was initially somewhat surprising due to the large increase in pK<sub>a1</sub> to pK<sub>a2</sub> of TBC (as will be discussed). This further alkylation is believed to be due to the disruption of the stabilisation mechanism that would secure the distal proton that is often responsible of pK<sub>a2</sub>. Conventionally the initial deprotonation results in a phenolic anion; this anion then stabilises the 3 other phenolic protons *via* a circular bonding and stabilisation mechanism that causes a pseudo covalent-hydrogen bond to form. The alkylation that occurs post deprotonation disrupts this stabilisation mechanism thus ‘resetting’ the pK<sub>a</sub>’s of the phenolic groups to those similar to the TBC starting material hence pK<sub>a1</sub> *ca.* pK<sub>a2</sub>

allowing for even weak bases such as  $K_2CO_3$  to result in formation of polyalkylated products.

**Table 3-1-** Etherification of *p*-*tert*-butylcalix-[4]-arenes with simple alkyl halides *via* 6 different methodologies. <sup>226,228–231</sup>

Product	Method	Yield	Reference
	(1)	30%	Diamond <sup>190</sup>
	(2)	75%	Shu <sup>226</sup>
	(3)	74%	Iwamoto <sup>228</sup>
	(6)	50%	Santoyo-Gonzalez <sup>230</sup>
	(4)	58%	Groenen <sup>229</sup>
	(5)	67%	

### 3.1.3.3 Etherification of the lower rim with functionalised alkyl halides

As previously discussed the introduction of specific functionalities in regards to sensor and extraction capabilities are a vital stepping stone in forming such compounds. In general, functionalised alkyl halides are in the structure  $XCH_2Y$ ; where X = leaving group (Cl, Br, I, OTs), and Y = functional group (alkene, alkyne, etc.) or  $XCH_2COY$  if Y contains a heteroatom *i.e.*  $NR_2$ , OH, Cl.<sup>233–236</sup> Throughout

literature there are infinite examples of etherification of the lower rim of TBC, however, the general methodologies follow the similar to those utilised with simple alkyl halides, Figure 3-9 with the functionalised reagents aforementioned, Figure 3-10.<sup>237</sup>

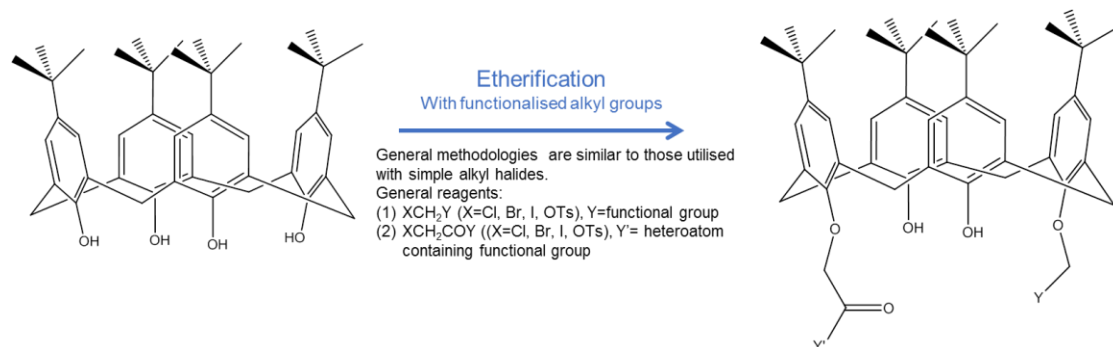


**Figure 3-10-** Etherification of *p-tert*-butylcalix-[4]-arenes with functionalised alkyl halides.<sup>233–236</sup>

### 3.1.3.4 Formation of intramolecular bridges on the lower rim

The formation of crown ether/cavitand type motifs on the lower rim of TBC is of great interest in regards to the application of TBC to sensors and extraction processes; integration of an intramolecular bridge is the main methodology to make such a compound similar to that's shown in Figure 3-6.<sup>212</sup> The first bridge species was formed *via* the acid catalysed (*p*-toluenesulphonic acid) etherification of TBC with diethylene glycol.<sup>238,239</sup> Since this initial success a large variety of glycol bridged species have been formed of various chain lengths, furthermore the formation of di-bridge compounds has also been achieved *via* a step-wise methodology utilising the mono-bridged product.<sup>233</sup> The synthetic methodologies utilised in the formation of bridges follow the same template as that of simple alkyl halides as shown in Figure 3-11.

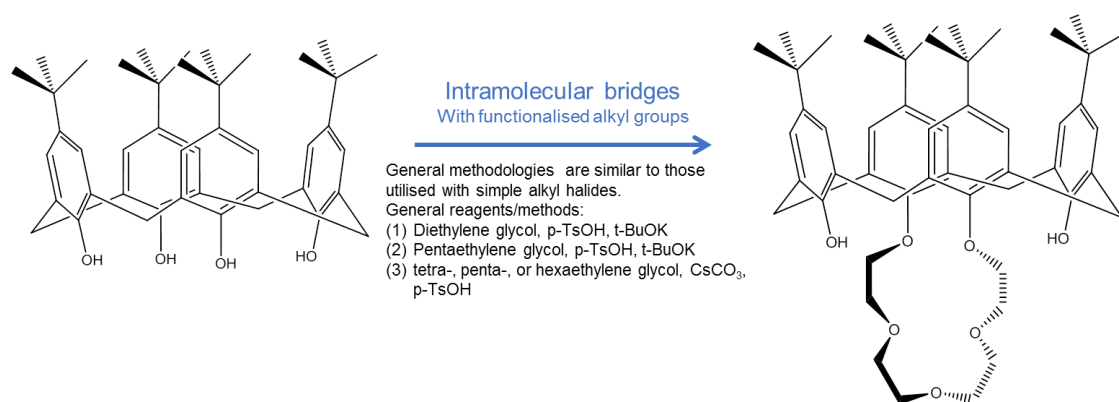


**Figure 3-11-** Formation of intramolecular bridges *p-tert*-butylcalix-[4]-arenes with glycols.<sup>238–240</sup>

### 3.1.3.5 $pK_a$ and conformations of *p-tert*-butylcalix-[4]-arenes

Conformations adopted by TBCs are of great interest for many reasons; aforementioned the functionalisation of TBC can have effects on the conformers achieved which, in turn can lead to difficulties in determining products achieved and furthermore in applications it can affect metal- $\pi$  interactions observed and the binding abilities due to changes in the lower rim cavity.

There are 4 conformations observed in TBC; cone, partial cone, 1,3-alternate and 1,2-alternate as shown in Figure 3-13.<sup>241</sup> This behaviour was initially determined by Cornforth *et al.* who whilst working with TBC arenes or as was previously termed cyclotetra-*m*-benzylene.<sup>167</sup> Munch *et al.* noted the change of  $-\text{CH}_2-$  linker groups as highlighted in Figure 3-12, with temperature hence indicating that the exchange between conformers is affected by temperature and solvent interactions. The  $-\text{CH}_2-$  exhibiting a quartet at 0 °C, doublet at 35 °C and singlet < 50 °C in chloroform with the singlet further sharpening with increasing temperature; an example of  $^1\text{H}$  NMR coalescence.<sup>242</sup> It should be noted that the cone conformer is preferred in TBC.

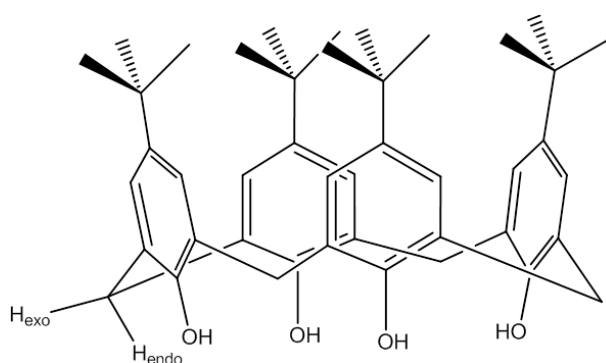


**Figure 3-12-** Cone conformer of *p-tert*-butylcalix-[4]-arene highlighting  $-\text{CH}_2-$  linker groups.

The interconversion is even more rapid upon the etheration of the lower rim. Gutsche *et al.* found that the mono-, di-, tri- and tetra-ethers of TBC are conformationally flexible and at room temperature interconvert at a rate of *ca.* 100  $\text{sec}^{-1}$ .<sup>243</sup> Furthermore, the length of the etheryl group impacts on the preferred conformation with smaller tetra-ethers (methyl, ethyl) preferring the partial cone and larger (propyl, butyl) preferring the cone conformation. It is evident throughout literature that the environment in which the TBC is solvated in, along with other factors such as steric bulk, temperature and pH can alter the conformation observed.



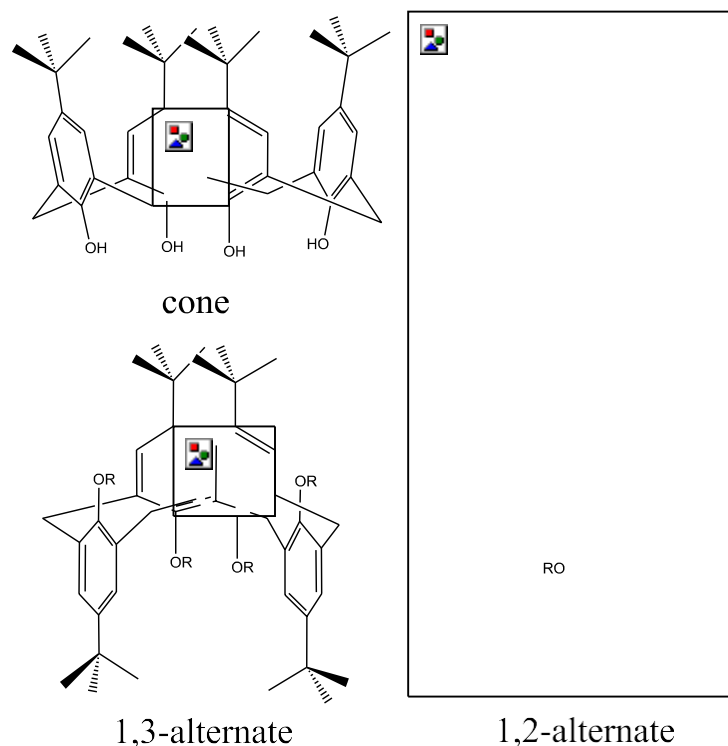


**Figure 3-13**-Conformers of *p*-*tert*-butylcalix-[4]-arene.

The determination of the  $pK_a$  of the phenolic protons of the TBC motif have been of great interest but has not been without challenges due to the low solubility of such compounds within aqueous solvents. Initial determinations *via* spectrophotometric and potentiometric techniques were made for *p*-nitro and *p*-sulfonate functionalised motifs by Reinhoudt and Shinkai.<sup>178,179,244</sup> The spectrophotometric technique involves the titration of the water solubilised calixarene motif and monitoring of the UV/Vis spectrum; specifically the band alluding to the phenolic proton (280 nm).<sup>245</sup> It should be noted that  $[N_{4444}][OH]$  has been utilised as a base source within these titrations however there have been no reports of isolation of such calixarate salt. Furthermore, it is more evident in potentiometric techniques as both a base and an electrolyte source.

In regards to *p*-*tert*-butylcalix-[4]-arene the  $pK_a$  was determined by Shinkai *et al.* *via* a 4-nitrophenolate titration in THF rather than the conventional protic solvent methods *i.e.*  $H_2O$ , MeOH and EtOH. The  $pK_{a1}$  was determined to be 4.11.<sup>171,178,179</sup> In comparison to *p*-*tert*-butylphenol which has a basic  $pK_a$  of 10.17 the acidic  $pK_a$  of TBC is believed to be due to conformational effects.<sup>246</sup> The *tert*-butyl motif on the calix-[4]-arene body has a significant effect on the dissociation constant of the phenolic proton; with *p*-methylcalix-[4]-arene and *p*-*tert*-butylcalix-[4]-arene having  $pK_a$ 's of 6.0 and 4.3 respectively. This large change in  $pK_a$  is believed to be due to

subtle conformational effects due to the differing sizes of the alkyl substituents.<sup>177,224</sup> The conformational effects mentioned are mainly due to the rigidity of the structure and proximity of 3 other phenolic protons which in turn can deprotonate and protonate simultaneously. The mobility of these protons is often described historically as the ‘super acidic’ protons.<sup>178</sup>

**Table 3-2**-pK<sub>a</sub>s of *p*-functionalisedcalix-[4]-arenes with R dictating the functional group para to the phenolic proton.

R	pK <sub>a1</sub>	pK <sub>a2</sub>	pK <sub>a3</sub>	pK <sub>a4</sub>	Ref
<i>t</i> -Bu	4.11				Shinkai <sup>178</sup>
SO <sub>2</sub> N(CH <sub>2</sub> CH <sub>2</sub> OH) <sub>2</sub>	0.8	9.7	12.5	>14	Shinkai <sup>179</sup>
NO <sub>2</sub>	2.9	10.9	12.3	>14	Shinkai <sup>179</sup>
SO <sub>3</sub> H	3.26-3.34	12.3	12.9	13.6	Ungaro <sup>247</sup>
SO <sub>3</sub> Na	3.26	11.8	12.8	14	Shinkai <sup>248</sup>

### 3.1.4 Acetate anion containing ionic liquids

Since the discovery of basic anions of ionic liquids such as acetates, dicyanamides and other carboxylates there has been a significant interest in their applications to base catalysis and as a solvent for acidic media.<sup>249</sup> Hence allowing for a non-volatile alternative to conventional bases such as triethylamine, potassium carbonate *etc.*

Imidazolium acetate ionic liquids were first reported in literature by scientists Ebel, Degen, Groll, Simer and Maase at BASF in 2004-2006. Synthesised *via* several methodologies listed below:

- (1) Oxaldehyde, acetic acid, acetone, and methyl amine in a water solvent.  
(Commonly referred to as the Debus-Radziszewski imidazole synthesis)  
<sup>250,251</sup>
- (2) Potassium *tert*-butoxide and [Emim][Cl] in *n*-butanol. (Commonly referred to as the Finkelstein method)<sup>252,253</sup>
- (3) [Emim][HSO<sub>4</sub>] and barium hydroxide in water.<sup>252</sup>
- (4) Methyl acetate and ethyl imidazole in methanol<sup>254</sup>

Within more recent literature, methodologies which encompass green syntheses principles and reactions have been utilised in the synthesis of imidazolium acetates. Dai *et al.* in 2010 were the first to report the use of dialkylcarbonates with alkyl imidazoles hence providing a 100 % atom efficient route.<sup>253</sup> It should be noted that method (4) by Degen and Ebel is also 100 % atom efficient, however, conversion is

reported to be significantly lower at 24 %.<sup>254</sup> The first report of tetradecyltriethylphosphonium acetate, [P<sub>66614</sub>][OAc] in literature was by Rebelo and co-workers in 2006 citing methodologies reported by Downard *et al.* for preparation of the phosphinate analogues in 2002.<sup>19,255</sup>

Since their initial discoveries there have been a significant number of studies regarding the physical and chemical properties. Densities, viscosities and melting point have been extensively studied by Rebelo *et al.*<sup>19,256,257</sup> In regards to the basicity of the acetate anions MacFarlane and co-workers were the first to classify the acetate anion containing ionic liquids as basic.<sup>249</sup> The significance of such classifications initiated the utilisation of these ILs in reactions conventionally base catalysed. Such basicity's of these ILs were determined by acid and base indicators such as alizarin red and bromocresol blue. A neat study by Seddon and co-workers utilised universal indicator to determine the relative basicity of base functionalised ionic liquid cations.<sup>258</sup> Universal indicator being a mixture of acid and bases such that proton exchange in the indicator is interrupted by the ionic liquid giving indications of the relative basicity.

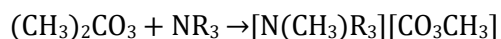
It is evident throughout literature that the most apparent applications of these acetate anion ionic liquids is in CO<sub>2</sub> capture and cellulose processing.<sup>259–264</sup> Carbon capture methods using these ILs work on the premise that the acetate anion forms a complex with the CO<sub>2</sub> molecule as determined by Shiflett *et al.*<sup>265,266</sup> The Lewis basicity of the anion was deemed vital as fluorinated analogues containing CF<sub>3</sub> group exhibited a significantly poorer CO<sub>2</sub> solubility as the electron withdrawing nature of the CF<sub>3</sub> reduced the Lewis basicity of the anion.

In regards to the application of acetate anion ionic liquids as catalyst Zhang *et al.* demonstrated the use of [Emim][OAc] as a catalyst in the cyanosilylation of carbonyl compounds such as benzaldehyde.<sup>267</sup> The [Emim][OAc] was demonstrated to have significant catalytic abilities at loadings as low as 0.0001 mol%; comparatively other anions which are not considered basic ionic liquids such as [Emim]Br did not demonstrate the same catalytic abilities.

### 3.1.5 Methyl carbonate anion ionic liquids

Methyl carbonate ionic liquids are a relatively new class of basic anion ionic liquids. First synthesised by Janson *et al.* by methylating trialkylamines with dimethyl carbonate, 'an environmentally benign alkylating reagent', affording a fully organic ionic liquid as shown in Equation 3-1.<sup>268,269</sup>

Equation 3-1



This methodology is 100% atom efficient and avoids the use of conventionally utilised alkyl halides. This methodology is not limited to ammonium and has been commercialised by Proionic GmbH who have developed the Carbonate Based Ionic Liquid Synthesis (CBILS®), which is a registered trademark of Proionic GmbH) which can form methyl carbonate anion ILs with and not limited to phosphonium, imidazolium, and pyrrolidinium cations. (Figure 3-14)<sup>3,262,263,270,271</sup>

Within the CBILS process the synthesis of the methyl carbonate anions step but the initial alkylations using the dialkyl carbonated provide opportunities for regeneration of the initial alkylating agent *via* a catalytic process with carbon dioxide. Furthermore, the carbon dioxide required can be utilised from the anion exchange steps in such that if a halide or other anion sourced from a Brønsted acid reacts with the methyl carbonate anion to give the desired product, methanol and CO<sub>2</sub>. This methodology is currently deemed the market leader in forming ultra-pure ionic liquids at large scale.<sup>2</sup> Discussions regarding the reactivity of the methyl carbonate anions in terms of acid base interactions with Roland Kalb of Proionic GmbH gave insight that within the experience of Proionic's development of these methodologies the anions would react in such a manner with species with a pK<sub>a</sub> >9.

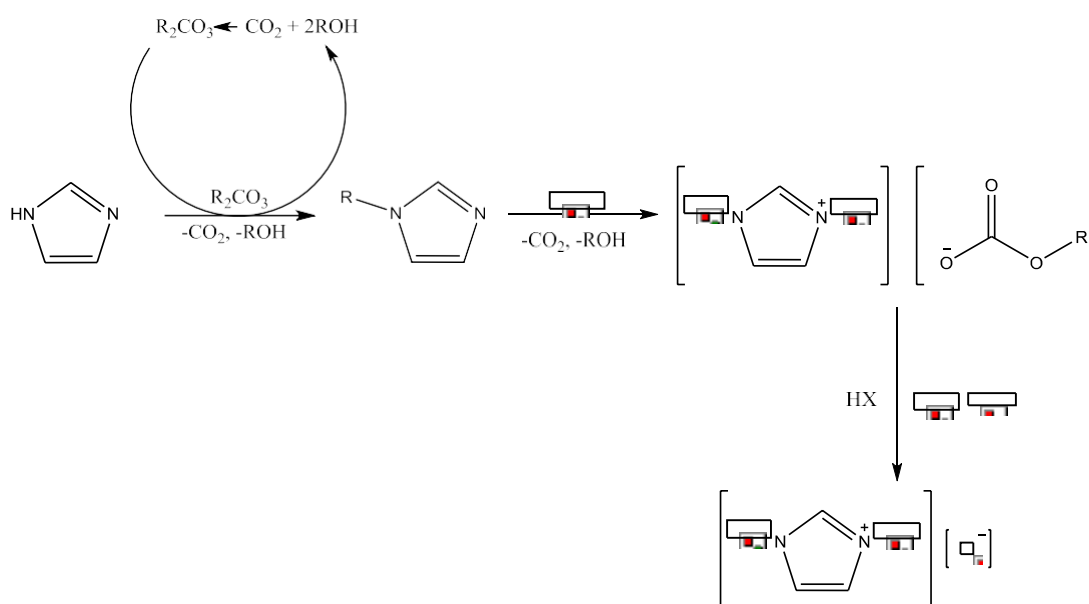


**Figure 3-14-** Carbonate Based Ionic Liquid Synthesis (CBILS®, which is a registered trademark of Proionic GmbH).<sup>2,3,270</sup>

## 3.2 Results and Discussion

Within the field of functionalised *p-tert*-butylcalix-[4]-arenes there are two significant roadblocks that are a detriment to the full utilisation of these compounds;

- (1) The low solubility of the starting material *p-tert*-butylcalix-[4]-arene hence requiring a significant amount of hazardous organic solvents to be utilised such as DMF. Furthermore, the sluggishness of such diluted reactions as a consequence of these dilutions.
- (2) The lack of selectivity demonstrated in alkylation and esterification reactions naturally lowers yields obtained and requires difficult and laborious separation techniques.

In this project it was aimed to solve both of these issues utilising ionic liquids with intrinsic basicity which aforementioned is critical in both solvation mechanisms and activation of phenolic sites for functionalisation.

### 3.2.1 Screening of ionic liquids

In this work, basic ionic liquids are utilised as a solvent for what would be determined as non-functionalised calix-[4]-arene motif *p-tert*-butylcalix-[4]-arene, TBC. The acetate anion in ionic liquids is well established for its strong basicity and have often been utilised in carbon capture and cellulose solvation as discussed.<sup>249,262,272</sup> It is this inherent basicity that makes the ionic liquids appealing whilst being a relatively non-polar solvent; focusing on simple phosphonium and imidazolium acetate ionic liquids it was wished to determine the solubility and the solvation mechanism of *p-tert*-butylcalix-[4]-arene.

Learning from previous methodologies in such that a base is used to facilitate both the solvation and functionalisation of the TBC motif in syntheses as discussed in section 3.1.2 it was believed that off the shelf basic ionic liquids with acetate anions could be utilised as both a solvent and intrinsic base with an overarching aim to improve yield, selectivity and purification of future alkylation products.

Arrays of common acetate anion ionic liquids were screened for *p-tert*-butylcalix-[4]-arene, TBC solubility. This screening included alkyl imidazolium acetate, and phosphonium acetate ionic liquids.

#### 3.2.1.1.1 Purity of the *p-tert*-butylcalix-[4]-arene starting material

*p-tert*-butylcalix-[4]-arene was obtained in 99% purity from Alfa Aesar. Upon <sup>1</sup>H NMR analysis dichloromethane impurities were detected. In regards to conformers

observed in the sample only a single cone conformer was observed matching data reported by Gutsche *et al.* and listed in Table 3-3<sup>243</sup>

***p*-tert-Butylcalix-4-arene:** <sup>1</sup>H NMR (400 MHz, CDCl<sub>3</sub>) δ 10.34(s, 4H, 4xOH), 7.05 (s, 8H, 8xAr-H), 4.26 (d, *J* = 19.4 Hz, 3.98H, 2xAr-CH<sub>2</sub>-Ar), 3.49 (d, *J* = 13.3 Hz, 3.91H, 2xAr-CH<sub>2</sub>-Ar), 1.55 (s, 35.64H, 4xt-C (CH<sub>3</sub>)<sub>3</sub>).

**Table 3-3-** Comparison of *p*-tert-butylcalix-[4]-arene samples via <sup>1</sup>H NMR spectroscopy.

Conformation	Ar-H	CH <sub>2</sub>	<i>t</i> -Bu	Reported by
Cone	singlet	Doublet of doublets ( <i>J</i> = 12 Hz)	singlet	Gutsche <sup>243</sup>
Commercial sample	singlet	Doublet of doublets ( <i>J</i> =19.4-13.3 Hz)	singlet	This work

### 3.2.1.2 Phosphonium acetate ionic liquids

The initial IL tested with *p*-tert-butylcalix-[4]-arene was trihexyltetradecyl phosphonium acetate, [P<sub>66614</sub>][OAc]; this IL along with having the basic acetate anion has a large phosphonium cation hence diffusing and decreasing the ionicity of the IL. It was observed that [P<sub>66614</sub>][OAc] could dissolve a significant amount of TBC; up to 25 mol% as shown in Figure 3-15 and listed in Table 3-4. The [P<sub>66614</sub>][OAc] upon addition of TBC solvation occurs within 4-6 hours resulting in a near identical solution. The solvation itself was found to be relatively rapid; within 4 hours of stirring at 40 °C (the elevated temperature to facilitate stirring) the crystalline TBC solid disappeared.

The acetate anion was suspected to strongly hydrogen bond to the phenolic protons of the TBC and eventually resulting in deprotonation. However, this was an initial speculation and a complete determination of this solvation mechanism is vital to any future applications due to the prerequisite deprotonating required for alkylations *etc.*

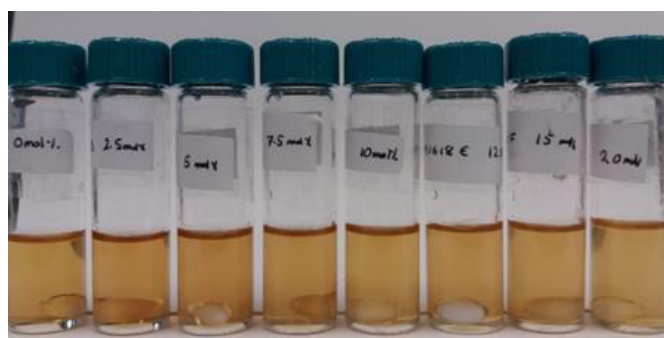


**Figure 3-15-** *p*-tert-butylcalix-[4]-arene dissolved in trihexyltetradecylphosphonium acetate (L-R: 0, 2.5, 5, 7.5, 10, 12.5, 15, 20 mol %).

**Table 3-4-** *p-tert*-butylcalix-[4]-arene, TBC dissolved in trihexyltetradecylphosphonium acetate, [P<sub>66614</sub>][OAc].

Sample	Mass/g		Moles		Concentration mol %
	IL	TBC	IL	TBC	
1	2.5	0	0.004605	0	0
2	2.5	0.076627	0.004605	0.000118	2.5
3	2.5	0.157286	0.004605	0.000242	5
4	2.5	0.242306	0.004605	0.000373	7.5
5	2.5	0.332049	0.004605	0.000512	10
6	2.5	0.42692	0.004605	0.000658	12.5
7	2.5	0.527372	0.004605	0.000813	15
8	2.5	0.74711	0.004605	0.001151	20

The solutions remained stable for several weeks in ambient conditions with no precipitations observed.

### 3.2.1.3 Imidazolium acetate liquids

Screening with 1-methyl-3-ethylimidazolium acetate, a commercially available IL was less successful than those observed with [P<sub>66614</sub>][OAc]. The TBC failed to form transparent solutions with minimal amounts of TBC added instead a hazy suspension was formed. The addition of a co-solvent, DMF that is known to dissolve TBC was added eventually affording a transparent solution, however, upon sitting for several days a crystalline solid appeared. The crystals were physically extracted from the liquor and measured using single crystal diffraction spectroscopy. The structure was determined to be that of 1-methyl-3-ethylimidazolium *p-tert*-butylcalix-[4]-arate; an ionic salt containing a mono-deprotonated TBC as shown in Figure 3-16.

The crystal structure exhibits many of the features that were aimed to be achieved *via* the use of ILs; firstly, the TBC is mono-deprotonated hence the cyclic hydrogen bonding has been disrupted *via* the IL, secondly the cyclic hydrogen bonding post-mono-deprotonation is reinitiated. The significance of this is crucial in providing a mono-deprotonated species; within conventional methods the base addition often results in multiple variations of the deprotonated species *i.e.* di-, tri- and tetra-deprotonated. The imidazolium cation mainly interacts with the lower rim of the TBC however, as shown, the cation sits within the cavity of the neighbouring the TBC.

The imidazolium cation lies 3.139 Å from the lower rim of the TBC and at its closest point it lies 3.00 Å from the neighbouring TBC molecule in which it is cradled but  $\pi$  interactions as shown in Figure 3-17.

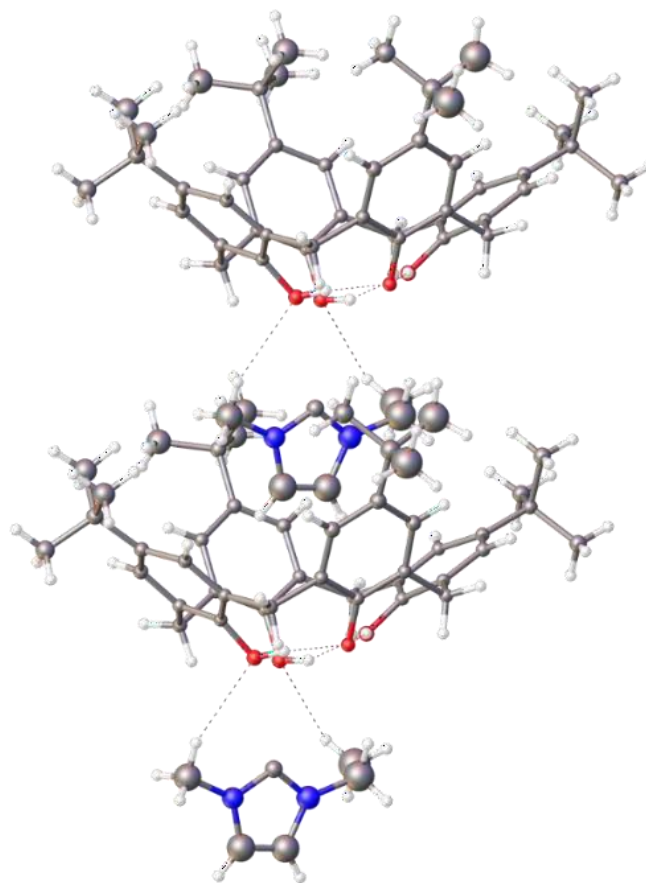


**Figure 3-16-**Single crystal X-ray diffraction spectroscopy determined structure of 1-methyl-3-ethylimidazolium p-tert-butylcalix-[4]-arate ionic salts.

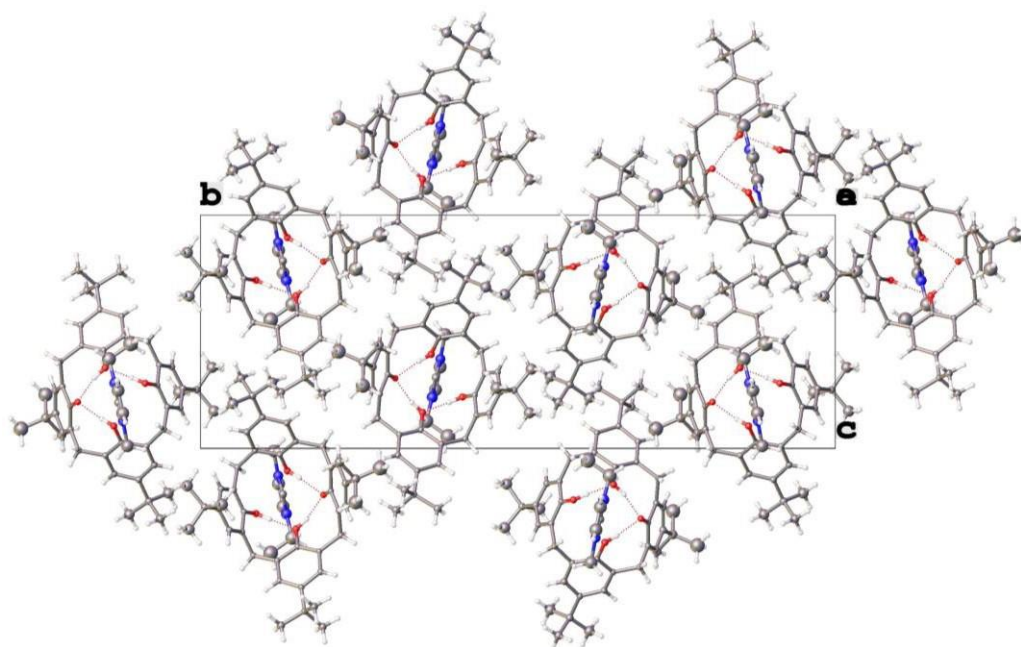


**Figure 3-17-** Single crystal X-ray diffraction spectroscopy determined structure of 1-methyl-3-ethylimidazolium p-tert-butylcalix-[4]-arate ionic salts.



### 3.2.2 Behaviour of *p*-tert-butylcalix-[4]-arenes in [P<sub>66614</sub>][OAc] ionic liquids

#### 3.2.2.1 Spectroscopic analysis-introduction

As aforementioned the determination of the solvation mechanism is vital to elucidating its use in future functionalisation syntheses. Work by Surov *et al.* also showed that the solubility of TBC and similar species is not only dictated by the ability to dissociate a proton but is also affected by the *endo*-solvent interaction.<sup>273</sup> In solvents that form complexes with calixarenes using only VDW interactions this is especially prevalent whereas the solvent molecule sits as a guest molecule that although it inhibits any conformation exchanges that may occur there is an increase in entropy and free energy as the solvent molecule is still free to move within the cavity. Hence it is not exclusively the behaviour and interactions of the IL with the phenolic protons that must be considered but also host-guest and VDW driven interactions.

#### 3.2.2.2 Nuclear Magnetic Resonance Spectroscopy

All measurements were completed using a Bruker Advance DPX 400 MHz NMR spectrometer with the neat mixtures of [P<sub>66614</sub>][OAc] and TBC to ensure no solvent interactions would disrupt the TBC and acetate anion interactions. [P<sub>66614</sub>][OAc] when observed in <sup>1</sup>H NMR spectroscopy gives rise to broad peaks and contains significant amount of overlapping peaks due to high viscosity and complexity of the cationic species therefore, it was determined that the sharp signals of a <sup>13</sup>C at 50 °C would be more beneficial to investigate the variation in acetate peaks due to the suspected TBC and acetate anion interaction as shown in Figure 3-19.

Upon increasing [TBC] the methyl peak of the acetate anion moves upfield indicating an increase in shielding *i.e.* an increase in electron density. From 0 mol% to 20 mol% TBC a shift greater than 2 ppm is observed as the CH<sub>3</sub>- of the acetate anion. It is suspected that this increase in electron density may be due to the acetate anion placing itself in the *endo* positioning the TBC as shown in Figure 3-18. The carbonyl peak, however, at 173.5 ppm shows no significant change with increasing TBC concentration, however, at 15 mol% and above a peak emerges at 169 ppm which may be indicative to that of acetic acid as shown in Figure 3-20. It should be noted that no peak at 21 ppm is observed to indicate the methyl group of the acetic acid suspected to be formed.<sup>274</sup> Conversely, due to proton exchange between the acetate anion and phenolic protons an averaging to the methyl peaks indicative of acetic acid and the acetate anion may be observed. This would be in

accordance with the up-field shift observed in Figure 3-19. The position of the acetate anion within this cavity is very likely in the liquid state; as a result of this there is likely to be shielding of the acetate anion by the aromatic cone walls causing upfield shift in the NMR analysis.

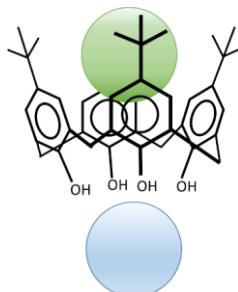


**Figure 3-18-** Representation of endo (green) and exo (blue) areas where acetate charge density may be located.

Previous experiments with imidazolium acetate ionic liquids have given us some indication that this may be the case with [Emim][OAc] being able to dissolve a small amount of TBC eventually crystallising to form a calixarate ionic salt with the imidazolium cation in a solution of what is suspected to be acetic acid and IL. However, it is unclear as to what extent of the anion exchange has occurred in these systems. It is not expected that  $[P_{66614}]^+$  to give similar crystalline results due to the large size and asymmetry of the phosphonium cation which also lends itself to the acetate anion being within the cavity as discussed. Furthermore, the studies when repeated at room temperature an identical trend was observed.

As previously discussed a rather peculiar up-field shift in  $^{13}\text{C}$  NMR studies of  $[P_{66614}][\text{OAc}]$  and TBC was observed, which has been suggested that they may be due to the acetate anion sitting in the cavity of the calix-[4]-arene body. Within phenol solutions it would not be expected to see this occurring with only minimal acetate- $\pi$  interactions within the aromatic species. Due to the size of the  $[P_{66614}]^+$  cation there is no possibility of the cation residing in the cavity of the cone calixarene motif; instead a more perched position is expected

As shown in Figure 3-21 the shift in the  $\text{CH}_3^-$  peak of the acetate anion at 26.1 ppm to 24 ppm with the addition of 20 mol% TBC is not observed to the same extent in analogous *tert*-butylphenol additions. Instead, a small shift to 25.6 ppm is observed indicating hydrogen bonding may only be present. From the  $^{13}\text{C}$  NMR studies it is indicated that the basic acetate anion strongly interacts with the phenolic protons of the TBC. Determination of deprotonation vs hydrogen bonding is as of yet not determined via NMR spectroscopy.

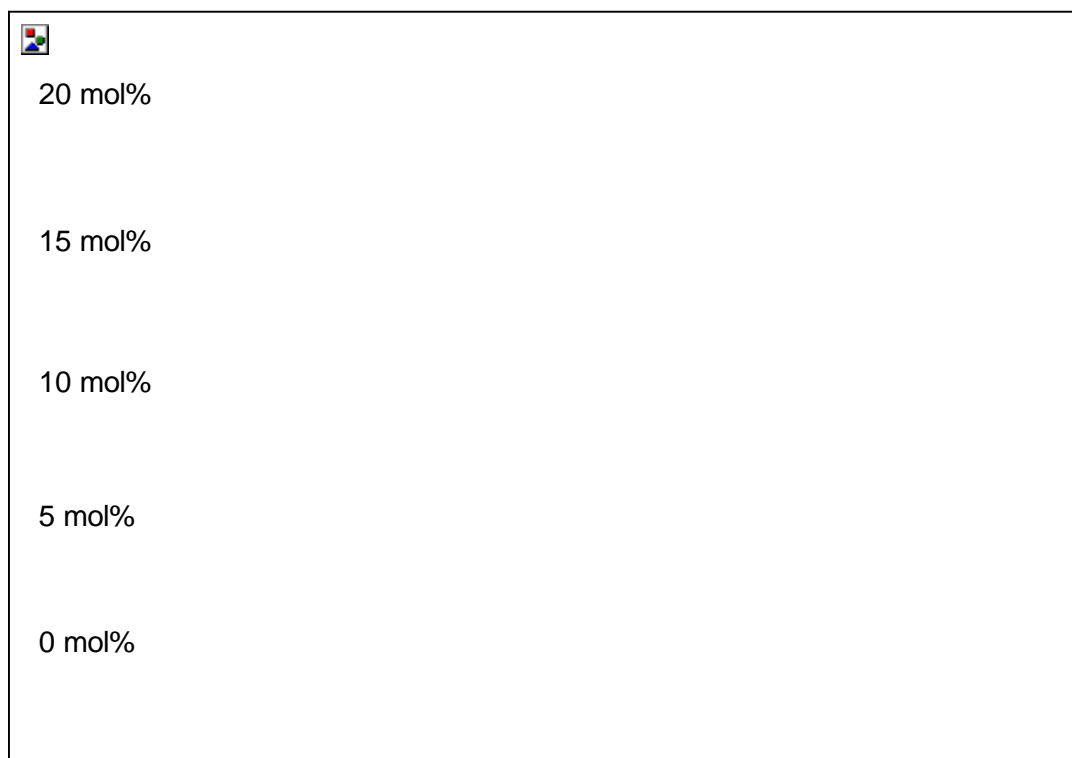


**Figure 3-19-** Partial  $^{13}\text{C}$  NMR spectra of  $[\text{P}_{66614}][\text{OAc}]$  and *p-tert*-butylcalix-[4]-arene. (top-bottom) 20, 15, 10, 5, 0 mol%. (37-13 ppm)

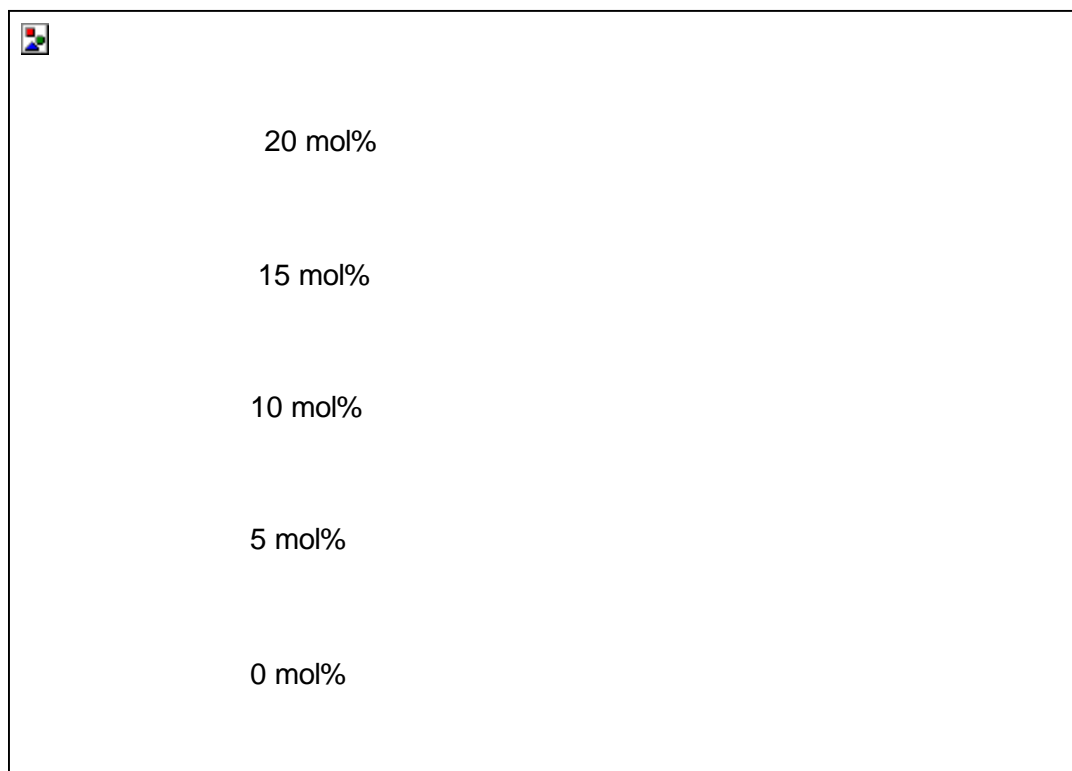


**Figure 3-20-** Partial  $^{13}\text{C}$  NMR spectra of  $[\text{P}_{66614}][\text{OAc}]$  and *p-tert*-butylcalix-[4]-arene. (top-bottom) 20, 15, 10, 5, 0 mol%. (176-122 ppm)

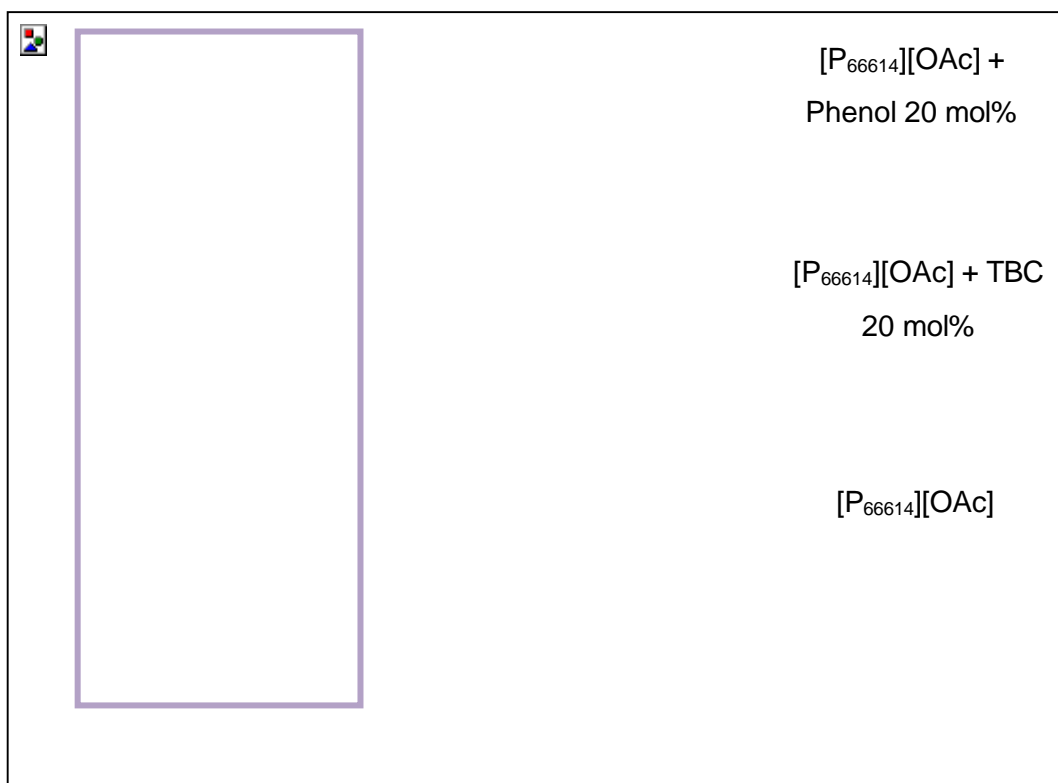


**Figure 3-21**-Partial  $^{13}\text{C}$  NMR spectra of  $[\text{P}_{66614}][\text{OAc}]$  solutions with phenol and *p*-tert-butylcalix-[4]-arene. (27-17 ppm)

### 3.2.2.2.1 *Dynamic equilibrium NMR study*

If the deprotonation of the TBC occurs, it is postulated that it will be a dynamic process due to the suspected formation of acetic acid. If so, it should be visible within variable temperature NMR studies to observe a change in the acetate functionality shift with differing temperatures due to variations in equilibrium due to thermodynamics. A simple study using 10 mol% TBC in  $[\text{P}_{66614}][\text{OAc}]$  at 3 different temperatures, 75 °C, 50 °C and 25 °C showed minimal changes with increasing temperature.

Increasing the temperature from 25 °C to 50 °C an improvement in resolution of the peaks as viscosity decreases is seen. Further changes which could also be determined as the temperature increased further from 50 °C to 75 °C the resolution decreased and the splitting of peaks became less visible; this is believed to be due to dynamic processes occurring between the TBC,  $[\text{OAc}]^-$ , and  $\text{H}[\text{OAc}]$ . This is further supported by the omission of a discrete  $\text{CH}_3^-$  peak at 21 ppm from the  $\text{H}[\text{OAc}]$ .

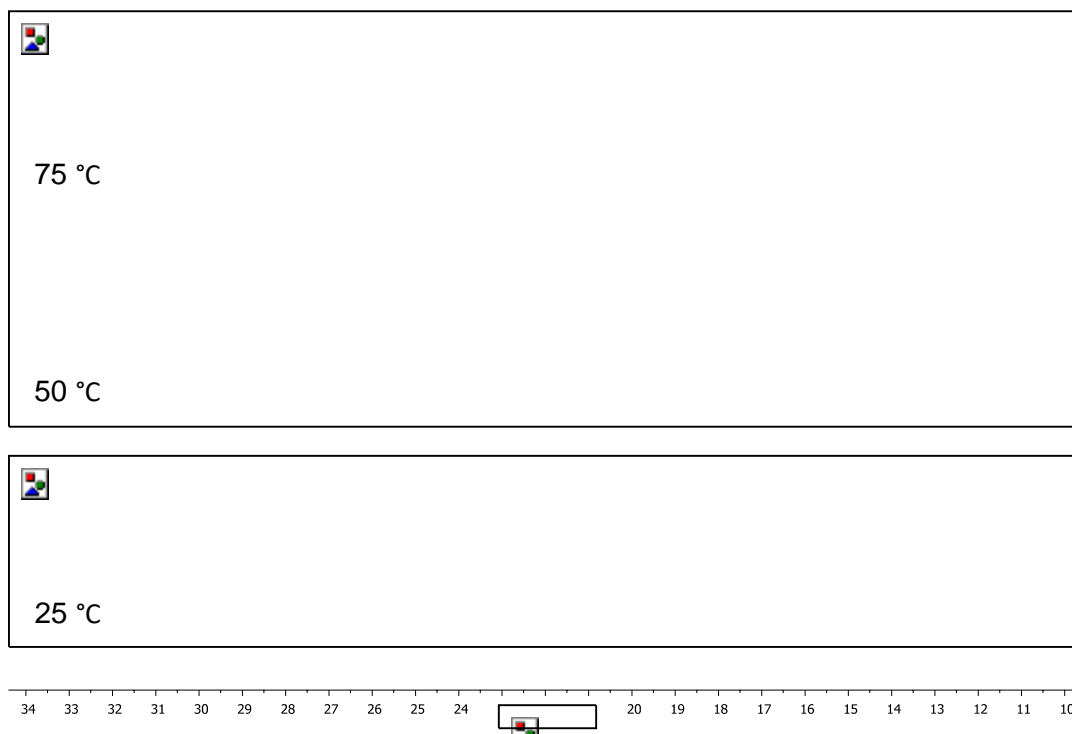


**Figure 3-22-** Partial  $^{13}\text{C}$  VT NMR study of 10 mol% TBC in  $[\text{P}_{66614}][\text{OAc}]$ . Top to bottom: 75 °C, 50 °C, 25 °C. (35-10 ppm)

### 3.2.2.3 UV/Vis spectroscopy

Previous work by Woolfall and Cunningham utilised UV/Vis spectroscopy as a methodology to determine the  $\text{pK}_a$  and deprotonation of TBC in acetonitrile.<sup>275</sup> They observed that with the addition of strong organic bases such as 1, 8-Diazabicyclo [5.4.0] undec-7-ene, DBU to TBC in acetonitrile there is a spectral change that corresponds to the first deprotonation of the phenolic TBC groups. The change itself consists of a shift in  $\lambda_{\text{max}}$  and a shoulder appearing as shown in Figure 3-23. It should be further noted that with the addition of excess of a strong acid such as triflic acid the shoulder formed and shift due to the strong base is reversed.

This study was repeated with our  $[\text{P}_{66614}][\text{OAc}]$  and TBC system in acetonitrile and to these solutions aliquots of DBU were added and spectra observed. It was postulated that if the TBC has already undergone the initial deprotonation no change in spectra should be observed with the addition of base, however, with the addition of a super acid such as triflic acid, a change in spectra should be observed. Hence, determining if a deprotonation had occurred during solvation and not solely hydrogen bonding between the anion and phenolic protons.

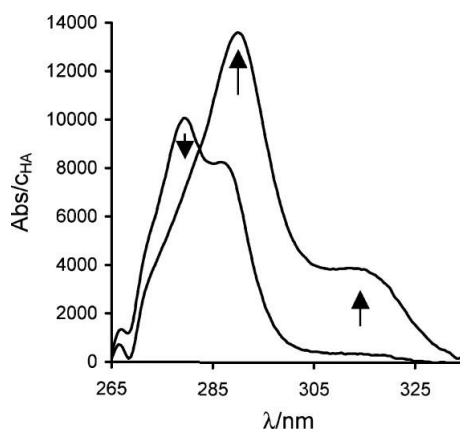


**Figure 3-23**-UV/Vis spectral change on addition of 1 equiv of DBU to *tert*-butylcalix-[4]-arene in MeCN by Woolfall and Cunningham.<sup>275</sup>

A standard solution of the  $[P_{66614}][OAc]$  -TBC solution was formed (20 mol %), a high concentration of TBC as to reduce the amount of ionic liquid present that is not involved within the deprotonation. The solution was diluted using acetonitrile and differing concentrations of the strong base DBU added in aliquots as listed in Table 3-5. No changes in spectra were observed with increasing DBU concentration indicating the TBC is already deprotonated *via* the  $[P_{66614}][OAc]$ . It should also be noted that the shape of the initial solutions is near identical to that reported by Woolfall as shown Figure 3-23.

The addition of 8 aliquots of DBU allows a near 1:2 ratio of TBC: DBU to be reached and no sign of deprotonation both with the initial aliquot and final aliquot as observed with the spectra remaining consistent as shown in Figure 3-24.

**Table 3-5**- UV/Vis investigation  $[P_{66614}][OAc]$  20 mol% TBC vs DBU in acetonitrile.

	TBC/ mmol	DBU/ mmol	Ratio TBC:DBU
Aliquot 1	1.78E-04	3.94E-05	4.52
Aliquot 2	1.78E-04	7.88E-05	2.26
Aliquot 3	1.78E-04	1.18E-04	1.51
Aliquot 4	1.78E-04	1.58E-04	1.13
Aliquot 5	1.78E-04	1.97E-04	0.90
Aliquot 6	1.78E-04	2.36E-04	0.75
Aliquot 7	1.78E-04	2.76E-04	0.65
Aliquot 8	1.78E-04	3.15E-04	0.56

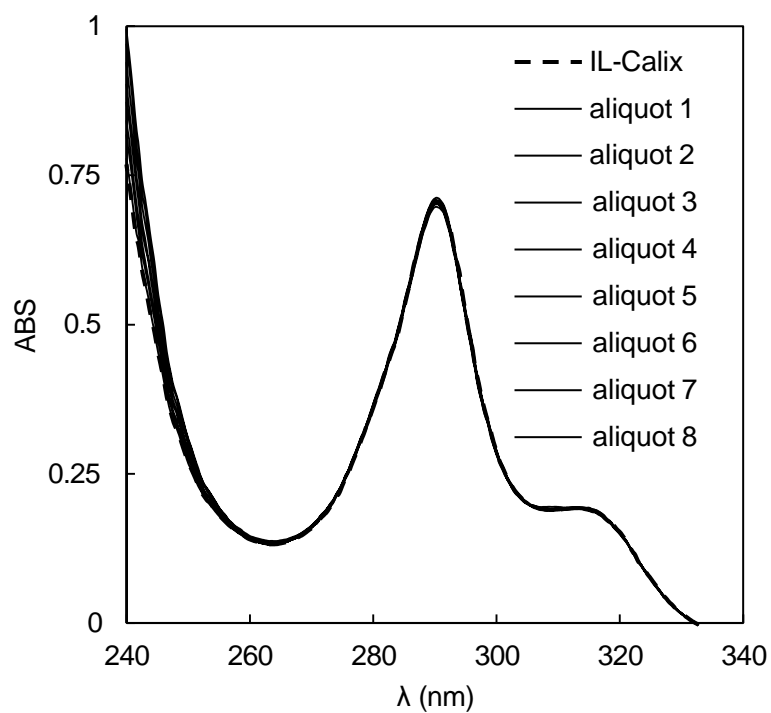


**Figure 3-24**-UV/Vis spectra of  $[P_{66614}][OAc]$  and TBC 20 mol % (IL-Calix) in MeCN with varying concentrations of DBU added.

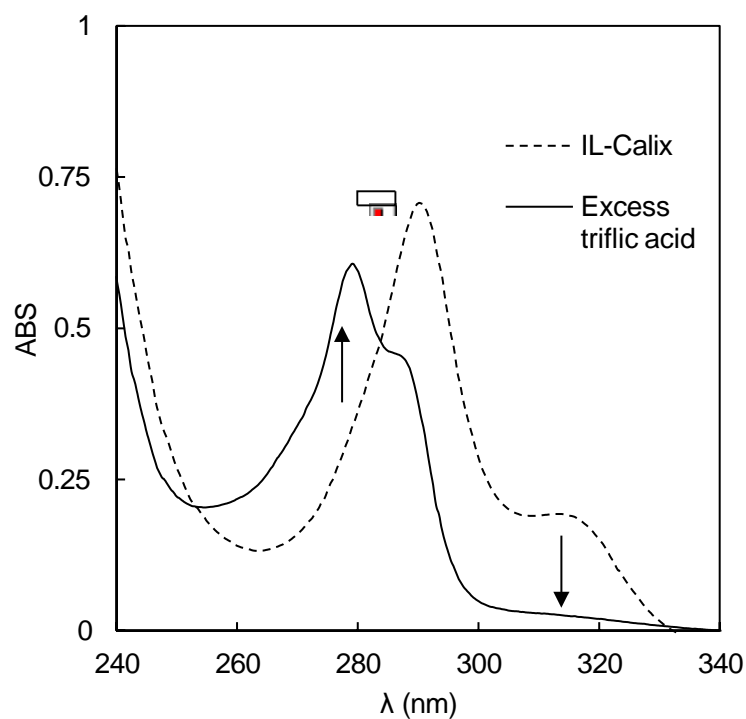


**Figure 3-25**-UV/Vis spectra of  $[P_{66614}][OAc]$  and TBC in MeCN.

The addition of triflic acid as shown in Figure 3-25 causes a significant shift in  $\lambda_{\max}$  and the loss of the shoulder previously assigned to the deprotonated TBC. The resultant spectrum is near identical to that of the original TBC-MeCN spectra as previously discussed. This UV/Vis spectroscopic study confirms the deprotonation has originally occurred *via* the solvation of TBC in the  $[P_{66614}][OAc]$  ionic liquid due to the acetate anion hence the addition of further base has no affect as the second deprotonation is exceeding difficult. Further to this, the first deprotonation can be reversed with the addition of a strong acid and is observed *via* UV/Vis spectroscopy.

To further confirm the deprotonation of the TBC is solely due to the acetate anion of the  $[P_{66614}][OAc]$  a control experiment in which TBC was pre-dissolved in an acetonitrile solution and  $[P_{66614}][NTf_2]$  was added in a 5-fold excess to TBC. The solution was stirred and allowed to equilibrate for 24 hours before UV/Vis spectra were recorded with again sequential aliquots of DBU added and shown in Figure 3-26. The shift in  $\lambda_{\max}$  as shown in Figure 3-26 indicates that deprotonation has not occurred within the  $[P_{66614}][NTf_2]$  system instead any interactions between the TBC and the IL are solely *via* hydrogen bonding and Van Der Waal contributions. Hence our initial speculations that a basic anion is critical to developing an efficient solvent system for TBC.

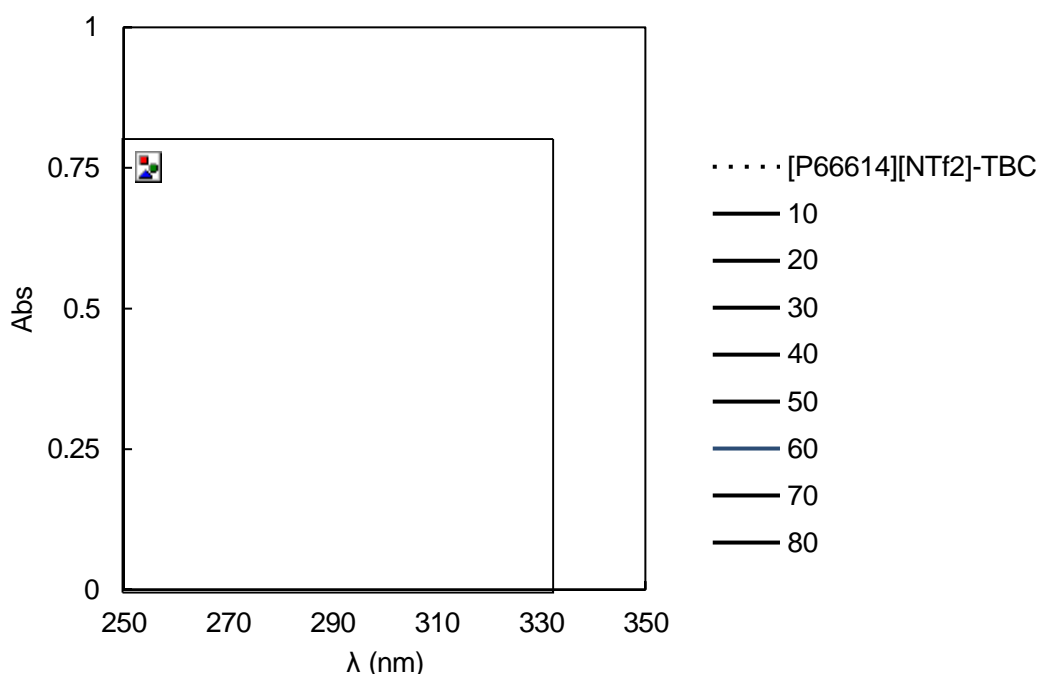


**Figure 3-26-** UV/Vis spectra of  $[P_{66614}][NTf_2]$  and TBC in MeCN with varying concentrations of DBU added.



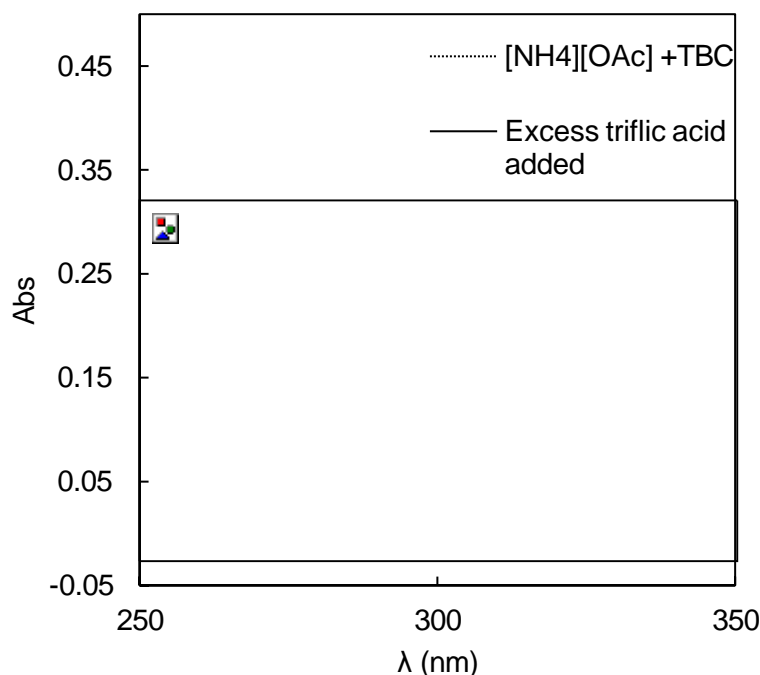


**Figure 3-27-** UV/Vis spectra of  $[\text{NH}_4][\text{OAc}]$  and TBC in MeCN/MeOH with excess triflic acid added (with varying concentrations of DBU added).

To confirm the cation does not impact on the deprotonation the as discussed  $[\text{P}_{66614}][\text{OAc}]$  study was repeated with ammonium acetate,  $[\text{NH}_4][\text{OAc}]$ . It should be noted that at ca. 5 wt% methanol in acetonitrile solution was utilised. Upon addition of DBU aliquots no changes in spectra were observed, however, upon addition of excess triflic acid as shown in identical behaviour to that in the Figure 3-25 is observed. Hence it can be determined that the acetate anion is the sole species causing the deprotonation to occur.

#### 3.2.2.4 Thermogravimetric analysis, TGA

$^1\text{H}$  NMR spectroscopic analysis of the *p-tert*-butylcalix-[4]-arene has shown that there are dichloromethane impurities within the crystalline starting material. This is again seen in thermogravimetric analysis, TGA of the commercial *p-tert*-butylcalix – [4]-arene in Figure 3-28 with a mass loss of  $\approx 5\%$  at  $200\text{ }^\circ\text{C}$ ; decomposition then gradually proceeds. This is a high temperature for DCM to be evaporated but it must be remembered that the DCM is essentially a dichloromethane of crystallisation (a solvate) and there are lattice energies to be overcome before evaporation/release at higher than expected temperatures.

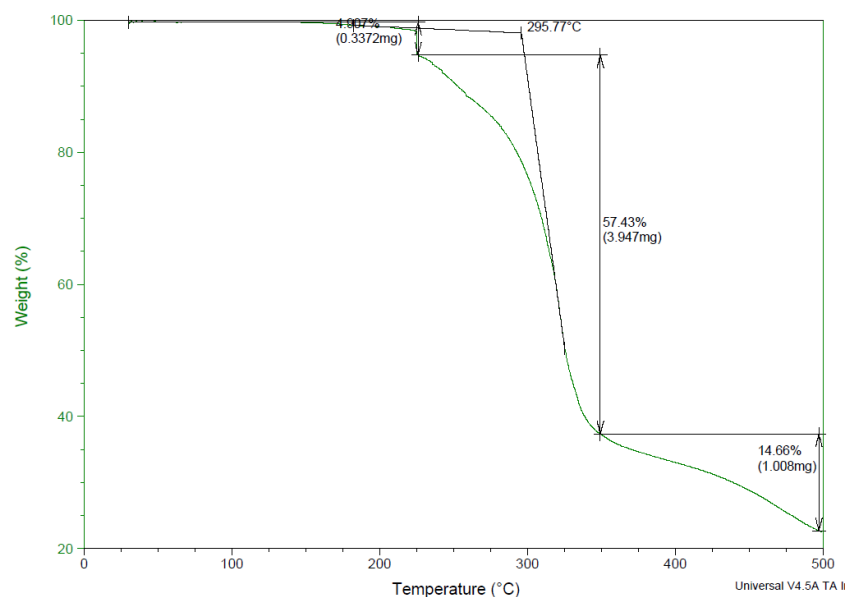


**Figure 3-28**-TGA of *p*-tert-butylcalix-[4]-arene (commercial sample). Rate of heating 1 °Cmin<sup>-1</sup>.

The neat IL under TGA analysis also shows some solvent impurities; most likely to be water or acetone below 200 °C as shown in Figure 3-29. After the impurities are removed the IL is stable 248.8°C as shown in Figure 3-29. When investigating our mixtures of [P<sub>66614</sub>][OAc] and TBC there are several considerations that must be taken account. Firstly, the initial impurities in the TBC and [P<sub>66614</sub>][OAc]; to remove water impurities and acetone the IL was placed on high vacuum for 24 hours at 75 °C, the DCM impurities in *p*-tert-butylcalix-[4]-arene are very difficult to remove due to the high melting point and point of solvent release; +200 °C. Hence it was deemed that the DCM impurities could not be removed.

Secondly, it must be considered as to what species may now be present as a buy product of solvation, most likely is acetic acid *via* the proton abstraction solvation mechanism of the TBC. Acetic acid has a boiling point of 118.5 °C.<sup>276</sup> Thirdly there is a significant difference in the decomposition temperature of the *p*-tert-butylcalix-[4]-arene and the IL hence the decomposition will cause a precipitation of the TBC if it has not already separated from solution.

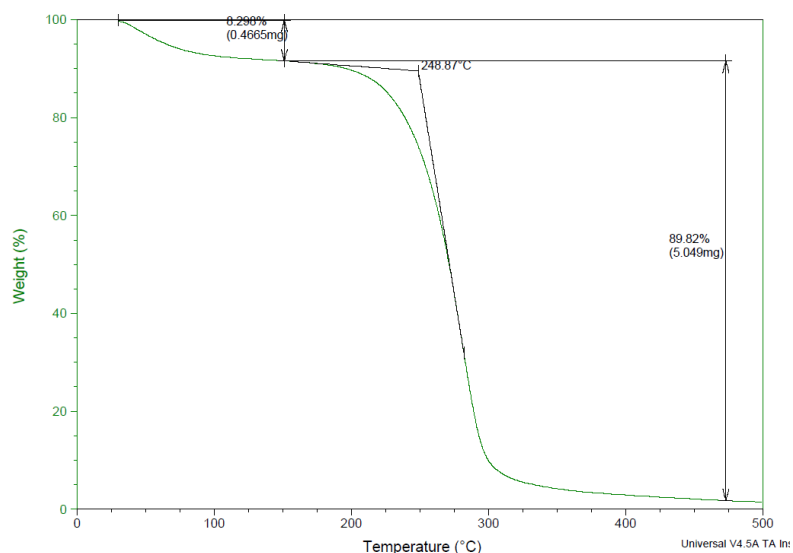


**Figure 3-29**-TGA of [P<sub>66614</sub>][OAc]. Rate of heating 1 °C min<sup>-1</sup>.

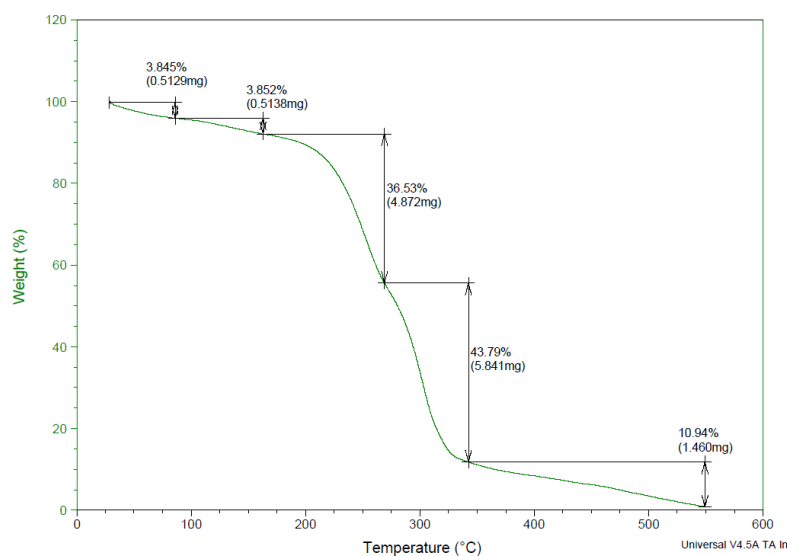


**Figure 3-30**-TGA of [P<sub>66614</sub>][OAc] and *p*-*tert*-butylcalix-[4]-arene 20 mol%. Rate of heating 1 °C min<sup>-1</sup>.

### 3.2.2.5 Density

The density of solutions rises with increasing concentration of *p*-*tert*-butylcalix-[4]-arene as shown in Figure 3-31. An increase of 0.0357 g/cm<sup>3</sup> is observed upon 20 mol% *p*-*tert*-butylcalix-[4]-arene. This increase in density is suspected to be due to the efficient packing of the IL-TBC liquid mix; this supports the assumption that the anion sits in the TBC cavity.

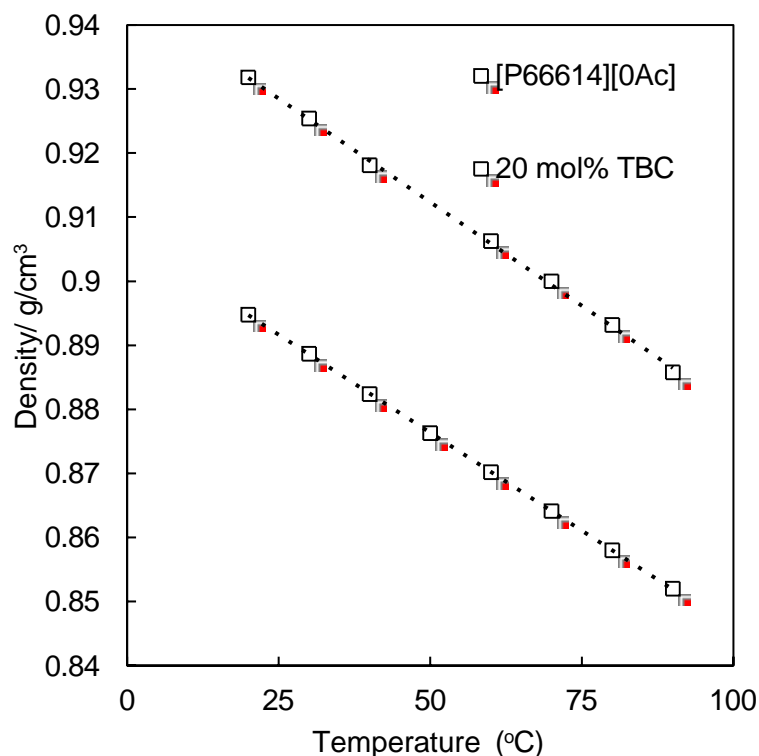


**Figure 3-31**-Density as a variation of temperature of [P<sub>66614</sub>][OAc] (circles) and [P<sub>66614</sub>][OAc] 20 mol% *p*-*tert*-butylcalix-[4]-arene (triangles)

### 3.2.2.6 Infrared Spectroscopy

Infrared spectroscopy is a useful tool in elucidating changes in bonding within systems especially those in which a carbonyl group is present. Functional groups such as carbonyls have a characteristic optical absorption called a chromophore. The typical wavenumbers,  $\nu$  for C=O stretches are 1640-1780  $\text{cm}^{-1}$ . As shown in Figure 3-33 and Figure 3-34 there are two prominent peaks that change intensity with increasing TBC concentration; 1375  $\text{cm}^{-1}$  and 1581  $\text{cm}^{-1}$ . In each case the peaks at 1375  $\text{cm}^{-1}$  and 1581  $\text{cm}^{-1}$  are at their most intense in the neat IL, however, the TBC molecules each contain four C-O contributions that must be accounted for. Currently it is concluded that the TBC is mono-deprotonated *via* the acetate anion hence it would be expected that the [OAc]<sup>-</sup> contribution to the spectra to cause a shift as electron density is varied as TBC-IL interactions increase with increasing TBC concentration. However, no shift is observed hence it is postulated that the molar extinction coefficient of any new stretched induced may be significantly lower than the initial IL IR bands.

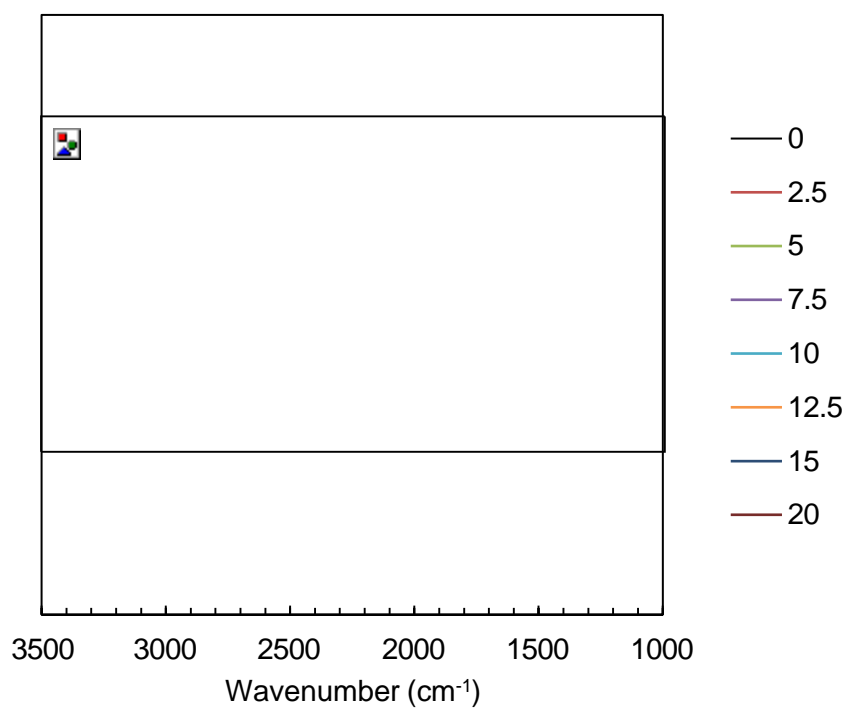


**Figure 3-32-** Partial IR Spectra of  $[P_{66614}][OAc]$  and *p-tert*-butylcalix-[4]-arene solutions. (3500-1000  $cm^{-1}$ )

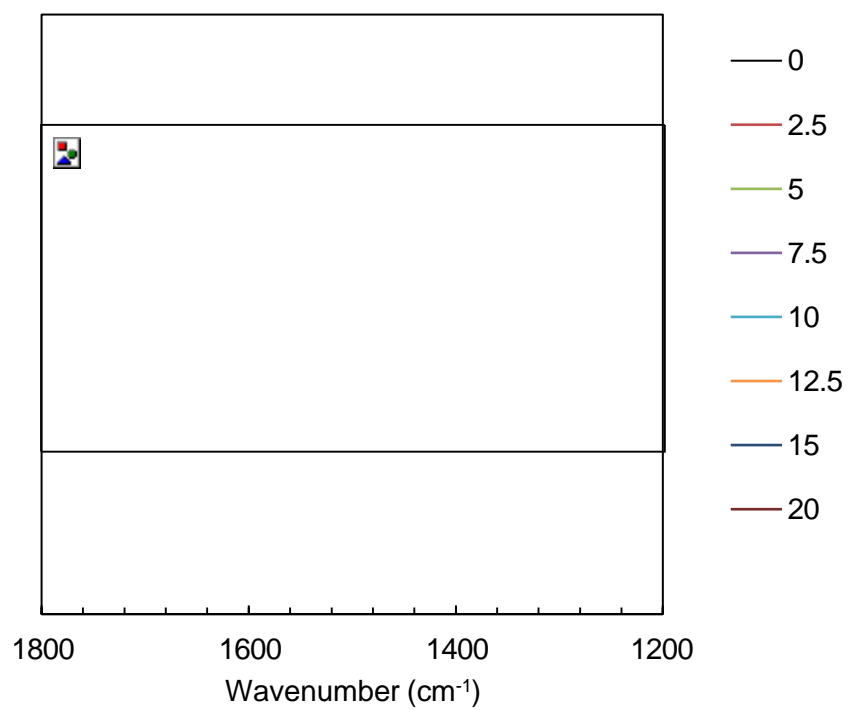


**Figure 3-33-** Partial IR Spectra of  $[P_{66614}][OAc]$  and *p-tert*-butylcalix-[4]-arene solutions. (1800-1200  $cm^{-1}$ )

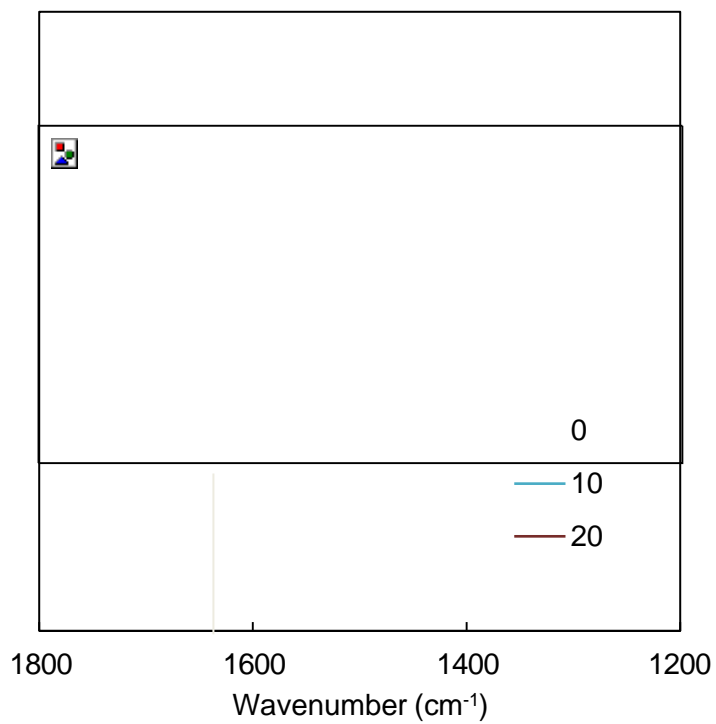


**Figure 3-34-** Partial IR Spectra of  $[P_{66614}][OAc]$  and *p-tert*-butylcalix-[4]-arene solutions. (1800-1200  $cm^{-1}$ )

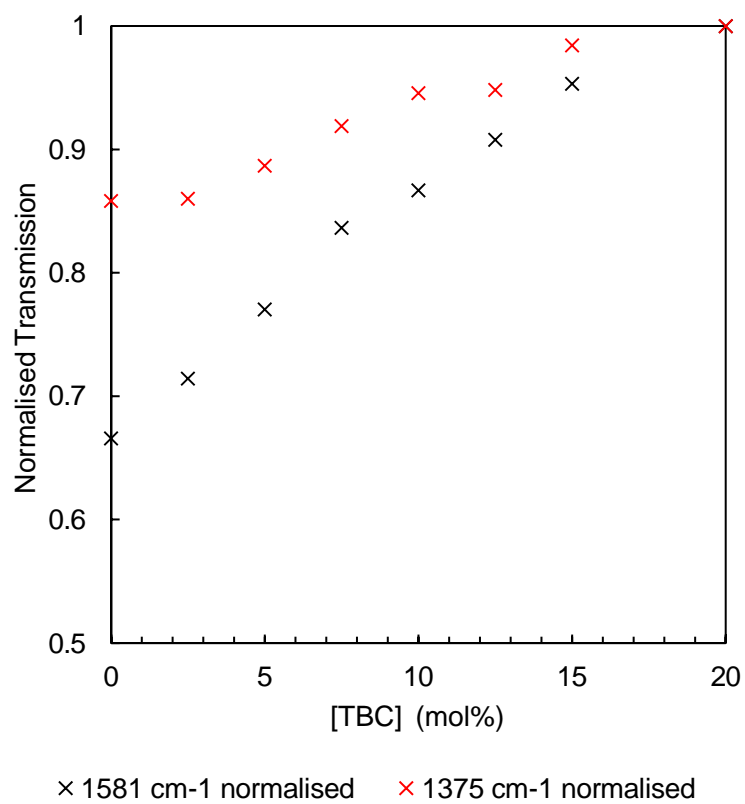


**Figure 3-35-** Normalised analysis of peak height of IR spectra of  $[P_{66614}][OAc]$  and *p-tert*-butylcalix-[4]-arene solutions.

The band at  $1581\text{ cm}^{-1}$  corresponds to that of the carbon oxygen bond of the acetate species as determined by an infrared spectrum of potassium acetate. As the TBC concentration increases there is greater interaction between the acetate and phenolic protons hence the bond order of the carbonyl stretch becomes more diffuse and hence the peak decreases and broadens.

The band at  $1466\text{ cm}^{-1}$  is believed to be due to the ionic liquid however its specific assignment is not known. The IR spectra of pure *p*-tert-butylcalix-[4]-arene has a broad hydroxyl band at  $3150\text{ cm}^{-1}$  and two distinctive bands at  $1740\text{ cm}^{-1}$  and  $1604\text{ cm}^{-1}$ . The somewhat low frequency of the hydroxyl bands is due to the strong intramolecular hydrogen bonding of the phenolic groups such that studies by Tobiasson *et al.*<sup>277</sup> In this study hydroxyl bands in the IL-TBC solutions are not observed, however, a broad series of peaks emerging at  $1600\text{ cm}^{-1}$  is seen and it must also be considered that the concentration of hydroxyl groups and the suggested hydrogen bonding interactions that occur between the phenolic protons and the acetate anion hence causing a broadening and a consequent disappearance of the hydroxyl bands.

#### **3.2.2.7 Solubility tests and merit in comparison to conventional solvents**

As discussed, the determination of the  $\text{pK}_a$  of TBC was not an easy feat; this was mainly due to its insolubility in aqueous and protic solvents. Even with the utilisation of bases the solubility of TBC is negligible in aqueous solvents. Within aprotic organic solvents the solubility is also low; no exact figures are available within literature, however, within this work it is found that TBC solvation in acetonitrile to be sluggish even at concentrations as low as *ca.* 215 micromolar.

### **3.2.3 Comparative systems**

To ensure conclusions regarding the  $[\text{P}_{66614}][\text{OAc}]$  and TBC systems are correct a series of comparative studies were carried out in which inorganic acetate salts, phenol and other similar species were investigated in a similar manner to elucidate trends in the solvation mechanism.

#### **3.2.3.1 Comparison to phenol and potassium acetate systems**

The first comparative system is utilising the key species in the solvation mechanism; a phenolic proton and an acetate anion. A series of solutions of potassium acetate,  $\text{K}[\text{OAc}]$  and phenol were prepared 0 mol% to 20 mol% solutions  $\text{K}[\text{OAc}]$  in phenol with only those below 15 mol% forming clear transparent solutions without residual potassium acetate. Details are listed in Table 3-6.

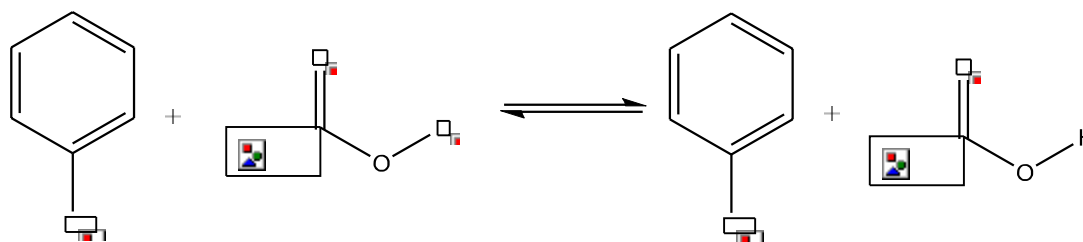


**Figure 3-36**-Phenol and potassium acetate interactions.

**Table 3-6**-Phenol and potassium acetate solutions formed. (Solvent less)

Sample	Mass/g		Moles/ mol		Concentration mol %
	Phenol	K[OAc]	Phenol	K[OAc]	
1	2	0	0.0213	0	0
2	2	0.11	0.0213	0.0011	5
3	2	0.23	0.0213	0.0024	10
4	2	0.37	0.0213	0.0038	15
5	2	0.52	0.0213	0.0053	20

Key consideration to take into account within this system is the significantly increased  $pK_a$  of the phenolic proton in comparison to TBC, an increase from  $\approx 4$  to  $\approx 10$  due to the lack of the *tert*-butyl group in the para position and the rigid conformational affects aforementioned.<sup>177</sup> Utilising the same series of spectroscopic techniques it was aimed to elucidate the TBC cavity-acetate anion interactions.

Phenol and benzene interactions have been noted by Moreau-Descoings *et al.* in such that the association s between phenol and benzene acting as a weak base for H-bonding causes shielding of the C-4 positions and de-shielding of the C-1 positions.<sup>278</sup> Utilising stronger bases such as picolines causes a more significant de-shielding of the C-1 from 155.02 ppm to 159.40 ppm and shielding of the C-4 position from 121.09 ppm to 119.40 ppm. To compare within the TBC-IL system it is observed that with increasing TBC concentration the C-1 is de-shielded from 153.340 ppm at 5 mol% to 153.543 ppm at 20 mol%. The increase in de-shielding with essentially a decrease in base may indicate that at higher concentration of TBC there is less base clustering occurring around the deprotonation site as a greater amount of H[OAc] is formed. The H[OAc] formed will also interact with the acetate anions hence explaining the increase in de-shielding observed with increasing TBC concentration and consequent increasing H[OAc] concentration the remaining basic acetate anions are clustering around the acid formed e.g. [AcO-H-OAc]<sup>-</sup>. Such clustering causes electron density of the acetate anions to be withdrawn but to a lesser extent if clustering occurs.<sup>279</sup>



As previously discussed a rather peculiar up-field shift is observed in  $^{13}\text{C}$  NMR studies of  $[\text{P}_{66614}][\text{OAc}]$  and *p*-*tert*-butylcalix-[4]-arene systems, which is suggested may be due to the acetate anion sitting in the cavity of the *p*-*tert*-butylcalix-[4]-arene or acid formation and a dynamic averaging of the acetyl  $\text{CH}_3$ . Within phenol solutions it is not expected to witness this occurring with only minimal acetate- $\pi$  interactions with the aromatic species.

#### 3.2.3.1.1 Infrared spectroscopy

As previously discussed infrared spectroscopy is a useful tool on elucidating the behaviour of carbonyl species. Within the  $\text{K}[\text{OAc}]$ -phenol system as shown in Figure 3-37, Figure 3-38, and Figure 3-39 there are significant changes in the carbonyl and carbon-oxygen single bond bands. The IR spectra show that the phenolic hydroxide band decreases with increasing acetate concentration. A decrease in the peak at  $1594\text{ cm}^{-1}$  is observed and a peak emerges at  $1550\text{ cm}^{-1}$  as shown in Figure 3-38, Figure 3-39. It is believed that this to be due to the acetate-phenolic interactions with the carbonyl stretch decreasing as electron density is transferred from the  $\text{C}=\text{O}$  to the hydrogen bond. Along with the carbon oxygen single bond increasing somewhat increasing in bond order as this resonance increases.

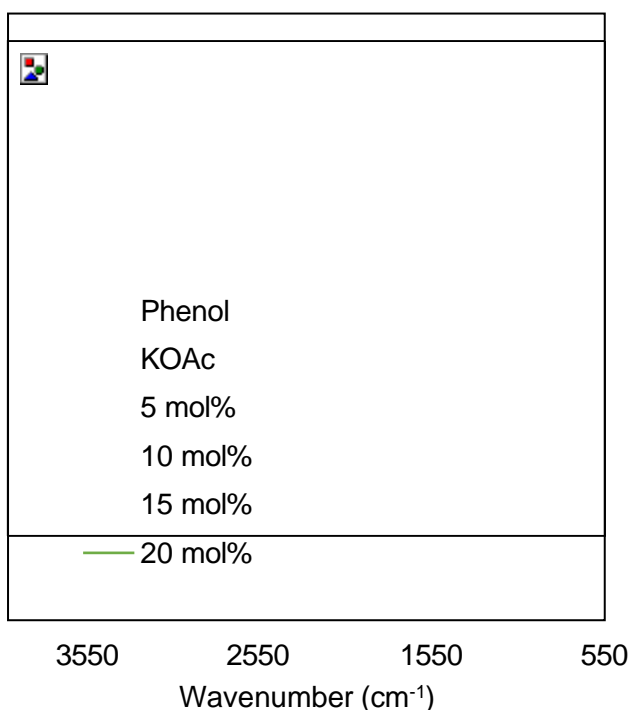


**Figure 3-37-** Infrared spectra of phenol, 5-20 mol%  $\text{K}[\text{OAc}]$  in phenol.

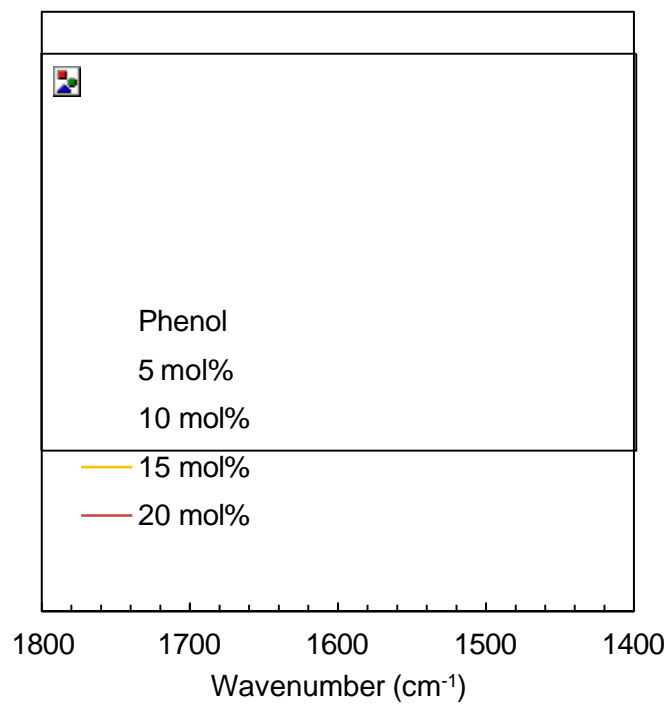


**Figure 3-38-** Partial IR spectra of phenol, 5-20 mol% K[OAc] in phenol. (1800-1400  $\text{cm}^{-1}$ ).

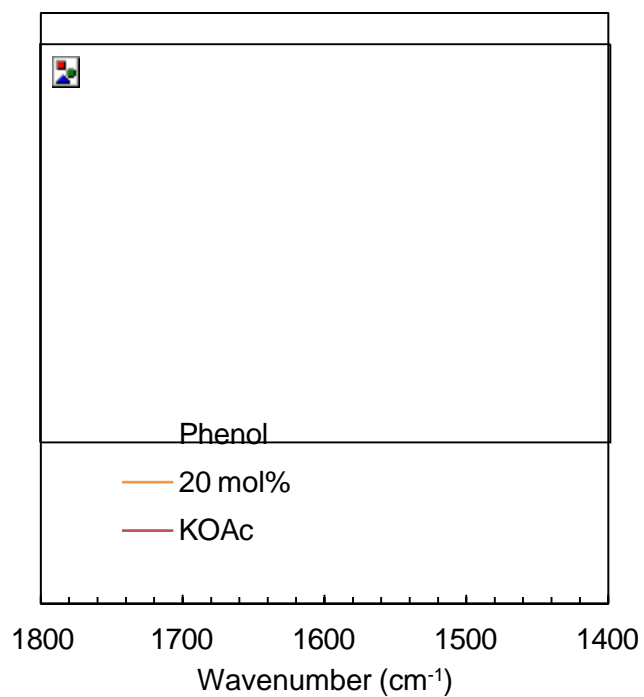


**Figure 3-39-** Partial infrared spectra of phenol, K[OAc] and 20 mol% K[OAc] in phenol. (1800-1400  $\text{cm}^{-1}$ ).

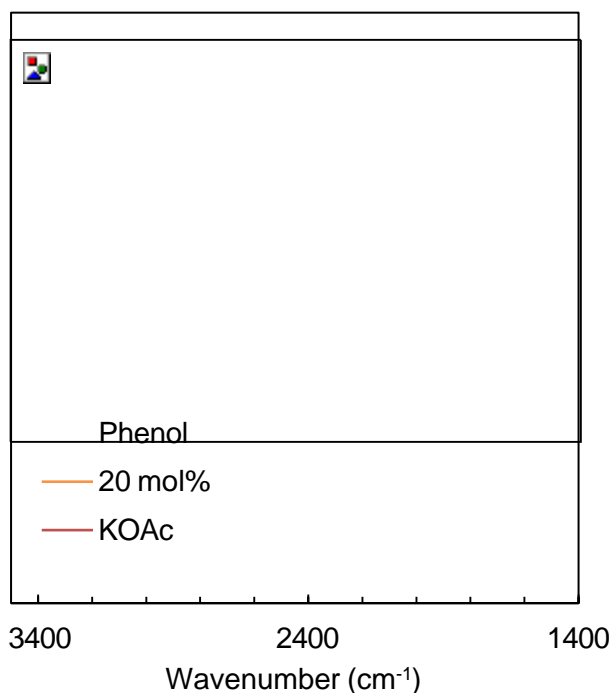


**Figure 3-40**-Infrared spectra of phenol, K[OAc] and 20 mol% K[OAc] in phenol.

A significant shift in the carbonyl stretch from  $1564\text{ cm}^{-1}$  to  $1544\text{ cm}^{-1}$  is observed moving from pure K[OAc] to the phenol/potassium acetate mixtures. This is rather a significant shift; however, it is not unsurprising as moving from hard cation in  $\text{K}^+$  to a mixture with a softer proton bases' cationic interaction from the phenolic proton. This was determined to be the carbonyl band of the  $[\text{OAc}]^-$  anion as no new bands emerge with increasing K[OAc] concentration at  $1564\text{ cm}^{-1}$ . Comparatively the IL-TBC system showed two distinct changes in the intensity of peaks at  $1375\text{ cm}^{-1}$  and  $1581\text{ cm}^{-1}$  with increasing TBC concentration *i.e.* increasing acid concentration. Although the  $\text{pK}_a$  of the phenol is approximately 9.1 in the presence of potassium acetate it would be expected that H-bonding interactions between the phenolic proton and the acetate anion. As shown in Figure 3-40, there is a shift in the hydroxyl band indicating that a strong hydrogen bond or deprotonation has occurred; there is also the emergence of a small series of bands *ca.*  $1800\text{ cm}^{-1}$  analogous to those observed in the TBC-IL system.

### 3.2.3.2 [Emim][OAc] and phenol comparison

1-Ethyl-3-methylimidazolium acetate, [Emim][OAc] is a useful ionic liquid for investigating the interaction phenolic proton and 'free' acetate anion. Although unsuccessful in dissolving a significant amount of *p-tert*-butylcalix-[4]-arene it is able to dissolve simple molecules which can emulate the phenolic motif *i.e.* phenol. Firstly, the interaction of phenol with the acetate anion was investigated. It should be

again noted that the  $pK_a$  of phenol is 9.1 hence significantly higher than that of *p-tert*-butylcalix-[4]-arene hence hydrogen bonding is suspected to prevail and not deprotonation as is observed in the TBC systems.

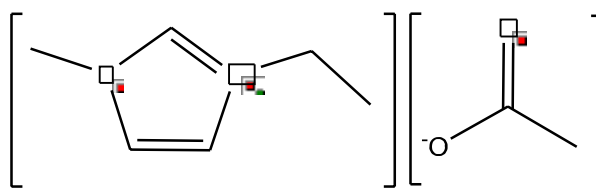


**Figure 3-41**-Structure of 1-Ethyl-3-methylimidazolium acetate, [Emim][OAc].

Stoichiometric mixtures of phenol and [Emim][OAc] are listed below in Table 3-7 with each forming liquids at room temperature. No single crystals were able to be grown / extracted from the series of mixtures investigated.

**Table 3-7**- Phenol and [Emim][OAc] solutions formed.

Sample	[Emim][OAc]		Phenol		Concentration/ mol%
	Mass/ g	Moles/ mol	Mass/ g	Moles/ mol	
1	1.00	0.0058	0.55	0.0058	50 mol%
2	1.50	0.0087	0.41	0.0044	33 mol%
3	1.75	0.0101	0.32	0.0034	25 mol%
4	2.00	0.0116	0.28	0.0029	20 mol%

### 3.2.3.2.1 Infrared spectroscopy

Again, infrared spectroscopy has been utilised to elucidate the acetate anion behaviour in the [Emim][OAc] system. Spectra of neat [Emim][OAc] gives rise to two major spectral bands at  $1562\text{ cm}^{-1}$  and  $1378\text{ cm}^{-1}$  as shown in Figure 3-42 and Figure 3-43. The peak at  $1562\text{ cm}^{-1}$  corresponds to the carbonyl peak from the acetate anion; with increasing phenol concentration this peak decreases in intensity with a shoulder arising at  $1594\text{ cm}^{-1}$  at high phenol concentrations. Spectra of neat phenol give rise to four major bands at  $1594\text{ cm}^{-1}$ ,  $1498\text{ cm}^{-1}$ ,  $1472\text{ cm}^{-1}$ ,  $1363\text{ cm}^{-1}$ ; the band at  $1472\text{ cm}^{-1}$  corresponds to the C-O of the phenol and decreases with decreasing phenol concentration. The decrease in intensity in each case is believed to be due to Beer-Lambert correlations to concentration of each species in the mixtures. The contribution from the hydroxyl group of the phenol is very much apparent in the neat spectra, however, upon the addition of the [Emim][OAc] the contribution decreases significantly and is non-existent at phenol concentrations above 33 mol%. As discussed previously within the original IL-TBC system, the hydroxyl band of the TBC was not observable similarly to the phenol K[OAc] system

in which the hydroxyl band of the phenol decreases with increasing phenol concentration as the mole equivalence of the phenol to base IL moves to 1:1 hence no base clustering occurs and the impact upon the phenolic group increases.

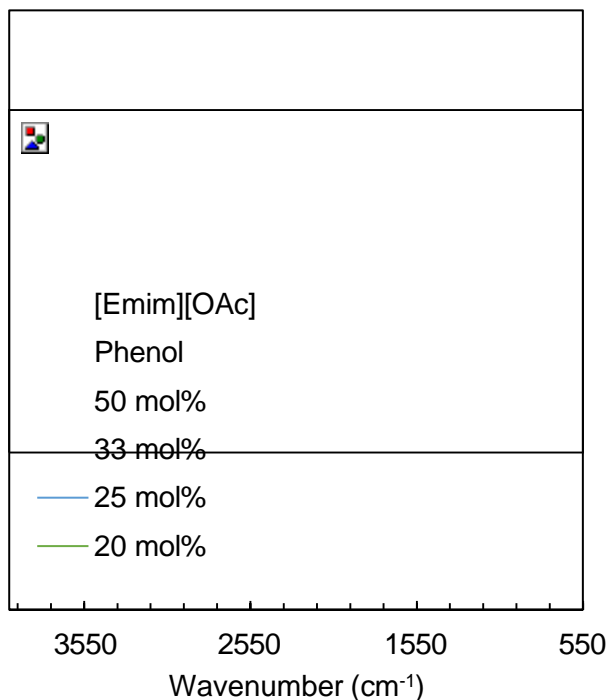


**Figure 3-42-** IR analysis of [Emim][OAc] and phenol mixtures.

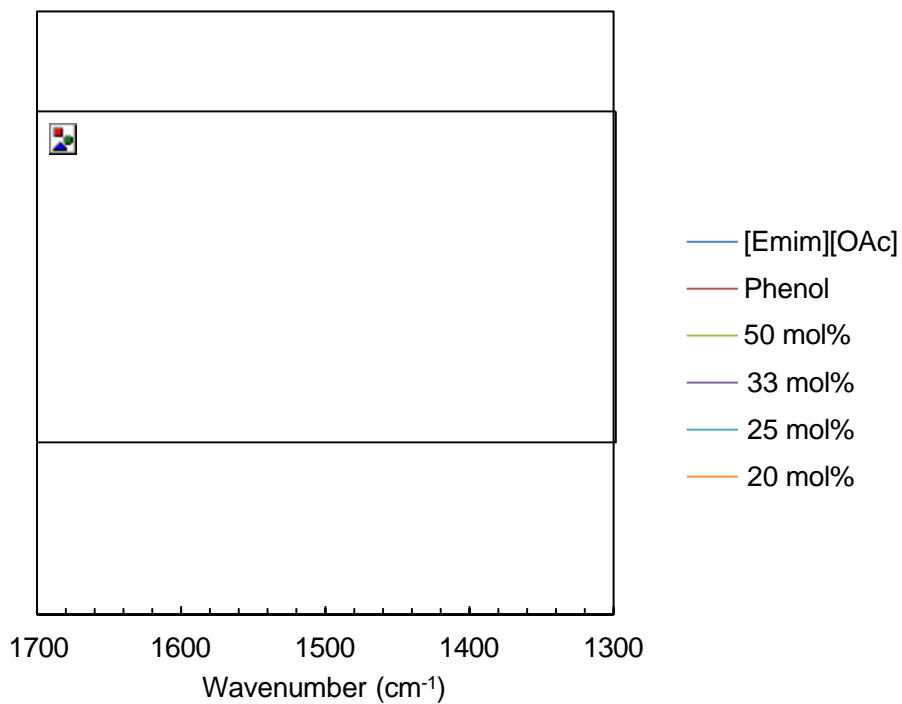


**Figure 3-43-**IR analysis of [Emim][OAc] and Phenol mixtures

### 3.2.3.2.2 $^1\text{H}$ Nuclear magnetic resonance spectroscopy

Proton NMR analysis of [Emim][OAc] and phenol mixtures show some rather significant changes in both the phenolic peaks and those of the imidazolium ionic liquid as shown in Figure 3-44. All spectra are referenced using a  $d_6$ -DMSO capillary. Phenolic peaks appear to shift slightly upfield with increasing phenol concentration indicating de-shielding *via* an interaction with the acetate anion. Furthermore, the imidazolium ring protons shifts significantly upfield with increasing phenol concentration as shown in Figure 3-44. This increase in shielding is believed to be due to decreased interactions between the [Emim] $^+$  cation and the acetate anion as it has a greater interaction with the increasing number of phenol species.

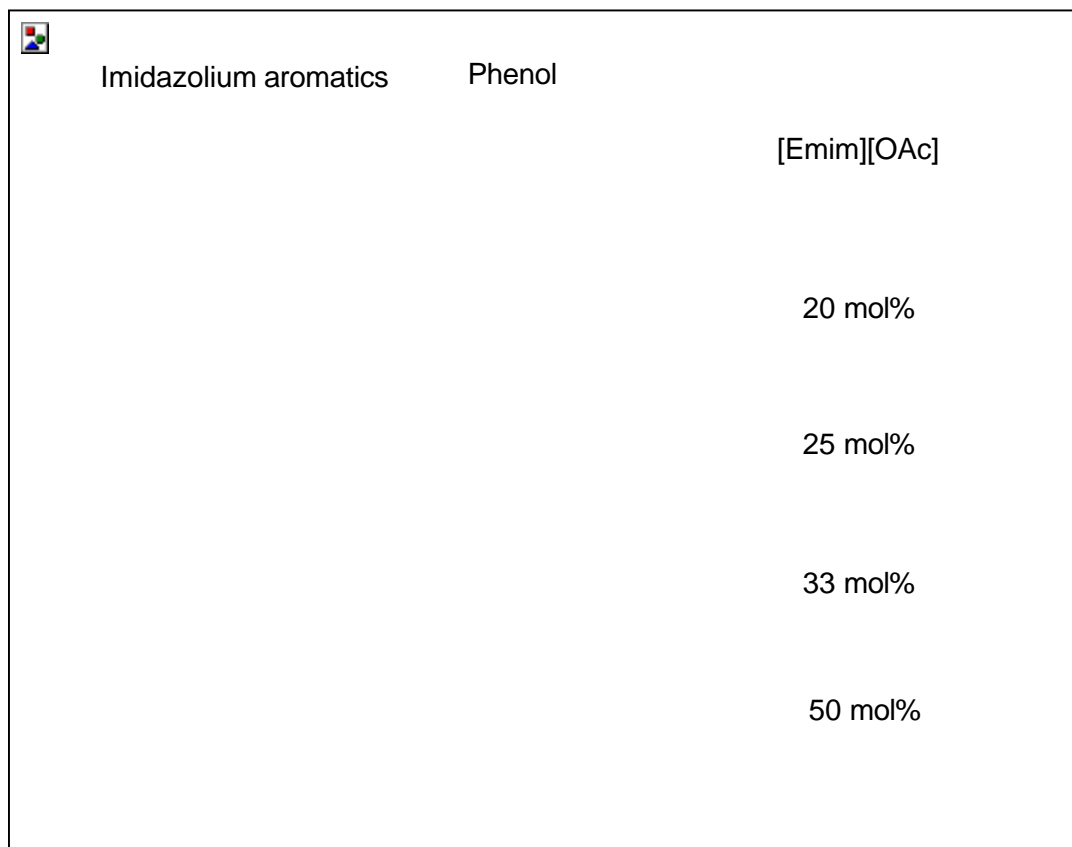


**Figure 3-44-**  $^1\text{H}$  NMR spectra of [Emim][OAc] and Phenol mixtures. Top to bottom: [Emim][OAc], 20 mol%, 25 mol%, 33 mol%, 50 mol%.

The alkyl substituents of the [Emim] $^+$ ; the methyl group a singlet at 3.55 ppm in neat IL and 3.40 ppm at 50 mol% phenol indicates an increase in electron density upon this substituent. The ethyl group; the  $-\text{CH}_2-$  a quartet at 3.82 ppm in neat IL and 3.68 ppm at 50 mol% phenol again indicates an increase in electron density upon this substituent; this is again see in the  $-\text{CH}_3$  group of the ethyl substituent a triplet at 0.636 ppm in neat IL and at 0.282 at 50 mol% phenol. This increase in electron

density upon the cation of the IL again corresponds to the disruption in cation and acetate anion interactions *via* the phenol such that the acetate anion is diverted/distracted by the phenolic proton. Comparing this to less basic anions with the [Emim]<sup>+</sup> such as chloride studies by Kosan *et al.* observed a similar trend in that the less basic the anion the greater the electron density upon the alkyl groups of the cation due to less attractions between the cation and anion.<sup>280</sup> In Figure 3-44 the peak at 2.50 ppm is believed to be due to the *d*<sub>6</sub>-DMSO residue and the peak at 1.15 ppm is due to the acetate anion of the [Emim][OAc] IL; minimal downfield shift is observed.

### 3.2.3.2.3 <sup>13</sup>C nuclear magnetic resonance spectroscopy

Analysis of the [Emim][OAc] and phenol mixtures has shown that the carbonyl peak at 174.22 ppm shows a downfield shift with increasing TBC concentration and a peak emerges at 158.51 ppm which may be indicative to that of acetic acid as shown in Figure 3-46. However, it should be noted that no peak at 21 ppm is observed to indicate the methyl group of the acetic acid. Conversely, due to proton exchange between the acetate anion and phenolic protons in the TBC- [P<sub>66614</sub>][OAc] systems an averaging of the methyl peaks indicative of acetic acid and the acetate anion was observed. This is not observed in the [Emim][OAc] systems hence indicating that the shift observed may not be solely due to acetic acid formation and dynamic averaging between the 'free' acetate anion and acetic acid. It is then postulated that the increase in shielding and increased electron density in the [P<sub>66614</sub>][OAc] systems may be due to anion and TBC cavity interactions.

Comparatively, [Emim][Cl] and [Emim][OAc] <sup>13</sup>C NMR spectra show that the [Emim]<sup>+</sup> interacts strongly with the acetate anion specifically with the alkyl substituents on the imidazolium centre specifically the –CH<sub>2</sub>– of the ethyl group (~47.54 ppm – 45.169 ppm) and the N-CH<sub>3</sub> methyl group (~36.55 ppm – 34.65 ppm). The [Emim]<sup>+</sup> show a minor upfield shift in regards to the carbons within the aromatic imidazolium centre with increasing phenol concentration. The alkyl substituents of the [Emim]<sup>+</sup> cations show no change with phenol addition. The phenol peaks, however, exhibit significant changes in regards to the C1 and C4 peaks. The C1 peak shifts downfield from 155.02 ppm to 158.57 ppm; with the largest downfield shift observed in the lowest phenol concentration investigated 20 mol%. The C4 peak shifts upfield from 121.09 ppm to 116.46 ppm again with the largest upfield shift observed in the lowest phenol concentration investigated 20 mol%. These shifts indicate the acid base interaction is again prevalent in this system *via* the acetate anion and the phenolic proton.

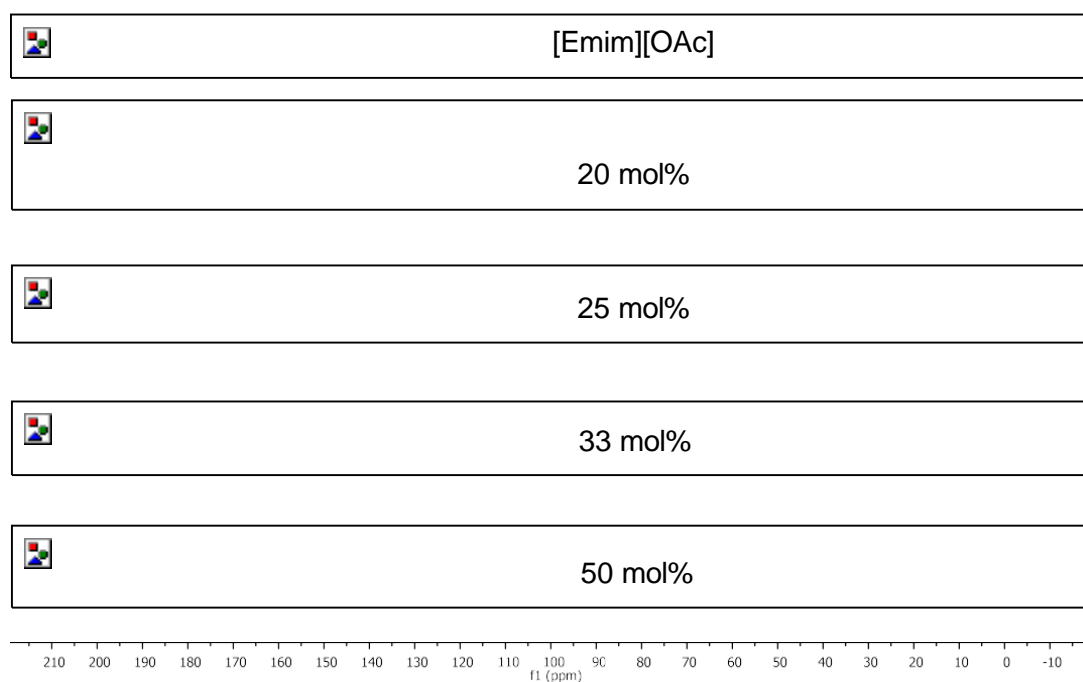


**Figure 3-45**- $^{13}\text{C}$  NMR spectra of [Emim][OAc] and Phenol mixtures. Top to bottom: [Emim][OAc], 20 mol%, 25 mol%, 33 mol%, 50 mol%.

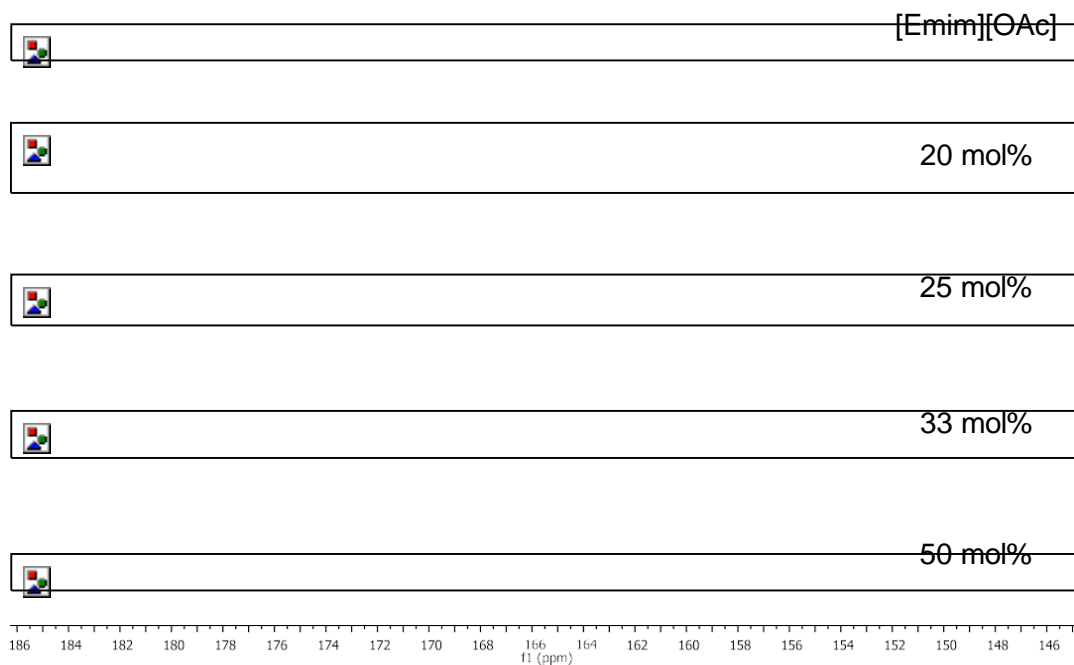


**Figure 3-46**-Partial  $^{13}\text{C}$  NMR spectra of [Emim][OAc] and phenol mixtures. Top to bottom: [Emim][OAc], 20 mol%, 25 mol%, 33 mol%, 50 mol%. (186-146 ppm)



### 3.2.3.3 Acetic Acid and Phenol Comparison

Previously interactions between the phenol and TBC have been investigated in regards to basic species such as acetate anion ionic liquids and inorganic bases such as potassium acetate. In this comparative system of acetic acid, H[OAc] and phenol mixtures, the interactions as suspected in the original [P<sub>66614</sub>][OAc] and TBC mixtures such that H[OAc] is formed as a consequence of solvation. Again, it must be reiterated that the pK<sub>a</sub> of the phenol and acetic acid are 9.1 and 4.75 respectively.

**Table 3-8-**Acetic acid in phenol solutions prepared.

Sample	Acetic acid		Phenol		Concentration phenol / mol%
	Mass/ g	Moles/ mol	Mass/ g	Moles/ mol	
1	0.96	0.0159	1.50	0.0159	50 mol%
2	1.27	0.0212	1.00	0.0106	33 mol%
3	1.43	0.0239	0.75	0.0080	25 mol%
4	1.26	0.0209	0.50	0.0053	20 mol%

#### 3.2.3.3.1 Infrared analysis

The infrared spectra of neat acetic acid has three main bands; 3055 cm<sup>-1</sup> (br) corresponding to the hydroxyl group, 1700 cm<sup>-1</sup> (s) corresponding to the C=O and 1412 cm<sup>-1</sup> (s) corresponding to the C-O as shown in Figure 3-47 and Figure 3-48. The infrared spectra of neat phenol have five 3250 cm<sup>-1</sup>(br), 1594 cm<sup>-1</sup>(s), 1498 cm<sup>-1</sup> (s), 1472 cm<sup>-1</sup>(s), 1363 cm<sup>-1</sup>(s); the peaks at 1498 cm<sup>-1</sup> and 1472 cm<sup>-1</sup> corresponds to the C-O of the phenol and decreases with decreasing phenol concentration.

This decrease in intensity in each case is believed to be due to Beer-Lambert correlations to concentration of each species. The hydroxyl band at 3250 cm<sup>-1</sup> in the phenol spectra depreciates significantly; comparatively the phenolic groups of the *p-tert*-butylcalix-[4]-arene are not apparent in the IL-TBC mixtures do not exhibit the broad hydroxyl bands observed in the phenol spectra this is due to the disrupted cyclic hydrogen bonding and deprotonation.

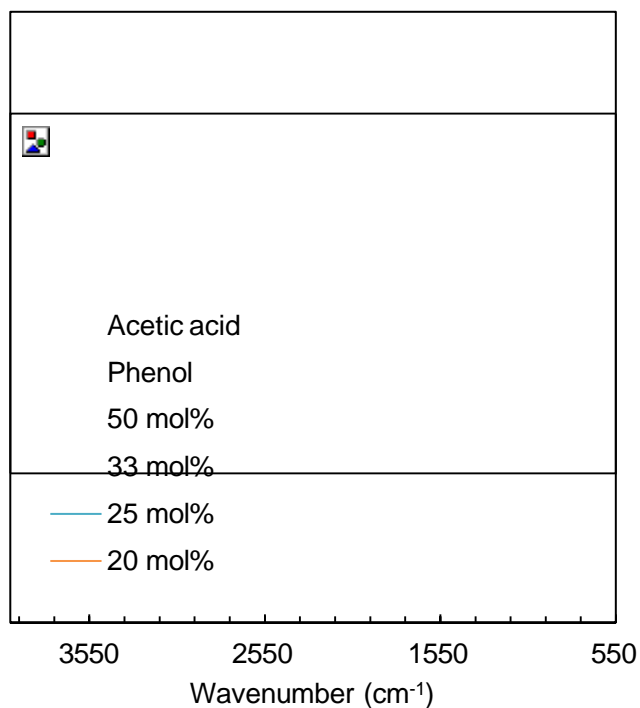


**Figure 3-47-** Infrared analysis of phenol in acetic acid mixtures of varying molar ratios.

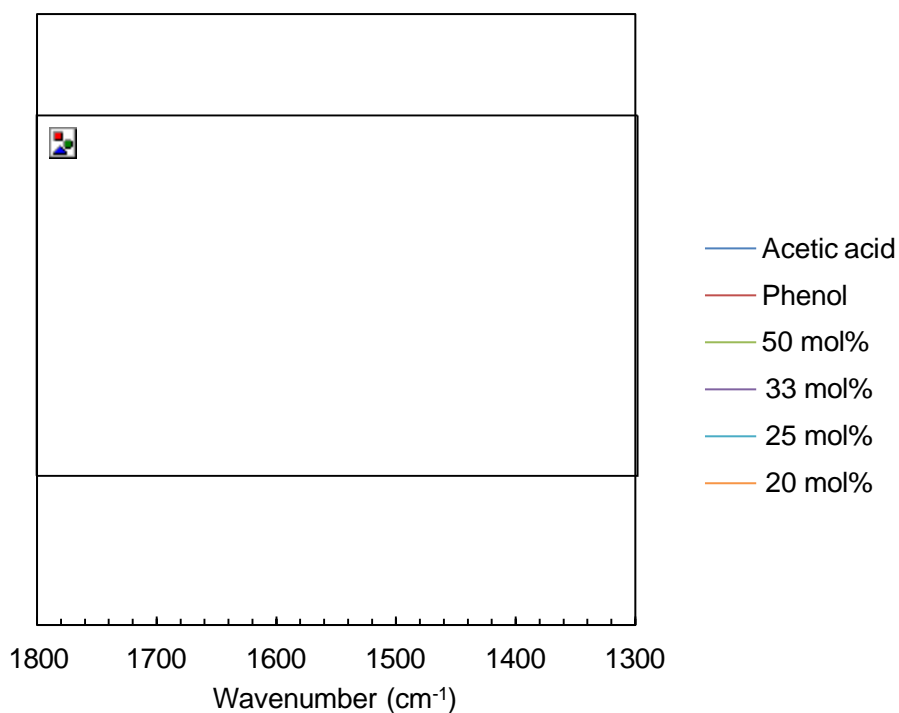


**Figure 3-48-** IR spectra of phenol in acetic acid mixtures of varying ratios. Acetic acid: Phenol.

### **3.2.3.3.2 <sup>1</sup>H Nuclear magnetic resonance spectroscopy**

Proton NMR spectra of acetic acid and various concentrations of phenol have shown some rather significant changes in the methyl group of the acetic acid; with

increasing phenol concentration the peak shifts upfield indicating an increase in electron density. Such an increase is believed to be due to proton dissociation and the formation of the conjugate acetate anion base in that in the neat acetic acid has its lowest electron density and at 80 mol% phenol its highest as shown in Figure 3-49.

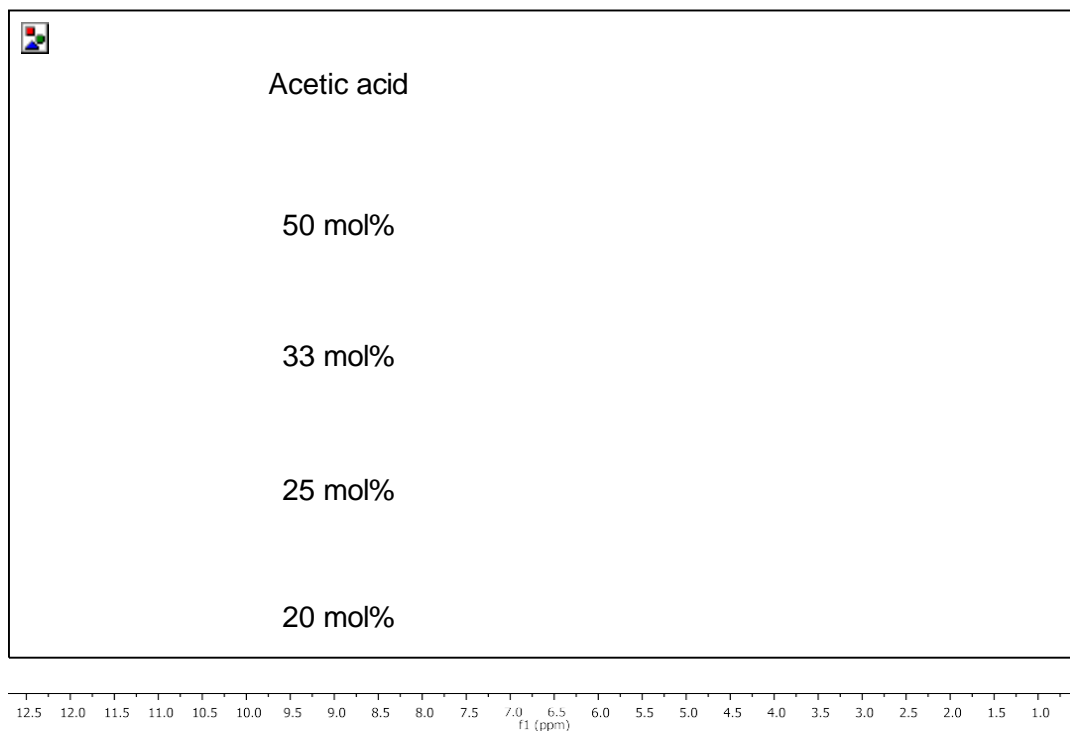


**Figure 3-49-**  $^1\text{H}$  NMR analysis of acetic acid and phenol mixtures. Top to bottom: acetic acid, 50 mol%, 33 mol%, 25 mol%, and 20 mol% (concentrations of acetic acid)

### 3.2.3.3.3 $^{13}\text{C}$ nuclear magnetic resonance spectroscopy

Within  $^{13}\text{C}$  NMR analysis of the phenol and acetic acid mixtures there are minimal changes in the spectra with increasing acetic acid concentration. The peak at 155 ppm is that of the C-1 on the phenol and would be expected to give the greatest shift upon phenolic interactions. The acetic acid peaks, at 178 ppm C=O and 19 ppm  $\text{CH}_3$  respectively, also show little variations again indicating that interactions are minimal.

From this it can be assumed that the acetic acid formation in the  $[\text{P}_{66614}][\text{OAc}]$  and TBC system will have a minimal effect on the NMR spectra except for averaging of the near equivalent  $\text{CH}_3$ - groups of the acetate anions and acetic acid due to exchange.

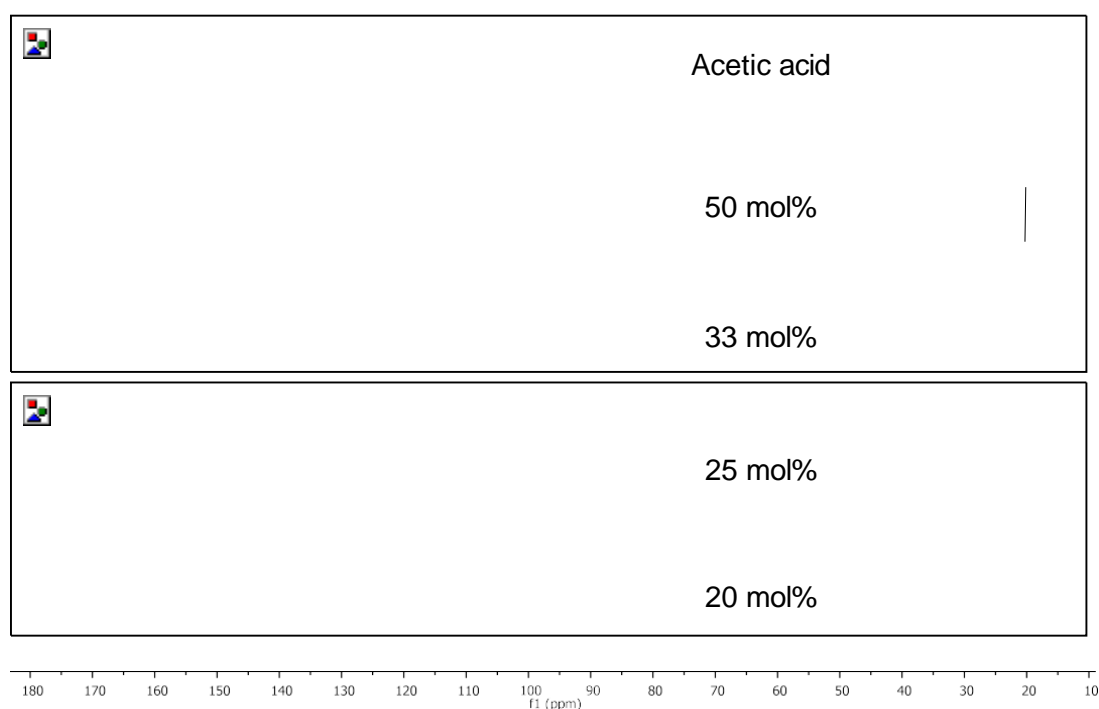


**Figure 3-50-** $^{13}\text{C}$  NMR analysis of phenol in acetic acid mixtures. Top to bottom: acetic acid, 50 mol%, 33 mol%, 25 mol%, and 20 mol%.

### 3.2.4 Interactions of *p*-*tert*-butylcalix-[4]-arenes and guanidine bases

Guanidine bases have recently been of great interest in regards to their strong non nucleophilic Brønsted basicity and unique properties as solvent. Specifically in regards to carbon capture in combination with primary amines and amino alcohols and cellulose processing.<sup>281,282</sup> Within cellulose processing these bases are utilised in a similar method invoking acid base chemistry with carbon dioxide to form reactive carbonate anions as shown in Figure 3-51, which in turn react with the alcohol groups of the glucose monomers in the cellulose structure.<sup>283,284</sup> These carbonate anions are intermediates that break up the inter-strand hydrogen bonding hence activating the solvation of cellulose for processing and manipulation.<sup>55,285,286</sup>

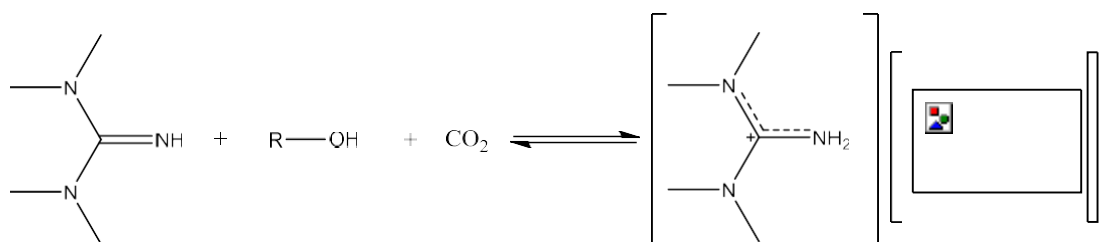


**Figure 3-51-**1,1,3,3-tetramethylguanidine reactions with alcohols and carbon dioxide.<sup>284</sup>

### 3.2.4.1 *p*-tert-butylcalix-[4]-arene and 1, 1, 3, 3-Tetramethylguanidine

#### 3.2.4.1.1 Interactions of *p*-tert-butylcalix-[4]-arenes in 1, 1, 3, 3-tetramethylguanidine - preparation and observations

In regards to interactions of guanidine bases with *p*-tert-butylcalix-[4]-arenes it has already been observed that in the previous work discussed by Woolfall and Cunningham that the use of the guanidine bases such as DBU, 1,8-Diazabicyclo[5.4.0]undec-7-ene has been shown to deprotonate TBC.<sup>275</sup> However, to compare with the [P<sub>66614</sub>][OAc] systems it was wished to further probe the effect of excess base. 1, 1, 3, 3-tetramethylguanidine, TMG is significantly smaller than its DBU counterpart and has been prevalent within a significant number of crystal structures registered on the CCDC (ca. 127 hits accessed: 04/04/2018). Hence it was aimed to utilise these properties to extract a single crystal structure of the TBC and base interactions. As shown in Figure 3-52 a simple 1:1 deprotonation is expected to form an ionic salt of mono deprotonated TBC. The interactions of the excess bases with this salt are the main focus of this study. The mixtures prepared are listed in Table 3-9 with the highest concentration of TBC studied a 1:1 mixture.

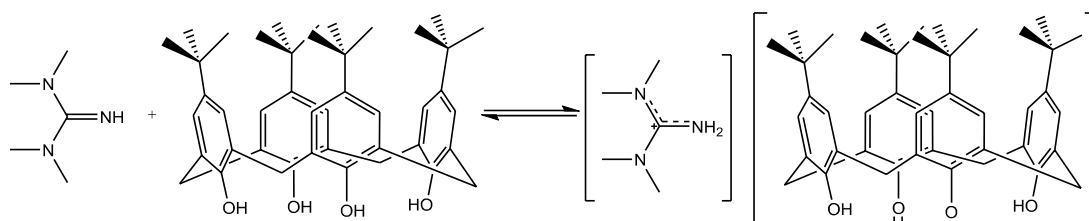


**Figure 3-52**-Predicted acid-base interactions of *p*-tert-butylcalix-[4]-arenes and 1, 1, 3, 3-tetramethylguanidine.

**Table 3-9**-Solutions of 1, 1, 3, 3-tetramethylguanidine, TMG and *p*-tert-butylcalix-[4]-arene, TBC.

Concentration TBC/ mol%	TMG: TBC	Observations
50 mol%	1:1	Ppt observed quickly after initial solvation
33 mol%	2:1	Ppt observed quickly after initial solvation
25 mol%	3:1	Ppt observed quickly after initial solvation
20 mol%	4:1	Ppt observed quickly after initial solvation
16.6 mol%	5:1	Ppt observed quickly after initial solvation
9 mol%	10:1	Ppt observed quickly after initial solvation
4.7 mol%	20:1	Colourless solution
0 mol%	TMG	Colourless solution

### 3.2.4.1.2 Nuclear Magnetic Resonance Spectroscopy

As a majority of mixtures of *p*-*tert*-butylcalix-[4]-arene and 1,1,3,3-tetramethylguanidine resulted in the formation of a precipitate, NMR studies were carried out in  $d_3$ -acetonitrile, an inert solvent that was able to dissolve the precipitate formed. Furthermore, this was also the solvent that Woolfall and Cunningham carried out the as aforementioned UV/Vis spectroscopic studies.

Again,  $^1\text{H}$  NMR showed some significant changes in the tetra-methyl functionality on the TMG base with an increase in de-shielding with increasing TBC concentration. Corresponding to decrease in electron density on the base indicating it has become a cationic species. Observing in greater detail the TMG methyl groups in Figure 3-54 and Table 3-10, the extent of the shift varies; the most dramatic changes are observed when the equivalents of TMG to TBC are less than 4:1 further indicating that the extent of base interaction on the salt is saturated at approximately 4:1 equivalents.

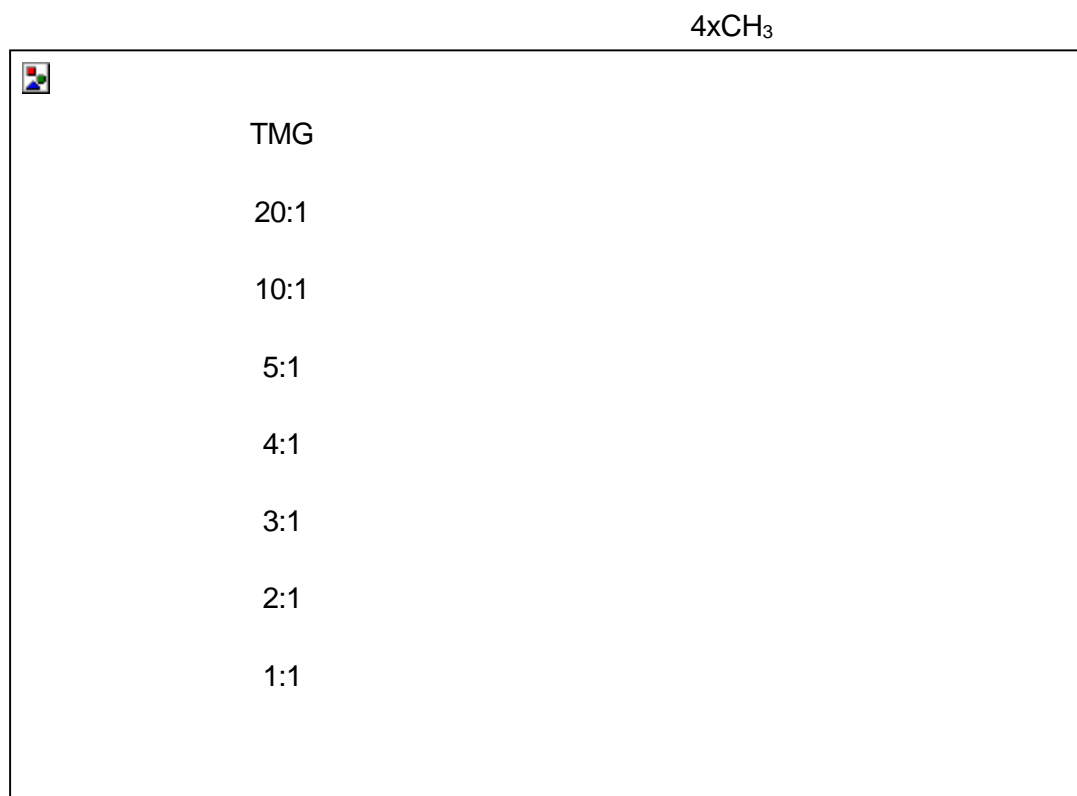


**Figure 3-53**  $^1\text{H}$  NMR spectra of *p*-*tert*-butylcalix-[4]-arene and 1, 1, 3, 3-tetramethylguanidine in  $d_3$ -acetonitrile. (top-bottom) 1,1,3,3-tetramethylguanidine in  $d_3$ -acetonitrile, 4.7 mol%, 9 mol%, 16.6 mol%, 20 mol%, 25 mol%, 33 mol%, 50 mol%.

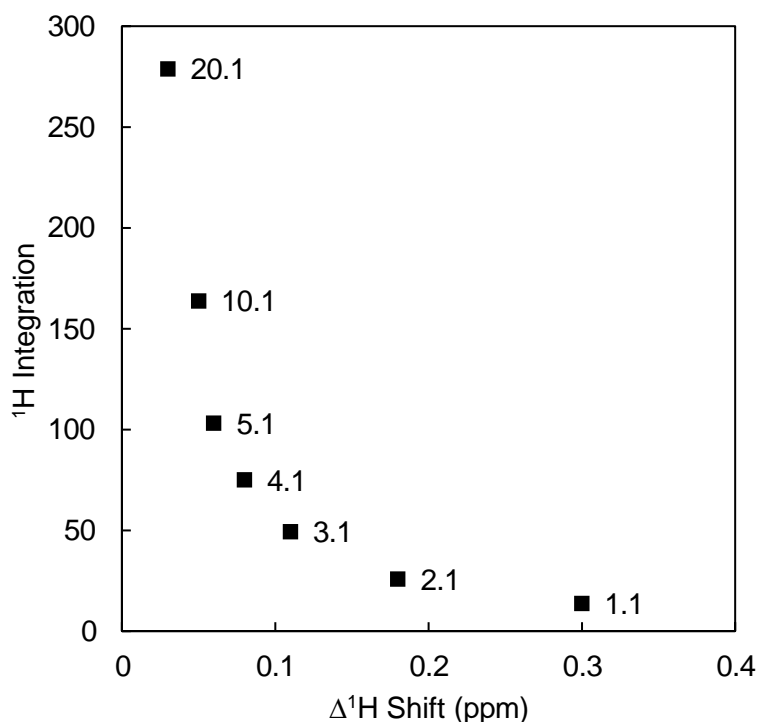


**Figure 3-54-** Delta shift from  $^1\text{H}$  NMR studies of TMG- $\text{CH}_3$  with varying ratios of TBC. Solvent- $d_3$ -acetonitrile.

**Table 3-10-** of *p*-*tert*-butylcalix-[4]-arene and 1,1,3,3-tetramethylguanidine  $^1\text{H}$  NMR shifts.

TMG:TBC	$^1\text{H}$ Shift/ ppm	$\Delta\text{Shift/ ppm}$	Integration	Observations
1.1	2.94	0.30	13.79	Ppt formed
2.1	2.82	0.18	25.82	Ppt formed
3.1	2.75	0.11	49.25	Ppt formed
4.1	2.72	0.08	74.99	Ppt formed
5.1	2.70	0.06	103.1	Ppt formed
10.1	2.69	0.05	163.7	Ppt formed
20.1	2.67	0.03	278.8	Colourless solution
TMG	2.64	0.00	12.00	Colourless solution

#### 3.2.4.1.3 UV/Vis spectroscopy

Utilising the Woolfall and Cunningham methodology, as previously mentioned, to a solution of TBC in acetonitrile there is a spectral change that corresponds to the first deprotonation within the four phenolic groups with the addition of aliquots of 1,1,3,3-tetramethylguanidine. The change itself consists of a shift in  $\lambda_{\text{max}}$  and a shoulder appearing at 315 nm, as shown in Figure 3-55. It was observed that the TBC is deprotonated after the addition of 1 equivalent of TMG.

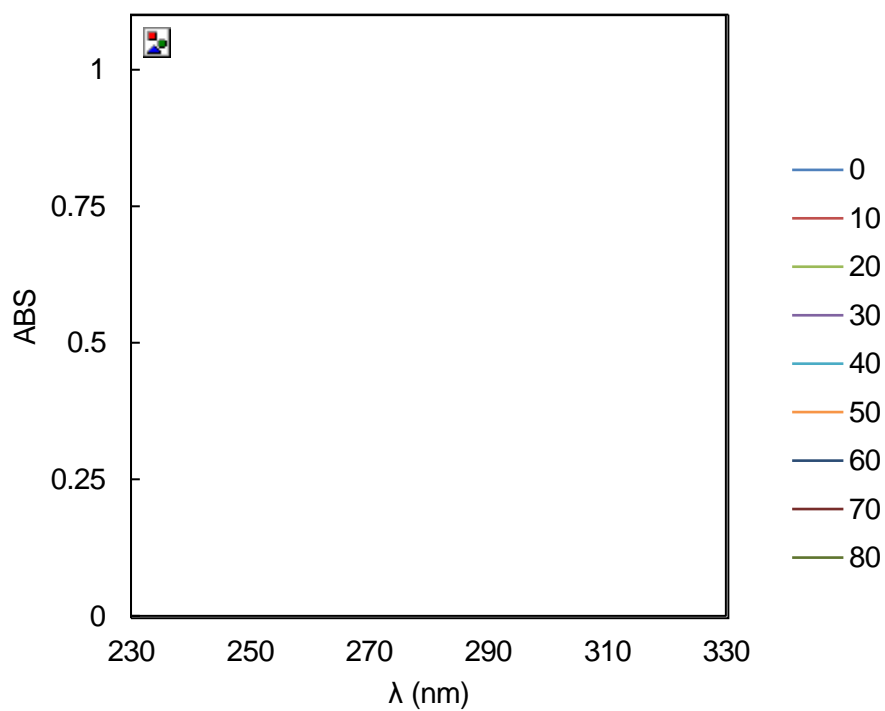


**Figure 3-55-** UV/Vis spectrum of *p*-*tert*-butylcalix-[4]-arene in MeCN with aliquots of 1, 1, 3, 3,- tetramethylguanidine added.

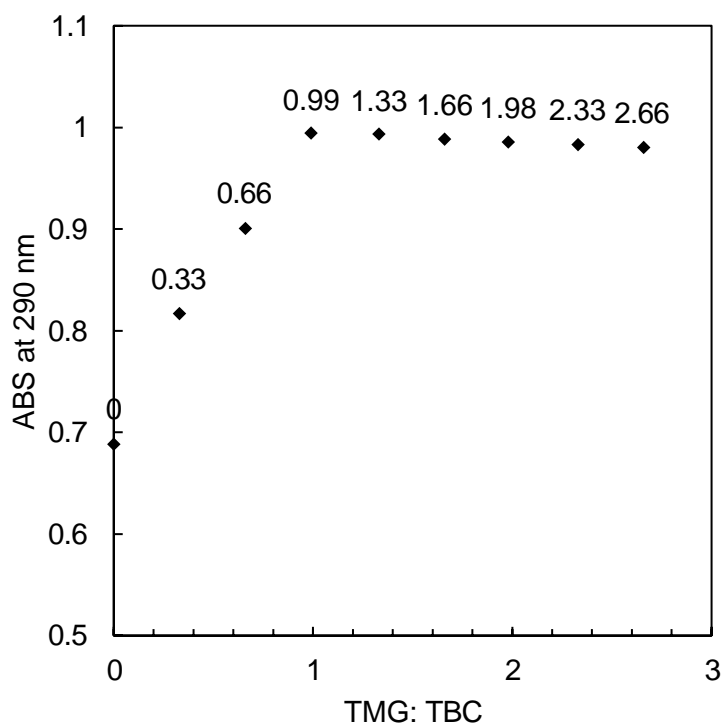


**Figure 3-56-** Plot of ABS at 290 nm as a function of TMG: TBC. Numbers above each point indicating the number of equivalents of TMG bas per TBC molecule.



**Table 3-11-** UV/Vis study of *p-tert*-butylcalix-[4]-arene vs 1, 1, 3, 3 – tetramethylguanidine.

Microliters of TMG solution	TMG/ mol	TBC/ mol	Ratio TMG:TBC	Absorption at 290 nm
0	0	1.85E-07	0	0.688
10	6.10E-08	1.85E-07	0.33	0.817
20	1.22E-07	1.85E-07	0.66	0.901
30	1.83E-07	1.85E-07	0.99	0.994
40	2.46E-07	1.85E-07	1.33	0.994
50	3.07E-07	1.85E-07	1.66	0.989
60	3.66E-07	1.85E-07	1.98	0.986
70	4.31E-07	1.85E-07	2.33	0.983
80	4.92E-07	1.85E-07	2.66	0.980

As shown in Figure 3-55 and the change in UV/Vis plateaus at 30  $\mu\text{L}$  which corresponds to approximately a 1:1 mix of TBC and TMG; to further confirm this the absorption at the original  $\lambda_{\text{max}}$ , 290 nm as a function of TMG:TBC ratio in Figure 3-56. The lack of change with additional base indicates the second de-protonation does not occur. This is interesting behaviour. The formation of a single deprotonation indicates that it is not base strength that depicts the lack of selectivity in the alkylation reactions as it is the free base that causes a second deprotonation.

#### **3.2.4.1.4 Single crystal X-ray diffraction**

As discussed, the main focus of this study was to determine the effect of excess base on the interaction of the deprotonated TBC. Of the mixtures of TBC and TMG prepared a majority resulted formation of a precipitate. The precipitates were extracted and recrystallized in acetonitrile with a single crystal obtained from a 2:1 TMG: TBC mixture. As shown in Figure 3-57, the mono-deprotonation of TBC has occurred with one of the TMG molecules present hence forming an ionic salt. The second TMG molecule present is a neutral species; however, there is a strong interaction from the free primary amine to the primary amine of the protonated base.

The protonated amine of the TMG lies 1.977 Å from the deprotonated phenolic group of the TMG. The neighbouring neutral TMG interacts with the protonated amine with the shortest hydrogen bonding interaction being 2.165 Å. In regards to packing the TBC molecules align themselves upper rim to upper rim in a staggered chain as shown in Figure 2-55; as consequence the TMG molecules interacting with the deprotonated lower rim of the TBC form a protonated and neutral base chain.

This clustering observed within this structure elucidates the continued changes in NMR spectroscopic methods as the interactions will impact the amount of de-

shielding observed in regards to the acetate anion. As the TMG is protonated an upfield shift is expected, however, this loss of electron density is compensated by base-base interactions hence the most significant upfield shift is observed at the 1:1 ratio of TMG: TBC, which is the lowest base concentration studies. Specifically, if you refer to the acetate shift in the  $[P_{66614}][OAc]$  and TBC systems; at low concentrations the greatest downfield shift of the  $CH_3^-$  of the acetate anion is found indicating an increase in de-shielding and decrease in electron density on the methyl group. With increasing TBC there is less acetate anions per TBC molecule hence the opportunity for base clustering declines causing a greater upfield shift.

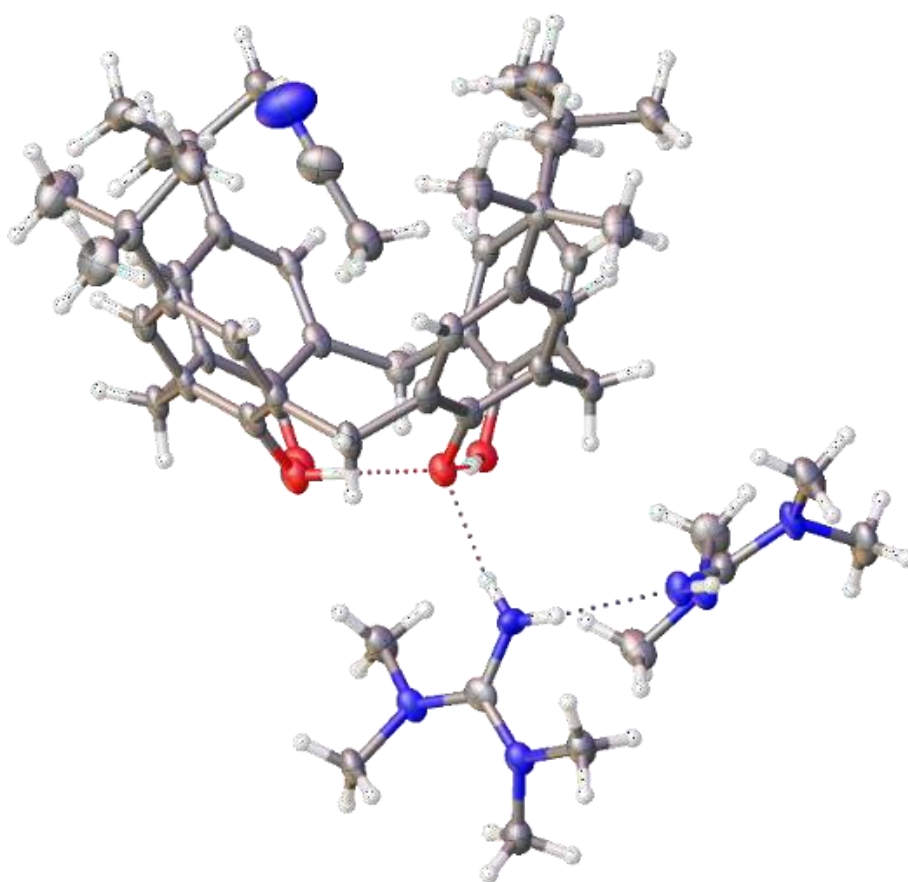


**Figure 3-57**-Single crystal diffraction determined structure of  $[TMG][TBC]$  and TMG interaction from a 2:1 mixture.

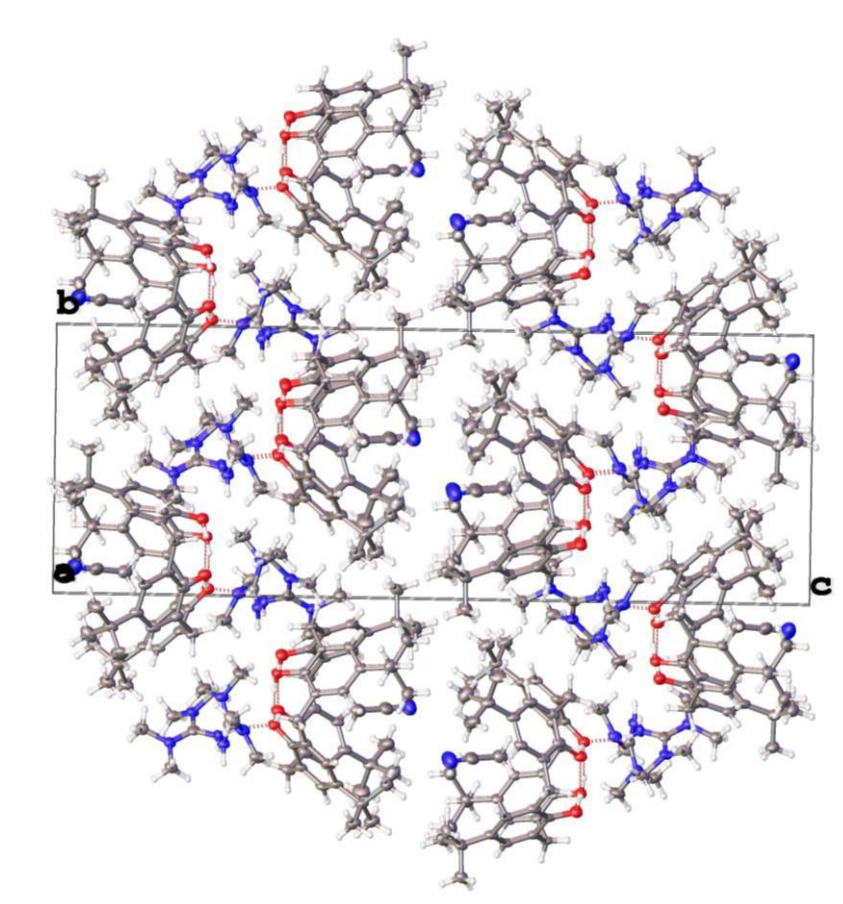


**Figure 3-58**-Single crystal diffraction determined structure of [TMG][TBC] and TMG interaction from a 2:1 mixture.

### 3.2.5 Behaviour of *p*-tert-butylcalix-[4]-arenes in methyl carbonate ionic liquids

Methyl carbonate anion ionic liquids were synthesised using a modified literature method within a screw cap pressure tube. The trialkylamine, methanol and dimethyl carbonate in a ratio of 0.04 mol amine, 0.25 mol methanol and 0.041 mol DMC stirred in a sealed glass tube over night at 150 °C. Solvent was removed before use *via* rotary evaporation. The reaction scheme is shown below in Figure 3-59.<sup>269</sup>

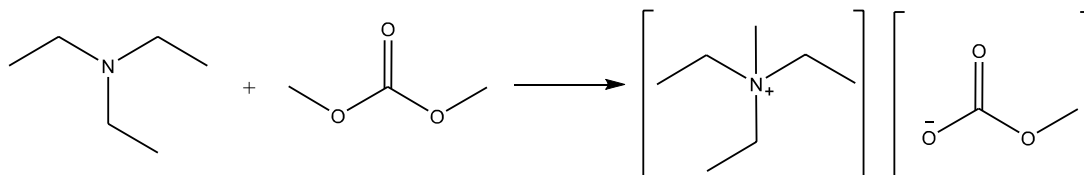


**Figure 3-59**-Synthesis of methyl carbonate anion ionic liquids.

Methyl carbonate basic anions have been utilised for many ionic liquid syntheses by Proionic GmbH and Kalb *et al.* as discussed in section 3.1.5.<sup>2,3,270,271</sup> The basic methyl carbonate anion in the presence of a Brønsted acid initiates a decomposition

mechanism in which the conjugate base anion is formed along with methanol and carbon dioxide as shown in Figure 3-60.

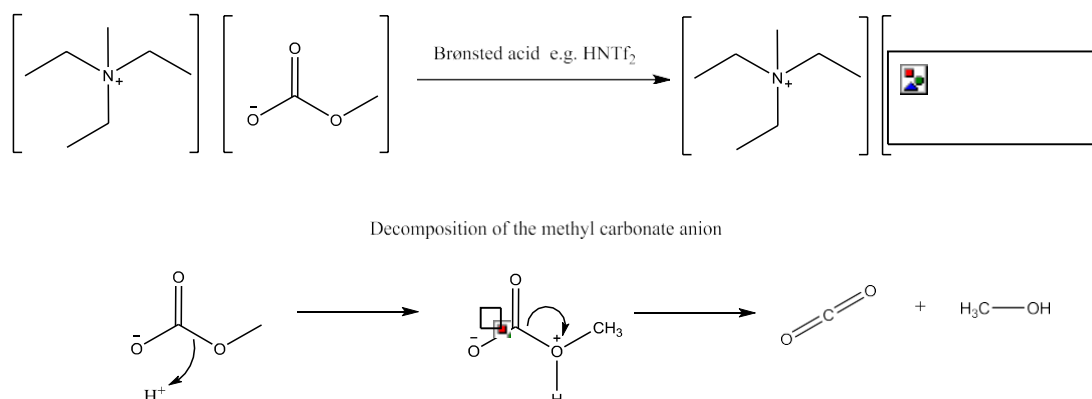


**Figure 3-60**-Decomposition of the methyl carbonate anion in the presence of a Brønsted acid.

Upon the addition of TBC to triethylmethylammonium,  $[N_{2221}]$ , tributylmethylammonium  $[N_{4441}]$  and tris(-2-methoxyethoxy)methylammonium  $[N_{peg}]$  methyl carbonate ionic liquids dissolved in acetonitrile, to facilitate stirring, effervescence and heat is observed. The solvent, once removed from the resulting liquor afford a white solid. As aforementioned, the stability of the basic anion is often viewed as a hindrance within the ionic liquids field, however, in this work, it is observed to seamlessly to provide a mono-deprotonation of *p-tert*-butylcalix-[4]-arene hence forming a calixarate salt of an organic cation as shown in Figure 3-61. The reaction proceeds cleanly and in near quantitative yield, which, in turn, allows for the production of utilisable  $[TBC]^-$  anion.

Such salts exhibit a dramatically improved solubility and scope as a starting material for mono-alkylations as will be discussed in 3.2.6. This acid-base reaction has been successful for a variety of cations including triethylmethylammonium,  $[N_{2221}]$ , tributylmethylammonium  $[N_{4441}]$  and tris (-2-methoxyethoxy) methylammonium  $[N_{peg}]$  (Figure 3-62). As will be discussed from the single crystal diffraction determined structure of  $[N_{2221}][TBC]$  is *via* the single deprotonation of the TBC motif causes a distortion in the cone conformer. The cation although hydrogen bonding dominantly occurs with the lower rim it is cradled by the upper rim of the neighbouring calixarene.

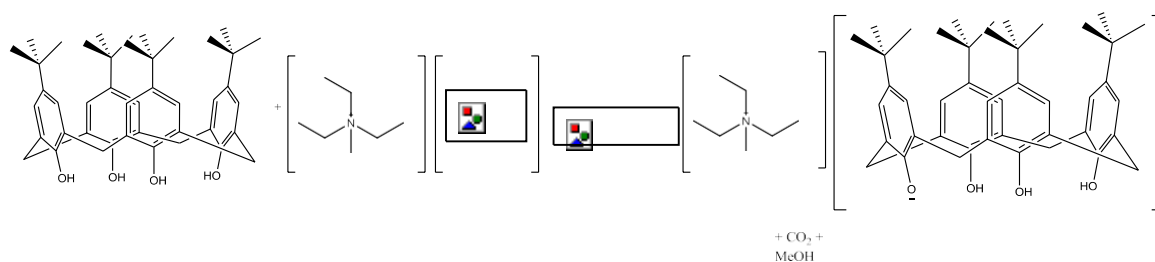


**Figure 3-61-** Synthesis of  $[N_{2221}][TBC]$  using methyl carbonate ionic liquids.

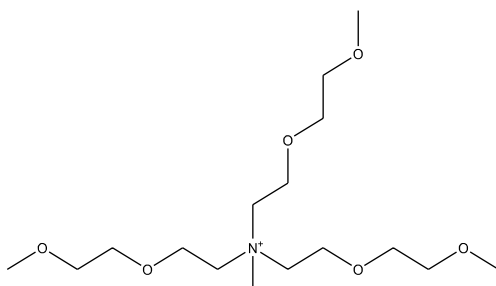


**Figure 3-62-** Structure of tris (-2-methoxyethoxy) methylamine [Npeg] cation.

### 3.2.5.1 Nuclear magnetic resonance spectroscopy

$^1H$  and  $^{13}C$  NMR spectra have alluded to the formation of the salt with integrations in the  $^1H$  spectra supporting a 1:1 cation and anion interactions are listed within the experimental methods and appendix (Figure 8-13, Figure 8-14, Figure 8-15, and Figure 8-16). Furthermore, the aromatic peak, at  $\sim 6.8$  ppm remains a sharp and singlet peak suggesting that the cone conformer remains despite the deprotonation and consequent disruption in cyclic hydrogen bonding in the lower rim phenolic protons.

### 3.2.5.2 UV/Vis spectroscopy

Again to determine whether if a single deprotonation has occurred methodology by Woolfall and Cunningham was utilised.<sup>275</sup> To further reiterate their findings; it was observed that with the addition of strong organic bases such as 1, 8-Diazabicyclo [5.4.0] undec-7-ene, DBU to TBC in acetonitrile there is a spectral change that corresponds to the first deprotonation within the four phenolic groups. The change itself consists of a shift in  $\lambda_{max}$  and a shoulder appearing at 315 nm however upon the addition of triflic acid the shift and shoulder formed is reversed.

This study was repeated with the calixarate salts in acetonitrile and to these solutions varying amounts of DBU was added and spectra observed. A standard solution of the calixarate salt was formed, the solution was diluted using acetonitrile and differing concentrations of the strong base DBU added. No changes in spectra were observed with increasing DBU concentration indicating the TBC is already

deprotonated. It should also be noted that the shape of the initial solutions is near identical to that reported for the TBC with 1 equivalent DBU as shown in Figure 3-63. The addition of triflic acid, however, showed a significant shift and loss of shoulder indicative of the formation of a neutral TBC species further confirming the deprotonation *via* the methyl carbonate anion. This deprotonation is also critical in interrupting the 'circular hydrogen bonding' within the phenolic protons which, is known especially for its strength in tetramer calix's as described by Tobiason and Shinkai *et al.*<sup>180,277</sup> This circular hydrogen bonding in the lower rim is also believed to significantly affect the stability of the cone conformer. The single deprotonation *via* the formation of this organic salt allows for a new opportunity for the single alkylation of TBC without the use of any bases. The removal of this base intrinsically prevents the formation of di-, tri- and tetra-alkylated species hence bypassing elaborate and laborious separation processes. The use of the organic salt also improves the solubility of the starting material allowing for reactions to be completed in concentrated solutions and under mild conditions. Further to this the initial issues regarding preferential solubility of the ether products over the *p-tert*-butylcalix-[4]-arene starting material *i.e.* a further preventative measure towards multiple alkylations.

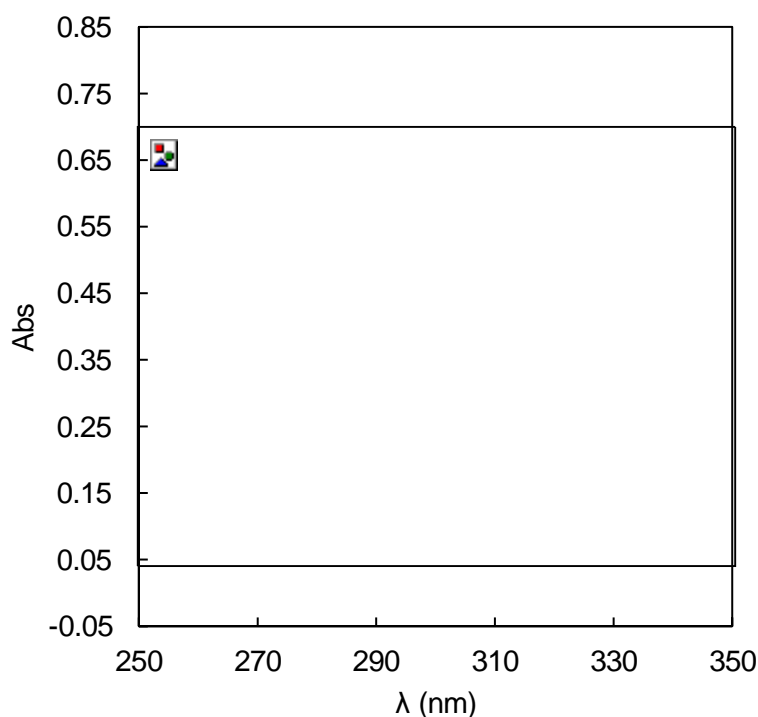


**Figure 3-63-** UV/Vis spectrum of  $[N_{2221}][TBC]$  in MeCN (dashed) and with excess triflic acid added. (solid).

### 3.2.5.3 Single crystal X-ray diffraction

As aforementioned, the calixarate salts formed were crystalline upon purification allowing for direct measurement *via* single crystal X-ray diffraction spectroscopy. Two of the calixarate salts were measured as shown in Figure 3-64 and Figure 3-66. As shown in Figure 3-64 and Figure 3-66 deprotonation occurs on the O4 position with the O1 –O3 phenolic groups orientating such that the O-H bond is directed towards this point of negative charge. In terms of cation and anion interactions in the  $[N_{2221}][TBC]$  structure, the majority of hydrogen bonding interactions occur between the lower rim of the TBC and the C-1 positions of the cation alkyl substituents. The  $[N_{2221}]$  cation is small and compact and was found to be cradled by the upper rim of the TBC with suspected  $\pi$  interactions. The  $[N_{2221}]$  cation lies at its closest point 2.182 Å from the lower rim and 2.812 Å from the aromatic carbons of the upper rim / calixarene cavity. In the  $[N_{4441}]$  example the cation cannot fit within the cavity instead it clusters around the lower rim of the deprotonated TBC in close proximity to another ion pair. Lying approximately 2.676 Å at its closes point to the lower rim the interaction is comparable with the smaller  $[N_{2221}]$  cation.

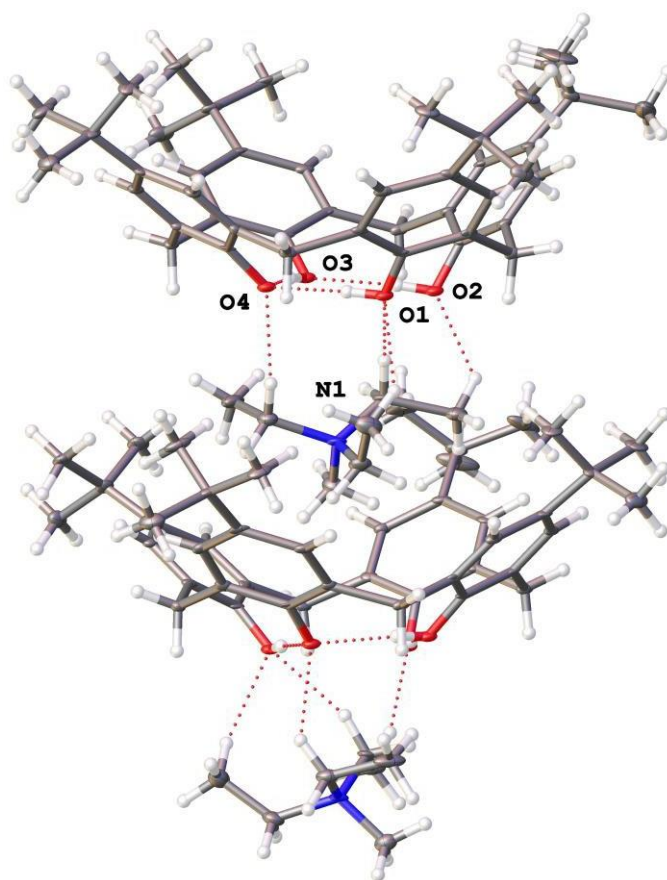


**Figure 3-64-** Single crystal diffraction determined structure of triethylmethylammonium p-tert-butylcalix-[4]-arate,  $[N_{2221}][TBC]$ .



**Table 3-12**-Single crystal data for triethylmethylammonium p-tert-butyl-calix-[4]-arate, [N 2 2 2 1][TBC].

Empirical formula	C <sub>51</sub> H <sub>73</sub> NO <sub>4</sub>
Formula weight	764.10
Crystal system	orthorhombic
Space group	Pna2 <sub>1</sub>
a/Å	15.4381(2)
b/Å	15.9969(2)
c/Å	18.31405(18)
α/°	90
β/°	90
γ/°	90

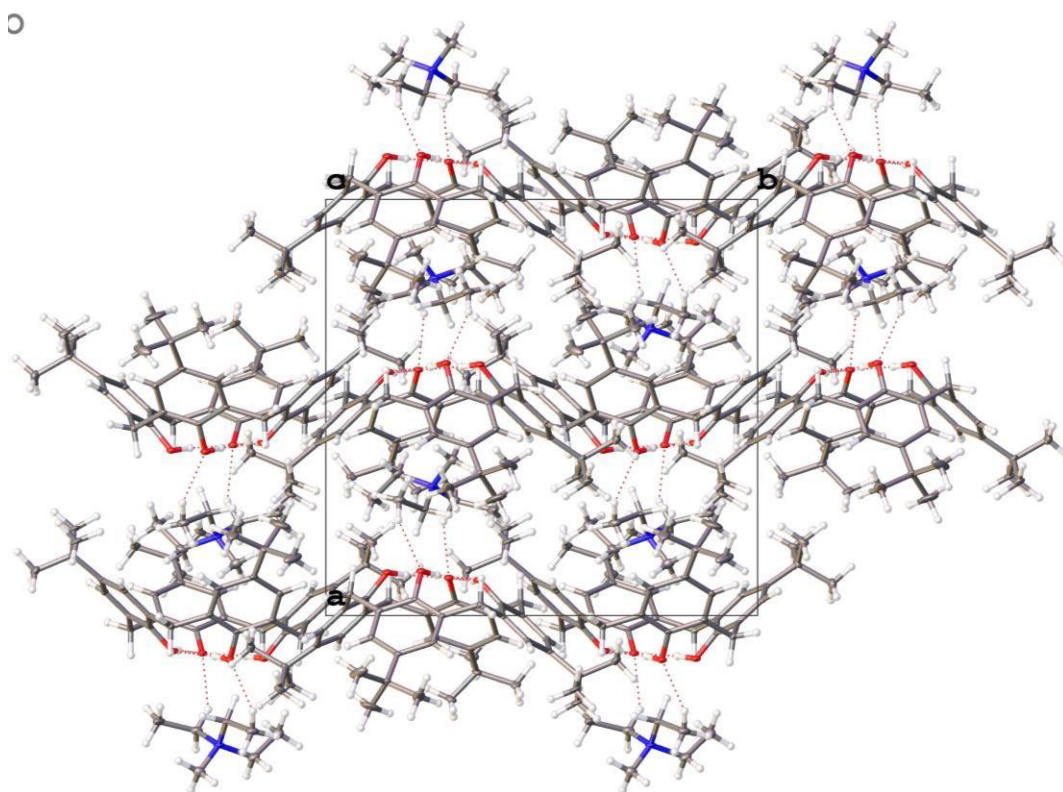


**Figure 3-65**- Single crystal diffraction determined structure of triethylmethylammonium p-tert-butyl-calix-[4]-arate, [N 2 2 2 1][TBC].



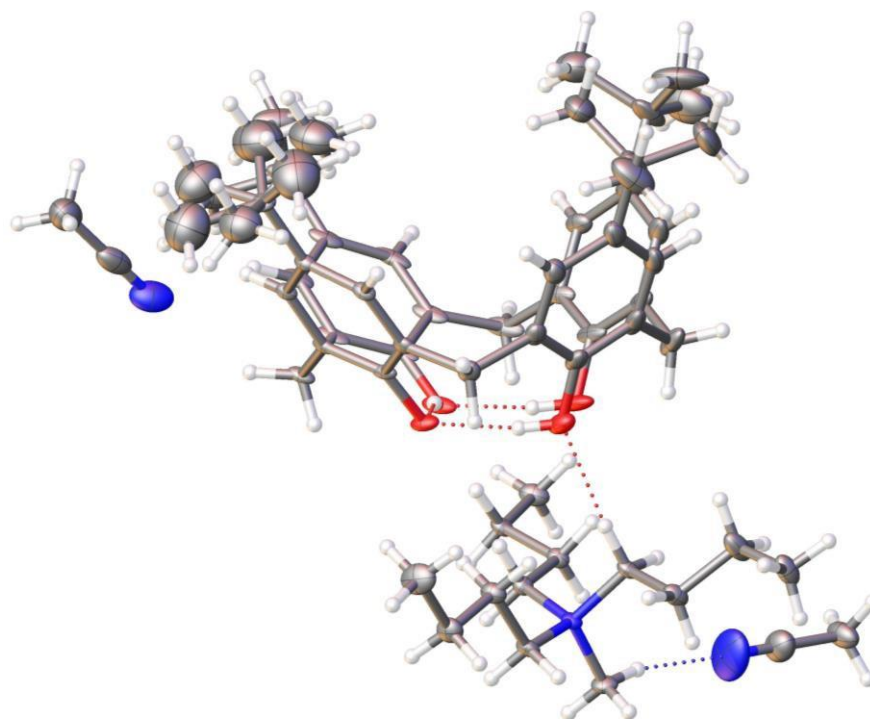


**Figure 3-66-** Single crystal diffraction determined structure of tributylmethylammonium p-tert-butylcalix-[4]-arate, [N 4 4 4 1][TBC].

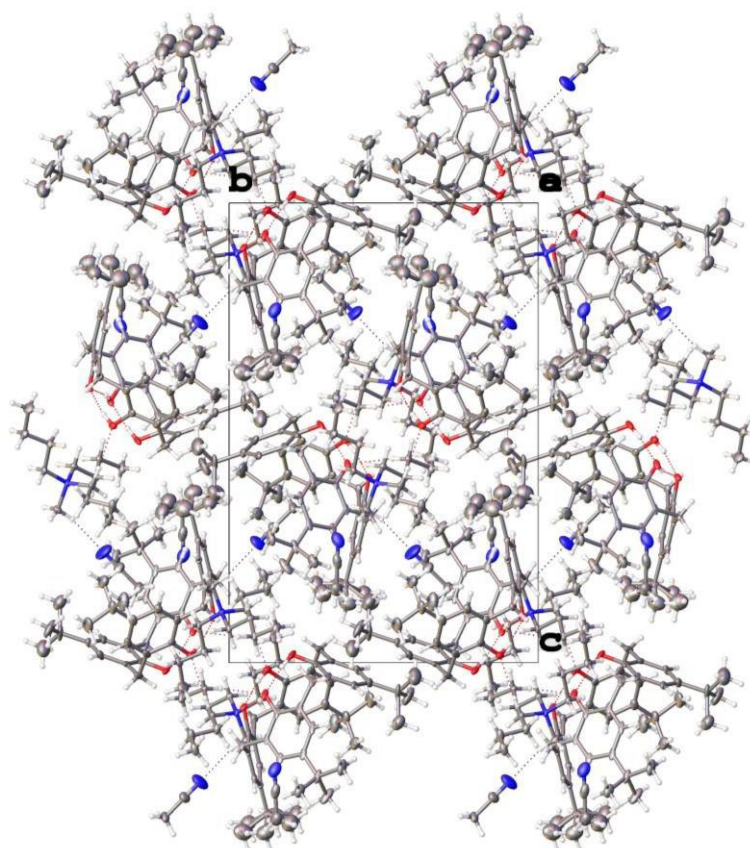


**Figure 3-67-** Single crystal diffraction determined structure of tributylmethylammonium p-tert-butylcalix-[4]-arate, [N 4 4 4 1][TBC].

**Table 3-13-** Single crystal data for triethylmethylammonium *p*-tert-butyl-calix-[4]-arate, [N<sub>2221</sub>][TBC].

Empirical formula	C <sub>64</sub> H <sub>100</sub> O <sub>4</sub> N <sub>3</sub>
Formula weight	975.49
Crystal system	Orthorhombic
Space group	P 2 <sub>1</sub> /c
<i>a</i> /Å	15.3846(2)
<i>b</i> /Å	15.7251(2)
<i>c</i> /Å	24.2062(3)
$\alpha$ /°	90
$\beta$ /°	105.0730(10)
$\gamma$ /°	90

### 3.2.6 Selective mono-alkylations of *p*-tert-butylcalix-[4]-arenes using ammonium calixarate salts

#### 3.2.6.1 Current methodologies for alkylations of *p*-tert-butylcalix-[4]-arenes

Synthesised by Zinke and Ziegler in 1948 *via* a series of condensation steps involving *p*-tert-butylphenol and formaldehyde; they were often referred as insoluble, high melting solids.<sup>162,164</sup> Since the synthesis of the basic calixarene motif there has been a huge interest in the solubility and functionalisation of these molecular baskets.<sup>2</sup> There are two evident aspects to this functionalisation; the first being enhancement of solubility *via* the attachment of a somewhat polar species to either the lower or upper rim utilising a variety of organic reactions including esterification, sulfonation and Claisen rearrangements to name but a few.<sup>224,287–289</sup> The second aspect of functionalisation focuses on the utilisation of the calixarene *via* the addition of a ligated species to assist in application to separations, host-guest complexes in many aspects of chemistry and biochemistry; including enhancement of rare earth luminescence.<sup>181,182,290</sup>

The mono-ethers of *p*-tert-butylcalix-[4]-arene are regularly used as starting materials for multi-functionalised calixarene host-molecules that require functionalisation of a single –OH group. Current methods of mono-alkylation primarily involve the use of a strong inorganic base such as Na[OMe], K[OAc], NaH, Cs[CO<sub>3</sub>] or CsF, which in each case carry their own issues regarding safety, solubility and the extent of deprotonation. Further details are available in section 3.1.3.<sup>213,225,226</sup> The solubility of the starting material (TBC) itself also determines the sluggishness of reactions where, especially, utilisation of weaker bases affords a greater mix of di-, tri- and tetra-ethers hence requiring elaborate separation techniques. Peculiarly, Na[OMe] in acetonitrile has shown to be an effective method

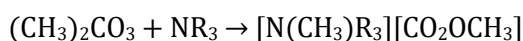
of monoalkylation producing a yield of approximately 75 % demonstrated by Shu *et al.*, which contravenes the idea that use of stronger bases should result in a greater proportion of multiple alkylations.<sup>226</sup> As of yet, no explanation for this result has been found.

Recent methods have been entailed to improve the green credentials of the mono-alkylations with a main shift towards utilisation of microwave (MW) irradiation and sulfonate alkylating reagents. Use of MW irradiation has rapidly decreased reaction times; however, the production of di-substituted species is still prevalent.<sup>291,292</sup> Sulfonates have also been utilised along with a silyl triether derivative with use of pendant phenolic groups for mono-alkylation that, although effective, require elaborate synthesis and poor atom efficiency.<sup>293</sup>

### 3.2.6.2 New methodology for mono-alkylation of *p*-*tert*-butylcalix-[4]-arenes

In this work, a simple method to obtain mono-etherated *p*-*tert*-butylcalix-[4]-arenes in which basic methyl carbonate ionic liquids are utilised to form mono-calix-[4]-arate salts is described. Methyl carbonate ionic liquids have been a somewhat new revelation within the ionic liquids field. The non-halogenated anion is very appealing in regards to the green impact and toxicity of it as a solvent, however, the intrinsic instability of the basic anion is often viewed as a hindrance. First synthesised by Janson *et al.* by methylating trialkylamines with dimethyl carbonate, ‘an environmentally benign alkylating reagent’, affording a fully organic ionic liquid (Equation 3-2).<sup>268</sup>

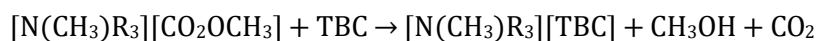
Equation 3-2



The determination the  $\text{pK}_a$  of TBC and other calixarenes has also been sought using a variety of methods including ammonium salts of *p*-nitrophenolate, 2,4-dinitrophenolate, and picrate, however, a majority of these measurements have only been possible in organic molecular solvents due to the very poor solubility of standard calixarene compounds such as TBC in aqueous and polar solvents.<sup>178,179</sup> The first  $\text{pK}_a$  measurement of a simple calix-[4]-arene was achieved by Böhmer, *et al.* by the addition of nitro-functionality in the upper rim to improve solubility.<sup>294</sup> However, as a consequence of the nitro addition to the upper rim the  $\text{pK}_a$  of the phenolic protons increases. It is plausible that the  $\text{pK}_a$ 's of hydroxyl groups in TBC determines the manner in which mono-alkylation can be attained. The higher basicity of the methyl carbonate anion compared to acetate is often noted; the

addition of a Brønsted acid of an anion of choice (*i.e.* TBC), the methyl carbonate anion decomposes into MeOH and CO<sub>2</sub> and the ionic salt with the conjugate base as the anion is obtained.<sup>2,3</sup>

**Equation 3-3**



The *p-tert*-butyl motif on the calix-[4]-arene has a significant effect on the dissociation constant of the phenolic proton; with *p*-methylcalix-[4]-arene and *p-tert*-butylcalix-[4]-arene having pK<sub>a</sub>'s of 6.0 and 4.3 respectively. This large change in pK<sub>a</sub> is believed to be due to subtle conformational effects due to the differing sizes of the alkyl substituents.<sup>177,294,295</sup> This structural effect and decrease in pK<sub>a</sub> allow for the acid base chemistry of the methyl carbonate anion to be utilised effectively as a new synthetic method.

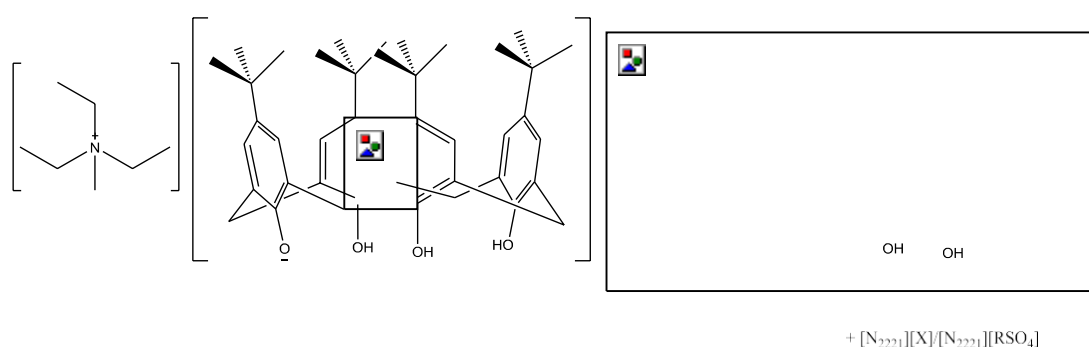


**Figure 3-68-** Reaction schematic for the alkylation of *p-tert*-butylcalix-[4]-arenes from organic *p-tert*-butylcalix-[4]-arate salts.

Mono-alkylations of [N<sub>2221</sub>][TBC] have been successfully carried out using both dialkyl sulphates and alkyl halides with good yield and minimal separation techniques. Using a standard procedure of dissolving [N<sub>2221</sub>][TBC] (0.262 mmol) in chloroform (2.5 mL) and 1.1 mole equivalents of an alkylating agent the solution is stirred at room temperature for 72 hours. Isolation simply requires washing with water and concentration under vacuum of the organic layer to afford an off-white solid in every case. Specifically, with small chain alkylating agents the by-product salt is readily removed with water, however, understandably in the alkyl sulphate by products as chain length increases the washing step requires greater attention.

Achieving high yields within methylation and methylation reactions the decrease in yield as chain length increases is believed to be due to general lack of reactivity of higher dialkyl sulphates. Current synthetic methods requiring mono-propylation or butylation require a top down approach *via* the selective removal of ether groups

from TBC again achieve comparable yields of approximately 35-95 %, however, this does not account for the initial alkylation step for the top down approach, which often incorporates the use of tags and protecting groups. Comparatively, from a bottom-up approach utilising a monosodium salt *via* Na[OMe] the highest yields reported for propylation and butylation are 47-75 %.<sup>225,227,296</sup>

In regards to the conformers achieved *via* this alkylation technique it is believed that different conformers may dominate depending on the alkylating agent is used, however, multiple variations are present in each product, which is observed *via* subtle changes in the <sup>1</sup>H NMR (as will be discussed). Asymmetry within the TBC after alkylation is evident from <sup>1</sup>H NMR spectroscopy together with the utilisation of electron spray mass spectroscopy to eliminate any ambiguity regarding the presence of only mono-alkylated TBCs.

However, the presence of multiple conformers is expected to be due to the aforementioned disruption in the circular phenolic hydrogen bonding due to mono-substitution. A simplistic view of possible conformers of TBC is represented in Figure 3-70; all conformers can exist in the mono-alkylated products with both solvent effects and by-products of each reaction possibly driving one conformer over another. From monitoring <sup>1</sup>H NMR as a function of time it is observed that a 100 % conversion is achieved in all dialkyl sulphates and alkyl iodides as shown in Figure 3-71. Studies with dimethyl carbonate were unsuccessful, but this is unsurprising as it is a significantly weaker methylating agent. In this work, the facile synthesis of organic mono-calix-[4]-arate salts in near quantitative yields from methyl carbonate ionic liquids has been demonstrated.

These organic salts have been successfully applied to selective alkylation reactions with dialkyl sulphates and alkyl halides to form single mono-alkylated products with high yield using only minimal amount of chloroform solvent. This method avoids the use of expensive alkali metal bases hence providing a safer and selective synthetic route that in future may also be successfully applied to further selective alkylations. The prevalence of the *p-tert*-butylcalix-[4]-arene motif and the development of a simplistic and new starting point for functionalisation allows for new perspective of on a variety of old synthetic routes.

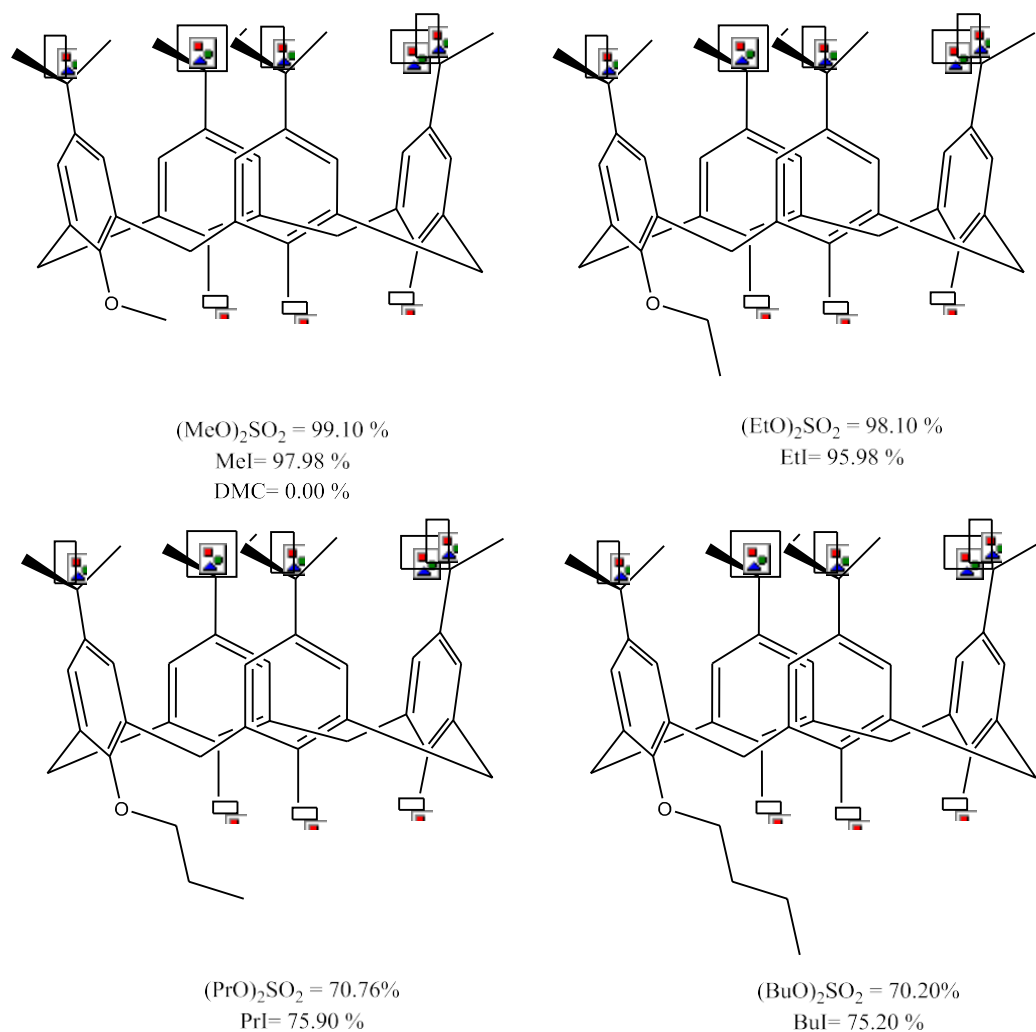


**Figure 3-69-** Products obtained with isolated yields for alkylations of  $[\text{N}_{2.2.2.1}]\text{TBC}$  with dialkyl sulphates and alkyl halides.

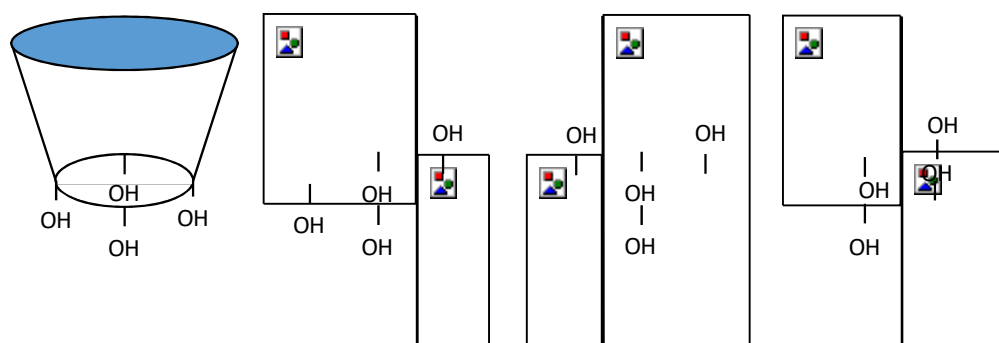


**Figure 3-70-** Conformers of TBC (L-R) cone, partial cone, 1, 3-alternate and 1, 2-alternate.

### 3.2.6.3 Comparison of separations with larger ammonium cations

A majority of the studies regarding mono-alkylations were completed using triethylmethylammonium *p*-*tert*-butylcalix-[4]-arate salts as preliminary studies utilising salts consisting of larger cations such as tributylmethylammonium,  $[\text{N}_{4441}]$  and the as aforementioned PEGylated form,  $[\text{N}_{\text{peg}}]$  required greater separation steps.

The larger the organic cation the less soluble in water the halide/alkyl sulphate by-product hence a greater number of washes are required and the uses of alternative solvents are required in the case of the  $[N_{\text{peg}}]$  salt. As discussed, one of main focuses of this new methodology is to eliminate laborious separations hence all studies were complexes using the triethylmethylammonium *p*-*tert*-butylcalix-[4]-arate salts,  $[N_{2221}][\text{TBC}]$ .

#### 3.2.6.4 $^1\text{H}$ nuclear magnetic resonance monitoring

Reaction studies in which isolated yield and products analysed were determined after a 72 hour reaction time. However, analysis of the reaction *via*  $^1\text{H}$  NMR as shown in Figure 3-71 show that the aromatic peak referring to the cone conformer of the *p*-*tert*-butylcalix-[4]-arene decreases and disappears after approximately 20 hours. Elucidation of the conformers present was not possible due to the complexity of the  $^1\text{H}$  NMR spectrum. When the reaction mixture was analysed by  $^1\text{H}$  NMR spectroscopy it revealed the presence of a mixture of conformers. However, due to the complexity of the spectra it was not possible assign signals for individual conformers.

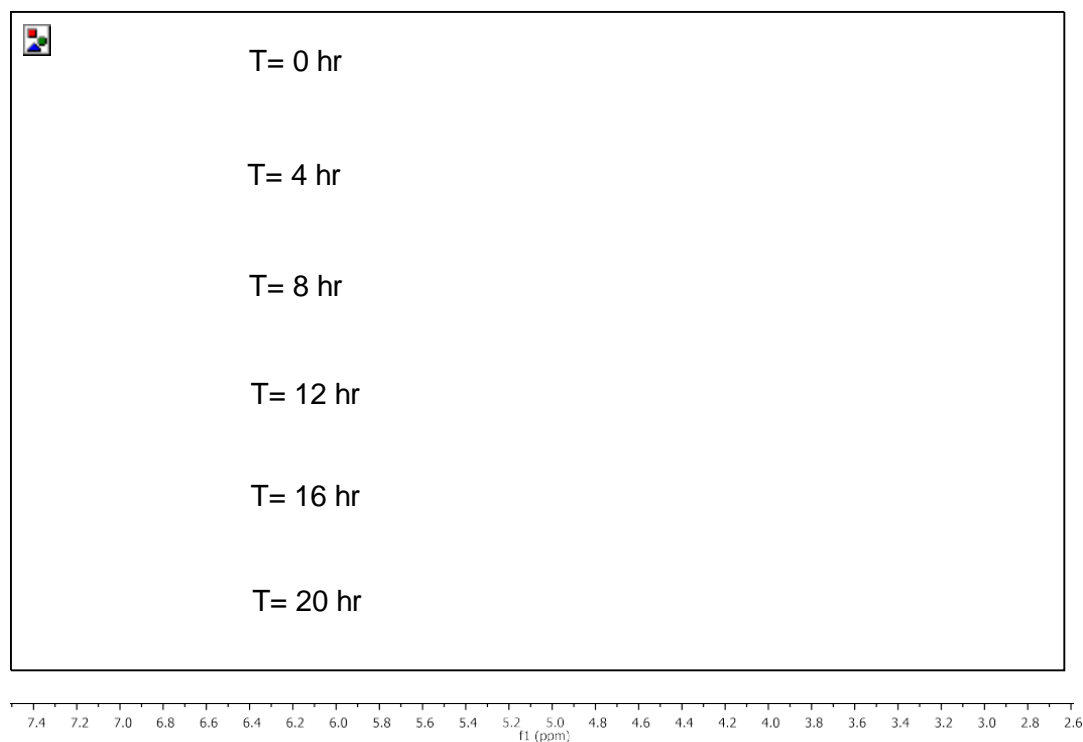


**Figure 3-71**  $^1\text{H}$  NMR monitoring of  $[N_{2221}][\text{TBC}]$  and dimethyl sulphate in  $d_3$ -chloroform.

As discussed, due to the complexity of the spectra it was not possible to pinpoint which conformers were present and in what proportion as shown in Figure 3-71. Work by Jaime *et al.* has demonstrated how elaborate  $^{13}\text{C}$  NMR of various of calix-

[4]-arenes can be, never mind their  $^1\text{H}$  counterparts.<sup>297</sup> Further work by Bifulco and Neri utilised computational techniques to compare the  $-\text{CH}_2-$  bridging peaks in  $^{13}\text{C}$  and  $^1\text{H}$  NMR; it was shown that between four different manipulation the TBC and the mono-methylated lower rim the  $^1\text{H}$  peak for the  $-\text{CH}_2-$  varied only 0.25 ppm and the  $^{13}\text{C}$  peak 5 ppm.<sup>298</sup> Such a slim margin in shift for different conformers again highlights the difficulty in identifying the conformers present.

Within this work reactions were monitored and products identified *via* the aromatic and etheryl peaks; such that asymmetry is observed and mono-alkylation occurs respectively.

### 3.2.6.5 Mass spectrometry

Mass spectrometry, MS was utilised as a technique to confirm the synthesis of a singly alkylated product. Mass spectrometry as analytic technique proceeds *via* four main steps; ionisation, acceleration, deflection and detection. Within MS species are deflected as per their mass charge ratios; the samples undergo ionization to the +1 state within conventional MS techniques and are accelerated to ensure all species have equivalent kinetic energy. Deflection of the accelerated species proceeds Electron spray methods utilise multiple charges species. As listed in Table 3-14 the isolated products in all cases matched the exact masses of the mono-alkylated products.

**Table 3-14-** Mass spectroscopic analysis of products from mono-alkylations of mono-anion *p-tert-butylcalix-[4]-arate* salts.

Alkylating agent	Calculated mass	Mass Spectrometry data of isolated product				
		Exact Mass	$[\text{M}+\text{H}]^+$	$[\text{M}+\text{Na}]^+$	$[\text{M}+\text{NH}_4]^+$	$[\text{M}+\text{K}]^+$
$\text{Me}_2\text{SO}_4$	663.4413	663.4413	663.4413		680.4679	
$\text{Et}_2\text{SO}_4$	677.4570	677.4595	677.4595	699.4402		
$\text{Pr}_2\text{SO}_4$	691.4726	691.0090	691.4727	713.4546	708.4992	
$\text{Bu}_2\text{SO}_4$	705.4883	705.4869	705.4883	727.4702	722.5140	743.4442
MeI	663.4413	663.4423	664.4454	685.4233		
EtI	677.4570	677.4570	678.4620	699.4389	694.4835	715.4128
PrI	691.4726	691.4733	691.4727	713.4546	708.4992	
BuI	705.4883	705.4861	705.4883	727.4702	722.5148	743.4442

There were no indications of di-, tri- or tetra-alkylated products within MS analysis further highlighting the effective selectivity of the alkylation methodology.



### 3.3 Conclusions

The solvation of *p*-*tert*-butylcalix-[4]-arene has been achieved in trihexyltetradecylphosphonium acetate, [P<sub>66614</sub>][OAc] up to a 20 mol% concentration; which is significantly higher than all known solvents in literature. Furthermore, extensive spectroscopic studies have elucidated the solvation mechanism which proceeds *via* the deprotonation of a single phenolic proton of the TBC. This deprotonation causes both base clustering of the remaining acetate anions, the deprotonated TBC and acetic acid formed to occur hence causing some peculiar NMR shifts and infrared spectroscopic observations. Such conclusions have been elucidated *via* a series of studies on a variety of comparative systems to support the spectroscopic observations.

Continuing on from the [P<sub>66614</sub>][OAc] system other basic anions were investigated; particularly methyl carbonate ionic liquids due to their acid sensitive anions. Upon addition of TBC to ammonium methyl carbonate ionic liquids in a small amount of acetonitrile effervescence is observed due to the evolution of CO<sub>2</sub> and a rapid solvation of the crystalline TBC. Removal of the acetonitrile solvent afforded a series of crystalline products, which were found to be ammonium mono-deprotonated calix-[4]-arate salts. These salts have been successfully applied to selective mono-alkylations of TBC in 100 % selectivity and high isolated yields.

In summary, this new synthetic route transforms a perceived weakness of methyl carbonate ionic liquids into a useful property.<sup>15</sup> Omitting the need for expensive, unpredictable inorganic bases (*i.e.* caesium carbonate, sodium methoxide) an intrinsically controlled method of mono-alkylation of TBC has been developed, without the need for strong inorganic bases which are often used in large excess. The products formed also require minimal water based work ups and no separation techniques as a single product is achieved in all cases. Transforming the first step of a majority of lower rim functionalisation reactions on the TBC to provide higher yields and selectivity provides greater accessibility to calixarene chemistry. There is also further scope to utilise this methodology on the second deprotonation of the TBC mono-alkylated products and sequential .

### 3.4 Future work

It is apparent that there is a great disparity between the behaviour of phenol and *p-tert*-butylcalix-[4]-arene in the acetate anion ionic liquids. In future it would be of merit to compare further uncycled *p-tert*-butylphenol units and larger calix-[6]-arenes and calix-[8]-arenes to compare the effect of the rigidity of the TBC unit and its effect on deprotonation vs. hydrogen bonding.

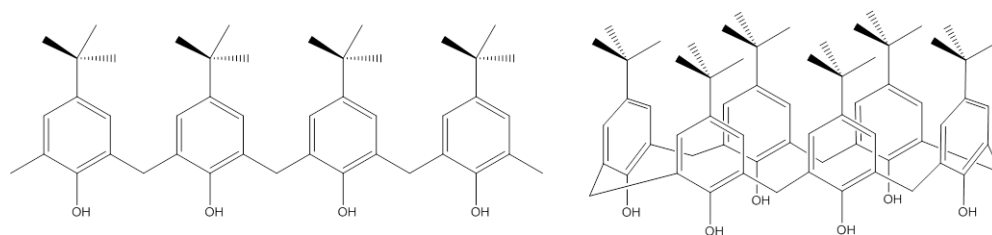


**Figure 3-72-** Uncycled *p-tert*-butylphenol units and *p-tert*-butylcalix-[6]-arenes.

Gaining a greater understanding of the behaviour and stability of similar supramolecular compounds will give scope for further applications of this methodology. One of the biggest accomplishments that could be achieved within etheryl functionalisation is the synthesis of a *p-tert*-butylcalix-[4]-arene with four different lower rim substituents. If the methyl carbonate anion deprotonation methods could be applied sequentially there is intrinsic control over the functionalisation steps as shown in Figure 3-73; along with avoiding laborious separation techniques this methodology allows for concentrated reaction mixtures, improved yields and control.

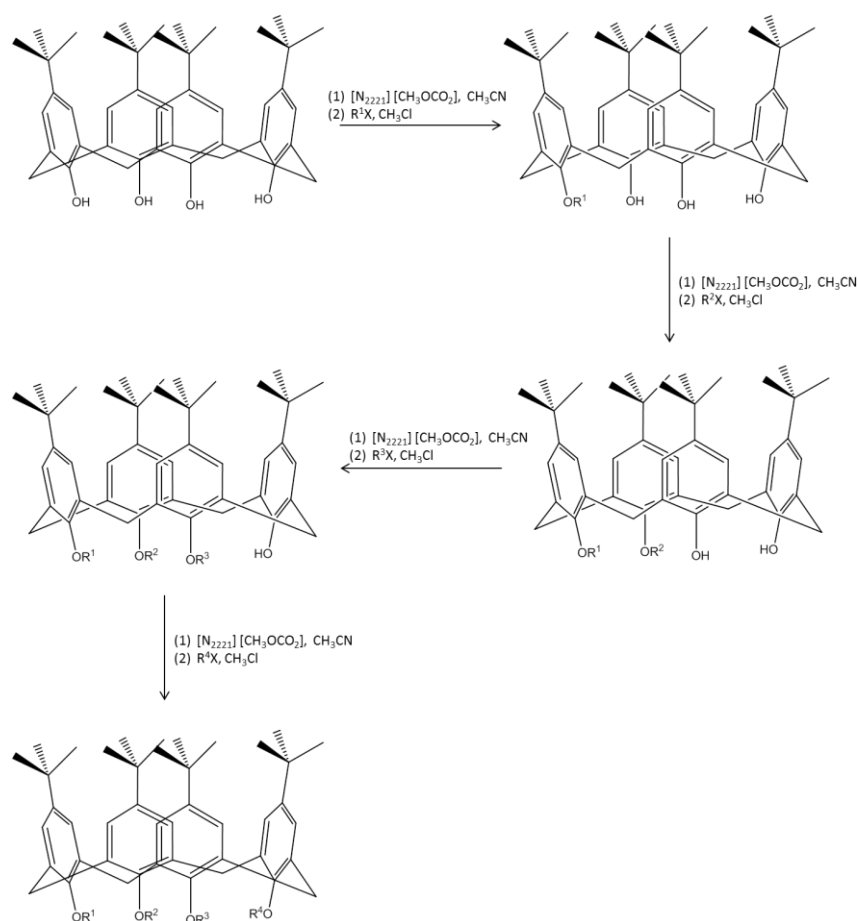


**Figure 3-73**-Sequential use of the methyl carbonate anion as a deprotonation method for tetra-functionalised *p*-*tert*-butylcalix-[4]-arene.

## 3.5 Experimental methods

### 3.5.1 Materials

*p*-*tert*-butylcalix-[4]-arene was obtained in 99% purity from Alfa Aesar. All solvents used were obtained from Honeywell and were of analytical purity. All alkylating agents were obtained from Sigma Aldrich with a minimum purity of 99%.

***p*-*tert*-butylcalix-[4]-arene:**  $^1\text{H}$  NMR (400 MHz,  $\text{CDCl}_3$ )  $\delta$  10.34(s, 4H, 4xOH), 7.05 (s, 8H, 8xAr-H), 4.26 (d,  $J = 19.4$  Hz, 3.98H, 2xAr- $\text{CH}_2$ -Ar), 3.49 (d,  $J = 13.3$  Hz, 3.91H, 2xAr- $\text{CH}_2$ -Ar), 1.55 (s, 35.64H, 4xt-C ( $\text{CH}_3$ )<sub>3</sub>).

Note: \*dichloromethane impurities are evident in this commercial sample from the  $^1\text{H}$  NMR. The cone conformer is solely present.

All alkylating reagents, salts and bases were purchased from Sigma-Aldrich or Alfa Aesar of *puriss* quality. Solvents were acquired from Honeywell.

Trihexyltetradecylphosphonium acetate,  $[P_{66614}][OAc]$  was prepared *via* adapted literature methods utilising potassium acetate in methanol to initiate the Finkelstein method.<sup>299,300</sup> The solution was concentrated to dryness and dry acetonitrile added to precipitate residual KCl salt. This method was repeated until a negative  $Ag[NO_3]$  test was observed. The solution was then washed with water and ethyl acetate. Halogen analysis of the sample was used to ensure the chloride concentration > 1 %.

Methyl carbonate ionic liquids were prepared *via* literature methods.<sup>3,269</sup>

### 3.5.2 Nuclear magnetic resonance spectroscopy

All NMR spectra were recorded on a Bruker Advance DPX 400 MHz spectrometer. The frequency of the measurements are  $^1H$  NMR 400 MHz and  $^{13}C$  100 MHz. Samples which were liquid at room temperature were recorded using  $d_6$ -DMSO capillaries as an external deuterium lock to prevent the solvent affecting the interactions present in the sample. Alkylation products and reaction monitoring studies were recorded in  $d$ -chloroform due to the solid nature of the starting material.

### 3.5.3 UV/Vis spectrometry

All spectra were measured on an Agilent Technologies Cary 60 UV/Vis spectrometer with a total range of 190 to 1100 nm using a 10 mm quartz cuvette sample holder.

Typical procedure for UV/Vis spectroscopic titrations. *p*-*tert*-butylcalix-[4]-arene (0.0073 g) was dissolved in MeCN (250 cm<sup>3</sup>) at 20 °C with 0.2 mole equiv IL. DBU (0.015 g) was dissolved in MeCN (50 cm<sup>3</sup>), giving a 3.94 μM solution. *p*-*tert*-butylcalix-[4]-arene solution (3.0 cm<sup>3</sup>) was added to a cuvette (10 mm), and a UV/Vis spectrum was taken at 25 °C on Agilent Technologies Cary 60 UV/vis Spectrophotometer. Successive aliquots (10 μL) of DBU solution were added to the cuvette using a micropipette, and a UV/vis spectrum was taken after each addition. A total of 8 aliquots were added, until a total of 80 μL had been added (1.8 mole equiv). All standard solutions were prepared at 20 °C, and the titrations were carried out at 20 °C. Triflic acid addition consisted of a single drop addition assumed to be excess.

### **3.5.4 Densimetry**

Density was measured using a U-shaped oscillating tube Anton Paar DMA 4500 density meter. The density meter was capable of holding a constant temperature,  $\pm 0.01\text{ }^{\circ}\text{C}$ , and measured density to an accuracy of  $\pm 0.0001\text{ gcm}^{-3}$ . Samples (1.3 mL) were sonicated for 20 minutes prior to measurement and loaded into syringes and transferred to the density meter. Measurements were completed at  $10\text{ }^{\circ}\text{C}$  increments to  $80\text{ }^{\circ}\text{C}$  from room temperature,  $20\text{ }^{\circ}\text{C}$ .

### **3.5.5 Thermogravimetric Analysis, TGA**

All measurements were carried out on TA instruments TGA Q 5000 instrument. Samples were placed in a haematic aluminium pan and were heated at  $1\text{ }^{\circ}\text{Cmin}^{-1}$  under a nitrogen flow with a  $\pm 0.1\%$  weighing accuracy.

### **3.5.6 Mass spectrometry**

All measurements were completed using a Waters LCT Premier Electrospray Time of Flight Mass Spectrometer (ESI-MS). Samples suspended in acetonitrile solvent.

### **3.5.7 Infrared spectroscopy**

All Infrared spectra were recorded on a PerkinElmer Spectrum-100 FTIR spectrometer with ATR attachment, with a total range of  $7800\text{ to }370\text{ cm}^{-1}$ , with a resolution of  $0.50\text{ cm}^{-1}$ . Liquid samples were measure *via* placement of a droplet of said sample was placed on the crystal of the ATR attachment and the contact placed on top. Solid samples were prepared in a similar method.

ATR-IR spectroscopy is a variation of conventional IR techniques in that the crystal in which the IR measurement is determine via the evanescent wave which is generated by the internal refraction of the crystal. Changes in the evanescent wave of the crystal are due to the sample placed on top of it hence generating an IR spectrum as shown in Figure 3-74.

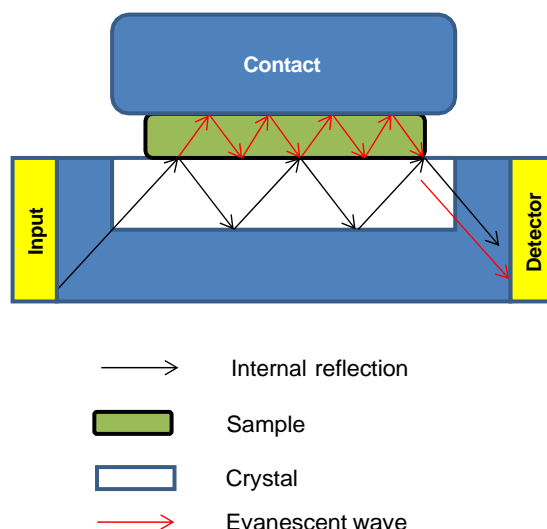


Figure 3-74- Attenuated Total Reflection Infrared spectroscopy technique.

### 3.5.8 Synthesis of *p*-*tert*-butylcalix-[4]-arate salts

**Triethylmethyammonium *p*-*tert*-butylcalix-[4]-arate, [N<sub>2 2 1</sub>][TBC]:** Equimolar amounts of triethylmethyammonium methyl carbonate (2.5 g, 13.07 mmol) and *p*-*tert*-butylcalix-4-arene (8.48 g, 13.07 mmol) were mixed together in acetonitrile (75 mL) and sonicated for 45 minutes until effervescence had ceased. The solution is concentrated under vacuum to form a white crystalline solid (9.76 g, 12.88 mmol, 98.0 %). This salt was used for other experiments without further purification.

<sup>1</sup>H NMR (400 MHz, CDCl<sub>3</sub>) δ (14.34 3 x Ar-OH), 6.97 (s, 8 H, 8x Ar-H), 4.41 (d, *J* = 12.1 Hz, 4 H, 2 x Ar-CH<sub>2</sub>-Ar), 3.55 – 3.41 (m, *J* = 30.0 Hz, 6 H, 3x N-CH<sub>2</sub>-R), 3.26 (d, *J* = 12.4 Hz, 4 H, 2 x Ar-CH<sub>2</sub>-Ar), 1.90 (s, 3 H, N-CH<sub>3</sub>), 1.40 (s, 9 H, 3 x N-CH<sub>2</sub>-CH<sub>3</sub>) 1.33 – 1.01 (m, 36 H, 4 x t-C(CH<sub>3</sub>)<sub>3</sub>).

<sup>13</sup>C NMR (101 MHz, CDCl<sub>3</sub>) δ 152.50, 140.57, 130.27, 124.95, 116.53, 77.48, 77.36, 77.16, 76.84, 56.08, 47.05, 34.23, 33.89, 31.81, 8.10, 1.47, 0.12.

**Tributylmethyammonium *p*-*tert*-butylcalix-[4]-arate, [N<sub>4 4 1</sub>][TBC]:** Equimolar amounts of tributylmethyammonium methyl carbonate, [N<sub>4 4 1</sub>][CO<sub>3</sub>Me] (0.25 g, 0.908 mmol) and *p*-*tert*-Butylcalix-[4]-arene, TBC (0.589 g, 0.908 mmol) are mixed in acetonitrile (15 ml) at 60 °C for 24 hours. Small amounts of residual TBC are removed via filtration through glass wool and the filtrate is concentrated to ¼ of its initial volume and from which colourless cubic crystals are obtained (0.656 g, 0.774 mmol, 85.23 %).

$^1\text{H}$  NMR (400 MHz,  $\text{CD}_3\text{CN}$ )  $\delta$  12.90 (s, 3 H, 3 x Ar-OH), 6.99 (s, 8 H, 8 x Ar-H), 4.34 (d,  $J = 11.7$  Hz, 4 H, 2 x Ar-CH<sub>2</sub>-Ar), 3.21 – 3.05 (m, 10 H, 2 x Ar-CH<sub>2</sub>-Ar and 3 x N-CH<sub>2</sub>-R), 2.87 (s, 3H, N-CH<sub>3</sub>), 1.69 – 1.59 (m, 6 H, 3 x N-CH<sub>2</sub>-CH<sub>2</sub>-R), 1.40 – 1.31 (m, 6 H, 3 x N-CH<sub>2</sub>-CH<sub>2</sub>-CH<sub>2</sub>-R), 1.16 (s, 36 H, 4 x t-C(CH<sub>3</sub>)<sub>3</sub>), 1.00 – 0.93 (m, 9 H, 3 x N-CH<sub>2</sub>-CH<sub>2</sub>-CH<sub>2</sub>-CH<sub>3</sub>).

### 3.5.9 Synthesis of mono-alkylated *tert*-butylcalix-4-arenes

**General procedure:** To a concentrated solution of [cation][TBC] (0.262 mmol) in chloroform (2.5 mL), dialkylsulfate/alkyl iodide (0.2882 mmol) was added and stirred for 72 hours at room temperature. The reaction mixture was washed with water (4x2 mL) and the organic layer was separated. The residual chloroform is removed under vacuum, affording off white solid.

The yields obtained for all alkylations are given in Table 3-15.

**Table 3-15-** Yields obtained from mono-alkylations of mono-anion *p-tert*-butylcalix-[4]-arate salts.

Alkylating agent	Isolated Yield %
Me <sub>2</sub> SO <sub>4</sub>	99.10
Et <sub>2</sub> SO <sub>4</sub>	98.10
Pr <sub>2</sub> SO <sub>4</sub>	70.76
Bu <sub>2</sub> SO <sub>4</sub>	70.20
Mel	97.98
Etl	95.98
PrI	75.90
Bul	75.20

#### 3.5.9.1 Nuclear magnetic resonance data of alkylation products via dialkylsulphates

***p-tert*-Butylcalix-[4]-arene mono methyl ester (methylated with dimethyl sulphate :**  $^1\text{H}$  NMR (400 MHz,  $\text{CDCl}_3$ )  $\delta$  10.34 (s, 1 H, Ar-OH), 10.14 (s, 1 H, Ar-OH), 9.55 (s, 1 H, Ar-OH), 7.15 – 6.67 (m,  $J = 112.2, 54.2, 51.0$  Hz, 8 H, 8 x Ar-H), 4.41 – 4.21 (m,  $J = 35.1, 13.3$  Hz, 4 H, 2 x Ar-CH<sub>2</sub>-Ar), 4.12 -3.94(s, 2.38H+0.62H, Ar-O-CH<sub>3</sub>), 3.43 (m,  $J = 13.4$  Hz, 4 H, 2 x Ar-CH<sub>2</sub>-Ar), 1.41 – 0.78 (m, 36 H, 4 x t-C(CH<sub>3</sub>)<sub>3</sub>).

$^{13}\text{C}$  NMR (101 MHz,  $\text{CDCl}_3$ )  $\delta$  207.25, 150.79, 148.65, 147.01, 143.94, 143.53, 133.74, 128.50, 128.22, 128.03, 126.81, 126.27, 126.11, 126.03, 125.98, 78.84,

77.66, 77.55, 77.35, 77.03, 63.56, 52.16, 34.57, 34.25, 33.33, 32.95, 32.45, 32.04, 31.81, 31.73, 31.58, 31.33, 31.25, 30.63, 11.99, 0.33.

$^1\text{H}$  NMR (400 MHz,  $\text{CDCl}_3 + \text{D}_2\text{O}$ )  $\delta$  7.14 – 6.71 (m, 8 H, 8 x Ar-H), 4.39 – 4.20 (m, 4 H, 2 x Ar-CH<sub>2</sub>-Ar), 4.12 -3.94(s, 2.35 H + 0.64 H, Ar-O-CH<sub>3</sub>), 3.45-3.28 (m, 4.06H, 2x Ar-CH<sub>2</sub>-Ar), 1.41 – 0.78 (m, 36 H, 4 x t-C(CH<sub>3</sub>)<sub>3</sub>).

***p*-tert-Butylcalix-[4]-arene mono ethyl ester (ethylated with diethyl sulphate) :**

$^1\text{H}$  NMR (400 MHz,  $\text{CDCl}_3$ )  $\delta$  10.34 (s, 0.17H, Ar-OH), 10.23 (s, 0.87 H, Ar-OH), 9.65 (s, 1.69 H, Ar-OH), 7.77 (s, 0.23 H, Ar-OH), 7.17 – 6.76 (m,  $J = 74.7, 38.2, 35.9$  Hz, 8 H, 8 x Ar-H), 4.39 – 4.04 (m, 6.21H, 2xAr-CH<sub>2</sub>-Ar and Ar-O-CH<sub>2</sub>-R), 3.49 – 3.25 (m, 4 H, 2 x Ar-CH<sub>2</sub>-Ar), 1.69 (dt,  $J = 54.6, 7.0$  Hz, 2.29+0.73 H, Ar-O-CH<sub>2</sub>-CH<sub>3</sub>), 1.39 – 0.96 (m, 36 H, 4x t-C(CH<sub>3</sub>)<sub>3</sub>).

$^{13}\text{C}$  NMR (101 MHz,  $\text{CDCl}_3$ )  $\delta$  149.27, 148.40, 148.13, 147.90, 143.57, 143.14, 133.68, 133.01, 128.27, 128.24, 128.11, 127.88, 126.35, 125.74, 125.71, 125.65, 125.48, 125.08, 77.33, 77.22, 77.02, 76.70, 72.40, 34.24, 33.99, 33.92, 33.04, 32.32, 31.98, 31.69, 31.49, 31.27, 31.10, 30.92, 15.27, 0.00.

$^1\text{H}$  NMR (400 MHz,  $\text{CDCl}_3 + \text{D}_2\text{O}$ )  $\delta$  7.15 – 6.76 (m, 8 H, 8 x Ar-H), 4.38 – 4.05 (m, 6 H, 2 x Ar-CH<sub>2</sub>-Ar and Ar-O-CH<sub>2</sub>-R), 3.48 – 3.28 (m, 4 H, 2 x Ar-CH<sub>2</sub>-Ar), 1.75 - 1.62(dt,  $J = 7.1$  Hz, , 3 H, Ar-O-CH<sub>2</sub>-CH<sub>3</sub>), , 1.34 – 0.98 (m, 36 H, 4 x t-C(CH<sub>3</sub>)<sub>3</sub>).

***p*-tert-butylcalix-[4]-arene mono propyl ester (propylated with dipropyl sulphate):**  $^1\text{H}$  NMR (400 MHz,  $\text{CDCl}_3$ )  $\delta$  10.34 (s, 0.20 H, Ar-OH), 10.20 (s, 0.86 H, Ar-OH), 9.61 (s, 1.68 H, Ar-OH), 7.86 (s, 0.21 H, Ar-OH), 7.01 (m, 8H, 8 x Ar-H), 4.40 – 4.21, 4.10 (m, t,  $J = 7.0$  Hz, 4.80 H + 1.71 H, 2xAr-CH<sub>2</sub>-Ar and Ar-O-CH<sub>2</sub>-R ), 3.50 – 3.25 (m, 4 H, 2xAr-CH<sub>2</sub>-Ar), 2.36 – 1.62 (m, 4 H, Ar-O-CH<sub>2</sub>-CH<sub>2</sub>-R, NB: acetone impurities), 1.31 – 0.98 (m, 39 H, 4x t-C(CH<sub>3</sub>)<sub>3</sub> and Ar-O-R-CH<sub>3</sub>).

$^{13}\text{C}$  NMR (101 MHz,  $\text{CDCl}_3$ )  $\delta$  148.73, 148.46, 143.47, 134.01, 128.60, 128.57, 128.21, 126.68, 126.28, 126.07, 126.04, 125.98, 77.67, 77.55, 77.35, 77.03, 72.73, 34.57, 34.32, 34.25, 33.36, 32.65, 31.81, 31.74, 31.60, 31.25, 15.60, 1.36, 0.33.

$^1\text{H}$  NMR (400 MHz,  $\text{CDCl}_3 + \text{D}_2\text{O}$ )  $\delta$  7.13 – 6.79 (m, 8H, 8 x Ar-H), 4.40 – 4.20, 4.10 (m, t,  $J = 31.8, 13.1, 4.9$  Hz, 4.74 H + 1.73 H, 2 x Ar-CH<sub>2</sub>-Ar and Ar-O-CH<sub>2</sub>-R), 3.50 – 3.25 (m, 4 H, 2 x Ar-CH<sub>2</sub>-Ar), 2.25 – 1.74 (dq, 4 H, Ar-O-CH<sub>2</sub>-CH<sub>2</sub>-R), 1.31 – 0.98 (m, 39 H, 4x t-C(CH<sub>3</sub>)<sub>3</sub> and Ar-O-R-CH<sub>3</sub>).

***p*-tert-butylcalix-[4]-arene mono butyl ester (butylated with dibutyl sulphate):**

$^1\text{H}$  NMR (400 MHz,  $\text{CDCl}_3$ )  $\delta$  10.34 (s, 1.06 H, Ar-OH), 10.19 (s, 0.55 H, Ar-OH ),



9.60 (s, 1.03 H, Ar-OH), 7.84 (s, 0.49H, Ar-OH), 7.12 – 6.79 (m, 8 H, 8 x Ar-H), 4.40 – 3.94 (m, 6 H, 2 x Ar-CH<sub>2</sub>-Ar and Ar-O-CH<sub>2</sub>-R), 3.41 (ddd,  $J = 52.0, 34.8, 13.3$  Hz, 4.08H, 2xAr-CH<sub>2</sub>-Ar), 2.14 – 1.90, 1.71 (m, 2 H, Ar-O-CH<sub>2</sub>-CH<sub>2</sub>-R), 1.71 (ddd,  $J = 22.5, 15.1, 7.6$  Hz, 2 H, Ar-O-CH<sub>2</sub>-CH<sub>2</sub>-CH<sub>2</sub>-R), 1.45 – 0.76 (m, 39 H, Ar-O-R-CH<sub>3</sub> and 4x t-C(CH<sub>3</sub>)<sub>3</sub>).

<sup>13</sup>C NMR (101 MHz, CDCl<sub>3</sub>)  $\delta$  148.42, 147.98, 146.62, 144.32, 143.03, 133.47, 128.29, 128.11, 127.73, 127.64, 126.34, 125.89, 125.64, 125.57, 125.41, 124.98, 77.27, 77.16, 76.96, 76.64, 34.17, 33.96, 33.86, 32.97, 32.57, 32.20, 31.82, 31.65, 31.44, 31.35, 31.20, 31.03, 19.15, 13.95, 0.97, -0.06.

<sup>1</sup>H NMR (400 MHz, CDCl<sub>3</sub>+ D<sub>2</sub>O)  $\delta$  7.13 – 6.75 (m, 8 H, 8 x Ar-H), 4.39 – 3.95 (m, 6.29H, 2 x Ar-CH<sub>2</sub>-Ar and Ar-O-CH<sub>2</sub>-R), 3.55 – 3.27 (m, 4 H, 2xAr-CH<sub>2</sub>-Ar), 2.16 – 1.94 (m, 2 H, Ar-O-CH<sub>2</sub>-CH<sub>2</sub>-R), 1.71 (ddd,  $J = 22.4, 14.9, 7.5$  Hz, 2 H, Ar-O-CH<sub>2</sub>-CH<sub>2</sub>-CH<sub>2</sub>-R), 1.43 – 0.78 (m, 39 H, Ar-O-R-CH<sub>3</sub> and 4 x t-C(CH<sub>3</sub>)<sub>3</sub>).

### 3.5.9.2 Nuclear magnetic resonance data of alkylation products via alkyl iodides

#### ***p*-tert-butylcalix-[4]-arene mono methyl ester (methylated with methyl iodide) :**

<sup>1</sup>H NMR (400 MHz, CDCl<sub>3</sub>)  $\delta$  [ 10.34 (s, 0.55 H), 10.15 (s, 0.94 H), 9.55 (s, 1.50 H) 3 x Ar-OH], 7.14 – 6.69 (m,  $J = 113.1, 54.6, 51.4$  Hz, 8H, 8 X Ar-H), 4.42 – 4.19 (m, 4H, 2 x Ar-CH<sub>2</sub>-Ar), 4.13-3.95 (s, s, 2.33 H + 0.67 H, Ar-O-CH<sub>3</sub>), 3.38 (dd,  $J = 42.3, 13.3$  Hz, 4 H, 2 x Ar-CH<sub>2</sub>-Ar), 1.44 – 0.82 (m, 36 H, t-C(CH<sub>3</sub>)<sub>3</sub>).

<sup>13</sup>C NMR (101 MHz, CDCl<sub>3</sub>)  $\delta$  150.46, 148.33, 147.81, 143.22, 133.43, 132.30, 128.19, 127.91, 126.49, 125.71, 125.66, 125.07, 77.35, 77.03, 76.71, 33.94, 33.01, 32.13, 31.73, 31.49, 31.41, 31.27, 31.02.

<sup>1</sup>H NMR (400 MHz, CDCl<sub>3</sub>+ D<sub>2</sub>O)  $\delta$  7.13 – 6.91 (m, 8 H, 8 x Ar-H), 4.31 (dd,  $J = 35.6, 13.3$  Hz, 9 H, 2 x Ar-CH<sub>2</sub>-Ar), 4.12-3.65 (M, 2.30 H+1.86 H, Ar-O-CH<sub>3</sub>), 3.43 (d,  $J = 13.6$  Hz, 4 H, 2xAr-CH<sub>2</sub>-Ar), 1.28 – 1.12 (m, 36 H, t-C(CH<sub>3</sub>)<sub>3</sub>).

#### ***p*-tert-butylcalix-[4]-arene mono ethyl ester (ethylated with ethyl iodide) :**

<sup>1</sup>H NMR (400 MHz, CDCl<sub>3</sub>)  $\delta$  10.34 (s, 0.54 H, Ar-OH), 10.14 (s, 0.80 H, Ar-OH), 9.55 (s, 1.72 H, Ar-OH), 7.16 – 6.65 (m,  $J = 113.1, 54.6, 51.4$  Hz, 8 H, 8 x Ar-H), 4.46 – 4.17 (m, 4 H, 2 x Ar-CH<sub>2</sub>-Ar), 3.73-3.71(q, 2 H, Ar-O-CH<sub>2</sub>-R) 3.50 – 3.27 (m, 4 H, 2 x Ar-CH<sub>2</sub>-Ar), 1.31 – 0.91 (m, 39.32H, 4 x t-C(CH<sub>3</sub>)<sub>3</sub> and Ar-O-R-CH<sub>3</sub>).

<sup>13</sup>C NMR (151 MHz, CDCl<sub>3</sub>)  $\delta$  150.80, 148.67, 148.63, 148.16, 148.07, 147.19, 143.95, 143.55, 141.87, 133.76, 132.63, 128.54, 128.53, 128.24, 126.83, 126.29,

126.13, 126.05, 126.00, 125.89, 125.41, 77.58, 77.37, 77.16, 63.87, 63.59, 58.85, 34.60, 34.35, 34.28, 34.25, 33.35, 32.97, 32.47, 32.07, 31.83, 31.76, 31.60, 31.36, 18.80, 1.38, 0.36.

$^1\text{H}$  NMR (400 MHz,  $\text{CDCl}_3 + \text{D}_2\text{O}$ )  $\delta$  7.16 – 6.65 (m,  $J = 113.1, 54.6, 51.4$  Hz, 8 H, 8x Ar-H), 4.46 – 4.17 (m, 4 H, 2 x Ar- $\text{CH}_2$ -Ar), 3.73-3.71(q, 2 H, Ar-O- $\text{CH}_2$ -R) 3.50 – 3.27 (m, 4.11H, 2 x Ar- $\text{CH}_2$ -Ar), 1.31 – 0.91 (m, 39 H, 4 x t-C( $\text{CH}_3$ )<sub>3</sub> and Ar-O-R- $\text{CH}_3$ ).

***p*-tert-butylcalix-[4]-arene mono propyl ester (propylated with propyl iodide):**

$^1\text{H}$  NMR (400 MHz,  $\text{CDCl}_3$ )  $\delta$  10.34 (s, 0.23H, Ar-OH), 10.22 (s, 0.79H, Ar-OH), 9.62 (s, 1.58H, Ar-OH), 7.77 (s, 0.39H, Ar-OH), 7.17 – 6.73 (m, 8H, 8xAr-H), 4.40 – 4.06 (m, 6.08H, 2xAr- $\text{CH}_2$ -Ar and Ar-O- $\text{CH}_2$ -R), 3.70 (dd,  $J = 16.7, 10.7$  Hz, 2H, Ar-O- $\text{CH}_2$ - $\text{CH}_2$ -R), 3.50 – 3.26 (m, 4H, 2xAr- $\text{CH}_2$ -Ar), 1.76 -1.32(dt,  $J = 7.1$  Hz, 2 H+1.01 H, Ar-O-R- $\text{CH}_3$ ), 1.43 – 0.85 (m, 36 H, 4x t-C( $\text{CH}_3$ )<sub>3</sub>).

$^{13}\text{C}$  NMR (151 MHz,  $\text{CDCl}_3$ )  $\delta$  151.42, 150.57, 150.05, 149.24, 148.38, 148.12, 147.89, 147.78, 143.55, 143.13, 140.52, 133.66, 133.02, 132.07, 128.25, 128.23, 128.10, 127.87, 126.34, 125.94, 125.73, 125.70, 125.64, 125.47, 125.08, 77.22, 77.01, 76.80, 72.40, 71.91, 58.50, 34.23, 33.98, 33.92, 33.81, 33.02, 32.30, 31.98, 31.68, 31.47, 31.40, 31.26, 31.10, 18.44, 15.27, 1.02.

$^1\text{H}$  NMR (400 MHz,  $\text{CDCl}_3 + \text{D}_2\text{O}$ )  $\delta$  7.01 (m,  $J = 77.5, 38.7, 36.3$  Hz, 8 H, 8 x Ar-H), 4.46 – 4.13 (m, 6 H, 2 x Ar- $\text{CH}_2$ -Ar + Ar-O- $\text{CH}_2$ -R), 4.08-3.62 (m, 1.07 H+0.94 H, Ar-O-R- $\text{CH}_2$ -R), 3.49 – 3.26 (m, 4 H, 2 x Ar- $\text{CH}_2$ -Ar), 1.75-1.62 (dt,  $J = 7.1$  Hz, 2.04 H+1.08 H), 1.33 – 0.98 (m, 36 H, 4 x t-C( $\text{CH}_3$ )<sub>3</sub>).

***p*-tert-butylcalix-[4]-arene mono butyl ester (butylated with butyl iodide):**

$^1\text{H}$  NMR (400 MHz,  $\text{CDCl}_3$ )  $\delta$  10.34 (s, 1.06H, Ar-OH), 10.19 (s, 0.55 H, Ar-OH), 9.60 (s, 1.14 H, Ar-OH), 7.84 (s, 0.49H, Ar-OH), 7.12 – 6.79 (m, 8 H, 8 x Ar-H), 4.39 – 4.21 (m, 4 H, 2 x Ar- $\text{CH}_2$ -Ar), 4.05 (dt,  $J = 13.0, 6.8$  Hz, 2 H, Ar-O- $\text{CH}_2$ -R), 3.41 (ddd,  $J = 52.0, 34.8, 13.3$  Hz, 4.26H, 2xAr- $\text{CH}_2$ -Ar), 2.15 – 1.95 (m, 2 H, Ar-O-R- $\text{CH}_2$ -R), 1.71 (ddd,  $J = 22.5, 15.1, 7.6$  Hz, 2 H, Ar-O-R- $\text{CH}_2$ -R), 1.41 – 0.95 (m, 39 H, Ar-O-R- $\text{CH}_3$  and 4 x t-C( $\text{CH}_3$ )<sub>3</sub>).

$^{13}\text{C}$  NMR (151 MHz,  $\text{CDCl}_3$ )  $\delta$  151.42, 150.57, 150.05, 149.24, 148.38, 148.12, 147.89, 147.78, 143.55, 143.13, 140.52, 133.66, 133.02, 132.07, 128.25, 128.23, 128.10, 127.87, 126.34, 125.94, 125.73, 125.70, 125.64, 125.47, 125.08, 77.22, 77.01, 76.80, 72.40, 71.91, 58.50, 34.23, 33.98, 33.92, 33.81, 33.02, 32.30, 31.98, 31.68, 31.47, 31.40, 31.26, 31.10, 18.44, 15.27, 1.02.

### **3.5.10 Single Crystal Analysis**

Data was collected using an Aligent SuperNova, Dual, Cu, EosS2 diffractometer. The crystals were kept at 100(2) K during data collection. Using Olex<sub>2</sub>, the structures were solved with the ShelXT, ShelXS and Superflip structure solution programs using Intrinsic Phasing and refined with the ShelXL refinement package using least squares minimization. Non-hydrogen atom positions were fully refined using anisotropic thermal parameters and the hydrogen atoms were initially located at idealized positions and then refined using riding coordinates.

**Table 3-16-** Single crystal data for [N<sub>2221</sub>][TBC] and [TMG][TBC].

	[N <sub>2221</sub> ][TBC]		[TMG][TBC]	
Bond precision:	C-C = 0.0052 Å	Wavelength=1.54184	C-C = 0.0074 Å	Wavelength=1.54184
Cell:	a = 15.4381(2) b = 15.9969(2) c = 18.31405(18)		a = 12.0531(3) b = 12.6401(4) c = 35.6963(11)	
	$\alpha = 90^\circ \beta = 90^\circ \gamma = 90^\circ$		$\alpha = 90^\circ \beta = 95.932(3)^\circ \gamma = 90^\circ$	
Temperature:	100 K		115 K	
	Calculated	Reported	Calculated	Reported
Volume	4522.87(9)	4522.86(9)	5409.3(3)	5409.3(3)
Space group	P n a 21	P n a 21	P 21/n	P 21/n
Sum formula	C <sub>51</sub> H <sub>73</sub> N O <sub>4</sub>	C <sub>51</sub> H <sub>73</sub> N O <sub>4</sub>	C <sub>56</sub> H <sub>85</sub> N <sub>7</sub> O <sub>4</sub>	C <sub>56</sub> H <sub>85</sub> N <sub>7</sub> O <sub>4</sub>
Mr	764.1	764.1	920.31	920.3
D <sub>x</sub> , g cm <sup>-3</sup>	1.122	1.122	1.13	1.13
Z	4	4	4	4
$\mu$ (mm <sup>-1</sup> )	0.533	0.533	0.556	0.556
F <sub>000</sub>	1672	1672	2008	2008
F <sub>000</sub> '	1676.4		2013.36	
(h, k, l) <sub>max</sub>	20,20,23	20,19,18	14,15,44	14,15,43
N <sub>ref</sub>	10327[ 5326]	8049	10722	10313

**Table 3-17-** Single crystal data for [N<sub>4441</sub>][TBC] and [Emim][TBC].

	[N <sub>4441</sub> ][TBC]		[Emim][TBC]	
Bond precision:	C-C = 0.0045 Å	C-C = 0.0045 Å	C-C = 0.0062 Å	Wavelength=1.54184
Cell:	a = 15.3846(2) b = 15.7251(2) c = 24.2062(3)		a = 9.32448(15) b = 35.4232(5) c = 13.6749(2)	
	$\alpha = 90^\circ \beta = 105.073(1)^\circ \gamma = 90^\circ$		$\alpha = 90^\circ \beta = 107.9778(17)^\circ \gamma = 90^\circ$	
Temperature:	100 K		100 K	
	Calculated	Reported	Calculated	Reported
Volume	5654.59(13)	5654.59(13)	4296.33(12)	4296.33(12)
Space group	P 21/c	P 21/c	P 21/n	P 1 21/n 1
Sum formula	C <sub>64</sub> H <sub>101</sub> N <sub>3</sub> O <sub>4</sub>	C <sub>64</sub> H <sub>101</sub> N <sub>3</sub> O <sub>4</sub>	C <sub>50</sub> H <sub>65</sub> N <sub>2</sub> O <sub>4</sub>	C <sub>50</sub> H <sub>65</sub> N <sub>2</sub> O <sub>4</sub>
Mr	976.48	976.48	758.04	758.04
Dx, g cm <sup>-3</sup>	1.147	1.147	1.172	1.172
Z	4	4	4	4
$\mu$ (mm <sup>-1</sup> )	0.534	0.534	0.568	0.568
F <sub>000</sub>	2152.0	2152.0	1644	1644
F <sub>000</sub> '	2157.0	2157.0	1648.43	
(h, k, l) <sub>max</sub>	19, 19, 29	19, 19, 29	11,43,16	11,43,16
N <sub>ref</sub>	11152	11152	8542	8262

## 4 Liquid coordination complexes of group 13 chlorometallates

*The Challenge:*

*Can a greater understanding of the speciation within gallium (III) and indium (III) chloride liquid coordination complexes be achieved?*

*Can EXAFS be utilised to gain greater insight into the speciation of such complexes?*

### 4.1 Introduction

#### 4.1.1 Group 13 chlorometallates in molecular solvents

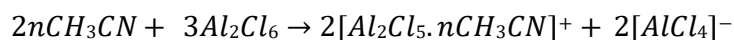
Historically, Gutmann investigated the behaviour of inorganic salts in non-aqueous solvents. He observed the formation of molecular complexes; including neutral adducts, cations and anions along with considerations of dimeric and trimeric species. Such species upon application to catalysis, inorganic synthesis and electrochemistry requires a significant amount of study to determine the species present and their impact on their respective application.

Walton reviewed the formation of non-transition metal halides in acetonitrile in 1965 investigating complex formation of Be, B, Al, Ge and Sn halides with a range of alkyl halides.<sup>301</sup> Walton's review demonstrated the large variety of metal halide that exhibit a wealth of complexes in molecular solvents; these metal halides have been utilised within a variety of catalytic reactions in molecular solvents and understanding of their behaviour is crucial in pinpointing active and detrimental species in these processes. Schmulbach in 1963 studied and identified the presence of three stable complexes within aluminium trichloride;  $\text{AlCl}_3 \cdot \text{MeCN}$ ,  $\text{Al}_2\text{Cl}_6 \cdot \text{MeCN}$ ,  $\text{AlCl}_3(\text{MeCN})_2$  all of which were originally isolated by Perrier *et al.* in the late 19<sup>th</sup> century.

Walton corroborated the presence of  $\text{AlCl}_3 \cdot \text{MeCN}$  and  $\text{AlCl}_3(\text{MeCN})_2$  within the systems, however, it was Walton and co-workers concluded that the  $\text{Al}_2\text{Cl}_6 \cdot \text{MeCN}$  could not be substantiated.<sup>301</sup> Further studies by Popov and Stute supported this theory, indicating that the solvation of  $\text{AlCl}_3$  in acetonitrile was dominated by  $\text{AlCl}_3 \cdot 2\text{CH}_3\text{CN}$  which is suspected to partially dissociate.<sup>302</sup> Schmulbach later postulated using new techniques, the cationic species  $[\text{Al}_2\text{Cl}_5 \cdot n\text{MeCN}]^+$  where  $n=2$ ,

4, 6 with  $[\text{AlCl}_4]^-$  as a counter anion. Equation 4-1 was determined *via* Raman spectroscopy and mass/elemental composition techniques.

Equation 4-1

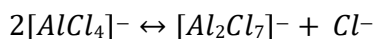


Dalibart *et al.* further noted the formation of penta- and hexa- coordinate species including cations such as  $[\text{Al}(\text{CH}_3\text{CN})_6]^{3+}$ ,  $[\text{AlCl}(\text{CH}_3\text{CN})_5]^{2+}$ , and  $[\text{AlCl}_2(\text{CH}_3\text{CN})_4]^+$ .<sup>303</sup> Fowles *et al.* found that simple 1:1 molecular adducts of  $\text{AlCl}_3$  and  $\text{GaCl}_3$  with trichloroacetonitrile could be prepared and analysed *via* X-ray diffraction techniques and Raman spectroscopy;  $\text{AlCl}_3 \cdot \text{CCl}_3\text{CN}$  and  $\text{GaCl}_3 \cdot \text{CCl}_3\text{CN}$ .<sup>304</sup> Within non-cyano solvents such as THF, DMSO *etc.* expanded coordination is also seen as well as simple 1:1 molecular adducts hence highlighting the amount of complexity that can occur in what is essentially a mix of two compounds.<sup>305</sup>

#### 4.1.2 Group 13 chlorometallate molten salts/ ionic liquids

The first observations of an chloroaluminate ionic liquid was one in which the formation of the ionic liquid/molten salt was not realised.<sup>1</sup> Organic chemists in the mid-19<sup>th</sup> century studying the Friedel-Crafts reaction noticed red coloured oil forming and separating from the reaction mixtures. This 'red oil' was upon later analysis found to be an organic cationic intermediate in the Friedel-Craft's reaction with a heptachloroaluminate counter-anion  $[\text{Al}_2\text{Cl}_7]^-$ . In 1948, Hurley and Weir formed the first chloroaluminate molten salt, a 2:1 mixture of  $\text{AlCl}_3$  and ethylpyridinium bromide.<sup>306,307</sup> This system gained great interest in regards to its use within electrochemistry due to its high metal ion content and notable high Lewis acidity.<sup>308</sup> One of the main drawbacks, however, was the electrochemical window of the ethylpyridinium cation; to overcome this Wilkes *et al.* in 1982 studied a number of alternative organic cations to which they found that 1,3-dialkylimidazolium salts were favourable candidates noting that 1-methyl-3-ethylimidazolium chloride was the best performing cation in regards to the electrochemical window of the systems.<sup>309</sup> The Lewis acidity of these chloroaluminate molten salts or as they are now more commonly termed, ionic liquids became of great interest to Osteryoung *et al.* who determined the heptachloroaluminate anion to be the Lewis acidic species and the dominant equilibrium present to be as described in Equation 4-2.<sup>310–312</sup>

Equation 4-2



The speciation of such molten salts/ionic liquids was confirmed by Seddon *et al.* and Ohno *et al.* in 1986 determining the role of the organic cation and the anionic chloroaluminate species in the system specifically that described in Equation 4-2 by single crystal x-ray diffraction techniques and diffraction of melts respectively.<sup>313,314</sup> Initially there were predictions of oligomeric anionic chloroaluminate species due to the high Lewis acidity observed, specifically  $[Al_3Cl_{10}]^-$  and  $[Al_4Cl_{13}]^-$  species, however, precipitation of  $Al_2Cl_6$  from higher mixtures (*i.e.*  $\chi_{AlCl_3} > 0.67$ ) indicates their instability and lifetime in the IL often resulting in precipitation of  $Al_2Cl_6$ .<sup>315,316</sup> This is described in Figure 4-1; which was determine *via* vapour pressure change of  $AlCl_3$  at various mole fractions of chloroaluminate ionic liquids.

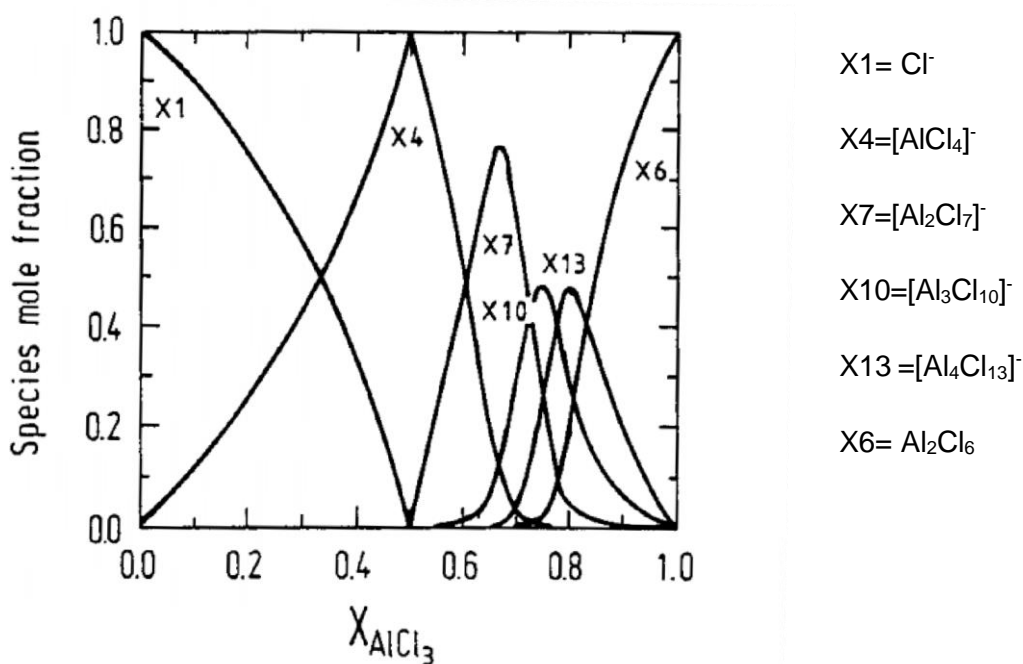


**Figure 4-1**-Plot demonstrating chloroaluminate species present in chloroaluminate ionic liquids by Wilkes *et al.*<sup>317</sup>

Since the discovery of the chloroaluminate salts by Hurley and Weir there was great interest from the U.S. Air Force in regards to applications of such ionic liquids to battery electrolytes. A team led by Wilkes, Carlin and King in the 1960-70s were focused on further studying the chloroaluminate ionic liquids with the addition of alkali metal chlorides such as NaCl and KCl.<sup>318,319</sup>



The development of this research centre led to many collaborations with Osteryoung and Mamantov, who later pioneered in the field of ionic liquid electrochemistry. Osteryoung and co-workers, in collaboration with the U.S. Air Force team synthesised and characterised the first 1-butylpyridinium chloride: aluminium chloride system; termed a low melting chloroaluminate salt (MP = 40 °C) in comparison of the NaCl-AlCl<sub>3</sub> salts initially focused on however, it was found to have inferior electrochemical properties in regards to its susceptibility to reduction.<sup>320</sup>

Charles Hussey and Wilkes collaborated and pioneered in the search for new organic cations for use in chloroaluminate ionic liquids aiming to find cations of greater stability and forming lower melting ionic liquids. Focusing on nitrogen-containing heterocycles in 1981 dialkylimidazolium cations were found to be promising alternatives to the pyridinium cations from a corroboration of current literature and their own knowledge of IL systems.<sup>321,322</sup> Forming a library of dialkylimidazolium chloride and iodides up to [C<sub>4</sub>mim]<sup>+</sup> they found these species were optimal for their applications.<sup>323</sup> Rapidly after discovery there was a deviation from the utilisation of chloroaluminates due to their water and air sensitivity to less sensitive anions such as [BF<sub>4</sub>]<sup>-</sup>, [PF<sub>6</sub>]<sup>-</sup> etc. by Zaworotko and Fuller.<sup>324,325</sup> More recently work by MacFarlane, and Ohno, has led the way towards a wealth of new anions; notable anions include dicyanamide [DCA]<sup>-</sup>,<sup>326</sup> bistriflamide [NTf<sub>2</sub>]<sup>-</sup>,<sup>327</sup> and amino acid-based anions.<sup>18</sup>

During the late 1980's and early 1990's the U.S. Air force collaborated with chemist Kenneth Seddon who became integral in the application of ionic liquids to many industrial processes. Initially, Seddon focused upon the behaviour of other metal salts with chloroaluminate ionic liquids including uranium<sup>328</sup>, molybdenum<sup>329</sup>, and iridium.<sup>330</sup> Later, moving towards the applications of ionic liquids to green chemistry citing his rationale towards this area of research as cited are the favourable non-volatile, non-flammable, liquid range, stability and tuneable properties of ionic liquids.<sup>331</sup> This step-change in the progression of ionic liquids research for battery electrolyte applications to applications in current industrial problems led to development of the Queen's University Ionic Liquids Laboratories, QUILL in 1999. Since 1999, QUILL has pioneered on multiple applications of ionic liquids to industrial processes including mercury removal from natural gas.<sup>332</sup>

Robin Rogers, of the University of Alabama initially studied under Jerry Atwood investigating the structures of haloaluminate liquid clathrates that were found to form ionic liquid type structures at high temperatures.<sup>333</sup> Moving forward with his own

research, Rogers became initially interested in the structure of the alkylaluminate salts such as  $[\text{NMe}_4][\text{AlMe}_3]$ .<sup>1</sup> Rogers later focused his work on integration into green processes such as cellulose processing,<sup>53</sup> extraction of commodity chemicals from mixtures,<sup>334</sup> carbon capture<sup>335</sup> and metal extraction.<sup>336</sup>

Austin Angell continued to develop a greater understanding of chloroaluminate electrochemical behaviours in their liquid and glassy states developing multiple characterisation methods and systems.<sup>337,338</sup> Angell continues to focus on energy storage solutions often utilising chloroaluminate anions.<sup>187,188</sup> Other notable ionic liquid-focused electrochemists include Grätzel and Wantanabe both of whom have focus on development of new ionic liquid-based electrolytes.<sup>341–344</sup> Recent work by the previously mentioned MacFarlane, has more recently has focused upon energy storage and solar cells composed of ionic liquids as electrolytes, conducting polymers and catalyst for water splitting processes.<sup>345,346</sup>

Chloroaluminate ionic liquids in regards to catalysis were initially utilised by Chauvin in nickel catalysed alkene dimerization reactions in the early 1990's and later Wilkes' utilised a similar melt in Ziegler-Natta catalysis.<sup>6,7</sup>

Tom Welton, a student of Seddon, continued to focus upon the application of ionic liquids in catalysis publishing a widely cited review in 1999,<sup>347</sup> and later an update review in which the number of references quoted are 5 times that of the original 1999 review hence demonstrating the popularity of ionic liquid based catalysis.<sup>348</sup> Peter Wasserscheid is one of the main pioneers of ionic liquid based catalysis often integrating Lewis acidic or basic anions in conjunction with transition metal catalysts.<sup>349</sup> Parshall is another pioneer of catalysis within molten salt media which as discussed is the starting point of chlorometallate ionic liquids.<sup>350</sup> An in-depth review in 1972 by Parshall highlighted the wealth of catalysis in molten salts which in a majority of cases is translatable to ionic liquids.

Chloroindate and chlorogallate ionic liquids came into focus in the late 1980's and early 1990's after the success and multiple applications of their chloroaluminate counterparts were realised. Research into chlorogallate ionic liquids is less abundant than chloroaluminates due to their increased costs. However, unlike their chloroaluminate counterparts, chlorogallates are able to form stable oligomeric species up to  $[\text{Ga}_3\text{Cl}_{10}]^-$  as observed by Raman spectroscopy. Furthermore, they are able to form ionic liquids up to  $\chi_{\text{MClx}} = 0.75$ , whereas chloroaluminate form ionic liquids up to  $\chi_{\text{MClx}} = 0.67$ .

First reported in 1987 by Gale, Wicelinski and Wilkes; chlorogallate molten salts formed of 1-methyl-3-ethylimidazolium chloride and gallium (III) chloride were found to be promising alternatives to the widely used chloroaluminate systems.<sup>351</sup> Whilst studies by multiple analytical techniques including electrochemical behaviours, Raman spectroscopy and mass spectroscopic techniques the speciation was fully corroborated by Seddon and co-workers utilising <sup>71</sup>Ga NMR spectroscopy and EXAFS spectroscopy in which a single peak is found at lower  $\chi_{\text{GaCl}_3}$  which later disappears to a broad peak indicating an asymmetric oligomeric species may be present.<sup>351–354</sup> This was indirectly corroborated *via* Gutmann acceptor number in which Lewis acidity increases and was monitored by an NMR probe triethylphosphine oxide.<sup>355</sup>

The speciation as shown in Table 4-1 highlights in formation of the Lewis acidic species at  $\chi_{\text{GaCl}_3} > 0.50$ . Such species have been found to be useful in regards to Lewis acid catalysis; specific applications includes applications to Baeyer–Villiger oxidations of the cyclic ketone 2-adamantanone,<sup>356</sup> oligomerisation of 1-decene,<sup>357</sup> formylation of toluene<sup>358</sup> and alkylation of isobutene/butene.<sup>359</sup> A thorough understanding of the speciation along with the chemical and physical properties as consequence provides a greater understanding of their use within catalytic applications.

**Table 4-1**-Speciation observed in chlorogallate ionic liquids.<sup>351,352,354,360,361</sup>

$\chi_{\text{GaCl}_3}$	Lewis acidity	Speciation
0.25	↓	$3[\text{cat}]\text{Cl} + \text{GaCl}_3 \rightarrow [\text{cat}][\text{GaCl}_4] + 2[\text{cat}]\text{Cl}$
0.50		$[\text{cat}]\text{Cl} + \text{GaCl}_3 \rightarrow [\text{cat}][\text{GaCl}_4]$
0.67		$[\text{cat}]\text{Cl} + 2\text{GaCl}_3 \rightarrow [\text{cat}][\text{Ga}_2\text{Cl}_7]$
0.75		Undetermined speciation <sup>362</sup> Species reported present include: [cat][GaCl <sub>4</sub> ] , [cat][Ga <sub>2</sub> Cl <sub>7</sub> ] and [cat][Ga <sub>3</sub> Cl <sub>10</sub> ]

Chlorogallates were demonstrated to be effective electrolytes for the electrodeposition of gallium thin films; Srinivasan *et al.* demonstrated that NaCl buffered systems of [C<sub>8</sub>mim][GaCl<sub>4</sub>] and [C<sub>8</sub>mim][Ga<sub>2</sub>Cl<sub>7</sub>] were lower in acidity and were able to provide uniform films of gallium on glossy carbon.<sup>363</sup> Endres and co-workers used GaCl<sub>3</sub> in conjunction with 1-Butyl-1-methylpyrrolidinium bis(trifluoromethylsulfonyl)- amide, [C<sub>1</sub>C<sub>4</sub>Py][NTf<sub>2</sub>] to form Ga(0) thin films on gold

substrates.<sup>364</sup> Zhang *et al.* also utilised GaCl<sub>3</sub> in conjunction with 1-butyl-3-methylimidazolium trifluoromethanesulfonate, [C<sub>4</sub>mim][OTf] to study the nucleation and diffusion properties of Ga(0) nanoparticles.<sup>365</sup>

Chloroindates were first discovered in 1994 by Carpenter and Verbrugge upon mixing of 1-methyl-3-ethylimidazolium chloride and indium(III) chloride analogous to that of the chloroaluminates by Wilkes.<sup>309,366</sup> Originally it was thought that the chloroindate systems would follow the speciation trends of the chloroaluminates and chlorogallates in that oligomeric species such as [In<sub>2</sub>Cl<sub>7</sub>]<sup>-</sup> would be present; hence initial applications of such ILs were utilising  $\chi_{\text{InCl}_3} = 0.67$  ILs.<sup>367,368</sup> Just as aluminium chloride precipitates in chloroaluminate ionic liquids when  $\chi_{\text{AlCl}_3} > 0.67$  indium(III) chloride precipitates from when  $\chi_{\text{InCl}_3} > 0.50$ . This indicates the anion [In<sub>2</sub>Cl<sub>7</sub>]<sup>-</sup> is not formed; this was indirectly confirmed *via* the Lewis acidity trends and EXAFS spectroscopy.<sup>355</sup> Yang *et al.* postulated that [InCl<sub>5</sub>]<sup>-</sup> and [InCl<sub>6</sub>]<sup>-</sup> may be present, however, which was not detected in the IL *via* EXAFS spectroscopic analysis.<sup>354,369</sup> In regards to the Lewis acidity trends observed in catalytic systems the moderate increase in activity  $\chi_{\text{InCl}_3} > 0.50$  was originally believed to be due to the oligomeric Lewis acidic species [In<sub>2</sub>Cl<sub>7</sub>]<sup>-</sup>. Estager and co-workers determined that the liquid phase does not increase in acidity when  $\chi_{\text{InCl}_3} > 0.50$  and thus increase in the catalytic activity of these turbid solutions is due to the precipitated InCl<sub>3</sub>.

Later, Hardacre and co-workers determined that the predicted anions [InCl<sub>5</sub>]<sup>2-</sup> and [InCl<sub>6</sub>]<sup>3-</sup> existed in the equilibria demonstrated in Equation 4-3.<sup>370</sup> This was determined *via* an (incongruent) melting point at 72.7 °C in the  $\chi_{\text{InCl}_3} = 0.25$  indicating [InCl<sub>6</sub>]<sup>3-</sup> and another melting point at 45 °C in  $\chi_{\text{InCl}_3} = 0.33$  indicating [InCl<sub>5</sub>]<sup>2-</sup> is present. Speciation was further confirmed *via* Raman spectroscopy and <sup>115</sup>In NMR spectroscopy.

#### Equation 4-3



Chloroindates and chlorogallates specifically [C<sub>4</sub>mim][MCl<sub>4</sub>] were found to be efficient catalysts in acetylation of benzaldehyde as shown in Figure 4-2 with yields of 70 % and 81 % respectively.<sup>371</sup> Mannich type reactions have also been found to be catalysed by [C<sub>4</sub>mim][BF<sub>4</sub>] and InCl<sub>3</sub> in combination by Chen *et al.*<sup>372</sup>

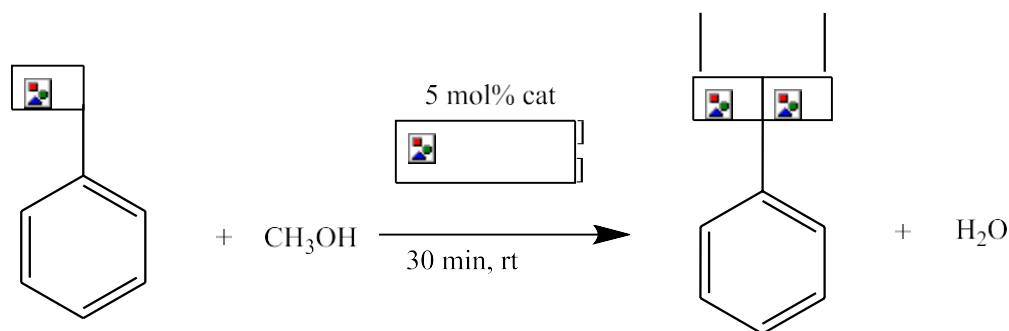


**Figure 4-2-** Acetylation of benzaldehyde with chlorogallate and chloroindate ionic liquids.

Estager *et al.* again utilised these high indium concentration liquids to attempt to form indium thin films however, the films did not form as expected instead resulting in the formation of indium (0) nanoparticles due to the disproportionation of the In(I) species to In(0) during the electrochemical reduction.<sup>373</sup> This methodology avoids the use of inorganic reducing agents such as  $\text{NaBH}_4$  and allows for simple extraction of the nanoparticles synthesised *via* simple washing with methanol.

Utilisation of such high metal containing liquids such as chloroindate ionic liquids is of great interest in regards to synthesis of indium containing functional materials for solar cell applications such as copper indium sulphide (CIS), copper indium selenide (CISe), copper indium gallium sulphide (CIGS) and copper indium gallium selenide (CIGSe). This has been demonstrated by Nockemann and co-workers who utilised chloroindate ionic liquids to form microcrystalline indium (III) selenide *via* a microwave-assisted reaction.<sup>374</sup>

### 4.1.3 Group 13 chlorometallate liquid coordination complexes

Liquid coordination complexes were first termed in 2013 by Coleman *et al.* who described them as liquids of very high metal concentrations formed from the heterolytic cleavage of metal halides in the presence of a donor ligand.<sup>22</sup> The first systems to be studied were chloroaluminates due to their as mentioned array of catalytic applications and chlorogallates, though their speciation was largely determined by analogy to chloroaluminates. Donor ligands were limited to donors with lone pairs situated on O-, N-, S- and P- atoms. Coleman utilised molar ratio,  $\chi_{\text{MCl}_x}$  as the main method of nomenclature of these systems with initially LCCs only described as LCC at  $\chi_{\text{MCl}_x} \geq 0.50$ , however, this has since been nullified.<sup>375</sup>

**Table 4-2-** The dynamic equilibrium exhibited by LCCs in comparison to ILs as deduced by spectroscopic studies.<sup>22</sup>

	LCC	IL
$\chi_{\text{MCl}_3}$	$2\text{MCl}_3 + 2\text{L}$	$\text{MCl}_3 + [\text{cation}]\text{Cl}$
0.5	$[\text{MCl}_2\text{L}_2][\text{MCl}_4] \rightleftharpoons 2[\text{MCl}_3\text{L}]$	$[\text{cation}][\text{MCl}_4]$
	$\downarrow +\text{MCl}_3$	$\downarrow +\text{MCl}_3$
0.6	$[\text{MCl}_2\text{L}_2][\text{M}_2\text{Cl}_7] \rightleftharpoons [\text{MCl}_3\text{L}] + [\text{M}_2\text{Cl}_6\text{L}]$	
	$\downarrow +\text{MCl}_3$	$\downarrow$
0.67	$[\text{MCl}_2\text{L}_2][\text{M}_3\text{Cl}_{10}] \rightleftharpoons 2[\text{M}_2\text{Cl}_6\text{L}]$	$[\text{cation}][\text{M}_2\text{Cl}_7]$

More recently liquid coordination complexes (LCCs) haven been termed eutectic mixtures of metal halides and organic donor molecules, typically liquid at ambient temperatures.<sup>22,376</sup> They have emerged as less expensive alternatives to ionic liquids and in recent years have been extensively studied as electrolytes and Lewis acidic catalysts.<sup>357,8,362,377,339</sup>

Initially Abbott and co-workers reported liquid mixtures of urea/amides and  $\text{AlCl}_3$ , postulating that they form ionic liquids, expanding upon this work Coleman *et al.* later determined the speciation of these eutectics formed by  $\text{AlCl}_3$  or  $\text{GaCl}_3$  with a range of donors (urea, thiourea, acetamide, phosphine oxide, or phosphine) to contain equilibrated cationic, anionic and neutral coordination complexes of the corresponding metal chlorides.<sup>22,376</sup> Fundamental studies into speciation of LCCs have also been of interest with the main focus on systems based on aluminium chloride; our group also worked with LCCs of gallium(III) chloride.<sup>22</sup>

Krossing and co-workers studied a range of aluminium halides coupled with 1-butylimidazole with varying  $\chi_{\text{AlX}_3}$  of these aluminium LCCs was in general it was shown to contain a mixture of cationic, anionic and neutral coordination complexes, in a dynamic equilibrium with each other. Krossing found that at low  $\chi_{\text{AlX}_3}$  ( $> 0.50$ ) the ionic  $[\text{AlL}_4\text{Cl}_2]\text{Cl}$  species dominated whereas higher chi values ( $\chi_{\text{AlX}_3} > 0.50$ ) tend to form neutral and ionic species that are oligomeric in nature such as  $[\text{Al}_2\text{Cl}_6\text{L}]$  and  $[\text{Al}_2\text{Cl}_7]^-$ . This demonstrated the importance in which the donicity of the ligand vs the strength of the M-X bond is decisive in determining the speciation present. Specifically, in aluminium systems the speciation has been integral in determining the electrodeposition character; Legrande *et al.* observed a change in speciation with temperature of dialkylsulfones- $\text{AlCl}_3$  as determined by  $^{27}\text{Al}$  NMR spectroscopy

and further noted that with temperature aluminium depositions changed in morphology and coulombic efficiency.<sup>305,378,379</sup> Nakayama observed that  $[\text{Al}_2\text{Cl}_7]^-$  is the active species in sulfone based Al electrolytes and conductivities vary as a function of  $\text{AlX}_3$ .<sup>380</sup>

Significant work by Hogg elucidated the speciation of  $\text{P}_{888}\text{E}-\text{AlCl}_3$  systems in great detail. Utilising a combination of NMR, Raman, IR spectroscopic techniques along with analysis of the physicochemical properties of the systems determined that the initially determined speciation equilibrium put forward by Coleman *et al.* was correct, however, the bias towards the neutral species could be more significant than initially thought depending on the donor atom and the metal halide source. The explanation for the effect of the donor atom on the speciation put forward by Hogg *et al.* is based upon the behaviour of diborane complexes.<sup>381</sup>

In the reactions of  $\text{BH}_3\cdot\text{THF}$  with ammonia it results in the formation of the  $\text{BH}_3\cdot\text{NH}_3$  adduct, which further reacts with another  $\text{BH}_3\cdot\text{THF}$  species, to form a dimeric intermediate and expelling a THF molecule. The intermediate consists of a B-H-B motif that Hogg postulates is the equivalent of the M-Cl-M species such that the cleavage of this bridge is dependent on which of the boron centres is attacked by the ligand present in solution ( $\text{NH}_3$ ). As shown in Figure 4-3 attack at B2 results in the homolytic cleavage and a neutral adducts forming ( $\text{BH}_3\text{NH}_3$ ); cleavage at B1, however, results in a heterolytic cleavage hence forming an ionic species ( $[\text{BH}_2(\text{NH}_2)_2][\text{BH}_4]$ ).

The cleavage that occurs is dependent on several factors including the concentration of the  $\text{BH}_3\cdot\text{THF}$  vs concentration of ligand ( $\text{NH}_3$ ) and the stability of the cleavage product specifically in regards to the ionic species as it was found to have an energy cost greater than the neutral species that was lowered *via*  $\delta$ hydrogen bonding effects making the pathways more comparable. It is crucial that the dimeric species is formed in this process if any ionic species later is found to be present in solution. The adduct species unlike the ionic can form regardless of the dimer formation.

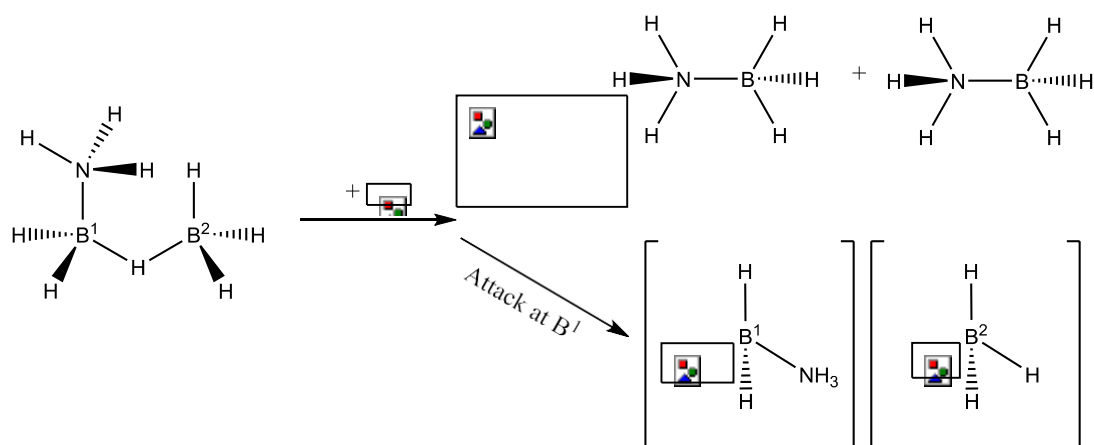


**Figure 4-3-**Homolytic and heterolytic cleavage of ammonia diborane complexes.<sup>382</sup>

Hogg<sup>382</sup> found comparisons of the  $\text{BH}_3$  system to that of  $\text{AlCl}_3$  and THF systems referencing work by Derouault<sup>383</sup> and Atwood<sup>384</sup> who, when reacting  $\text{AlCl}_3$  with THF, both reported the formation of the ionic product,  $[\text{AlCl}_2\text{THF}_4][\text{AlCl}_4]$ . Conversely, Cowley found the molecular species,  $[\text{AlCl}_3\text{THF}_2]$ .<sup>385</sup> What appear to be comparable systems at face value are differentiated by their starting material in which Derouault and Atwood used neat  $\text{AlCl}_3$  and Cowley used  $(\text{Me}_2\text{N})_3\text{SiCl}\cdot\text{AlCl}_3$ . By using the  $(\text{Me}_2\text{N})_3\text{SiCl}\cdot\text{AlCl}_3$  precursor rather than the  $\text{Al}_2\text{Cl}_6$  dimer, the formation of the dimeric intermediate is prevented and hence no opportunity for heterolytic cleavage occurs.

As mentioned, the LCCs previously reported have shown that there is different speciation with differing ligand species that are of comparable sterics, hence indicating that donor strength is an important factor in determining the species present. Hogg again referred to literature to gain greater understanding of such systems quoting a study by Gandon *et al.*<sup>386</sup> in which the behaviours of  $\text{GaX}_3$  ( $\text{X} = \text{Cl}, \text{Br}, \text{I}$ ) and N-heterocyclic carbene bases were monitored. Gandon found that bases of differing strengths resulted in the formation different natured products.

The nature of the donor ligand and the cleavage observed was concluded to be that a stronger donor promotes heterolytic cleavage as it is able to attack the  $\text{Ga}^1$  position as the bridging  $\text{Ga}^1\text{-Cl}$  bond is weakened by the initial  $\text{Ga}^1\text{-L}$  bond hence causing heterolytic cleavage. In weak ligand systems the initial  $\text{Ga}^1\text{-L}$  bond formed does not weaken the bridging  $\text{Ga}^1\text{-Cl}$  bond hence the second donor ligand attacks the  $\text{Ga}^2$  centre as the LUMO moves to the other gallium causing a homolytic cleavage. The use of stronger donor ligands means that the initial  $\text{Ga}^1\text{-L}$  bond formed does significantly weakens the bridging  $\text{Ga}^1\text{-Cl}$  bond hence the second donor ligand attacks the  $\text{Ga}^1$  centre as the LUMO remains on  $\text{Ga}^1$ . In regards to the  $\text{P}_{888}\text{E}$



species the trend follows;  $P_{888}O$  ligands are stronger/harder and the ionic contribution is greater than that of  $P_{888}S$  and  $P_{888}Se$ , softer donors. Hogg found that the stronger donor species such as  $P_{888}O$  had a greater prevalence of ionic species in  $AlCl_3$  LCCs than the softer  $P_{888}Se$ .

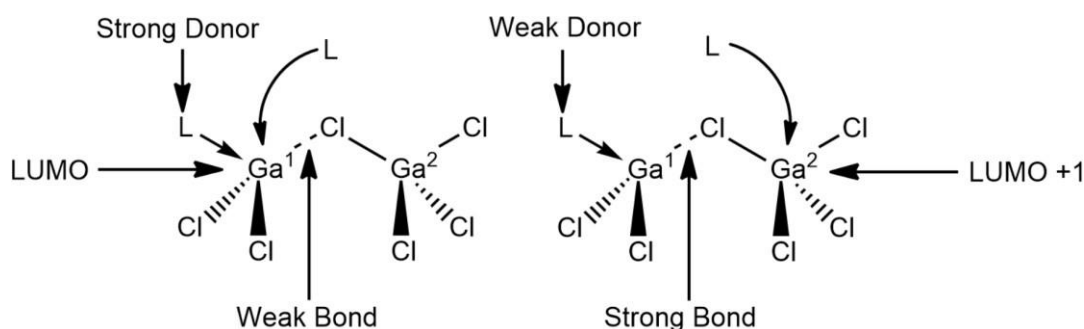


**Figure 4-4-** Pictorial representation of  $Ga^1-Cl$  bond strength as a function of L donor strength in  $L-GaCl_2-(\mu Cl)-GaCl_3$ bu Hogg.<sup>382</sup>

Hogg and co-workers further studied the behaviours of multiple chlorometallates with  $P_{888}$  and  $P_{888}O$  donor ligands.<sup>387</sup> Investigating  $AlCl_3$ ,  $GaCl_3$ ,  $InCl_3$ ,  $SbCl_3$ ,  $SnCl_2$ ,  $SnCl_4$ ,  $TiCl_4$  and  $ZnCl_2$  via multinuclear NMR techniques including quantification of Lewis acidity using the Gutmann acceptor number method. Key findings included redox occurring in the  $SnCl_4$  and  $SbCl_3$  systems,  $P_{888}$ ,  $P_{888}O-AlCl_3$ ,  $P_{888}O-GaCl_3$ , formed both neutral adducts and ionic species with  $P_{888}$  and  $P_{888}O$ ,  $InCl_3$ ,  $ZnCl_2$  and  $TiCl_4$  formed neutral adducts.

A recent review by Rogers and co-workers provided a detailed insight into the vast array of applications for these Lewis acidic liquids; demonstrating that chloroaluminates, chlorogallates and chloroindates have significant impact upon many catalytic processes hence any form in which such anions can be suspended in good purity, predictability and with relative ease is naturally an encouraged development within the field.<sup>360</sup> Examples of current applications include:

- Alkylations of benzene with 1-decene<sup>377</sup> ( $P_{888}O-GaCl_3$ , Urea-  $GaCl_3$ , DMA-  $GaCl_3$ )
- Conversion of 1-decene to C20 product<sup>357</sup> ( $P_{888}O-MCl_3$ ,  $P_{888}-MCl_3$ , Ur-  $MCl_3$ , AcA-  $MCl_3$ , SUr-  $MCl_3$ ,  $P_{888}O-MCl_3$ ,  $C_7CN-MCl_3$  where  $M=Ga / Al$ )
- Diels–Alder reaction of cyclopentadiene and ethyl acrylate<sup>387</sup> ( $P_{888}O-MCl_x$   $M=Ti / Sn / Al / Ga / In / Sb / Zn$ )
- Isobutane butane alkylations for high octane gasoline.<sup>8</sup> ( $AcA-AlCl_3$ )

Whilst the field of LCCs catalysis is forming, their use in materials synthesis is yet to be investigated. Similar to Ionic Liquids, LCCs have a high metal content but also possess potential advantages over the former such as:

- No spectator cations
- Intrinsic capping agent
- Cations, anions and neutral species are precursor containing
- Low volatility hence high reaction temperatures can be reached.

Previous success with ionic liquids could be replicated if not improved *via* the use of LCCs as donor ligands such as P<sub>888</sub> and P<sub>888</sub>O are typical capping agents in a majority of semiconductor nanoparticle syntheses.

#### 4.1.4 Experimental techniques for speciation elucidation

As demonstrated in the previous chapter the complexity and determination of the speciation of these solutions is difficult and requires a multitude of spectroscopic techniques. Using a multipronged approach to determine the speciation of such complex solutions it is aimed to gain a greater understanding of both, the techniques used and the information they can provide, along with the speciation of the system itself. In regards to the physiochemical properties density, viscosity and conductivity of solutions will be investigated hence giving insight into complex size with different ligands and  $\chi_{\text{MCl}_3}$  values. Spectroscopic techniques including multinuclear NMR, infrared, Raman spectroscopy are the affectionately termed bread-and-butter spectroscopic techniques for the characterisation of inorganic compounds.

Extended X-ray Absorption Fine Structure Spectroscopy, EXAFS is a powerful spectroscopic technique that has been proven to be a useful tool in further confirming speciation trends in chlorometallate ionic liquids.<sup>354</sup> The technique itself is based upon the excitation of a core shell electron of an absorber atom; this excitation energy is unique to the central atom under investigation. Upon excitation a photoelectron is ejected from the atom and the interactions within the atom and its neighbours are observable as a function of energy and transmission/fluorescence hence providing information about the oxidation state, geometry and local environment of the atom under investigation. Elucidation of this information from the raw spectra can be difficult and in the next few pages aim to give a brief overview of this technique from a chemist's perspective and a practical approach to data analysis.<sup>388</sup>

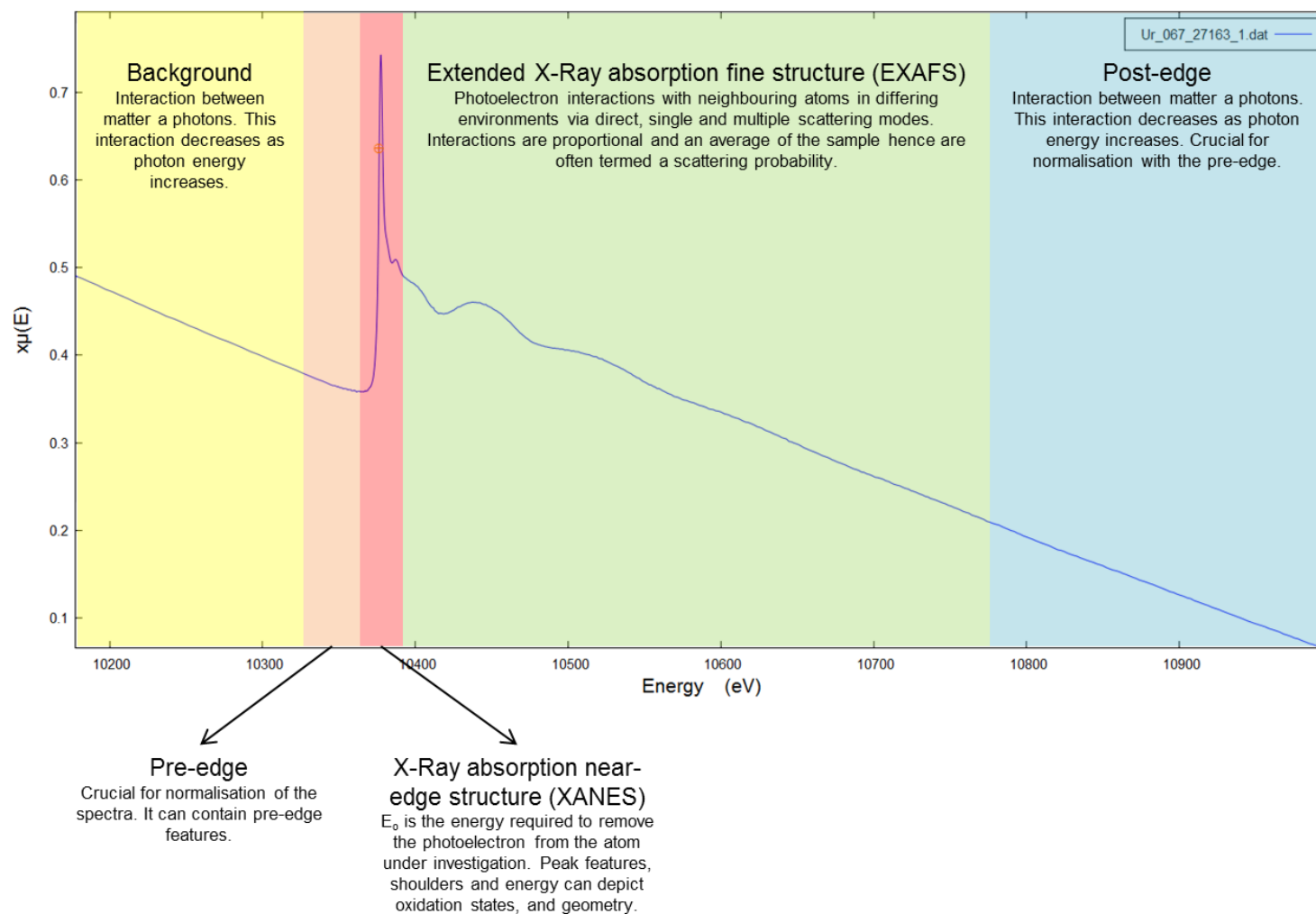


**Figure 4-5-** Diagram showing a typical EXAFS spectrum.

#### 4.1.4.1 The fundamentals of EXAFS

An EXAFS experiment and resultant spectrum is consisted of five main features as shown in Figure 4-5:

- (1) **Background**-The background of each spectrum generally defines the interaction between the photon beam and matter. In general absorption increases with increasing photon energy this is due to photoelectric absorption which is defined in Equation 4-4. The linear absorption coefficient,  $\mu$  depends on many factors including energy, density, atomic number and atomic mass as defined by Pascarelli in Equation 4-5.

Equation 4-4

$$\mu(E)t = -\ln\left(\frac{I}{I_0}\right)$$

$\mu(E)$  = Linear absorption coefficient at energy E  
t = Sample thickness  
 $I_0$  = Intensity of incident photons  
I = Intensity of transmitted photons

Equation 4-5

$$\mu \approx \frac{\rho Z^4}{AE^3}$$

E = Photon energy  
Z = Atomic number  
 $\rho$  = density  
A = Atomic mass

- (2) **Pre-edge** –This in general a relatively featureless part of the spectrum and is majorly utilised in the determination of the pre-edge line in data processing for normalisation. However, there are cases in which a pre-edge feature may be observed such as multiple oxidation states of the element under study causing what appear to be multiple edges. An example by Radovanovic *et al.* is shown in Figure 4-7; this example clearly demonstrates the significant effect changes in oxidation state can have on the spectra achieved i.e. the position of the edge changes hence pre-edges can also change.<sup>389</sup>

The pre-edge feature is also affected by dipolar selection rules and electronic transitions into empty bound states resulting in bumps in the spectra. Dipolar selection rules or the 'Laporte rule' applies to centrosymmetric molecules in that they contain an inversion centre. The

Laporte rule states that like to like orbital transitions are forbidden e.g.  $g \rightarrow g$  and  $u \rightarrow u$ . ( $g$  = gerade,  $u$  = ungerade)<sup>390,[1]</sup>

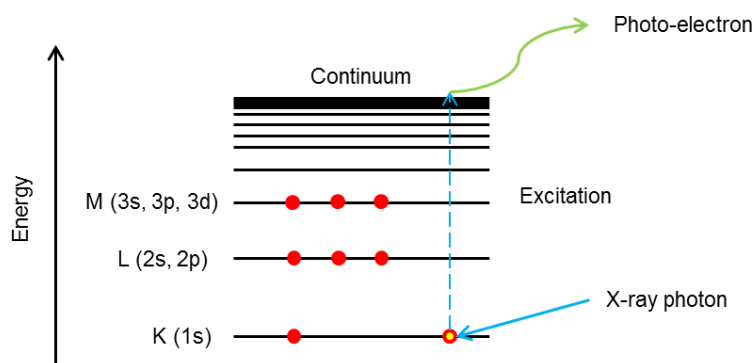


Figure 4-6- Generation of a photo-electron in EXAFS spectroscopy.

(3)  **$E_0$  / Edge / XANES-**  $E_0$  is the energy at which the photoelectric effect occurs; this excitation results in a sudden increase in intensity as shown in Figure 4-5. The photoelectric effect is the absorption of an x-ray photon by an atom at which a core level electron (either at k, l or m shell) is ejected from the atoms to the continuum to form a photoelectron as shown in Figure 4-6. This is somewhat analogous to an ionisation. However, it is a core electron that is ejected not a valance electron; it should be further noted that any excess energy from the photons are transferred to the photoelectron. As mentioned the electrons ejected can come from the k, l or m levels these are commonly referred to in regards to edges as the k, l or m - edges. K-edges are most commonly utilised.

**XANES** X-ray absorption near edge structure as shown in Figure 4-5 is the spectra immediately after the edge and is measures with low energy photo-electrons. This area of the spectra allows for not only charge to be determined but also the geometry of the local coordination environment *i.e.* specific pre-edges indicate specific geometries and the position of the edge determines the oxidation state (EXAFS extends beyond the neighbouring atom and is mainly analysed *via* single scattering contributions, high energy photo-electrons). Bastion *et al.* was the first to correlate the XANES measurement to a concept termed coordination charge in 1967.<sup>391</sup> This concept encompasses the oxidation state of inorganic halide salts, consequent changes in bond strength and coordination. Since this correlation a significant number of studies have utilised it to determine

<sup>1</sup> Gerade and ungerade refer to symmetry operations of the molecular orbitals of atoms. Gerade refers to a change in parity upon inversion and ungerade results in no change in parity with inversion.

structures within amorphous materials, inorganic complexes and glasses.<sup>392–</sup>

394

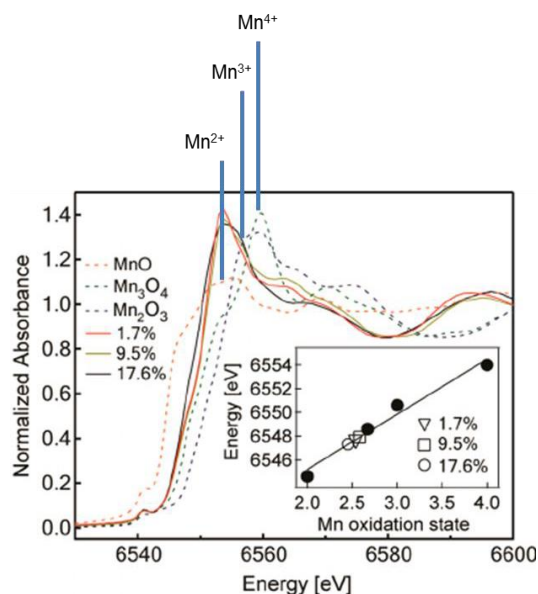


**Figure 4-7-** Reproduced and annotated EXAFS spectra of mixed oxidation state manganese oxide doped materials.<sup>389</sup>

**(4) Extended X-ray Absorption Fine Structure, EXAFS;** this is the most information packed aspect of the spectra. After the excitation and generation of the photo-electron as shown in Figure 4-6 it interacts with atoms in its local environment as shown Figure 4-8. The photo-electron generated here is higher in energy than in the XANES analysis; any energy exceeding that of the excitation is converted to kinetic energy of the photo-electron which in turn affects the wavelength and frequency of the photo-electron.

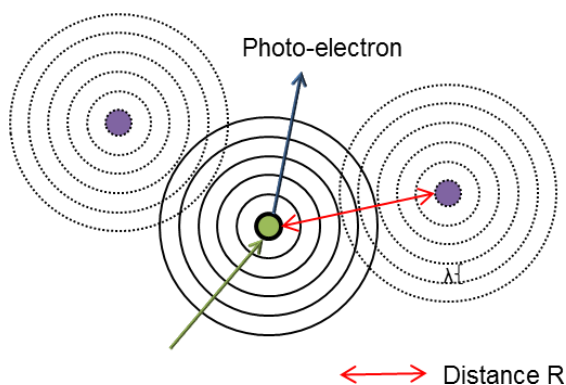


**Figure 4-8-**EXAFS single scattering in condensed matter.

The relationship between wavelength, velocity and frequency is described in Equation 4-6. Applying this to the photo-electron it must be considered as to

how the influence of kinetic energy can have upon these characteristic features of the photoelectron as shown in Equation 4-7.

Equation 4-6

$$\lambda = \frac{v}{f}$$

$\lambda$ =wavelength

$v$ = velocity

$f$ =frequency

Equation 4-7

$$E_{kinetic} = E - E_0 = \frac{p^2}{2m} = \frac{\hbar^2 k^2}{2m} \quad \text{Where} \quad \lambda = \frac{2\pi}{k}$$

$E$ = Photon energy

$E_0$ = Edge energy

$p$ = momentum of the photo-electron

$m$ =mass of electron

$\hbar$ =reduced Planck's constant

$K$ =wavenumber

Once the photoelectron has gained its edge energy,  $E_0$  it gains kinetic energy and scatters elastically with the neighbouring atoms. The distance and nature of these neighbouring atoms causes a scattering and consequent oscillation in the resultant  $E$  signal. There are multiple factors which affect the multitude of interactions that occur as described in the overarching EXAFS equation, Equation 4-8, such that it has been broken down into its key features to allow for a chemist's interpretation.

Equation 4-8

Scattering intensity and distance factor			Photo-electron scattering	
Number of scattering atoms			Disorder term, $\sigma^2$ Debye-Waller factor	
Sum of scattering atoms				
$\chi(k) = S_0^2 \sum_i N_i \frac{f_i(k)}{k D_i^2} e^{-\frac{2D_i}{\lambda(k)}} e^{-2k^2 \sigma_i^2} \sin(2kD_i + \delta_i(k))$				
Amplitude reduction term			Interference factor	

*Amplitude reduction term,  $S^2_0$*  is a factor that identifies intrinsic losses due to the de-excitation processes in which the electron hole formed during excitation and photo-electron generation is not compensated hence initial and final quantum states are non-identical. Commonly, this factor should equal one; failure to do so indicate the model is invalid or there is an error or distortion in the spectra collected.

*Sum of scattering atoms,  $\Sigma$*  highlights that EXAFS is an average of the local environments of the absorber atoms hence multiple crystallographic models and paths are required for a true EXAFS fit. Hence different bonding modes and path can be quantified and differentiated within a single system as the spectrum achieved is an overall average of the atom of interest.

*Number of scattering atoms or degeneracy  $N_i$*  indicates that correlations the amplitude and no of scattering atoms can be determined. It is effectively the coordination number of the absorbing atom such that the sum of all  $N_i$  must be a reasonable approximation of the total coordination number of said element.

*Scattering intensity and distance factor;  $f(k)$*  is a crucial component of the EXAFS equation and defines the scattering probability. It is a proportionality constant that is also proportional to the probability of elastic scattering of neighbouring atoms. The photo-electron itself does not behave as a plane wave but a spherical wave that due to its isotropic spread the scattering probability falls as a function of the square of the distance,  $D$ . Spherical waves can be visualised as a buoy causing ripples on the water's surface. The  $f(k)$  can be greatly impacted by phase shift and consequent interference hence it is often determined by modern IFEFFIT/FEFF codes.<sup>395</sup>

*Photo-electron scattering;* the key aspect to this contribution is the mean free path,  $\lambda$  this term defines the behaviours of the photoelectron that is not due to elastic scattering. Inelastic scatter such that the energy is lost by the photon results in a change in the wavelength /frequency of the photo-electron. This change in parameters can affect multiple aspects of the signal including interferences, suppression of the main EXAFS signal and generation of an Auger electron. This parameter determines that distant scattering ( $<10 \text{ \AA}$ ) at which these scenarios are most probable is negligible.



*Disorder term,  $\sigma^2$* ; This factor is also termed the Debye-Waller factor and corresponds to the variation in D, the distance from the absorbing atom and scattering atom due to disorder. This is in general higher in more disordered systems such as liquids and those in which a heat source is applied. Disorder causes noisy spectra hence extraction of fine structural information becomes more difficult especially as energy increases away from the edge. A common experimental technique to reduce this disorder is simply *via* cooling the sample.

*Interference factor*; The  $\delta(k)$  term relates to the change in phase of the photo-electron. This specifically refers a photo-electron as it approaches a scattering atom; upon approach it enters a potential well causing an acceleration which can cause a shift in phase. As discussed EXAFS is an interference effect; the wavenumber, K is a useful term in which to observe the interactions hence the EXAFS spectra undergoes Fourier transform to K space in which the oscillations can be amplified to the power of 2 and 3 most commonly.

- (5) Post edge**; similarly, to the pre edge the post edge is determined by photon and matter interactions. The post-edge is defined as the aspect of the spectra in which oscillations of the EXAFS are no longer distinguishable as shown in Figure 4-5. This post-edge is also used in alignment; subtractions of background and consequent normalisation of the EXAFS spectra. All of these functions and signal processing are completed using the Athena program from the Demeter Software package; this will be discussed further in future.

**EXAFS and R-space**; As aforementioned the EXAFS signal elucidates the number of and type of neighbouring atoms along with their distance from the atom investigated. Fourier transform of this signal into R space provides a photo-electron scattering profile in respect to the distance from the absorber R. This profile is analogous to a radial distribution function within QM.

**The EXAFS experiments.** The air sensitive nature of the samples in this work required the sample holders to be air tight. The most commonly used stainless steel sample holders are also unsuitable due to the high acidity and corrosive nature of the samples. Within this work sample holders were fastened from Kapton foil/tape and a polycarbomer spacer such that the thickness of the central window was variable as shown in Figure 4-9. Solid samples were pressed into pellets with boron

nitride. All samples were prepared under glovebox conditions and were position on a PEEK auto sampler. Each sample was measured 3 times hence any degradation of the sample in beam could be monitored. Samples can be measured in transmission or fluorescence.

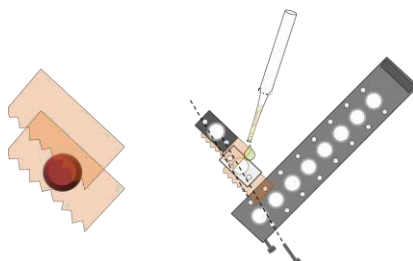


**Figure 4-9-** EXAFS sample holders (left) thin liquid samples sandwiched between Kapton tape with a 1mm polycarbomer spacer (right) solid pellet sealed with Kapton tape.

#### 4.1.4.2 Signal processing and the fitting process

**EXAFS interpretation and the Demeter software package;** Bruce Ravel a pioneer of XAS data interpretation developed a series of graphical programs that utilises IFEFFIT code to facilitate EXAFS analysis. The package consists of three key programs; Artemis, Athena and Hephaestus. Athena is a GUI interface for the IFEFFIT library (see scattering intensity and distance factor,  $f(k)$ ) and utilises Gnuplot for data plotting.<sup>395–397</sup> The main function of the Athena software is the processing and plotting of EXAFS data in preparation for fitting and analysis. Artemis is also a GUI interface with an integrated toolkit for EXAFS data fitting; it utilises IFEFFIT and Larch to complete FEFF fits of paths to spectra.<sup>398</sup> Hephaestus is a toolkit for experimentalists containing useful physical data for EXAFS measurements.

#### 4.1.4.3 The fitting process

The fitting process is summarised in Figure 4-10. There are three main aspects to the fitting process; preparation and processing of raw data (Athena), determination of the species to be fitted and sourcing suitable structures in which the fit can be based and completing the fit. The fitting process itself is built upon a foundation of chemical knowledge of the system and quality structures/structural predictions in which models can be a basis of a robust assembly of scattering paths with adequate parameterisation. As shown in Figure 4-10, the raw energy data, measured either in transmission or fluorescence is initially processed in Athena allowing for calibration, alignment, merging of multiple spectra and background normalisation to be

performed. The data is then Fourier transformed into  $\mu(E)$ , where it is then imported to the fitting program Artemis. Before the fit can be performed the chemist must have a reasonable chemical foundation on the makeup of their system under study. For example, as will be discussed within the chlorogallate LCC system studies in this work, multinuclear NMR has indicated that the neutral species dominates at high  $\chi_{\text{GaCl}_3}$ , densimetry and viscosity have alluded to the formation of oligomeric species and using chemical knowledge the structures present are predicted. Furthermore, bond distances of the predicted structures are required for a scattering path to be generated by IFEFFIT this can be acquired from with a single crystal structure (.cif) or *via* a computationally derived structure from energy and geometry optimisation calculations.

Once adequate structures have been obtained and a reasonable determination of the makeup of the sample has been determined the fitting model can be prepared. Artemis; the interface for IFEFFIT and FEFF8 allows for the previously mentioned predicted structures to be imported along with the EXAFS data set. In this program the predicted paths are calculated and parameterised by a number of factors and fits calculated. Each fit resulted in a plot and fit log allowing for the user to identify the success or lack of in their fit model.

#### 4.1.4.4 The statistics of an EXAFS fit

EXAFS are not a simple yes or no in regards to its fitting methodology and interpretation. Instead a statistical and comparative approach must be completed.

**Independent points,  $N_{\text{ind}}$** - The number of independent points equates to the number of points that are truly independent from absorptions at neighbouring energies. Variation in the number of independent points analysed within the fit is dependent on the fitting window; the fitting window is the range in both k-space and R-space the fit is occurring. It is crucial that the fitting window is wide enough to account for the path being fitted but not too wide as to skew the fit to noise or additional path contributions.

**Variables,  $f$** - A variable relates to the number of guess parameters that have been imposed on the paths modelled. The general rule in regards to independent point,  $N_{\text{ind}}$  vs. fitting variables,  $f$  is that the number of variables must not exceed two thirds of the number of independent points. If exceeded there is no freedom of fit and the honesty of the fit to the real data is skewed to a dishonest fit.

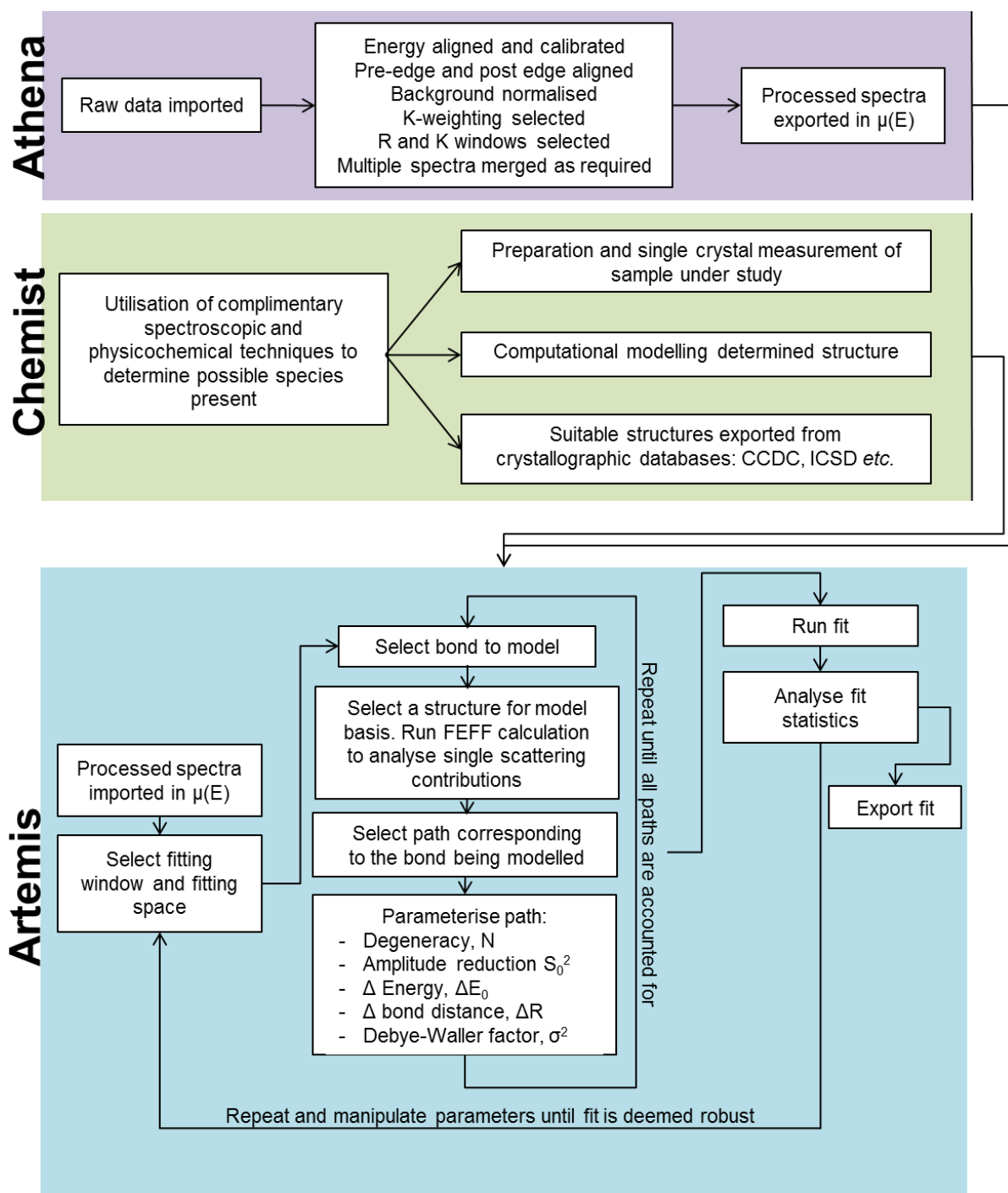


Figure 4-10-EXAFS fitting procedure using the Demeter software package.

**R-factor-** R-factor is a statistical parameter that is rarely used outside of the EXAFS field. It is defined as the sum of the squared difference between each data point and fit point and is normalised *via* division of the sum of all data points squared see Equation 4-9.<sup>388</sup>

Equation 4-9

$$R = \frac{\sum_{i=1}^N (data - fit)^2}{\sum_{i=1}^N (data)^2}$$

In reality the R-factor is a measure of the relative fit to the data; the general rule maintains that a fit is feasible if the R-factor is below 0.05. R-factor is hugely affected by the fitting window selected; other factors such as noise and disorder at the end of the spectrum can cause fitting to be attempted at long range to a non-existent species.

**$\chi^2$  and reduced  $\chi^2$ -** Similar to R-factor, chi-squared,  $\chi^2$  accounts for the relative fit however it takes into account the measurement uncertainties  $\varepsilon_i$  as shown in Equation 4-10. Uncertainty is a measure of random and systematic errors in measurement and is commonly combined to an averaged single term rather than per independent point.

Equation 4-10

$$\chi^2 = \sum_{i=1}^{N_{ind}} \frac{(data - fit)^2}{\varepsilon_i^2}$$

Uncertainties within EXAFS are calculated automatically within the Aretmis software fitting procedures and are taken into account.

Reduced chi-squared,  $\chi^2$  (Equation 4-11) accounts for the degrees of freedom within the fit. A degree of freedom,  $\nu$  is the difference between the number of independent points,  $N_{ind}$  and variables,  $f$ . ( $\nu = N_{ind} - f$ ).

Equation 4-11

$$\chi_v^2 = \frac{N_{ind}}{\nu N} \sum_{i=1}^{N_{ind}} \frac{(data - fit)^2}{\varepsilon_i^2}$$

## 4.2 Results and Discussion

As discussed, the main aim of this work is to elucidate the complex speciation of chlorogallate and chloroindate liquid coordination complexes. Continuing on from the foundations put in place for the well reported chloroaluminate LCCs it is aimed to further the field of LCCs and to look further into applications to inorganic materials syntheses.

### 4.2.1 Chlorogallate liquid coordination complexes

#### 4.2.1.1 Synthesis and observations of chlorogallate liquid coordination complexes

Initially, LCCs of equimolar quantities of  $\text{GaCl}_3$  and  $\text{P}_{888}\text{E}$  ( $\text{E} = \text{O}, \text{S}, \text{Se}$ ) were synthesised and characterised according to those reported by Coleman *et al.*<sup>22</sup> Subsequently, selected samples with excess of metal chloride ( $\chi_{\text{MCl}_3} > 0.50$ ) were synthesised to explore speciation of suspected oligonuclear complexes as listed in Table 4-3. All samples prepared resulted in the formation of viscous yellow liquids.

**Table 4-3-** Combinations of  $\text{GaCl}_3$  and  $\text{P}_{888}\text{E}$  ( $\text{E}=\text{O}, \text{S}, \text{Se}$ ) ligands that formed LCCs at given  $\chi_{\text{MCl}_3}$  values.

$\text{MCl}_x$	$\chi_{\text{MCl}_x}$	$\text{P}_{888}\text{O}$	$\text{P}_{888}\text{S}$	$\text{P}_{888}\text{Se}$
$\text{GaCl}_3$	0.50	yellow liquid <sup>a</sup>	yellow liquid	yellow liquid
	0.60	yellow liquid <sup>a</sup>	yellow liquid	yellow liquid
	0.67	yellow liquid <sup>a</sup>	yellow liquid	yellow liquid
	0.75	yellow liquid <sup>a</sup>	yellow liquid	yellow liquid

<sup>a</sup> Previously reported.<sup>22</sup>

#### 4.2.1.2 Density measurements

Densities were measured for a range of  $\text{P}_{888}\text{E}-\text{GaCl}_3$   $\chi_{\text{GaCl}_3} = 0.50, 0.60, 0.67, 0.75$  each with a variety of donor atoms;  $\text{E} = \text{O}, \text{S}, \text{Se}$ . All densities were studied as a function of temperature exhibiting an as expected decrease in density with increasing temperature. For all measured LCCs, linear density vs. temperature relationships were found, typically with very good correlations ( $R^2 > 0.99$ ), as summarised in Table 4-4. This is in agreement with earlier reports on ionic liquids, halometallate by Fannin *et al.* and non-halometallate alike.<sup>318,399,400</sup> In comparison to  $\text{AlCl}_3$  liquid coordination complexes reported by Hogg they were in general less dense than their  $\text{GaCl}_3$  counterparts due to the higher density of  $\text{GaCl}_3$  over  $\text{AlCl}_3$ .<sup>382</sup>

In contrast, changing the donor atom of the  $P_{888}E$  from oxygen to sulphur and further to a selenium atom ( $P_{888}O > P_{888}S > P_{888}Se$ ) the density only marginally increased the density of the liquid coordination complex formed as shown in Figure 4-11. Each sulphur atom is approximately double the mass of an oxygen atom but does not radically alter the size of the donor molecule or the sterics induced by its Tolman cone angle.<sup>401</sup> Tolman cone angle or the ligand cone angle,  $\Theta$  is method of quantifying steric bulk *via* visualisation of the ligand as a cone in which, the whole ligand is encapsulated with the metal centre acting as the vertex.

Referring back to the density data, as density relates to both the number of heavier atoms, steric bulk and  $\chi_{GaCl_3}$ . Tolman cone angle eliminates sterics as a factor with ligands having very similar results hence the changes in density are related to the increased mass of the species formed as a function of  $\chi_{GaCl_3}$ .

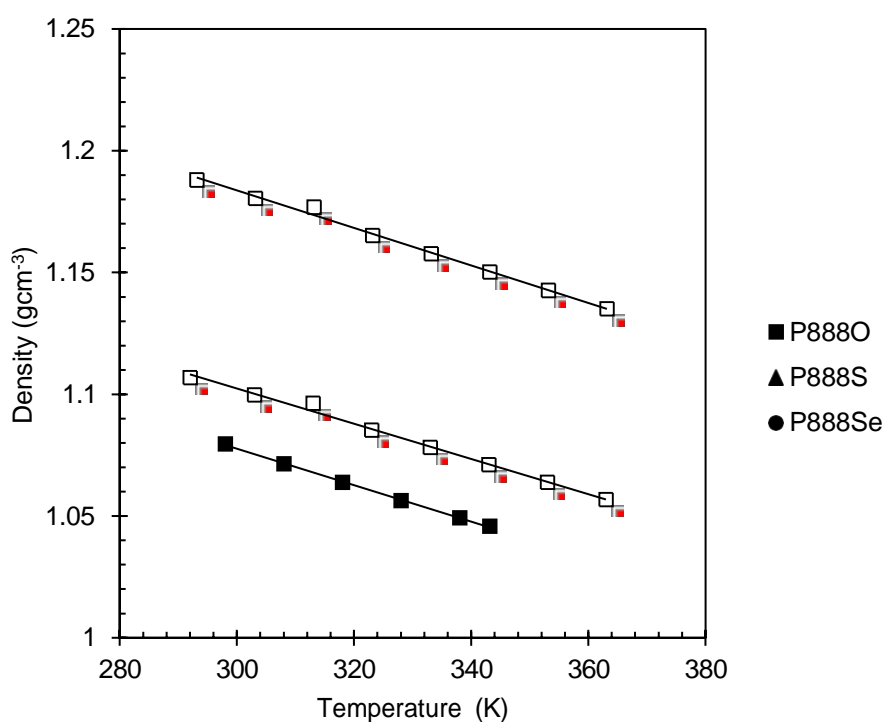


**Figure 4-11**-Density of  $P_{888}E-GaCl_3$   $\chi_{GaCl_3} = 0.50$ .

**Table 4-4-**Table of density fit data for chlorogallate LCCs.

$\chi$ GaCl <sub>3</sub>	Ligand								
	P <sub>888</sub> O			P <sub>888</sub> S			P <sub>888</sub> Se		
	M	C	R <sup>2</sup>	M	C	R <sup>2</sup>	M	C	R <sup>2</sup>
0.5	-0.0008	1.3027	0.999	-0.0007	1.3195	0.994	-0.0008	1.4124	0.994
0.6	-0.0008	1.3884	1	-0.0008	0.4173	0.994	-0.0008	1.5044	0.993
0.67	-0.0008	1.4842	1	-0.0008	1.5042	0.994	-0.0009	1.5865	0.994
0.75	-0.0009	1.6359	0.999	-0.0009	1.6415	0.994	-0.001	1.7099	0.994

#### 4.2.1.3 Viscosity measurements

In parallel with the density studies, viscosities were measured for GaCl<sub>3</sub>-LCCs with P<sub>888</sub>E (E = O, S, Se) donor ligands. Dynamic viscosities were recorded using a falling ball viscometer, which allows for accurate measurement of air sensitive liquids due to its closed system set up.<sup>2</sup> The use of the sealed tube, pre-loaded in a glovebox, prevents reaction of the material with atmospheric moisture. Viscosities were measured over a temperature range at 3 angles, 15 °, 20 °, 30 °; the dynamic viscosities were averaged from three measurements per angle.

The temperature-viscosity profile was plotted and then fitted to a Vogel-Fulcher-Tammann (VFT) (Equation 4-12)<sup>402,403</sup>

#### Equation 4-12

$$\log \eta = A + B / (T - T_0)$$

Where:

$\eta$  = viscosity,

A, B = fitting parameters,

$T_0$  = ideal glass transition temperature,

T = temperature

<sup>2</sup> Kinematic vs dynamic viscosities: Dynamic viscosity is a measure of a liquids resistance to shear flow when an external force is applied. Kinematic viscosity is a measure of dynamic viscosity as a function of density hence being a descriptor of a liquids resistance to shear flow under gravity. No external forces are applied.

It follows, that ;

$$\text{Kinematic viscosity (cSt)} \times \text{density} = \text{Dynamic viscosity (cP)}$$

Dynamic viscosity is measure in centipoise, cP or mPas

Kinematic viscosity is measured in centistokes, cSt or mm<sup>2</sup> s<sup>-1</sup>



In conventional systems the Arrhenius equation is commonly used to model viscosity, however, Jacquemin *et al.* determined that the VFT equations provides a better fit to IL type systems.<sup>400,404</sup> The VFT equation is composed of both physical and arbitrary parameters including; ideal glass transition temperature  $T_0$ , temperature  $T$ , and,  $A$  and  $B$ , which have no direct physical meaning. The VFT fitting parameters are listed in Table 4-5 ( $P_{888}E-GaCl_3$ ) and plots are shown in Figure 4-13 ( $P_{888}O$ ), Figure 4-14 ( $P_{888}S$ ), and Figure 4-15 ( $P_{888}Se$ ). In contrast to density, it is clear in Figure 4-12 that the donating atom can have a large effect on the viscosity of the LCCs at low/room temperatures and there is a variation with the chlorometallate species also, specifically in comparison to the chloroaluminate analogues analysed by Hogg *et al.*<sup>382</sup> It is further noted that similar trends relating to decreasing donor hardness and the subsequent increase in viscosity was also observed in the chloroaluminate systems but to a lesser extent than the observations in this work.

Observing the trends of the chlorogallate LCC systems in greater detail it is seen that as donor hardness decreases the viscosity increases significantly. At 323 K,  $P_{888}O$   $\chi_{GaCl_3} = 0.50$  has a viscosity of 51.28 cP vs. 183.63 cP for  $P_{888}Se$   $\chi_{GaCl_3} = 0.50$ ; this trend of increasing viscosity with decreasing donor hardness is observed at higher  $\chi_{GaCl_3}$  as shown in Figure 4-12. Furthermore, as  $\chi_{GaCl_3}$  increases the LCC viscosity decreases indicating the formation of oligomeric species such as  $[Ga_2Cl_7]^-$  similarly to what has previously been observed within chloroaluminate species in both LCCs as discovered by Hogg. and in ionic liquids as determined by Fannin *et al.*<sup>318,382</sup>

With increasing  $\chi_{GaCl_3}$  the viscosity decreases, indicating that the predicted oligomeric species are present as the negative charge is more dispersed over the anionic species hence weakening intermolecular ionic and hydrogen bonding. This is observed in all  $P_{888}E-GaCl_3$  systems studied.<sup>349</sup>

Within the ionic liquids field there have been several studies and theories regarding the diffusion of ions within ionic liquids.<sup>405</sup> Initial correlations to conventional salts in aqueous solutions were found to be inadequate. In classical models a single ions transport/diffusion is modelled at infinite dilution, however, upon the discovery of molten salts this model was not seen to correlate with experimental data. Bockris found that as ionic liquids and molten salts are composed of two ionic species it is more accurate to model the transport of the ion holes rather than that of two discrete ions. Reverting back to diffusion it was found that the ion holes diffuse through the

solutions relative to the size and mass of the ions present. Stokes law determined that the mass of the diffusion must be accounted for and that the size of the species must also be included. The sizes of the ions were initially modelled as hard spheres but this was found to be ineffective, however, later models accounting for ion asymmetries were found to be effective. The Stokes-Einstein equation, previously used in classical gas models they did not account for motion within a liquid species, however, it was found to be a surprisingly good model for ionic liquids above their glass transition temperatures.

In summary, the Stokes-Einstein equation is an effective method of correlating ion mass, ion size, conductivity, and viscosity to determine the diffusion coefficient of ionic liquids. The main observation in this LCC viscosity data is the decreased viscosity with increasing  $\chi_{\text{GaCl}_3}$  hence indicating larger ions are present, specifically, oligomeric chlorogallate species hence confirming that postulated by Fannin and Hogg.

**Table 4-5.-** VFT fit parameters for  $\text{P}_{888}\text{E-GaCl}_3$

VFT fit according to $Y=10^{A+(B/(T-T_0))}$	$\text{P}_{888}\text{O-GaCl}_3$			
	0.5	0.6	0.67	0.75
A	-1.35376	-1.2295	-1.0655	-0.8688
B	547.23872	526.88893	485.68992	410.41956
$T_0$	144.52966	143.54344	146.91057	160.9753
	$\text{P}_{888}\text{S-GaCl}_3$			
	0.5	0.6	0.67	0.75
A	-1.65659	-1.39853	-1.12849	-0.9176
B	703.3058	634.39945	552.5303	464.34631
$T_0$	139.10436	141.98603	151.61204	163.32539
	$\text{P}_{888}\text{Se-GaCl}_3$			
	0.5	0.6	0.67	0.75
A	-1.96571	-1.32219	-1.22159	-0.98005
B	828.32222	620.21036	591.38062	498.89627
$T_0$	127.31288	145.86717	148.60426	158.6625

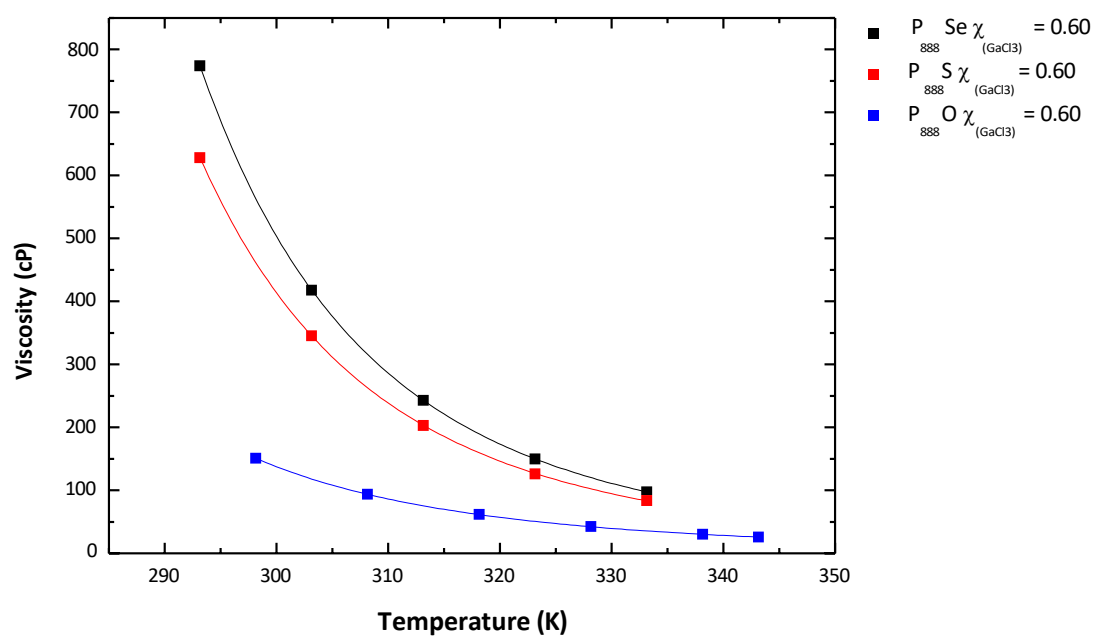


Figure 4-12- VFT plot of  $P_{888}E-GaCl_3$  LCCs  $\chi_{GaCl_3} = 0.60$ .

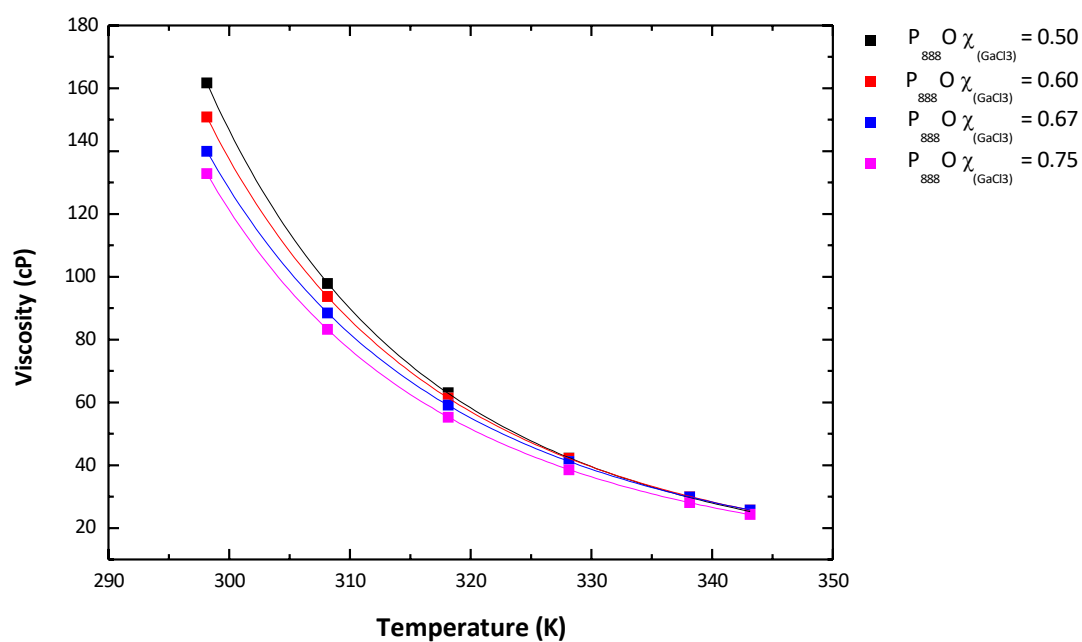


Figure 4-13- VFT plot of  $P_{888}O-GaCl_3$  LCCs.

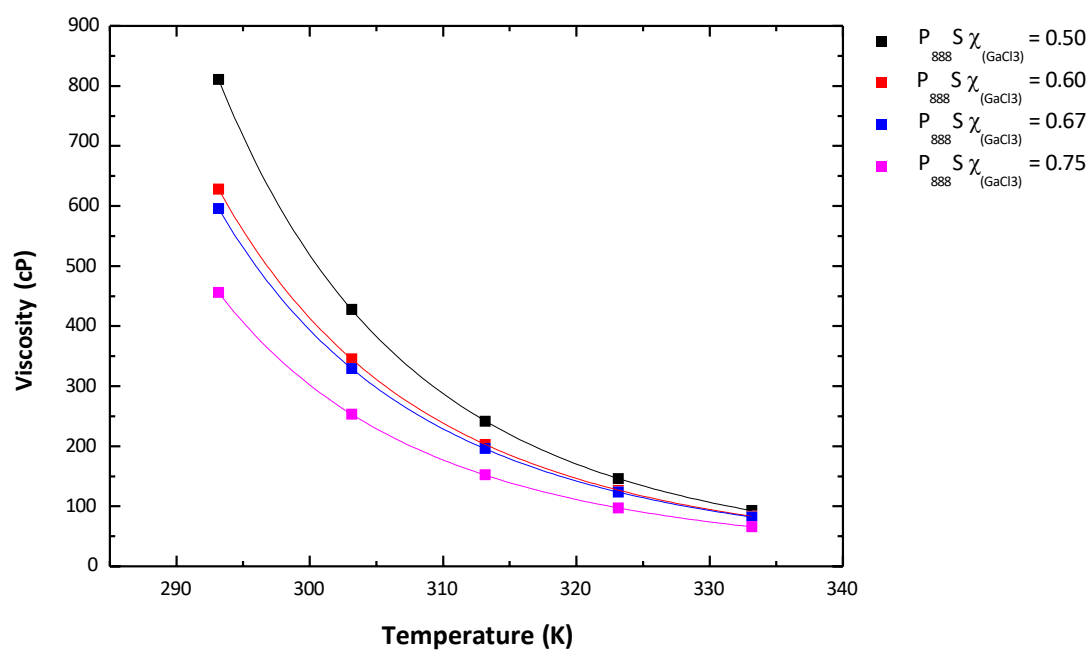


Figure 4-14- VFT plot of  $P_{888}S-GaCl_3$  LCCs.

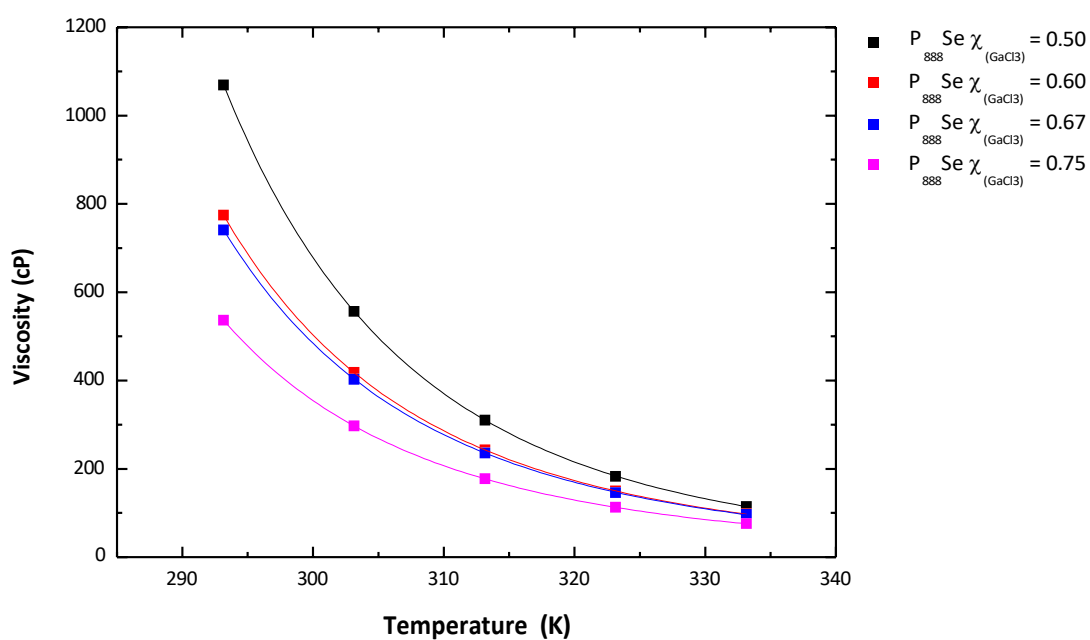


Figure 4-15- VFT plot of  $P_{888}Se-GaCl_3$  LCCs.

#### 4.2.1.4 Nuclear resonance spectroscopy

Multinuclear NMR is a valuable tool in elucidating speciation within metal-containing liquids; the ability to probe a solution from multiple perspectives allows for a systematic approach to the determination of the species present.<sup>375</sup> Previous

speciation studies with multinuclear NMR techniques have been proven to be effective with  $\text{AlCl}_3$ ,  $\text{GaCl}_3$ ,  $\text{InCl}_3$ ,  $\text{SbCl}_3$ ,  $\text{SnCl}_4$ ,  $\text{SnCl}_2$ ,  $\text{ZnCl}_2$  and  $\text{TiCl}_4$ , LCCs formed with trioctylphosphine ( $\text{P}_{888}$ ), and trioctylphosphine oxide ( $\text{P}_{888}\text{O}$ ) systems, however, as will be discussed, NMR alone may not give a comprehensive representation of the speciation. Factors such as NMR timescale, overlapping peaks and multiple outcomes in regards to assignment can be at the detriment of the technique.

As LCCs have been shown to be equilibrated charged and neutral species, care must be taken during the NMR measurement to prevent perturbation of system being measured. The addition of solvent, the temperature of the system and other stimuli can affect the speciation present. The addition of a solvent causes changes in the liquid coordination complexes formed and/or equilibrium present, for example Lewis acidic anions will readily be coordinated by basic solvents. To prevent such interactions and changes in speciation a deuterated solvent capillary is utilised such that the neat LCC is placed in a standard NMR tube under glovebox conditions and the sealed capillary added.

Within these LCC studies  $^1\text{H}$ ,  $^{13}\text{C}$ ,  $^{31}\text{P}$  and  $^{77}\text{Se}$  NMR nuclei have been utilised. Attempts at  $^{71}\text{Ga}$  NMR resulted in broad uninterpretable spectra as was previously seen with high  $\text{GaCl}_3$  content ionic liquids.<sup>354</sup> The broadness of the spectra achieved were due to several factors including; the quadrupole nuclei, the viscosity of the neat solutions, and the postulated presence of oligomeric gallium chloride species. Phosphorous  $^{31}\text{P}$  NMR, is a highly sensitive, 100 % abundance and spin half nucleus hence it plays a crucial role in the determination of  $\text{P}_{888}\text{E-GaCl}_3$  LCCs. The phosphorous nucleus not only varies greatly with coordination number and charge but also exhibits clear shielding and de-shielding shift with subtle changes in electron density.<sup>406</sup> Selenium  $^{77}\text{Se}$  NMR is less sensitive than the  $^{31}\text{P}$  nuclei and less abundant, 7.63 %, however, it does exhibit a spin half nucleus making it useful in speciation studies of the  $\text{P}_{888}\text{Se-GaCl}_3$  systems.

The  $^{31}\text{P}$  NMR spectra of the three  $\text{P}_{888}\text{E-GaCl}_3$   $\chi_{\text{GaCl}_3} = 0.50$  LCC systems are compared in Figure 4-16. In all three cases, there are two sets of signals in the  $^{31}\text{P}$  NMR spectra; the more shielded ones correspond to a neutral adduct species,  $[\text{GaCl}_3(\text{P}_{888}\text{E})]$ , with the considerably smaller, relatively de-shielded peaks corresponding to the charged species,  $[\text{GaCl}_2(\text{P}_{888}\text{E})_2]^+$ .<sup>375</sup> Comparatively to  $\text{P}_{888}\text{O-AlCl}_3$  there is a significant bias to the neutral adduct for  $\text{P}_{888}\text{O-GaCl}_3$ . With  $\text{P}_{888}\text{S/Se-GaCl}_3$  systems, the downfield peaks corresponding to the ionic species  $[\text{GaCl}_2(\text{P}_{888}\text{E})_2]^+$  increase compared to  $\text{P}_{888}\text{S/Se-AlCl}_3$  as the donor ligand becomes

softer.<sup>375</sup> This is both expected and unexpected behaviour; as the donor atom decreases in hardness it would be expected that the prominence of the ionic species to increase significantly relative to the neutral species, however, the neutral species remains dominant throughout all studies.

**Table 4-6**-Integration of ionic vs. neutral peak in  $^{31}\text{P}$  NMR spectra of chloroaluminate LCCs at  $\chi_{\text{GaCl}_3} = 0.50$  by Hogg and chlorogallate in this work.<sup>382</sup>

	$\text{P}_{888}\text{O}$	$\text{P}_{888}\text{S}$	$\text{P}_{888}\text{Se}$
$\text{AlCl}_3$	1:2	1:12	Trace:1
$\text{GaCl}_3$	1:4	1:4	1:3

Using some rudimentary integration of the peaks (Table 4-6) it was observed that the relative ratio of ionic to neutral species in  $\text{P}_{888}\text{E-GaCl}_3$  systems to shift as follows  $\text{P}_{888}\text{O}$  1:4,  $\text{P}_{888}\text{S}$  1:4 and  $\text{P}_{888}\text{Se}$  1:3 in  $\text{P}_{888}\text{E-GaCl}_3$  LCC systems. The  $^{31}\text{P}$  NMR spectrum of  $\text{P}_{888}\text{Se-GaCl}_3$   $\chi_{\text{GaCl}_3} = 0.50$  features a singlet at 47.51 ppm, accompanied by satellites arising from  $^{77}\text{Se}$  coupling ( $^1J_{\text{P-Se}} = 463.98$  Hz), with only trace downfield peak (and a trace feature from  $\text{P}_{888}\text{O}$  impurity). The corresponding  $^{77}\text{Se}$  NMR (Figure 4-18) shows a doublet environment and a trace of a relatively de-shielded peak in a similar fashion to the  $^{31}\text{P}$  NMR spectrum. This positively confirms that the molecular adduct is still preferred over the charged species for complexes with phosphine sulphide and selenide. The downfield nature of the peak shift arises from the greater de-shielding experienced by oligomeric species at higher  $\chi_{\text{GaCl}_3}$ . Furthermore, the coupling constant between  $^{31}\text{P}$  and  $^{77}\text{Se}$  is seen to decrease by ca. 207 Hz upon complexation of the ligand to  $\text{AlCl}_3$ . This is consistent with the decrease in coupling constant seen by Burford *et al.* upon complexation of  $\text{Ph}_3\text{PSe}$  to  $\text{AlCl}_3$  which would be expected to be replicated within the gallium systems.<sup>407</sup>

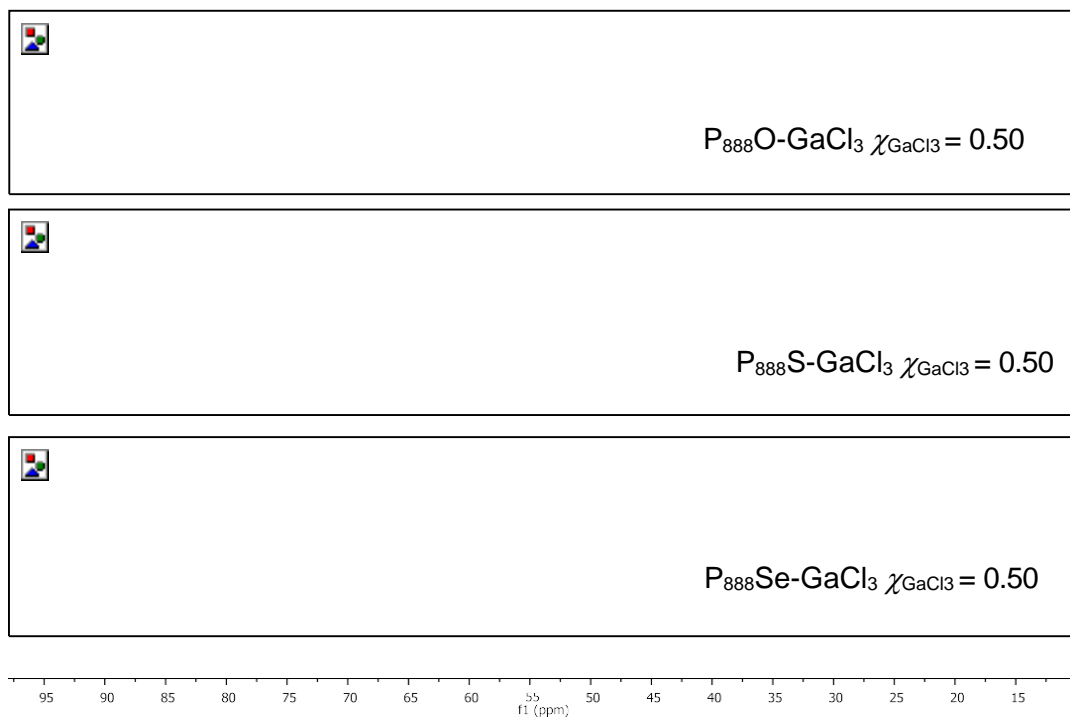


**Figure 4-16.**  $^{31}\text{P}$  NMR spectra of  $\text{P}_{888}\text{O-GaCl}_3$   $\chi_{\text{GaCl}_3} = 0.50$  (top),  $\text{P}_{888}\text{S-GaCl}_3$   $\chi_{\text{GaCl}_3} = 0.50$  (middle) and  $\text{P}_{888}\text{Se-GaCl}_3$   $\chi_{\text{GaCl}_3} = 0.50$  (bottom).

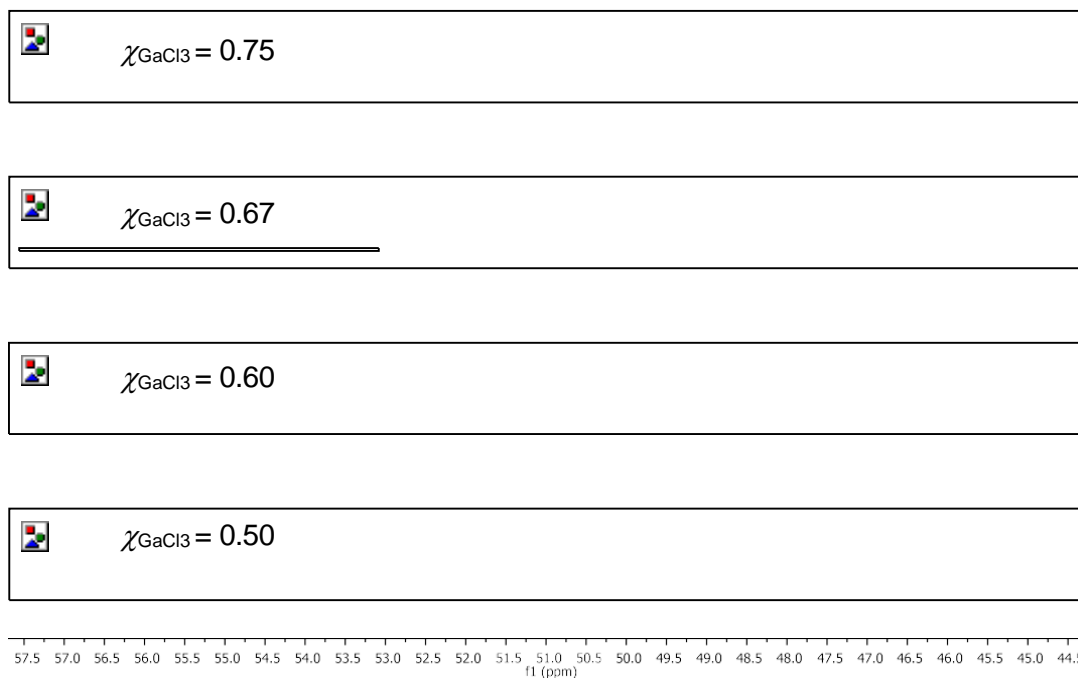


**Figure 4-17.**  $^{31}\text{P}$  NMR spectra of  $\text{P}_{888}\text{Se-GaCl}_3$   $\chi_{\text{GaCl}_3} = 0.75$ ,  $\chi_{\text{GaCl}_3} = 0.67$ ,  $\chi_{\text{GaCl}_3} = 0.60$ ,  $\chi_{\text{GaCl}_3} = 0.50$ .

As discussed in section 4.1.3, Hogg put forward a theory based on the work by Shore and Gandon, that hetero- vs. homolytic splitting was due to the donor strength

and its effect on the transition state dimer  $\text{LGaCl}_2\text{-}\mu\text{Cl-GaCl}_3$ . Gallium is softer than aluminium and sulphur and selenium are softer donors than oxygen.

Group 13 chlorometallates are often seen as hard, moderate and soft acceptors as you move down the group from Al to Ga to In, however, this narrative is not as clear cut as one would initially think. Yes, hardness of these metals does decrease but it is realised that gallium is still a hard species and as is indium. The Kobayashi scale is a method of quantifying the hardness of these species *via* the comparison of reaction products in a competitive addition reaction of aldehydes and aldimines to silyl enol ether.<sup>408</sup> The scale classifies species as active, weak and neutral with aluminium, indium and gallium chlorides classified as active and aldehyde selective hence indicating the similar nature of these metal centres.

Investigating greater  $\chi_{\text{GaCl}_3}$  values, gallium's increased ability to form oligomeric species such as  $[\text{Ga}_2\text{Cl}_7]^-$ ,  $[\text{Ga}_3\text{Cl}_{10}]^-$  and further postulated  $[\text{Ga}_4\text{Cl}_{13}]^-$  must be accounted for.<sup>409</sup> The downfield shift that is seen with increasing  $\chi_{\text{GaCl}_3}$  is attributed to the greater de-shielding of the ligand experienced when coordinated to oligomeric species. As seen in Figure 8-62 moving from  $\chi_{\text{GaCl}_3} = 0.50$  to  $\chi_{\text{GaCl}_3} = 0.60$  only a single peak in the  $^{31}\text{P}$  NMR spectra in  $\text{P}_{888}\text{S}$  and  $\text{P}_{888}\text{Se}$  indicating only the neutral species is present. However, the  $^{77}\text{Se}$  NMR spectrum, Figure 4-18 indicated that at  $\chi_{\text{GaCl}_3} = 0.60$  there may still be a significant presence of the ionic species as significant broadening occurred that did not correlate to the increased viscosity, as viscosity to decrease with increasing  $\chi_{\text{GaCl}_3}$ . In order to investigate this further a small amount of  $d_2$ -dichloromethane (a non-coordinating solvent which is expected to have a minimal effect on speciation as demonstrated by Liu *et al.*)<sup>410</sup> was added to the NMR sample and the spectra were measured at 20 °C, 10 °C, 0 °C, -10 °C, and -20 °C. (Figure 4-20) This cooling and dilution enabled us to slow the dynamic equilibrium present and observed ionic species in the solution, specifically in the  $^{77}\text{Se}$  spectra as shown in Figure 4-19. The second observed species ( $\delta \text{ } ^{77}\text{Se} = -167$  ppm) species is attributed to the ionic species arose.



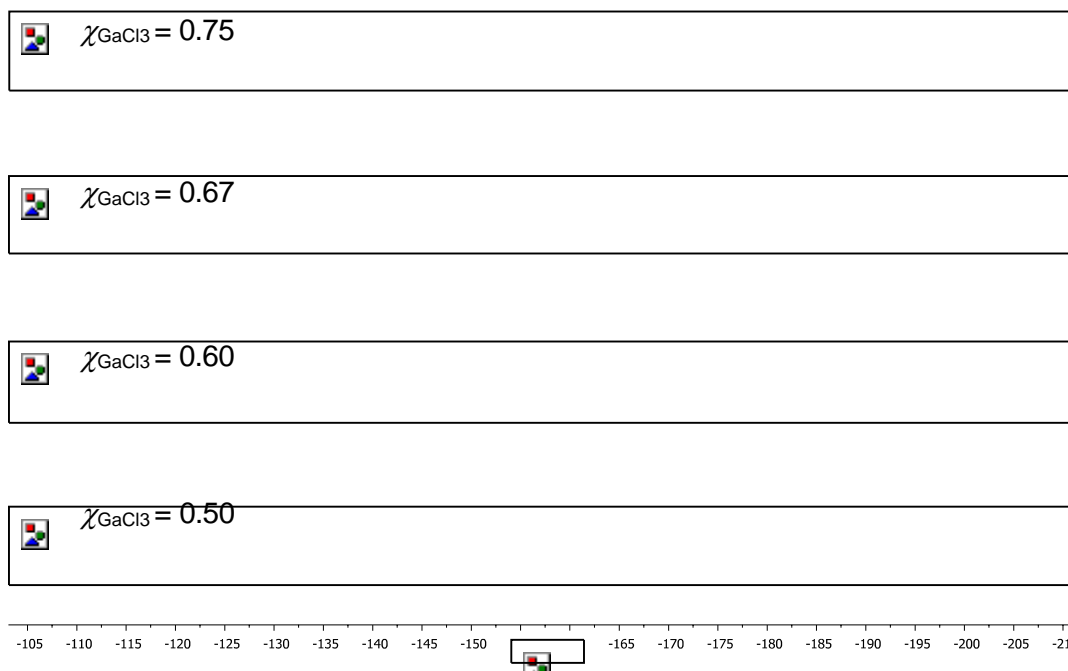


**Figure 4-18-** $^{77}\text{Se}$  NMR spectra of  $\text{P}_{888}\text{Se-GaCl}_3$   $\chi_{\text{GaCl}_3} = 0.75$ ,  $\chi_{\text{GaCl}_3} = 0.67$ ,  $\chi_{\text{GaCl}_3} = 0.60$ ,  $\chi_{\text{GaCl}_3} = 0.50$ .

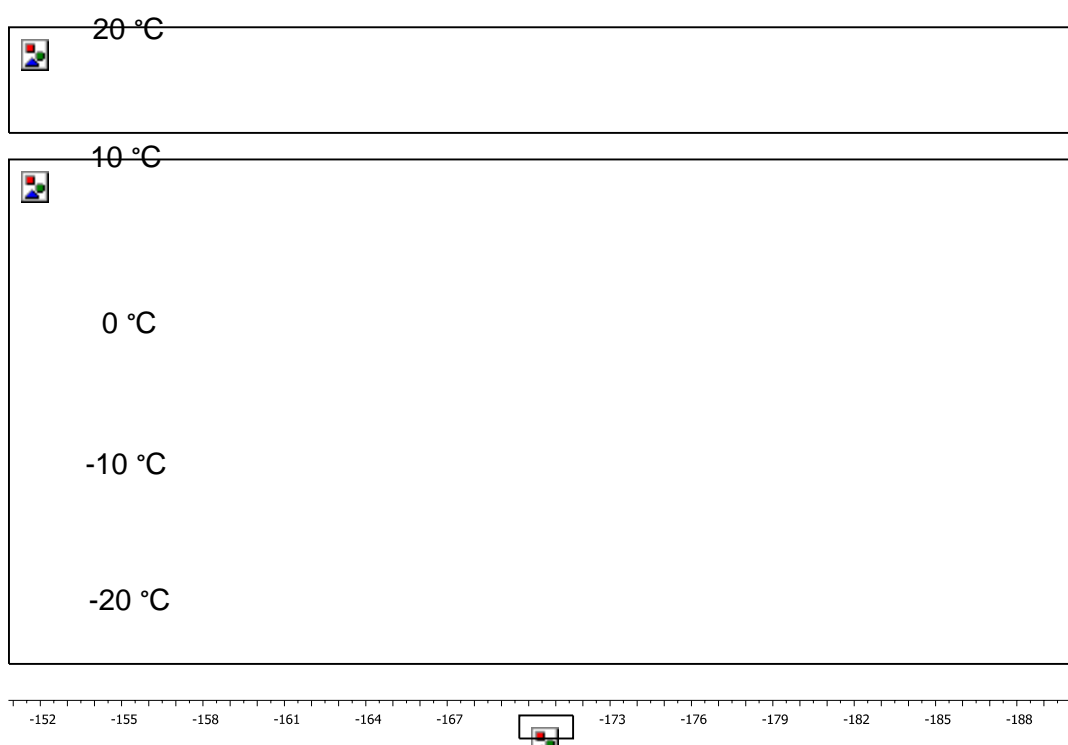


**Figure 4-19-** $^{77}\text{Se}$  NMR of  $\text{P}_{888}\text{Se-GaCl}_3$   $\chi_{\text{GaCl}_3} = 0.60$  in *d*-dichloromethane at 20, 10, 0, -10, -20 °C.

Furthermore, this allowed for coupling constants to be deduced as described in Table 4-7. The single peaks observed in the  $^{31}\text{P}$  NMR spectra of  $\text{P}_{888}\text{S}$  and  $\text{P}_{888}\text{Se}$

systems with increasing  $\chi_{\text{GaCl}_3}$  was initially believed to be due to the predominance of the neutral adduct. As the  $^{77}\text{Se}$  NMR spectrum of  $\text{P}_{888}\text{Se-GaCl}_3$   $\chi_{\text{GaCl}_3} = 0.60$  showed this was not the case, as will be discussed in chapter 4.2.1.8, the conductivity measurements have shown that at higher  $\chi_{\text{GaCl}_3}$  there is a significant increase in conductivity, it was reasoned that there may still be ionic species present in these samples.

It is postulated that the rate of exchange between the neutral and ionic species increases as donor softness increases. Such that the timescale of the NMR spectra is greater than the timescale of the exchange processes, causing an averaging of peaks within the  $^{31}\text{P}$  spectrum and the variation in speciation and relative abundance of both neutral and ionic species along with the formation of oligomeric species depicts the shift of the averaged  $^{31}\text{P}$  peak.

**Table 4-7-**  $^{31}\text{P}$  and  $^{77}\text{Se}$  shift and coupling in  $\text{P}_{888}\text{Se-GaCl}_3$  LCCs.

LCCs	$\delta ^{31}\text{P}$ (ppm)	$^1\text{J} (^{31}\text{P} - ^{77}\text{Se})$ (Hz)	$\delta ^{77}\text{Se}$ (ppm)	$^1\text{J} (^{31}\text{P} - ^{77}\text{Se})$ (Hz)
$\text{P}_{888}\text{Se}$	36.41	678.25	-388.57	709.68
$\text{P}_{888}\text{Se-GaCl}_3$ $\chi_{\text{GaCl}_3} = 0.50$	47.51	471.42	-161.245	463.98
	50.33	466.56	-183.585	468.54
$\text{P}_{888}\text{Se-GaCl}_3$ $\chi_{\text{GaCl}_3} = 0.60$	49.53	456.84	-167.25*	467.4*
	50.37*	N/A	-182.535*	459.42*
$\text{P}_{888}\text{Se-GaCl}_3$ $\chi_{\text{GaCl}_3} = 0.67$	51.13	442.26	-147.27	444.6
$\text{P}_{888}\text{Se-GaCl}_3$ $\chi_{\text{GaCl}_3} = 0.75$	51.98	447.12	-135.23	434.34

\*Coupling constants determined using NMR at  $-20^\circ\text{C}$  in  $d$ -dichloromethane

Initial measurements of  $\text{P}_{888}\text{S-GaCl}_3$   $^{31}\text{P}$  NMR spectra (Figure 4-20) were significantly broader than those of the  $\text{P}_{888}\text{Se}$  hence the dynamic NMR experiment was repeated showing that as aforementioned, a dynamic process is present. The cooling of the  $\text{P}_{888}\text{S-GaCl}_3$   $\chi_{\text{GaCl}_3} = 0.60$  allowed the once believed to be the single peak of the neutral adduct to be resolved into the neutral and ionic contributions, again indicating that within the gallium systems ionic species are more likely to be present with softer donors than is observed with the aluminium counterparts. This experimental methodology was not applied to Al systems, however it is apparent that at  $\chi_{\text{MCl}_3} = 0.50$  (where the peaks were well resolved and not subject to rapid intermolecular exchange) that indeed  $\text{GaCl}_3$  LCCs form more ionic species with softer donors. However, it should be noted that the position of equilibrium with LCCs

has previously been observed to change with temperature by Coleman and Legrande.<sup>22,378</sup> Hence, this cooling study indicates that the ionic species is achievable in the  $P_{888}Se-GaCl_3$   $\chi_{GaCl_3} = 0.60$ , Figure 4-19, but thermodynamics will favour the neutral adducts at ambient temperatures; however, it is also due to rapid exchange processes. It is also observable at lower temperatures due to the decrease in the exchange processes as characterised by the shape and resolution of the NMR peak with lowering temperatures, however, it is difficult to fully elucidate the distribution in regards to the rate of exchange within the systems at ambient temperature. Unfortunately, the  $^{31}P$  of the cooled system failed to resolve at the temperatures investigated; differences in the NMR nuclei investigated are believed to be due to differing measurement frequencies,  $^{31}P$  243 MHz and  $^{77}Se$  114 MHz and relaxation times, T1 of each nuclei.

Similarly, upon cooling of the  $P_{888}S-GaCl_3$   $\chi_{GaCl_3} = 0.60$  LCC, as shown in Figure 4-20 the  $^{31}P$  NMR spectra resolved from a single peak to 2 discrete singlets which, is indicative of both the neutral and ionic species being present. The resolved peaks further confirm that exchange processes are present and can be observed as they are slowed with cooling. As listed in Table 4-8 the ionic vs. neutral species are in a 1: 2.15 ratio at -60 °C.

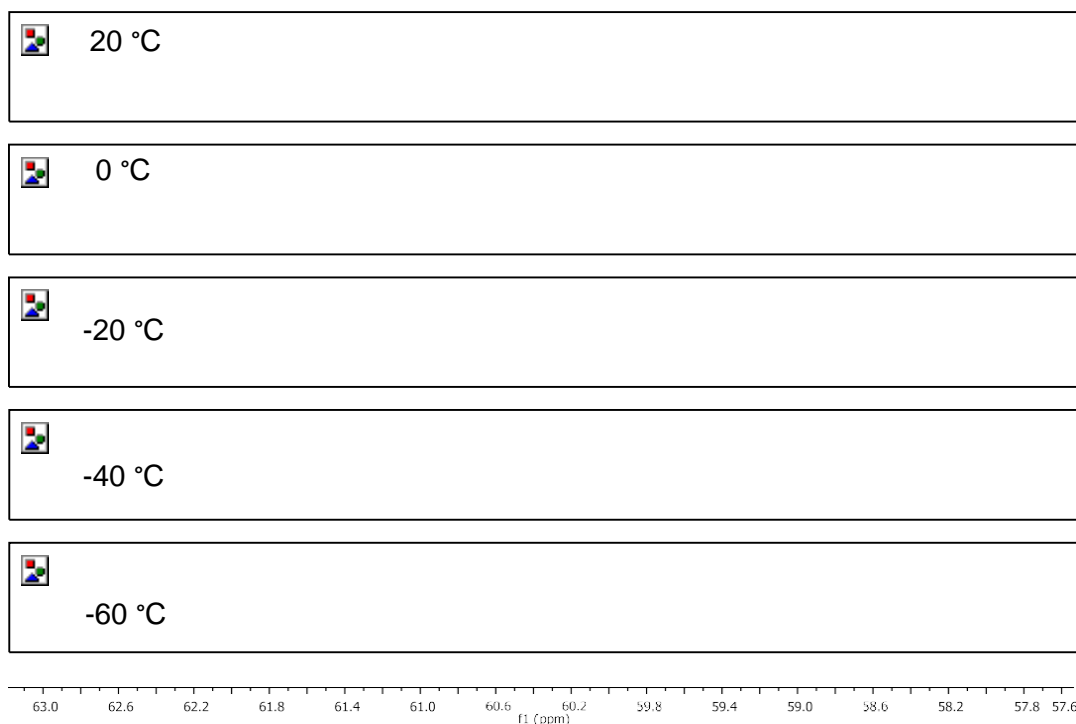


**Figure 4-20-** $^{31}P$  NMR spectra of  $P_{888}S-GaCl_3$   $\chi_{GaCl_3} = 0.60$  in *d*-dichloromethane at 20 °C, 0 °C, -20 °C, -40 °C, -60 °C .

**Table 4-8-**<sup>31</sup>P integration analysis of ionic vs. neutral species in P<sub>888</sub>S-GaCl<sub>3</sub> cooled LCCs.

LCC	<sup>31</sup> P integration analysis ionic: neutral
P <sub>888</sub> S-GaCl <sub>3</sub> $\chi_{\text{GaCl}_3} = 0.60$ -40 °C	1:2.35
P <sub>888</sub> S-GaCl <sub>3</sub> $\chi_{\text{GaCl}_3} = 0.60$ -60 °C	1:2.15

With P<sub>888</sub>O-GaCl<sub>3</sub> systems more complex <sup>31</sup>P NMR spectra are observed in comparison to the P<sub>888</sub>S and P<sub>888</sub>Se systems. Instead of a signal peak being observed at higher  $\chi_{\text{GaCl}_3}$  values *i.e.*  $\chi_{\text{GaCl}_3} = 0.67$ , two signals are observed at 81.31 ppm and 83.41 ppm corresponding to the cationic and neutral adduct, respectively (Figure 4-21).<sup>375</sup> Again moving to  $\chi_{\text{GaCl}_3} = 0.75$  there are 3 major overlapping signals observed that had previously been assigned to a “number of equilibrated oligomeric species”, however, this is not observed in either the P<sub>888</sub>S or the P<sub>888</sub>Se  $\chi_{\text{GaCl}_3} = 0.75$  system hence there is a difference in speciation between these systems. It is speculated that the peaks observed in the higher  $\chi_{\text{GaCl}_3} = 0.75$  of the P<sub>888</sub>O system are due to an ionic species such as [Ga<sub>2</sub>Cl<sub>7</sub>]<sup>-</sup> and [Ga<sub>3</sub>Cl<sub>10</sub>]<sup>-</sup> that are slower in exchange than that observed in the P<sub>888</sub>S and P<sub>888</sub>Se counterparts.

From these experiments it appears that the neutral species is dominant at ambient temperature, but the suspected ionic species is still present but in an unquantifiable amount *via* NMR studies due to the rapid exchange rate and somewhat instability of the ionic species that is exhibited upon NMR spectroscopy at cooler temperatures. This was not elucidated further by Hogg *et al.*<sup>382</sup> in which only ambient NMR studies of the chloroaluminate LCCs were completed hence concluded that the neutral species dominated at high  $\chi_{\text{AlCl}_3} > 0.67$ . It may prove prudent in light of the results obtained here to test this assertion by performing variable temperature NMR spectroscopy upon the AlCl<sub>3</sub> LCC systems. Furthermore, there may be some cases for other chlorometallate systems, which Hogg *et al.* have determined to consist of neutral species to be revisited in light of the results obtained here.

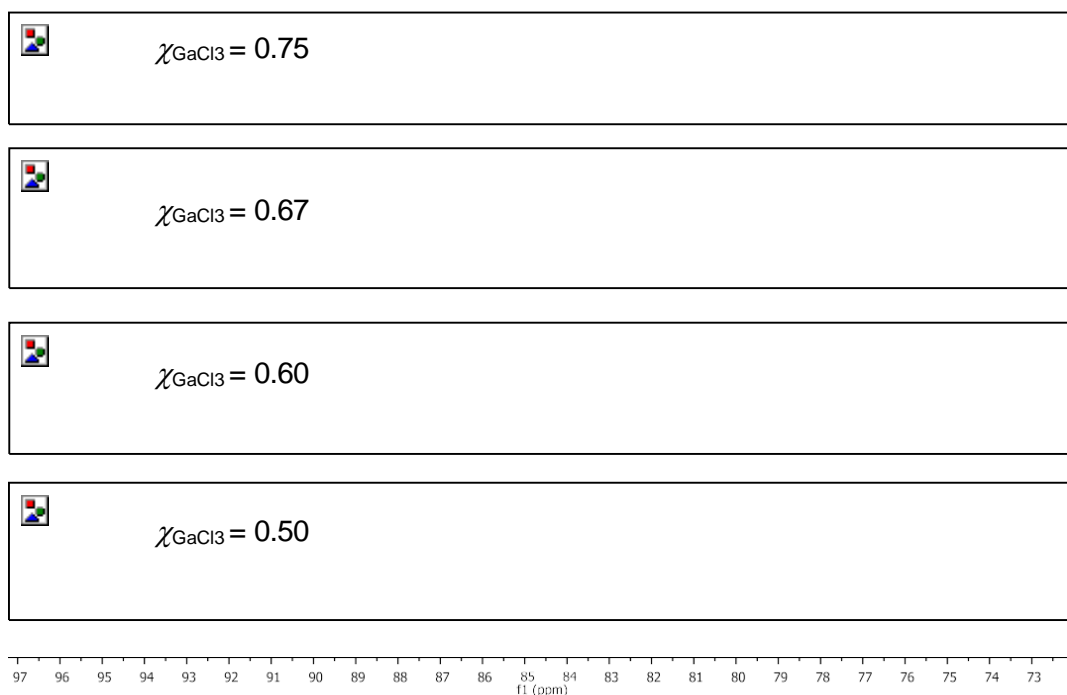


**Figure 4-21-**  $^{31}\text{P}$  NMR spectra of  $\text{P}_{888}\text{O-GaCl}_3$  mixtures (top-bottom)  $\chi_{\text{GaCl}_3} = 0.75, 0.67, 0.60, 0.50$ .

An observation by Coleman *et al.* in the  $\text{Ur-AlCl}_3$   $\chi_{\text{AlCl}_3} = 0.60$  initially indicated the temperature dependence of the speciation of LCCs, however, this has of yet not been fully understood.<sup>22</sup> Such a significant change in speciation with temperature could be hugely influential on catalytic applications of such compound and upon their applications. This is seen by Haumann *et al.*<sup>411</sup> in Lewis acid assisted hydrogenations of toluene in which and by Liu *et al.*<sup>412</sup> in isobutene alkylation. Haumann utilised solid catalysts with ionic liquid catalysts, comparing a standard chloroaluminate IL,  $[\text{C}_4\text{mim}][\text{Al}_2\text{Cl}_7]$  vs. an LCC,  $\text{Ur-AlCl}_3$   $\chi_{\text{AlCl}_3} = 0.67$ . With increasing temperature there was a slight increase in catalytic activity of the IL, however, within the LCC system there was a huge increase in activity; from  $X_{60}/\% = 11.3\%$  at  $40^\circ\text{C}$  to  $99.9$  at  $80^\circ\text{C}$ . Liu *et al.* completed all experiments at  $15^\circ\text{C}$ , however, comparing catalytic activity and the products obtained as a function of temperature would be of merit as speciation is expected to shift, It is suggested that a comprehensive computational study may allow for comparison of the energies of each possible species and kinetics of their associated equilibria could be quantified and compared to give rationale with their behaviours with temperature.

#### 4.2.1.5 Raman spectroscopy

Raman spectroscopy is another spectroscopic technique which can elucidate the structures of the metal species under study. As a vibrational spectroscopic

technique, Raman measures changes in the modes of vibration of a molecule. The Raman spectra measured are also subject to selection rules relating to the symmetry of the molecule under study and can therefore impart geometric information. Raman spectroscopy works upon the premise that a molecular vibration will give rise to a band in the Raman spectra if the symmetry/vector of the vibration has the same alignment as the polarizability tensor,  $\alpha$  hence causing a change in the molecular polarizability, comparatively infrared spectroscopy responds to a change in dipole. Furthermore, if a molecule has a centre of inversion e.g. methane of  $T_d$  symmetry it must follow the exclusion rule in that none of its vibrational modes can be both IR and Raman active.

Raman spectroscopy has previously been carried out on a variety of donor ligands that are specifically  $P_{888}E$  where  $E = O, S$  and  $Se$  coordinating atoms. Vibrational bands corresponding to the chlorogallate anions have been found to fall within 300-400  $cm^{-1}$ . In these anions the terminal gallium-chlorine bond has a clear distinct shift depending on the nature of the anion. This bond is observed at as  $[GaCl_4]^-$  ( $Ga-Cl^t = 346\text{ cm}^{-1}$ ),  $[Ga_2Cl_7]^-$  ( $Ga-Cl^t = 365\text{ cm}^{-1}$ ) and  $[Ga_3Cl_{10}]^-$  ( $Ga-Cl^t = 392\text{ cm}^{-1}$ ) at  $\chi_{GaCl_3} > 0.50$  as previously reported by Coleman *et al.* [NB: Cl<sup>t</sup> indicating a terminal chlorine atom]<sup>22,352</sup> Within chlorogallate ionic liquids Wicelinski *et al.*, were to able identify  $[Ga_2Cl_7]^-$ , symmetry  $C_{2V}$ , at 414  $cm^{-1}$  in  $\chi_{GaCl_3} > 0.50$ , rather than the neutral  $Ga_2Cl_6$  symmetry  $D_{3d}$ . This was determined by polarised Raman spectroscopy, such that the depolarization intensity;  $\rho$  is the ratio between peak intensity in the perpendicular/parallel modes that indicated symmetric species present when  $\rho = I_{perp}/I_{parr} < 0.75$  i.e. totally symmetric vibrations generate polarised bands.<sup>4,352</sup> thus molecular species which a centre of inversion is present it gives rise to depolarised bands  $\rho = 0.75$ .

The tetrachlorogallate anion,  $[GaCl_4]^-$  has  $Ga-Cl^t$  stretches ( $a_1 + t_2$ ) at 346  $cm^{-1}$  and 386  $cm^{-1}$ , respectively.<sup>413</sup> Within the phosphine chalcogenide donor system, there are also considerations for the  $P=S$  and  $P=Se$  contributions. It is expected that  $\nu(P=Se)$  uncoordinated to give rise to bands from 473-577  $cm^{-1}$ , however, upon complexation to transition metals such as Co, Ni and Zn with trimethylphosphine selenide this vibrational mode is observed at 408-414  $cm^{-1}$ .<sup>414,415</sup> It is expected to observe  $\nu(P=S)$  uncoordinated from 635<sub>Ph3P=S</sub>-539<sub>iPr3P=S</sub>  $cm^{-1}$  hence in this work no uncoordinated  $P_{888}S$  or  $P_{888}Se$  is observed. The position of  $P=S$  upon may indicate the relative amount of  $S(p\pi)-P(d\pi)$  bonding. Any such multiple bonding will tend to delocalize sulphur electrons causing a decrease of the basicity of the sulphur while

increasing the frequency of P=S vibration upon complex formation to a transition metal such as Cu(I), polarization of the electrons of the sulphur donor atom is expected to cause a decrease in the S(p $\pi$ ) -P(d $\pi$ ) bonding and consequently a decrease in  $\sim$ (P=S). This decrease should be greatest for a ligand possessing the greatest amount of multiple bonding in the un-complexed ligand.<sup>416–418</sup>

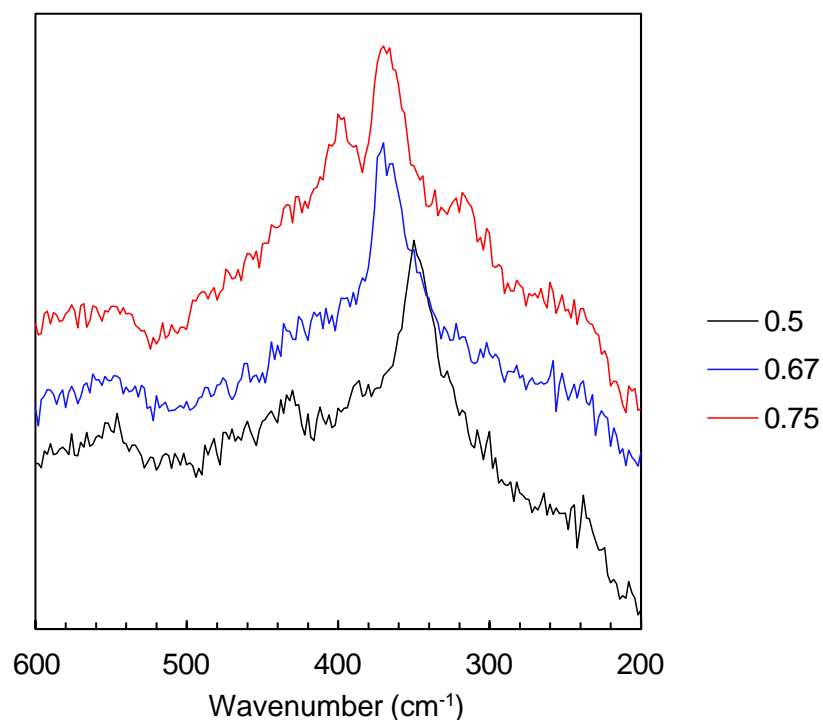


**Figure 4-22**-Stacked plot of Raman spectra of P<sub>888</sub>S-GaCl<sub>3</sub> LCCs. (top-bottom)  $\chi_{\text{GaCl}_3}$  = 0.75, 0.67, 0.60, 0.50.

**Table 4-9**-Raman stretching frequencies of P<sub>888</sub>E-GaCl<sub>3</sub> LCCs.

	Frequency (cm <sup>-1</sup> )
P <sub>888</sub> O-GaCl <sub>3</sub> $\chi_{\text{GaCl}_3}$ = 0.50	370
P <sub>888</sub> S-GaCl <sub>3</sub> $\chi_{\text{GaCl}_3}$ = 0.50	350
P <sub>888</sub> S-GaCl <sub>3</sub> $\chi_{\text{GaCl}_3}$ = 0.67	370
P <sub>888</sub> S-GaCl <sub>3</sub> $\chi_{\text{GaCl}_3}$ = 0.75	366, 400
P <sub>888</sub> Se-GaCl <sub>3</sub> $\chi_{\text{GaCl}_3}$ = 0.50	374
P <sub>888</sub> Se-GaCl <sub>3</sub> $\chi_{\text{GaCl}_3}$ = 0.60	372
P <sub>888</sub> Se-GaCl <sub>3</sub> $\chi_{\text{GaCl}_3}$ = 0.67	374
P <sub>888</sub> Se-GaCl <sub>3</sub> $\chi_{\text{GaCl}_3}$ = 0.75	376

As shown in Figure 4-22, increasing the  $\chi_{\text{GaCl}_3}$  from 0.50 to 0.75 the main observable peak shifts from  $350 \text{ cm}^{-1}$   $\chi_{\text{GaCl}_3}$  to  $370 \text{ cm}^{-1}$  when  $\chi_{\text{GaCl}_3} > 0.67$ . When  $\chi_{\text{GaCl}_3} = 0.75$  there is multiple bands now present, the highest of which arising at  $398 \text{ cm}^{-1}$ . As discussed there are multiple species that can arise within this area of the Raman spectrum including the anionic chlorogallates and bands due to the  $\text{P}_{888}\text{E}$  adducts as seen in Table 4-10.

Unlike those observed in the chloroaluminate systems there is no distinct peaks that could be assigned to the neutral adducts.<sup>382</sup> The location of the Ga-E stretches in molecular adducts studied by Reid *et al.* have found that they may be located within what was primarily assigned to the Ga-Cl<sup>t</sup> stretches of the anionic contributions; Characteristic Raman shifts are displayed in Table 4-10. It is shown that previous assignments of anionic species Ga-Cl<sup>t</sup> stretches between  $349\text{-}392 \text{ cm}^{-1}$  overlap with those of the neutral adducts, hence it can only be established that Ga-Cl stretches are present and not fully assign them to the Ga-Cl<sup>t</sup> stretching frequencies of either species, however, NMR indicates that these bands are statistically more likely to arise from the neutral species specifically at  $\chi_{\text{GaCl}_3} > 0.50$  LCCs. The Raman spectra recorded have a weak resolution, hence a greater amount of averaging is observed hence the more dominant species will prevail. Unfortunately, the Raman spectrum does not exhibit discrete and assignable bands and has created limitations in the speciation data that can be elucidated.

**Table 4-10-** Characteristic Raman shifts of gallium chloride molecular adducts and ionic species.

Molecular adduct	Raman shift, $\text{cm}^{-1}$	Literature
$[\text{GaCl}_3(\text{SeMe}_2)]$	371 Ga-Cl	Reid <sup>413</sup>
$[(\text{GaCl}_3)_2\{\text{I-MeS}(\text{CH}_2)_2\text{SMe}\}]$	356 (s), 346 (m) Ga-Cl	
$[\text{GaCl}_3(\text{Me}_3\text{PO})]$	1100(br) P=O 387, 358 Ga-Cl	Reid <sup>419</sup>
$[\text{GaCl}_3(\text{Ph}_3\text{P})]$	387 s, 347 (m) Ga-Cl	
Ionic species	Raman shift, $\text{cm}^{-1}$	Literature
$[\text{GaCl}_4]^-$	386, 346 Ga-Cl	Wicelinski <sup>352</sup>
$[\text{Ga}_2\text{Cl}_7]^-$	365, 414 Ga-Cl	
$[\text{Ga}_3\text{Cl}_{10}]^-$	392 Ga-Cl	
$[\text{Ga}(\text{DMSO})_6][\text{GaCl}_4]_3$	498 (m), 381(m), 347 (vs), 314 (m), 263 (w)	Carty <sup>420</sup>



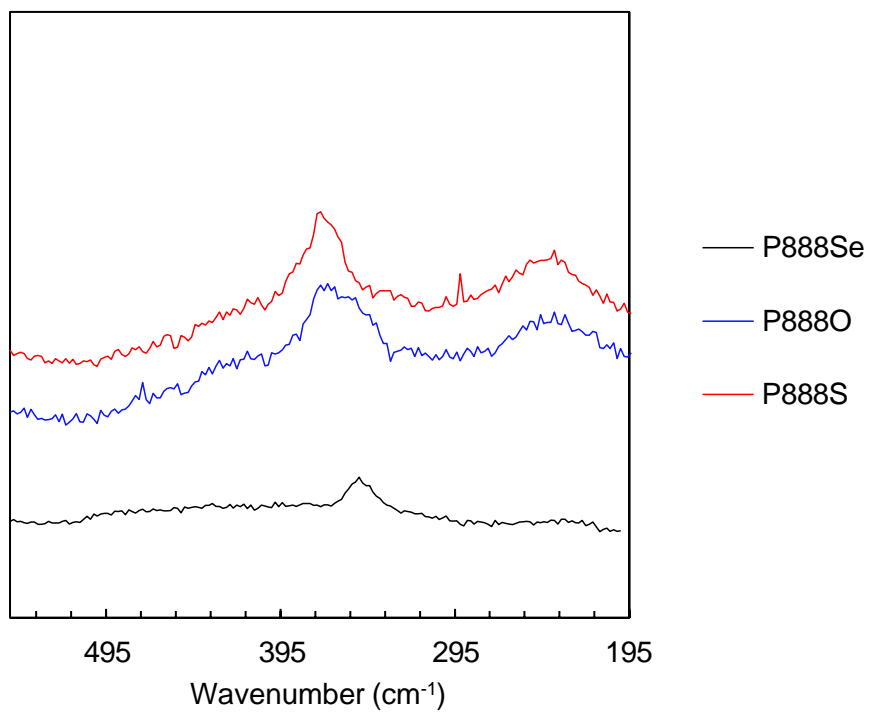


**Figure 4-23-** Stacked plot of Raman spectra of P<sub>888</sub>E-GaCl<sub>3</sub> LCCs.  $\chi_{\text{GaCl}_3}$  = 0.50.

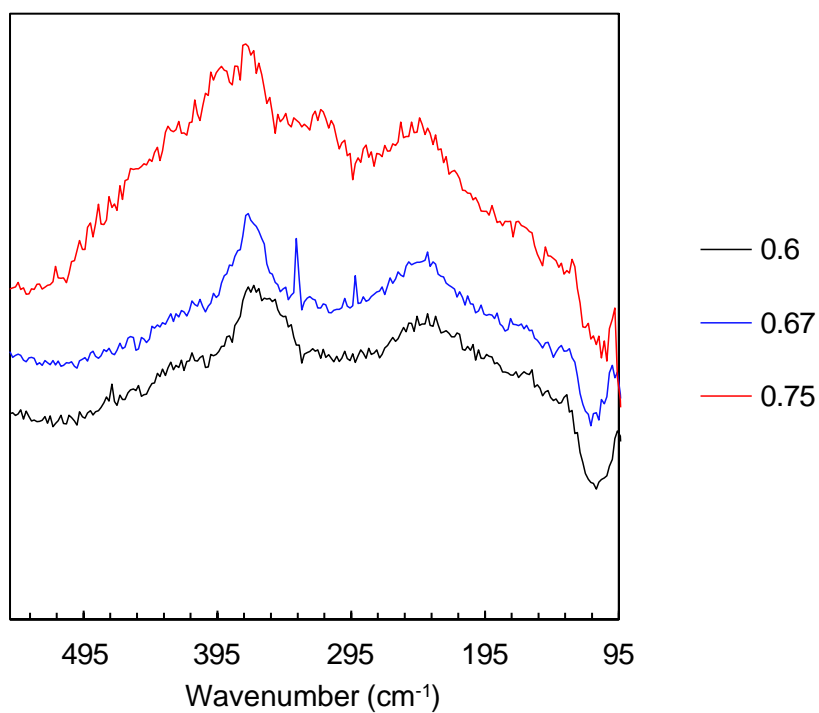


**Figure 4-24-** Stacked plot of Raman spectra of P<sub>888</sub>Se-GaCl<sub>3</sub> LCCs. (top-bottom)  $\chi_{\text{GaCl}_3}$  = 0.75, 0.67, 0.60, 0.50.

#### 4.2.1.6 Infrared spectroscopy

Infrared spectroscopy of the chlorogallate liquid coordination complex systems does not contain any Ga-Cl or Ga-E bands, however, it has confirmed that the ligand species remains intact and no water contamination has occurred hence no hydroxyl band is present. All Infrared spectra are available in the supplementary data. The lower limit of the ATIR spectrometer means that the stretching frequencies of the  $P_{888}Se$  are unavailable. The oligomeric species are more Lewis acidic in character, hence the donor ligands coordinated to these species are more tightly bound than their monomeric and neutral adduct counterparts. Infrared spectroscopy of the  $P_{888}S$  LCC systems indicated a shift in the P=S band there is a decrease in wavenumber within increasing  $\chi_{GaCl_3}$ . This increase as shown Table 4-1 and Figure 4-25 confirms the presence of more Lewis acid species at higher  $\chi_{GaCl_3}$ .

**Table 4-11-** Infrared stretching frequencies of  $P_{888}S-GaCl_3$ .

$P_{888}S-GaCl_3$	P=S wavenumber ( $cm^{-1}$ )
$\chi_{GaCl_3} = 0$	599
$\chi_{GaCl_3} = 0.50$	548
$\chi_{GaCl_3} = 0.60$	543
$\chi_{GaCl_3} = 0.67$	541
$\chi_{GaCl_3} = 0.75$	541

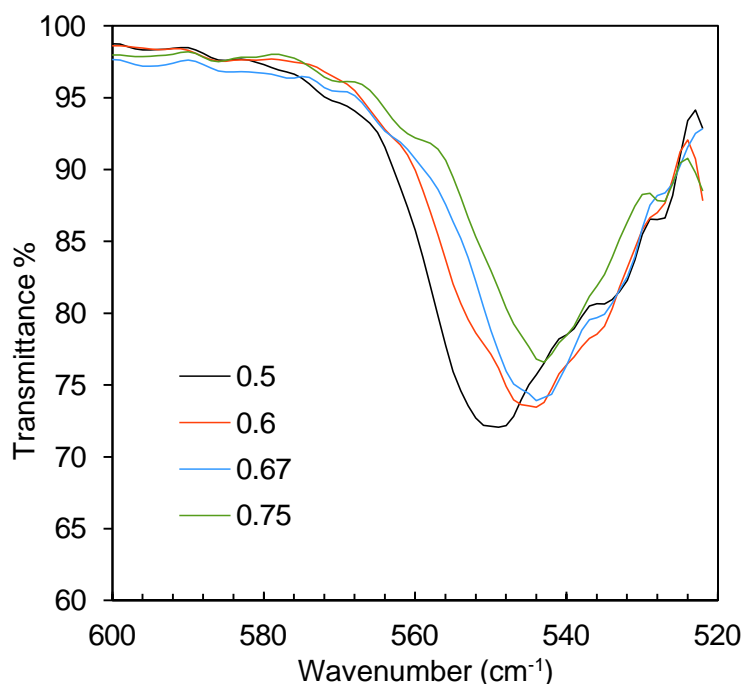


**Figure 4-25-**Expanded Infrared spectra of  $P_{888}S-GaCl_3$  LCCs.

#### 4.2.1.7 Extended X-ray fine structure

Extended X-ray absorption fine structure spectroscopy, EXAFS is a powerful spectroscopic technique that has proven to be a useful tool in confirming speciation trends in chlorometallate ionic liquids.<sup>354</sup> The technique itself is based upon the excitation of a core shell electron of an absorber atom; this excitation energy is unique to the central atom under investigation. Upon excitation, a photoelectron is ejected from the atom and the interactions between the atom and its neighbours are observable as a function of energy and transmission / fluorescence, hence providing information about the oxidation state, geometry and local environment of the atom under investigation. Elucidation of this information from the raw spectra can be difficult and in the next few pages aim to give a brief overview of this technique from a chemist's perspective and a practical approach to data analysis.<sup>388</sup>

##### 4.2.1.7.1 Application of EXAFS to speciation determination of chlorogallate liquid coordination complexes

The key aim of the study was determination of the species presents within gallium (III) chloride liquid coordination complexes and confirmation of the Ga-Cl and Ga-donor atom bonds. The main species which requires elucidation is the dimeric species formed in the neutral aspect of the equilibrium. As of yet it has not been determined as to whether the chlorine or the donor atom of the ligand acts as the bridging atom.

A variety of LCCs were examined using EXAFS based on the LCCs reported by Coleman *et al.* including mixtures of GaCl<sub>3</sub> with acetamide (AcA), dimethylacetamide (DMA), urea (Ur), thiourea (SUr), trioctylphosphine (P<sub>888</sub>), trioctylphosphine oxide (P<sub>888</sub>O) and trioctylphosphine selenide (P<sub>888</sub>Se). EXAFS measurements were completed at the Diamond light source, UK beamline B18 and I20. Liquid samples were protected from atmospheric moisture by sealing them in Kapton cells as detailed in 4.5.3.

Using the Demeter software package, initially an ambitious attempt was made to quantify the equilibrium within the systems *via* parameterising the amplitude factor of the neutral vs ionic species, however; the chaotic but similar nature of the systems bonding nodes resulted in the fit being less conclusive than initially hoped.<sup>396</sup>

Instead a data-driven approach was taken with the contributions of each path of neutral vs ionic being identical in bond contributions *i.e.* each side of the equilibrium will contain equal Ga-Cl and Ga-E contributions which are quantified *via* coordination number, N and a non-integer used to ensure the Ga centre has a

maximum coordination number of 4. Further to this the Ga-Ga contributions are apparent within the data hence they were also taken into account.

Fits occurred in K-space up to  $K_{\max}$  19.9  $\text{cm}^{-1}$  due to the high quality of the data recorded. This expanded fit and corroboration of the bond distances from known crystal structures,<sup>419,421,422</sup> crystal structures prepared (SUr-GaCl<sub>3</sub>) and the chemical knowledge determined from NMR alluding to a dynamic equilibria means that good fits are achieved when both neutral and ionic species are quantified. Specifically, observation of oligomeric species in the system evidently *via* the need for bridging chlorine to be accounted for within the fit.

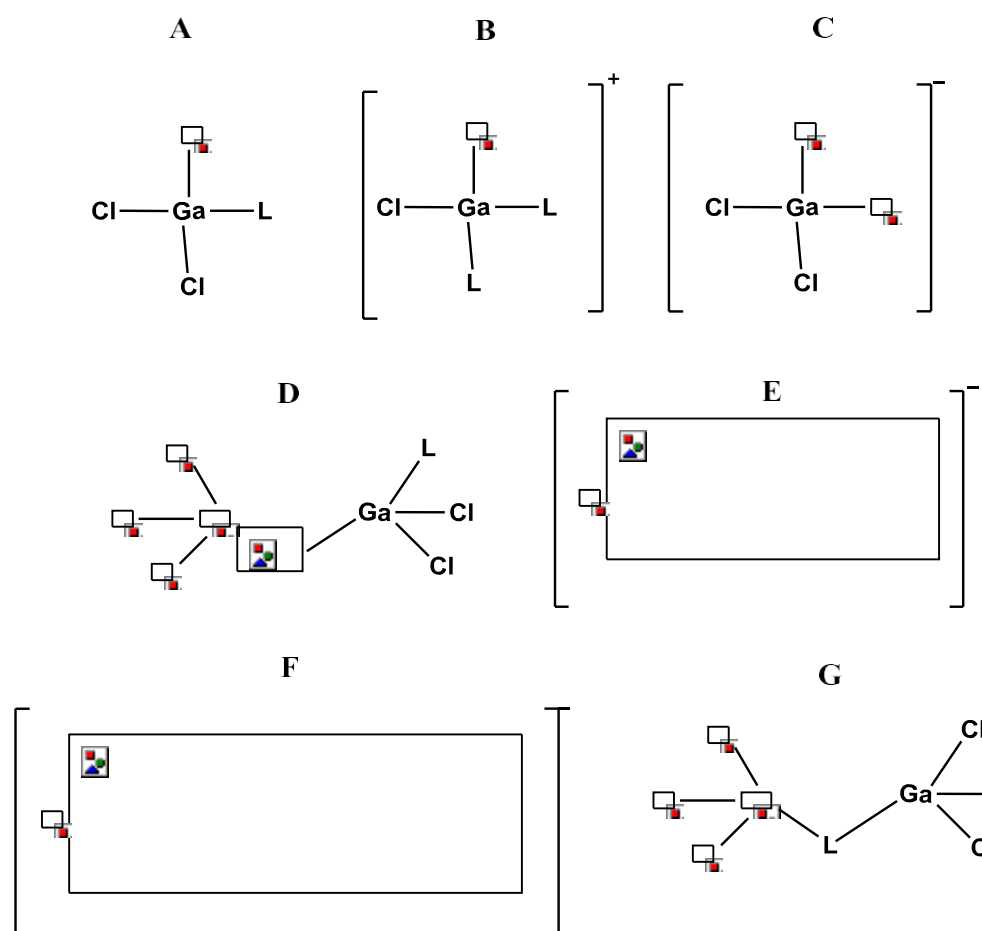


**Figure 4-26-** Possible species within chlorogallate LCCs.

Furthermore, there was initially ambiguity in regards to the neutral oligomeric species and whether the bridging atom would be chlorine or the donor atom of the ligand as shown in Figure 4-26(D & G). It was evident, that a trial and error approach requiring combinations of species depicted in Figure 4-26 would elucidate the preferred species. The best fits in all cases where those, in which species G were excluded. This provides strong evidence that all bridging atoms, in both neutral and

ionic species, are chlorine atoms. In summary the species used within fits were as follows;  $\chi_{\text{GaCl}_3} = 0.50$  (A, B, C),  $\chi_{\text{GaCl}_3} = 0.60$  (A, B, D, E),  $\chi_{\text{GaCl}_3} = 0.67$  (B, D, E, F). It was evident that as  $\chi_{\text{GaCl}_3}$  increased the data quality decreased as shown in Figure 4-28, further indicating a greater disorder present; this is also expected with the liquid nature of the samples.<sup>388</sup> Comparing fits of the  $\text{P}_{888}\text{O}$  and  $\text{P}_{888}\text{Se}$  LCCs at  $\chi_{\text{GaCl}_3} = 0.50$  it is observed that the Ga-E bond increases from 1.861 to 2.523 Å; furthermore, this increase in bond length observed in the EXAFS spectra confirms the donor ligand coordination is present as greater deviation from the Ga-Cl bond length, ca. 2.17 Å is observed.

As expected, the Ga-Se bond length is greater than that of the Ga-O counterpart; this is due to the increased size and poorer orbital overlap of the selenium atom with gallium and the bond strength of the Ga-Se bond being lower hence a more rapid exchange between species. The species in question were initially thought to be significantly bias, if not fully neutral, however, if the ionic or neutral species were exclusively modelled the fit quality declined furthermore as  $\chi_{\text{GaCl}_3}$  increased the oligomeric species and bridging chlorine species was essential to a conclusive fit. Hence it can be concluded that at higher at  $\chi_{\text{GaCl}_3}$  there are both ionic and neutral species present that as the chalcogenides increase in size and become weaker Lewis bases, exchange increases, hence the NMR itself is inconclusive at determining the speciation present. Instead, a variety of analytical techniques must be utilised to give a full and in-depth knowledge of the systems under investigations due to their complex nature. Furthermore, the exchange rate between species at high at  $\chi_{\text{GaCl}_3}$  is visibly faster with larger chalcogenide donor atoms.

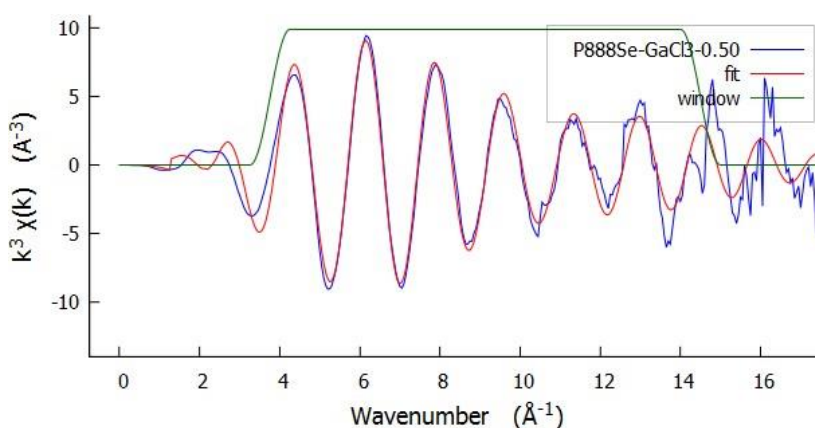


**Figure 4-27-** EXAFS fit for  $\text{P}_{888}\text{Se-GaCl}_3$   $\chi_{\text{GaCl}_3} = 0.50$  in k-space.

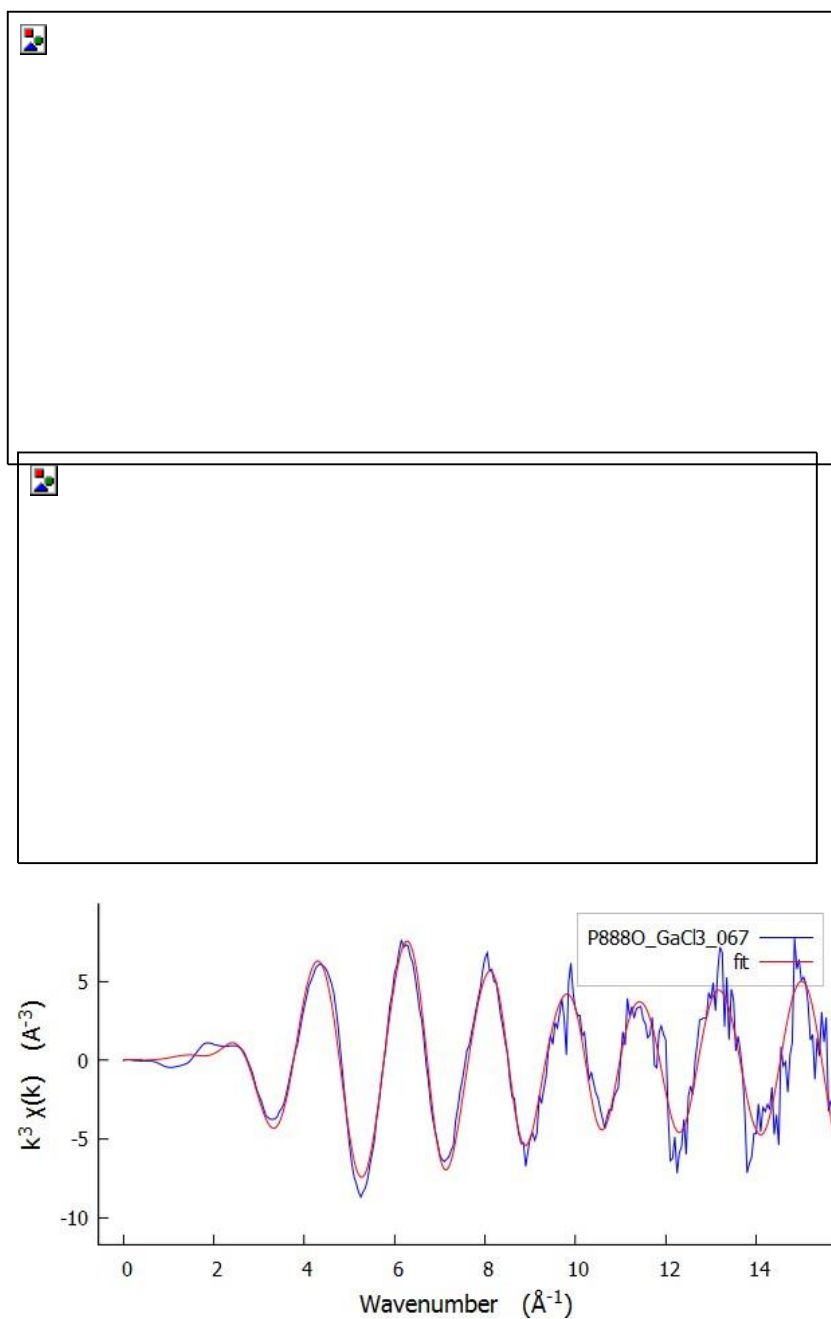


**Figure 4-28**-EXAFS fits for P<sub>888</sub>O-GaCl<sub>3</sub> (top-bottom)  $\chi_{\text{GaCl}_3} = 0.50, 0.60, 0.67$  in k-space.

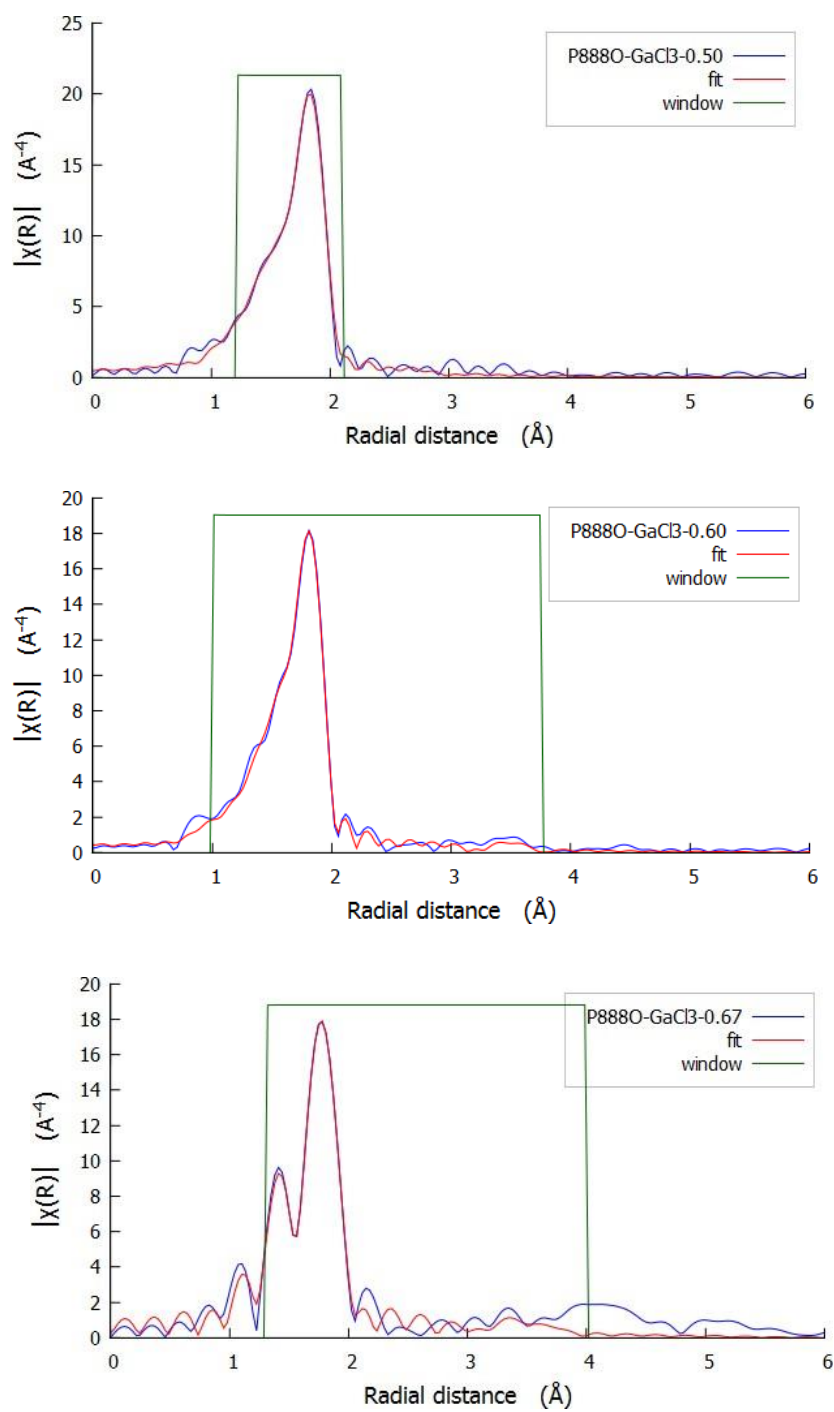


**Figure 4-29-** EXAFS fit for  $\text{P}_{888}\text{O-GaCl}_3$  (top-bottom)  $\chi_{\text{GaCl}_3} = 0.50, 0.60, 0.67$  in R-space.

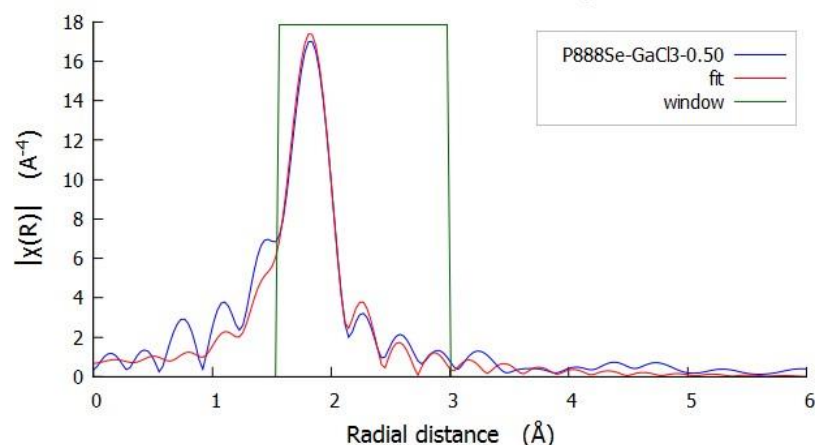


**Figure 4-30-** EXAFS fit for  $\text{P}_{888}\text{Se-GaCl}_3$   $\chi_{\text{GaCl}_3} = 0.50$  in R-space

Naturally, as  $\chi_{\text{GaCl}_3}$  increases from 0.50 to 0.67 as shown in Figure 4-29 the fitting window widens; this is to account for the increasing path lengths of the bridging species fitted and the Ga-Ga interactions. Furthermore, as previously discussed, the number of independent points is related to the fitting window which is dependent on data quality along with the effective path length of the species modelled. With increasing  $\chi_{\text{GaCl}_3}$  it is expected that the formation of oligomeric species will occur hence the bridging chlorine and gallium-gallium interactions must be accounted for, causing the fit window to be extended from 2.1 Å to 4.0 Å. This also allows for a greater number of paths to be modelled and a better fit integrity in regards to number of independent points vs. variables. The choices of fitting window in all cases begin and end on a spectral node.

As shown in Table 4-12 the statistics of the fit for  $\text{P}_{888}\text{O-GaCl}_3$  LCCs in the molar ratio  $\chi_{\text{GaCl}_3} = 0.50$  -0.67. The R-factor for  $\chi_{\text{GaCl}_3} = 0.50$  and  $\chi_{\text{GaCl}_3} = 0.60$  remains approximately 0.02, which is the desired value indicating the fit, interpretation and model are adequate. The R-factor for  $\chi_{\text{GaCl}_3} = 0.67$  is higher than the desired 0.02 at 0.053 however this does not necessarily indicate the model is flawed but can also be due to the lower data quality which is apparent in comparison to spectra the in Figure 4-29. The model for  $\chi_{\text{GaCl}_3} = 0.67$  is broadly correct and deemed adequate especially due to the liquid nature of the sample, the number of possible species present and increased noise.



**Table 4-12-** EXAFS fitting statistics for P<sub>888</sub>O-GaCl<sub>3</sub> LCCs.

P <sub>888</sub> O-GaCl <sub>3</sub>	$\chi_{\text{GaCl}_3} = 0.50$	$\chi_{\text{GaCl}_3} = 0.60$	$\chi_{\text{GaCl}_3} = 0.67$
Independent points	9.3515625	29.6376953	21.5800781
Number of variables	6	12	10
Chi-square	401926114.2528110	2610159962.5667877	83293333.8034178
Reduced chi-square	119922010.7793935	132915798.9789840	7192812.7689914
R-factor	0.0237798	0.0176012	0.0535626

This behaviour was consistent throughout a variety of donor ligands all of which are listed within the appendix. In all cases a chloride bridge resulted in better fits and the donor atoms resulted in poorer fits if regarded as a bridging species. Hence EXAFS confirms the nature of the neutral adducts formed and the presence of oligomeric species *via* the Ga-Ga interaction observed.

#### 4.2.1.8 Conductivity measurements

Conductivity is a useful tool in determining the ionic vs neutral composition of the LCCs *via* the availability of the charge carrying species. In order to determine the variation of speciation as a function of conductivity, a cross section of samples were utilised as described in Table 4-13.<sup>423</sup> The electrochemistry of chlorogallate and chloroaluminate ionic liquid systems have been well documented with the aprotic acid-base equilibrium well understood in such the [Al<sub>2</sub>Cl<sub>7</sub>]<sup>-</sup> is the acid and the Cl<sup>-</sup> anion is the base. Thus in ionic liquids the concentration of charge carrying species is known, however, in LCCs there is ionic and neutral contributions which must be accounted for; the position temperature dependent equilibria is unknown.<sup>424–426</sup> Conductivity in its simplistic form is dependent on the viscosity and an intrinsic constant of the solution as described in Equation 4-13.

**Equation 4-13**

$$\Lambda\eta = k$$

Where:

$\Lambda$  = the conductivity of the sample

$\eta$  = the viscosity of the sample

k = a constant

From the NMR results described in Table 4-13, particularly one would expect increasing deviation from the behaviour of the KCl solution (a standard for conductivity), as the molecular weight of chalcogenide increases.

The conductivity was found to increase with increasing  $\chi_{\text{GaCl}_3}$  in both  $\text{P}_{888}\text{O}$  and  $\text{P}_{888}\text{Se}$  systems indicating a greater number of charge carrying species is present. At  $\chi_{\text{GaCl}_3} = 0.50$  the  $\text{P}_{888}\text{O-GaCl}_3$  exhibits approximately double the conductivity of the  $\text{P}_{888}\text{Se-GaCl}_3$  system hence contains approximately double the number of charge carriers. This is in agreement with the NMR data that suggests that a greater number of neutral species are formed as the donor ligand becomes softer in character. At  $\chi_{\text{GaCl}_3} = 0.75$  the  $\text{P}_{888}\text{O-GaCl}_3$  exhibits a similar conductivity to the  $\text{P}_{888}\text{Se-GaCl}_3$  system it is postulated that the rate of exchange between the ionic and neutral species increases with increasing  $\chi_{\text{GaCl}_3}$  hence the similar despite donor strength is unsurprising as the equilibrium is significantly more rapid in the  $\text{P}_{888}\text{Se}$  system as demonstrate via the dynamic NMR studies carried out and the observed averaging of  $^{31}\text{P}$  peaks at ambient temperature.

**Table 4-13-**Table of conductivity of LCC species.

	$\text{P}_{888}\text{O-GaCl}_3$		$\text{P}_{888}\text{Se-GaCl}_3$	
$\chi_{\text{GaCl}_3}$	0.5	0.75	0.5	0.75
Conductivity Measurement	Conductivity $\mu\text{S/cm}$			
1	62.78	226.0	27.82	198.4
2	61.65	216.5	28.21	200.3
3	62.04	213.6	27.78	198.8
4	61.64	207.2	28.21	198.4
5	61.98	188.0	28.27	198.0
6	61.91	182.6	28.27	198.3
Average	62.00	205.7	28.09	198.7
Standard deviation	0.417	16.97	0.229	0.825

Naturally, a Walden plot is something that is considered when quantifying the conductivity of a species, however, within literature there are reports of chloroaluminate molten salts and ionic liquids (most commonly with the addition of alkali metal halides) but as of yet no reports of LCCs electrochemical data. Walden

plots explore the relationship between  $\log [\text{conductivity (Scm}^{-1}\text{mol}^{-1})]$  as a function of  $\log [1 / \text{viscosity (poise}^{-1})]$  and is often used as a method of determining more or less ionic liquids specifically for battery applications. A key factor in this plot is the per mole quantification; the use of a conventional dip probe in neat solution along with the unknown number of charge carrying species present means that this term cannot be truly quantified. Already the spectroscopic techniques utilised have not elucidated the position of equilibrium hence an approximation cannot be made on the number of charge carrying species.

#### 4.2.1.9 Speciation and explanations

Hogg found within chloroaluminate systems that with decreasing donor hardness the prevalence of the neutral species in the equilibria is greater than the ionic species. Within the chlorogallate systems, density, viscosity and ambient temperature NMR studies, this was also found however, use of other spectroscopic and physicochemical techniques have found that the dominance of the neutral species is still present however, not to the extent previously seen in chloroaluminate systems.

Cooling NMR studies, Raman spectroscopy and EXAFS have found that even at higher  $\chi_{\text{GaCl}_3}$  the ionic contribution is significant. Cooling NMR studies found that with slowing of the rates of exchange the dynamic averaged spectra measured at ambient temperature that was initially assigned as the neutral species resolved into two peaks in the  $^{31}\text{P}$  spectra. The need to use cooling NMR measurements when the  $\text{P}_{888}\text{S}$  and  $\text{P}_{888}\text{Se}$  ligands were used, alluded to the fact that with decreasing donor hardness the rate of exchange between the species increases. The Raman spectra were found to be ambiguous with both neutral and ionic species resulting in similar bands hence a specific determination could not be made. EXAFS spectroscopy determined that without consideration of the ionic component good fits could not be made. Further to this, EXAFS found that the bridging species at  $\chi_{\text{GaCl}_3} > 0.50$ , bridge *via* the chloride species and not *via* the ligand species. This is a somewhat peculiar preference towards a non-symmetric species.

Conductivity measurements also confirmed that in hard donor systems the bias lies more towards the ionic component than a softer species in which the neutral component is bias. The rate of exchange is found to increase with increasing  $\chi_{\text{GaCl}_3}$  and increasing donor softness, hence the conductivity of  $\text{P}_{888}\text{Se}$  solutions increases to a comparable conductivity of  $\text{P}_{888}\text{O}$  at  $\chi_{\text{GaCl}_3} = 0.75$ . Further indicating, the presence of ionic species at higher  $\chi_{\text{GaCl}_3}$ .

**Table 4-14-** Predicted speciation of chlorogallate liquid coordination complexes.

	LCC
$\chi_{\text{MCl}_3}$	$2\text{MCl}_3 + 2\text{L}$
0.50	$[\text{MCl}_2\text{L}_2][\text{MCl}_4] \rightleftharpoons 2[\text{MCl}_3\text{L}]$
	$\downarrow \quad \quad \quad +\text{MCl}_3$
0.60	$[\text{MCl}_2\text{L}_2][\text{M}_2\text{Cl}_7] \rightleftharpoons [\text{MCl}_3\text{L}] + [\text{M}_2\text{Cl}_6\text{L}]$
	$\downarrow \quad \quad \quad +\text{MCl}_3$
0.67	$[\text{MCl}_2\text{L}_2][\text{M}_3\text{Cl}_{10}] \rightleftharpoons 2[\text{M}_2\text{Cl}_6\text{L}]$
0.75	Undetermined polymeric species

## 4.2.2 Chloroindate liquid coordination complexes

As discussed in section 4.1.2, chloroindate based ionic liquids have been of great interest in regards to their Lewis acid properties, application in catalysis and for the synthesis of inorganic compounds. Ionic liquids, however, carry their own drawbacks with the purity often under question due to their elaborate organic cations. Incorporating the  $\text{InCl}_3$  species of interest into LCCs will aid in avoiding such impurities.

### 4.2.2.1 Synthesis and observations

Initially, LCCs of equimolar quantities of  $\text{InCl}_3$  and  $\text{P}_{888}\text{E}$  ( $\text{E} = \text{O}, \text{S}, \text{Se}$ ) were synthesised and characterised according to those reported by Coleman *et al.*<sup>22</sup> The  $\chi_{\text{MClx}} = 0.50$  synthesised resulted in formation of a small amount of precipitate. Upon PXRD analysis of the precipitate from  $\text{P}_{888}\text{Se-InCl}_3$   $\chi_{\text{InCl}_3} = 0.50$  it was found to not match any reported PXRD diffraction patterns of  $\text{InCl}_3$ , hence it can be deduced that it is not starting material. Subsequently, sub-stoichiometric mixtures of  $\text{InCl}_3$  and  $\text{P}_{888}\text{E}$  ( $\chi_{\text{InCl}_3} < 0.50$ ) were synthesised to explore speciation. All samples were prepared with  $\chi_{\text{InCl}_3} < 0.50$  resulted in the formation of colourless liquids.

**Table 4-15-** Combinations of  $\text{InCl}_3$  and  $\text{P}_{888}\text{E}$  ( $\text{E}=\text{O}, \text{S}, \text{Se}$ ) ligands that formed LCCs at given  $\chi_{\text{MClx}}$  values.

$\text{MCl}_x$	$\chi_{\text{MClx}}$	$\text{P}_{888}\text{O}$	$\text{P}_{888}\text{S}$	$\text{P}_{888}\text{Se}$
$\text{InCl}_3$	0.25	colourless liquid	colourless liquid	colourless liquid
	0.33	colourless liquid	colourless liquid	colourless liquid
	0.40	colourless liquid	colourless liquid	colourless liquid
	0.50	colourless liquid <sup>a</sup>	colourless liquid <sup>b</sup>	colourless liquid <sup>b</sup>

<sup>a</sup> Previously reported. <sup>b</sup> A small amount of precipitate present.

### 4.2.2.2 Density measurements

Densities were measured for  $\text{P}_{888}\text{E-InCl}_3$   $\chi_{\text{InCl}_3} = 0.25, 0.33, 0.40$  each with a variety of donor atoms;  $\text{E} = \text{O}, \text{S}, \text{Se}$ . All densities were studied as a function of temperature.  $\text{P}_{888}\text{E-InCl}_3$   $\chi_{\text{InCl}_3} = 0.50$  were omitted from measurement due to the presence of precipitate. An identical measurement and experimental methodology to that utilised in the chlorogallate LCCs was adopted. For all measured LCCs, linear density vs. temperature relationships were found, typically with very good correlations ( $R^2 > 0.99$ ), as summarised in Table 4-4. This is in agreement with earlier reports on ionic liquids, halometallate and non-halometallate alike.<sup>318,399,400</sup>

$\text{AlCl}_3$  complexes were in general less dense than their  $\text{GaCl}_3$  counterparts due to the higher density of  $\text{GaCl}_3$  over  $\text{AlCl}_3$ .  $\text{InCl}_3$  complexes are less comparable as the highest  $\chi_{\text{InCl}_3}$  synthesised without precipitate was  $\chi_{\text{InCl}_3} = 0.40$  however, in relation to the  $\chi_{\text{MCl}_3} = 0.50$  systems of aluminium and gallium the indium solution sit in-between. At 343 K, for  $\text{P}_{888}\text{S}$  the density trend is as follows  $\text{AlCl}_3$  ( $0.9853 \text{ g/cm}^3$ )  $< \text{InCl}_3$  ( $1.0547 \text{ g/cm}^3$ )  $< \text{GaCl}_3$  ( $1.071 \text{ g/cm}^3$ ).

In contrast, changing the oxygen atom for a sulphur atom and further to a selenium atom ( $\text{P}_{888}\text{O} > \text{P}_{888}\text{S} > \text{P}_{888}\text{Se}$ ) only marginally increased the density of the complex. Comparing sulphur and oxygen the most apparent difference between the species is the mass each species being 32 and 16 *au.* respectively. As discussed in 4.2.1.2 this change in mass does not affect the size of the donor ligand.

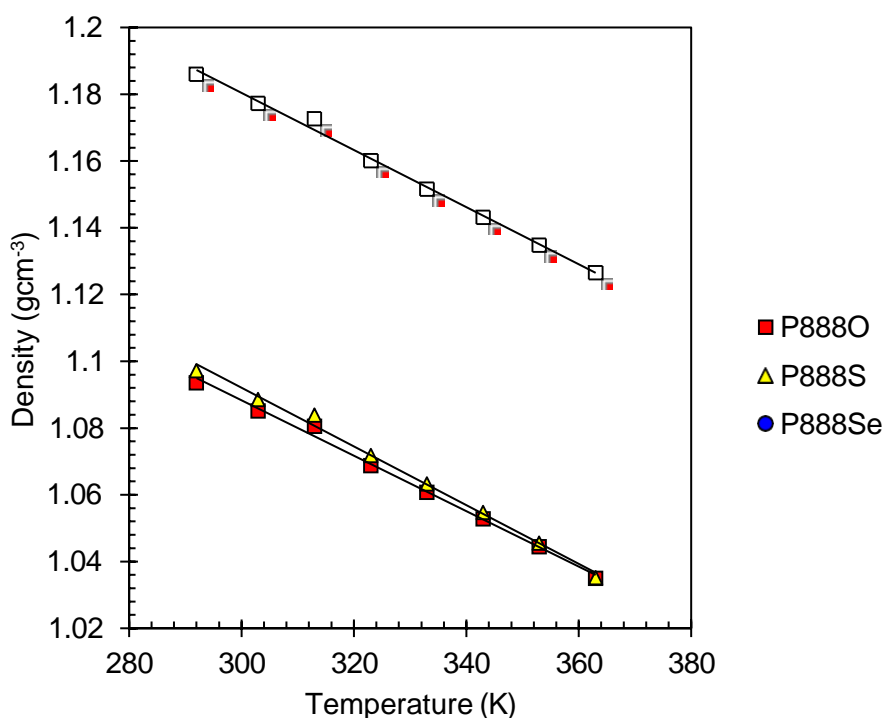


Figure 4-31- Density plot of  $\text{P}_{888}\text{E}-\text{InCl}_3$   $\chi_{\text{InCl}_3} = 0.40$ .

#### 4.2.2.3 Viscosity measurements

In parallel with the density studies, viscosities were measured for  $\text{InCl}_3$ -LCCs with  $\text{P}_{888}\text{E}$  ( $\text{E} = \text{O}, \text{S}, \text{Se}$ ) donor ligands in an identical methodology to that utilised in the chlorogallate LCC systems previously discussed. Viscosities were measured over a temperature range at 3 angles,  $15^\circ$ ,  $20^\circ$ ,  $30^\circ$ ; the dynamic viscosities were averaged and the temperature-viscosity profile were plotted and fitted using a Vogel-Fulcher-Tammann (VFT) (Equation 4-12)<sup>402,403</sup> The  $\text{P}_{888}\text{E}-\text{InCl}_3$   $\chi_{\text{InCl}_3} = 0.50$  was

again omitted from measurement due to the fine precipitate present in all donor ligands tested.

The VFT fitting parameters are listed in Table 4-16  $P_{888}E-InCl_3$  and plots are shown in Figure 4-32 ( $P_{888}O$ ), Figure 4-33 ( $P_{888}S$ ), and Figure 4-34 ( $P_{888}Se$ ). In contrast to density, it is clear in Figure 4-35 that the donating atom can have a large effect on the viscosity of the LCCs at low/room temperatures and there is a variation with the chlorometallate species also, specifically in comparison to the chloroaluminate analogues analysed by Hogg *et al.*<sup>382</sup>, and chlorogallates synthesised earlier in this work, it is noted that the similar trends in regards to decreased donor hardness resulting in subsequent increases in viscosity not mirrored in the chloroindate LCCs. The viscosity of the  $P_{888}O-InCl_3$  system is significantly higher than that of  $P_{888}S-InCl_3$  and  $P_{888}Se-InCl_3$ , which exhibit very similar viscosities. Generally, as observed in the  $P_{888}E-GaCl_3$  systems as  $\chi_{MCl_3}$  increases, viscosity increases however, in the  $P_{888}O-InCl_3$  system this is not observed instead the highest viscosity is seen in  $\chi_{MCl_3} = 0.33$ . This may indicate a significant shift towards neutral adducts and specifically those which may be larger in size/coordination number.

**Table 4-16**-VFT fit parameters for  $P_{888}E-InCl_3$ .

VFT fit according to $Y=10^{A+(B/(T-T_0))}$	$P_{888}O-InCl_3$		
	0.25	0.33	0.4
A	-2.96974	-0.59907	-0.20085
B	1162.16883	428.75844	290.09757
$T_0$	107.63185	189.11649	215.3946
	$P_{888}S-InCl_3$		
	0.25	0.33	0.4
A	-1.79896	-1.51084	-1.86665
B	557.67212	485.93664	642.22951
$T_0$	167.27713	183.49793	162.86655
	$P_{888}Se-InCl_3$		
	0.25	0.33	0.4
A	-1.48922	-1.40236	-1.76866
B	505.73152	493.58178	627.85347
$T_0$	174.48698	183.59729	168.77853

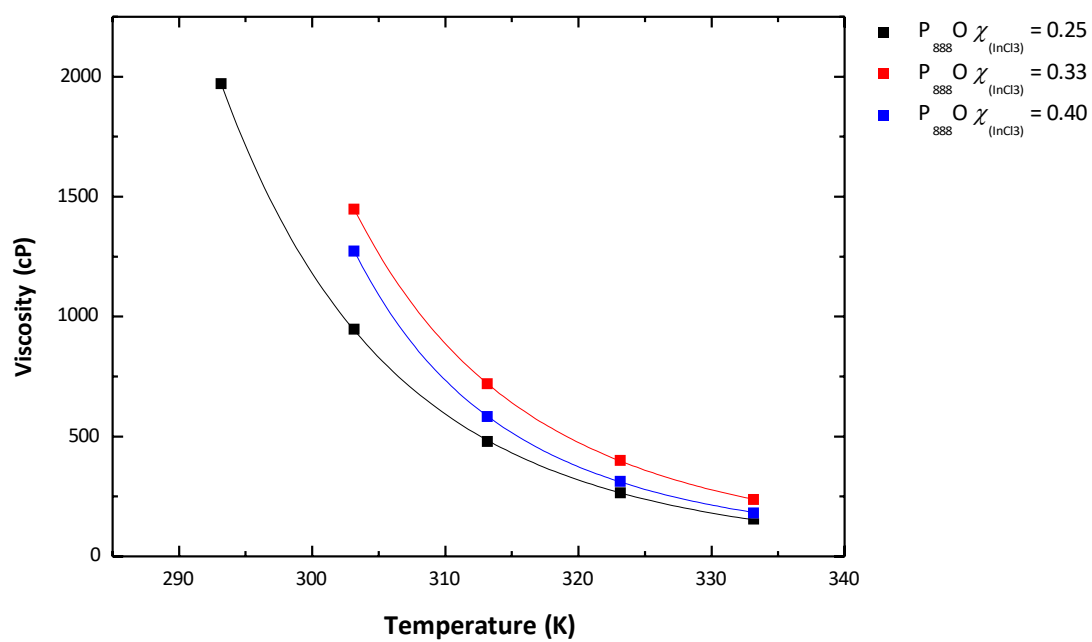


Figure 4-32- VFT fit of  $P_{888}O-InCl_3$  LCCs  $\chi_{InCl_3} = 0.25, 0.33, 0.40$ .

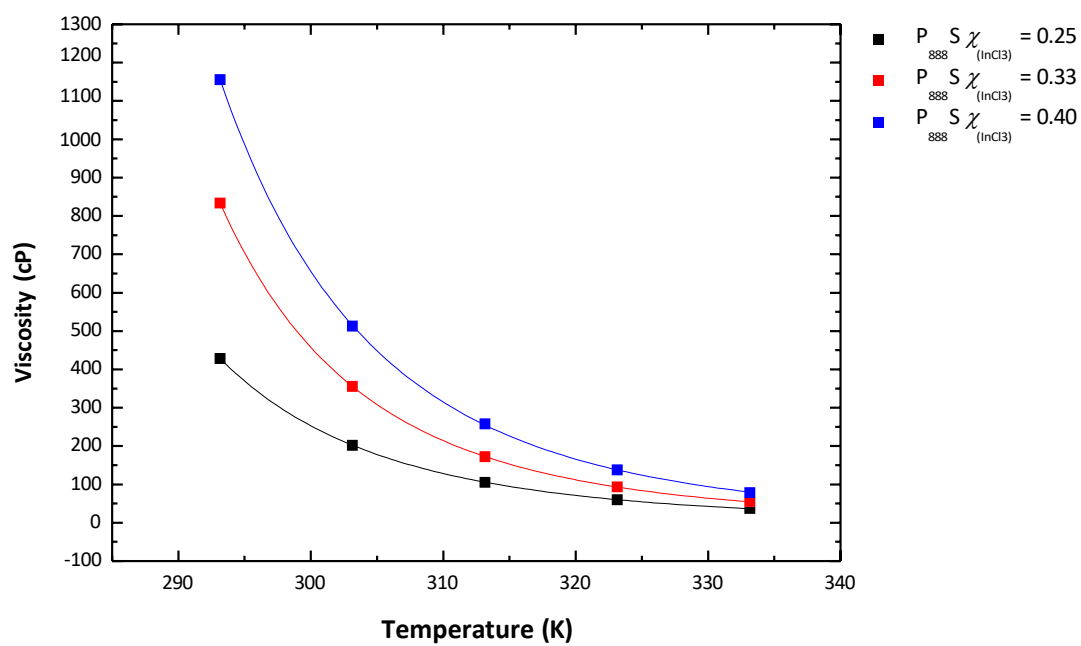
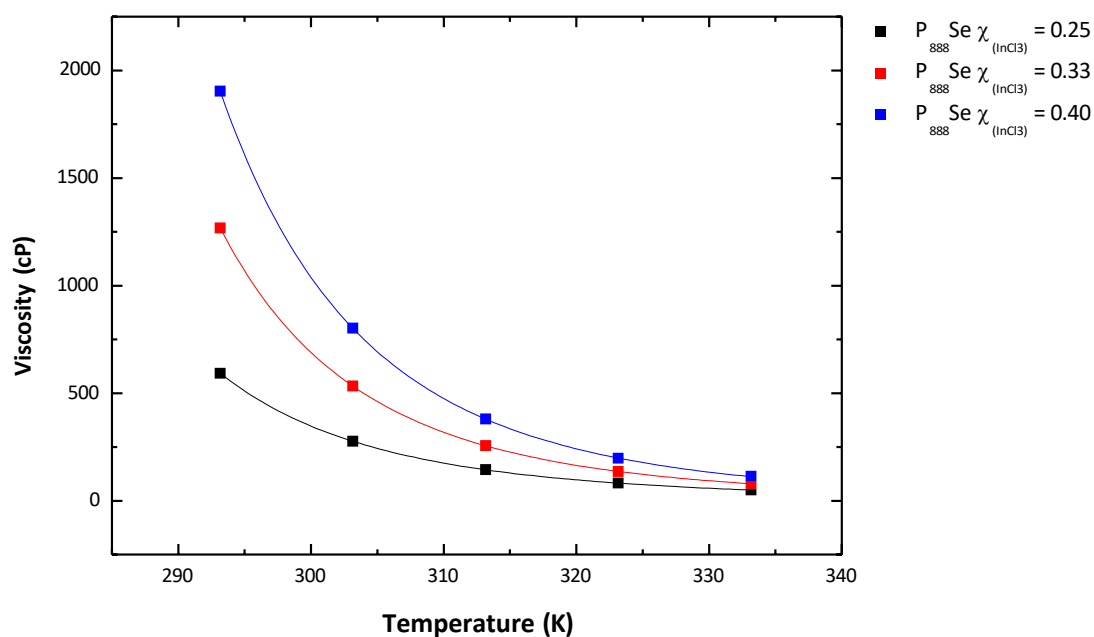
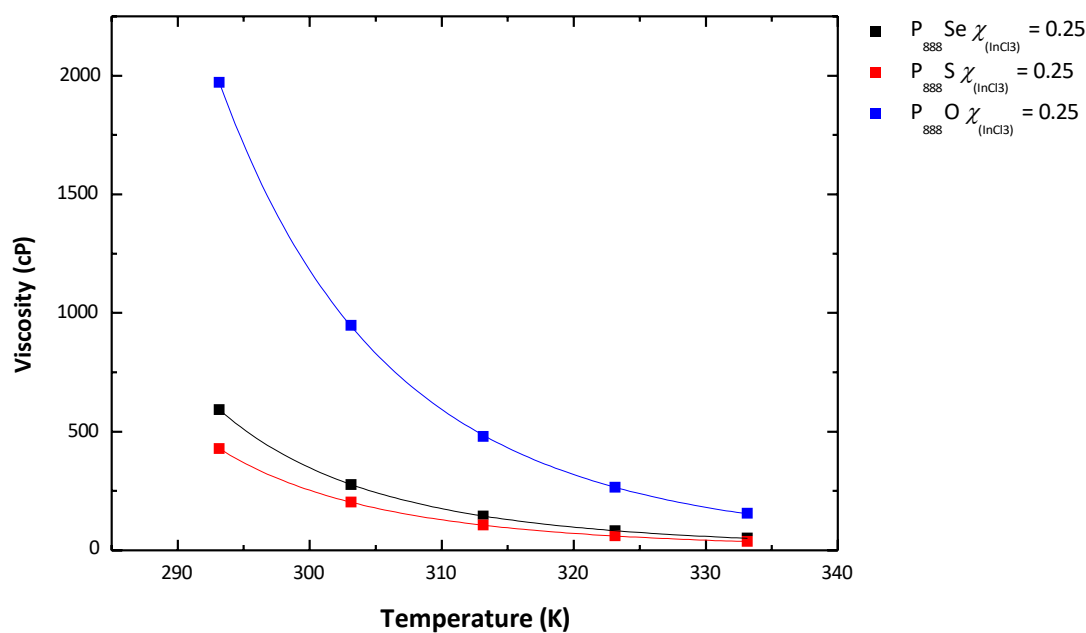


Figure 4-33- VFT fit of  $P_{888}S-InCl_3$  LCCs  $\chi_{InCl_3} = 0.25, 0.33, 0.40$ .





**Figure 4-34-** VFT fit of  $P_{888}Se-InCl_3$  LCCs  $\chi_{InCl_3} = 0.25, 0.33, 0.40$ .



**Figure 4-35-** VFT fit of  $P_{888}E-InCl_3$  LCCs  $\chi_{InCl_3} = 0.25$ .

Unlike the viscosity that is observed in the chlorogallate and chloroaluminate systems, viscosity does not decrease with increasing  $\chi_{InCl_3}$  that would be indicative of oligomeric species forming such as  $[In_2Cl_7]^-$  found in chloroindate ionic liquids is

not observed. The increase in viscosity with increasing  $\chi_{\text{InCl}_3}$  indicates that the larger coordination sphere of the In(III) is utilised and it expands beyond the tetra coordinate species previously observed instead moving to penta- and hexa-coordinate species.<sup>349,427</sup>

#### 4.2.2.4 Nuclear resonance spectroscopy

In all  $^{31}\text{P}$  NMR spectra of the chloroindate LCCs a downfield shift is observed and a singular peak at  $\chi_{\text{InCl}_3} = 0.50$  (Figure 4-36). However, at lower  $\chi_{\text{InCl}_3}$  values specifically in the  $\text{P}_{888}\text{O-InCl}_3$  system, the spectrum resolves into 3 peaks at  $\chi_{\text{InCl}_3} = 0.25$ . Previous work by Atwood *et al.* suggest that the  $\text{InX}_3$  system's behaviour with triphenylphosphine oxides is dependent on the nature of the anion present.<sup>428</sup> The asymmetric cleavage that occurs to form ionic species is observed in  $\text{InBr}_3$  systems, however, the hexa-coordinate neutral adducts are observed in  $\text{InCl}_3$  systems. Further to this, work by Robinson *et al.* determined that within the solid state combinations of  $\text{InCl}_3$  and  $\text{Ph}_3\text{P=O}$  hexa- and penta-coordinate complexes form at  $\chi_{\text{InCl}_3} = 0.25$  and  $0.33$  respectively.<sup>429</sup>

Tuck and Carty postulated that both neutral and ionic species of  $\text{InX}_3$ -ligand systems are possible; however, they further postulated that the ionic and neutral components are affected by the presence of solvent. It is further noted that this trend has only been confirmed within solid state products.<sup>430</sup> Baker *et al.* further investigated the formation of adducts of  $\text{InI}_3$  and  $\text{GaI}_3$  with  $\text{PPh}_3$  and found that the indium species formed mainly five coordinate neutral adducts, whereas the gallium species formed a variation of four coordinate neutral and anionic species<sup>431</sup>. Again, it should be further noted that these species were determined from crystallisations in ether.  $^{31}\text{P}$  NMR spectra of the indium solutions exhibited subtle variations with the donor ligands. In  $\text{P}_{888}\text{S}$  and  $\text{P}_{888}\text{Se}$ , a single peak was observed that broadens with increasing  $\chi_{\text{InCl}_3}$  (Figure 4-36 and Figure 4-37) In  $\text{P}_{888}\text{O}$  however, at  $\chi_{\text{InCl}_3} = 0.33$  and  $0.25$  two and three peaks are observed respectively (Figure 4-38).

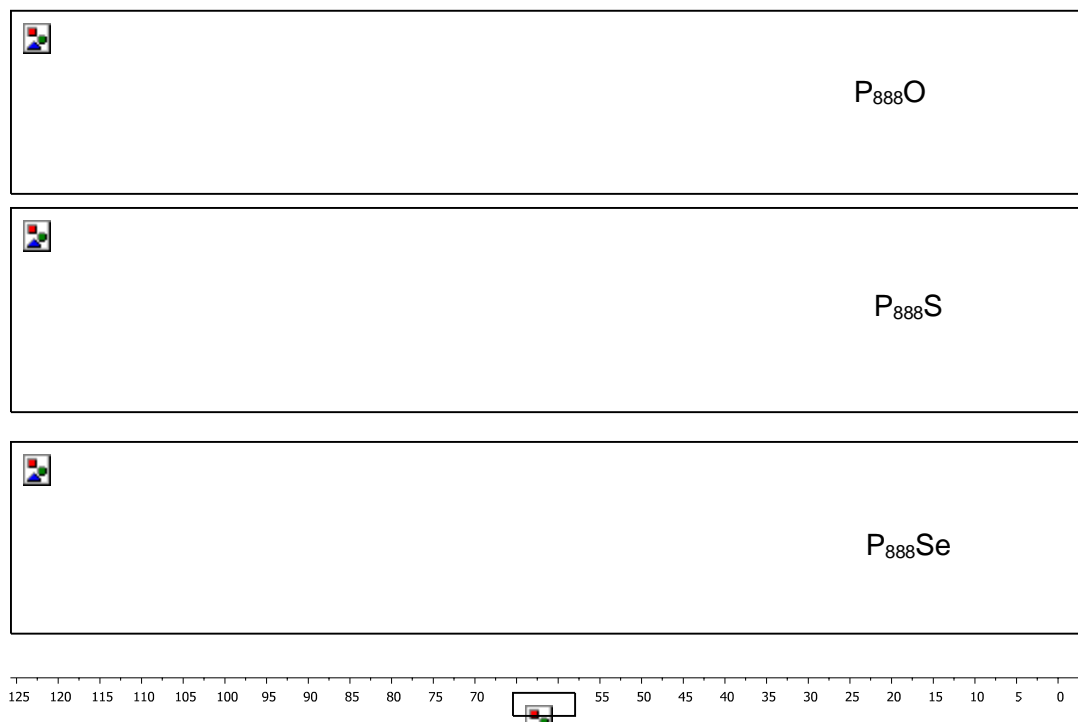


**Figure 4-36**- $^{31}\text{P}$  NMR spectra of  $\text{P}_{888}\text{O-InCl}_3$   $\chi_{\text{InCl}_3} = 0.50$  (top),  $\text{P}_{888}\text{S-InCl}_3$   $\chi_{\text{InCl}_3} = 0.50$  (middle) and  $\text{P}_{888}\text{Se-InCl}_3$   $\chi_{\text{InCl}_3} = 0.50$ . (Bottom)

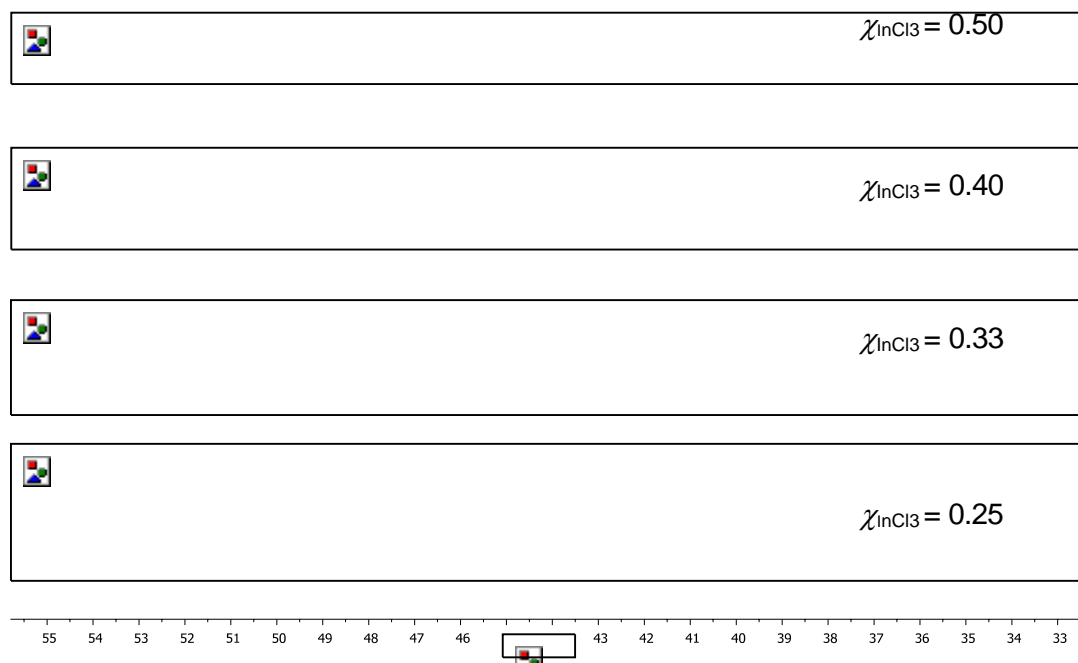


**Figure 4-37**- $^{31}\text{P}$  NMR spectra of  $\text{P}_{888}\text{Se-InCl}_3$  LCCs (top-bottom)  $\chi_{\text{InCl}_3} = 0.50, 0.40, 0.33$  &  $0.25$ .

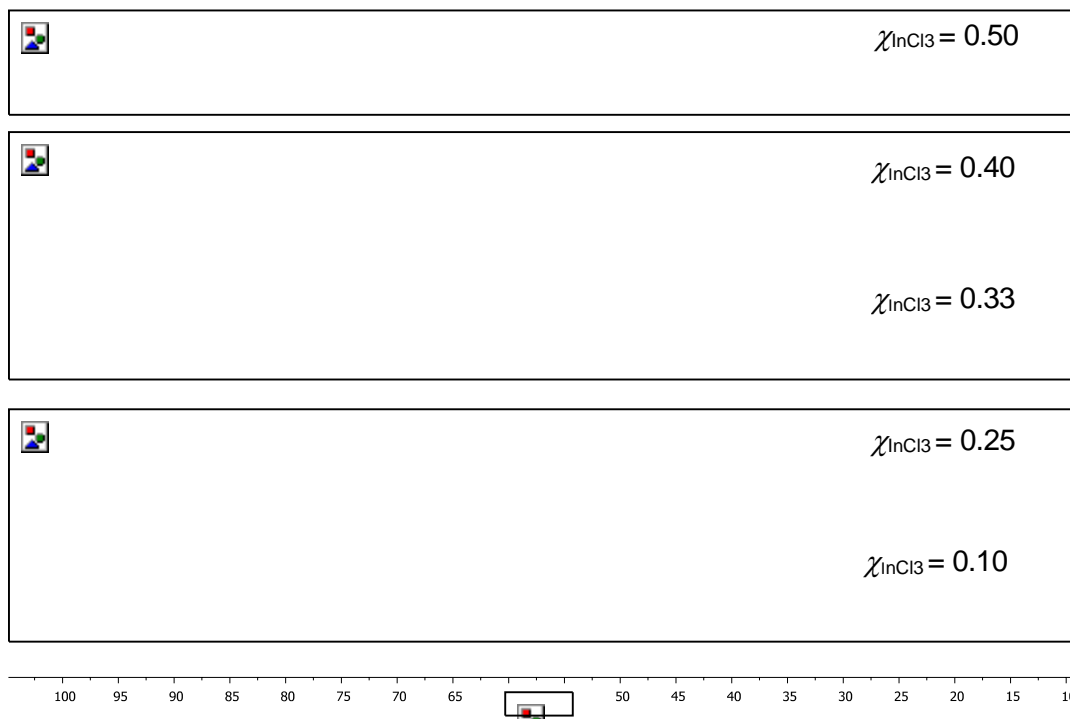


**Figure 4-38-**  $^{31}\text{P}$  NMR spectra of  $\text{P}_{888}\text{O}-\text{InCl}_3$   $\chi_{\text{InCl}_3} = 0.50$ ,  $\chi_{\text{InCl}_3} = 0.40$ ,  $\chi_{\text{InCl}_3} = 0.33$ ,  $\chi_{\text{InCl}_3} = 0.25$ ,  $\chi_{\text{InCl}_3} = 0.10$ \* \*NMR spectra recorded at  $70^\circ\text{C}$ . (Top-bottom)

Utilising the correlation of viscosity vs.  $\chi_{\text{MCl}_x}$  and the width at half peak height vs.  $\chi_{\text{MCl}_x}$ , an insight into the speciation trends of these LCCs can be observed.<sup>432</sup> Peak width within a  $^{31}\text{P}$  NMR spectrum is dependent on two separate properties of the sample-viscosity and symmetry of the species present. In order to correlate this to the viscosity data aforementioned and the somewhat inconclusive NMR data, a plot constructed showed how the trends do not follow direct proportionality indicating that with increasing  $\chi_{\text{MCl}_x}$  the speciation changes and the broadening of the  $^{31}\text{P}$  peak indicative of the neutral species broadened not only as a function of viscosity but as a function of the speciation trends. Hogg *et al.* also postulated that molecular adducts were present in regards to  $^{31}\text{P}$  NMR spectra citing work by Robinson as mentioned, for structural determination.<sup>375,429</sup>

Furthermore, due to the larger coordination sphere of indium, it is postulated that as  $\chi_{\text{InCl}_3}$  decreases the stoichiometry lends itself to form the penta- and hexacoordinate species may form e.g.  $[\text{InCl}_3(\text{L})_2]$  and  $[\text{InCl}_3(\text{L})_3]$  adducts, which complicates speciation because of possible isomerisation e.g. *fac* and *mer* isomers for the hexacoordinate neutral species. Compositions with intermediate  $\chi_{\text{InCl}_3}$  values could potentially contain a mixture of tetra-, penta- and hexa-coordinate species e.g.  $[\text{InCl}_3(\text{L})_3]$ ,  $[\text{InCl}_3(\text{L})_2]$  and  $[\text{InCl}_3(\text{L})]$  adducts. At  $\chi_{\text{InCl}_3} = 0.50$  it is believed that the

$[\text{InCl}_3(\text{L})]$  adduct dominates with the precipitate indicating the system moves towards lower  $\chi_{\text{InCl}_3}$  values. As aforementioned, the PXRD of the precipitate collected from  $\text{P}_{888}\text{Se-InCl}_3$  solutions was observed to not match literature diffraction patterns for indium(III) chlorides, hence it can be deduced that it is not due to unreacted starting material.<sup>433–438</sup> At  $\chi_{\text{InCl}_3} = 0.40$  and  $0.33$  it is also predicted that the trigonal bipyramidal complex forms; within this structure the ligands can exist axial or planar to each other hence either equivalent or inequivalent environments can increase the complexity of the NMR spectrum. The proposed speciation is shown in Table 4-17.

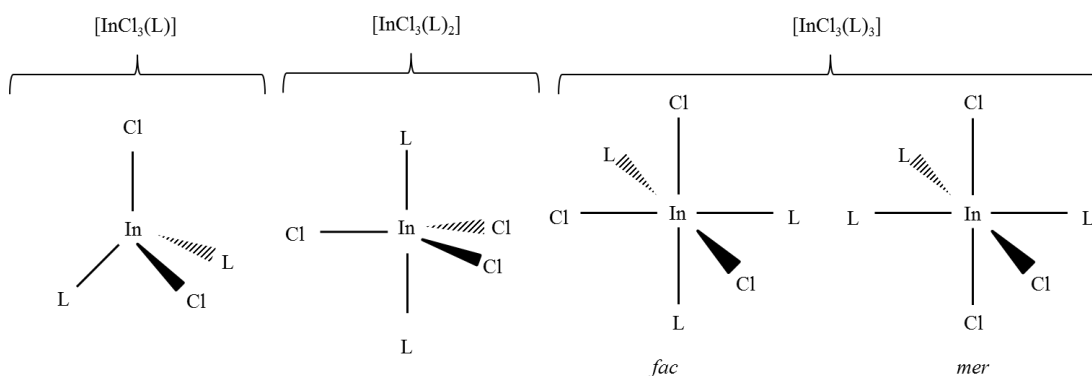


**Figure 4-39-** Suggested structures present in  $\text{P}_{888}\text{E-InCl}_3$  LCCs.

**Table 4-17-** Suggested speciation of  $\text{P}_{888}\text{E-InCl}_3$  LCCs.

$\chi_{\text{InCl}_3}$	Speciation	
0.25	$\text{InCl}_3 + 3\text{L}$	$\rightleftharpoons [\text{InCl}_3(\text{L})_3]$
0.33	$2\text{InCl}_3 + 4\text{L}$	$\rightleftharpoons 2[\text{InCl}_3(\text{L})_2] \rightleftharpoons [\text{InCl}_3(\text{L})] + [\text{InCl}_3(\text{L})_3]$
0.40	$2\text{InCl}_3 + 3\text{L}$	$\rightleftharpoons [\text{InCl}_3(\text{L})_2] + [\text{InCl}_3(\text{L})]$
0.50	$\text{InCl}_3 + \text{L}$	$\rightleftharpoons [\text{InCl}_3(\text{L})]$

This speciation is comparable to those already reported by Carty *et al.*<sup>430,439</sup> with a variety of oxygen and sulphur containing ligands such as urea and thiourea. Selenium,  $^{77}\text{Se}$  NMR was found to be a useful tool within speciation determination in the chlorogallate species, however, the quality and resolution of spectra obtained at lower  $\chi_{\text{InCl}_3}$  is poor and results in only one broad signal being observed. At  $\chi_{\text{InCl}_3} = 0.50$ , however, a more defined spectrum consisting of a less pronounced broad signal -219.7 ppm and a relatively sharp doublet at -242.79- -246.23 ppm are observed as shown in Figure 4-40. The broad peak appears to match the peaks

observed in the lower  $\chi_{\text{InCl}_3}$  LCCs such that with increasing  $\chi_{\text{InCl}_3}$  electron density on the selenium atom decreases hence indicating a stronger binding that it would be expected in more chlorine rich, ligand poor environments such as  $[\text{InCl}_3\text{L}_2]$  suspected to be a major component at  $\chi_{\text{InCl}_3} = 0.40$ . The sharp doublet at -242.79 - -246.23 ppm may indicate some un-precipitated  $[\text{InCl}_3\text{L}]$ ; being the simplest  $\text{InCl}_3$ - $\text{P}_{888}\text{Se}$  adduct, there is no through space coupling, inequivalent Se environments etc. hence giving the greatest opportunity for identification. The precipitation and the presence of a second peak in the  $\chi_{\text{InCl}_3} = 0.50$  spectrum support the theory that the precipitate formed is that of  $[\text{InCl}_3\text{L}]$  hence causing a relative decrease in the  $\chi_{\text{InCl}_3}$  of the residual solution hence more expanded coordination adducts form such as  $[\text{InCl}_3\text{L}_2]$ .

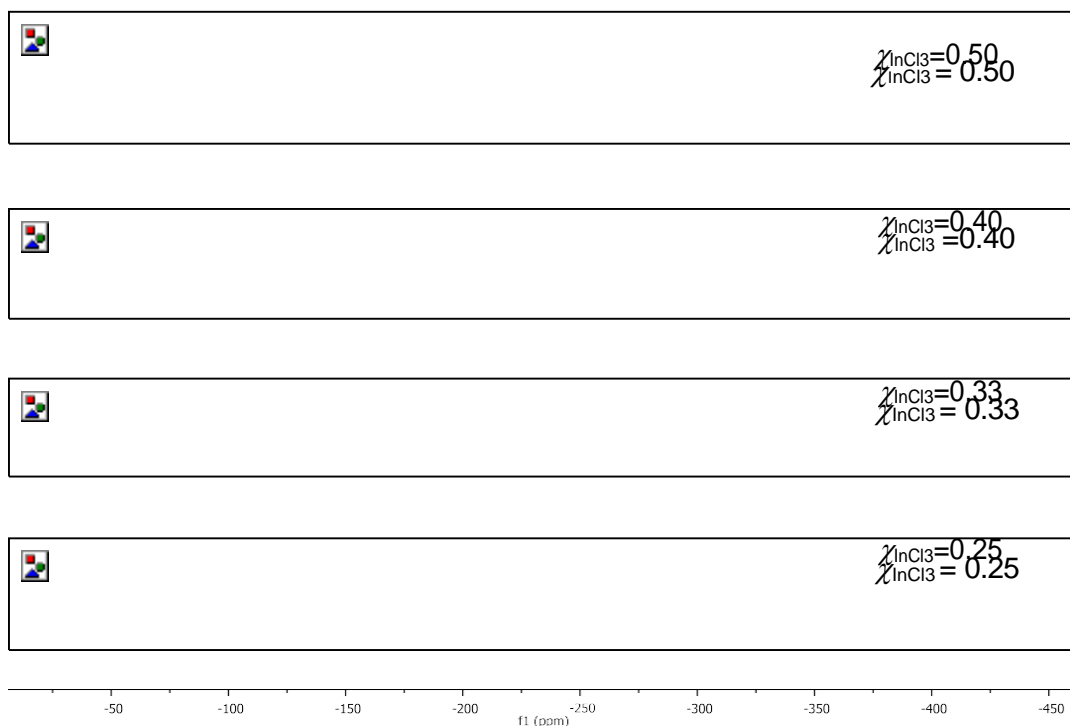


**Figure 4-40.**  $^{77}\text{Se}$  NMR spectra of  $\text{P}_{888}\text{Se}-\text{InCl}_3$   $\chi_{\text{InCl}_3} = 0.50$ ,  $\chi_{\text{InCl}_3} = 0.40$ ,  $\chi_{\text{InCl}_3} = 0.33$ ,  $\chi_{\text{InCl}_3} = 0.25$ . (Top-bottom)

#### 4.2.2.5 Raman spectroscopy

It was intended that Raman spectroscopy could elucidate the suspected neutral species present. Single crystal investigations, as mentioned by Carty *et al.* have determined that indium chloride adducts can form tetrahedral, trigonal bipyramid and octahedral complexes.<sup>430,440,441,442,443</sup> Utilising known Raman spectra of neutral and ionic indium chloride adducts it was aimed to deduce what species may be present in the LCCs formed. Summarised in Table 4-18 are listed the most prominent adducts found in literature; it is generally seen that the vibration bands for In-Cl are

288-259  $\text{cm}^{-1}$  for octahedral coordination, 342-286  $\text{cm}^{-1}$  for trigonal bipyramidal coordination and 340-256  $\text{cm}^{-1}$  for tetrahedral coordination.

It is expected that ionic contributions such as  $[\text{InCl}_4]^-$  to give rise to two Raman active stretches at 321  $\text{cm}^{-1}$  and 337  $\text{cm}^{-1}$ .<sup>413</sup> From literature it is observed that there is significant overlap in the expected Raman-bands for each coordination environment for the In-Cl bond, hence specific assignment to species is difficult. Due to limitations of the Raman spectrometer only  $\text{P}_{888}\text{S}$  and  $\text{P}_{888}\text{Se}$  systems were studied as shown in Figure 4-41 and Figure 4-42 respectively. As shown in each system, there is a broad band at 320-324  $\text{cm}^{-1}$  which can be assigned to multiple In-Cl neutral and ionic contributions in multiple coordination environments. In the  $\text{P}_{888}\text{S}$  systems there are also small peaks arising at 292  $\text{cm}^{-1}$  in  $\chi_{\text{InCl}_3} = 0.33$  and at 272  $\text{cm}^{-1}$  in  $\chi_{\text{InCl}_3} = 0.25$ ; although the exact assignment is nearly impossible it should be noted that his emergence of new peaks with increasing  $\chi_{\text{InCl}_3}$  indicates a possible change in coordination.

**Table 4-18-** Characterising Raman shifts of indium chloride molecular adducts and ionic species.

Molecular adduct	Coordination Number	Raman shift ( $\text{cm}^{-1}$ )	Literature
$[(\text{InCl}_3)_2\{\text{MeS}(\text{CH}_2)_2\text{SMe}\}_2]$	4	302(vs), 268(m), 256(w).	Reid <sup>413</sup>
$[\text{InCl}_3\{\text{MeC}(\text{CH}_2\text{SMe})_3\}]$	4	295(s), 276(m), 260(m), 238(m).	Reid <sup>413</sup>
$[\text{InCl}_2\{\text{i-PrS}(\text{CH}_2)_2\text{SiPr}_2\}][\text{InCl}_4]$	4	369(w), 340(sh)*, 319(s)*, 287(w), 267(s).	Reid <sup>413</sup>
$[(\text{InCl}_3)_2\{\text{MeSe}(\text{CH}_2)_2\text{SeMe}\}_2]$	4	298(s), 278(m), 250(m).	Reid <sup>413</sup>
$[\text{InCl}_3((\text{Me}_2\text{N})_3\text{PO})_2]$	5	327	Carty <sup>430</sup>
$[\text{InCl}_3(2,6\text{-lutidine N-oxide})_2]$	5	286	Brown <sup>444</sup>
$[\text{InCl}_3(\text{Ph}_3\text{PO})_2]$	5	342(vs), 332(sh), 116	Carty <sup>445</sup>
$[\text{InCl}_3(\text{DMSO})_3]$	6	288(s), 276(s), 259(s), 120	Carty <sup>445</sup>
$[\text{InCl}_3(\text{DMSO})_3]$	6	449 (m), 441(sh), 346 (m), 310 (m), 267 (vs)	Carty <sup>420</sup>

\* $[\text{InCl}_4]^-$  Ga-Cl stretches

**Table 4-19-** Raman shifts of Indium chloride LCCs.

LCC	$\chi_{\text{InCl}_3}$	Raman shift ( $\text{cm}^{-1}$ )
$\text{P}_{888}\text{S-InCl}_3$	0.25	272,322
	0.33	292, 326
$\text{P}_{888}\text{Se-InCl}_3$	0.25	324
	0.33	322

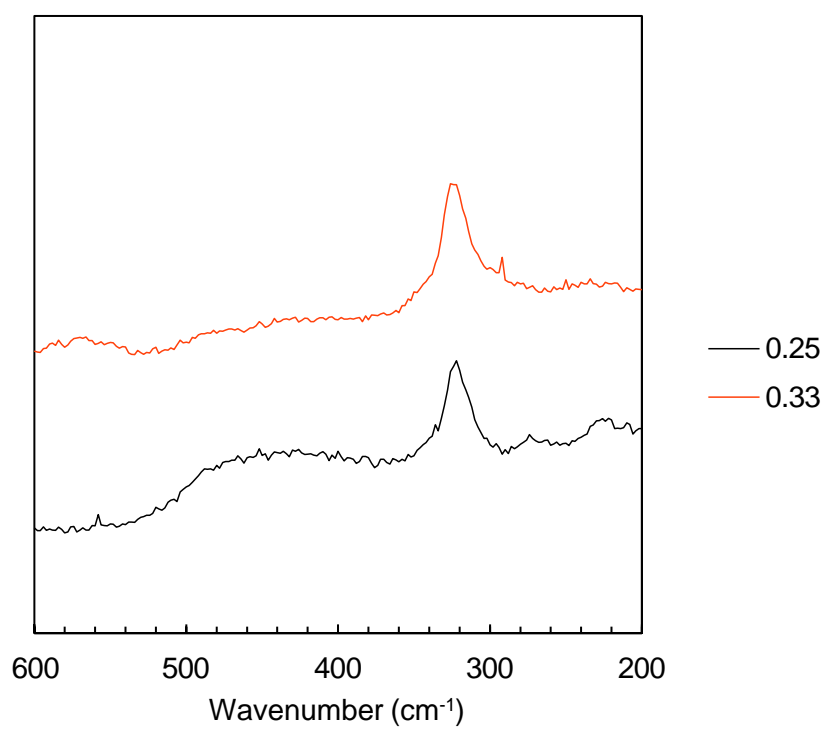


**Figure 4-41-** Rescaled stacked plot of Raman spectra of  $\text{P}_{888}\text{S-InCl}_3$  LCCs. (top-bottom)  $\chi_{\text{InCl}_3} = 0.33$ , 0.25.



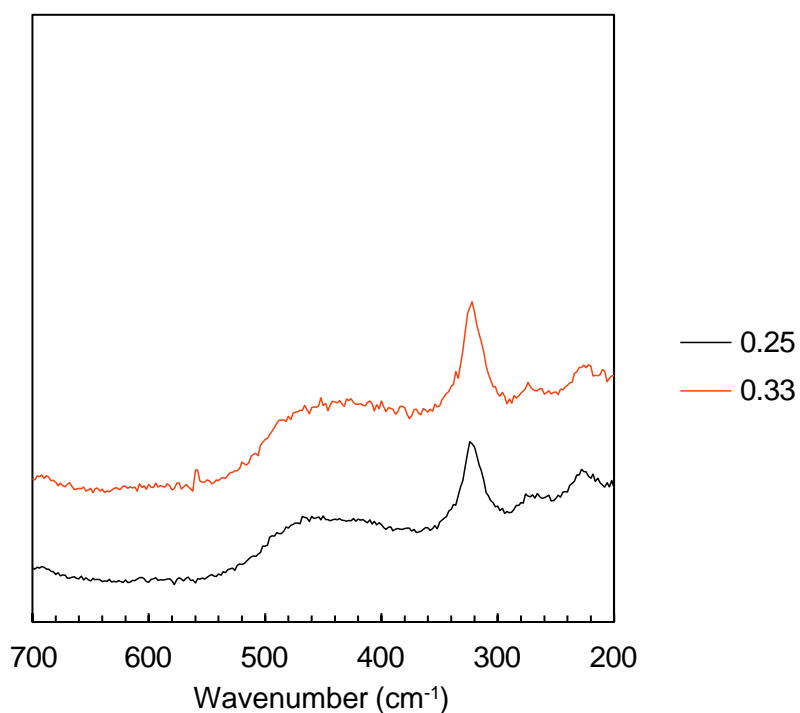


**Figure 4-42**-Rescaled stacked plot of Raman spectra of  $P_{888}Se-InCl_3$  LCCs. (top-bottom)  $\chi_{GaCl_3} = 0.33$ , 0.25.

#### 4.2.2.6 Infrared spectroscopy

Infrared spectroscopy of the chloroindate liquid coordination complex systems does not contain any In-Cl or In-E bands, however, it has been confirmed that the ligand species remains intact and no water contamination has occurred, hence no hydroxyl band is present. All Infrared spectra are available in the appendix and the  $P_{888}S-InCl_3$  system listed in Table 4-20 and shown in Figure 4-43.

**Table 4-20**- Infrared stretching frequencies of  $P_{888}S-GaCl_3$ .

$P_{888}S-InCl_3$	P=S wavenumber ( $cm^{-1}$ )
$\chi_{InCl_3} = 0$	599
$\chi_{InCl_3} = 0.25$	559
$\chi_{InCl_3} = 0.33$	554
$\chi_{InCl_3} = 0.40$	551

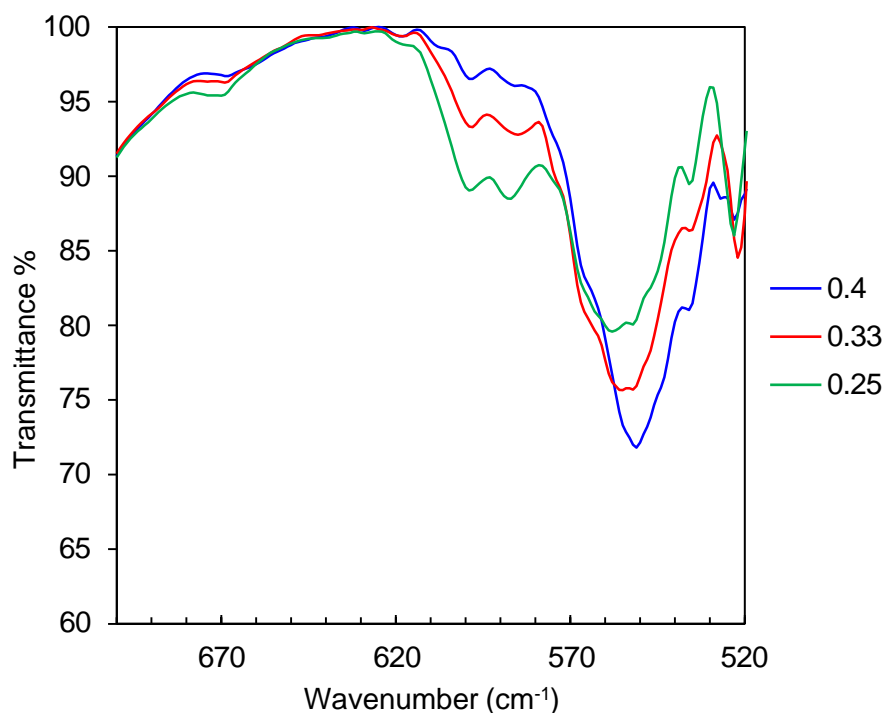


**Figure 4-43-** Expanded Infrared spectra of  $P_{888}S-InCl_3$  LCCs.

In the  $P_{888}S$  systems the wavenumber of the  $P=S$  bond decreases from  $599\text{ cm}^{-1}$  of the unbound donor ligand to  $551\text{ cm}^{-1}$  at  $\chi_{InCl_3} = 0.40$ . In the chlorogallate LCCs it was observed that the  $P=S$  bond upon complexation to the Lewis acidic chlorogallates at  $\chi_{GaCl_3} = 0.75$  ( $549\text{ cm}^{-1}$ ); the  $P=E$  stretch was observed to lower to this frequency with increasing  $\chi_{GaCl_3}$  as a result of the formation of greater Lewis acidic oligomeric species being formed. In the chloroindate systems from the input stoichiometries it is apparent that oligomeric species are highly unlikely to be present. This lowering in frequency of the  $P=S$  bond with increasing  $\chi_{InCl_3}$  is not unexpected and minimal. This small shift is an indication of the changing bond strength between S and In, suggesting the ligand becomes more tightly bound with increasing  $\chi_{InCl_3}$  value, it follows that this shift is indicative decrease in the coordination number around the Indium atom from low to high  $\chi_{InCl_3}$  values. Within literature neutral complexes such as  $[InCl_3(Me_3PS)_2]$  ( $\nu(P=S) = 541\text{ cm}^{-1}$ )<sup>446</sup> and  $[InCl(N\{Pr^i_2PS\}_2)_2]$  ( $\nu(P=S) = 540, 563\text{ cm}^{-1}$ )<sup>447</sup> exhibit stretches similar to those observed in these LCC systems.

#### 4.2.2.7 Speciation and explanations

The speciation of the chloroindate liquid coordination complexes is vastly different to that exhibited in the chlorogallate. It has been determined from literature and

multiple spectroscopic techniques that molecular adducts form at all  $\chi_{\text{InCl}_3}$  values. This is particularly evident from the viscosity data. Generally, as observed in the  $\text{P}_{888}\text{E-GaCl}_3$  systems as  $\chi_{\text{MCl}_3}$  increases, viscosity increases however in the  $\text{P}_{888}\text{O-InCl}_3$  system this is not observed instead the highest viscosity was observed at  $\chi_{\text{MCl}_3} = 0.33$ . Indicating a significant shift towards neutral adducts and specifically those which may be larger in size/coordination number.  $^{31}\text{P}$  NMR data also indicates a neutral species has formed with multiple peaks indicating multiple adducts may be present. The reason for such differing behaviour compared to chlorogallate and chloroaluminate systems is believed to be simply due to the larger size of the indium centre and consequent expanded coordination shell.

### 4.3 Conclusions

A variety of liquid coordination complexes of group 13 chlorometallates and trioctylphosphine chalcogenides have been studied extensively in regards to their chemical and physicochemical properties, hence their speciation has been determined with a good degree of confidence. Corroboration of multiple spectroscopic techniques including multinuclear NMR, Raman, Infrared and EXAFS spectroscopy; along with a solid basis of physicochemical properties including density and viscosity a good prediction has been made in regards to the speciation of each system. It was shown the vital need to corroborate results across multiple measurement techniques and the need to probe the existence of equilibria present to ensure a worthwhile prediction of the speciation of these systems.

Cooling VT NMR studies carried out on the LCC systems gave a new insight to the previously un-investigated variation of speciation with temperature. Upon recent applications to catalysis the change in speciation with temperature is a vital factor in the catalytic activity hence possibly allowing for the catalytically active species present to be determined.

It was evident that the chlorogallate and chloroindate systems differed significantly in regards to their complex formation properties. The chlorogallate LCCs resembled the analogous chloroaluminate LCC systems studied by Hogg and co-workers in that both ionic and neutral species existed and exchange is varied dependent on the nature of the donor ligand. The chloroindate species however, was found to form only neutral adducts and hence only sub-stoichiometric amounts of  $\text{InCl}_3$  could be utilised, as the dimeric species  $[\text{In}_2\text{Cl}_7]^-$  are inaccessible.

#### 4.4 Future Work

As will be discussed in chapter 5 the main application of the LCCs within the remit of this project is synthesis of semiconductor materials specifically group 13 chalcogenides. Within conventional synthesis elaborate solvothermal methods are utilised require solvents, capping agents and specific salts of the precursors. Ionothermal microwave-assisted methodologies to synthesise indium (III) selenides have been very effective hence the similarity of LCC donor ligands to the conventional capping agents and ionic liquids it is a natural step to replicate this success with LCCs and if not, improving it.<sup>374</sup>

Referring back to speciation a good approximation of the species present has been made however as always there is more to be confirmed. Conductivity is a physicochemical property that has only been rudimentarily quantified; in future the use of impedance spectroscopy and Nyquist plots as a function of variable  $\chi_{\text{GaCl}_3}$  will hopefully give greater insight into the position of the equilibria.

Experiments performed in this work which provided crucial evidence on the rate of intermolecular exchange between ionic and neutral species were not performed on  $\text{P}_{888}\text{S}/\text{Se AlCl}_3$  LCCs and would provide evidence as to whether previous conclusions were valid.<sup>375</sup>

Furthermore, a quantification of the vapour pressure of these species is also of interest; do they truly compare with ionic liquids? A TGA method developed by Styring and co-workers would allow for the vapour pressure to be determined and the use of an *in situ* GCMS or Raman spectrometer would allow for identification of the species in the vapour phase.<sup>448</sup>

Repetition of the Raman experiments would be sought with the use of a Raman microscope to improve data quality and to complete spectra at multiple temperatures.

#### 4.5 Experimental methods

All experiments were performed in a glovebox (MBraun labmaster dp, < 0.3 ppm of  $\text{H}_2\text{O}$  and  $\text{O}_2$ ) or using standard argon Schlenk techniques. All glassware was dried overnight in an oven (ca. 100 °C) before use. Aluminium (III) chloride (99.999 %) and gallium (III) chloride (99.999 %) were purchased in sealed ampules, under argon from Alfa Aesar. Sulphur (99.95 %) and selenium ( $\approx 200$  mesh, 99.95 %) were purchased from Sigma Aldrich and were all dried under reduced pressure (80 °C, < 1 mbar, 48 h) before use. Trioctylphosphine oxide (99.5 %) was provided by Cytec

and dried as described above. Urea, acetamide, thiourea were obtained from Sigma Aldrich in *puriss* grade and were dried *via* heating under vacuum. (65 °C, 48 hours)

#### 4.5.1 Synthesis of donor ligands and liquid coordination complexes

**Trioctylphosphine chalcogenide.** Trioctylphosphine sulphide and trioctylphosphine selenide were synthesised using an equimolar mix of trioctylphosphine and selenium/sulphur, modified from literature methods.<sup>449</sup> In a typical procedure, elemental sulphur/selenium (0.7961 g, 24.83 mmol / 1.7562 g, 22.24 mmol) was added slowly in portions to the trioctylphosphine (9.2039 g, 24.83 mmol/ 8.2438 g, 22.24 mmol), with rapid stirring (500 rpm) allowing for the heat from the exothermic reaction to cool. The last additions of chalcogenide elements are sluggish and require stirring overnight. The reaction mixtures were then filtered to give clear, colourless liquids. Purity was analysed by <sup>31</sup>P NMR spectroscopy.

P<sub>888</sub>S: <sup>31</sup>P-NMR (243 MHz, DMSO capillary)  $\delta$  (ppm): 44.91 (1P, s, P=S)

P<sub>888</sub>Se: <sup>31</sup>P-NMR: (243 MHz, DMSO capillary)  $\delta$  (ppm): 36.41 (1P, d, P=Se, <sup>1</sup>J<sub>P-Se</sub> 678 Hz), 48.35 (1P, s, P=O)

**Liquid coordination complexes.** LCCs were synthesised on a 2 -12 g scale, following the literature procedure.<sup>22</sup> All syntheses were carried out in a nitrogen-filled glovebox (MBraun LabMaster dp, > 0.6 ppm O<sub>2</sub> and H<sub>2</sub>O). To the neutral donor ligand the metal chloride (GaCl<sub>3</sub> / InCl<sub>3</sub>) was added in portions. Heat was generated upon each metal chloride addition hence the flask was allowed to cool before the next portion was added. To allow for the equilibria to settle the LCC was allowed to stir for 12 hours under glovebox conditions resulting in homogeneous liquids in all cases.

#### 4.5.2 Raman and IR spectroscopy

Infrared spectra were measured using a PerkinElmer Spectrum-100 IR spectrometer with ATR attachment, with a total range of 7800 to 370 cm<sup>-1</sup>, with a resolution of 0.5 cm<sup>-1</sup>. Air-sensitive samples were loaded into a screw cap GC vial under glovebox conditions and sealed with parafilm. Then, the vial was removed from the glovebox and transferred to the IR spectrometer. The vial was then opened and rapidly placed over the crystal of the ATR attachment, allowing for the liquid sample to flow onto the crystal. The glass vial was left over the sample during measure to provide an inert atmosphere.

Raman spectra were measured using a PerkinElmer Raman station 400F spectrometer, with a 785 nm focused laser beam. As samples were often air sensitive, the quartz cuvette (1 mm diameter) was filled under glovebox conditions and sealed using parafilm.

#### 4.5.3 Extended X-ray Fine Structure spectroscopy

EXAFS measurements on the liquid coordination complexes,  $\text{L-GaCl}_3$ ,  $\chi_{\text{GaCl}_3} = 0.50, 0.60, 0.67$  and  $0.75$ , were carried out at the Diamond Light Source (I20-scanning beamline and B-18 core EXAFS beamline)<sup>450,451</sup> at the Ga K-edge. A four-bounce scanning Si(111) monochromator was used<sup>452,453</sup>, and the rejection of higher harmonics was achieved by using a pair of rhodium coated mirrors operating at 5 mrad incident angle. The measurements were performed at room temperature in transmission mode. Two ion chambers filled with the appropriate gas mixture to absorb 15% and 80% of the intensity of the radiation were used for I0 and It respectively. All samples were prepared in a MBraun Labmaster dp glovebox (up to 0.6 ppm of  $\text{H}_2\text{O}$  and  $\text{O}_2$ ). For liquid samples, a drop of neat sample was captured between two layers of an adhesive Kapton film, stuck directly to a Kapton or PTFE spacer (127 -500  $\mu\text{m}$ ). Sealed samples were mounted onto a PEEK sample holder with 8 mm window. Three to five spectra were recorded and then merged, calibrated, normalized and background subtracted using Athena.<sup>396,454</sup> The spectra were then fitted using Artemis to calculate interatomic distances and their root-mean-square variations ( $\sigma^2$ ).

#### 4.5.4 Viscosimetry

Viscosity was measured using an Anton Paar AMVn automated rolling ball viscometer. An identical methodology to Hogg was utilised.<sup>382</sup>

#### 4.5.5 Densitymetry

Density was measured using a U-shaped oscillating tube Anton Paar DMA 4500 density meter. Samples were prepared under glovebox conditions and transferred to the density meter in Parafilm sealed syringes. An identical methodology to Hogg was utilised.<sup>382</sup>

#### 4.5.6 Conductivity

Conductivity was measured using a Fischer Scientific Accumet AB200 and Fisherbrand Accumet probe temperature compensated two-cell conductivity probe (Pt, cell constant =1 cm<sup>-1</sup>). The cell constant was calibrated to a 0.01 M KCl aqueous solution. Samples were prepared under glovebox conditions and transferred to the conductivity meter under a flow of nitrogen where the probe was secured in place using parafilm. The samples were heated to 50 °C, allowed to equilibrate for 30 minutes and conductivities recorded at 5-minute intervals.

#### 4.5.7 Nuclear magnetic resonance spectroscopy

Multinuclear NMR was used throughout this body of work. All NMR spectra were recorded on either a Bruker Advance DPX 400 MHz, or a Bruker Advance DPX 600 MHz spectrometer. The frequencies of the measurements are summarised below in Table 4-21. Samples which were liquid at room temperature were recorded using DMSO capillaries as an external deuterium lock to prevent the solvent affecting the equilibria present in the sample.

**Table 4-21-** Summary of the frequency of measurements used for each spectrometer

Nuclei	Bruker Advance DPX 400 Frequency of Measurement (MHz)	Bruker Advance DPX 600 Frequency of Measurement (MHz)
<sup>1</sup> H	400	600
<sup>13</sup> C	100	150
<sup>31</sup> P	162	243
<sup>77</sup> Se	-	114

Cooling NMR experiments required the use of an alternative deuterium lock within the LCC solutions to prevent freezing. *D2-dichloromethane* and *d*-chloroform were used and spectra were recorded at cooling intervals until freezing was observed. The samples under test were armed and the initial spectra repeated to indicate if any degradation *etc.* had occurred.

##### 4.5.7.1 Ligands

**Trioctylphosphine oxide, P<sub>88</sub>O** <sup>31</sup>P (d-DMSO capillary, 162 MHz): 49.91(1P, s, P=S)

**Trioctylphosphine sulphide, P<sub>88</sub>S** <sup>31</sup>P (d-DMSO capillary, 243 MHz) δ (ppm): 44.91 (1P, s, P=S)

**Trioctylphosphine selenide,  $P_{888}Se$**   $^{31}P$  (d-DMSO capillary, 243 MHz)  $\delta$  (ppm): 36.41 (1P, d, P=Se,  $^1J_{P-Se}$  = 678 Hz), 48.35 (1P, s, P=O);  $^{77}Se$  (d-DMSO capillary, 114 MHz)  $\delta$  (ppm): -388.57 (1Se, d, P=Se,  $^1J_{P-Se}$  = 709.68)

#### 4.5.7.2 Liquid Coordination complexes

##### **Trioctylphosphine oxide – gallium (III) chloride LCC, $P_{888}O-GaCl_3$**

$\chi_{GaCl_3} = 0.50$   $^{31}P$  (d-DMSO capillary, 243 MHz)  $\delta$  (ppm): 80.15 (s), 76.50 (s)

$\chi_{GaCl_3} = 0.60$   $^{31}P$  (d-DMSO capillary, 243 MHz)  $\delta$  (ppm): 81.23 (s), 79.97(s)

$\chi_{GaCl_3} = 0.67$   $^{31}P$  (d-DMSO capillary, 243 MHz)  $\delta$  (ppm): 83.41 (s), 81.31 (s)

$\chi_{GaCl_3} = 0.75$   $^{31}P$  (d-DMSO capillary, 243 MHz)  $\delta$  (ppm): 89.06 (s), 85.21 (s), and 84.37(s)

##### **Trioctylphosphine sulphide – gallium (III) chloride LCC, $P_{888}S-GaCl_3$**

$\chi_{GaCl_3} = 0.50$   $^{31}P$  (d-DMSO capillary, 243 MHz)  $\delta$  (ppm): 64.66 (s, P=O), 60.15 (s), 57.93 (s)

$\chi_{GaCl_3} = 0.60$   $^{31}P$  (d-DMSO capillary, 243 MHz)  $\delta$  (ppm): 66.35 (s, P=O), 61.12 (s), 59.54 (s)

$\chi_{GaCl_3} = 0.67$   $^{31}P$  (d-DMSO capillary, 243 MHz)  $\delta$  (ppm): 67.35 (s, P=O), 62.33 (s), 60.42 (s)

$\chi_{GaCl_3} = 0.75$   $^{31}P$  (d-DMSO capillary, 243 MHz)  $\delta$  (ppm): 68.43 (s, P=O), 61.42 (s), 60.85 (s)

##### **Trioctylphosphine selenide – gallium (III) chloride LCC, $P_{888}Se-GaCl_3$**

$\chi_{GaCl_3} = 0.50$   $^{31}P$  (d-DMSO capillary, 243 MHz)  $\delta$  (ppm): 47.51 (t, P=Se-Ga,  $^1J_{P-Se}$  = 471.42 MHz), 50.33 (t, P=Se-Ga,  $^1J_{P-Se}$  = 466.56 MHz) ;  $^{77}Se$  (d-DMSO capillary, 114 MHz)  $\delta$  (ppm): -161.245 (d, P=Se-Ga,  $^1J_{P-Se}$  = 463.98 MHz), -183.585(d, P=Se-Ga,  $^1J_{P-Se}$  = 468.54 MHz)

$\chi_{GaCl_3} = 0.60$   $^{31}P$  (d-DMSO capillary, 243 MHz)  $\delta$  (ppm): 49.53 (t, P=Se-Ga,  $^1J_{P-Se}$  = 456.84 MHz), 50.37 (t, P=Se-Ga,  $^1J_{P-Se}$  = N/A\*);  $^{77}Se$  (d-DMSO capillary, 114 MHz)  $\delta$  (ppm): -167.255\* (d, P=Se-Ga,  $^1J_{P-Se}$  = 467.4 MHz), -182.535\* (d, P=Se-Ga,  $^1J_{P-Se}$  = 459.42 MHz)

\*Obtained using cooling NMR techniques



$\chi_{\text{GaCl}_3} = 0.67$   $^{31}\text{P}$  (d-DMSO capillary, 243 MHz)  $\delta$  (ppm): 51.13 (t, P=Se-Ga,  $^1J_{\text{P-Se}} = 442.26$  MHz);  $^{77}\text{Se}$  (d-DMSO capillary, 114 MHz)  $\delta$  (ppm): -147.27 (d, P=Se-Ga,  $^1J_{\text{P-Se}} = 444.6$  MHz)

$\chi_{\text{GaCl}_3} = 0.75$   $^{31}\text{P}$  (d-DMSO capillary, 243 MHz)  $\delta$  (ppm): 51.98 (t, P=Se-Ga,  $^1J_{\text{P-Se}} = 447.12$  MHz);  $^{77}\text{Se}$  (d-DMSO capillary, 114 MHz)  $\delta$  (ppm): -135.27 (d, P=Se-Ga,  $^1J_{\text{P-Se}} = 434.34$  MHz)

#### **Trioctylphosphine oxide – indium (III) chloride LCC, $\text{P}_{888}\text{O-InCl}_3$**

$\chi_{\text{InCl}_3} = 0.25$   $^{31}\text{P}$  (d-DMSO capillary, 243 MHz)  $\delta$  (ppm): 55.92(s), 60.90(s), 63.11(s)

$\chi_{\text{InCl}_3} = 0.33$   $^{31}\text{P}$  (d-DMSO capillary, 243 MHz)  $\delta$  (ppm): 60.56(s), 63.16(s)

$\chi_{\text{InCl}_3} = 0.40$   $^{31}\text{P}$  (d-DMSO capillary, 243 MHz)  $\delta$  (ppm): 54.52(s), 66.63(s)

$\chi_{\text{InCl}_3} = 0.50$   $^{31}\text{P}$  (d-DMSO capillary, 243 MHz)  $\delta$  (ppm): 71.76 (s)

#### **Trioctylphosphine sulphide – indium (III) chloride LCC, $\text{P}_{888}\text{S-InCl}_3$**

$\chi_{\text{InCl}_3} = 0.25$   $^{31}\text{P}$  (d-DMSO capillary, 243 MHz)  $\delta$  (ppm): 49.9(s), 50.66(s), 57.60(s)

$\chi_{\text{InCl}_3} = 0.33$   $^{31}\text{P}$  (d-DMSO capillary, 243 MHz)  $\delta$  (ppm): 60.56(s), 63.16(s)

$\chi_{\text{InCl}_3} = 0.40$   $^{31}\text{P}$  (d-DMSO capillary, 243 MHz)  $\delta$  (ppm): 54.52(s), 66.63(s)

$\chi_{\text{InCl}_3} = 0.50$   $^{31}\text{P}$  (d-DMSO capillary, 243 MHz)  $\delta$  (ppm): 71.76(s)

#### **Trioctylphosphine selenide – indium (III) chloride LCC, $\text{P}_{888}\text{Se-InCl}_3$**

$\chi_{\text{InCl}_3} = 0.25$   $^{31}\text{P}$  (d-DMSO capillary, 243 MHz)  $\delta$  (ppm): 40.10 (d, P=Se-In,  $^1J_{\text{P-Se}} = 305.1$  Hz), 49.80 (s, P=O);  $^{77}\text{Se}$  (d-DMSO capillary, 114 MHz)  $\delta$  (ppm): -254.99 (d, P=Se-In)

$\chi_{\text{InCl}_3} = 0.33$   $^{31}\text{P}$  (d-DMSO capillary, 243 MHz)  $\delta$  (ppm): 41.79 (d, P=Se-In,  $^1J_{\text{P-Se}} = 288.88$  Hz), 51.232 (s, P=O);  $^{77}\text{Se}$  (d-DMSO capillary, 114 MHz)  $\delta$  (ppm): -219.75 (d, P=Se-In)

$\chi_{\text{InCl}_3} = 0.40$   $^{31}\text{P}$  (d-DMSO capillary, 243 MHz)  $\delta$  (ppm): 44.36 (d, P=Se-In,  $^1J_{\text{P-Se}} = 261.11$  Hz), 54.47(1P, s, P=O);  $^{77}\text{Se}$  (d-DMSO capillary, 114 MHz)  $\delta$  (ppm): -210.07 (d, P=Se-In)

$\chi_{\text{InCl}_3} = 0.50$   $^{31}\text{P}$  (d-DMSO capillary, 243 MHz)  $\delta$  (ppm): 49.09 (s, P=Se-In), 58.79 (s, P=O);  $^{77}\text{Se}$  (d-DMSO capillary, 114 MHz)  $\delta$ : -220.01 (1Se, s, br, P=Se-In), -243.77 (1Se, s, br, P=Se-In), -247.62 (1Se, s, br, P=Se-In),

#### 4.5.8 Powder X-ray diffraction

Solid products were analysed via a powder diffraction experiment on an Aligent Supernova single crystal spectrometer. Due to the small amount of product collected a conventional PXRD diffractometer was not utilised. Using a nylon loop the solid was fixed using vacuum grease and mounted.

## 5 Liquid coordination complexes of chlorocuprates

Can liquid coordination complexes be formed from chlorocuprates?

If yes, can the speciation of such complexes be elucidated?

Can LCCs be used as precursors for semiconductor synthesis?

### 5.1 Introduction

The main aim of this work is to gain greater understanding of speciation in chlorocuprate LCCs and methodologies that can be utilised to determine it. One of the many applications that LCCs have been earmarked for is in semiconductor synthesis; specifically, binary, tertiary and ternary Group 13 chalcogenides with the addition of copper to form copper indium gallium selenides, CIGS. As discussed in the previous chapter the speciation of chlorogallate and chloroindate LCCs with phosphine chalcogenide donor ligands is now well understood, however, there are as of yet no reports of chlorocuprate LCCs. In this chapter, the formation and speciation of Cu(I) and Cu(II) chlorocuprates will be investigated in a multi-technique approach and proof-of-concept semiconductor synthesis studies will be carried out.

#### 5.1.1 Chlorocuprates in classical molecular solvents and ionic liquids.

Chlorocuprates in molecular solvents have been of great interest for several years with a significant number of studies completed by Ishiguro *et al.*, which have shown that the speciation of copper(II) chloride in dimethylformide, DMF and acetonitrile solutions with  $0.1 \text{ mol dm}^{-3}$  ammonium perchlorate varies with the solvent present.<sup>455,456</sup> Specifically, the presence of the neutral species, which appears to be more prevalent in the acetonitrile solutions *i.e.* a nitrogen donor than in DMF solutions, an oxygen donor, where charged species are more prevalent as is shown in Figure 5-1 and Table 5-1.

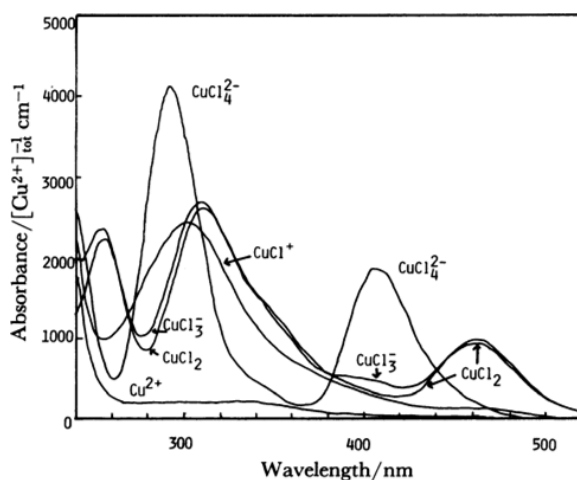


**Figure 5-1-** Speciation studies of Cu (II) by Ishiguro *et al.* in acetonitrile solvent.

**Table 5-1-**UV/Vis spectroscopic studies absorption maxima of copper (II) chloride complexes in acetonitrile and dimethylformide. <sup>455–457</sup>

	Acetonitrile	DMF
[CuCl] <sup>+</sup>	300	268
[CuCl <sub>2</sub> ]	255	265
	308	
	460	
[CuCl <sub>3</sub> ] <sup>-</sup>	255	
	380	300
	460	
[CuCl <sub>4</sub> ] <sup>2-</sup>	290	296
	405	410

Further studies by Elleb *et al.* have alluded to a more detailed designation of the DMF-CuCl<sub>2</sub> ionic solutions using electronic spectroscopy specifically focusing on three species, [CuCl]<sup>+</sup>, [CuCl<sub>3</sub>]<sup>-</sup>, and [CuCl<sub>4</sub>]<sup>2-</sup>.<sup>458</sup> [CuCl]<sup>+</sup> exhibits a band at 268 nm with an expanded branch with a very low absorption between 400 and 500 nm.<sup>459</sup> [CuCl<sub>3</sub>]<sup>-</sup> exhibits a band at 300 nm and a second band of lower intensity at 440 nm. This spectrum is also characterised by a large shoulder around 380 nm. [CuCl<sub>4</sub>]<sup>2-</sup>, the tetra-coordinated complex has two intense bands at 296 nm and 410 nm. It should be noted that Elleb *et al.* confirmed the absence of CuCl<sub>2</sub> neutral species as predicted by Hubacek and Gutmann due to its self-dissociation into [CuCl]<sup>+</sup> and [CuCl]<sup>3-</sup> as fast as it was formed, hence not being visible in the UV/Vis spectra.

**Table 5-2**-Near IR assignments of copper (II) chloride species in DMF.

Species	Band	Reference
DMF-solvated copper(II) ion- square planar geometry $[\text{CuCl}_4]^{2-}$	790 nm	Elleb <sup>459</sup>
<i>Pseudo</i> -tetrahedral $[\text{CuCl}_4]^{2-}$	1180 nm	Furlani and Morpurgo <sup>460</sup>
Mono-chlorocuprate $[\text{CuCl}]^+$	870 nm	Elleb
Tri-chlorocuprate $[\text{CuCl}_3]^-$	1110 nm	Elleb
Tetra-chlorocuprate $[\text{CuCl}_4]^{2-}$	1200 nm	Elleb

Elleb further noted the remarkable increase in stability of the DMF-Cu(II) complexes in comparison to their water equivalents, specifically a  $10^3$  and  $10^{10}$  increase in the rate constants of the formation of the  $[\text{CuCl}]^+$  and  $[\text{CuCl}_3]^-$  species respectively hence indicating the formation of ionic pairs of Cu(II) complexes. This corroborates Guttmann's views, that auto complex formation has to be expected in this system, as the solvent DMF and the anionic ligand  $\text{Cl}^-$  have similar donor numbers hence taking into account auto complexation and the suspected geometries of the complexes of copper(II) it would be expected that the solution would follow the complexation in Figure 5-2. The cationic species being in the square planar geometry and the anion in a tetrahedral geometry.<sup>459</sup>

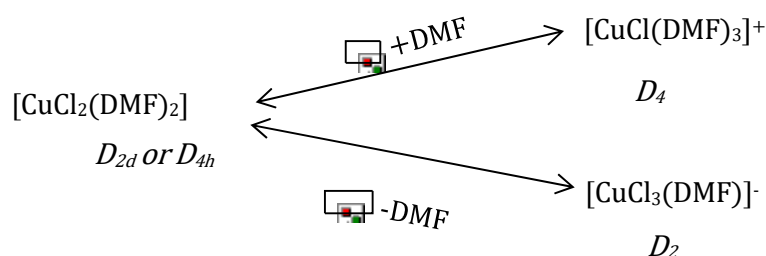
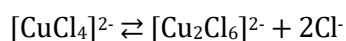


**Figure 5-2**-Suspected auto complexation by Gutmann and Elleb-(adapted figure).<sup>459</sup>

There is still ambiguity over the coordination of DMF with X-ray diffraction studies indicating that either 4 or 6 solvent molecules can be coordinated. The solvent molecules and the counter anions appear to be the determining factor for the coordination number of the copper species and the nature of the complexes formed.<sup>455</sup> Utilising DMSO as an analogous example to the DMF system it would be expected that you would observe very similar results, however, this is not the case with differing enthalpies of formation *i.e.* DMSO is a more associative solvent causing different species to form.<sup>457</sup>

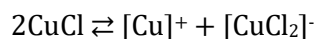
Studies with copper (II) salts in acetonitrile by Manahan and Iwanoto show that again there are three predominant and stable species charged present  $[\text{CuCl}]^+$ ,  $[\text{CuCl}_3]^-$ ,  $[\text{CuCl}_4]^{2-}$ .<sup>461</sup> The presence of the neutral and ionic species  $[\text{CuClL}_3]^+$ ,  $[\text{CuCl}_2\text{L}_2]$ ,  $[\text{CuCl}_3\text{L}]^-$  and  $[\text{CuCl}_4]^{2-}$  (L = AN) has also been analysed *via* polarography (electrochemical methods) and reduction of the solutions *via* two step electron reductions.<sup>462</sup> In these studies, no dimeric copper species were reported, which may be present at higher concentrations of copper salts with donor ligands. Kharitonov and Golubeva have identified two anionic copper chloride species may exist; the aforementioned  $[\text{CuCl}_4]^{2-}$  and  $[\text{Cu}_2\text{Cl}_6]^{2-}$  as per Equation 5-1.  $[\text{Cu}_2\text{Cl}_6]^{2-}$  visible as a band at 388 nm.<sup>463</sup>

**Equation 5-1**



Copper(I) chloride is a more difficult species to quantify due to its instability in a variety of molecular solvents and consequent disproportionation to elemental copper and a Cu(II) species. Manahan and Iwanoto suggested the following equilibrium existed in acetonitrile solutions.<sup>461</sup>

**Equation 5-2**



In regards to bonding with acetonitrile computational studies have indicated formation of a dative bond between the monovalent copper cation is accompanied by back donation due to the radial contraction of the s-/p- shells and expansion of the d-/f- shells.<sup>464</sup> Studies by Rodgers *et al.* have further suggested the possibility of  $[\text{Cu}(\text{CH}_3\text{CN})_x]^+$  clusters where  $x = 1-5$ .<sup>465</sup> Tetrakis(acetonitrile)copper salts were initially synthesised and characterised by Morgan *et al.* *via* reduction of silver nitrate with copper powder in acetonitrile.<sup>466,467</sup> They have been a useful tool in a variety of copper complex synthetic chemistry with the hexafluorophosphate salt being the anion of choice due to its diffuse nature.<sup>468</sup> It should be further noted that the cationic copper acetonitrile complex is referred to have a near ideal tetrahedral geometry as determined by single crystal X-ray diffraction.

The linear two-coordinate copper (I) complexes were initially synthesised using bulky amine ligands such as substituted pyrazoles, imidazoles and along with functionalised-calixarenes *etc.*<sup>469,470</sup> Jameson and Sorrell have also reported two-coordinated copper(I) complexes synthesised *via* repeated recrystallisation of the

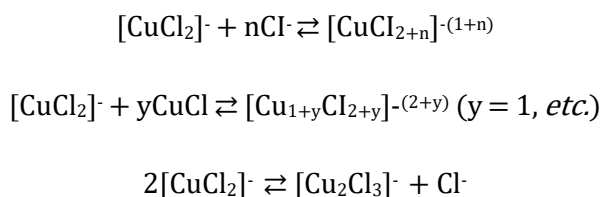
tetra-coordinated acetonitrile complexes.<sup>471</sup> Fused salts of triethylammonium chloride and copper (I) chloride result in the formation of a molten salt containing the  $[\text{CuCl}_2]^-$  anion. However, at higher concentration the presence of the  $[\text{Cu}_2\text{Cl}_3]^-$  anion is detected via Raman spectroscopy with broad unresolved peaks from 270-300  $\text{cm}^{-1}$  which is distinct from the sharp band indicating  $[\text{CuCl}_2]^-$  at 302  $\text{cm}^{-1}$ .<sup>472,473</sup>

In summary, the behaviour of Cu(I) and Cu(II) species in molecular solvents has a vast array of coordination possibilities; within literature it is evident that the nature of the solvent/ligand and the environment has a huge impact on what species is present. Furthermore, the stability of each species varies on its coordination environment. Chlorocuprates in ionic liquids, as will be discussed, have a more predictable speciation such that an anionic species is always formed and the species present are readily identified using spectroscopic techniques.<sup>4</sup>

#### 5.1.1.1 Chlorocuprate ionic liquids

One of the first reports of Cu(I) ionic liquids was the crystal structure determination of bis(trimethylammonium) decabromotetracuprate(II) salt.<sup>474</sup> Significant work by Yoke and co-workers in 1973 studied the vibrational spectroscopy of Cu(I) halide and phosphonium and ammonium cations.<sup>475</sup> It was found that species such as  $[\text{CuCl}_2]^-$ ,  $[\text{CuCl}_3]^{2-}$  and  $[\text{Cu}_2\text{Cl}_3]^-$  were present in these ionic liquids. Further investigations into the physicochemical properties of these ionic liquids found that the lowest melting points were achieved at  $\chi_{\text{CuCl}} = 0.50$  indicating that in the chloride poor acid salts *i.e.* higher  $\chi_{\text{CuCl}}$  oligomeric species such as  $[\text{Cu}_2\text{Cl}_3]^-$  are formed. In chloride rich basic salts *i.e.* lower  $\chi_{\text{CuCl}}$ , chloride rich species such as  $[\text{CuCl}_3]^{2-}$  are formed. The equilibria follow chloride anion transfer according to Equation 5-3.

Equation 5-3



Copper(II) ionic liquids have also been studied and under anhydrous conditions been found to form  $[\text{CuCl}_4]^{2-}$  anions.<sup>476</sup> Chlorocuprate ionic liquids have been well documented in literature for their interesting coordination and redox behaviour for several decades. Specific examples of utilisation of copper's unique redox behaviour is evident in a variety of chlorocuprate ionic liquids including mercury capture<sup>332,477</sup>,

preparation of copper containing thin films<sup>478</sup>, and radical polymerisations.<sup>479</sup> In regards to protic ionic liquids and their interactions with chlorocuprate ions; Nakama *et al.* have completed an intricate study surrounding the interactions of N-alkyldiethylenetriamine and copper(II) salts.<sup>480</sup> Use of the polydentate amine ligands has been popular within PILs including N-hexaethylenediamine<sup>481</sup>.

Fulton and co-workers found that chlorocuprates and the chlorocuprate anions found are varied dependent on their water content with low  $\chi_{\text{H}_2\text{O}}$  content exhibiting a tetrahedral chlorocuprate species and at higher  $\chi_{\text{H}_2\text{O}}$  content an octahedral or square pyramidal species forms with the latter exhibiting no Cu-Cl bonding as shown in Figure 5-3.<sup>482</sup> This speciation was determined *via* UV/Vis spectroscopy, XANES and DFT modelling.

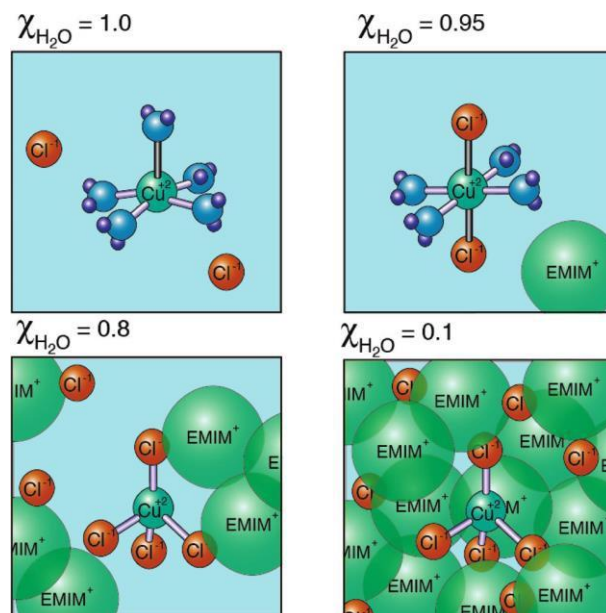


**Figure 5-3**-Reproduced schematic of various cation-anion structures in ionic liquid-water mixture for various mole fractions of water as indicated by Fulton and co-workers.<sup>482</sup>

Cu(I) salts within literature commonly adopt coordination numbers of 2, 3 or 4, which in theory corresponds to  $\chi_{\text{CuCl}} = 0.50$ , 0.33 and 0.25.<sup>483–487</sup> Indeed, studying coordination chemistry of CuCl and triphenylphosphine ( $\text{PPh}_3$ ) in several organic solvents, Reichie and Jardine demonstrated that a range of coordination modes is possible, with crystal structures of  $[\text{CuCl}(\text{PPh}_3)]$ ,  $[\text{CuCl}(\text{PPh}_3)_2]$  and  $[\text{CuCl}(\text{PPh}_3)_3]$  recorded for crystals grown under various conditions.<sup>487,488</sup> However, both demonstrated that more complicated scenarios are also possible with both cyclic and oligomeric systems possible. The reaction of 1-decylimidazole,  $\text{C}_{10}\text{im}$ , and  $\text{CuBr}$  yielded an ionic compound,  $[\text{Cu}(\text{C}_{10}\text{im})][\text{CuBr}_2]$ , where crystal structure featured

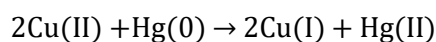


linear coordination of both the cation and anion, with close contact of two copper centres.<sup>489</sup>

Similar observations have been made by Frisch and co-workers for 0.1 M CuCl solution in a choline chloride-urea deep eutectic solvent, where a mixture of  $[\text{CuCl}_2]^-$  and  $[\text{CuCl}_3]^{2-}$  was reported studied by EXAFS (average coordination number  $N_{\text{Total}} = 2.5$ ), despite chloride anions being in excess, available for Cu(I) to access higher coordination numbers.<sup>490</sup> Also utilising EXAFS spectroscopy Van Deun and co-workers determined the speciation of CuCl<sub>2</sub> in choline chloride water mixtures finding that the behaviour of the copper centre follows that observed by Fulton in chlorocuprate ionic liquids such that high water contents cause fully hydrated molecules to form.<sup>478</sup>

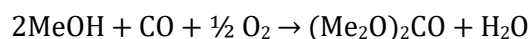
As briefly mentioned, there are several applications of chlorocuprate ionic liquids within literature. A high-profile application is in the extraction of mercury from natural gas using 1-butyl-3-methylimidazolium chlorocuprate(II) ionic liquids. This process works via a redox reaction in which elemental mercury is oxidised to Hg(II) and the Cu(II) reduced to Cu(I) as per Equation 5-4 via a sequence of multiple redox steps. The Cu(I) species formed remains as a  $[\text{CuCl}_2]^-$  anion.

Equation 5-4



Wasserscheid and co-workers utilised supported chlorocuprate ionic liquids in the gas-phase oxycarbonylation of methanol to form dimethyl carbonate as per Equation 5-5.<sup>491</sup> A supported ionic liquid of various anions (chloride, triflate and acetate) are doped with various concentrations of Cu(I) and Cu(II) salts which undergo redox catalysis causing oxidation of the methanol and reduction of the carbon monoxide.

Equation 5-5

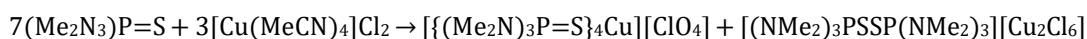
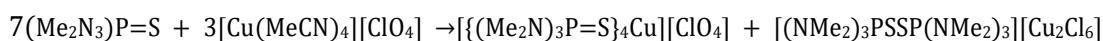


### 5.1.2 Chlorocuprate liquid coordination complexes

Liquid coordination complexes, LCCs classically, are defined as eutectic mixtures of metal halides and organic donors. Initial work surrounding LCCs has been focused upon the group 4, 12-15 metal halides, however, little work has been focused on other transition metals such as copper.<sup>22,375</sup> Already, interesting redox behaviour has been observed in LCC systems containing trioctylphosphine with SbCl<sub>3</sub> and SnCl<sub>4</sub>,

specifically as redox reactions. As aforementioned, the speciation of copper chloride species at high concentration in molecular solvents such as DMSO, DMF and acetonitrile have been studied in depth, however, the neutral species that may be present are still somewhat uncertain. Use of what would be termed more classical donor ligands such as phosphines is not novel; reports of reductions by copper(II) and antimony(V) with phosphine selenides and sulphides have been investigated by Reid *et al.*<sup>492</sup> Ainscough and Meek both suggested the Cu(II) driven reductions of P<sub>111</sub>S proceeded *via* Equation 5-6 with Cu(ClO<sub>4</sub>)<sub>2</sub> and CuCl<sub>2</sub>.<sup>493,494</sup>

#### Equation 5-6



Similar behaviour has been reported in regards to Cu(II) complexes with thiourea in that the thiourea forms a formamidine disulphide cation  $[(\text{NH}_2)_2\text{CS} - \text{SC}(\text{NH}_2)_2]^{2+}$  with a copper containing counter anion hence care must be taken when selecting a donor ligand.<sup>495</sup> Similar behaviours can be found in phosphorous containing compounds, in which  $[\text{R}_3\text{PX}]\text{X}$  like species can be formed with the first report by Webster, Beattie and Livingston in 1965 in which adducts of the  $[\text{PCl}_4]^+$  cation were formed with phenathroline and pyridine.<sup>496,497</sup> More recently, such compounds have been utilised within catalytic processes, specifically in phosphorus (V)-mediated nucleophilic substitution reaction in the chlorination and bromination reactions of alcohols. A P(V) species,  $[\text{R}_3\text{PX}]\text{X}$  mediates the reaction. Initially, a  $\text{R}_3\text{PO}$  species is reduced to  $\text{R}_3\text{P}$  and is then oxidised *via* a reaction with the halogenated starting materials to form the  $[\text{R}_3\text{PX}]\text{X}$ .<sup>498</sup>

Copper (I) salts with phosphine sulphide have been reported throughout literature in multiple geometries and compositions. Meek and co-workers initially predicted 2-coordinate and 4-coordinate geometries;  $[\text{CuL}_4][\text{CuCl}_2]$  and  $[\text{CuL}_2][\text{CuX}_2]$  however, later confirming that 3-coordinate geometries were also evident.<sup>494,499</sup> Black and Levason studied the behaviour of  $\text{Cu}[\text{OTf}]$ ,  $\text{Cu}[\text{BF}_4]$  and  $\text{Cu}[\text{PF}_6]$  salts with sulphur, selenium and tellurium donors.<sup>500</sup> It was observed, that the addition of sulphur, selenium and tellurium donors the salts formed  $[\text{CuL}_x][\text{A}]$  where  $x = 2-4$  ( $\text{A} = \text{OTf}$ ,  $\text{BF}_4$ ,  $\text{PF}_6$ ) indicating that 2- to 4- coordinate geometries are observed. The latter tetra-coordinate geometry was not as evident as initially though even in significant ligand excess; previous studies in which the  $[\text{CuL}_4]^+$  cations were obtained utilised

anhydrous methanol as a co-solvent which may be key in stabilising the species formed.<sup>485</sup>

A series of studies by Binnemans and co-workers surrounded copper(I) salts such as CuNTf<sub>2</sub> with acetonitrile.<sup>501</sup> Forming new ionic complexes such as [Cu(CH<sub>3</sub>CN)<sub>n</sub>]<sup>+</sup>[Tf<sub>2</sub>N]<sup>-</sup> (n = 2, 4) with n changeable upon heating, these low melting complexes (n = 4, 70 °C) somewhat mid-point between the ionic liquids and liquid coordination complexes. Notably, the tetrahedral coordinated copper is dissociated from the bistriflamide anion whereas in the n = 2 species the Cu(I) centre is in a trigonal planar geometry with 2 acetonitrile molecules coordinated and a bond from the central nitrogen of the bistriflamide anion. Such species have been used in redox flow batteries exploiting the high metal concentrations achieved and the redox behaviour of copper.<sup>502</sup>

As stated in chapter 4.1, the composition of liquid coordination complexes contains multiple equilibrated coordination complexes, rather than a single well-defined structure. When defining speciation the most obvious answer is not always the correct one.<sup>387</sup>

#### **5.1.2.1 Conventional ionothermal methodologies to synthesis copper / gallium / indium chalcogenide semiconductor materials**

Copper indium selenide, CIS were first synthesised in 1993 by Nadenau, Ruckh and co-workers who highlighted the possible applications of such materials to solar cells due to their 1.04 eV band gaps *i.e.* within the range of visible light excitations.<sup>503,504</sup> O'Brien and co-workers in 1999 refined the hot injection techniques using P<sub>888</sub>Se, P<sub>888</sub> and P<sub>888</sub>O with InCl<sub>3</sub> and CuCl, however, the methodology requires several elaborate reagent additions, and temperature stabilisations to form CuInSe<sub>2</sub> and Cu<sub>2-x</sub>Se nanoparticles of 4 - 6 nm.<sup>505</sup> Conventional methodologies require the use of long chain alkyl amines such as triethanolamine, oleyamine *etc.* and conventional capping agents such as P<sub>888</sub>O. However, these methodologies require precise control over a variety of reaction conditions such as temperature, hence scalability is difficult as control is crucial in nucleation and growth of such compounds in regards to desired morphology for application.<sup>506</sup>

Chikan and Kelley notably utilised the P<sub>888</sub>Se ligand as a precursor in which gallium (II) selenide was formed.<sup>507</sup> This methodology encompassed a mixture of P<sub>888</sub> and P<sub>888</sub>O with elemental selenium added, hence forming P<sub>888</sub>Se to which trimethylgallium was added *via* a hot injection method. The GaSe formed highly luminescent nanoparticles of 4 - 6 nm. It is believed that greater understanding of

the starting materials and a greater homogeneity of the precursor like that within the group 13 and trioctylphosphine chalcogenide liquid coordination complexes rather than the often expensive and impure ionic liquid-containing precursors will provide a simple and effective alternative. Synthesis of binary compounds is relatively successful at larger scale, however, moving from binary to ternary compounds such as CIGS is challenging. Control of composition and morphology is the main task of such syntheses as especially in ternary compound multiple compositions (phases) can exist.<sup>508</sup>

In regards to the ionothermal synthesis of copper indium selenide, CIS, Tyrell *et al.* found that a two-step process incorporating the use of  $[\text{C}_8\text{mim}][\text{InCl}_4]$  with  $\text{Ph}_2\text{Se}_2$  for an initial reaction that is presumed to form  $\text{In}_2\text{Se}_3$  although this intermediate was not clarified; followed by the addition of a stoichiometric amount for  $\text{CuCl}$  and a further microwave-assisted reaction.<sup>509</sup> Although showing incorporation and homogeneity of the precursor materials the true potential of the ionic liquids was not fully discovered and the inelegancy of a two-step process could be improved upon. Furthermore, ionic liquids cations add an extra step, and therefore cost, to the synthesis and are a known source of potential impurities, hence LCCs were believed to be the solution to these issues being a purer, less expensive and more controllable alternative neoteric solvent-precursor. Other methods by Tyrell with smaller organic cations such as  $[\text{C}_2\text{mim}][\text{CuCl}_2]$  with  $\text{Ph}_2\text{Se}_2$  and  $[\text{C}_2\text{mim}][\text{InCl}_4]$  resulted in the formation of intermediate species of formula  $[\text{CuCl}(\text{Se}_2\text{Ph}_2)_2]_n$ . (Figure 5-55 ) which resembles a typical LCC species.<sup>509</sup>

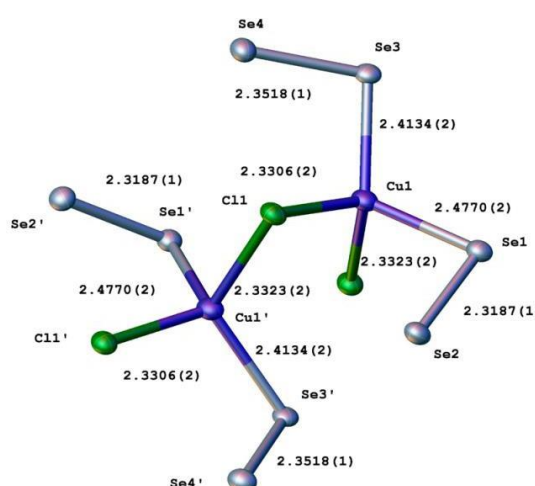


**Figure 5-4-** Part of the crystal structure of the polymeric  $[\text{CuCl}-(\text{Se}_2\text{Ph}_2)_2]_n$ . Ellipsoids are shown at a 50% probability level.<sup>509</sup>

LCCs provide an alternative reagent to the previously used ionic liquid methods along with the donor ligand acting as an intrinsic source of chalcogenides ( $P_{888}E$ ,  $E = S, Se$ ) and as a capping agent.

## 5.2 Results and Discussion

Firstly, forming LCCs with Cu(I) and Cu(II) chlorocuprate salts, the stability and  $\chi_{CuClx}$  achievable will be assessed, and moving forward a similar approach to that taken with the elucidation of the Group 13 chlorometallate LCCs such that multinuclear NMR, IR, Raman and EXAFS spectroscopy will be utilised with the addition of XANES and UV/Vis spectroscopic techniques. Upon gaining greater understanding of the LCCs speciation there will be attempts to integrate these LCCs along with those studied previously to semiconductor synthesis to form binary and ternary compounds.

### 5.2.1 Chlorocuprate liquid coordination complexes

#### 5.2.1.1 Synthesis and observations

Copper (I) chloride formed a wealth of LCCs with trioctylphosphine oxide, trioctylphosphine sulphide and trioctylphosphine selenide when handled similarly to the chlorogallate LCCs. Comfortably forming solutions up to  $\chi_{CuCl} = 0.50$  and more sluggishly  $\chi_{CuCl} = 0.50$ , a variation in colour of the solutions is observed specifically for  $P_{888}O$  forming blue/green solutions,  $P_{888}$ -colourless,  $P_{888}S$  and  $P_{888}Se$ - forming dark solutions at higher  $\chi_{CuCl}$  values. All solutions prepared are listed in Table 5-3.

**Table 5-3**-Summary of chlorocuprate liquid coordination complexes prepared.

Ligand	Copper chloride, CuCl <sub>x</sub>	$\chi_{\text{CuCl}_x}$	Observations
P <sub>888</sub>	CuCl	0.25	Colourless solution
		0.33	Colourless solution
		0.50	Colourless solution
	CuCl <sub>2</sub>	0.25	light yellow solid
		0.33	light yellow solid
		0.50	light yellow solution
		0.60	light yellow solution
P <sub>888</sub> O	CuCl	0.25	Light blue/green solution
		0.33	Light blue/green solution
		0.50	Light blue/green solution
	CuCl <sub>2</sub>	0.25	red/orange solution
		0.33	red/orange solution
		0.50	red/orange solution
		0.60	-
P <sub>888</sub> S	CuCl	0.25	light yellow solution
		0.33	light yellow solution
		0.50	dark brown solution
	CuCl <sub>2</sub>	0.50	red solution with yellow precipitate
P <sub>888</sub> Se	CuCl	0.25	light yellow solution
		0.33	light yellow solution
		0.50	dark brown solution
	CuCl <sub>2</sub>	0.50	red solution with black ppt

### 5.2.1.2 Nuclear resonance spectroscopy

Multinuclear NMR has been utilised to elucidate binding within the systems specifically the <sup>31</sup>P nucleus. <sup>65</sup>Cu and <sup>63</sup>Cu NMR are quadrupolar nuclei hence it was deemed inadequate to provide information on speciation as only symmetry could be determined if clarity was maintained as the quadrupolar moment of these nuclei is substantial. For example  $^1J(^{63/65}\text{Cu}-^{31}\text{P}) = \text{ca. } 1200 \text{ Hz}$  of  $[(\text{CH}_3\text{O})_3\text{P}]_4\text{CuCl}$  in  $\text{CH}_3\text{CN}$  have been found to produce a single broad peak at -200 ppm with peak width at half peak height approximately 130 ppm.<sup>510</sup>

Levason and Black investigated the NMR spectra of several Cu(I) phosphine, phosphine sulphides and phosphine selenides. Tertiary and quaternary phosphines were found to give mixed results in <sup>31</sup>P and <sup>63</sup>Cu NMR spectra; depending on the nature of the ligand. As shown in Figure 5-5, resolved spectra were obtained for  $[\text{Cu}(\text{PPhH}_2)_4]^+$ , whereas fast exchange of species such as  $[\text{Cu}(\text{PEt}_3)_4]^+$  resulted in a singlet at all temperatures.<sup>500</sup>

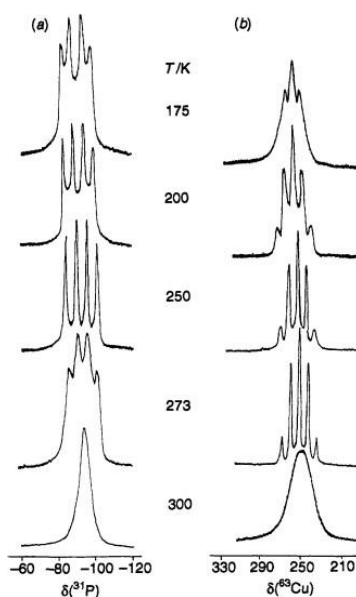


**Figure 5-5**-Variable temperature NMR  $^{31}\text{P}$ - $\{^1\text{H}\}$  and  $^{63}\text{Cu}$  NMR spectra of  $[\text{Cu}(\text{PPhH}_2)_4]^+$ .<sup>500</sup>

Phosphine sulphides and phosphine selenides of the  $[\text{Cu}(\text{L})_4]^+$  ( $\text{L} = \text{R}_3\text{P}=\text{S}$  or  $\text{R}_3\text{P}=\text{Se}$ ) composition showed similar spectra with exchange being prevalent throughout and spectra being somewhat resolved at low temperatures. As discussed, the  $^{63}\text{Cu}$  NMR spectra are not expected to elucidate the speciation to the extent that was achieved by Levason and Black with  $[\text{Cu}(\text{PPhH}_2)_4]^+$  (Figure 5-5) as both cationic, anionic and neutral species are expected to form in 2-4 coordinate systems with bridging species also present. Dimethyl sulphide studies with Cu(I) salts such as  $\text{Cu}[\text{PF}_6]$ ,  $\text{Cu}[\text{BF}_4]$ , and  $\text{Cu}[\text{SO}_2\text{CF}_3]$  found that the presence of excess sulphide ligand assisted with the ability to obtain a  $^{63}\text{Cu}$  NMR spectrum, however, only at very low temperature of ca. 180 – 250 K, which is not accessible in the LCC type systems as the addition of any solvent will affect the equilibria present in the system hence not giving a true insight into the LCC systems.

#### 5.2.1.2.1 Copper(I) chloride liquid coordination complexes

$^{31}\text{P}$  NMR spectroscopy has alluded to the formation of the Cu-P and Cu-X=P bonding motifs with shifts observed in each donor ligand used. However, as shown in Figure 5-6, Figure 5-7 and Figure 5-8 little variations in the shifts are observed as  $\chi_{\text{CuCl}}$  is increased. Within the  $\text{P}_{888}$  system it is observed that the  $^{31}\text{P}$  peak for  $\text{P}_{888}$  shifts from -29.44 ppm for the unbound trioctylphosphine ligand to -20.7 ppm when bound to copper at  $\chi_{\text{CuCl}} = 0.50$ . It is observed that the peak does not shift with increasing  $\chi_{\text{CuCl}}$  compared to the aforementioned chlorogallate studies by Hogg *et al.*, in which the  $^{31}\text{P}$  peaks referring to the  $\text{P}_{888}$  is found between 40-50 ppm.<sup>387</sup> The change in charge and electrophilicity of each of the central metals such as  $\text{Cu}^+$  is

significantly less electrophilic than  $\text{Ga}^{3+}$  hence binding will naturally be weaker especially due to the atom's comparable sizes being period 4 elements.

$\text{P}_{888}\text{S-CuCl}$  and  $\text{P}_{888}\text{Se-CuCl}$  systems exhibit a small shift with the addition of copper (I) chloride from 46.78 ppm to 51.35 ppm ( $\chi_{\text{CuCl}} = 0.50$ ) and 35.65 ppm to 37.84 ppm ( $\chi_{\text{CuCl}} = 0.50$ ) respectively. The downfield shift with increasing  $\chi_{\text{CuCl}}$  indicates Cu-E=P/ Cu-P bonding occurs.

**Table 5-4-** $^{31}\text{P}$  NMR signals of neat  $\text{P}_{888}$  and liquid coordination complexes of  $\text{CuCl}$  and  $\text{P}_{888}$ .

$\chi_{\text{CuCl}}$	$\delta_{31\text{P}}$ (ppm)	$\Delta\delta_{31\text{P}}$ compared to neat $\text{P}_{888}$ (ppm)	Reference
0 (neat $\text{P}_{888}$ )	-29.44	-	Hogg <sup>375</sup>
0.25	-22.33 -9.03*	7.11 20.41*	this work
0.33	-20.92 -23.37 -7.17*	8.52 6.07 22.27*	this work
0.50	-20.70 -24.22 -7.65*	9.04 5.26 21.79*	this work
$\text{P}_{888}\text{-ZnCl}_2$ , $\chi_{\text{ZnCl}_2} = 0.50$	-20.03	9.41	Hogg <sup>375</sup>

\* Impurity due to 99% purity trioctylphosphine



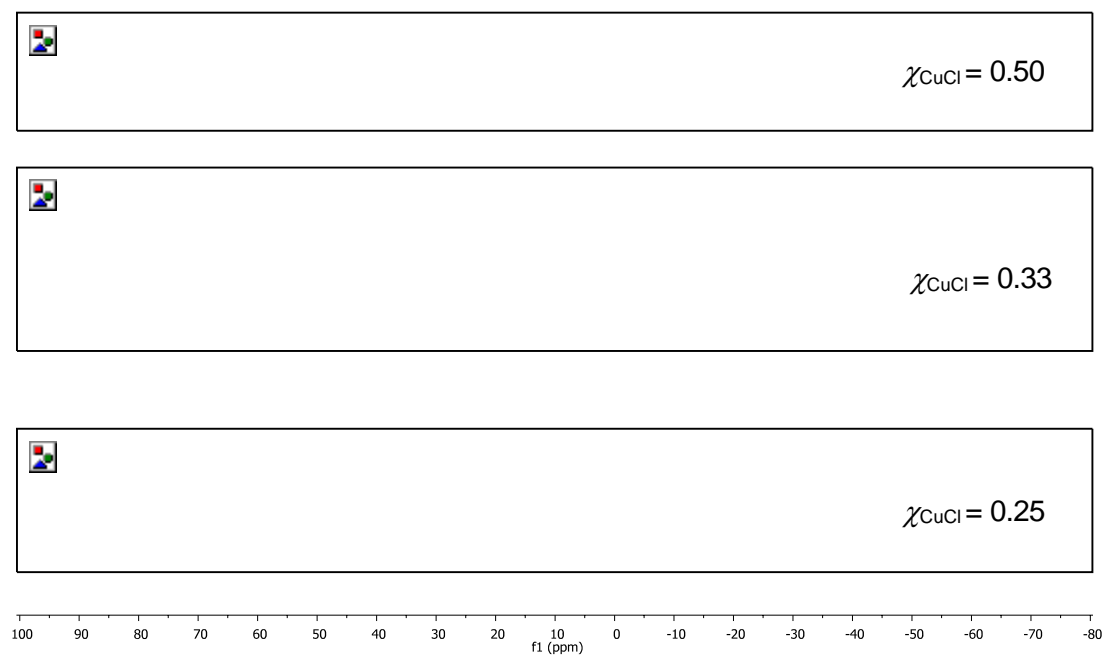


**Figure 5-6-** $^{31}\text{P}$  NMR spectra of  $\text{P}_{888}\text{-CuCl}$   $\chi_{\text{CuCl}} = 0.50, 0.33, 0.25$ . (Top-bottom).

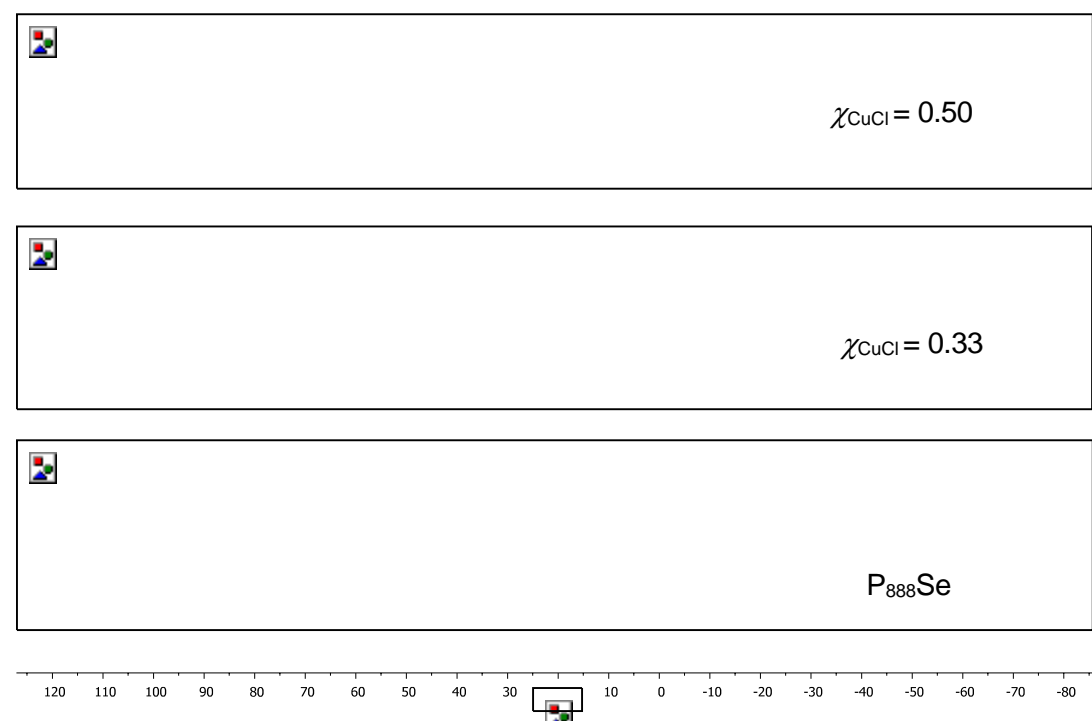


**Figure 5-7-** $^{31}\text{P}$  NMR of  $\text{P}_{888}\text{Se-CuCl}$   $\chi_{\text{CuCl}} = 0.50, 0.33$ .  $\text{P}_{888}\text{Se}$ . (Top to bottom)

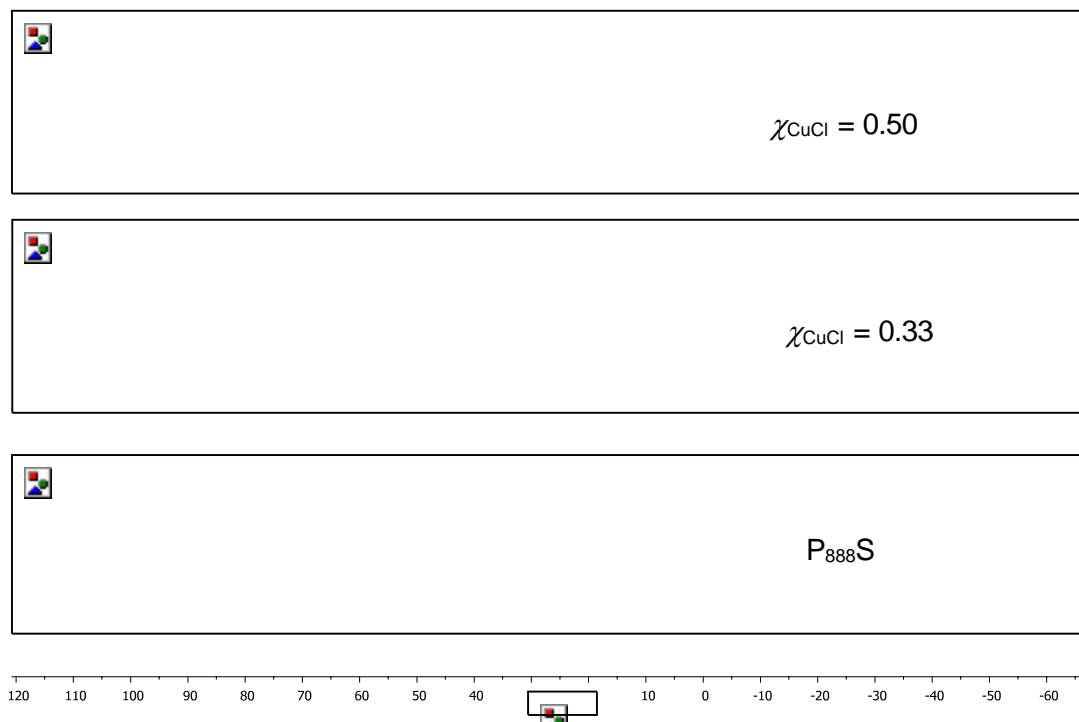


**Figure 5-8-**  $^{31}\text{P}$  NMR of  $\text{P}_{888}\text{S-CuCl}$   $\chi_{\text{CuCl}} = 0.50$ ,  $0.33$  and  $\text{P}_{888}\text{S}$ . (Top-bottom)

The  $\text{P}_{888}\text{S-CuCl}$  compounds shift with coordination to 46.8 ppm is similar to that observed by Levason and Black for  $[\text{Cu}(\text{Ph}_3\text{PS})_3]^+$  salts at 39.3 ppm. The  $\text{P}_{888}\text{Se}$  compounds shift with coordination to 37.8 ppm is also similar to that observed by Levason and Black for  $[\text{Cu}(\text{Ph}_3\text{PSe})_3]^+$  salts at 29.7 ppm.<sup>500</sup>

**Table 5-5-**  $^{31}\text{P}$  NMR signals of neat  $\text{P}_{888}\text{S}$  and  $\text{P}_{888}\text{Se}$  liquid coordination complexes of  $\text{CuCl}$  and  $\text{P}_{888}$ .

Ligand	$\chi_{\text{CuCl}}$	$\delta_{31\text{P}}$ (ppm)	$\Delta\delta_{31\text{P}}$ compared to neat $\text{P}_{888}\text{E}$ (ppm)
$\text{P}_{888}\text{S}$	0	49.49	-
	0.33	50.05	0.56
	0.50	50.97	1.48
$\text{P}_{888}\text{Se}$	0	36.41	-
	0.33	37.64	1.23
	0.50	37.85	1.44

Black and Levasons' cooling method was applied to the  $\text{P}_{888}\text{-CuCl}$   $\chi_{\text{CuCl}} = 0.25$  LCC system. Unlike the resolution of peaks observed with  $[\text{Cu}(\text{PPhH}_2)_4]^+$  (Figure 5-5) no resolution of the peak was observed with cooling.<sup>500</sup> The  $\text{P}_{888}\text{-CuCl}$   $\chi_{\text{CuCl}} = 0.25$  LCC was suspended in *d*-chloroform and was cooled to 223 K;  $^{31}\text{P}$  NMR spectra were recorded and a single peak at *ca.* -22.33 ppm was observed throughout.

#### 5.2.1.2.2 Copper(II) chloride liquid coordination complexes

Significant changes in behaviour have been observed moving between Cu (I) and Cu (II) chloride and chalcogenide donor ligands. Unlike its Cu (I) counterpart, Cu (II) did not form LCCs with chalcogenide donors,  $P_{888}E$  ( $E = S, Se$ ) instead a deep blood red solution formed and instantaneous precipitation of the chalcogenide was observed. This precipitate was confirmed to be the elemental chalcogenide species via SEM/EDX microscopy as shown in Figure 5-10.

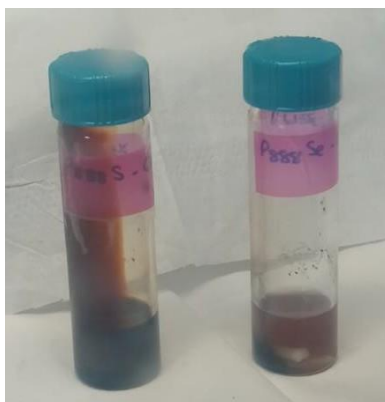


Figure 5-9- LCCs (L-R)  $P_{888}S-CuCl_2$   $\chi_{CuCl_2}=0.50$  and  $P_{888}Se-CuCl_2$   $\chi_{CuCl_2}=0.50$ .

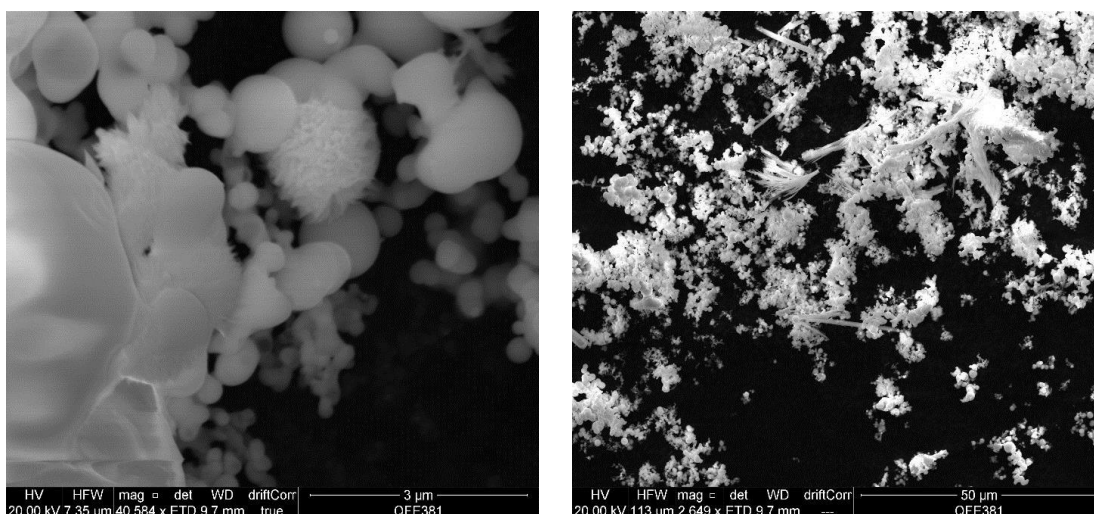
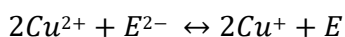


Figure 5-10- SEM analysis of  $P_{888}Se-CuCl_2$   $\chi_{CuCl_2}=0.50$  precipitate.

The driving force for this breakdown in the donor ligand is somewhat peculiar in the respect that the Cu (II) moves to the Cu (I) state, which is well documented for its instability and consequent reversion to the Cu (II) and Cu(0) species.<sup>511</sup> It has been proposed that the redox occurs in accordance with Equation 5-7.

Equation 5-7



E= sulphur/selenium

As mentioned, the precipitation is suspected to be due to a redox reaction between the chalcogenide and for the chlorocuprate it was suspected that copper (I) is present and not the paramagnetic copper (II) species, hence NMR analysis is obtainable. Again, the  $^{31}\text{P}$  nucleus was utilised and attaining a clear spectrum as shown in Figure 5-11 and Figure 5-12 for  $\text{P}_{888}\text{S}$  and  $\text{P}_{888}\text{Se}$ , respectively. As shown in Figure 5-11 the spectrum obtained from the  $\text{CuCl}_2$  mixture indicates that there is  $\text{P}_{888}\text{S}-\text{CuCl}$  present *via* a peak at 49.54 ppm. The sharp peak observed at 103.64 ppm is indicative to a P(V) species, specifically  $[\text{P}_{888}\text{Cl}]\text{Cl}$ , previously identified by Denton *et al.*  $^{498}\text{As}$  shown in Figure 5-12, a similar trend to that observed in the  $\text{P}_{888}\text{S}$  systems is seen such that there is  $\text{P}_{888}\text{Se}-\text{CuCl}$  present *via* a peak at 37.71 ppm. The sharp peak observed at 102.68 ppm is indicative to a P(V) species,  $[\text{P}_{888}\text{Cl}]\text{Cl}$ . These chlorophosphonium salts as described by Denton *et al.*, have been noted to form *via* reactions with phosphine oxides and oxalyl chloride,  $(\text{COCl})_2$ . These compounds have been successfully applied to the Appel reaction substitution of secondary long chain alcohols to chlorides.

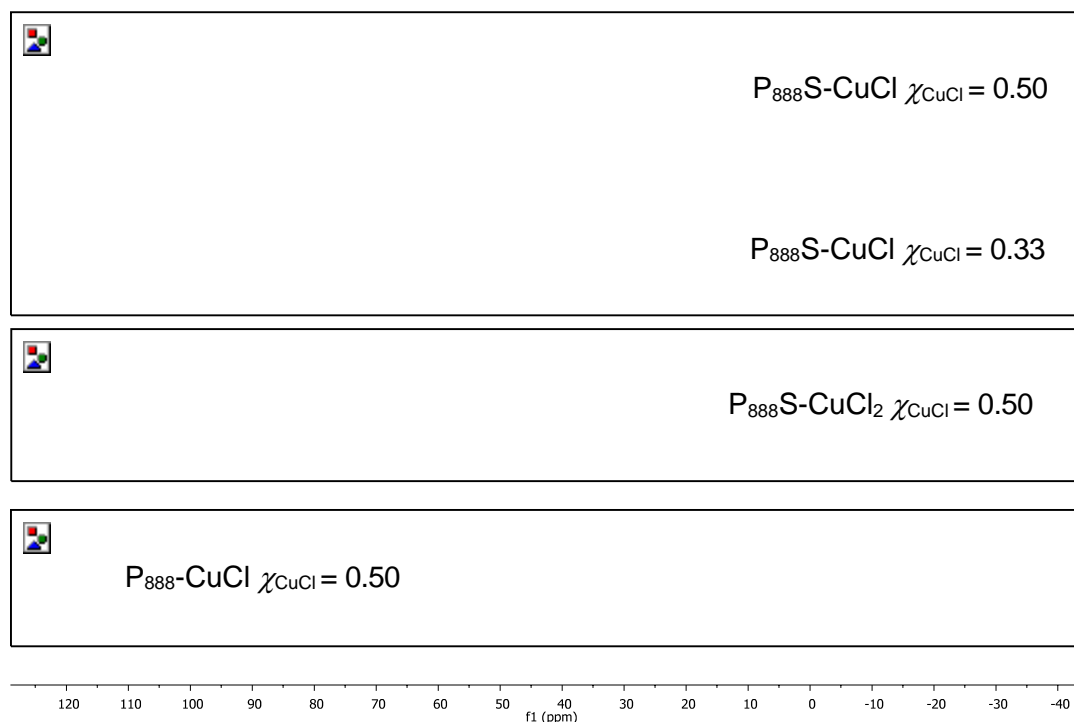


**Figure 5-11.**  $^{31}\text{P}$  NMR of  $\text{P}_{888}\text{S}-\text{CuCl}$   $\chi_{\text{CuCl}} = 0.50$ ,  $\text{P}_{888}\text{S}-\text{CuCl}$   $\chi_{\text{CuCl}} = 0.33$ ,  $\text{P}_{888}\text{S}-\text{CuCl}_2$   $\chi_{\text{CuCl}_2} = 0.50$  and  $\text{P}_{888}-\text{CuCl}$   $\chi_{\text{CuCl}} = 0.50$ . (Top-bottom)

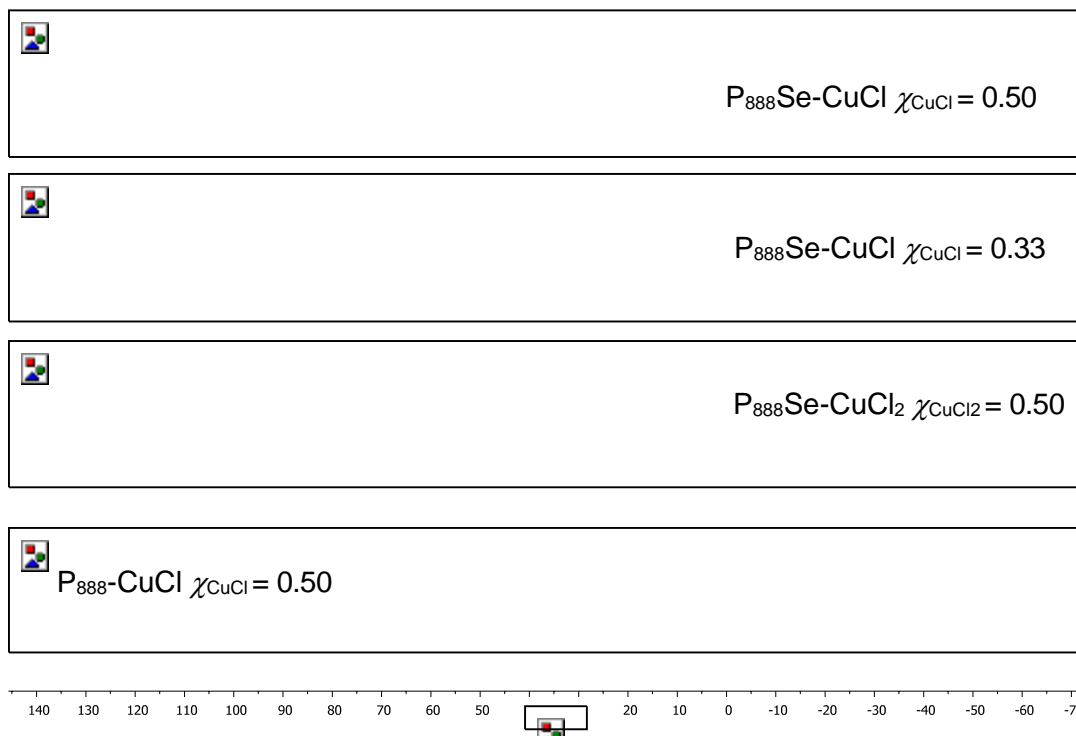
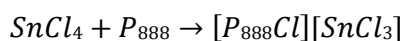


**Figure 5-12**  $^{31}\text{P}$  NMR of  $\text{P}_{888}\text{Se}$ ,  $\text{P}_{888}\text{Se}-\text{CuCl}$   $\chi_{\text{CuCl}} = 0.50$ ,  $\text{P}_{888}\text{Se}-\text{CuCl}_2$   $\chi_{\text{CuCl}_2} = 0.50$  and  $\text{P}_{888}-\text{CuCl}$   $\chi_{\text{CuCl}} = 0.50$ . (Top-bottom)

This behaviour in regards to redox has also not only been observed by the chlorocuprate species in this work, but also in  $\text{P}_{888}-\text{SnCl}_4$  in which the  $\text{Sn}^{4+}$  reduces to  $\text{Sn}^{2+}$  *via* oxidation of P(III) to P(V) as described in Equation 5-8 by Hogg *et al.*<sup>375</sup>

#### Equation 5-8



It is also suspected that the species identified as  $[\text{P}_{888}\text{Cl}]\text{Cl}$  could react with the  $\text{CuCl}$  generated to form chlorocuprate anions,  $[\text{P}_{888}\text{Cl}][\text{CuCl}_2]$ ,  $[\text{P}_{888}\text{Cl}][\text{Cu}_2\text{Cl}_4]$  *etc.*, hence significantly increasing the complexity of an already complex system. In the NMR analysis of the  $\text{P}_{888}-\text{CuCl}_2$  system no peaks referring to a P(V) species are initially observed, however, it eventually becomes apparent that these are not stable solutions as shown in Figure 5-13. It is unusual to gain a spectrum of this clarity of a paramagnetic species; however, broadening is evident in comparison to  $\text{Cu(I)}$ . It was deemed unnecessary to study higher  $\chi_{\text{CuCl}_2}$  values due to the increased concentration of the paramagnetic source. It must also be considered that any phosphorus species directly in contact with the paramagnetic  $\text{Cu(II)}$  species may not be visible in the NMR spectrum as was demonstrated in work by Nockemann,

Swadzba-Kwasny and co-workers, in which acetate anions of  $[\text{C}_4\text{mim}][\text{OAc}]$  coordinate to CuO complexes causing the acetate  $^{13}\text{C}$  peak to disappear.<sup>512</sup>

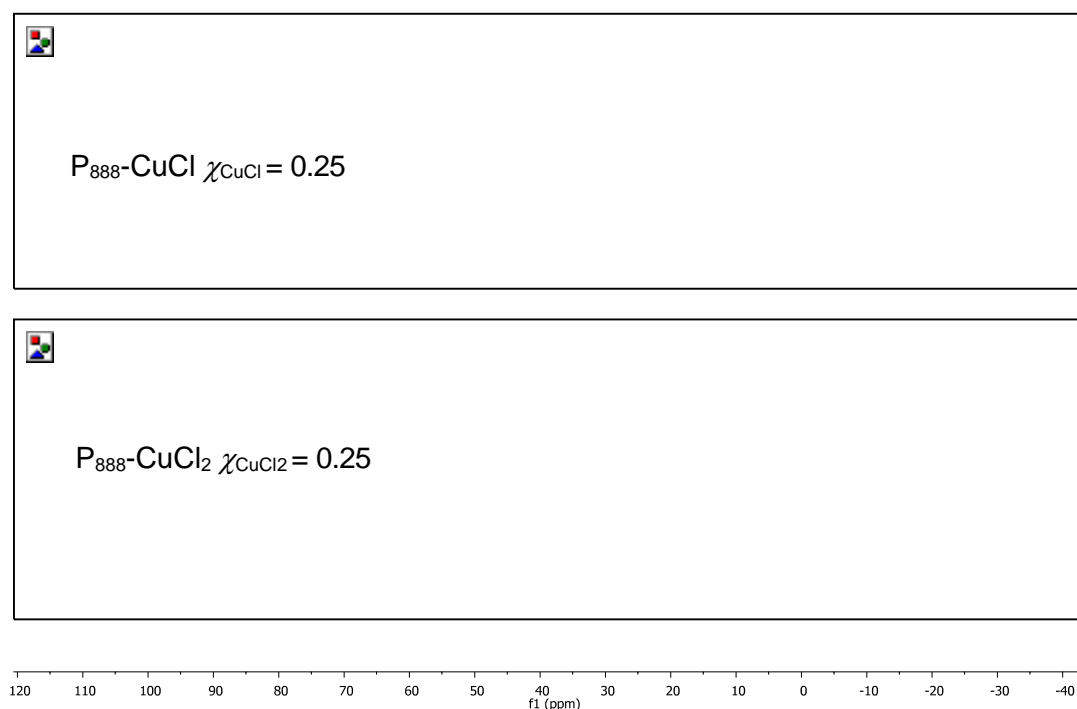


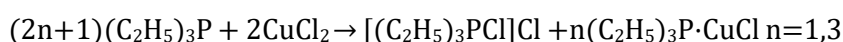
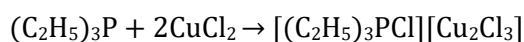
**Figure 5-13**- $^{31}\text{P}$  NMR of P<sub>888</sub>-CuCl  $\chi_{\text{CuCl}} = 0.25$ , and fresh P<sub>888</sub>-CuCl<sub>2</sub>  $\chi_{\text{CuCl}_2} = 0.25$ .

However, the lack of a peak at *ca.* 100 ppm indicates that no  $[\text{P}_{888}\text{Cl}][\text{Cl}]$  types species is present as the  $[\text{P}_{888}\text{Cl}]^+$  cation should be affected by the presence of Cu(II) species in fresh solutions. This then lead to questions surrounding the stability of P<sub>888</sub>O systems with Cu(II); this is of specific importance to the field of deep eutectic solvents for extraction capabilities. If the stability of the P<sub>888</sub>O, which is often suspected to be the driving force behind extraction capabilities, is not as stable as first thought the composition of the DES will be altered dramatically upon application.

Jardine noted that tertiary phosphines were able to reduce Cu(II) if the anion of the salt was poorly coordinating.<sup>487</sup> Collier *et al.* further noted the formation of Cu(I) phosphines from Cu(II) chloride salts as a preparative method, however, reactions were completed in ethanol solvent and the under atmospheric conditions, Further studies by Choudhry *et. al* with thiolate containing ligands and Cu(II) salts found that again the ligand was able to reduce the Cu(II) to Cu(I).<sup>513</sup> It is well reported in literature that with group 15 ligands resulted in reduction of the Cu(II) species it is somewhat unusual that this is not seen within the of P<sub>888</sub>-CuCl<sub>2</sub>  $\chi_{\text{CuCl}_2} = 0.25$   $^{31}\text{P}$  NMR as it is also understood that the by-product of such reduction specifically being

chloride salts is  $[P_{888}Cl]^+$  which should be present at ca. 100 ppm.<sup>487,514</sup> To investigate possible kinetic barriers of the predicted decomposition in the original sample of  $P_{888}-CuCl_2$   $\chi_{CuCl_2} = 0.25$  was heated with a heat gun for several minutes and  $^{31}P$  NMR spectra recorded and no change was observed. Often the use of Cu(II) salt in preparative methods utilises a polar solvent such as ethanol with heat and it is often described as a rapid process.<sup>515</sup> One of the most similar reports in literature to this work is by Axtell and Yoke who reported the redox of trimethylphosphine and copper (II) chloride in anhydrous conditions.<sup>516</sup> They found that the redox proceeds *via* two methods as shown in Equation 5-9 to which the  $[P_{222}Cl]^+$  cation was observed at 112 ppm in  $^{31}P$  NMR spectra.

Equation 5-9



In regards to  $P_{888}.CuCl_2$  and the lack of this is an unexpected and unexplainable result; throughout literature it has been demonstrated that Cu(II) reduced in the presence of phosphine ligands. The  $P_{888}-CuCl_2$  upon mixing forms a colourless solution at room temperature, and there is no significant colour change except for the solvation of the brick-red solid  $CuCl_2$  in the  $P_{888}$ . There is no obvious exotherm observed, however, this is difficult to detect under glovebox conditions. Studies by Zelonka and Baird found that Cu(II) phosphine complexes could be prepared without a redox reaction occurring with use of the bidentate ligand hexafluoroacetylacetonate to form 1:1 adducts, however, the addition of excess ligand result in the aforementioned redox processes. Piloni and co-workers formed Cu(I) and Cu(II) complexes stabilised with phosphine oxides specifically 1,1'-bis(oxodiphenylphosphoranyl)ferrocene, odppf to form  $[Cu(odppf)_2(EtOH)](BF_4)_2$  and  $[Cu(odppf)_2](BF_4)_2$ .<sup>517</sup>

Observing the sample over time it was found that redox eventually occurred together with the formation of two phases. As shown in Figure 5-14, the samples appeared to remain stable for under ambient glovebox conditions for at least 3-4 weeks. Samples aged approximately 3 months showed that reduction had been initiated and at 6 months complete. The peak emerging at 102 ppm only appears in the 3 month and 6-month-old samples and is indicative of the previously elusive  $[P_{888}Cl]^+$  cation. There is no indication of this within the 3-week-old sample.

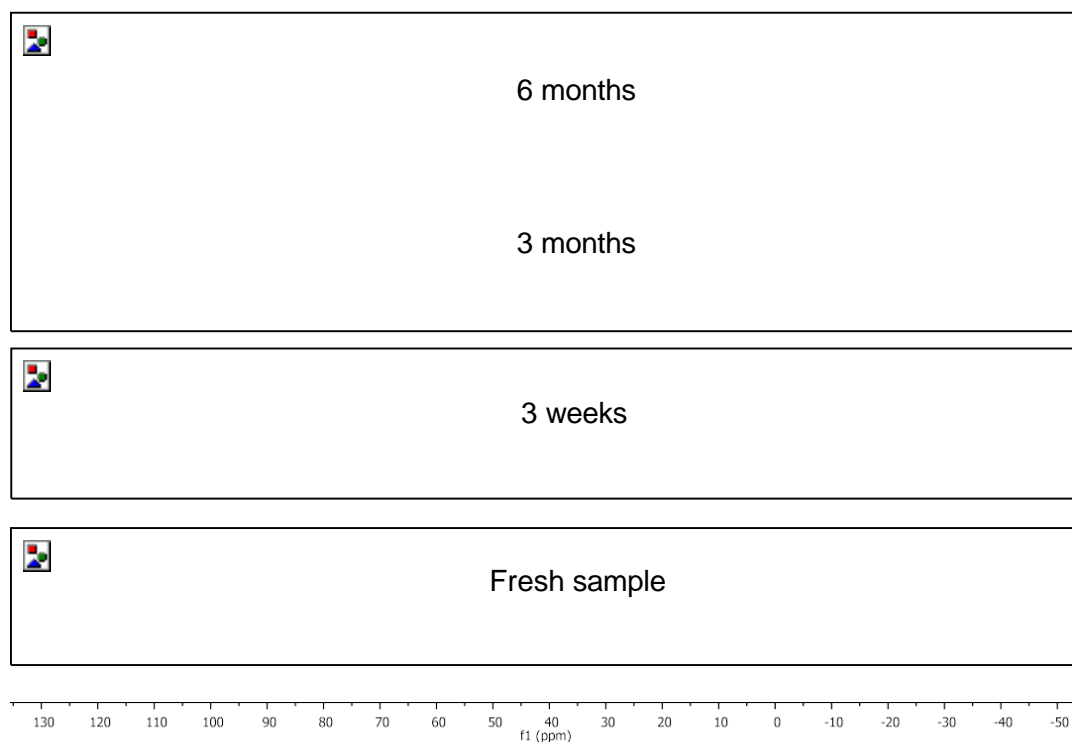


**Figure 5-14**–<sup>31</sup>P NMR of P<sub>888</sub>-CuCl<sub>2</sub> LCCs made fresh, after 3 weeks, 3months and 6 months.

The sluggishness of this reaction is surprising and unexpected, especially in comparison to that observed in trimethylphosphine by York and Axell.<sup>516</sup> They observed that the copper(II) chloride and triethylphosphine undergoes an exothermic redox reaction, slowly at -45 °C and more rapidly above -23 °C. With the LCCs formed at room temperature it would be expected that the redox would occur rapidly, but this is not observed. The reason for this is not yet known.

A summary of the NMR shift observed in the copper(II) chloride and phosphine/ phosphine chalcogenide LCCs is available in Table 5-6.

**Table 5-6**–<sup>31</sup>P NMR signals of P<sub>888</sub>, P<sub>888</sub>S and P<sub>888</sub>Se liquid coordination complexes of CuCl<sub>2</sub>.

Ligand	$\chi_{\text{CuCl}}$	$\delta_{31\text{P}}$ (ppm)	$\Delta\delta_{31\text{P}}$ compared to neat P <sub>888</sub> E (ppm)
P <sub>888</sub>	0	-29.44	
	0.50 (fresh)	-22.33	7.11
	0.50 (aged)	102.56	132.0
P <sub>888</sub> S	0	49.49	-
	0.50	49.54	0.05
		103.64	54.15
P <sub>888</sub> Se	0	36.41	-
	0.50	37.71	1.30
		102.68	66.27



### 5.2.1.3 Raman spectroscopy

Raman spectroscopy has been previously found to be a useful tool in determining the nature of M-X bonds within chlorometallate ionic liquid and LCC systems.<sup>4,22</sup> Edwards and co-workers noted that Cu-P stretches in Raman should occur at  $233\text{ cm}^{-1}$  and in the infrared spectra at  $231\text{ cm}^{-1}$  for tris triphenylphosphine copper(I) chloride. The Cu-Cl stretches in Raman should occur at  $283\text{ cm}^{-1}$  and is not visible in the Infrared spectra.<sup>518</sup> As shown in the Raman spectra collected for  $\text{P}_{888}\text{-CuCl}$   $\chi_{\text{CuCl}} = 0.25, 0.33$  and  $0.50$  showed little to no distinguishable features below  $300\text{ cm}^{-1}$  hence not elucidating any of the bonding motifs in the systems.

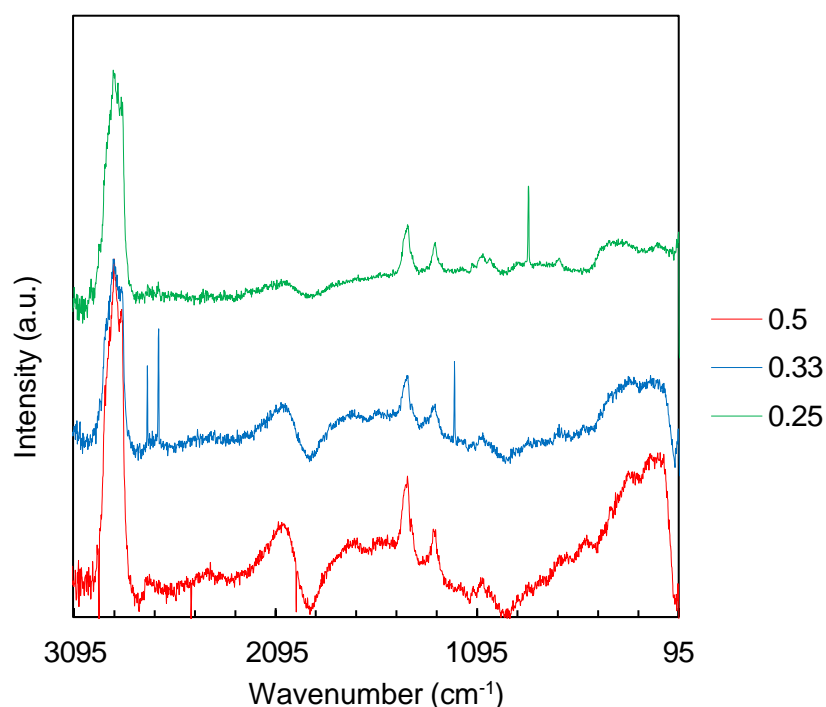


**Figure 5-15-** Raman spectra of  $\text{P}_{888}\text{-CuCl}$   $\chi_{\text{CuCl}} = 0.25, 0.33$  &  $0.50$ .

The lowest wavenumbers achievable in ATIR Infrared spectrometers available are  $550\text{ cm}^{-1}$  hence no Cu-P or Cu-Cl stretches are observable.

### 5.2.1.4 UV/Vis spectroscopy

It is apparent throughout literature that the Cu(II) species is significantly stronger in absorption than its Cu(I) counterpart, as highlighted in section 5.1.1. Carlsson and Wettermark found that the Cu(I) chloride UV/Vis spectra had weak absorbance. The anionic species  $[\text{CuCl}_2]^-$  affording a weak absorption maxima at 210 nm and the anionic species  $[\text{CuCl}_3]^{2-}$  affords a strong absorption at 230 nm and 276 nm.<sup>519</sup>

Copper(I) LCCs were examined using UV/Vis spectroscopy. As shown in Figure 5-16 there is an oversaturation ca. 291 nm and 251 nm in  $\chi_{\text{CuCl}} = 0.25$  and 0.50 respectively. All measurements were carried out in a Hellma QS Suprasil 0.5 mm quartz UV/Vis cell. These cells are cited as having a lower spectral limit of 230 nm. This alludes to oversaturation due to the spectral band present; to overcome this further dilution using a non-coordinating solvent is possible, however, the polarity of the solvent can impact the equilibrium present.

The difference in oversaturation between the  $\chi_{\text{CuCl}} = 0.25$  and 0.50 spectra may suggest that at  $\chi_{\text{CuCl}} = 0.25$  the  $[\text{CuCl}_3]^{2-}$  anionic species may be present with previous absorption maxima noted to be at 230 nm and 276 nm. The shift in oversaturation in the  $\chi_{\text{CuCl}} = 0.50$  and an apparent shoulder at 289 nm may indicate that a small amount of the  $[\text{CuCl}_3]^{2-}$  anionic species is present but it is more likely that the  $[\text{CuCl}_2]^-$  species is present ca. 210 nm.

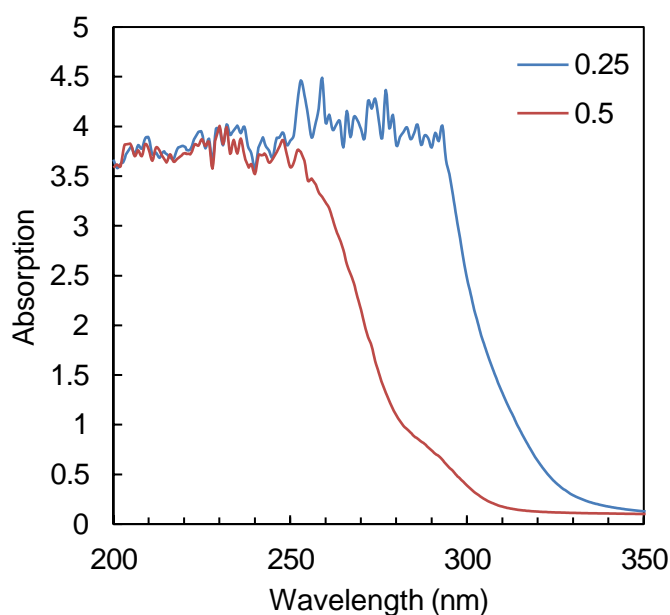


**Figure 5-16-** UV/Vis spectra of P888-CuCl  $\chi_{\text{CuCl}} = 0.25$  and 0.50.

To elucidate this matter further, sandwich-type cells fashioned from two quartz plates were used to contain the LCC. According to Beer-Lambert law, the absorption of the band should decrease as a function of sample thickness in relation to the molar extinction coefficient of that band. As shown in Figure 5-17, the oversaturation points of the  $\chi_{\text{CuCl}} = 0.25$  LCC lowers from 291 nm to 261 nm with what appears to be a shoulder peak at ca. 291 nm believed to be due to the  $[\text{CuCl}_3]^{2-}$  anionic species.

This sandwich-type cell was also used on the  $\chi_{\text{CuCl}} = 0.50$  LCC and as shown in Figure 5-18 the oversaturation point remains at 261 nm and the previously seen shoulder peak at 291 nm disappears. From this it can be determined that the spectral limit of the quartz cell is most likely 261 nm and the peak at 291 nm is a real peak that elucidates that in the  $\chi_{\text{CuCl}} = 0.25$  LCC the  $[\text{CuCl}_3]^{2-}$  species is more abundant than in the  $\chi_{\text{CuCl}} = 0.50$  LCC.

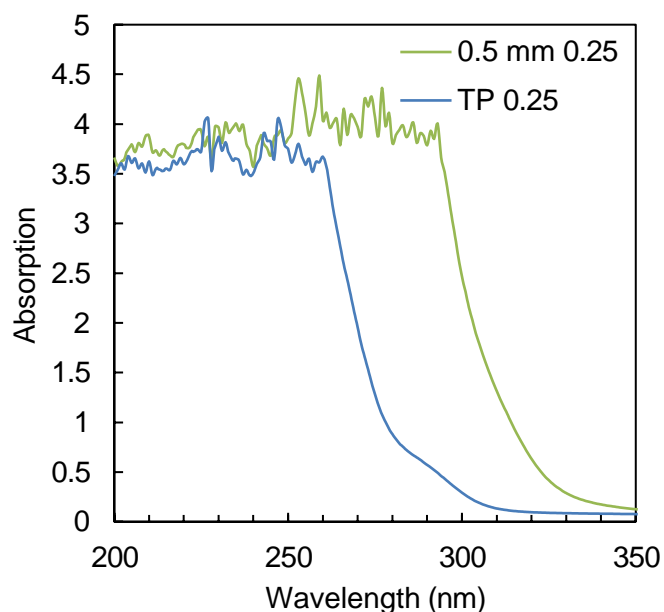


**Figure 5-17-** UV/Vis spectra of P<sub>888</sub>-CuCl  $\chi_{\text{CuCl}} = 0.25$  in a 0.50 mm UV/Vis and quartz thin plate (TP).

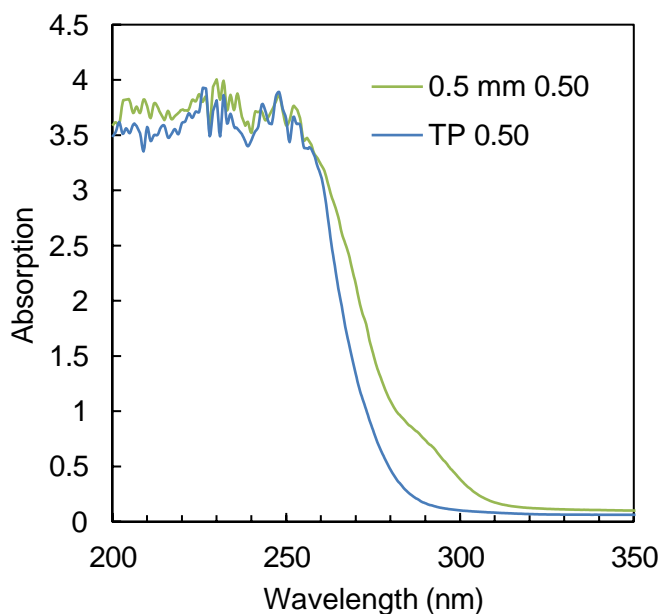


**Figure 5-18-** UV/Vis spectra of P<sub>888</sub>-CuCl  $\chi_{\text{CuCl}} = 0.50$  in a 0.50 mm UV/Vis and quartz thin plate (TP).

### 5.2.1.5 Infrared spectroscopy

Infrared spectroscopy of the  $P_{888}$ ,  $P_{888}O$ ,  $P_{888}S$  and  $P_{888}Se$  systems confirmed the coordination of the respective phosphines to the copper centre; Figure 5-19, Figure 5-21, Figure 5-22, Figure 5-23 respectively and listed in Table 5-7. As mentioned, the P-Cu stretches lie below the limit of the IR spectrometer hence cannot be monitored. The  $P_{888}O$ ,  $P_{888}S$  and  $P_{888}Se$  systems, however, exhibit stretching frequencies *ca.* 1100-550  $cm^{-1}$  and have been monitored *via* infrared spectroscopy. Using an ATIR technique, the solutions were measured in their liquid state. In the  $P_{888}O$  systems the frequency of the P=O bond decreases from 1195  $cm^{-1}$  of the unbound donor ligand to 1124  $cm^{-1}$  in Cu(I) and 1107  $cm^{-1}$  in Cu(II) LCCs.

**Table 5-7**-Infrared stretching frequencies of  $P_{888}E$ -CuCl LCC systems.

LCC	P=E stretching frequency ( $cm^{-1}$ )	Ref
$Ph_3P=O$	1195	Cotton <sup>520</sup>
$P_{888}O$ -CuCl $\chi_{CuCl} = 0.25, 0.33 \text{ \& } 0.50$	1124	This work
$P_{888}O$ -CuCl <sub>2</sub> $\chi_{CuCl_2} = 0.25, 0.33 \text{ \& } 0.50$	1107	This work
$R_3P=S$	730, 587	Chittenden <sup>521</sup>
$P_{888}S$ -CuCl $\chi_{CuCl} = 0.25, 0.33$	722, 555	This work
$P_{888}S$ -CuCl <sub>2</sub> $\chi_{CuCl_2} = 0.50$ liquor	722, 560 (peak at 560 is decreased in absorption)	This work
$R_3P=Se$	443	Sukhov <sup>522</sup>

In the  $P_{888}S$  systems the frequency of the P=S bond decreases from 587  $cm^{-1}$  of the unbound donor ligand to 555  $cm^{-1}$  in Cu(I) and 560  $cm^{-1}$  in Cu(II) LCCs with a notable decrease in the absorption band intensity. As discussed, the Cu(II) system results in the precipitation of elemental sulphur, hence it is unsurprising that the P=S bond is less. In the  $P_{888}Se$  systems the frequency of the P=Se bond is below the IR spectrometer limit, hence is not measurable.

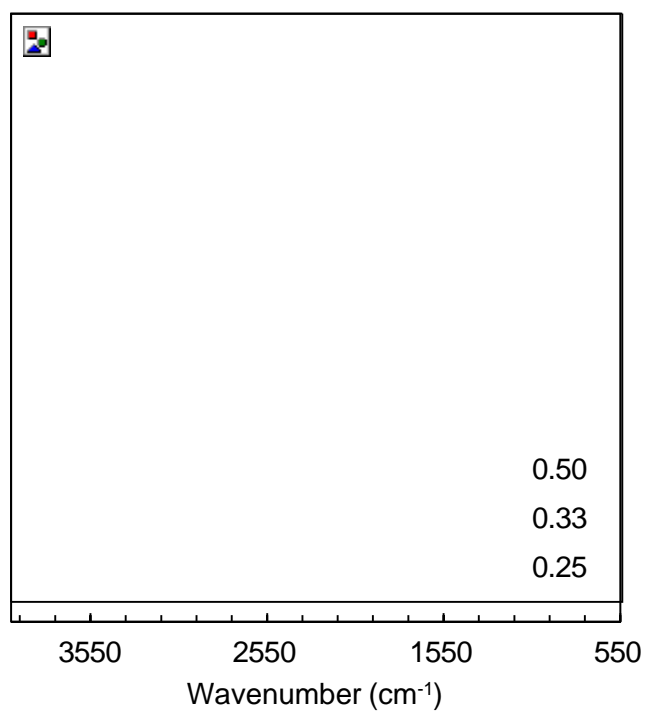


**Figure 5-19-**Infrared spectra of P<sub>888</sub>-CuCl  $\chi_{\text{CuCl}}$  = 0.50, 0.33, 0.25.

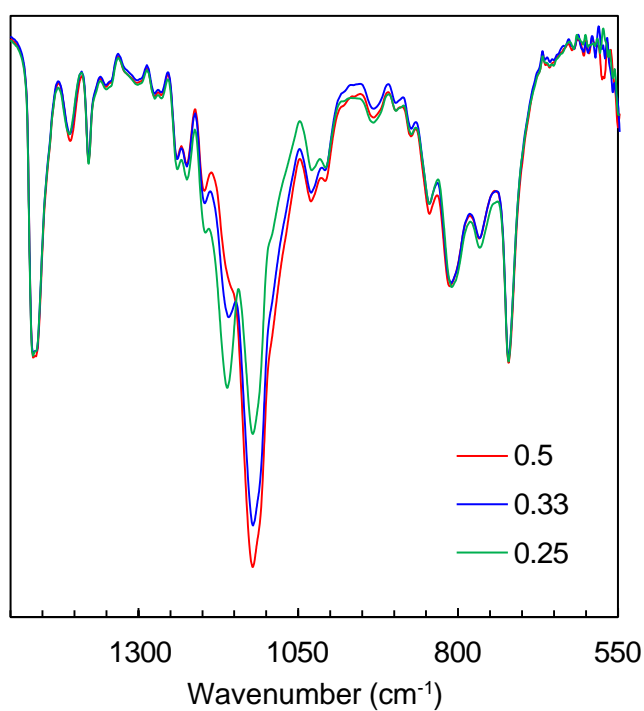


**Figure 5-20-** Infrared spectra of P<sub>888</sub>O-CuCl  $\chi_{\text{CuCl}}$  = 0.50, 0.33, 0.25.

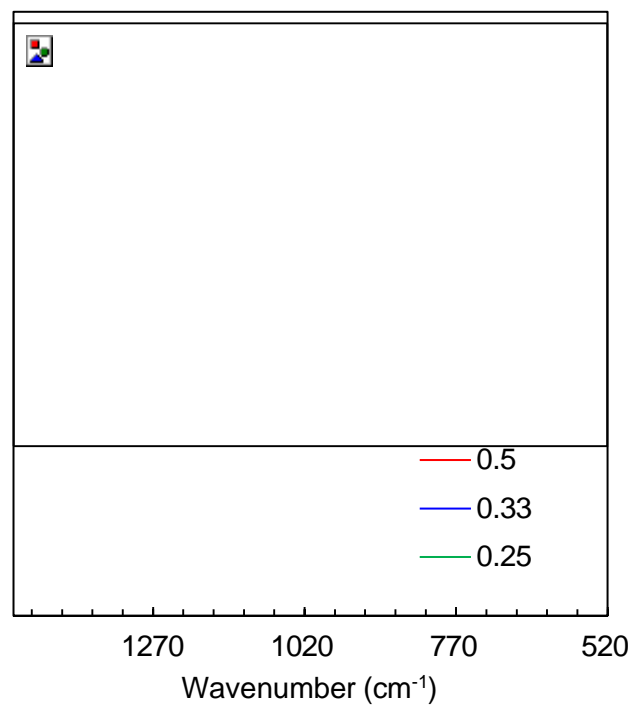


**Figure 5-21-** Infrared spectra of  $\text{P}_{888}\text{O}-\text{CuCl}_2$   $\chi_{\text{CuCl}_2} = 0.50, 0.33, 0.25$ .

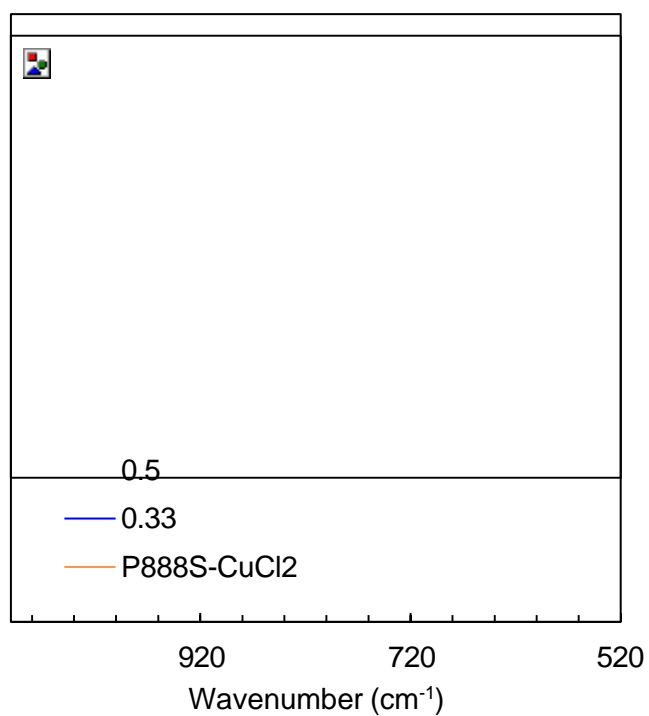


**Figure 5-22-** Infrared spectra of  $\text{P}_{888}\text{S}-\text{CuCl}$   $\chi_{\text{CuCl}} = 0.50, 0.33, 0.25$  and  $\text{P}_{888}\text{S}-\text{CuCl}_2$   $\chi_{\text{CuCl}_2} = 0.50$  liquor.

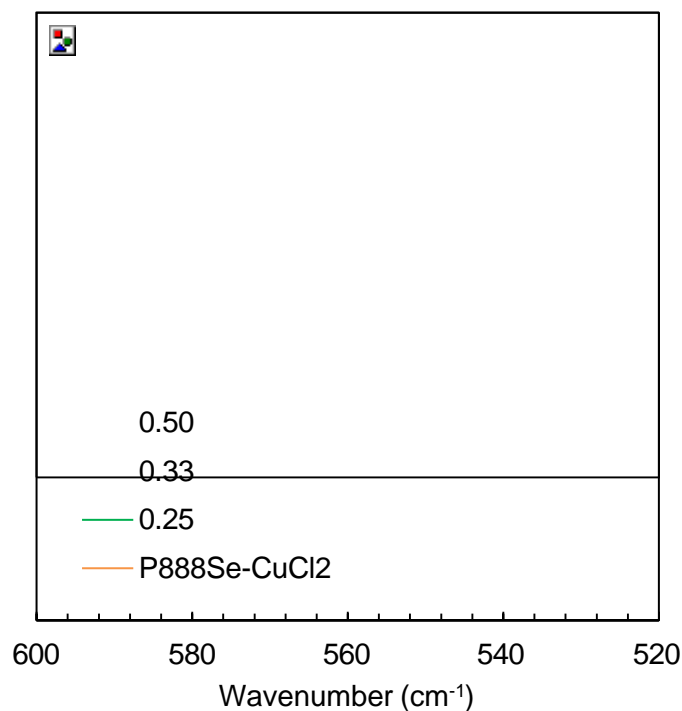


**Figure 5-23-** Infrared spectra of  $P_{888}Se-CuCl$   $\chi_{CuCl} = 0.50, 0.33, 0.25$  and  $P_{888}Se-CuCl_2$   $\chi_{CuCl_2} = 0.50$  liquor.

The linear and tetrahedral geometries of Cu(I) were initially well reported due to the  $d^{10}$  configuration of the Cu(I) ion; the charged and uncharged ligands fill the 4 s and 4p orbitals to form variously hybridized complexes.<sup>523</sup> Meek and co-workers found that the  $R_3P=S$  ligand can form multiple complex species with Cu(I) species with the donor ligand acting as both a terminal and bridging species.<sup>494</sup> Furthermore, it was found that the Cu(I) species with these ligands commonly result in a three-coordinate geometry; Eller and Corfield found that the  $[Cu(SPMe_3)_3][ClO_4]$  salt resulted in the trigonal planar species shown in Figure 5-24 to be adopted.<sup>524</sup>

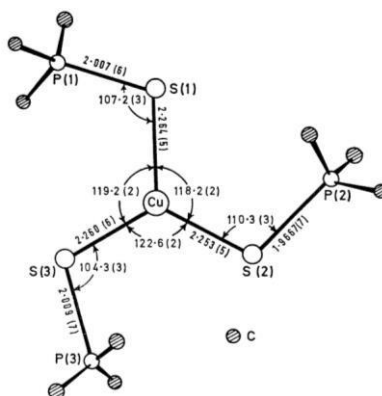


**Figure 5-24-** Figure by Eller and Corfield of  $[Cu(SPMe_3)_3][ClO_4]$  salt as determined by single crystal diffraction.<sup>524</sup>

The bridging species discussed by Meek and Reichie highlighted that an equilibrium is present in solution.<sup>488,494</sup> These 3-coordinate species were found to be dimeric or monomeric in nature depending on the counter anion affinity. It was found that the addition of excess ligand could result in dissociation of a donor ligand and a further formation of the [L-Cu-X] complex and not the tetrahedral species [CuL<sub>4</sub>]<sup>+</sup>.<sup>416</sup> Complexes of the type [CuL<sub>4</sub>]X where X=Cl, Br, or I have never been isolated.

Meek further postulated that the ligand bulkiness should decrease the stability of the 3-coordinate complex based upon observation made by Lippard and Mayerle, in which they postulated the equilibria shown in Figure 3-64 may be present in such systems.

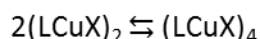
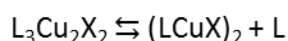
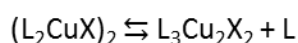
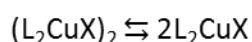
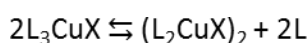
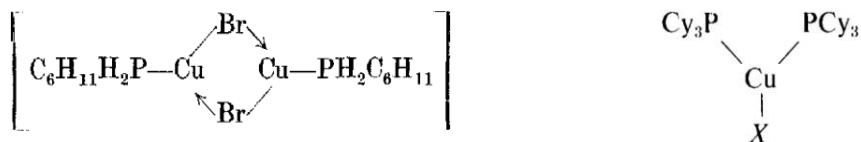


Figure 5-25-Equilibria predictions by Lippard and Mayerle<sup>525</sup>

Within Infrared analysis there is no indication of free ligand within the P<sub>888</sub>S or P<sub>888</sub>O systems, hence the discrete equations (1),(3) and (4) do not exist as discrete equilibria but as a component in an expand system in which the free ligand is further coordinated. Lippard and Mayerle investigated the effects of many parameters on such equilibria. Using the addition of solvents such as acetone as a probe, it was found that ligand dissociation is greater in chloride species following the order that Cl > Br > I and basicity of the ligand is another variant on the speciation.<sup>525</sup>

The size of the donor ligand also affects the species formed with Moers and Op Het Veld postulating the formation of monomeric species with bulky ligands such as tricyclohexylphosphine in solution with linear or trigonal planar geometries.<sup>526</sup> Issleib and Haftendorn postulated that dimeric structures also exist in solution, hence the complexity of the species in solution is somewhat ambiguous, however, it is notable that a majority of reported species are neutral adducts.<sup>527,528</sup>





**Figure 5-26**-Postulated structures of tricyclohexylphosphine and Cu(I) salts in solution.<sup>526,527</sup>

### 5.2.1.6 Extended X-ray fine structure

Within literature, EXAFS analysis of copper species in DES systems has been useful in elucidating the predominantly anionic species present. Studies by Van Deun and co-workers<sup>478</sup>, and Abbott and co-workers<sup>490</sup> elucidated the speciation of Cu(II) and Cu(I) in DES and ionic liquid media *via* EXAFS. However, little has been reported recently in which Cu speciation is both neutral, cationic and ionic has been analysed and quantified using such a technique.

Coordination of Cu(I) in the three compositions of the P<sub>888</sub>-CuCl system ( $\chi_{\text{CuCl}}$  = 0.25, 0.33 and 0.50) were determined using EXAFS on I20-scanning beamline at Diamond. All data were fitted to single shell coordination, consistent with Cu(I) complexes such that the coordination number, N tested ranged from 2 to 4 characteristic of Cu(I) complexes. For each  $\chi_{\text{CuCl}}$ , spectra were fitted with a variation of total coordination numbers, N<sub>total</sub> and within such the ratio of Cu-Cl and Cu-P bonds varied. The R-factor was utilised to determine the best fits. In all cases the fits occurred in K-space with identical K and R ranges to ensure a true comparison could be made.

At first glance, it is observed that with variation of the  $\chi_{\text{CuCl}}$ , the EXAFS spectra change, as shown in Figure 5-27, Figure 5-28 and Figure 5-29; indicating a change in bonding modes present and consequent speciation with  $\chi_{\text{CuCl}}$ . Fitting such a complex system is difficult and requires a methodical approach to elucidating the speciation present. Utilising previously reported literature, it is apparent that the coordination range of Cu(I) is most likely to lie between 2 - 4, hence fits were carried out with a variation of total coordination numbers, N<sub>total</sub> = 2, 2.5, 2.67, 3, 4 for each system. Within each N<sub>total</sub> the ratio of Cu-P and Cu-Cl was varied and the best fit as determined by the R-factor parameter was selected. Observing the spectra in k-space, it is clear that the phase of the spectra changes with  $\chi_{\text{CuCl}}$  as shown in Figure 5-29 especially at higher wavenumber indicating that the longer range single scattering varies more significantly with variable  $\chi_{\text{CuCl}}$ .

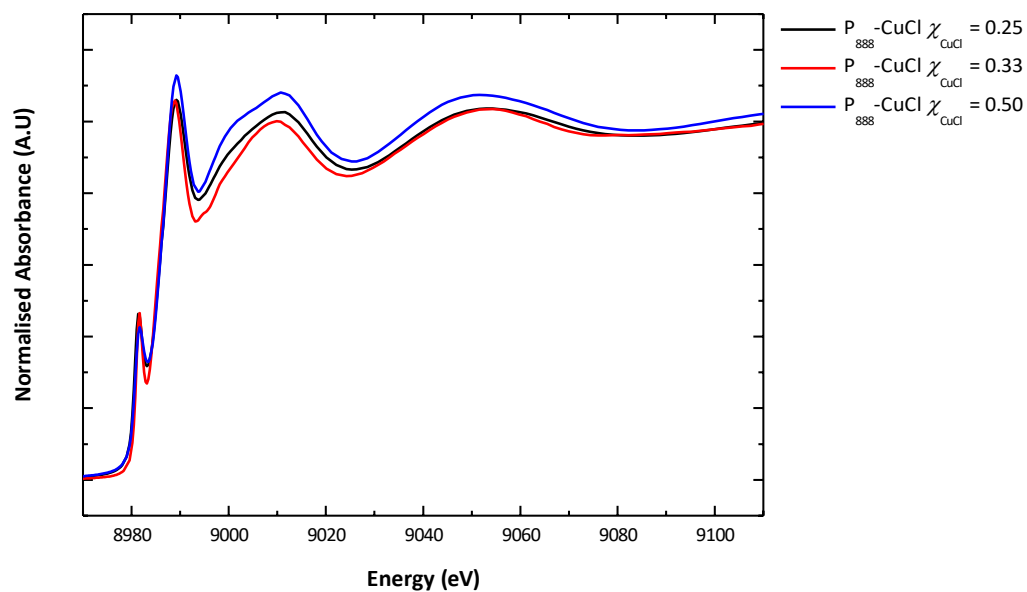


**Figure 5-27-** Normalized overlaid EXAFS spectra of  $P_{888}\text{-CuCl}$   $\chi_{\text{CuCl}} = 0.25, 0.33$  &  $0.50$ .

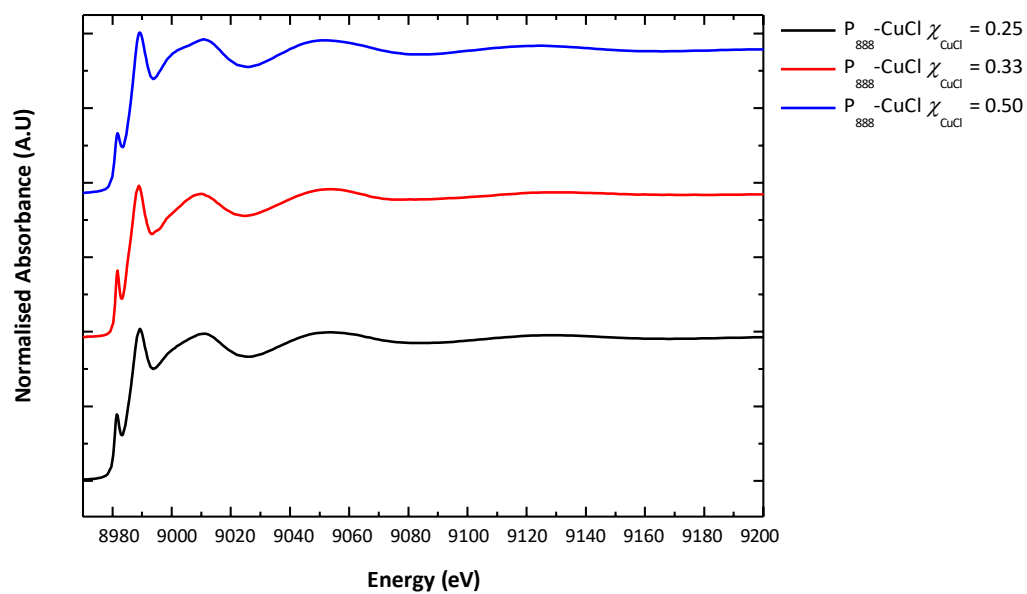


**Figure 5-28-** Normalized stacked EXAFS spectra of  $P_{888}\text{-CuCl}$   $\chi_{\text{CuCl}} = 0.25, 0.33$  &  $0.50$ .

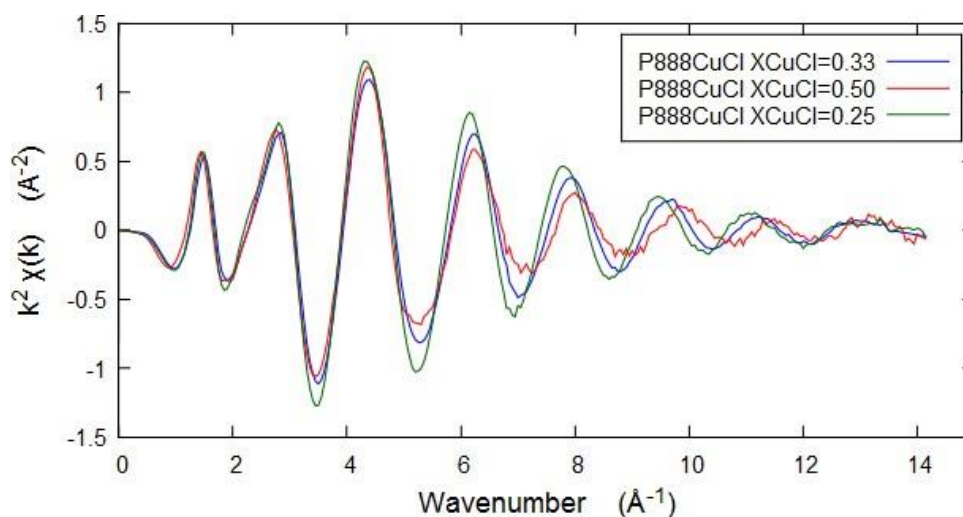


**Figure 5-29.** Normalized overlaid EXAFS spectra of P<sub>888</sub>-CuCl  $\chi_{\text{CuCl}} = 0.25, 0.33$  &  $0.50$  in  $k$ -space.

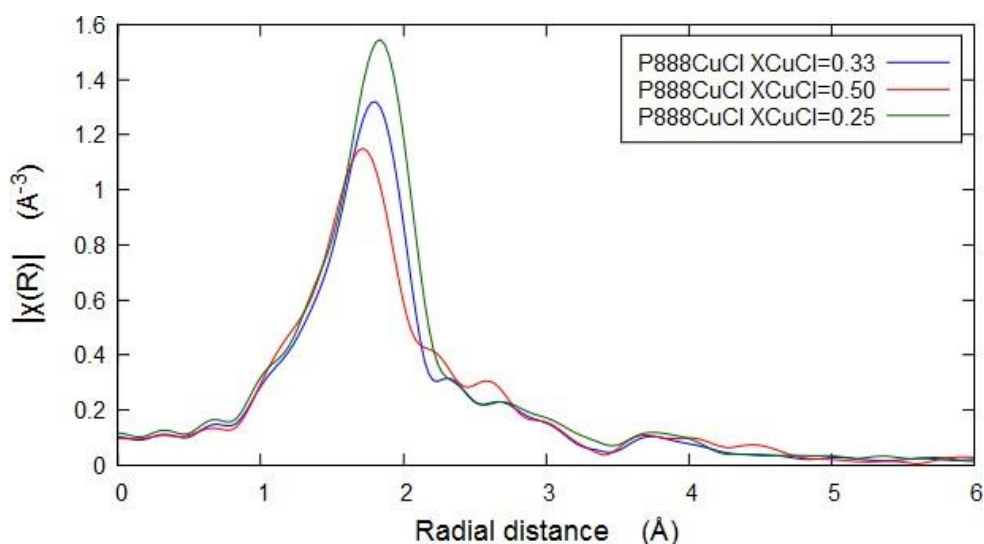


**Figure 5-30.** Normalized overlaid EXAFS spectra of P<sub>888</sub>-CuCl  $\chi_{\text{CuCl}} = 0.25, 0.33$  &  $0.50$  in  $R$ -space.

Spacing between maxima in the EXAFS plot and intensity of the first shell peak in pRDF are narrowing with increasing  $\chi_{\text{CuCl}}$  value (Figure 5-30) which points to coordination becoming more consistent with increasing  $\chi_{\text{CuCl}}$ . Furthermore, the increasing intensity and broadening of the signal in  $R$ -space with decreasing  $\chi_{\text{CuCl}}$  indicates that coordination expands as ligand concentration increases. The numerical value for  $N_{\text{total}}$  cannot be a priori assumed based on stoichiometry, because it is affected by bridging coordination modes, including potential cubane structures, combined with the observation that some ligands may remain uncoordinated. Therefore, for all three data sets, a range of data fitting exercises were carried out. All data were fitted in  $k$  space, and a single coordination shell around the copper centre was considered. In theory, the value of  $N_{\text{Cu-Cl}}/N_{\text{total}} = \chi_{\text{CuCl}}$

in each studied LCC sample. In practice, this ratio was expected to deviate due to bridging and/or free ligand present. For each fit, the  $R$  factor was recorded, which reflects the goodness of fit between the model and the collected data.

Plotting  $R$ -factor as a function of  $N_{\text{Cu-Cl}}/N_{\text{total}}$  with variable  $N_{\text{total}}$  as shown in Figure 5-31 there are trends observed such that at  $\chi_{\text{CuCl}} = 0.50$  best fits are achieved at  $N_{\text{Total}} = 2.67$  and  $N_{\text{total}} = 3$ . The trends in each  $N_{\text{total}}$  tested show that with decreasing  $N_{\text{Cu-Cl}}/N_{\text{total}}$  fits improve until a sudden jump in  $R$ -factor is observed as highlighted by a dashed line in Figure 5-31. Upon further inspection, as shown in Figure 5-31 the lowest  $R$ -factor was achieved for  $N_{\text{total}} = 2.67$  with  $N_{\text{total}} = 3$  being a close second. The lowest  $R$ -factor was achieved for an  $N_{\text{Cu-Cl}}/N_{\text{total}} = 0.44$ - $0.45$ , as highlighted in the shaded square, which corresponds to a near equimolar mixture of Cu-L and Cu-Cl mixture.

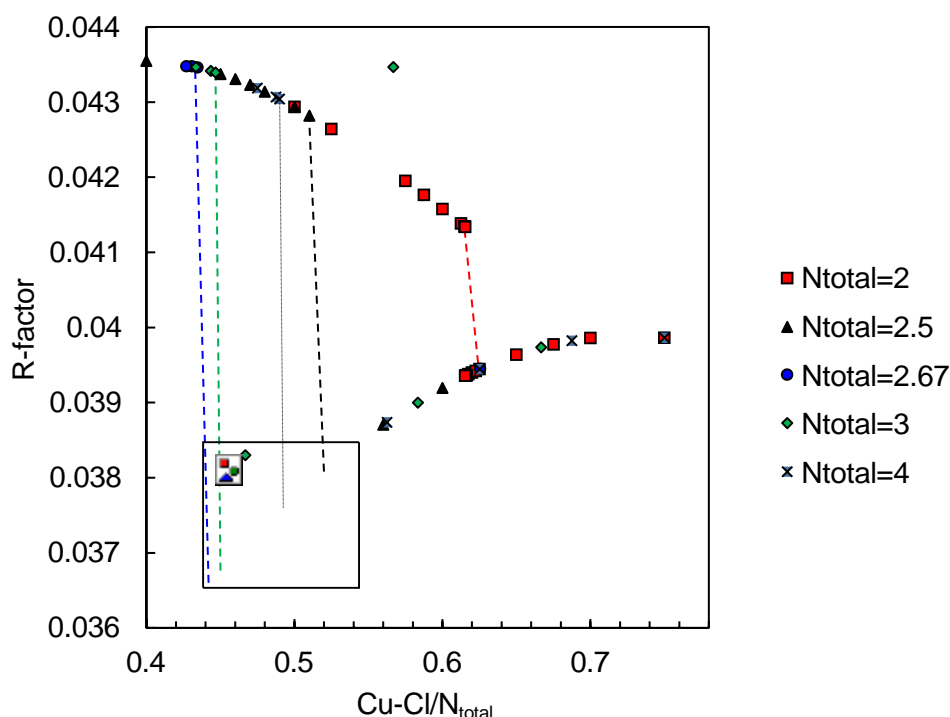


**Figure 5-31-**  $R$ -factor of EXAFS fits of  $\text{P}_{888}\text{-CuCl}$   $\chi_{\text{CuCl}} = 0.50$  as a function of  $N_{\text{Cu-Cl}}/N_{\text{total}}$ .

Upon initial inspection, from the stoichiometry one would expect at  $\chi_{\text{CuCl}} = 0.50$  that the copper centre to be 2-coordinate, however, as shown it is clear that the best fits are achieved with an average coordination of 2.67-3. As listed in Figure 5-32, 2-3 coordinate species are possible within this system and using the EXAFS fits it is predicted that the  $[\text{CuL}_2][\text{Cu}_2\text{Cl}_3\text{L}]$  species is most likely to be present at  $\chi_{\text{CuCl}} = 0.50$  as it exhibits the average copper coordination of 2.67. Further to this, the  $N_{\text{Cu-Cl}}/N_{\text{total}}$  ratio indicates that at this fit there is unaccounted Cu-Cl species as it does not reach

the desired  $N_{\text{Cu-Cl}}/N_{\text{total}} = 0.50$ . This can be rationalised by the presence of auto complexation species such as  $[\text{CuL}_3]\text{Cl}$  in which no Cu-Cl is observed. Notably, structures with bridging phosphines in Cu(I) complexes are not known, in contrast to abundant examples of chloride bridges.

For the  $\text{P}_{888}\text{-CuCl}$  systems at  $\chi_{\text{CuCl}} = 0.25$  fits are of greater quality at  $N_{\text{total}} > 2$  with the best fits achieved at  $N_{\text{Total}} = 4$  indicating that four coordination copper species are present as shown in Figure 5-33 and Figure 5-34. Predicted speciation is described in Table 5-8; at  $\chi_{\text{CuCl}} = 0.25$  the average coordination is most commonly 4 however, ionisation may occur rather than the auto-complexation as described by Gutmann to form the 3- coordinate  $[\text{CuL}_3]\text{Cl}$  species. This accounts for the good fits observed in  $N_{\text{total}} = 2.67$  and  $N_{\text{total}} = 3$ , highlighted in the shaded area of Figure 5-34.

In general,  $\chi_{\text{CuCl}} = 0.25$  follows the expected trend of a higher coordination number in comparison to the  $\chi_{\text{CuCl}} = 0.50$  system which as discussed has a preferred average coordination of 2.67 whereas  $\chi_{\text{CuCl}} = 0.25$  has a preferred average coordination of 4. The  $N_{\text{Cu-Cl}}/N_{\text{total}}$  ratio at the best fit has the  $N_{\text{Cu-Cl}}/N_{\text{total}}$  value of 0.19, which is lower than the stoichiometric expectation for  $\chi_{\text{CuCl}} = 0.25$ , however, combination of the  $N_{\text{Cu-Cl}}/N_{\text{total}}=2.67$  and 3.0 fits indicating a mixed speciation will allow for the desired 0.25 to be reached. There are on average less chlorides around the copper(I) centre than anticipated from stoichiometry. Once more, this points towards the presence of free chloride within the sample, with some chlorides in bridging modes to make up for the lower  $\chi_{\text{CuCl}}$  than expected.

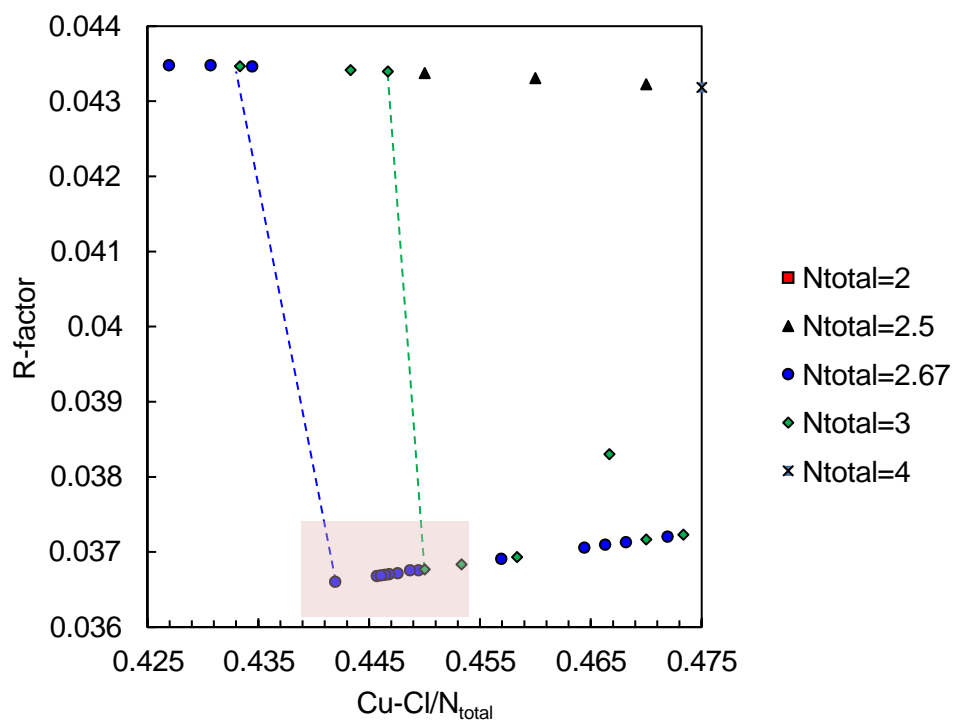


**Figure 5-32-** R-factor of EXAFS fits of  $P_{888}\text{-CuCl}$   $\chi_{\text{CuCl}} = 0.50$  as a function of  $N_{\text{Cu-Cl}}/N_{\text{total}}$ .

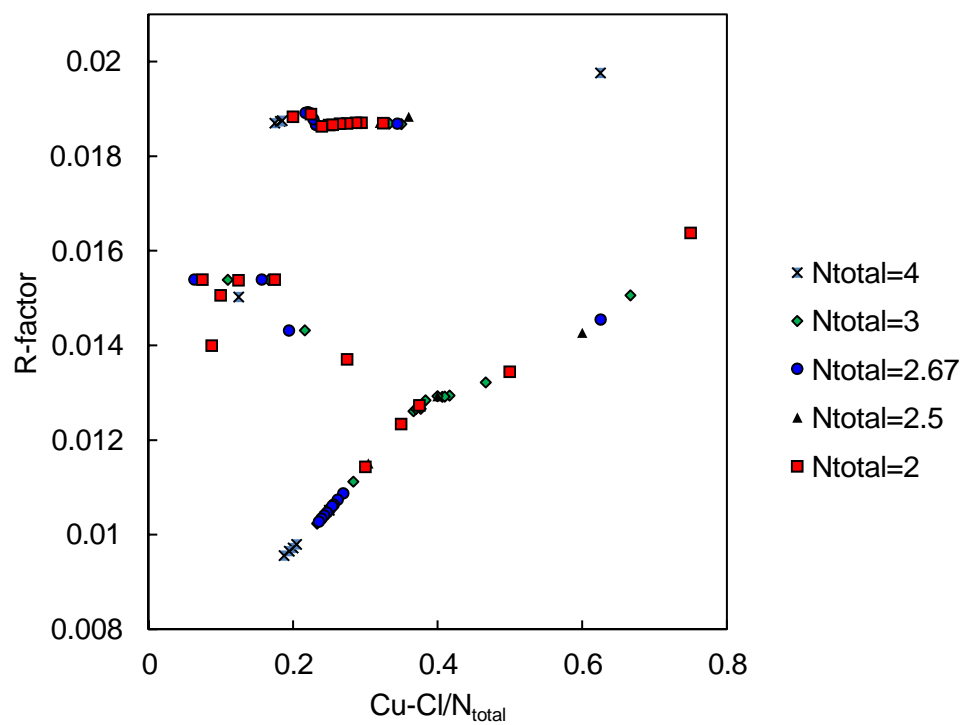


**Figure 5-33-** R-factor of EXAFS fits of  $P_{888}\text{-CuCl}$   $\chi_{\text{CuCl}} = 0.25$  as a function of  $N_{\text{Cu-Cl}}/N_{\text{total}}$ .

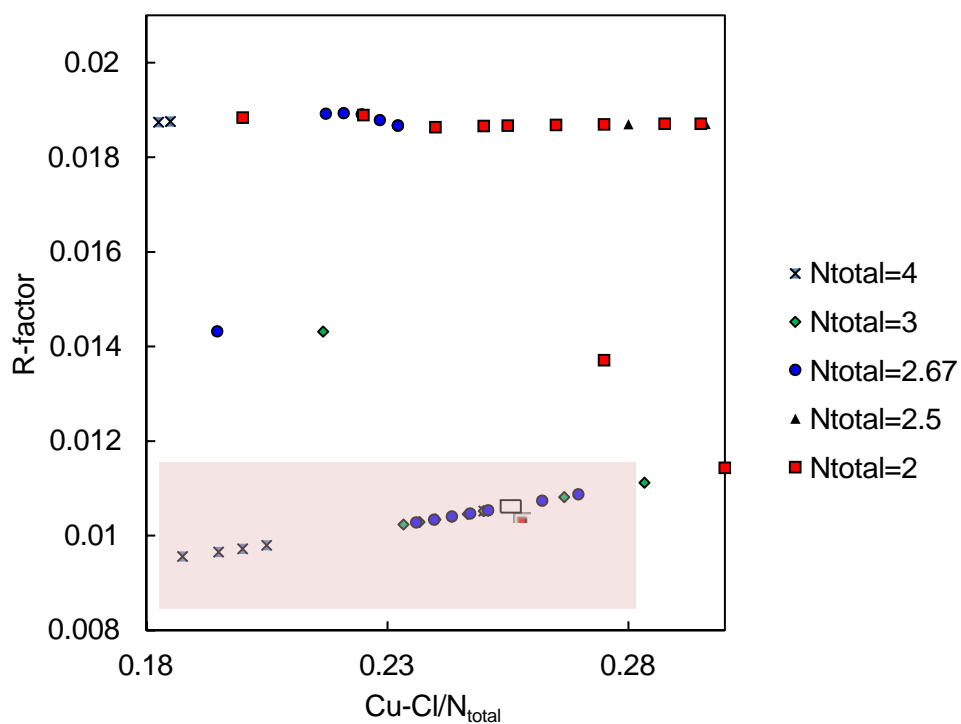


**Figure 5-34-** R-factor of EXAFS fits of  $P_{888}\text{-CuCl}$   $\chi_{\text{CuCl}} = 0.25$  as a function of  $N_{\text{Cu-Cl}}/N_{\text{total}}$ .

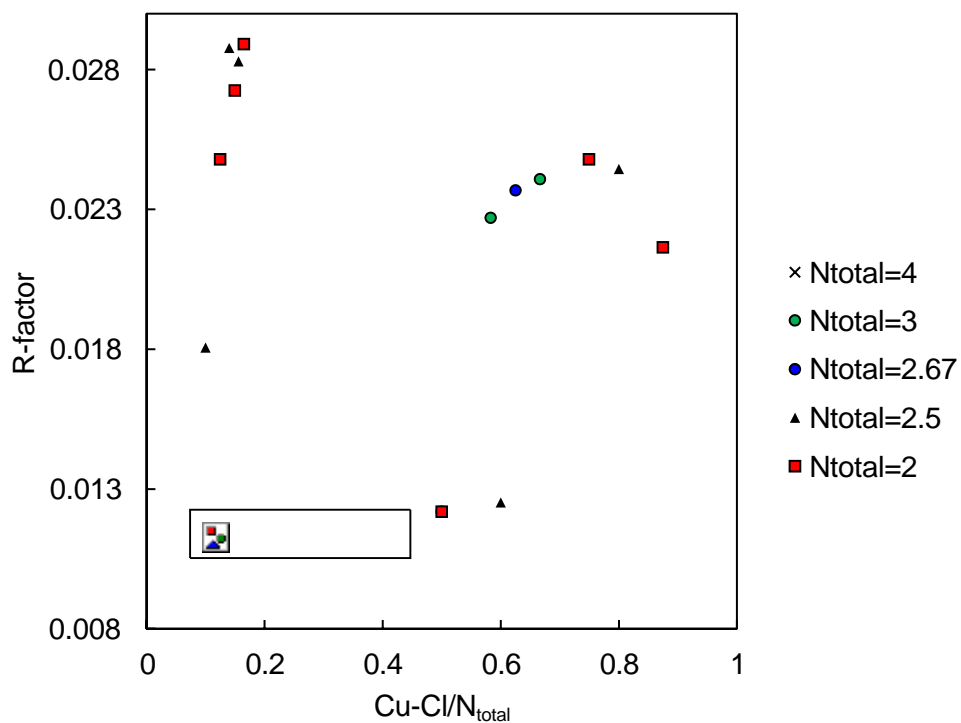


**Figure 5-35-** R-factor of EXAFS fits of  $P_{888}\text{-CuCl}$   $\chi_{\text{CuCl}} = 0.33$  as a function of  $N_{\text{Cu-Cl}}/N_{\text{total}}$ .

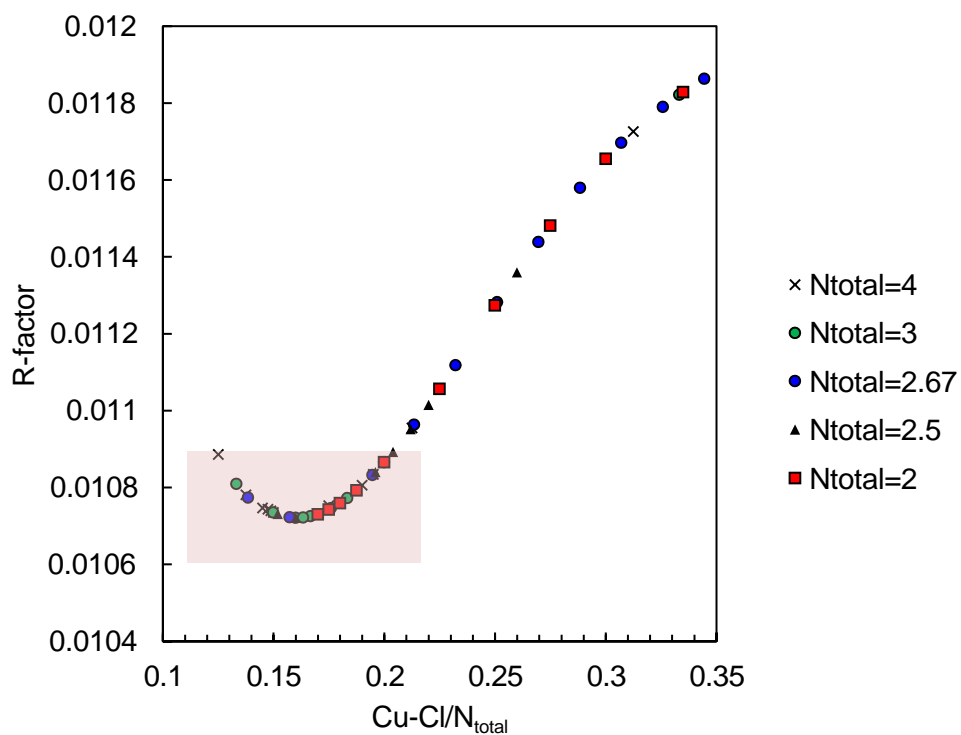


**Figure 5-36-** R-factor of EXAFS fits of P<sub>888</sub>-CuCl  $\chi_{\text{CuCl}} = 0.33$  as a function of  $N_{\text{Cu-Cl}}/N_{\text{total}}$ .

**Table 5-8-** Predicted speciation of P<sub>888</sub>-CuCl systems. (L=P<sub>888</sub>)

	Speciation	Average coordination number
$\chi_{\text{CuCl}} = 0.25$		
2CuCl + 6L	$[\text{CuL}_3\text{Cl}] \leftrightarrow [\text{CuL}_3]\text{Cl}$	3.5
	$[\text{CuL}_4][\text{CuL}_2\text{Cl}_2]$	4
$\chi_{\text{CuCl}} = 0.33$		
CuCl + 2L 2CuCl + 4L 3CuCl + 6L	$[\text{CuL}_2]\text{Cl} \leftrightarrow [\text{CuL}_2\text{Cl}]$ $[\text{CuL}_3]\text{Cl} + [\text{CuLCl}]$	2.5
	$[\text{CuL}_3][\text{CuCl}_2\text{L}] \leftrightarrow [\text{CuL}_4][\text{CuCl}_2]$ $[\text{CuL}_2][\text{CuL}_2\text{Cl}_2] \leftrightarrow [\text{CuL}_4][\text{CuCl}_2]$ $[\text{CuL}_3][\text{Cu}_2\text{L}_3\text{Cl}_3] \leftrightarrow [\text{CuL}_2\text{Cl}][\text{Cu}_2\text{L}_3\text{Cl}_2]$	3
$\chi_{\text{CuCl}} = 0.50$		
2CuCl + 2L 3CuCl + 3L	$2[\text{CuClL}] \leftrightarrow [\text{CuL}_2][\text{CuCl}_2]$	2
	$[\text{Cu}_2\text{L}_2\text{Cl}_2]$	3
	$[\text{CuL}_2][\text{Cu}_2\text{Cl}_3\text{L}]$	2.67



The  $P_{888}$ -CuCl systems at  $\chi_{CuCl} = 0.33$  fits were indistinguishable in regards to the preferred average coordination number of copper. As shown in Figure 5-35 and Figure 5-36, it is not possible to differentiate the preferred  $N_{total}$ ; instead it is presumed that all coordination numbers from 4 to 2 are present. Elucidation of the geometries present will allow for reasonable speciation predictions to be made. Furthermore, the lower  $N_{Cu-Cl}/N_{total}$  ratio, at which the plateau in R-factor is observed, is nearly half of the desired 0.33; it is believed that this is due to the auto complexation process and the formation of free chloride in the system. Fitted EXAFS data are shown in Figure 5-37, and the corresponding *pseudo*-radial distribution functions (*p*RDFs) are also shown. Fitting parameters are listed in Table 5-9. EXAFS fitting parameters for  $P_{888}$ -CuCl LCCs, at compositions:  $\chi_{CuCl} = 0.25$  and 0.50 show that the fits are relatively good, however, it should be noted that the crystal structures from which the Cu-P and Cu-Cl are modelled from are bridging species from a triphenylphosphine copper chloride cubane type structure as shown in Figure 5-38, hence a truly terminal species will be shorter in reality.

The good fits achieved for  $\chi_{CuCl} = 0.50$  indicating a 2.67-3 coordinate geometry is in good agreement with both the geometries postulated in the previously reported tricyclohexylphosphine-Cu(I) complexes.<sup>526–528</sup> However, the  $\chi_{CuCl}$  calculated indicate that a bridging chloride is likely to be present but given the  $P_{888}E$  species can also act as a bridging species but if this was present the  $\chi_{CuCl}$  would be closer to its calculated value and not the fit predicted value.

EXAFS spectroscopy has successfully elucidated the preferred copper coordination at extreme  $\chi_{CuCl}$  allowing for reasonable predictions of the speciation to be made. EXAFS by nature is an averaging technique hence it is unsurprising that the intermediate  $\chi_{CuCl} = 0.33$  in which a mixture of species is present at  $\chi_{CuCl} = 0.50$  and  $\chi_{CuCl} = 0.25$  are expected to be in equilibrium. This somewhat ambiguity shown in the  $\chi_{CuCl} = 0.33$  system lead to an  $N_{Total} = 3.33$  to be selected as an input driven fit parameter *i.e.* at  $\chi_{CuCl} = 0.25$  and  $\chi_{CuCl} = 0.50$  the best fits were achieved at  $N_{Total} = 4$  and  $N_{Total} = 2.67$  under the assumption at  $\chi_{CuCl} = 0.33$  a midpoint is reached, the midpoint  $N_{Total} = 3.33$ . Again, the ratio of Cu-P and Cu-Cl contributions were input as the solution input would dictate, a  $\chi_{CuCl} = 0.14$  ratio as determined by the screening study.

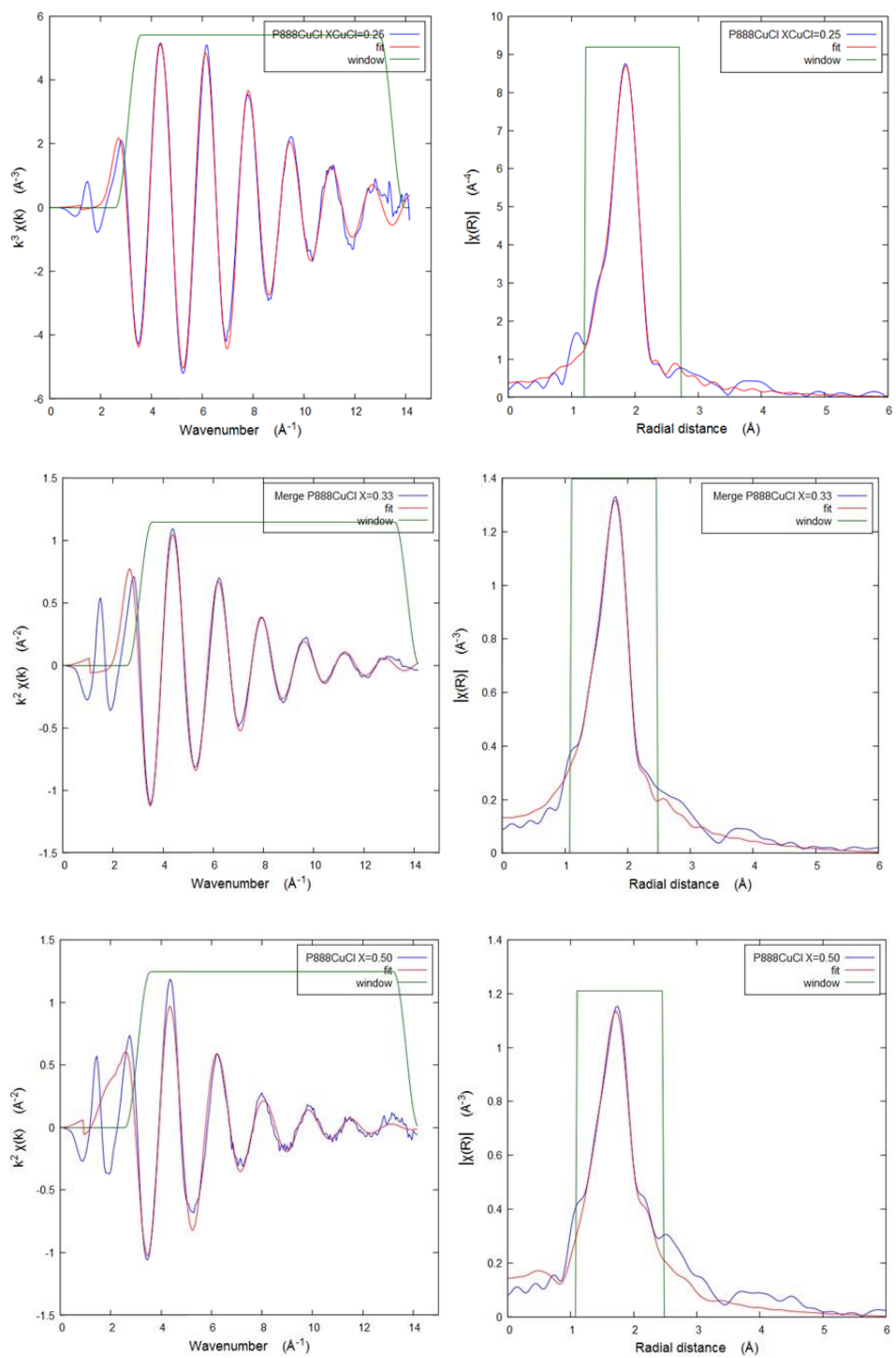


**Figure 5-37-** EXAFS fits for  $\text{P888-CuCl}$   $\chi_{\text{CuCl}} = 0.25, 0.33$  and  $0.50$ .  $\text{P888-CuCl}$   $\chi_{\text{CuCl}} = 0.25$   $N_{\text{total}} = 4$   $N_{\text{Cu-P}} = 3.18$   $N_{\text{Cu-Cl}} = 0.82$ ;  $\chi_{\text{CuCl}} = 0.33$   $N_{\text{total}} = 3.33$   $\text{Cu-Cl} = 0.476$   $\text{Cu-P} = 2.854$ ;  $\text{P888-CuCl}$   $\chi_{\text{CuCl}} = 0.50$   $N_{\text{total}} = 2.67$   $N_{\text{Cu-P}} = 1.49$   $N_{\text{Cu-Cl}} = 1.18$ .

**Table 5-9-** EXAFS fitting parameters for P<sub>888</sub>-CuCl LCCs, at the compositions:  $\chi_{\text{CuCl}} = 0.25, 0.33$  and 0.50.

$\chi_{\text{CuCl}}$	Bond	Coordination number, $N$	$\sigma^2$ (Å <sup>2</sup> ) <sup>a</sup>	$R$ -factor	$\delta R$ (Å)	R
0.25	Cu-P	3.18	0.00782	0.0072325	0.11026	2.28726
	Cu-Cl	0.82	0.00716		0.16259	2.40958
0.33	Cu-P	2.854	0.00886	0.0094661	0.09193	2.26893
	Cu-Cl	0.476	0.00575		0.18154	2.42854
0.50	Cu-P	1.49	0.01634	0.0356617	0.22293	2.39993
	Cu-Cl	1.18	0.00995		-0.05936	2.18764
<sup>a</sup> Debye-Waller factor (mean-square disorder in $R$ )						

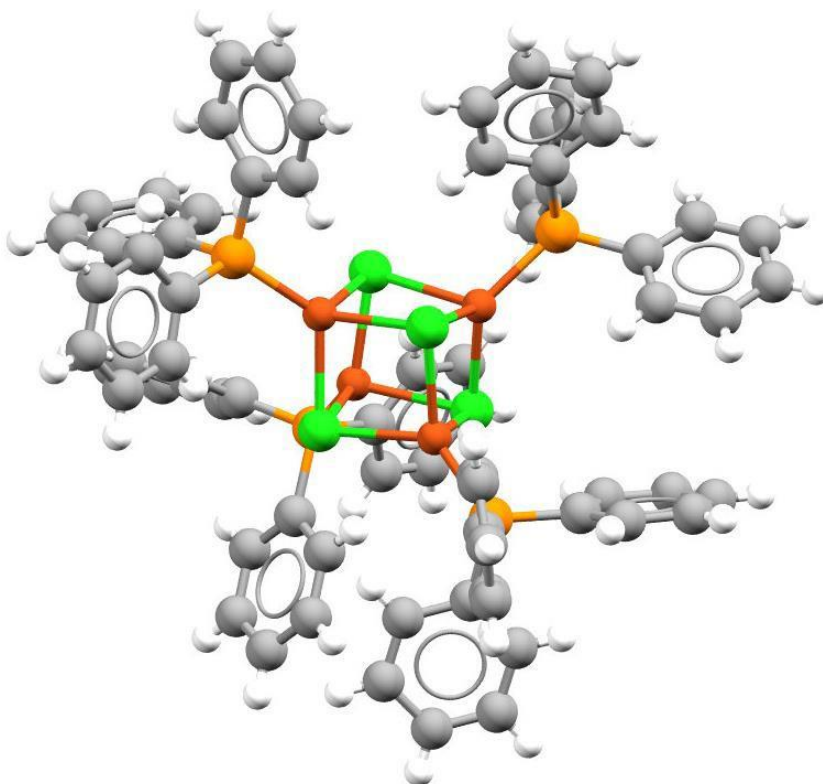


**Figure 5-38-** Triphenylphosphine copper(I) chloride complex from which EXAFS fits were modelled. CCDC- TPCUCL12.

Analysis of fitting parameters, listed in Table 5-9, reveals that the ratio of  $N_{\text{Cu-P}}$  to  $N_{\text{Cu-Cl}}$  is always higher than would appear from stoichiometry, with total coordination

number higher than that expected from stoichiometry, except for stoichiometric  $N_{\text{total}} = 4$  at  $\chi_{\text{CuCl}} = 0.25$ . This suggests two simultaneously occurring phenomena: the presence of free (uncoordinated) chloride in the LCC sample, contributing to 'excess' of phosphine around the copper(I) centre, and chloride bridging coordination modes, which account for total coordination numbers. Chloride bridges are suggested by notably long Cu-Cl bonds, which in  $\chi_{\text{CuCl}} = 0.25$  and 0.33 compositions average ca. 2.4 Å. Shorter average Cu-Cl bond length in  $\chi_{\text{CuCl}} = 0.50$  (ca. 2.19 Å) can be associated with contributions from dicoordinate species,  $[\text{CuCl}(\text{P}_{888})]$ . Within the literature of Cu(I) structures it is apparent that within those containing trialkylphosphines and Cu(I)Cl the cubane structure is commonly found in the solid state. Looking at three examples of Cu(I) species that do not adopt a cubane structure it is seen that the Cu-Cl bond does vary.

Fit parameters are relatively similar for the  $\chi_{\text{CuCl}} = 0.25$  and 0.33 compositions, with *R*-factor slightly higher for the latter. All Debye-Waller and *R*-factor values for all these two samples are below 0.01. In contrast, fitting parameters for the  $\chi_{\text{CuCl}} = 0.50$  compositions are less favorable: Debye-Waller values are 0.016 Å<sup>2</sup> for Cu-P and 0.010 Å<sup>2</sup> for Cu-Cl, despite lower coordination number and thus expectedly shorter bonds, and *R*-factor has tripled. Interestingly, the bond length for Cu-P is suggested to be longer than that for Cu-Cl, again, in contrast to the two other samples (attempts to fix bond lengths at values similar to the other samples resulted in worse fit). This suggests a major difference in bonding modes for  $\chi_{\text{CuCl}} = 0.50$  compared to other samples. It is possible, that with low ligand availability, phosphine binds in bridging mode, which results in elongated Cu-P bonds. Possibly, there is a larger number of bonding modes in the system, which results in a worse fit when only two bond types are used in the model fit.

Discrete linear complexes such as  $[\text{CuCl}_2]^-$  exhibit shorter Cu-Cl bond lengths of 2.017 Å,<sup>529</sup> whereas the discrete tricoordinate species,  $[\text{CuCl}_2\text{PPh}_3]^-$  exhibit a longer Cu-Cl bond distances ca. 2.23 Å.<sup>530</sup> Hence is apparent that the bridging species in cubanes do have comparable Cu-Cl bond lengths to discrete Cu-Cl terminal coordination. As a final comparison within the dimeric species  $[\text{Cu}_2\text{Cl}_4(\text{PPh}_3)_2]$  the Cu-Cl terminal and Cu-Cl bridging range from 2.242-2.246 Å to 2.369-2.554 Å respectively.<sup>531</sup>

In conclusion, EXAFS spectroscopy was instrumental in elucidating the averaged copper coordination numbers and pointed to the existence of free chloride and bridging chloride ligands in the system. High energy resolution fluorescence

detected XANES was subsequently employed to gain additional insight into the LCC, shedding light on geometry of copper species.

#### **5.2.1.7 High energy resolution fluorescence detected X-ray absorption near edge structure (HERFD-XANES)**

High- energy resolution X-ray absorption near-edge structure (HERFD-XANES) is sensitive both to coordination number and site geometry of the studied element, complementary to EXAFS. It is particularly suitable for the study of first-row transition elements, where pre-edge features are always observed on the low-energy side of k-absorption edges. Factors that can affect the copper pre-edge and white line energy can include both the coordination number and geometry. The intensity of such features is related to symmetry around the studied element, with low-symmetry environments producing very strong pre-peak features, and highly symmetrical coordination spheres result in weak pre-peak signals. Hodgen, Spira-Solomon, Penner-Hahn and co-workers have successfully utilised XANES to determine both the electronic nature and geometry of multiple copper systems including enzymatic systems<sup>532</sup>, those in molecular solvents such as acetonitrile<sup>533</sup>, catalytic systems<sup>534</sup> and organocuprate reagents.<sup>535</sup>

The use of high-energy resolution fluorescence detected XANES (HERFD-XANES) enhances features present in the edge region of the absorption spectrum by reducing the core-hole lifetime<sup>536</sup>. This technique has been used in the present study, making the intensity of the transition at 8983 eV significantly larger, allowing the determination of subtle differences between the different samples studied.

In Cu(I) compounds, two-coordinate complexes display a prominent  $1s \rightarrow 4p$  transition at 8983 eV, which decreases with increasing coordination number. The reasoning for such a change in pre-peak intensity with increasing coordination number is due to geometry induced splitting of the copper's 4 orbitals as shown in Figure 5-39. In two coordinate systems a linear geometry is adopted causing the  $p_z$  orbital to be repulsed and split from the triply degenerate starting  $4p_{x,y,z}$  to a higher energy. This increase in energy of the  $p_z$  orbital allows for two pre-peak transitions to occur;  $1s \rightarrow 4p_{x,y}$  (at lower energy) and  $1s \rightarrow p_z$  (at higher energy); the transition at lower energy will manifest as a conventional pre-peak, whereas at higher energies there is an increased chance of overlap with the white line, hence appearing as a shoulder. These energies can be further affected by covalent overlap of the ligand orbitals along the z axis causing a decrease in intensity.

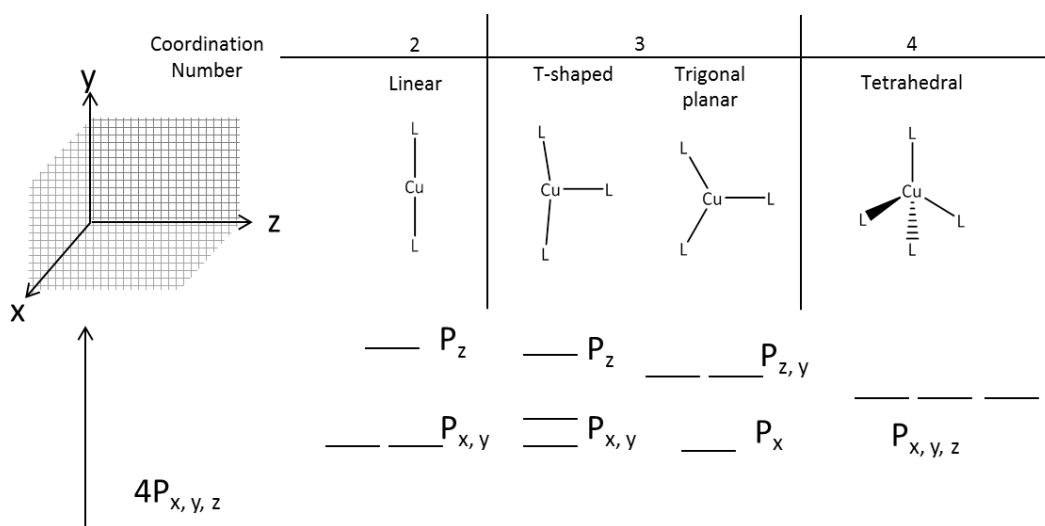


**Figure 5-39.** Figure reproduced from Hodgson and co-workers highlighting the 4p orbital splitting that occurs in in Cu(I) complexes. <sup>533</sup>

Moving from 2-coordinate to 3-coordinate there are two possible geometries present, T-shaped and trigonal planar. The pre-peak in the T-shape Cu(I) geometry is similar to that observed in the linear geometry as only a slight alteration in the  $p_y$  orbital is observed. In trigonal planar geometries a greater splitting of the  $p_y$  orbital occurs. This increase in energy in  $p_y$  would initially suggest an increase in pre-peak intensity at higher energies than the 2- coordinate, however; the ligand coordination weakens this transition hence lowering the pre-peak intensity. Furthermore, in the trigonal planar geometry  $p_y$  and  $p_z$  become degenerate, hence the pre-peak is majorly the  $1s \rightarrow p_x$  transition so intensity again lowers in this case. Moving further from 3-coordinate to a 4-coordinate species only a tetrahedral system is likely to exist in solution. In this geometry the  $p_{x,y,z}$  orbital increase in energy as are triply degenerate hence any  $1s-p$  transitions occur at higher energy and with reduced intensity as there are 4 ligand species with covalent overlap hence further reducing the intensity of the pre-peak.

As shown in Figure 5-41 and Figure 5-42, High resolution XANES data, recorded for the four samples of the  $P_{888}$ -CuCl system ( $\chi_{CuCl} = 0.10, 0.25, 0.33$  and  $0.50$ ) are compared in. Intensities of the pre-peak at ca. 8983 eV, for normalised scans, are compared in Table 5-10. It is clear from the HERFD-XANES data collected that with increasing  $\chi_{CuCl}$  from 0.10 to 0.50 the pre-peak intensity increases dramatically indicating that coordination decreases. This is in agreement with that observed in the EXAFS analysis, in which the average Cu coordination decreases from 4-coordinate at  $\chi_{CuCl} = 0.25$  to 2.67-coordinate at  $\chi_{CuCl} = 0.50$ . It is also apparent that within increasing  $\chi_{CuCl}$  a shoulder feature on the white line increases in intensity

indicating that 3-coordinate along with two coordinate species are present again, supporting the total coordination of  $\chi_{\text{CuCl}} = 0.50$  being 2.67 and not purely a 2-coordinate linear system. This result supports the formation of dimeric species in solution as shown in Table 5-8 rather than the linear geometry equilibria initially suspected. At  $\text{P}_{888}\text{-CuCl}$   $\chi_{\text{CuCl}} > 0.25$ , it is apparent that there is still a prominent pre-edge visible but at a significantly lower intensity; this indicates that the geometry may not be solely tetrahedral. A trigonal planar species may exist *via* auto complexation in that the Cu(I) does not directly coordinate to chlorine forming  $[\text{CuL}_3]\text{Cl}$  as described by Gutmann. This would explain the low  $\chi_{\text{CuCl}}$  value (0.19) obtained at  $\chi_{\text{CuCl}} = 0.25$  as there are less Cu-Cl contributions than expected.

**Table 5-10-** Numerical analysis of pre-peak and edge intensities of  $\text{P}_{888}\text{-CuCl}$  LCCs HRXANES spectra.

$\chi_{\text{CuCl}}$	Ratio pre edge area(1) to edge area(2)	Ratio pre edge area(1) to edge area(3)
0.10	5.9892	20.6041
0.25	5.1788	16.8446
0.33	4.9835	15.7584
0.50	4.6643	12.7831

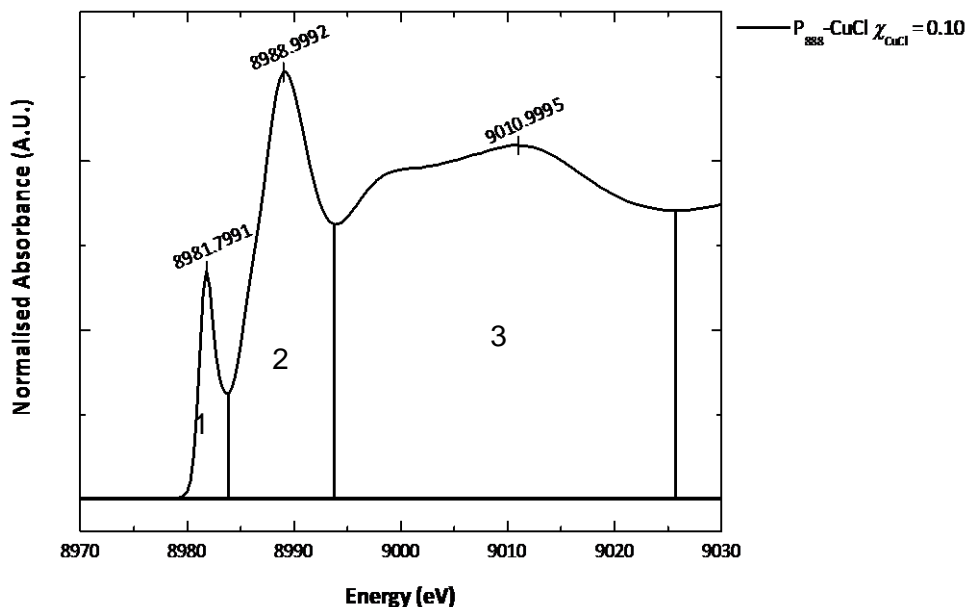


**Figure 5-40-** Pictorial representation of the sources of the numerical analysis in Table 5-10.

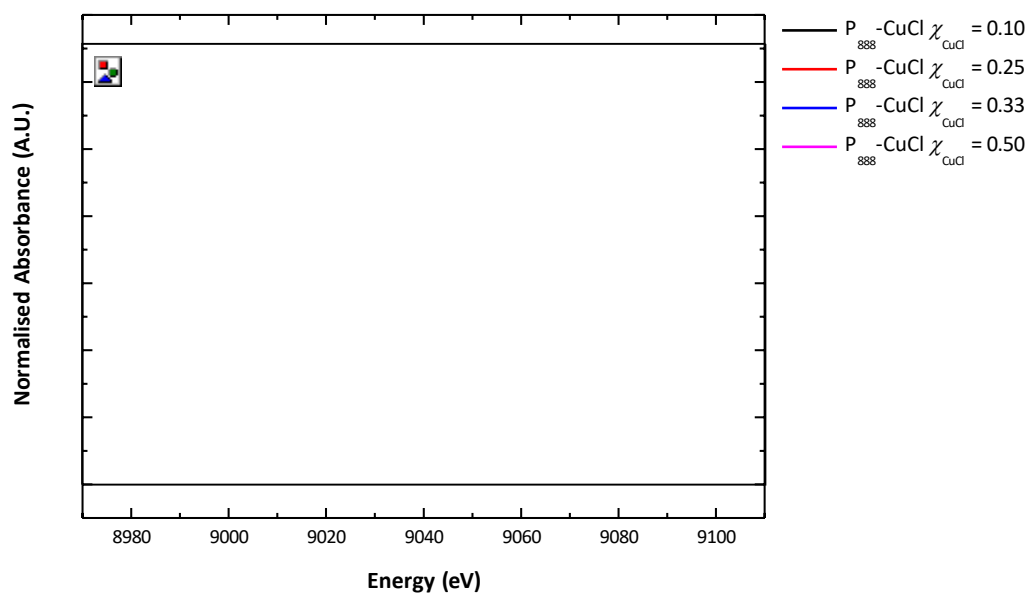


**Figure 5-41.** Overlaid plot of high resolution XANES of  $\text{P}_{888}\text{-CuCl } \chi_{\text{CuCl}} = 0.10, 0.25, 0.33, 0.50$ .

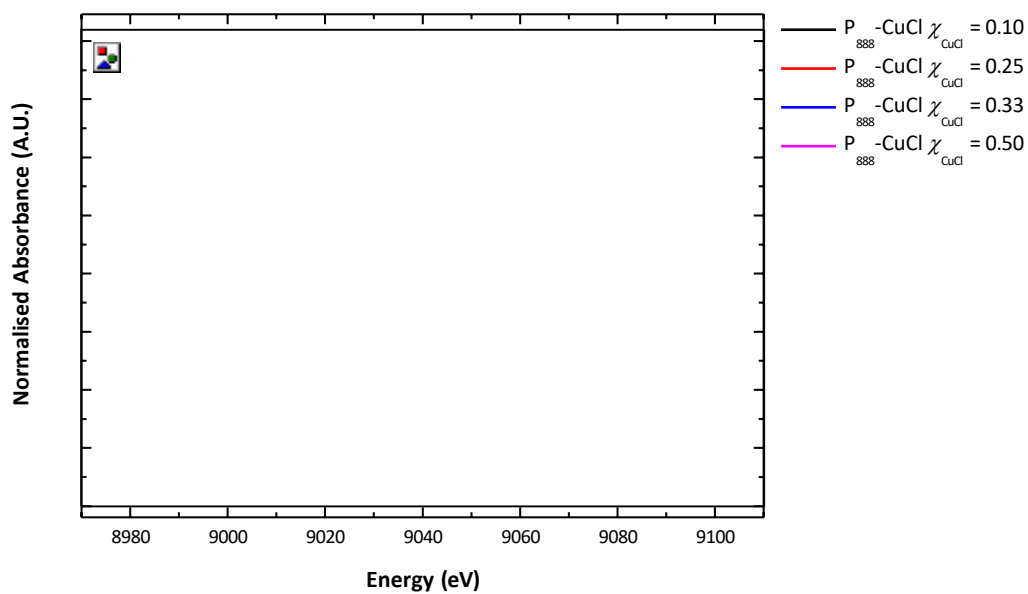


**Figure 5-42.** Stacked plot of high resolution XANES of  $\text{P}_{888}\text{-CuCl } \chi_{\text{CuCl}} = 0.10, 0.25, 0.33, 0.50$ .

On the other hand, the pre-edge feature is visible even for  $\chi_{\text{CuCl}} = 0.10$ , which shows that even at a large excess of donor ligands, the geometry around the copper centre is not purely tetrahedral. In conclusion, Cu(I) is neither exclusively di-coordinate in ligand-poor environment ( $\chi_{\text{CuCl}} = 0.50$ ), nor is fully coordinationally-saturated in a



ligand-rich environment ( $\chi_{\text{CuCl}} = 0.10$ ), but in all samples there is contribution from multiple coordination modes. This sort of behavior was seen in DES studies by Abbott and co-workers, in which Cl<sup>-</sup> rich DES with the addition of chlorocuprates did not result in coordinationally saturated copper centres.<sup>490</sup>

EXAFS and HERFD-XANES of the Cu(I)/Cu(II) and P<sub>888</sub>E containing species were found to degrade on the beam with bubbles formed *in situ* and a black liquid obtained. No reproducible spectra were able to be recorded. A sample of P<sub>888</sub>-CuCl<sub>2</sub> is shown in Figure 5-43 after a single scan exposure.



**Figure 5-43**-Visible sample degradation in P<sub>888</sub>-CuCl<sub>2</sub> samples upon exposure to X-ray beam.

#### 5.2.1.8 Speciation and explanations

##### **Copper(I)**

Copper (I) chloride LCCs formed readily up to  $\chi_{\text{CuCl}} = 0.50$  with turbid solutions forming at higher  $\chi_{\text{CuCl}}$ . Colourless in appearance these elusive LCCs were a challenge to elucidate what could be present as it is evident within literature that there is a multitude of species that are viable and are both ionic and neutral in nature. Standard spectroscopic techniques such as UV/Vis, IR and Raman spectroscopy give insight that ionic species may be present specifically the [CuCl<sub>3</sub>]<sup>2-</sup> anion. IR spectroscopy suggested that multiple Cu-E=P species are present whereas Raman techniques did not provide any assignable peaks. Multinuclear NMR confirmed the Cu-P/Cu-E=P bond, however, little change was observed with variable  $\chi_{\text{CuCl}}$ . EXAFS and HERFD-XANES were valuable tools in the elucidation of the coordination within these LCCs.

A new approach to EXAFS fitting that is data driven allowed for the deduction of the average total coordination number of the Cu(I) species in LCCs composed of

Cu(I)Cl and trioctylphosphine at multiple  $\chi_{\text{CuCl}}$  compositions. This information, combined with the EXAFS derived  $\chi_{\text{CuCl}}$  value, indicates the presence of bridging species and a coordination lower and higher than expected for  $\chi_{\text{CuCl}} = 0.25$  and  $\chi_{\text{CuCl}} = 0.50$ , respectively. Furthermore, the calculated Cu-Cl: Cu-P coordination ratio indicates that there is a small degree of ionisation present with free chloride present. HERFD-XANES provides further confirmation of a geometry change due to the increase of the pre-edge feature going from low to high  $\chi_{\text{CuCl}}$  values, indicating a change in average Cu(I) environment from higher geometries such as tetracoordinate ( $\chi_{\text{CuCl}} = 0.25$ ) to linearly coordinated ( $\chi_{\text{CuCl}} = 0.50$ ) copper(I) species. Through this work a partial insight into the speciation was given and summarised in Table 5-8 and Table 5-11.

**Table 5-11-** Final best fit coordination numbers for  $\text{P}_{888}\text{-CuCl}$   $\chi_{\text{CuCl}} = 0.25, 0.33$  and  $0.50$ .

$\chi_{\text{CuCl}}$	$N_{\text{total}}$	$N_{\text{Cu-Cl}}$	$N_{\text{Cu-P}}$
0.25	4	3.18	0.82
0.33	3.33	0.476	2.854
0.50	2.67	1.18	1.49

This innovative approach to EXAFS and XANES fit-driven speciation has been found to be a valuable methodology with significant scope to future speciation determination studies of complex metal-containing liquids such as LCCs, deep eutectic solvents and ionic liquids.

### **Copper(II)**

Upon mixing of  $\text{CuCl}_2$  with  $\text{P}_{888}\text{S}$  and  $\text{P}_{888}\text{S}$ , there is an instantaneous precipitation of the elemental chalcogen, however, this phenomenon is not observed as rapidly with non-chalcogenide donors *i.e.*  $\text{P}_{888}$  instead a similar set of solutions to the Cu(I) are observed as shown in Figure 5-44. At  $\chi_{\text{CuCl}_2} \geq 0.50$ , the LCCs are liquid at room temperature with  $\chi_{\text{CuCl}_2} \leq 0.50$  forming low-melting point solids. As discussed over several months, the reduction of Cu(II) occurs with the  $\text{P}_{888}$  ligand resulting in a two-phase system forming.

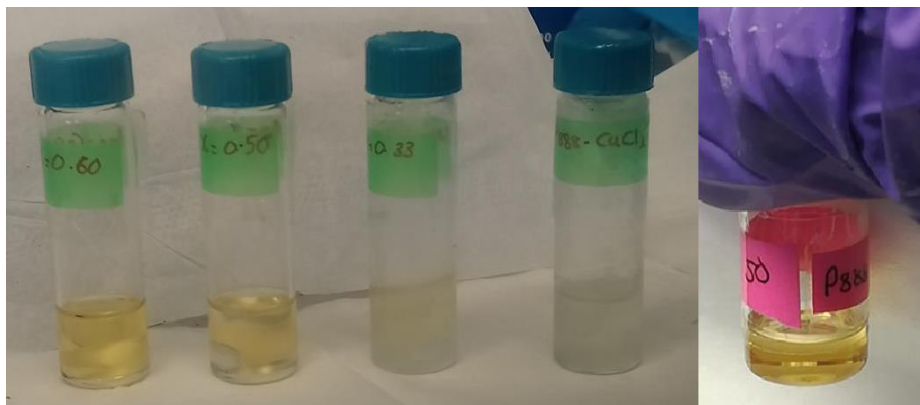


**Figure 5-44** |  $P_{888}$ - $CuCl_2$  LCCs (L-R)  $\chi_{CuCl_2} = 0.60, 0.50, 0.33, 0.25$  and the two-phase solution that forms after 3 months.

Copper (II) chloride redox behaviour is not unknown within chemistry. *Kotocova et al.* describes that the availability of reducible ligands in the coordination sphere of  $Cu^{2+}$  in regards to thermodynamics is showing that it is a relatively facile process.<sup>537</sup> The reduction of  $Cu(II)$  is not uncommon and has been utilised in synthesis of disulphides from mercaptans *via* facile reductions of mercaptans upon coordination and consequent reduction.<sup>538</sup>

It is also found in nature, specifically, within copper-containing electron transfer proteins as described by Thompson *et al.* such that histidine type complexes of  $Cu(II)$  can undergo reduction in the present of a mercaptan species with many other examples in literature of biomimetic complexes.<sup>513,539,540</sup> An extensive review by Jardine highlights the frequency at which these redox reactions occur and are utilised in synthesis of their  $Cu(I)$  complex analogues.<sup>487</sup>

In regards to the speciation of the initial  $P_{888}$ - $CuCl_2$  LCC prior to redox little is determined from  $^{31}P$  NMR and Infrared spectroscopy, however, after solvation it is evident that the  $[P_{888}Cl]^+$  cation is present. As a counter anion to this it is suspected that both  $Cl^-$  and  $[Cu_xCl_{x+1}]^-$  is present as per literature reports by Yoke and Axtell.<sup>516</sup> The presence of significantly smaller  $P_{888}S$  and  $P_{888}E$ , peaks in the  $^{31}P$  NMR spectra indicate that little  $P_{888}E$ - $CuCl$  is present in comparison to the  $[P_{888}Cl]^+$  species.

## 5.2.2 Copper (I) chloride – trioctylphosphine liquid coordination complexes and chalcogenide interactions

### 5.2.2.1 Observations

Copper (I) chloride- trioctylphosphine liquid coordination complexes  $P_{888}$ - $CuCl$ , as aforementioned may have scope in regards to synthesis of copper containing semiconductor materials such as copper selenides *etc.* Utilisation of element

sources of the chalcogenide species is preferential as it eliminated the need for alkyl of halogenated precursors. To investigate the interactions of chalcogenides with these solutions, small portions of elemental sulphur, selenium and tellurium were added to  $P_{888}$ -CuCl  $\chi_{CuCl} = 0.33, 0.50$  LCCs and observations noted in Table 5-12 .

**Table 5-12-** Copper (I) chloride- trioctylphosphine liquid coordination complexes  $P_{888}$ -CuCl and elemental chalcogens.

LCC	$\chi_{CuClx}$	Element	Observation
$P_{888}$ -CuCl	0.5, 0.33	S	Dissolves readily (less so at $\chi_{CuClx} = 0.33$ )
	0.5, 0.33	Se	Dissolves readily (less so at $\chi_{CuClx} = 0.33$ )
	0.5, 0.33	Te	Black suspension forms

### 5.2.2.2 Nuclear magnetic resonance spectroscopy

Multinuclear NMR has been utilised to elucidate binding within the systems specifically the  $^{31}P$  nucleus as shown in Figure 5-45, Figure 5-46 and Figure 5-47.  $^{31}P$  NMR spectroscopy has alluded to the formation of the Cu-X=P bonding motifs upon the addition of sulphur and selenium at 35.56 ppm and 50.84 ppm respectively. There is no indication of  $P_{888}Te$  formation with the  $P_{888}$  peak at -19.84 ppm hence indicating no solvation has occurred *via*  $P_{888}Te$  formation. In the sulphur and selenium systems there is residual  $P_{888}$  despite being a saturated solution with excess chalcogenide added. The reason for this is currently unknown.

**Table 5-13-** $^{31}P$  NMR signals of  $P_{888}$ -CuCl  $\chi_{CuCl} = 0.50$  with the addition of elemental chalcogenide.

Chalcogenide	$\delta_{31P}$ (ppm)	$\Delta\delta_{31P}$ compared to LCC
-	-20.70	-
S	35.56	56.26
Se	50.84	71.54
Te	-19.84	0.86

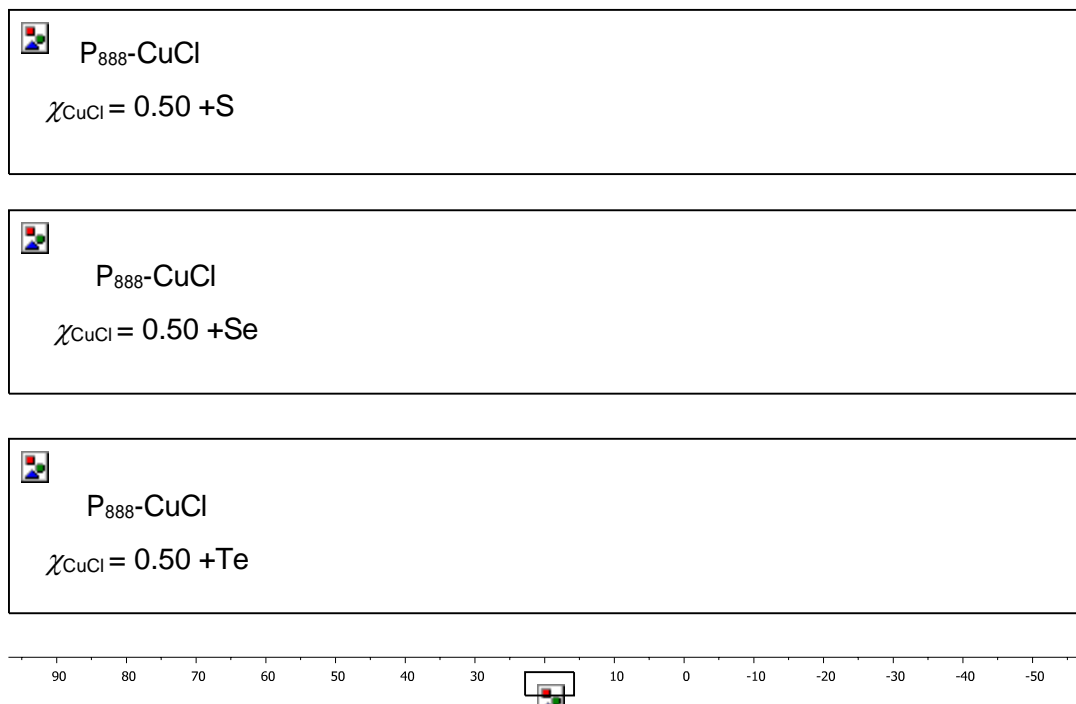


**Figure 5-45-(top -bottom)**  $^{31}\text{P}$  NMR of  $P_{888}\text{-CuCl}$   $\chi_{\text{CuCl}} = 0.50$  + elemental sulphur,  $P_{888}\text{-CuCl}$   $\chi_{\text{CuCl}} = 0.50$  + elemental selenium,  $P_{888}\text{-CuCl}$   $\chi_{\text{CuCl}} = 0.50$  + elemental tellurium.

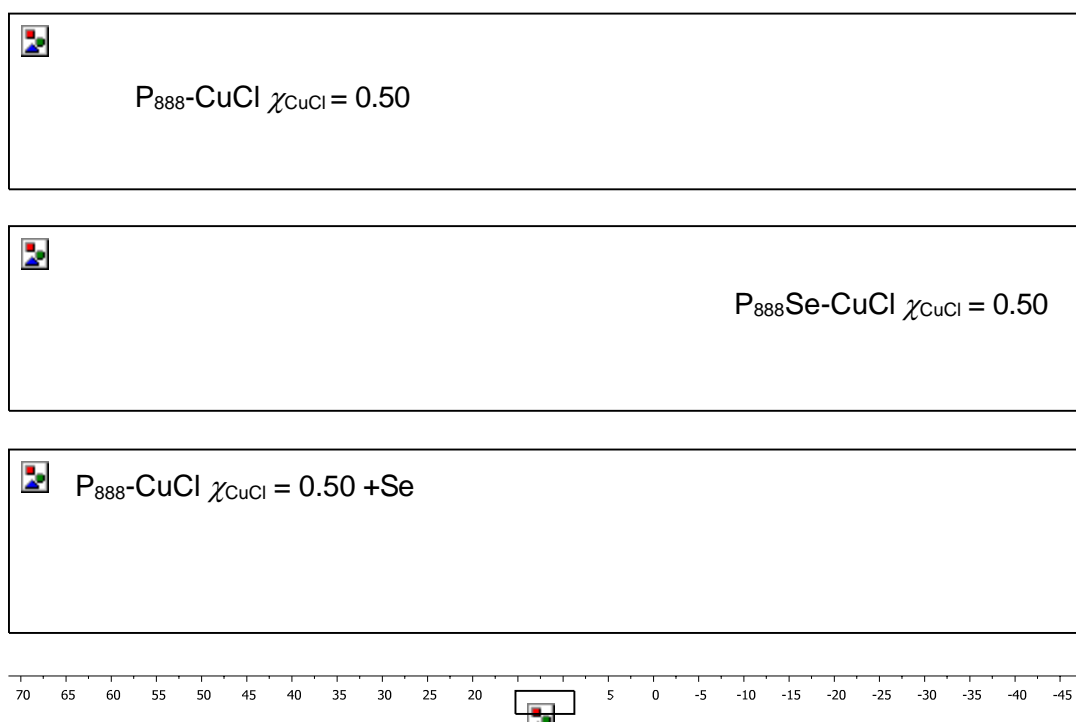


**Figure 5-46-(top -bottom)**  $^{31}\text{P}$  NMR of  $P_{888}\text{-CuCl}$   $\chi_{\text{CuCl}} = 0.50$ ,  $P_{888}\text{Se-CuCl}$   $\chi_{\text{CuCl}} = 0.50$ ,  $P_{888}\text{-CuCl}$   $\chi_{\text{CuCl}} = 0.50$  + elemental selenium.

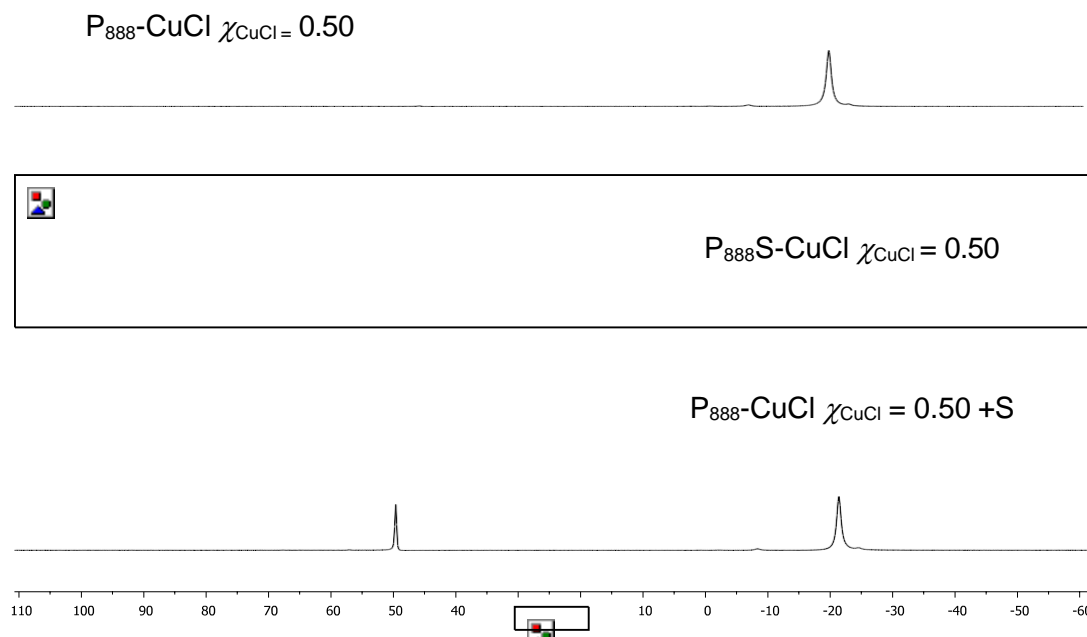


**Figure 5-47**--(top -bottom)  $^{31}\text{P}$  NMR of  $\text{P}_{888}\text{-CuCl}$   $\chi_{\text{CuCl}} = 0.50$ ,  $\text{P}_{888}\text{S-CuCl}$   $\chi_{\text{CuCl}} = 0.50$ , and  $\text{P}_{888}\text{-CuCl}$ ,  $\chi_{\text{CuCl}} = 0.50$  and elemental sulphur.

### 5.2.2.3 Infrared spectroscopy

Infrared spectroscopy of  $\text{P}_{888}\text{-CuCl}$   $\chi_{\text{CuCl}} = 0.50$  with the addition of elemental chalcogenides as is shown in Figure 5-48 and Figure 5-49. The main observation is the formation of the  $\text{P}=\text{S}$  bond upon the addition of sulphur at  $553\text{ cm}^{-1}$  which is in accordance with that found in  $\text{P}_{888}\text{S-CuCl}$  LCCs as listed in Table 5-7. In regards to  $\text{P}=\text{Te}$  it is expected to generate a band *ca.*  $450\text{ cm}^{-1}$ , hence is not visible in the IR spectra.<sup>541</sup>

**Table 5-14**- Infrared spectra of  $\text{P}_{888}\text{-CuCl}$   $\chi_{\text{CuCl}} = 0.50$  with elemental sulphur, selenium and tellurium.

LCC	P-C/P=E stretching frequency ( $\text{cm}^{-1}$ )	Ref
$\text{Ph}_3\text{P}=\text{O}$	1195	Cotton <sup>520</sup>
$\text{R}_3\text{P}=\text{S}$	730, 587	Chittenden <sup>521</sup>
$\text{R}_3\text{P}=\text{Se}$	443	Sukhov <sup>522</sup>
$\text{P}_{888}\text{-CuCl}$ $\chi_{\text{CuCl}} = 0.50 + \text{S}$	722 (increased absorption), 553	This work
$\text{P}_{888}\text{-CuCl}$ $\chi_{\text{CuCl}} = 0.50 + \text{Se}$	722 (increased absorption)	This work
$\text{P}_{888}\text{-CuCl}$ $\chi_{\text{CuCl}} = 0.50 + \text{Te}$	No change	This work

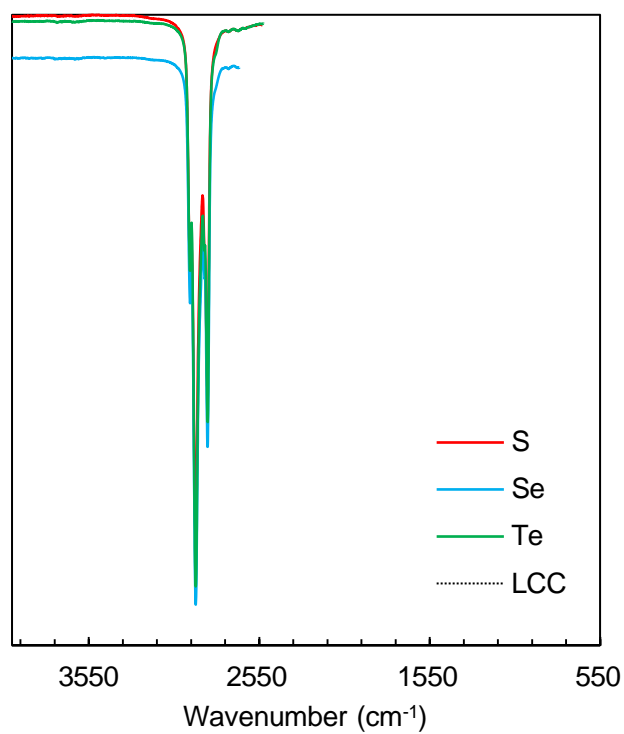


**Figure 5-48-** Infrared spectra of  $P_{888}\text{-CuCl}$   $\chi_{\text{CuCl}} = 0.50$  with elemental sulphur, selenium and tellurium.

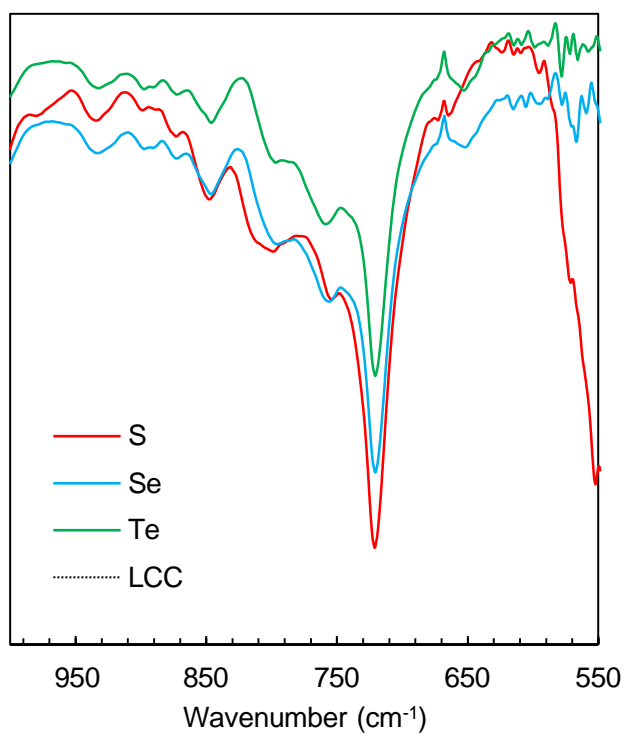


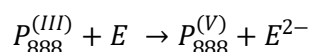
**Figure 5-49-** Infrared spectra of  $P_{888}\text{-CuCl}$   $\chi_{\text{CuCl}} = 0.50$  with elemental sulphur, selenium and tellurium.

The clear formation of  $P_{888}S$  in the Infrared spectra validates what is shown in the  $^{31}P$  NMR spectra such that upon solvation of the elemental sulphur under goes a redox process with the P(III) phosphine to form a new donor ligand,  $P_{888}S$ .

#### 5.2.2.4 Solvation mechanism

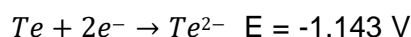
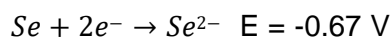
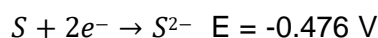
It is evident that the addition of a chalcogenide, specifically sulphur and selenium resulting in the formation of  $P_{888}E$ , as described in Equation 5-10. There is no suggestion that the chlorocuprate interacts with the elemental chalcogenide; instead solvation is driven *via* redox with the phosphine. The tellurium fails to show any solvation in the  $P_{888}$ -CuCl LCCs; this is somewhat unsurprising due to the greater standard reduction potential of the tellurium species in comparison to selenium and sulphur as shown in Equation 5-11.<sup>542</sup>

Equation 5-10



Where E= S or Se

Equation 5-11



In comparison, the standard reduction potential for  $P^{(V)}$  to  $P^{(III)}$  is -1.12 V, which is very similar to that of tellurium, hence there is no positive potential difference for the redox to occur. It is pertinent that the standard reduction potentials are a preliminary guide to redox couples that may occur as the complexity of these solutions can impact the conditions and consequent changes in redox properties. Mishra *et al.* found that there are differences in behaviour of copper(I) chlorides and copper(II) chlorides with dimethyl selenides.<sup>543</sup> The  $Cu^+$  species proceeds cleanly to form  $[Cu(\mu-Cl)(\mu-SeMe_2)]_2$  a 2D framework, whereas  $Cu^{2+}$  forms  $[Me_3Se][CuCl_4]$  and an unidentified brown product. The formation of the  $[Me_3Se]^{2+}$  cation eludes to the reduction of  $Se^{2-}$  to  $Se^{5-}$  if  $Cu^{2+}$  remains, hence a counter oxidation must have occurred.



## 5.2.3 Copper (II) chloride – trioctylphosphine liquid coordination complexes and chalcogenide interactions

### 5.2.3.1 Observations

Copper (II) chloride- trioctylphosphine liquid coordination complexes  $P_{888}\text{-CuCl}_2$ , have already shown some interesting redox properties in regards to  $E^{2-}$  donor ligands such as  $P_{888}\text{S}$  and  $P_{888}\text{Se}$ . Furthermore, the precipitation of sulphur and selenium is, as aforementioned indicative of redox behaviour in regards to the  $\text{Cu}^{2+}$  cation. Investigating elemental sulphur, selenium and tellurium in the fresh 'stable' solutions of  $P_{888}\text{-CuCl}_2$ , we observe, as listed in Table 5-15, solvation occurs readily in the cases of sulphur and selenium and in the tellurium sample a colour change is observed from colourless to a light green solution.

**Table 5-15-** Copper (II) chloride- trioctylphosphine liquid coordination complexes  $P_{888}\text{-CuCl}_2$  and elemental chalcogens.

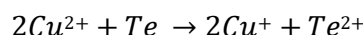
LCC	$\chi_{\text{CuCl}_2}$	Element	Observation
$P_{888}\text{-CuCl}_2$	0.50, 0.33	S	Dissolves readily
	0.50, 0.33	Se	Dissolves readily
	0.50, 0.33	Te	Hazy green solution forms

#### 5.2.3.1.1 Nuclear magnetic resonance spectroscopy

Multinuclear NMR has been again utilised to elucidate binding within the systems, specifically the  $^{31}\text{P}$  nucleus as shown in Figure 5-50.  $^{31}\text{P}$  NMR spectroscopy has alluded to the formation of the  $\text{Cu-X=P}$  bonding motifs with shifts observed in each donor ligand used from P(III) of  $P_{888}$  to the P(V) of  $P_{888}\text{E}$ . Within the sulphur and selenium solvation there is the formation of  $P_{888}\text{S}$  and  $P_{888}\text{Se}$  at 50.35 ppm and 37.54 ppm, respectively. However, another peak arises at ca. 102 ppm in all chalcogens tested; S, Se and Te indicating the presence of the as discussed  $[\text{P}_{888}\text{Cl}]\text{Cl} / [\text{P}_{888}\text{Cl}][\text{Cu}_x\text{Cl}_{x+1}]$  species. This species, as we have studied is not present in the  $P_{888}\text{-CuCl}_2$  LCCs hence it is postulated that it is a product of the degradation of  $P_{888}\text{E}$  formed upon the addition of the chalcogenide. This is supported by the increase in  $[\text{P}_{888}\text{Cl}]\text{Cl} / [\text{P}_{888}\text{Cl}][\text{Cu}_x\text{Cl}_{x+1}]$  species with increasing  $\chi_{\text{CuCl}_2}$ , as shown in Figure 5-50. The most obscure result was obtained upon the addition of elemental tellurium, similar to the selenium and sulphur studies the  $[\text{P}_{888}\text{Cl}]\text{Cl} / [\text{P}_{888}\text{Cl}][\text{Cu}_x\text{Cl}_{x+1}]$  species was observed, however, no evidence of  $P_{888}\text{Te}$  was observed; the  $P_{888}\text{Te}$  is significantly more difficult to form than the  $P_{888}\text{S}$  and  $P_{888}\text{Se}$  counterparts.

Within this work, attempts to synthesise  $P_{888}Te$  resulted in a mix of products, unreacted starting material and suspected  $P_{888}O$  formed due to contaminants. This difficulty in formation of  $P_{888}Te$  and the  $^{31}P$  NMR spectrum showing the  $[P_{888}Cl]Cl / [P_{888}Cl][Cu_xCl_{x+1}]$  species indicates that the solvation of the elemental tellurium species to possibly form a cationic telluride species *via* the reduction of  $Cu^{2+}$  as shown in Equation 5-12. It is suspected, that the tellurium is oxidised to the 2+ state as it is one of the most common cationic telluride species reported, however, tellurium has been reported to exist in up to the 6+ state.<sup>544</sup> Furthermore, solvation *via* this method accounts for the formation of the  $[P_{888}Cl]Cl / [P_{888}Cl][Cu_xCl_{x+1}]$  as  $Cu^{2+}$  reduces to  $Cu^+$  the preferred coordination of the central copper changes for 6 / 4 to 4 / 2, hence releasing a donor ligand and chloride to form the as mentioned species.

**Equation 5-12**



The appearance of a doubling of peaks at *ca.* -20 ppm is believed to be due to the formation of complexes with cationic telluride species.<sup>545</sup> As the elemental sulphur and selenium can proceed *via* two pathways either forming the  $P_{888}Se$  *via* redox with the P(III) and then consequent redox with the Cu(II) or *via* a more direct redox with the Cu(II) to a cationic species.  $^{77}Se$  NMR spectra of  $P_{888}-CuCl_2$  saturated with elemental selenium showed a single doublet at -332 ppm, which corresponds to an anion  $Se^{2-}$  species (Figure 5-52). If it was a cation species formed *via* direct redox with the Cu(II) it would be expected to observe a peak above 0 ppm. However, it is suspected that the  $P_{888}Se$  formed is a free ligand due to the -332 ppm shift; in comparison to that obtained by Levason and Black in Cu(I) and  $Ph_3P$  complexation studies.<sup>500</sup>

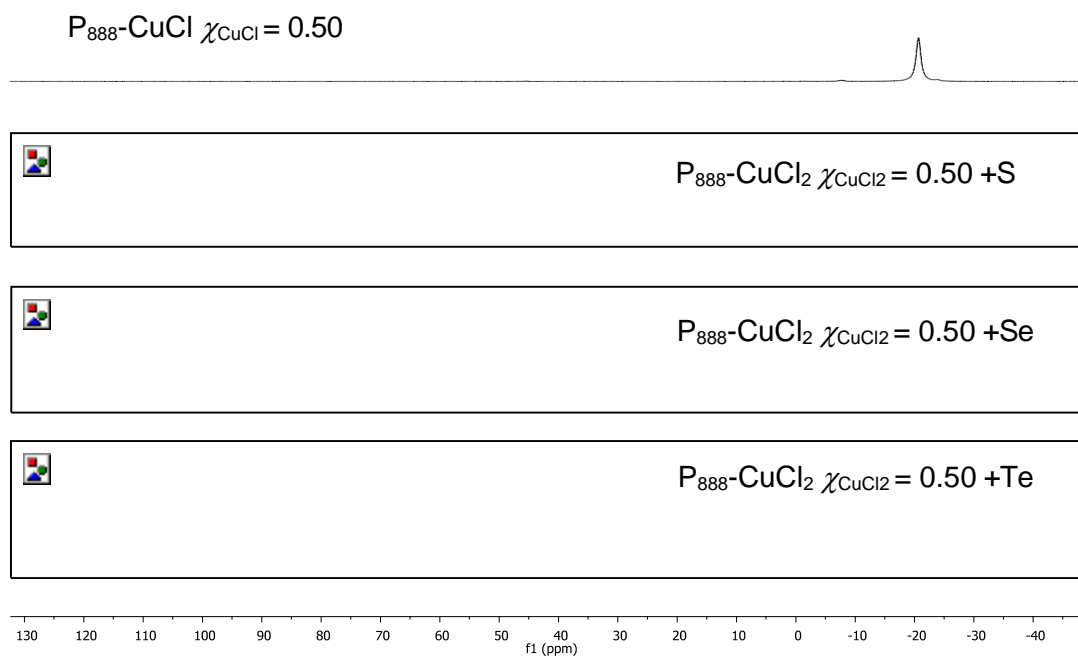


**Figure 5-50-**(top-bottom)  $^{31}\text{P}$  NMR of  $P_{888}\text{-CuCl} \chi_{\text{CuCl}} = 0.50$ ,  $P_{888}\text{-CuCl}_2 \chi_{\text{CuCl}_2} = 0.50$  + elemental sulphur,  $P_{888}\text{-CuCl}_2 \chi_{\text{CuCl}_2} = 0.50$  + elemental selenium,  $P_{888}\text{-CuCl}_2 \chi_{\text{CuCl}_2} = 0.50$  + elemental tellurium.

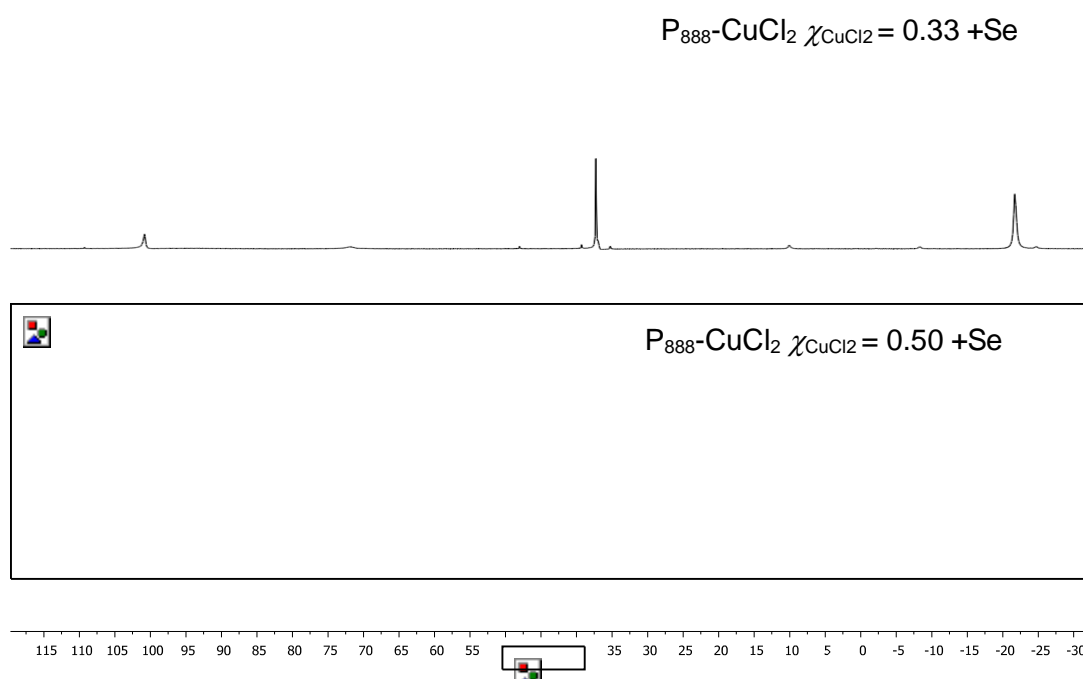


**Figure 5-51-**  $^{31}\text{P}$  NMR of  $P_{888}\text{-CuCl}_2 \chi_{\text{CuCl}_2} = 0.33$  and  $0.50$  + elemental selenium.

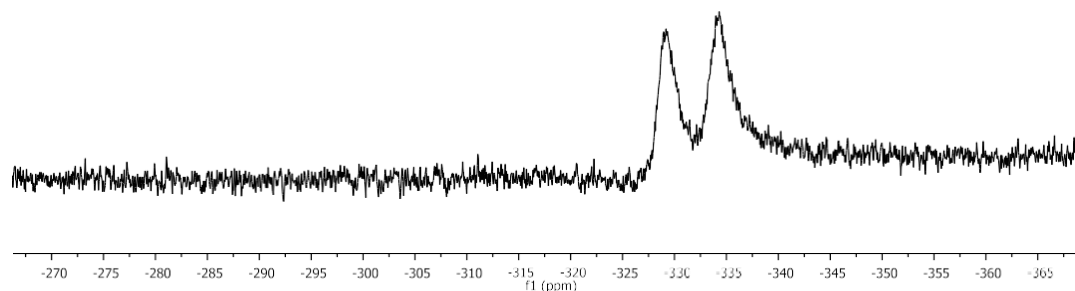


**Figure 5-52**– $^{77}\text{Se}$  NMR of  $\text{P}_{888}\text{-CuCl}_2$   $\chi_{\text{CuCl}_2} = 0.50$  + elemental selenium.

### 5.2.3.2 Infrared spectroscopy

Infrared spectroscopy of the fresh  $\text{P}_{888}\text{-CuCl}_2$   $\chi_{\text{CuCl}_2} = 0.50$  with the addition of chalcogenides is shown in Figure 5-53. The main observation is the formation of the  $\text{P}=\text{S}$  bond upon the addition of sulphur at  $554\text{ cm}^{-1}$ , which is in accordance with that found in  $\text{P}_{888}\text{S-CuCl}$  LCCs, as listed in Table 5-7. In regards to P-Te it is expected to generate a band *ca.*  $450\text{ cm}^{-1}$  hence is not visible in the IR spectra.<sup>541</sup>

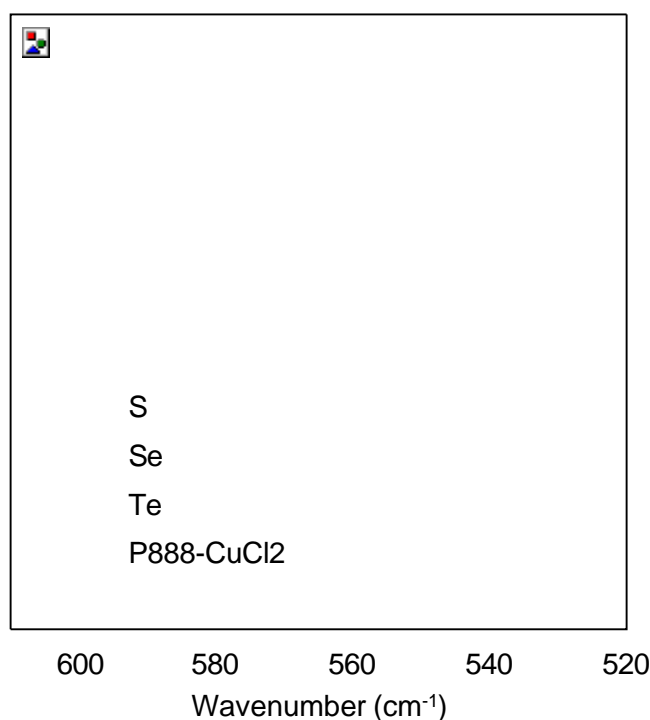


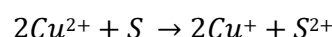
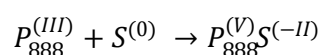
**Figure 5-53**–Infrared spectra of  $\text{P}_{888}\text{-CuCl}_2$   $\chi_{\text{CuCl}_2} = 0.50$  with elemental sulphur, selenium and tellurium.

### 5.2.3.3 Solvation mechanism

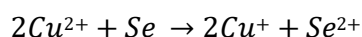
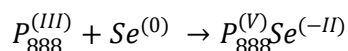
It is apparent that there are both similarities and difference in the solvation mechanism of chalcogenides in the  $\text{P}_{888}\text{-CuCl}_2$  LCC system compared to  $\text{P}_{888}\text{-CuCl}$

LCC systems. Within the sulphur and selenium solutions the  $P_{888}E$  species is formed in a similar manner to the  $P_{888}\text{-CuCl}$  LCC system, in that a redox with the phosphorus donor ligand occurs. However, the tellurium is believed to proceed differently to that of sulphur and selenium, in that solvation is solely driven by redox with the  $\text{Cu}^{2+}$  (Equation 5-12) as no interaction with the phosphine was observed in the  $P_{888}\text{-CuCl}$  LCC system unlike sulphur and selenium. Solvation *via* direct reaction of the chalcogenide and chlorocuprate cannot be exclusively found in the tellurium experiment but it is suspected to work in tandem with the phosphine method of solvation hence explaining the lack of residual  $P_{888}$  in the sulphur and selenium test with  $P_{888}\text{-CuCl}_2$ , whereas there is  $P_{888}$  present in the tellurium sample as only a single method of solvation is active.

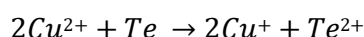
**Equation 5-13**



**Equation 5-14**



**Equation 5-15**

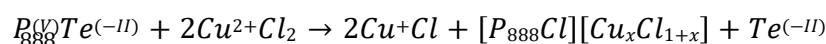
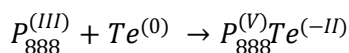


Although, as discussed, the direct reaction of the sulphur and selenium species is possible it is believed that the formation of the phosphine chalcogenide is preferential as no evidence of a cationic selenium species is detected in the  $^{77}\text{Se}$  NMR spectra. Furthermore, cationic sulphur and selenium species are often coloured. In both the sulphur and selenium solvation experiments there are no colour changes observed with the solutions remaining a transparent and yellow throughout.

The acceleration in the formation of the  $P(V)$  species with the addition of elemental tellurium indicates that there must be an interplay with the phosphorous species that is not accounted for in Equation 5-15. There are two possible mechanisms which can account for the formation of the  $P(V)$  species. The first of which is *via* the

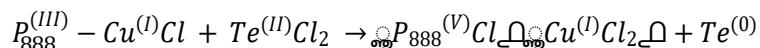
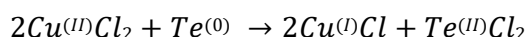
formation of  $P_{888}Te$  and the consequent reduction *via* the  $Cu^{2+}$  species as per Equation 5-16.

Equation 5-16



However, if this mechanism did occur the formation of  $P_{888}Te$  would have also been detected in the Cu(I) LCC systems and it is not. The second and most likely mechanism, in which the P(V) species is formed is *via* the formation of acationic tellurium species by a redox reaction with the Cu(II) species. The cationic telluride species is suspected to form  $TeCl_2$ , which in turn undergoes redox with  $P_{888}$  to form P(V) and  $Te(0)$ . This mechanism is listed in Equation 5-17.

Equation 5-17



Confirmation of this mechanism could be sought *via* XPS spectroscopy to determine the oxidation states of the copper and telluride species. Furthermore, the use of a non-redox-active ligand may allow detection and ultimately utilisation of the cationic telluride species in inorganic synthesis along with confirming the first step of the solvation mechanism.

### 5.2.3.4 Summary of chlorocuprate liquid coordination complexes and chalcogenide interactions

A summary of the chlorocuprate LCC and chalcogenide interactions is listed in Figure 5-54.

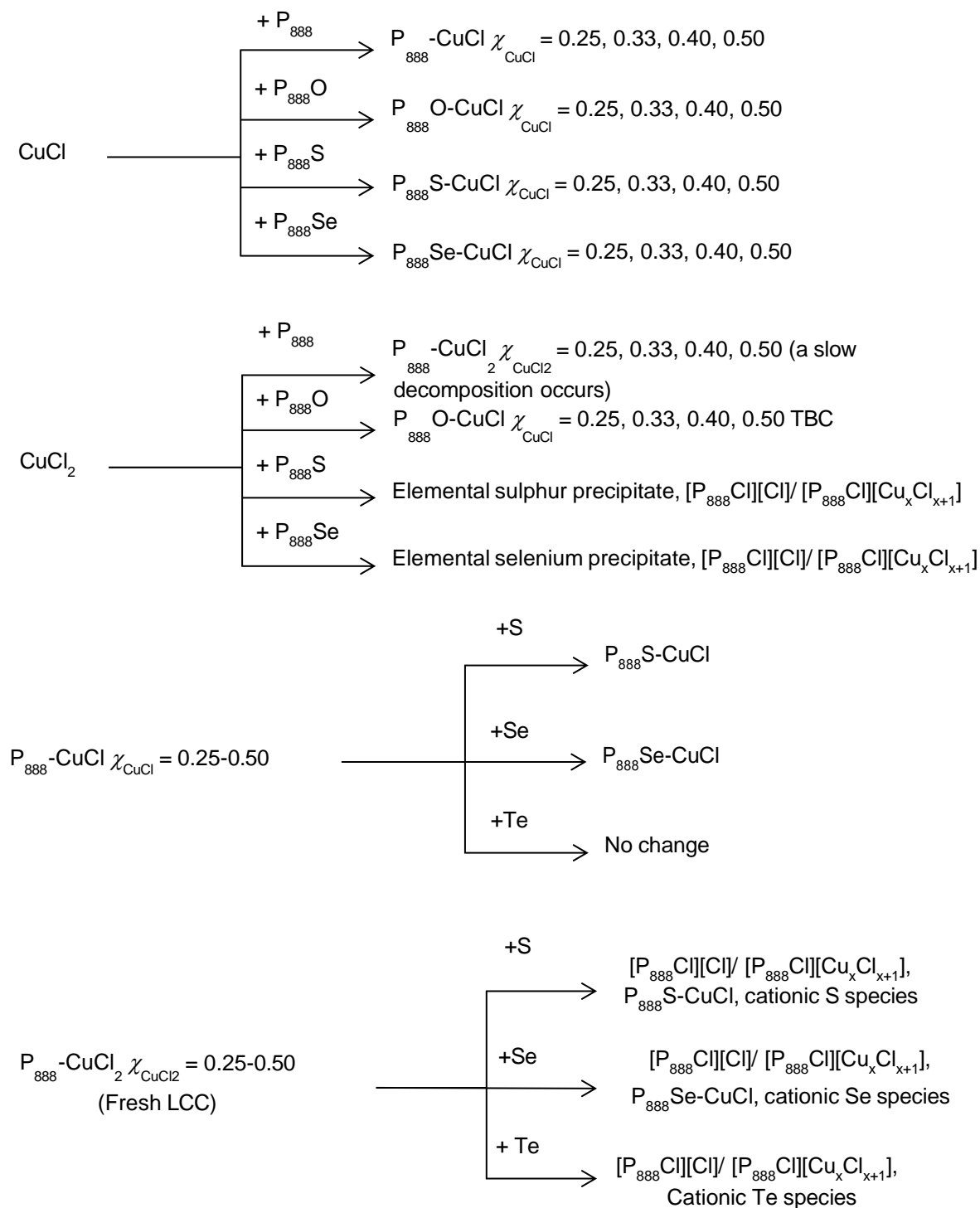


**Figure 5-54-** Summary of chlorocuprate liquid coordination complexes and chalcogenide interactions.

## 5.2.4 Liquid coordination complexes as precursors for semiconductor materials

As discussed in 5.1.2.1, LCCs can provide a cheaper and simpler alternative to current conventional and ionothermal methods to synthesise transition metal and group 13 chalcogenide semiconductors. Here, a series of proof-of-concept reactions have been carried out to investigate the suitability of LCCs to inorganic syntheses of binary and ternary compounds.

### 5.2.4.1 Gallium selenides

Comparisons to previous work regarding the microwave synthesis of gallium (III) selenide have been hampered by malfunctions of the microwave reactor. One comparative reaction was completed using  $P_{888}Se-GaCl_3$   $\chi_{GaCl_3} = 0.50$ . The sample was heated at 20 °C intervals for 30 seconds until a reaction was observed. The power settings were set to not exceed 150 Watts. A reaction was observed at 80 °C with an exotherm observed increasing the recorded temperature to 115 °C forming a red/brown suspension that with DCM washes results in a fine red powder. This reaction temperature is approximately 115 °C lower than that previously achieved on the Anton Paar microwave reactor using the same LCC.

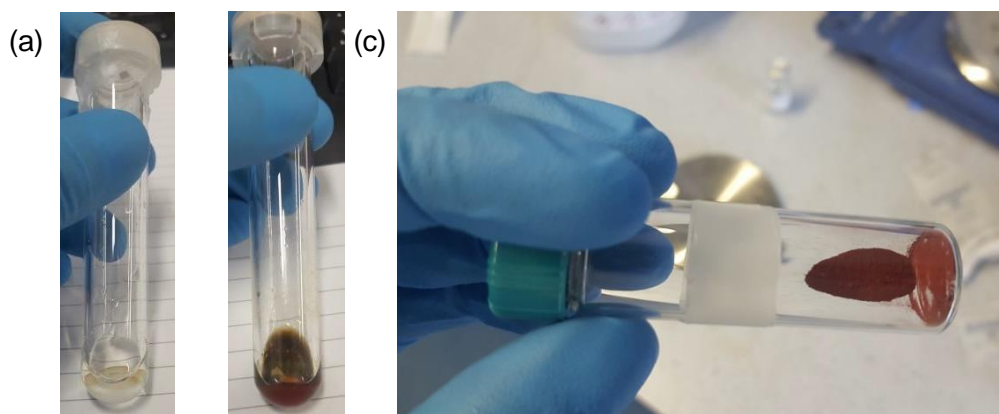


**Figure 5-55-**  $P_{888}Se-GaCl_3$   $\chi_{GaCl_3} = 0.50$  (a) LCC, (b) after microwave irradiation 80 °C for 30 s (c) isolated product

The powder formed has been analysed using pXRD and SEM-EDX techniques (Figure 5-56, Figure 5-57 and Figure 5-58); and was determined to be gallium(III) selenide microspheres. The average particle size was determined to be 1.48  $\mu m$  diameter (standard deviation 0.493  $\mu m$ , 20 samples.)



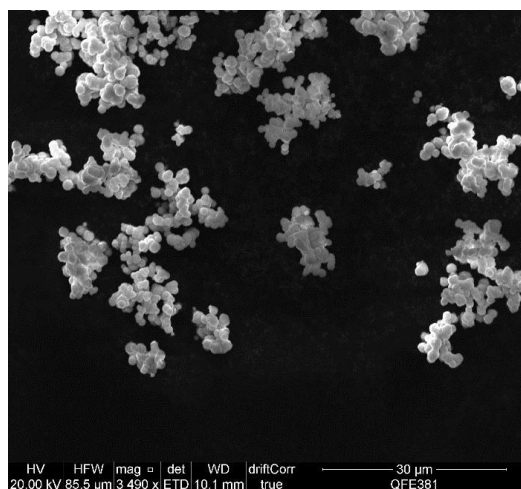


**Figure 5-56**-SEM image of microwave irradiated product of  $P_{888}Se-GaCl_3$   $\chi_{GaCl_3} = 0.50$ .

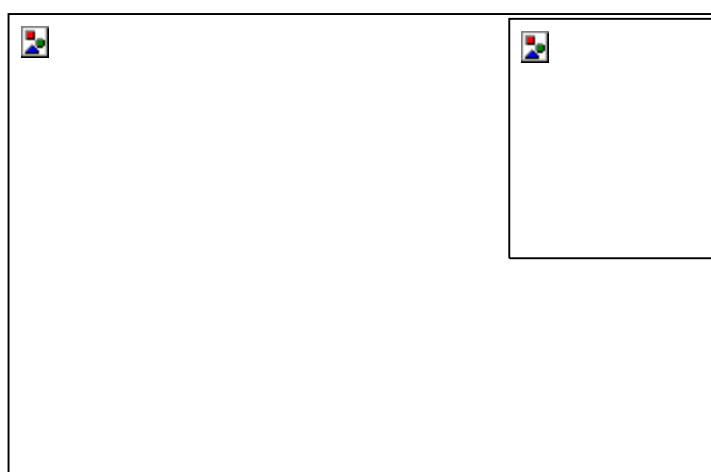


**Figure 5-57**-EDX analysis of microwave irradiated  $P_{888}Se-GaCl_3$   $\chi_{GaCl_3} = 0.50$ .

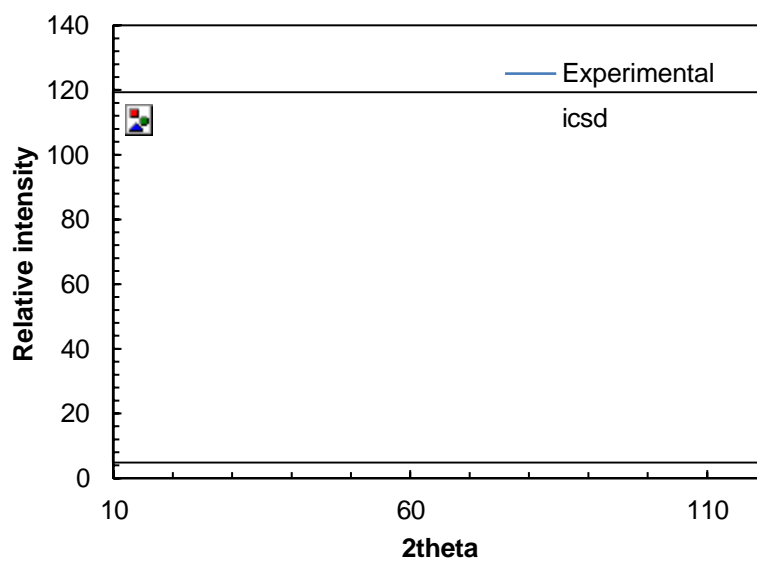


**Figure 5-58**-pXRD diffraction pattern of microwave irradiated  $P_{888}Se-GaCl_3$   $\chi_{GaCl_3} = 0.50$  and ICSD PXR pattern by Flahaut *et al.*<sup>546</sup>

The pXRD pattern matches that obtained by Flahaut *et al.*<sup>546</sup> with reflections at 28.5, 47.3, 55.5, 68.7, 76.4, 86., 93.7 and 106.6 ° determining a:

*'the entirely ordered monoclinic phase of Ga<sub>2</sub>Se<sub>3</sub> is a superstructure of the basic distorted sphalerite-type.'*

**Table 5-16**-Elemental distribution of isolated product of P<sub>888</sub>Se-GaCl<sub>3</sub>  $\chi_{\text{GaCl}_3}$  = 0.50 microwave reaction.

	mm	wt%	mol %	mol ratio	elemental ratio
Ga	69.72	30.90	0.4431	0.4041	1
Se	78.97	51.60	0.6534	0.5959	1.474

The success observed with the microwave-assisted reactions lead to further investigations into the use of a more classical bench-top approach. Due to the air sensitive nature of the compound; ampoules were utilised to allow for prolonged heating outside the glove box. As with the microwave-assisted reactions the ampoules were heated and the temperature increased at 20 °C increments until a significant change in appearance was observed. The solutions tested initially were P<sub>888</sub>Se-GaCl<sub>3</sub>  $\chi_{\text{GaCl}_3}$  = 0.60 and  $\chi_{\text{GaCl}_3}$  = 0.67 with significant changes in the appearance of both samples observed at 215 °C to which heating was continued for a further 1 hour 30 minutes. Upon work-up, it was observed that no isolatable precipitate was present in the darkened  $\chi_{\text{GaCl}_3}$  = 0.60 solution however, a white-cream precipitate was collected from  $\chi_{\text{GaCl}_3}$  = 0.67 solutions. The white powder was found to be air sensitive; turning red over prolonged exposure to the atmosphere as shown in Figure 5-59.

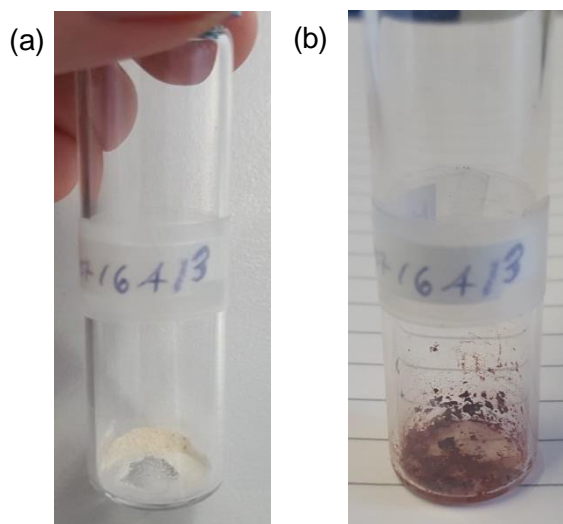


**Figure 5-59**-(a) product formed with  $P_{888}Se-GaCl_3$   $\chi_{GaCl_3} = 0.67$  (b) product after 96 hours exposure to air.

Upon repetition both precipitates had similar morphology under SEM analysis forming clusters of rod like structures with average length  $11.55 \mu m$  ( $\chi_{GaCl_3} = 0.67$ , Figure 5-60) and  $14.47 \mu m$  ( $\chi_{GaCl_3} = 0.67$ , Figure 5-60 ); EDX analysis has shown a slight discrepancy in composition between samples as shown in Figure 5-61. PXRD diffraction of the isolated solid did not elucidate the composition or structure of the mystery white powder. It is suspected that the compound is an intermediate of the reaction in which the gallium (III) selenide is formed in microwave-assisted reactions. The compound is believed to be an approximate equimolar mix of gallium selenium and chlorine. To further investigate the unknown compound attempts were made to recrystallize the solid, however, no crystals were achieved in solutions that remained stable and melting was not achieved with the solid turning red at higher temperatures.

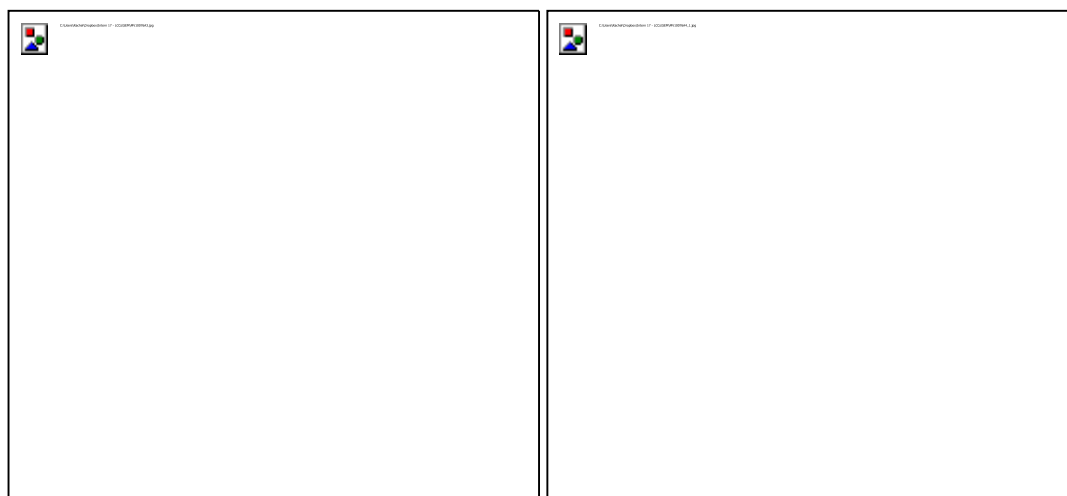


**Figure 5-60**-SEM analysis of ionothermal  $P_{888}Se-GaCl_3$   $\chi_{GaCl_3}=0.67$  reaction products.



**Figure 5-61**-EDX analysis of ionothermal  $P_{888}Se-GaCl_3$   $\chi_{GaCl_3} = 0.67$  reaction product.

#### 5.2.4.2 Indium selenides

Previous work by Tyrrell *et al.* utilised chloroindate ionic liquids with diphenyl diselenide in microwave-assisted ionothermal reactions to form microspheres of  $\gamma$ - $In_2Se_3$ .<sup>374</sup> Ideally similar reaction conditions in regards to the use of a microwave reactor would have been preferred in investigating the use LCCs as precursors, however, as mentioned the hardware was not available. Unlike the previous ionothermal work the  $P_{888}E-InCl_3$ , LCCs have a built-in chalcogenide precursor hence a greater control over stoichiometry and homogeneity is achieved in comparison to the methods demonstrated by Tyrrell in which pre-heating and mixing of the precursor is required. Similarly, to the chlorogallate LCCs, investigated  $InCl_3-P_{888}Se$   $\chi_{InCl} = 0.25$  (0.7520 g) was placed in an ampoule, sealed and as with the microwave-assisted reactions the ampoules were heated and the temperature increased at 20 °C increments until a significant change in appearance was observed (heated in oil at 250 °C for 60 hr.) The reaction mixture became red/brown in appearance and upon work up a red/brown powder was isolated. SEM analysis of the isolated powder as shown in Figure 5-62 found that oblong rice like structures were achieved with an average long edge diameter of 519 nm as determined using Image J software (35 structures measured). EDX analysis found that the formula  $InSe_{1.32}$  is present *via* a mapping technique as shown in Figure 5-62, Figure 5-63 and Table 5-17.

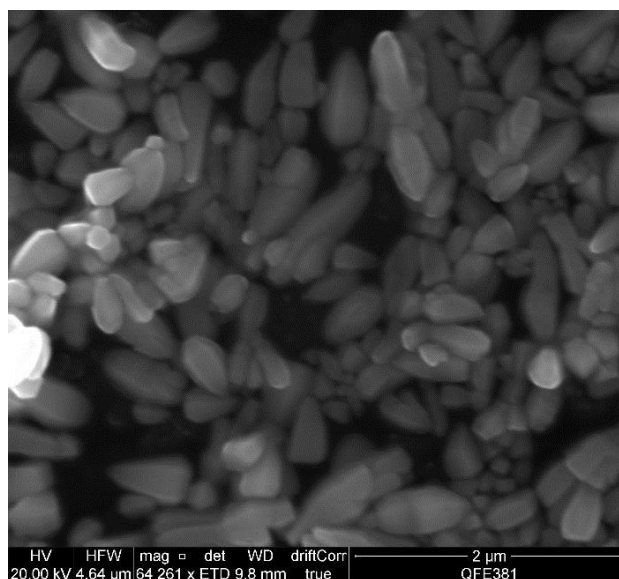


**Figure 5-62**-SEM analysis of ionothermal  $P_{888}Se-InCl_3$   $\chi_{InCl_3} = 0.25$  reaction product.

**Table 5-17**-Elemental distribution of  $P_{888}Se-InCl_3$   $\chi_{InCl_3} = 0.25$  reaction product.

	rmm	wt%	mol %	mol ratio	elemental ratio
In	114.82	45.8	0.3989	0.4309	1
Se	78.97	41.6	0.5268	0.5691	1.32

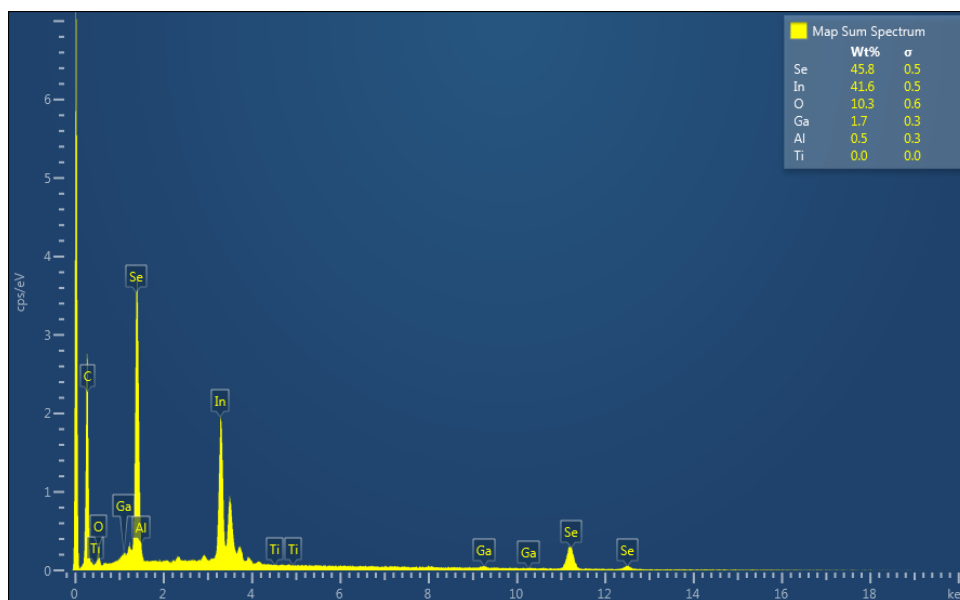


**Figure 5-63**-EDX analysis of ionothermal  $P_{888}Se-InCl_3$   $\chi_{InCl_3} = 0.25$  reaction product.

PXRD diffraction patterns of the isolated powder indicate that the  $\text{InSe}_{1.32}$  is formed in the  $\text{Al}_2\text{S}_3$  structure (Figure 5-64). Matched to simulated powder pattern of the single crystal structure determined by D. Carre *et al.* the In centres are coordinated either tetrahedrally or pentagonally resulting in a distorted Wurzite like structure.<sup>547</sup>

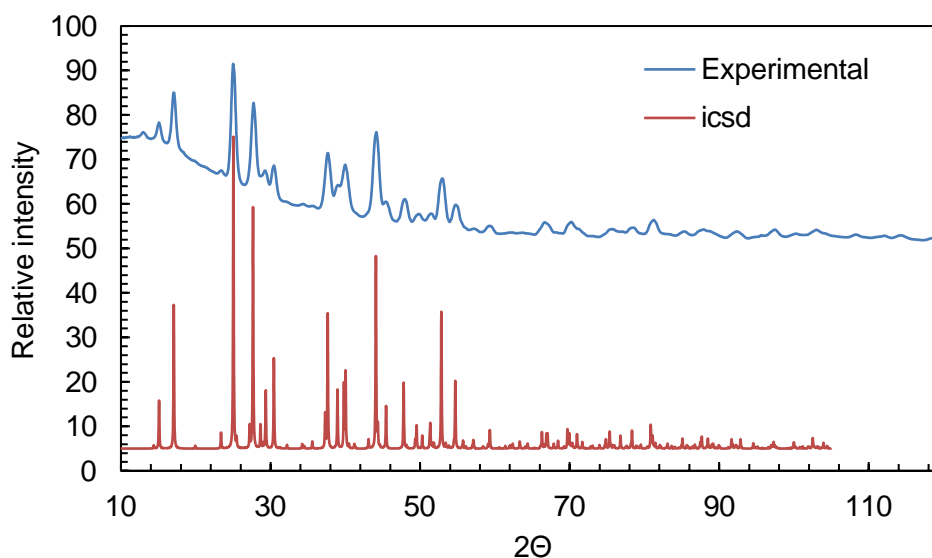


**Figure 5-64**—PXRD analysis of ionothermal  $\text{P}_{888}\text{Se-InCl}_3$   $\chi_{\text{InCl}_3} = 0.25$  reaction product and ICSD PXRD pattern by D. Carre *et al.*<sup>547</sup>

This phase of indium selenide is the  $\gamma$  form, which has a direct band gap of 1.29 eV hence it is utilisable in optoelectrics.<sup>548</sup> For a second time,  $\text{P}_{888}\text{E}$  donor ligand LCCs have been successfully utilised to form group V-VI semiconductor materials without use of further capping agents, solvents and elaborate synthetic methods.

#### 5.2.4.3 Copper chalcogenides

Synthesis of copper selenides in ionic liquid media have been previously reported by Zheng and co-workers who used the ionic liquid precursor, 1-n-butyl-3-ethylimidazolium methyl selenite ( $[\text{C}_4\text{mim}][\text{SeO}_2(\text{OCH}_3)]$ ) in a hydrothermal synthetic method with  $\text{Cu}(\text{SO}_4)$  to form copper selenides with further reports of selenide synthesis *via* this methodology with other transition metals such as zinc.<sup>549–551</sup> However, integration of both the copper and selenium precursors into the ionic liquid systems has as of yet not been reported and it was this that led to the investigation of chlorocuprate and  $\text{P}_{888}\text{E}$  LCCs as precursors.

The  $\text{CuCl-P}_{888}\text{Se}$   $\chi_{\text{MCl}} = 0.33$  system was selected as the nature of this system is believed to be due to a mixture of 2-, 3- and 4-coordinate species, hence providing the greatest opportunity for reaction to occur. Similarly, to the chlorogallate LCCs investigated  $\text{CuCl-P}_{888}\text{Se}$   $\chi_{\text{CuCl}} = 0.33$  (1.0 g) was placed in an ampoule, sealed and

as with the microwave assisted reactions, the ampoules were heated and the temperature increased at 20 °C increments until a significant change in appearance was observed (heated in oil at 180 °C for 60 minutes.) The initially colourless liquid became dark and near black upon reacting; the isolated product after work up procedures was black in colour. SEM analysis of the isolated powder as shown in Figure 5-65 found that nanospheres of average diameter 54.42 nm (as determined by ImageJ software, 35 spheres sampled). EDX analysis as shown in Figure 5-66 and Table 5-18 found that the product formula is  $\text{Cu}_{1.73}\text{Se}$

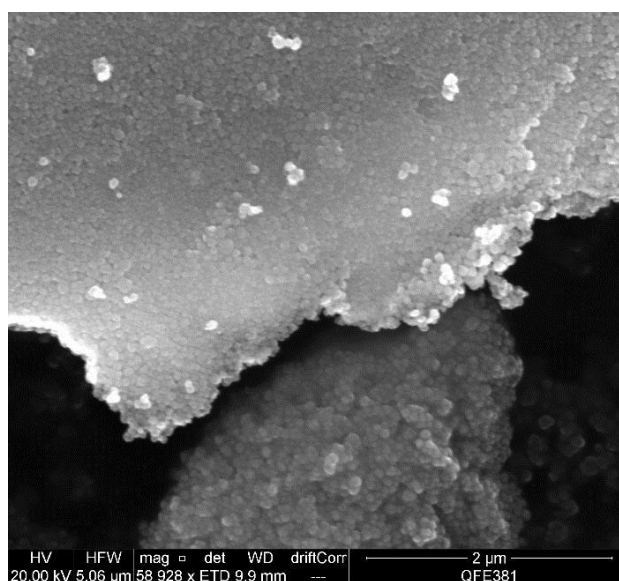


**Figure 5-65**-SEM analysis of  $\text{P}_{888}\text{Se-CuCl}$   $\chi_{\text{CuCl}} = 0.33$  reaction product.

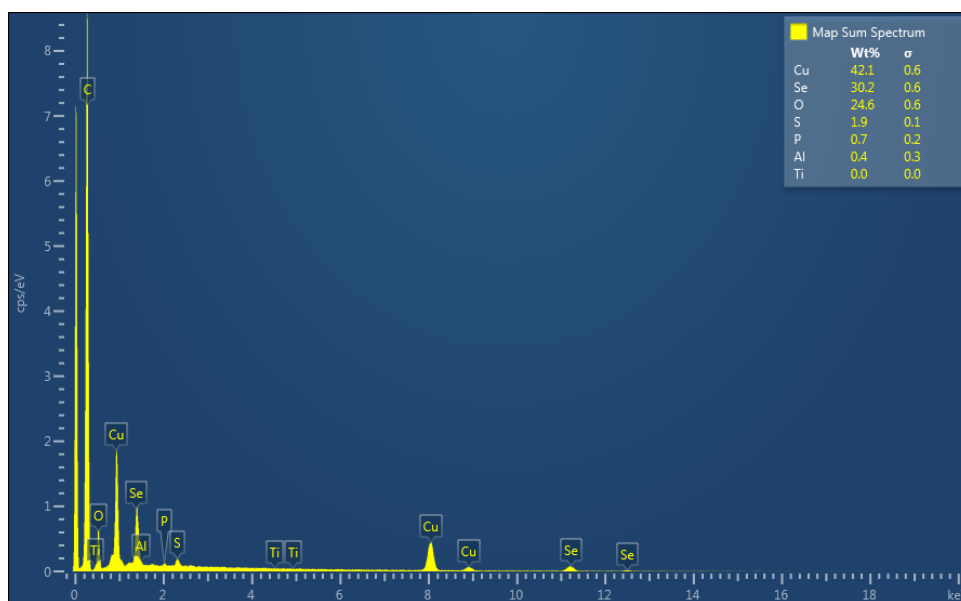


**Figure 5-66**- Elemental distribution of  $\text{P}_{888}\text{Se-CuCl}$   $\chi_{\text{CuCl}} = 0.33$  reaction product.

**Table 5-18-** Elemental distribution of  $P_{888}Se-CuCl$   $\chi_{CuCl} = 0.33$  reaction product.

	rmm	wt%	mol %	mol ratio	elemental ratio
Cu	63.55	42.1	0.6625	0.6340	1.73
Se	78.97	30.2	0.3824	0.3660	1

PXRD analysis as shown in Figure 5-67, has been successfully matched to a previously reported structure of molecular formula  $Cu_{1.75}Se$  and unit cell  $Fm-3m$ .

<sup>552</sup> A copper-rich copper selenide indicates that the copper remains majorly in the Cu(I) state with matching reflections at 31.3, 44.9, 52.9, 55.1, 71.5, 88.9°.

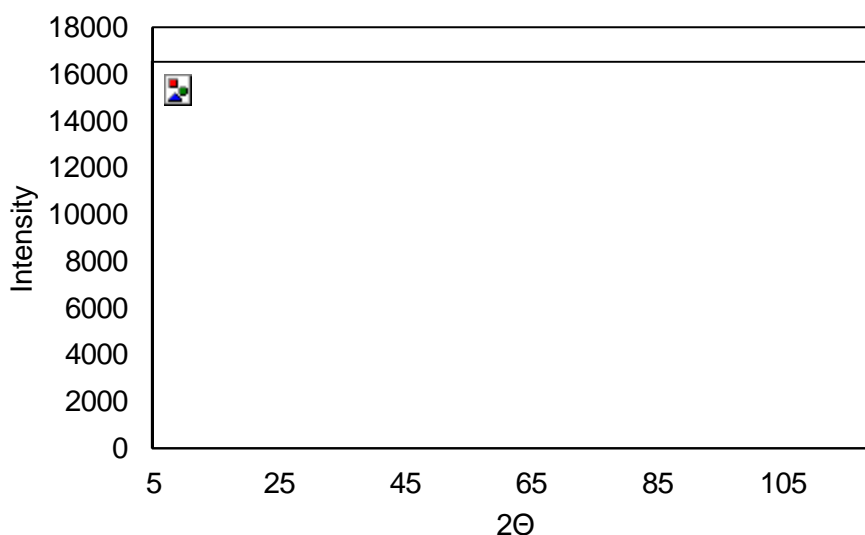


**Figure 5-67-** pXRD analysis of  $P_{888}Se-CuCl$   $\chi_{CuCl} = 0.33$  reaction product (black) and ICSD reported  $Cu_{1.75}Se$  reported structure (red). <sup>552</sup>

Copper sulphides are also of great interest in regards to applications to solar cells and semiconductor materials, hence the  $P_{888}S-CuCl$   $\chi_{CuCl} = 0.33$  system was again selected as the nature of this system is believed to be due to a mixture of 2-, 3- and 4-coordinate species hence providing the greatest opportunity for reaction to occur. Similarly, to the chlorogallate LCCs investigated  $P_{888}S-CuCl$   $\chi_{CuCl} = 0.33$  (1.0 g) was placed in an ampoule, sealed and as with the microwave-assisted reactions, the ampoules were heated and the temperature increased at 20 °C increments until a significant change in appearance was observed (heated in oil at 250 °C for 60 minutes.) The initially colourless liquid became dark and near black upon reacting; the isolated product after work up procedures was black in colour. From SEM analysis of the isolated powder as shown in Figure 5-68, and it is clear that a



mixture of products was achieved with small flower-like spherical clusters and larger irregular agglomerations of elemental sulphur. EDX mapping analysis of the sample indicated a 1:1 mixture of copper and sulphur as shown in Table 5-19.

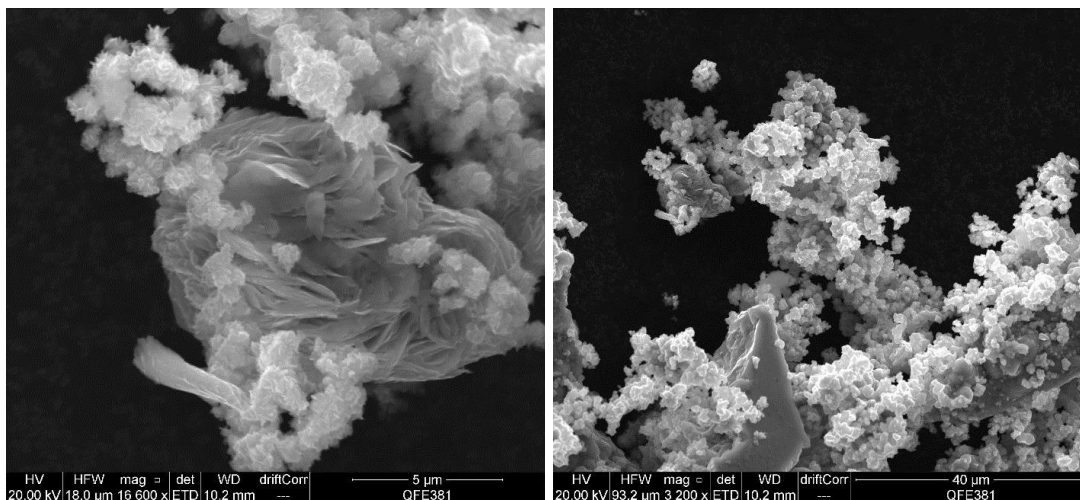


**Figure 5-68-** SEM analysis of  $P_{888}S-CuCl$   $\chi_{CuCl} = 0.33$  isolated reaction product.

**Table 5-19-** EDX analysis of  $P_{888}S-CuCl$   $\chi_{CuCl} = 0.33$  isolated reaction product.

Element	Wt%	mm	mol%	Elemental ratio
Cu	55.3	63.55	0.8702	1.03
S	27.2	32.07	0.8482	1.00

EDX mapping analysis (Figure 5-69) highlighted that the two reaction products, although differing in appearance, showed similar distributions of copper and sulphur. Furthermore, the mapping technique highlighted phosphorous (ca. 1.5 %) and chloride (ca. 1 %) impurities are evident.

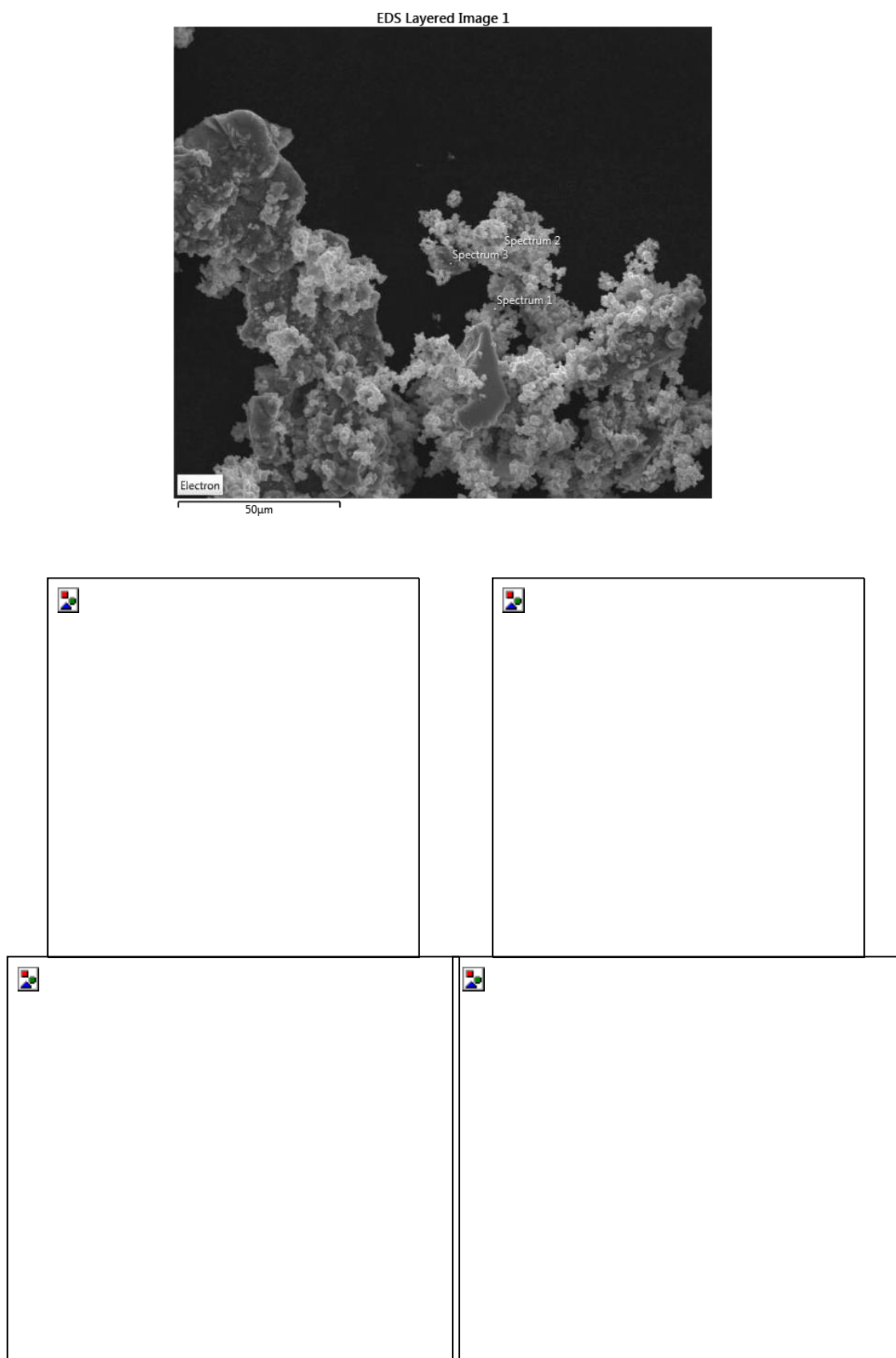


**Figure 5-69**-EDX mapping analysis of  $P_{888}S-CuCl$   $\chi_{CuCl} = 0.33$  isolated reaction product.

#### 5.2.4.4 Mixed metal chalcogenides

The overall aim of this project is to integrate both the group 13 and group 16 precursors of solar cell materials into a single precursor liquid system. Liquid coordination complexes have already been successful in forming the components of commercial solar cells *i.e.* indium selenide, gallium selenide and copper selenide. Commercial solar cells are most commonly composed of wafers of crystalline silicon however second generation solar cells specifically with a focus on the development of thin film cells have sought alternative materials such as copper indium gallium selenide, CIGS which has been found to outperform silicon on a molecular level however upon scaling up the efficiency decreases hence hampering application of these efficient materials.<sup>553</sup> Current methods require elaborate synthetic techniques such as chemical vapour deposition, electrospray methods, sputtering techniques; all of which commonly require selenisation as a separate step after initial film preparation. Overall, current methods require expensive instrumentation and fail to provide reproducible materials on the large scale.<sup>554</sup>

Initial investigations sought the formation of  $\text{CuInGaSe}_2$  *via* mixing of  $\text{P}_{888}\text{Se-CuCl}$   $\chi_{\text{CuCl}} = 0.50$ ,  $\text{P}_{888}\text{Se-GaCl}_3$   $\chi_{\text{GaCl}_3} = 0.50$  and  $\text{P}_{888}\text{-InCl}_3$   $\chi_{\text{InCl}_3} = 0.50$  in a 1:1:1 molar ratio with a total reaction mass of 1 g. The near-colourless liquid similarly to the chlorogallate LCCs investigated was placed in an ampoule, sealed and as with the microwave-assisted reactions the ampoules were heated and the temperature increased at 20 °C increments until a significant change in appearance was observed. The solution darkened at 180 °C and was held at this temperature for a further 18 hours, cooled and the solid formed was then washed with DCM and dried under argon. SEM analysis of the isolated powder as shown in Figure 5-70 shows a brittle shard like material is formed. Unlike previous semiconductor syntheses with LCCs, no apparent particles are found, instead a homogeneous block-like solid is achieved. EDX mapping analysis, as shown in Figure 5-71, Table 5-20 and Figure 5-72 showed a homogeneous distribution of copper, indium and selenium; no gallium was detected hence failing to form the desired CIGS, however, the elemental distribution equates to a  $\text{Cu}_{0.8}\text{InSe}_{1.98}$  formula. Oxygen impurities were evident in EDX analysis; however, mapping determined it to be a background impurity that was consistent throughout the sample. The PXRD diffraction pattern of the sample was found to match that of  $\text{Cu}_{0.923}\text{InSe}_2$  reported by Zahn and Paufler. The compound having a chalcopyrite structure with a  $I-42d$  space group.<sup>555</sup>

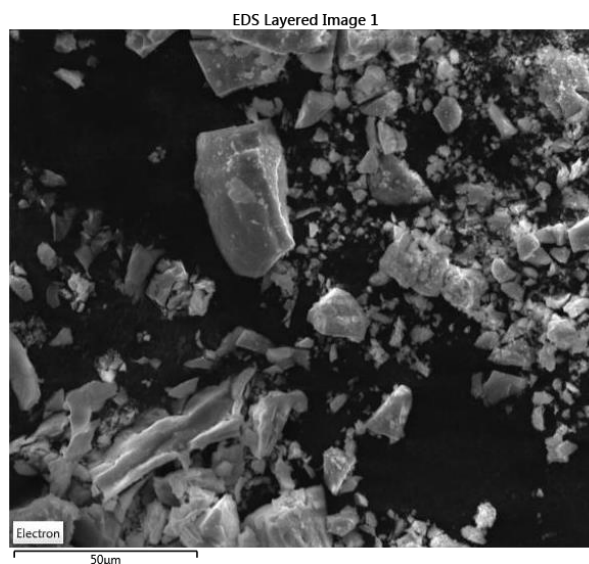


**Figure 5-70**-SEM analysis of  $P_{888}Se-CuCl$   $\chi_{CuCl} = 0.50$ ,  $P_{888}Se-GaCl_3$   $\chi_{GaCl_3} = 0.50$  and  $P_{888}-InCl_3$   $\chi_{InCl_3} = 0.50$  in a 1:1:1 molar ratio isolated reaction product.

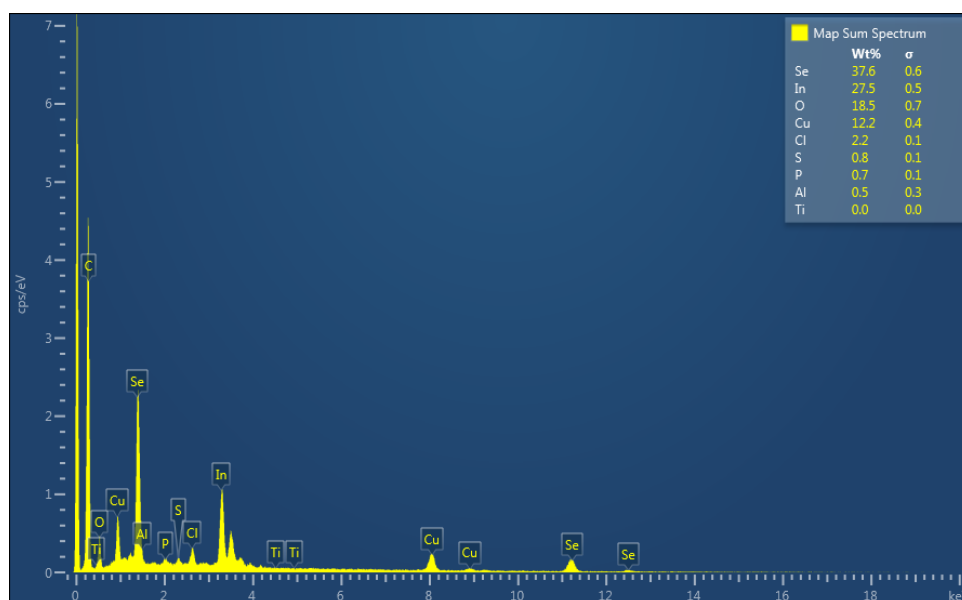


**Figure 5-71**- EDX analysis of  $P_{888}Se-CuCl$   $\chi_{CuCl} = 0.50$ ,  $P_{888}Se-GaCl_3$   $\chi_{GaCl_3} = 0.50$  and  $P_{888}-InCl_3$   $\chi_{InCl_3} = 0.50$  in a 1:1:1 molar ratio isolated reaction product.

**Table 5-20**-EDX elemental distribution of  $P_{888}Se-CuCl$   $\chi_{CuCl} = 0.50$ ,  $P_{888}Se-GaCl_3$   $\chi_{GaCl_3} = 0.50$  and  $P_{888}-InCl_3$   $\chi_{InCl_3} = 0.50$  in a 1:1:1 molar ratio isolated reaction product.

Element	Wt%	RAM	mol%	Ratio
Cu	12.2	63.55	0.192	1
In	27.5	114.82	0.240	1.25
Se	37.6	78.97	0.476	2.48

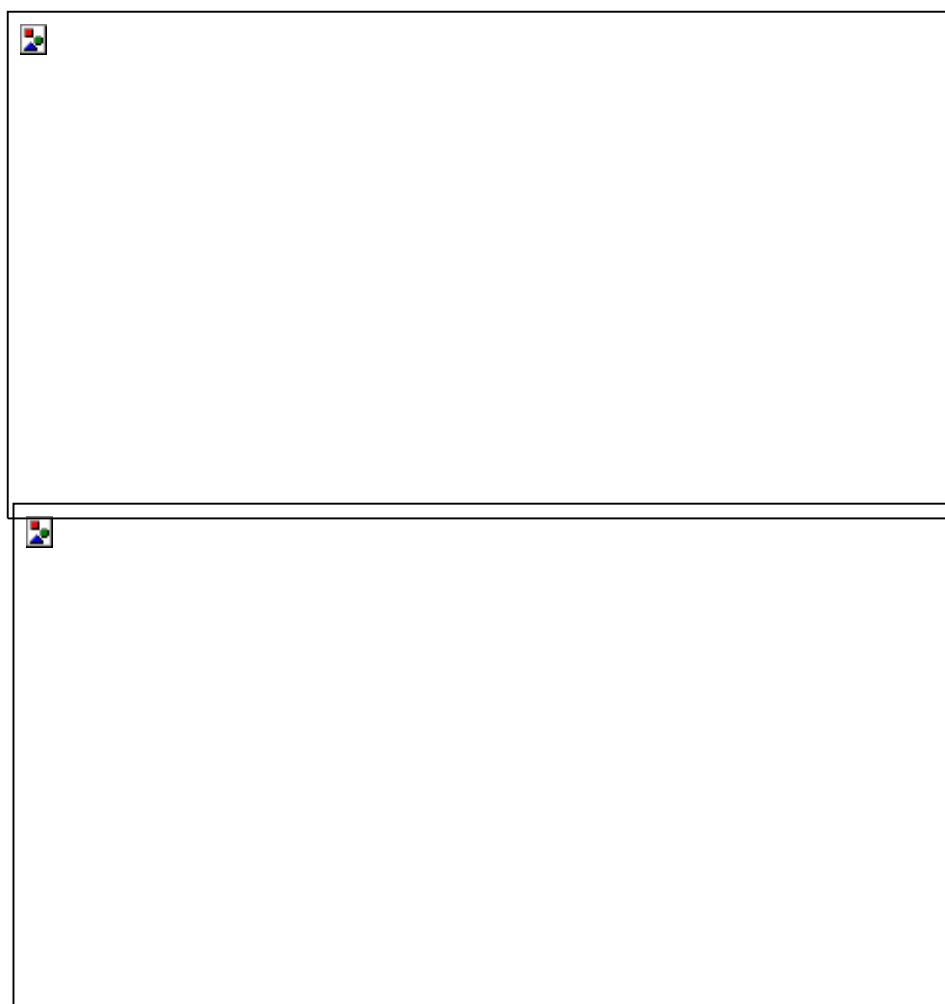


**Figure 5-72-** EDX mapping of  $P_{888}Se-CuCl$   $\chi_{CuCl} = 0.50$ ,  $P_{888}Se-GaCl_3$   $\chi_{GaCl_3} = 0.50$  and  $P_{888}-InCl_3$   $\chi_{InCl_3} = 0.50$  in a 1:1:1 molar ratio isolated reaction product.

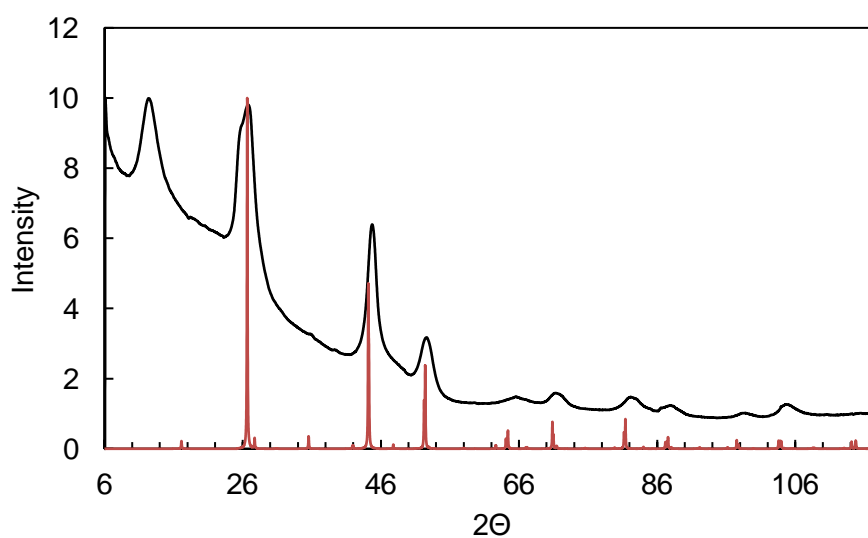


**Figure 5-73-** pXRD analysis of  $P_{888}Se-CuCl$   $\chi_{CuCl} = 0.50$ ,  $P_{888}Se-GaCl_3$   $\chi_{GaCl_3} = 0.50$  and  $P_{888}-InCl_3$   $\chi_{InCl_3} = 0.50$  in a 1:1:1 molar ratio isolated reaction product.

The copper indium selenide, CIS formed although not what was originally desired exhibiting good homogeneity and crystallinity, however, in pursuit of the gallium-containing compound incorporation of elemental gallium was sought. In the final product the gallium is required to be in the Ga(II)/Ga(I) state therefore the addition of Ga(0) was aimed to result in incorporation of the gallate species.

Mixing of  $P_{888}\text{Se-CuCl}$   $\chi_{\text{CuCl}} = 0.50$ ,  $P_{888}\text{Se-GaCl}_3$   $\chi_{\text{GaCl}_3} = 0.50$  and  $P_{888}\text{-InCl}_3$   $\chi_{\text{InCl}_3} = 0.50$  in a 1:1:1 molar ratio with a total reaction mass of 1 g and elemental gallium was added (0.2 g). The near colourless liquid and a metallic droplet similarly to the chlorogallate LCCs investigated was placed in an ampoule, sealed and as with the microwave assisted reactions the ampoules were heated and the temperature increased at 20 °C increments, until a significant change in appearance was observed. The solution darkened again at 180 °C and was held at this temperature for a further 18 hours, cooled and the solid formed was then washed with DCM and dried under argon. It was evident during work up that a large amount of the gallium droplet remained with smaller dispersed droplets present in the precipitate collected. SEM analysis of the isolated powder as shown in Figure 5-74 resembled the previous product in Figure 5-70 and the EDX distribution (Figure 5-75, Table 5-21) was similar with the compounds formula being  $\text{Cu}_{0.83}\text{InSe}_{2.11}$ .

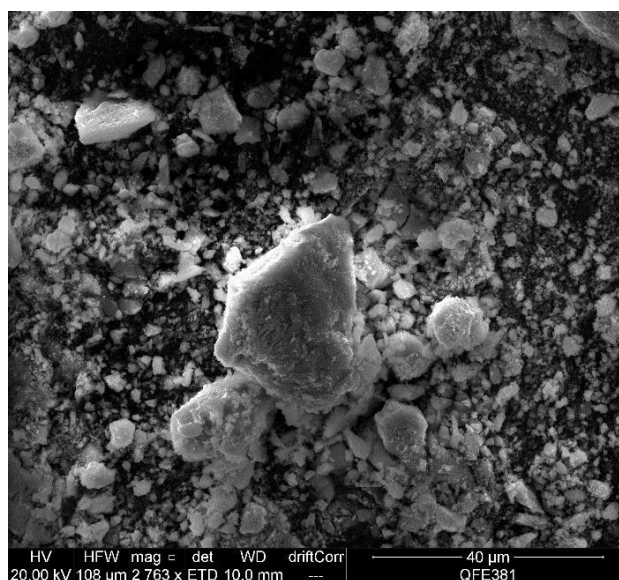


**Figure 5-74**-SEM analysis of  $P_{888}\text{Se-CuCl}$   $\chi_{\text{CuCl}} = 0.50$ ,  $P_{888}\text{Se-GaCl}_3$   $\chi_{\text{GaCl}_3} = 0.50$  and  $P_{888}\text{-InCl}_3$   $\chi_{\text{InCl}_3} = 0.50$  in a 1:1:1 molar ratio and elemental gallium isolated reaction product.

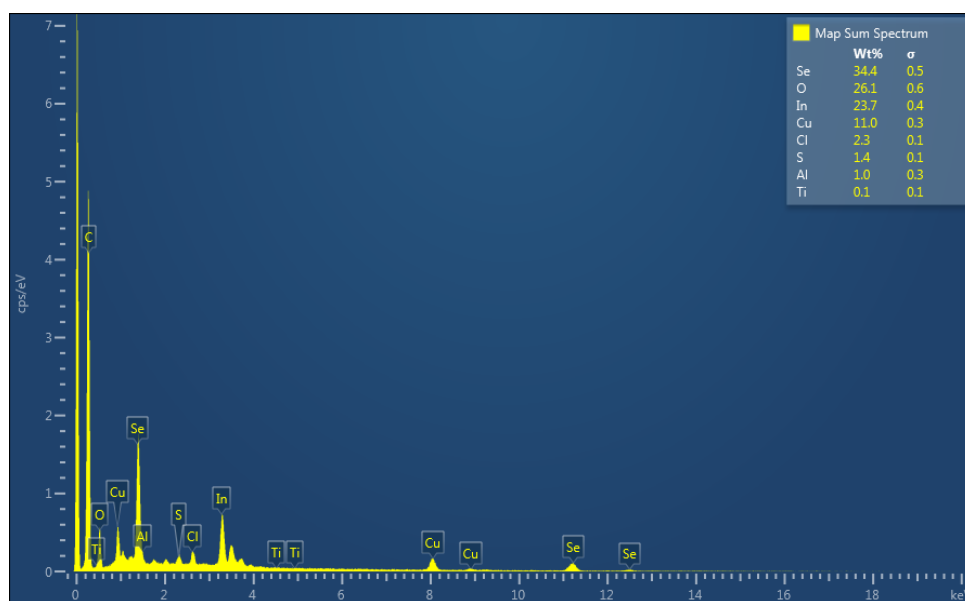


**Figure 5-75**-EDX analysis of  $P_{888}\text{Se-CuCl}$   $\chi_{\text{CuCl}} = 0.50$ ,  $P_{888}\text{Se-GaCl}_3$   $\chi_{\text{GaCl}_3} = 0.50$  and  $P_{888}\text{-InCl}_3$   $\chi_{\text{InCl}_3} = 0.50$  in a 1:1:1 molar ratio and elemental gallium isolated reaction product.

**Table 5-21**- Elemental distribution of  $P_{888}\text{Se-CuCl}$   $\chi_{\text{CuCl}} = 0.50$ ,  $P_{888}\text{Se-GaCl}_3$   $\chi_{\text{GaCl}_3} = 0.50$  and  $P_{888}\text{-InCl}_3$   $\chi_{\text{InCl}_3} = 0.50$  in a 1:1:1 molar ratio and elemental gallium isolated reaction product.

Element	Wt%	rmm	mol%	Ratio
Cu	11	63.546	0.173103	1
In	23.7	114.818	0.206414	1.192433
Se	34.4	78.971	0.435603	2.516439

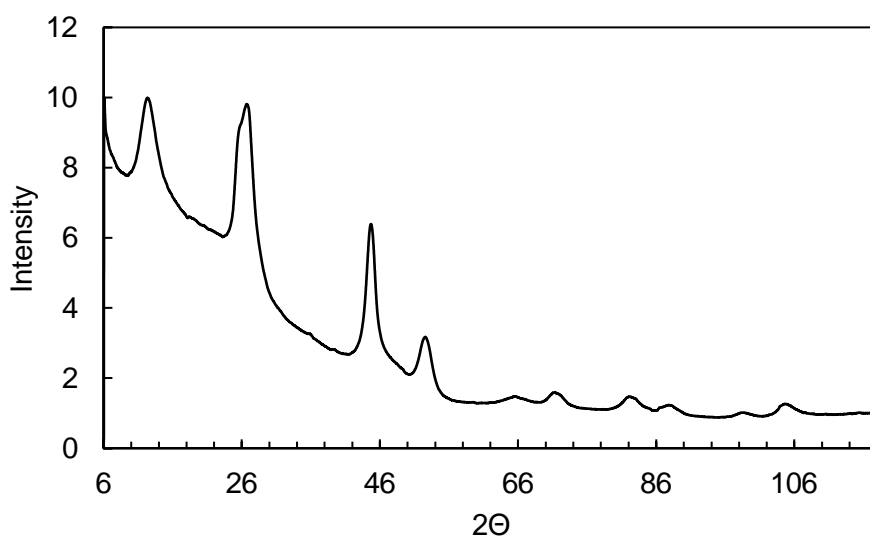


**Figure 5-76**-PXRD analysis of  $P_{888}\text{Se-CuCl}$   $\chi_{\text{CuCl}} = 0.50$ ,  $P_{888}\text{Se-GaCl}_3$   $\chi_{\text{GaCl}_3} = 0.50$  and  $P_{888}\text{-InCl}_3$   $\chi_{\text{InCl}_3} = 0.50$  in a 1:1:1 molar ratio and elemental gallium isolated reaction product.

The PXRD pattern matched that observed in the reaction omitting elemental gallium as shown in Figure 5-75 and Figure 5-73 hence determining the identical reaction product was achieved and the integration of gallium into the species was not achieved *via* elemental gallium addition hence the decision was made to omit indium from the reaction mixture in the prospect of encourage the gallium species to be formed. Mixing of  $\text{P}_{888}\text{Se-CuCl}$   $\chi_{\text{CuCl}} = 0.50$  and  $\text{P}_{888}\text{Se-GaCl}_3$   $\chi_{\text{GaCl}_3} = 0.50$  in a 1:1 molar ratio with a total reaction mass of 1 g. The near colourless liquid, similarly to the chlorogallate LCCs investigated was placed in an ampoule, sealed and as with the microwave-assisted reactions the ampoules were heated and the temperature increased at 20 °C increments until a significant change in appearance was observed. The solution darkened again at 180 °C and was held at this temperature for 18 hours. A dark precipitate formed which was consequently washed with DCM and dried under argon. SEM analysis, as shown in Figure 5-77 the morphology of the reaction product is similar in appearance to that obtained in the copper selenide synthesis in Figure 5-65.

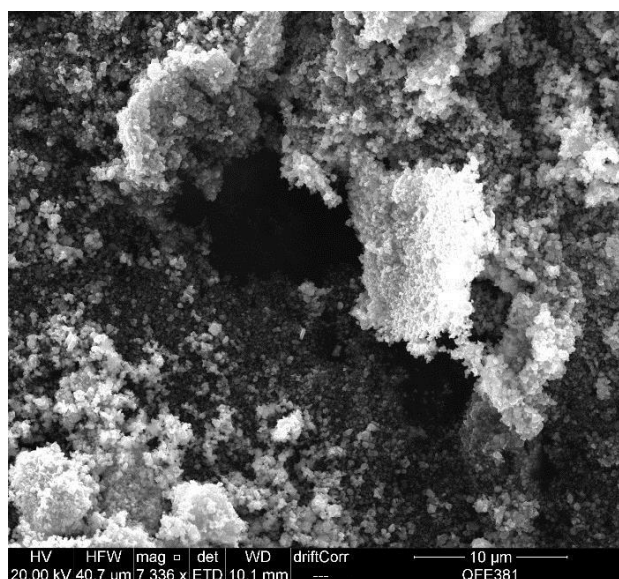


**Figure 5-77**-SEM analysis of  $\text{P}_{888}\text{Se-CuCl}$   $\chi_{\text{CuCl}} = 0.50$ , and  $\text{P}_{888}\text{Se-GaCl}_3$   $\chi_{\text{GaCl}_3} = 0.50$  in a 1:1 molar ratio isolated reaction product.

EDX analysis as shown in Figure 5-78 and Table 5-22, indicated the copper selenide formation of the formula  $\text{Cu}_{1.5}\text{Se}$ , hence gallium failed to react and integrate into the compound. The lack of chlorogallate throughout these synthesis experiments is believed to be due to the limited heating methods and rate of heating. A rapid thermal gradient is suspected to be preferred.



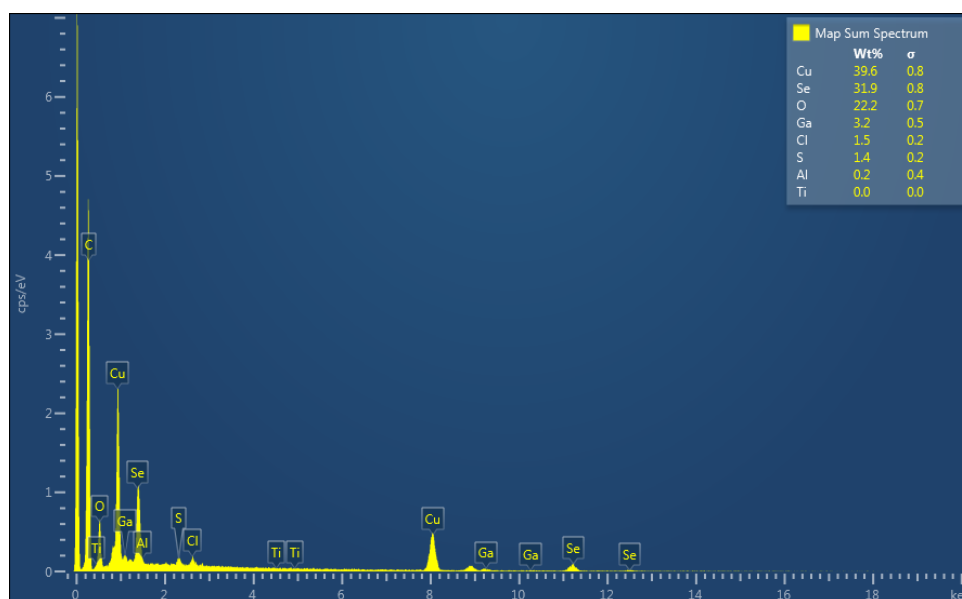


**Figure 5-78**-EDX analysis of  $\text{P}_{888}\text{Se-CuCl}$   $\chi_{\text{CuCl}} = 0.50$ , and  $\text{P}_{888}\text{Se-GaCl}_3$   $\chi_{\text{GaCl}_3} = 0.50$  in a 1:1 molar ratio isolated reaction product.

**Table 5-22**-Elemental distribution of  $\text{P}_{888}\text{Se-CuCl}$   $\chi_{\text{CuCl}} = 0.50$ , and  $\text{P}_{888}\text{Se-GaCl}_3$   $\chi_{\text{GaCl}_3} = 0.50$  in a 1:1 molar ratio isolated reaction product.

Element	Wt%	rmm	mol%	Ratio
copper	39.6	63.55	0.6232	1.54
selenium	31.9	78.97	0.4039	1

### 5.3 Conclusions

Currently within literature there are no reports of chlorocuprate liquid coordination complexes; with an overall aim to utilise these high metal-concentration liquids in materials synthesis, a full understanding must be achieved of the liquid speciation. The chlorocuprate systems are of great interest in the formation of CIGS ternary semiconductor compounds. Using multiple spectroscopic techniques including NMR, IR, Raman, EXAFS and HERFD-XANES spectroscopy a good estimation of the chlorocuprate LCCs has been made.

The EXAFS and XANES spectroscopic analysis of the chlorogallate and chlorocuprate LCCs has been vital in regards to the elucidation of the speciation present. Within the chlorogallate systems, EXAFS analysis determined the presence of oligomeric species that are formed *via* chlorine bridges. It also highlighted the presence of ionic species at high  $\chi_{\text{GaCl}_3}$  values. In the chlorocuprate species, EXAFS elucidated that the copper centres were bonded to both the chloride and ligand species. Furthermore, the EXAFS fit was quantified as a function of the R-

factor for multiple total coordination numbers with the best fit for each  $\chi_{\text{CuCl}}$  being selected and the preferred geometry determined along with a relative  $\chi_{\text{CuCl}}$  value calculated to elucidate if the species was prone to forming dimeric species.

The studied liquid coordination complexes have then been successfully used in the synthesis of group13-15 semiconductor materials;  $\text{Ga}_2\text{Se}_3$ ,  $\text{In}_2\text{Se}_3$ ,  $\text{Cu}_{1.75}\text{Se}$ ,  $\text{Cu}_{0.8}\text{InSe}_{1.98}$ ; which have been characterised *via* SEM, EDX and PXRD analysis. The ability to form such compounds in such a simplistic method can overcome the previous synthetic difficulties and scale up issues found in current methods. Moving forward, translation of the conventional heating methods that have been found to already be successful to microwave assisted synthesis is expected to further improve the rate, yield and uniformity of the products achieved.

## 5.4 Future work

The first series of experiments that should be carried out is preparation of LCCs with significantly smaller donor ligands such as trimethylphosphine, urea and thiourea in an attempt to crystallise and to isolate some of the complexes present. Furthermore, a more in-depth Raman study would be sought using a Raman microscope of a different wavelength to reduce any issues with fluorescence.

This work is the first report of Cu(I)Cl containing liquid coordination complexes; chlorocuprate ionic liquids have been utilised in a wide variety of applications including mercury capture,<sup>556</sup> capture of carbon monoxide in flue gas streams<sup>557</sup> and separation of olefins and aliphatic monomers.<sup>558</sup> The application of LCCs as a substitute is one that should be sought due to their potentially greener credentials and minimal synthesis required.

Development of a robust and scalable method of semiconductor synthesis, whether it is binary, tertiary or ternary compounds, is the main issue in regards to application of these compounds compared to ultra-pure silicon wafers. The first study that would be merited is the application of the combined  $\text{P}_{888}\text{S}$  and  $\text{P}_{888}\text{Se} - \text{GaCl}_3 / \text{InCl}_3 / \text{CuCl}$  LCCs to microwave assisted methods that have previously been successfully applied in ionothermal methods.<sup>49,559</sup> With a more long-term outlook on the project, the progression of printable circuitry is more and more popular as electronic devices strive to be more and more compact in nature. Semiconductors in solar cells and within conventional circuitry are an important component to integrate into this process. LCCs provide a possible delivery method to 'print' semiconductors directly onto a substrate.

As shown in Figure 5-79, the system would involve delicate placement of the selected LCC onto the substrate and then the reaction would be initiated *via* direct heating or microwave irradiation to form the semiconductor species. The reaction areas would then be washed with organic solvent and the process repeated.

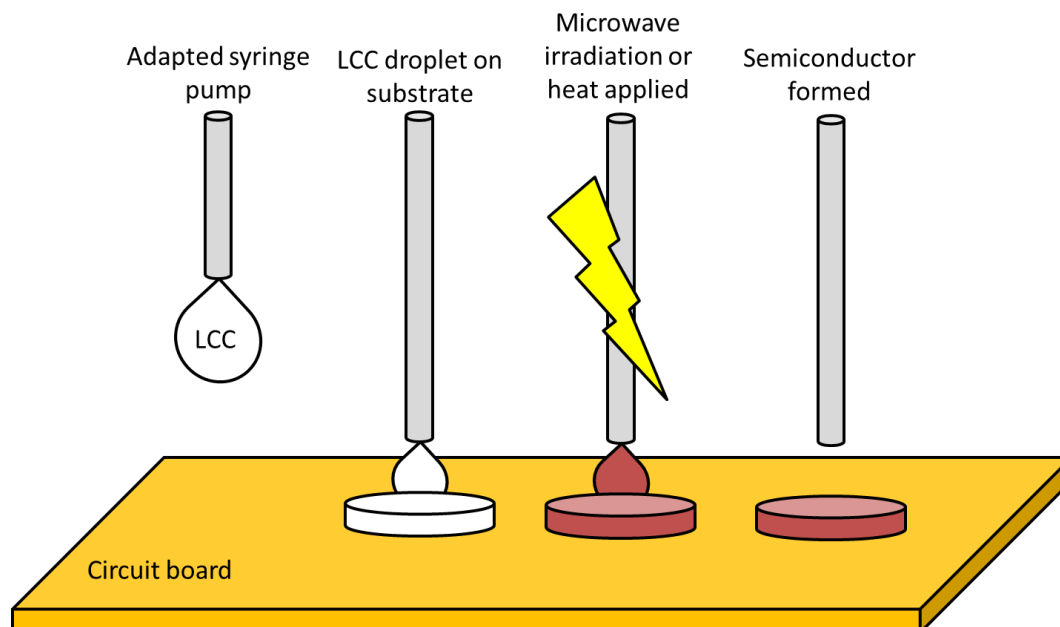


**Figure 5-79**-Pictorial representation of LCC 'printing' of semiconductors.

The studies regarding the addition of chalcogenide species to  $P_{888}$ -CuCl LCCs were completed under the guise of further simplifying synthetic processes. If an LCC of  $P_{888}$ -CuCl could be accurately measured out, hence the total copper content known the chalcogenide species can be added stoichiometrically to the mixture. Once a homogeneous liquid is achieved the heating or microwave irradiation could be applied forming a stoichiometrically ideal semiconductor material.

Further investigation into the formation of the suspected telluride species would be of merit. Use of XPS spectroscopy will allow for identification of the telluride species and its oxidation states. Furthermore, application of the suspected telluride-containing species in the Cu(II) LCCs to the synthesis of CuTe materials.

Thin films are also a useful form of these semiconductor materials; there are two possible approaches to achieving this;

- (1) Conventional electrochemical methods in which LCCs are held at a reduction potential for the metal species to deposit on the electrode surface. The chalcogenide species will most likely be introduced after film formation via  $H_2Se$  or  $H_2S$  gas.

- (2) Dip coating of a substrate with the LCC of choice and exposure to heat treatment to initiate semiconductor formation. The substrates could be a simple indium tin oxide coated piece of glass. ITO is a common charge carrying material used within semiconductor setups.

The application of LCCs to inorganic materials synthesis has barely been investigated. There is significant scope in the materials already studied and further work to be completed on templating effects, donor ligand influence on particle size, morphology and composition along with scale-up studies.

## 5.5 Experimental Methods

All experiments were performed in a glovebox (MBraun labmaster dp, <0.3 ppm of H<sub>2</sub>O and O<sub>2</sub>) or using standard argon Schlenk techniques. All glassware was dried overnight in an oven (ca.100 °C) before use. Sulphur (99.95 %) and selenium (≈200 mesh, 99.95 %) were purchased from Sigma Aldrich and were all dried under reduced pressure (80 °C, < 1 mbar, 48 h) before use. Trioctylphosphine oxide (99.5 %) was provided by Cytec and dried as described above. Copper (I) chloride (99.99%) and copper(II) chloride (99.99 %) were obtained in sealed ampoules under argon from Alfa Aesar.

### 5.5.1 Synthesis of donor ligands and liquid coordination complexes

**Trioctylphosphine chalcogenide.** Trioctylphosphine sulphide and trioctylphosphine selenide were synthesised using an equimolar mix of trioctylphosphine and selenium/sulphur, modified from literature methods.<sup>449</sup> In a typical procedure, elemental sulphur/selenium (0.7961 g, 24.83 mmol / 1.7562 g, 22.24 mmol) was added slowly in portions to the trioctylphosphine (9.2039 g, 24.83 mmol/ 8.2438 g, 22.24 mmol), with rapid stirring (500 rpm) allowing for the heat from the exothermic reaction to cool. The last additions of chalcogenide elements are sluggish and require stirring overnight. The reaction mixtures were then filtered to give clear, colourless liquids. Purity was analysed by <sup>31</sup>P NMR spectroscopy.

P<sub>888</sub>S: <sup>31</sup>P-NMR (243 MHz, DMSO capillary) δ (ppm): 44.91 (1P, s, P=S)

P<sub>888</sub>Se: <sup>31</sup>P-NMR: (243 MHz, DMSO capillary) δ (ppm): 36.41 (1P, d, P=Se, <sup>1</sup>J<sub>P-Se</sub> 678 Hz), 48.35 (1P, s, P=O)

**Liquid coordination complexes.** Liquid coordination complexes. LCCs were synthesised on a 2 -12 g scale, following the literature procedure.<sup>22</sup> All syntheses were carried out in a nitrogen-filled glovebox (MBraun LabMaster dp, > 0.6 ppm O<sub>2</sub>

and H<sub>2</sub>O). To the neutral donor ligand the metal chloride (CuCl / CuCl<sub>2</sub>) was added in portions. Heat was generated upon each metal chloride addition hence the flask was allowed to cool before the next portion was added. To allow for the equilibria to settle the LCC was allowed to stir for 12 hours under glovebox conditions resulting in homogeneous liquids in Cu(I) LCCs and a variation of results were observed in the Cu(II) LCCs.

### 5.5.2 Raman and IR spectroscopy

Infrared spectra were measured using a PerkinElmer Spectrum-100 IR spectrometer with ATR attachment, with a total range of 7800 to 370 cm<sup>-1</sup>, with a resolution of 0.50 cm<sup>-1</sup>. Air-sensitive samples were loaded into a vial in the glovebox and sealed with parafilm. Then, the vial was removed from the glovebox and transferred to the IR spectrometer. The vial was inverted and placed over the crystal of the ATR attachment, allowing for the liquid sample to flow onto the crystal, protecting the sample from contact with air. Raman spectra were measured using a PerkinElmer Raman station 400F spectrometer, with a 785 nm focused laser beam. As samples are air sensitive, the quartz cuvette was loaded in the glovebox and sealed using parafilm.

### 5.5.3 Extended X-ray Fine Structure spectroscopy

EXAFS measurements on the liquid coordination complexes, P<sub>888</sub>-CuCl,  $\chi_{\text{CuCl}} = 0.25$ , 0.33 and 0.50, were carried out at the Diamond Light Source (I20-scanning beamline)<sup>450,451</sup> at the Cu K-edge (8979 eV). A four-bounce scanning Si(111) monochromator was used<sup>452,453</sup>, and the rejection of higher harmonics was achieved by using a pair of rhodium coated mirrors operating at 5mrad incident angle. The measurements were performed at room temperature in transmission mode. Two ion chambers filled with the appropriate gas mixture to absorb 15% and 80% of the intensity of the radiation were used for I0 and It respectively. All samples were prepared in an MBraun Labmaster dp glovebox (up to 0.6 ppm of H<sub>2</sub>O and O<sub>2</sub>). For liquid samples, a drop of neat sample was captured between two layers of an adhesive Kapton film, stuck directly to a Kapton or PTFE spacer (127 -500  $\mu\text{m}$ ). Sealed samples were mounted onto a PEEK sample holder with 8 mm window. Samples of solid standards: Cu(I)Cl, was ground with dry boron nitride and pressed into a pellet (8 mm diameter) with a pellet press placed inside the glovebox. The optimum amount of sample calculated using the XAFS mass program<sup>560</sup> was mixed with BN to prepare the pellets. Those were sealed between two layers of adhesive

Kapton film and mounted onto a PEEK sample holder with 8 mm window. Three to five spectra were recorded and then merged, calibrated, normalized and background subtracted using Athena.<sup>396,454</sup> The spectra were then fitted using Artemis<sup>454</sup> to calculate interatomic distances and their root-mean-square variations ( $\sigma^2$ ).

#### 5.5.4 High-Energy Resolution Fluorescence Detected XANES

High-Energy Resolution Fluorescence Detected XANES (HERFD-XANES) measurements on the liquid coordination complexes,  $P_{888}\text{-CuCl}$ ,  $\chi_{\text{CuCl}} = 0.25, 0.33$  and  $0.50$ , and on standards:  $\text{Cu(I)Cl}$ , dispersed in boron nitride pellets, was carried out at the I20-scanning beamline at Diamond Light Source. A X-ray emission spectrometer based on a 1m diameter Rowland circle operating in the Johann configuration in the vertical plane<sup>561</sup> was used for the experiment. The spectrometer was equipped with three 100 mm Si(444) spherical analyser crystals were used to select the Cu  $K\alpha$  emission line (8047.8 eV). An ion chamber filled with the optimum gas mixture to absorb 15% of the incident radiation at the Cu K-edge energy was used as incident monitor, while a medipix area detector<sup>562</sup> was used to collect the intensity of the emission line.

#### 5.5.5 Nuclear magnetic resonance spectroscopy

Multinuclear NMR was used throughout this body of work. All NMR spectra were recorded on either a Bruker Advance DPX 400 MHz, or a Bruker Advance DPX 600 MHz spectrometer. The frequencies of the measurements are summarised below in Table 4-21. Samples which were liquid at room temperature were recorded using DMSO capillaries as an external deuterium lock to prevent the solvent affecting the equilibria present in the sample.

**Table 5-23-** Summary of the frequency of measurements used for each spectrometer

Nuclei	Bruker Advance DPX 400 Frequency of Measurement (MHz)	Bruker Advance DPX 600 Frequency of Measurement (MHz)
$^1\text{H}$	400	600
$^{13}\text{C}$	100	150
$^{31}\text{P}$	162	243
$^{77}\text{Se}$	-	114

Cooling NMR experiments required the use of an alternative deuterium lock within the LCC solutions to prevent freezing.  $d^2$ -dichloromethane and  $d$ -chloroform were used and spectra were recorded at cooling intervals until freezing was observed.

The samples under test were armed and the initial spectra repeated to indicate if any degradation etc. had occurred.

#### 5.5.5.1 Ligands

**Trioctylphosphine oxide,  $P_{888}O$**   $^{31}P$  (d-DMSO capillary, 162 MHz): 49.91(1P, s, P=S)

**Trioctylphosphine sulphide,  $P_{888}S$**   $^{31}P$  (d-DMSO capillary, 243 MHz)  $\delta$  (ppm): 44.91 (1P, s, P=S)

**Trioctylphosphine selenide,  $P_{888}Se$**   $^{31}P$  (d-DMSO capillary, 243 MHz)  $\delta$  (ppm): 36.41 (1P, d, P=Se,  $^1J_{P-Se}=678$  Hz), 48.35 (1P, s, P=O);  $^{77}Se$  (d-DMSO capillary, 114 MHz)  $\delta$  (ppm): -388.57 (1Se, d, P=Se,  $^1J_{P-Se}=709.68$ )

#### **Trioctylphosphine – copper(I) chloride LCC, $P_{888}-CuCl$**

$\chi_{CuCl}=0.25$   $^{31}P$  (d-DMSO capillary, 243 MHz)  $\delta$  (ppm): -22.33(s), -9.03(s)

$\chi_{CuCl}=0.33$   $^{31}P$  (d-DMSO capillary, 243 MHz)  $\delta$  (ppm): -20.92(s), -23.37(sh), -7.17\*(s)

$\chi_{CuCl}=0.50$   $^{31}P$  (d-DMSO capillary, 243 MHz)  $\delta$  (ppm): -20.70(s), -22.22(sh), -7.65\*(s)

\*impurity due to 99% purity  $P_{888}$

(sh) shoulder peak

#### **Trioctylphosphine sulphide – copper(I) chloride LCC, $P_{888}S-CuCl$**

$\chi_{CuCl}=0.33$   $^{31}P$  (d-DMSO capillary, 243 MHz)  $\delta$  (ppm): 50.05 (s)

$\chi_{CuCl}=0.50$   $^{31}P$  (d-DMSO capillary, 243 MHz)  $\delta$  (ppm): 50.97

#### **Trioctylphosphine selenide – copper(I) chloride LCC, $P_{888}Se-CuCl$**

$\chi_{CuCl}=0.33$   $^{31}P$  (d-DMSO capillary, 243 MHz)  $\delta$  (ppm): 37.64

$\chi_{CuCl}=0.50$   $^{31}P$  (d-DMSO capillary, 243 MHz)  $\delta$  (ppm): 37.85

#### 5.5.6 Chalcogenide solvation experiments

The LCC (1 g) under test was prepared according to described methods. The elemental chalcogenides were added in 10 mg portions until saturation occurred.

NMR and IR analysis were completed using the capillary methods and ATR methods described.

### **5.5.7 Synthesis of binary and ternary semiconductor materials**

#### **5.5.7.1 Microwave assisted reactions**

To a GS10 microwave reaction vial containing a stirrer bar TOPSe-GaCl<sub>3</sub> was added under an inert atmosphere. The total mass of reaction not exceeding 1 g. Using a CEM Discover microwave reactor the mixture was then exposed to microwave irradiation at variable temperature and time with consistent stirring at 600 rpm. Once the formation of a suspension is achieved the reaction mixture is allowed to cool before using dichloromethane to extract reaction by-products from the particles formed. Once extracted the particles were dried under a flow of argon gas then stored in an inert atmosphere.

#### **5.5.7.2 Conventional heating reactions**

LCC were mixed in molar ratios dictated by the stoichiometry of the final compound in a screw cap vial and were stirred to form a homogeneous mixture for 1 hour. The resultant solution was transferred to an 8 mm diameter glass ampoule under glovebox conditions and was sealed with parafilm. Transferred outside of the glovebox the ampoule was sealed under flame. The ampoule was heated in an oil bath to allow for observations to be made whilst heating. Heating from room temperature the temperature was increases initially at 20 °C intervals to 100 °C and then in 10 °C intervals until a reaction was observed. Once a reaction was observed the temperature was held until enough material was deemed to be adequate for isolation. The ampoule was then allowed to cool and opened. The reaction suspension was then washed with dichloromethane (3x10 mL minimum) affording a clean solid which was dried under a flow of argon.

#### **5.5.7.3 Scanning electron microscopy and EDX analysis**

Solid products obtained were mounted on carbon tape covered stainless steel holders. Product morphology was analysed using a FEI Quanta FEG- Environmental SEM Oxford Ex-ACT scanning electron microscope. EDX analysis was carried out using both a point and ID and, mapping technique.

#### **5.5.7.4 Powder X-ray diffraction**

Solid products were analysed *via* a powder diffraction experiment on an Aligent supernova single crystal spectrometer. Due to the small amount of product collected



a conventional PXRD spectrometer was not utilised. Using a nylon loop the solid was fixed using vacuum grease and mounted.

## 6 Conclusions

This work has demonstrated how the 'designer capabilities' of ionic liquids can improve current synthetic methods within both inorganic and organic chemistry. The term 'reactive ionic liquids' are ones that are integral to the reaction process to which they have been applied. This can be both as a catalyst, reagent or as a solvent to which dissolution of a reagent is not available in conventional solvents. This project aimed to investigate three new types of ionic liquids for three specific applications to demonstrate the true designer properties of these solvents.

The first application that was targeted was an ionic liquid to dissolve alkali metals at room temperature and above. This goal was achieved *via* an aminopyridinium cation that provided a primary amine functionality to mimic ammonia along with an aromatic functionality to stabilise the solvated electrons formed upon solvation. This solvation mechanism was been studied extensively with a variety of spectroscopic techniques, comparative studies and computational techniques. Applications to single electron reductions were also studied with initial success in inorganic applications with lead resulting in characterisation of sodium bistriflamide. This is the first report of alkali metal solvation in an ionic liquid and is a step in bridging the "temperature gap" from solvothermal to solid state syntheses, and potentially opens up new pathways for inorganic synthesis of low-oxidation state, metastable compounds.

The second application was based upon *p-tert*-butylcalix-[4]-arenes, TBC which, are well-known for their useful derivatives in sensors and extraction applications. However, they are often subject to unselective and poor-yielding functionalisation reactions along with the initial calixarene motif's poor solubility in many organic solvents. Basic anion-ionic liquids were found to be a suitable alternative to conventional inorganic bases, specifically methyl carbonate-anion ionic liquids that were found to be effective in mono-deprotonating TBC and consequently forming calixarate salts. These salts were found to be an effective reagent in mono-alkylations of the TBC lower rim with 100 % selectivity, high yield and no need for elaborate separations.

The final application is based on the inorganic synthesis of semiconductor species. This study utilised liquid coordination complexes, LCCs as a new generation ionic liquids composed of a halometallate and donor ligand, in which cationic, anionic and neutral complexes are formed in equilibria and exhibit ionic liquid like properties in regards to their low volatility. These LCCs have been studied extensively *via* a

variety of spectroscopic techniques including multinuclear NMR, IR, Raman and EXAFS spectroscopy to elucidate their speciation. Key findings include the significant variation in speciation as a function of temperature and the presence of ionic species even at higher  $\chi_{\text{GaCl}_3}$  values. The chloroindate LCCs were found to form solely neutral adducts with no ionic contribution detected. Chlorocuprate LCCs were found to be specifically difficult to elucidate the equilibria present. Conventional in-house spectroscopic techniques gave little insight into the Cu(I) speciation. The Cu(II) LCCs were found to result in unstable redox-active systems such that the addition of  $\text{P}_{888}\text{S}$  or  $\text{P}_{888}\text{Se}$  resulted in elemental chalcogenide being precipitated.

The inconclusive in-house speciation studies on the chlorocuprate LCCs equilibria lead to the development of new methodology for speciation determination using EXAFS techniques. Using plots of R-factor as a function of total coordination number and relative bond ratios; local minima can determine the total coordination number of the centre under investigation and the relative molar ratio of each bonding species. This allowed for the average coordination and the ligand vs. chloride contribution of three  $\chi_{\text{CuCl}}$  mole ratios to be determined. These LCCs have also been shown to be good candidates for binary and tertiary semiconductor synthesis *via* conventional heating methods in ampoule conditions. Both binary and tertiary compounds have been formed using LCC precursors.

This project has shown three examples of reactive ionic liquids to which the designer properties of reactive ionic liquids have been realised. Cation manipulation has been carried out successfully solvate alkali metals; methyl carbonate anions have been utilised to mono-deprotonated calixarenes for functionalisation reactions; LCCs have allowed integration of semiconductor materials.

### ***Future Work***

***Alkali metal solvation*** There is significant scope in monitoring the stability of this IL under radiative and flash photolytic techniques. Within sodium and potassium solvation experiments the ionic liquid has been found to be stable, hence making it a prime candidate for these studies with further scope for atomistic simulations to further confirm the behaviour of the sodium cation formed. In regards to application of this new method of sodium solvation to reduction chemistry it would be sought to repeat the Zintl-type reduction reactions with a variety of elements including lead, tin, antimony and chalcogenides in an attempt to replicate the anionic clusters formed by Ruck and co-workers.<sup>40</sup> Using more controlled cooling methods and post

reaction treatment with liquid ammonia or ethylene diamine may allow for extraction and growth of the suspected cluster products formed. Further to this, the addition of organic solvents/reagent such as ethene, butene *etc.* is of merit for application to polymerisations and other radical initiated reactions. Furthermore, the use of this ionic liquid with other redox-active species such as iron or copper as a cation may provide some interesting behaviours.

***p*-tert-butylcalix-[4]-arenes** It is apparent that there is a great disparity between the behaviour of phenol and *p*-tert-butylcalix-[4]-arene in the acetate anion ionic liquids. In future it would be of merit to compare further uncyclised *p*-tert-butylphenol units and larger calix-[6]-arenes and calix-[8]-arenes to compare the effect of the rigidity of the TBC unit and its effect on deprotonation vs. hydrogen bonding. Gaining a greater understanding of the behaviour of similar supramolecular compounds will give scope for further applications of this methodology. One of the biggest accomplishments that could be achieved within etheryl functionalisation is the synthesis of a *p*-tert-butylcalix-[4]-arene with four different lower rim substituents. If the methyl carbonate anion deprotonation methods could be applied sequentially there is intrinsic control over the functionalisation steps, along with avoiding laborious separation techniques this methodology allows for concentrated reaction mixtures, improved yields and control.

**Gallium and indium LCCs** Conductivity is a physicochemical property that has currently only been rudimentarily quantified; in future the use of impedance spectroscopy and Nyquist plots as a function of variable  $\chi_{\text{GaCl}_3}$  will hopefully give greater insight into the position of the equilibria. Experiments performed in this work, which provided crucial evidence on the rate of intermolecular exchange between ionic and neutral species were not performed on  $\text{P}_{888}\text{S}/\text{Se AlCl}_3$  LCCs and would provide evidence as to whether previous conclusions were valid.<sup>375</sup> Furthermore analysis of variable temperature NMR on other LCCs within literature to observe how it can vary with temperature and its respective influence on catalytic applications.<sup>387,411</sup>

**Copper LCCs** Further spectroscopic analysis is required on the LCCs specifically using alternative donor ligands to facilitate single crystal diffraction studies. Physical properties of these new LCCs also require study *i.e.* density, viscosity and TGA analysis. Further development of the semiconductor syntheses utilising microwave-assisted methodologies should be sought and moving onto studies regarding reproducible synthesis of ternary semiconductors should also be completed. In a

push to further simplify this methodology the use of LCCs composed of the metal chloride and  $P_{888}$ , with the addition of elemental chalcogenide should be investigated as a possible method of stoichiometric control over the final product.

**EXAFS and HERFD XANES** This methodology using R-factor as an indication of preferred coordination number and molar ratios should be applied to other LCC systems. Specifically those discussed within recent publications by Hogg *et al.*<sup>375</sup> such as Zn, Tl and Sn metal chlorides.

## 7 References

- 1 J. S. Wilkes, *Green Chem.*, 2002, **4**, 73–80.
- 2 R. S. Kalb, M. Damm and S. P. Verevkin, *React. Chem. Eng.*, 2017, **2**, 432–436.
- 3 R. S. Kalb, E. N. Stepurko, V. N. Emel'yanenko and S. P. Verevkin, *Phys. Chem. Chem. Phys.*, 2016, **18**, 31904–31913.
- 4 J. Estager, J. D. Holbrey and M. Swadźba-Kwaśny, *Chem. Soc. Rev.*, 2014, **43**, 847–886.
- 5 M. Maase and K. Massonne, *Ionic Liquids IIIB: Fundamentals, Progress, Challenges, and Opportunities*, American Chemical Society, Washington, DC, 2005, vol. 902.
- 6 Y. Chauvin, B. Gilbert and I. Guibard, *J. Chem. Soc. Chem. Commun.*, 1990, 1715.
- 7 R. T. Carlin and J. S. Wilkes, *J. Mol. Catal.*, 1990, **63**, 125–129.
- 8 P. Hu, Y. Wang, X. Meng, R. Zhang, H. Liu, C. Xu and Z. Liu, *Fuel*, 2017, **189**, 203–209.
- 9 P. Nockemann, K. Binnemans and K. Driesen, *Chem. Phys. Lett.*, 2005, **415**, 131–136.
- 10 R. E. Del Sesto, T. M. McCleskey, C. Macomber, K. C. Ott, A. T. Koppisch, G. A. Baker and A. K. Burrell, *Thermochim. Acta*, 2009, **491**, 118–120.
- 11 B. Wang, L. Qin, T. Mu, Z. Xue and G. Gao, *Chem. Rev.*, 2017, **117**, 7113–7131.
- 12 F. Ricciardi and M. M. Joullié, *Org. Prep. Proced. Int.*, 1983, **15**, 17–28.
- 13 M.-C. Tseng, H.-C. Kan and Y.-H. Chu, *Tetrahedron Lett.*, 2007, **48**, 9085–9089.
- 14 S. Chempath, J. M. Boncella, L. R. Pratt, N. Henson and B. S. Pivovar, *J. Phys. Chem. C*, 2010, **114**, 11977–11983.
- 15 C. M. Gordon, J. D. Holbrey, A. R. Kennedy and K. R. Seddon, *J. Mater. Chem.*, 1998, **8**, 2627–2636.
- 16 M. G. Freire, C. M. S. S. Neves, I. M. Marrucho, J. A. P. Coutinho and A. M. Fernandes, *J. Phys. Chem. A*, 2010, **114**, 3744–3749.
- 17 F. Larsson, P. Andersson, P. Blomqvist and B.-E. Mellander, *Sci. Rep.*, 2017, **7**, 10018.
- 18 K. Fukumoto, M. Yoshizawa and H. Ohno, *J. Am. Chem. Soc.*, 2005, **127**, 2398–2399.

- 19 J. M. S. S. Esperança, H. J. R. Guedes, M. Blesic and L. P. N. Rebelo, *J. Chem. Eng. Data*, 2006, **51**, 237–242.
- 20 S. Coffie, J. M. Hogg, L. Cailler, A. Ferrer-Ugalde, R. W. Murphy, J. D. Holbrey, F. Coleman and M. Swadźba-Kwaśny, *Angew. Chemie Int. Ed.*, 2015, **54**, 14970–14973.
- 21 T. Belhocine, S. A. Forsyth, H. Q. N. Gunaratne, M. Nieuwenhuyzen, P. Nockemann, A. V Puga, K. R. Seddon, G. Srinivasan and K. Whiston, *Green Chem.*, 2011, **13**, 3137–3155.
- 22 F. Coleman, G. Srinivasan and M. Swadźba-Kwaśny, *Angew. Chemie Int. Ed.*, 2013, **52**, 12582–12586.
- 23 Q. Zhang, K. De Oliveira Vigier, S. Royer and F. Jérôme, *Chem. Soc. Rev.*, 2012, **41**, 7108.
- 24 A. P. Abbott, D. Boothby, G. Capper, D. L. Davies and R. K. Rasheed, *J. Am. Chem. Soc.*, 2004, **126**, 9142–9147.
- 25 A. P. Abbott, J. C. Barron, K. S. Ryder and D. Wilson, *Chem. - A Eur. J.*, 2007, **13**, 6495–6501.
- 26 A. Zhu, T. Jiang, B. Han, J. Zhang, Y. Xie and X. Ma, *Green Chem.*, 2007, **9**, 169–172.
- 27 S. Riaño, M. Petranikova, B. Onghena, T. Vander Hoogerstraete, D. Banerjee, M. R. S. Foreman, C. Ekberg and K. Binnemans, *RSC Adv.*, 2017, **7**, 32100–32113.
- 28 D. V. Wagle, H. Zhao, C. A. Deakyne and G. A. Baker, *ACS Sustain. Chem. Eng.*, 2018, **6**, 7525–7531.
- 29 Y. Dai, J. van Spronsen, G.-J. Witkamp, R. Verpoorte and Y. H. Choi, *Anal. Chim. Acta*, 2013, **766**, 61–68.
- 30 J. H. Davis James, *Chem. Lett.*, 2004, **33**, 1072–1077.
- 31 J. H. Davis, K. J. Forrester and T. Merrigan, *Tetrahedron Lett.*, 1998, **39**, 8955–8958.
- 32 J. Pernak, A. Syguda, D. Janiszewska, K. Materna and T. Praczyk, *Tetrahedron*, 2011, **67**, 4838–4844.
- 33 M. R. Cole, M. Li, B. El-Zahab, M. E. Janes, D. Hayes and I. M. Warner, *Chem. Biol. Drug Des.*, 2011, **78**, 33–41.
- 34 J. L. Shamshina, O. A. Cojocaru, S. P. Kelley, K. Bica, S. P. Wallace, G. Gurau and R. D. Rogers, *ACS Omega*, 2017, **2**, 3483–3493.
- 35 H. Q. N. Gunaratne, P. Nockemann and K. R. Seddon, *Chem. Commun.*, 2015, **51**, 4455–4457.
- 36 A. D. Sawant, D. G. Raut, N. B. Darvatkar and M. M. Salunkhe, *Green Chem.*

- Lett. Rev.*, 2011, **4**, 41–54.
- 37 D. Freudenmann, S. Wolf, M. Wolff and C. Feldmann, *Angew. Chemie Int. Ed.*, 2011, **50**, 11050–11060.
  - 38 M. Jost, L. H. Finger, J. Sundermeyer and C. von Hänisch, *Chem. Commun.*, 2016, **52**, 11646–11648.
  - 39 A. M. Guloy, Z. Tang, R. Ramlau, B. Böhme, M. Baitinger and Y. Grin, *Eur. J. Inorg. Chem.*, 2009, **2009**, 2455–2458.
  - 40 E. Ahmed, E. Ahrens, M. Heise and M. Ruck, *Zeitschrift für Anorg. und Allg. Chemie*, 2010, **636**, 2602–2606.
  - 41 M. Wolff, J. Meyer and C. Feldmann, *Angew. Chemie*, 2011, **123**, 5073–5077.
  - 42 K. Binnemans, *Chem. Rev.*, 2007, **107**, 2592–2614.
  - 43 A.-V. Mudring and S. Tang, *Eur. J. Inorg. Chem.*, 2010, **2010**, 2569–2581.
  - 44 P. Nockemann, B. Thijs, K. Lunstroot, T. N. Parac-Vogt, C. Görller-Walrand, K. Binnemans, K. Van Hecke, L. Van Meervelt, S. Nikitenko, J. Daniels, C. Hennig and R. Van Deun, *Chem. - A Eur. J.*, 2009, **15**, 1449–1461.
  - 45 P. Nockemann, K. Servaes, R. Van Deun, K. Van Hecke, L. Van Meervelt, K. Binnemans and C. Görller-Walrand, *Inorg. Chem.*, 2007, **46**, 11335–11344.
  - 46 S. Santner, J. Heine and S. Dehnen, *Angew. Chemie Int. Ed.*, 2016, **55**, 876–893.
  - 47 R. E. Morris, *Chem. Commun.*, 2009, 2990.
  - 48 E. Ahmed and M. Ruck, *Coord. Chem. Rev.*, 2011, **255**, 2892–2903.
  - 49 S. Tyrrell, G. Behrendt, Y. Liu and P. Nockemann, *RSC Adv.*, 2014, **4**, 36110–36116.
  - 50 J. Dupont, G. S. Fonseca, A. P. Umpierre, P. F. P. Fichtner and S. R. Teixeira, *J. Am. Chem. Soc.*, 2002, **124**, 4228–4229.
  - 51 C. L. Hussey, *Pure Appl. Chem.*, 1988, **60**, 1763–1772.
  - 52 M. Nieuwenhuyzen, K. R. Seddon, F. Teixidor, A. V Puga and C. Vinas, *Inorg Chem*, 2009, **48**, 889–901.
  - 53 R. P. Swatloski, S. K. Spear, J. D. Holbrey and R. D. Rogers, *J. Am. Chem. Soc.*, 2002, **124**, 4974–4975.
  - 54 F. Hermanutz, F. Gähr, E. Uerdingen, F. Meister and B. Kosan, *Macromol. Symp.*, 2008, **262**, 23–27.
  - 55 K. N. Onwukamike, T. Tassaing, S. Grelier, E. Grau, H. Cramail and M. A. R. Meier, *ACS Sustain. Chem. Eng.*, 2018, **6**, 1496–1503.
  - 56 E. D. Bates, R. D. Mayton, I. Ntai and J. H. Davis, *J. Am. Chem. Soc.*, 2002, **124**, 926–927.



- 57 C. Wang, H. Luo, D. Jiang, H. Li and S. Dai, *Angew. Chemie*, 2010, **122**, 6114–6117.
- 58 P. Nockemann, B. Thijs, S. Pittois, J. Thoen, C. Glorieux, K. Van Hecke, L. Van Meervelt, B. Kirchner and K. Binnemans, *J. Phys. Chem. B*, 2006, **110**, 20978–20992.
- 59 P. Nockemann, B. Thijs, K. Van Hecke, L. Van Meervelt and K. Binnemans, *Cryst. Growth Des.*, 2008, **8**, 1353–1363.
- 60 J. Gorke, F. Srienc and R. Kazlauskas, *Biotechnol. Bioprocess Eng.*, 2010, **15**, 40–53.
- 61 X. Sun, H. Luo and S. Dai, *Chem. Rev.*, 2012, **112**, 2100–2128.
- 62 P. E. Mason, F. Uhlig, V. Vaněk, T. Buttersack, S. Bauerecker and P. Jungwirth, *Nat. Chem.*, 2015, **7**, 250–254.
- 63 C. A. Kraus and W. W. Lucasse, *J. Am. Chem. Soc.*, 1921, **43**, 2529–2539.
- 64 J. L. Dye, K. D. Cram, S. a Urbin, Y. Redko, J. E. Jackson and M. Lefenfeld, *J. Am. Chem. Soc.*, 2005, **127**, 9338–9339.
- 65 H. Abourahma, L. Bradley, N. M. Lareau and M. Reesbeck, *J. Chem. Educ.*, 2014, **91**, 443–445.
- 66 P. Nandi, J. L. Dye and J. E. Jackson, *J. Org. Chem.*, 2009, **74**, 5790–5792.
- 67 G. E. Gibson and T. E. Phipps, *J. Am. Chem. Soc.*, 1926, **48**, 312–326.
- 68 M. K. Faber, O. Fussa-Rydel, J. B. Skowrya, L. E. H. McMills and J. L. Dye, *J. Am. Chem. Soc.*, 1989, **111**, 5957–5958.
- 69 S. Windwer and B. R. Sundheim, *J. Phys. Chem.*, 1962, **66**, 1254–1258.
- 70 R. R. Dewald and J. L. Dye, *J. Phys. Chem.*, 1964, **68**, 128–134.
- 71 T. Cuvigny, J. Normant and H. Normant, *COMPTES RENDUS*, 1964, **258**, 3502.
- 72 N. Gremmo and J. E. B. Randles, *J. Chem. Soc. Faraday Trans. 1 Phys. Chem. Condens. Phases*, 1974, **70**, 1480.
- 73 N. Gremmo and J. E. B. Randles, *J. Chem. Soc. Faraday Trans. 1 Phys. Chem. Condens. Phases*, 1974, **70**, 1488.
- 74 J. L. Dye, M. G. DeBacker and V. A. Nicely, *J. Am. Chem. Soc.*, 1970, **92**, 5226–5228.
- 75 J.-M. Lehn, in *Alkali Metal Complexes with Organic Ligands*, Springer-Verlag, Berlin/Heidelberg, pp. 1–69.
- 76 D. J. Cram and J. M. Cram, *Science (80- )*, 1974, **183**, 803–806.
- 77 C. J. Pedersen, *J. Am. Chem. Soc.*, 1967, **89**, 7017–7036.
- 78 J. L. Dye, M. Y. Redko, R. H. Huang and J. E. Jackson, *Adv. Inorg. Chem.*, 2006, **59**, 205–231.

- 79 J. M. Ceraso and J. L. Dye, *J. Chem. Phys.*, 1974, **61**, 1585–1587.
- 80 F. J. Tehan, B. L. Barnett and J. L. Dye, *J. Am. Chem. Soc.*, 1974, **96**, 7203–7208.
- 81 J. Kim, A. S. Ichimura, R. H. Huang, M. Redko, R. C. Phillips, J. E. Jackson and J. L. Dye, *J. Am. Chem. Soc.*, 1999, **121**, 10666–10667.
- 82 H. Davy, *Philos. Trans. R. Soc. London*, 1808, **98**, 333–370.
- 83 J. B. Hannay and J. Hogarth, *Sci. Am.*, 1880, **9**, 3585–3586.
- 84 G. E. Gibson and W. L. Argo, *Phys. Rev.*, 1916, **7**, 33.
- 85 C. A. Kraus, *J. Am. Chem. Soc.*, 1907, **29**, 1557–1571.
- 86 A. J. Birch, *J. Chem. Soc.*, 1944, 430–436.
- 87 A. J. Birch, *Q. Rev. Chem. Soc.*, 1950, **4**, 69–93.
- 88 M. J. Wagner and J. L. Dye, 1996.
- 89 J. L. Dye, *Science (80-. )*, 2003, **301**, 607–608.
- 90 A. Greenfield and U. Schindewolf, *Berichte der Bunsengesellschaft für Phys. Chemie*, 1998, **102**, 1808–1814.
- 91 J. L. Dye, M. Y. Redko, R. H. Huang and J. E. Jackson, in *Radiation Physics and Chemistry*, American Chemical Society, 2006, vol. 59, pp. 205–231.
- 92 L. G. Boxall, H. L. Jones and R. a Osteryoung, *J. Electrochem. Soc.*, 1973, **120**, 223–231.
- 93 I. C. Quarmby, R. A. Mantz, L. M. Goldenberg and R. A. Osteryoung, *Proc - Electrochem Soc*, 1994, **13**, 483–490.
- 94 F. Wu, N. Zhu, Y. Bai, L. Liu, H. Zhou and C. Wu, *ACS Appl. Mater. Interfaces*, 2016, **8**, 21381–21386.
- 95 D. Si, K. Chen, J. Yao and H. Li, *J. Phys. Chem. B*, 2016, **120**, 3904–3913.
- 96 K. Takahashi, K. Suda, T. Seto, Y. Katsumura, R. Katoh, R. A. Crowell and J. F. Wishart, *Radiat. Phys. Chem.*, 2009, **78**, 1129–1132.
- 97 I. A. Shkrob and M. C. Sauer, *J. Phys. Chem. A*, 2002, **106**, 9120–9131.
- 98 J. F. Gavlas, F. Y. Jou and L. M. Dorfman, *J. Phys. Chem.*, 1974, **78**, 2631–2635.
- 99 J. Belloni and J. L. Marignier, *Int. J. Radiat. Appl. Instrumentation. Part C. Radiat. Phys. Chem.*, 1989, **34**, 157–171.
- 100 J. F. Wishart and P. Neta, *J. Phys. Chem. B*, 2003, **107**, 7261–7267.
- 101 C. Xu and C. J. Margulis, *J. Phys. Chem. B*, 2015, **119**, 532–542.
- 102 C. J. Margulis, H. V. R. Annapureddy, P. M. De Biase, D. Coker, J. Kohanoff and M. G. Del Pópolo, *J. Am. Chem. Soc.*, 2011, **133**, 20186–20193.
- 103 A. Skrzypczak and P. Neta, *J. Phys. Chem. A*, 2003, **107**, 7800–7803.
- 104 L. Y. Yuan, M. Sun, L. Mei, L. Wang, L. R. Zheng, Z. Q. Gao, J. Zhang, Y. L.

- Zhao, Z. F. Chai and W. Q. Shi, *Inorg. Chem.*, 2015, **54**, 1992–1999.
- 105 S. H. Ha, R. N. Menchavez and Y.-M. Koo, *Korean J. Chem. Eng.*, 2010, **27**, 1360–1365.
- 106 T. E. Sutto, *Conf. proceeding sHonolulu PRiME 2012*, 2012, 3687.
- 107 C. Jagadeeswara Rao, K. A. Venkatesan, B. V. R. Tata, K. Nagarajan, T. G. Srinivasan and P. R. Vasudeva Rao, *Radiat. Phys. Chem.*, 2011, **80**, 643–649.
- 108 I. A. Shkrob, T. W. Marin, S. D. Chemerisov, J. Hatcher and J. F. Wishart, *J. Phys. Chem. B*, 2012, **116**, 9043–9055.
- 109 I. A. Shkrob, T. W. Marin, S. D. Chemerisov, J. L. Hatcher and J. F. Wishart, *J. Phys. Chem. B*, 2011, **115**, 3889–3902.
- 110 I. A. Shkrob, T. W. Marin, R. A. Crowell and J. F. Wishart, *J. Phys. Chem. A*, 2013, **117**, 5742–5756.
- 111 I. A. Shkrob, T. W. Marin, J. R. Bell, H. Luo and S. Dai, *J. Phys. Chem. B*, 2013, **117**, 14400–14407.
- 112 R. P. Morco, J. M. Joseph and J. C. Wren, *RSC Adv.*, 2015, **5**, 28570–28581.
- 113 H. J. Hageman, *Prog. Org. Coatings*, 1985, **13**, 123–150.
- 114 D. WATTS, *Dent. Mater.*, 2005, **21**, 27–35.
- 115 Z. Xue, D. He and X. Xie, *Polym. Chem.*, 2015, **6**, 1660–1687.
- 116 A. . Mesquita, M. . Mori, J. . Vieira and L. G. A. e Silva, *Radiat. Phys. Chem.*, 2002, **63**, 465–468.
- 117 A. J. Carmichael, D. M. Haddleton, S. A. F. Bon and K. R. Seddon, *Chem. Commun.*, 2000, 1237–1238.
- 118 P. L. Arnold, E. Hollis, F. J. White, N. Magnani, R. Caciuffo and J. B. Love, *Angew. Chemie Int. Ed.*, 2011, **50**, 887–890.
- 119 S. Pfirrmann, C. Limberg, C. Herwig, R. Stößer and B. Ziemer, *Angew. Chemie Int. Ed.*, 2009, **48**, 3357–3361.
- 120 P. Holze, T. Corona, N. Frank, B. Braun-Cula, C. Herwig, A. Company and C. Limberg, *Angew. Chemie - Int. Ed.*, 2017, **56**, 2307–2311.
- 121 G. P. Connor and P. L. Holland, *Catal. Today*, 2017, **286**, 21–40.
- 122 M. D. Morse, *Chem. Rev.*, 1986, **86**, 1049–1109.
- 123 E. W. Abel and F. G. A. Stone, *Q. Rev. Chem. Soc.*, 1970, **24**, 498.
- 124 E. Zintl and A. Harder, *Z. Phys. Chem., Abt. A*, 1931, **154**, 47–91.
- 125 J. D. Corbett, D. G. Adolphson, D. J. Merryman, P. A. Edwards and F. J. Armatis, *J. Am. Chem. Soc.*, 1975, **97**, 6267–6268.
- 126 S. M. Kauzlarich, S. R. Brown and G. Jeffrey Snyder, *Dalt. Trans.*, 2007, 2099.

- 127 A. M. Guloy, R. Ramlau, Z. Tang, W. Schnelle, M. Baitinger and Y. Grin, *Nature*, 2006, **443**, 320–323.
- 128 D. Sun and T. Hughbanks, *Inorg. Chem.*, 2000, **39**, 1964–1968.
- 129 E. Ahmed, D. Köhler and M. Ruck, *Zeitschrift für Anorg. und Allg. Chemie*, 2009, **635**, 297–300.
- 130 H. Zhang, Y. Shi, L. Wang, C. Wang, H. Zhou, W. Guo and T. Ma, *Chem. Commun.*, 2013, **49**, 9003.
- 131 T. F. Fässler and R. Hoffmann, *J. Chem. Soc. Dalt. Trans.*, 1999, 3339–3340.
- 132 H. Abramczyk and J. Kroh, *Chem. Phys.*, 1991, **157**, 373–379.
- 133 P. E. Mason, T. Buttersack, S. Bauerecker and P. Jungwirth, *Angew. Chemie - Int. Ed.*, 2016, **55**, 13019–13022.
- 134 L. Berthon, S. I. Nikitenko, I. Bisel, C. Berthon, M. Faucon, B. Saucerotte, N. Zorz and P. Moisy, *Dalt. Trans.*, 2006, 2526.
- 135 T. H. U. of J. Insitute of Chemistry, 23 Na NMR, <http://chem.ch.huji.ac.il/nmr/techniques/1d/row3/na.html>.
- 136 D. F. Evans, *J. Chem. Soc.*, 1959, 2003.
- 137 P. Atkins and J. De Paula, *Elements of physical chemistry*, Oxford University Press, USA, 2013.
- 138 D. T. Wilkinson and H. R. Crane, *Phys. Rev.*, 1963, **130**, 852.
- 139 E. V Saenko, K. Takahashi and V. I. Feldman, *J. Phys. Chem. Lett.*, 2013, **4**, 2896–2899.
- 140 W. G. Schrenk, *Appl. Spectrosc.*, 1986, **40**, xix–xxviii.
- 141 J. F. W. Herschel, *Treatises on physical astronomy, light and sound contributed to the Encyclopaedia metropolitana*, J. J. Griffin, London, 1848.
- 142 P. M. Hald, *J. Biol. Chem.*, 1947, 499–510.
- 143 E. Zurek, P. P. Edwards and R. Hoffmann, *Angew. Chemie Int. Ed.*, 2009, **48**, 8198–8232.
- 144 L. Ben Haj Hassen, Z. Denden, Y. Rousselin and H. Nasri, *Acta Crystallogr. Sect. E Crystallogr. Commun.*, 2015, **71**, m215–m216.
- 145 K. Matsumoto, T. Matsui, T. Nohira and R. Hagiwara, *J. Fluor. Chem.*, 2015, **174**, 42–48.
- 146 H. Rzepa, The mechanism of the Birch reduction. Part 2: a transition state model., <http://www.ch.imperial.ac.uk/rzepa/blog/?p=8508>.
- 147 C. F. Nutaitis, *J. Chem. Educ.*, 1989, **66**, 673.
- 148 M. I. J. Hutter F. Schiffmann and J. Vande Vondele, *Wiley Interdiscip. Rev. Comput. Mol. Sci*, 2014, **4**, 15–25.
- 149 J. P. Finley, *Mol. Phys.*, 2004, **102**, 627–639.

- 150 J. VandeVondele and J. Hutter, *J. Chem. Phys.*, 2007, **127**, 114105.
- 151 J. M. del Campo, J. L. Gázquez, S. B. Trickey and A. Vela, *J. Chem. Phys.*, 2012, **136**, 104108.
- 152 O. V. Dolomanov, L. J. Bourhis, R. J. Gildea, J. A. K. Howard and H. Puschmann, *J. Appl. Crystallogr.*, 2009, **42**, 339–341.
- 153 G. M. Sheldrick, *Acta Crystallogr. Sect. A Found. Adv.*, 2015, **71**, 3–8.
- 154 G. M. Sheldrick, *Acta Crystallogr. Sect. A Found. Crystallogr.*, 2008, **64**, 112–122.
- 155 L. Palatinus and G. Chapuis, *J. Appl. Crystallogr.*, 2007, **40**, 786–790.
- 156 F. Vogle and H. Uwe, *Modern Cyclophane Chemistry*, Wiley-VCH Verlag GmbH & Co. KGaA, Weinheim, FRG, 2004.
- 157 A. Zinke and S. Pucher, *Monatshefte für Chemie/Chemical Mon.*, 1948, **79**, 26–41.
- 158 A. Baeyer, *Berichte der Dtsch. Chem. Gesellschaft*, 1872, **5**, 280–282.
- 159 Classical Art Research Centre, Calyx-krater, <http://www.beazley.ox.ac.uk/tools/pottery/shapes/calyx.htm>, (accessed 21 March 2018).
- 160 V. Powers, *Am. Chem. Soc. Natl. Hist. Chem. Landmarks*, 1993, 1–2.
- 161 C. S. Day, in *Calixarenes Revisited*, ed. C. D. Gutsche, Royal Society of Chemistry, Cambridge, 1989, pp. 1–9.
- 162 A. Zinke and E. Ziegler, *Berichte der Dtsch. Chem. Gesellschaft (A B Ser.)*, 1941, **74**, 1729–1736.
- 163 A. Zinke, R. Ott and F. H. Garrana, *Monatshefte für Chemie und verwandte Teile anderer Wissenschaften*, 1958, **89**, 135–142.
- 164 A. Zinke, G. Zigeuner, G. Weiss and E. Wiesenberger, *Monatshefte für Chemie*, 1949, **80**, 160–169.
- 165 C. D. Gutsche, M. Iqbal and D. Stewart, *J. Org. Chem.*, 1986, **51**, 742–745.
- 166 F. Vocanson, R. Lamartine, C. Duchamp and J. B. Regnouf de Vains, *Chromatographia*, 1995, **41**, 204–206.
- 167 J. W. Cornforth, P. D'Arcy Hart, G. A. Nicholls, R. J. W. Rees and J. A. Stock, *Brit. J. Pharmacol.*, 1955, **10**, 73–86.
- 168 L. C. Craig and O. Post, *Anal. Chem.*, 1949, **21**, 500–504.
- 169 J. D. Glennon, S. Hutchinson, S. J. Harris, A. Walker, M. A. McKervey and C. C. McSweeney, *Anal. Chem.*, 1997, **69**, 2207–2212.
- 170 Y. Zhang and I. M. Warner, *J. Chromatogr. A*, 1994, **688**, 293–300.
- 171 C. D. Gutsche, in *Calixarenes, an introduction*, 2008, pp. 61–76.
- 172 B. T. Hayes and R. F. Hunter, *J. Appl. Chem.*, 2007, **8**, 743–748.

- 173 V. Böhmer, P. Chhim and H. Kämmerer, *Die Makromol. Chemie*, 1979, **180**, 2503–2506.
- 174 G. Sartori, F. Bigi, C. Porta, R. Maggi and R. Mora, *Tetrahedron Lett.*, 1995, **36**, 2311–2314.
- 175 M. Bergamaschi, F. Bigi, M. Lanfranchi, R. Maggi, A. Pastorio, M. A. Pellinghelli, F. Peri, C. Porta and G. Sartori, *Tetrahedron*, 1997, **53**, 13037–13052.
- 176 A. Wolff, V. Boehmer, W. Vogt, F. Ugozzoli and G. D. Andreetti, *J. Org. Chem.*, 1990, **55**, 5665–5667.
- 177 C. D. Gutsche, *Acc. Chem. Res.*, 1983, **16**, 161–170.
- 178 A. Koji, I. Koji, S. Seiji and M. Tsutomu, *Bull. Chem. Soc. Jpn.*, 1990, **63**, 3480–3485.
- 179 S. Shinkai, K. Araki, P. D. J. Grootenhuis and D. N. Reinhoudt, *J. Chem. Soc. Perkin Trans. 2*, 1991, 1883–1886.
- 180 A. Koji, M. Hiroto, O. Fumio and S. Seiji, *Chem. Lett.*, 1992, **21**, 539–542.
- 181 N. Sabbatini, M. Guardigli, A. Mecati, V. Balzani, R. Ungaro, E. Ghidini, A. Casnati and A. Pochini, *J. Chem. Soc. Chem. Commun.*, 1990, 878–879.
- 182 J. J. Rebek, *Chem. Commun.*, 2000, 637–643.
- 183 M. L. Dietz, *Sep. Sci. Technol.*, 2006, **41**, 2047–2063.
- 184 K. Shimojo and M. Goto, *Anal. Chem.*, 2004, **76**, 5039–5044.
- 185 S. Kojiro and G. Masahiro, *Chem. Lett.*, 2004, **33**, 320–321.
- 186 R. Grigg, J. M. Holmes, S. K. Jones and W. D. J. A. Norbert, *J. Chem. Soc. Chem. Commun.*, 1994, 185–187.
- 187 Y. Kubo, S. Hamaguchi, K. Kotani and K. Yoshida, *Tetrahedron Lett.*, 1991, **32**, 7419–7420.
- 188 T. Werner, J. M. Kürner, C. Krause and O. S. Wolfbeis, *Anal. Chim. Acta*, 2000, **421**, 199–205.
- 189 M. Kubinyi, I. Mohammed-Ziegler, A. Grofcsik, I. Bitter and W. J. Jones, *J. Mol. Struct.*, 1997, **408–409**, 543–546.
- 190 M. McCarrick, B. Wu, S. J. Harris, D. Diamond, G. Barrett and M. A. McKerver, *J. Chem. Soc. Chem. Commun.*, 1992, **3593**, 1287.
- 191 M. McCarrick, B. Wu, S. J. Harris, D. Diamond, G. Barrett and M. A. McKerver, *J. Chem. Soc. Perkin Trans. 2*, 1993, 1963.
- 192 J. S. Kim, O. J. Shon, J. W. Ko, M. H. Cho, I. Y. Yu and J. Vicens, *J. Org. Chem.*, 2000, **65**, 2386–2392.
- 193 M. R. Ganjali, Z. Memari, P. Norouzi, B. Shaabani, M. Emamalizadeh, Y. Hanifehpour and F. Faridbod, *Anal. Lett.*, 2010, **43**, 2220–2233.

- 194 S. K. Menon, N. R. Modi, B. Patel and M. B. Patel, *Talanta*, 2011, **83**, 1329–1334.
- 195 A. Ali, R. Joseph, B. Mahieu and C. P. Rao, *Polyhedron*, 2010, **29**, 1035–1040.
- 196 B. Castellano, E. Solari, C. Floriani, N. Re, A. Chiesi-Villa and C. Rizzoli, *Organometallics*, 1998, **17**, 2328–2336.
- 197 M. Giusti, E. Solari, L. Giannini, C. Floriani, A. Chiesi-Villa and C. Rizzoli, *Organometallics*, 1997, **16**, 5610–5612.
- 198 V. Videva, A.-S. Chauvin, S. Varbanov, C. Baux, R. Scopelliti, M. Mitewa and J.-C. G. Bünzli, *Eur. J. Inorg. Chem.*, 2004, **2004**, 2173–2179.
- 199 D. Buccella and G. Parkin, *J. Am. Chem. Soc.*, 2006, **128**, 16358–16364.
- 200 A. Yilmaz, B. Tabakci, E. Akceylan and M. Yilmaz, *Tetrahedron*, 2007, **63**, 5000–5005.
- 201 A. Ikeda, H. Tsuzuki and S. Shinkai, *J. Chem. Soc., Perkin Trans. 2*, 1994, 2073–2080.
- 202 V. K. Gupta, R. N. Goyal, M. Al Khayat, P. Kumar and N. Bachheti, *Talanta*, 2006, **69**, 1149–1155.
- 203 Y. Yang, X. Cao, K. Surowiec and R. A. Bartsch, *J. Incl. Phenom. Macrocycl. Chem.*, 2014, **78**, 387–395.
- 204 P. M. Marcos, J. R. Ascenso, M. A. P. Segurado and J. L. C. Pereira, *J. Incl. Phenom. Macrocycl. Chem.*, 2002, **42**, 281–288.
- 205 H. Zhou, K. Surowiec, D. W. Purkiss and R. A. Bartsch, *Org. Biomol. Chem.*, 2005, **3**, 1676.
- 206 M. Yilmaz, *Synth. React. Inorg. Met. Chem.*, 1998, **28**, 1759–1768.
- 207 Y. Liu, H. Wang, L.-H. Wang, Z. Li, H.-Y. Zhang and Q. Zhang, *Tetrahedron*, 2003, **59**, 7967–7972.
- 208 S.-K. Chang and I. Cho, *J. Chem. Soc. Perkin Trans. 1*, 1986, 211.
- 209 S. Bozkurt, M. Durmaz, A. Sirit and M. Yilmaz, *J. Macromol. Sci. Part A Pure Appl. Chem.*, 2007, **44**, 159–165.
- 210 A. Casnati, A. Pochini, R. Ungaro, C. Bocchi, F. Ugozzoli, R. J. M. Egberink, H. Struijk, R. Lugtenberg, F. De Jong and D. N. Reinhoudt, *Chem. Eur. J.*, 1996, **2**, 436–445.
- 211 A. F. D. de Namor, F. J. S. Velarde and M. C. Cabaleiro, *J. Chem. Soc., Faraday Trans.*, 1996, **92**, 1731–1737.
- 212 C.-M. Jin and J. M. Shreeve, *Inorg. Chem.*, 2004, **43**, 7532–7538.
- 213 A. D. Iampolska, S. G. Kharchenko, Z. V. Voitenko, S. V. Shishkina, A. B. Ryabitskii and V. I. Kalchenko, *Phosphorus. Sulfur. Silicon Relat. Elem.*,

- 2016, **191**, 174–179.
- 214 A. Muravev, F. Galieva, O. Bazanova, D. Sharafutdinova, S. Solovieva, I. Antipin and A. Konovalov, *Supramol. Chem.*, 2016, **28**, 589–600.
- 215 M. Wehbie, G. Arrachart, L. Ghannam, I. Karamé and S. Pellet-Rostaing, *Dalt. Trans.*, 2017, **46**, 16505–16515.
- 216 M. M. Nigra, A. J. Yeh, A. Okrut, A. G. DiPasquale, S. W. Yeh, A. Solovyov and A. Katz, *Dalt. Trans.*, 2013, **42**, 12762.
- 217 N. de Silva, J.-M. Ha, A. Solovyov, M. M. Nigra, I. Ogino, S. W. Yeh, K. A. Durkin and A. Katz, *Nat. Chem.*, 2010, **2**, 1062–1068.
- 218 M. Twain, R. Ungaro, N. York, J. Smid, A. Pochini, R. Cornforth, G. Andreetti and C. Lbc, .
- 219 P. Karásek, J. Planeta and M. Roth, *J. Chem. Eng. Data*, 2014, **59**, 2433–2436.
- 220 H. J. No, K. and Koo, *Bull. Korean Chem. Soc.*, 1994, **15**, 483–488.
- 221 S. K. Sharma, I. Alam and C. D. Gutsche, *Synthesis (Stuttg.)*, 1995, **1995**, 1089–1096.
- 222 S. K. Sharma and C. D. Gutsche, *Synthesis (Stuttg.)*, 1994, **1994**, 813–822.
- 223 C.-M. Shu, W.-C. Liu, M.-C. Ku, F.-S. Tang, M.-L. Yeh and L.-G. Lin, *J. Org. Chem.*, 1994, **59**, 3730–3733.
- 224 C. D. Gutsche and J. A. Levine, *J. Am. Chem. Soc.*, 1982, **104**, 2652–2653.
- 225 O. A. Yesypenko, V. I. Boyko, M. A. Klyachina, S. V. Shishkina, O. V. Shishkin, V. V. Pyrozhenko, I. F. Tsymbal and V. I. Kalchenko, *J. Incl. Phenom. Macrocycl. Chem.*, 2012, **74**, 265–275.
- 226 C. M. Shu, W. S. Chung, S. H. Wu, Z. C. Ho and L. G. Lin, *J. Org. Chem.*, 1999, **64**, 2673–2679.
- 227 J. Bois, J. Espinas, U. Darbost, C. Felix, C. Duchamp, D. Bouchu, M. Taoufik and I. Bonnamour, *J. Org. Chem.*, 2010, **75**, 7550–7558.
- 228 K. Iwamoto, K. Araki and S. Shinkai, *Tetrahedron*, 1991, **47**, 4325–4342.
- 229 L. C. Groenen, B. H. M. Ruël, A. Casnati, W. Verboom, A. Pochini, R. Ungaro and D. N. Reinhoudt, *Tetrahedron*, 1991, **47**, 8379–8384.
- 230 F. Santoyo-González, A. Torres-Pinedo and A. Sánchez-Ortega, *J. Org. Chem.*, 2000, **65**, 4409–4414.
- 231 S. Shinkai, T. Arimura, H. Kawabata, H. Murakami, K. Araki, K. Iwamoto and T. Matsuda, *J. Chem. Soc. Chem. Commun.*, 1990, **32**, 1734.
- 232 K. Iwamoto, K. Araki and S. Shinkai, *Tetrahedron*, 1991, **47**, 4325–4342.
- 233 T. S. Eliot, L. Gidding and C. Poems, in *Calixarenes Revisited*, ed. C. D. Gutsche, Royal Society of Chemistry, Cambridge, 1994, pp. 79–145.



- 234 A. Arduini, A. Pochini, S. Reverberi, R. Ungaro, G. D. Andreetti and F. Ugozzoli, *Tetrahedron*, 1986, **42**, 2089–2100.
- 235 F. Arnaud-Neu, G. Barrett, S. J. Harris, M. Owens, M. A. McKerver, M. J. Schwing-Weill and P. Schwinte, *Inorg. Chem.*, 1993, **32**, 2644–2650.
- 236 F. Arnaud-Neu, E. M. Collins, M. Deasy, G. Ferguson, S. Harris, B. Kaitner, A. J. Lough, A. McKerver, E. Marques, B. L. Ruhl, M. J. Schwing-Weill and E. M. Seward, *J. Am. Chem. Soc.*, 1989, **111**, 8681–8691.
- 237 V. Böhmer, *Angew. Chemie Int. Ed. English*, 1995, **34**, 713–745.
- 238 A. Arduini, A. Casnati, L. Dodi, A. Pochini and R. Ungaro, *J. Chem. Soc. Chem. Commun.*, 1990, 1597.
- 239 C. Alfieri, E. Dradi, A. Pochini, R. Ungaro and G. D. Andreetti, *J. Chem. Soc. Chem. Commun.*, 1983, 1075.
- 240 A. Casnati, A. Pochini, R. Ungaro, F. Ugozzoli, F. Arnaud, S. Fanni, M.-J. Schwing, R. J. M. Egberink, F. de Jong and D. N. Reinhoudt, *J. Am. Chem. Soc.*, 1995, **117**, 2767–2777.
- 241 S. Shinkai, *Tetrahedron*, 1993, **49**, 8933–8968.
- 242 J. H. Munch, *Die Makromol. Chemie*, 1977, **178**, 69–74.
- 243 C. D. Gutsche, B. Dhawan, J. A. Levine, K. Hyun No and L. J. Bauer, *Tetrahedron*, 1983, **39**, 409–426.
- 244 P. D. J. Grootenhuis, P. A. Kollman, L. C. Groenen, D. N. Reinhoudt, G. J. Van Hummel, F. Ugozzoli and G. D. Andreetti, *J. Am. Chem. Soc.*, 1990, **112**, 4165–4176.
- 245 L. P. Hammett and A. J. Deyrup, *J. Am. Chem. Soc.*, 1932, **54**, 2721–2739.
- 246 K. M. Williamson, Kenneth L. Masters, *Macroscale and Microscale Organic Experiments*, 2016.
- 247 G. Arena, R. Cali, G. G. Lombardo, E. Rizzarelli, D. Sciotto, R. Ungaro and A. Casnati, *Supramol. Chem.*, 1992, **1**, 19–24.
- 248 I. Yoshida, N. Yamamoto, F. Sagara, D. Ishii, K. Ueno and S. Shinkai, *Bull. Chem. Soc. Jpn.*, 1992, **65**, 1012–1015.
- 249 D. R. MacFarlane, J. M. Pringle, K. M. Johansson, S. A. Forsyth and M. Forsyth, *Chem. Commun.*, 2006, 1905–1917.
- 250 PCT/EP2008/067014, 2008.
- 251 Z. Wang, *Comprehensive Organic Name Reactions and Reagents*, John Wiley & Sons, Inc., Hoboken, NJ, USA, 2010.
- 252 2004.
- 253 W. Xiao, X. Wang, Q. Chen, T. Wu, Y. Wu, L. Dai and C. Song, *Chem. Lett.*, 2010, **39**, 1112–1113.

- 254 BASF AG, 2006.
- 255 C. J. Bradaric, A. Downard, C. Kennedy, A. J. Robertson and Y. Zhou, *Green Chem.*, 2003, **5**, 143–152.
- 256 M. Tariq, P. A. S. Forte, M. F. C. Gomes, J. N. C. Lopes and L. P. N. Rebelo, *J. Chem. Thermodyn.*, 2009, **41**, 790–798.
- 257 V. Losetty and M. Sivapragasam, *Chem. Sci. J.*, , DOI:10.4172/2150-3494.1000128.
- 258 S. A. Forsyth, U. Fröhlich, P. Goodrich, H. Q. N. Gunaratne, C. Hardacre, A. McKeown and K. R. Seddon, *New J. Chem.*, 2010, **34**, 723.
- 259 Y. Zhang and J. Y. G. Chan, *Energy Environ. Sci.*, 2010, **3**, 408–417.
- 260 M. S. Shannon and J. E. Bara, *Sep. Sci. Technol.*, 2012, **47**, 178–188.
- 261 J.-M. Andanson, A. A. H. Pádua and M. F. Costa Gomes, *Chem. Commun.*, 2015, **51**, 4485–4487.
- 262 G. Gurau, H. Rodríguez, S. P. Kelley, P. Janiczek, R. S. Kalb and R. D. Rogers, *Angew. Chemie Int. Ed.*, 2011, **50**, 12024–12026.
- 263 P. Janiczek, R. S. Kalb, G. Thonhauser and T. Gamse, *Sep. Purif. Technol.*, 2012, **97**, 20–25.
- 264 F. Hermanutz, F. Gähr, E. Uerdingen, F. Meister and B. Kosan, *Macromol. Symp.*, 2008, **262**, 23–27.
- 265 M. B. Shiflett, D. W. Drew, R. A. Cantini and A. Yokozeki, *Energy & Fuels*, 2010, **24**, 5781–5789.
- 266 M. B. Shiflett and A. Yokozeki, *J. Chem. Eng. Data*, 2008, **54**, 108–114.
- 267 B. Ullah, J. Chen, Z. Zhang, H. Xing, Q. Yang, Z. Bao and Q. Ren, *Sci. Rep.*, 2017, **7**, 42699.
- 268 B. Albert and M. Jansen, *Zeitschrift für Anorg. und Allg. Chemie*, 1995, **621**, 1735–1740.
- 269 J. D. Holbrey, W. M. Reichert, I. Tkatchenko, E. Bouajila, O. Walter, I. Tommasi and R. D. Rogers, *Chem. Commun.*, 2003, 28–29.
- 270 WO2008052860 and EP2079705B1
- 271 WO2005021484, EP1658262B1 and US8075803B2,
- 272 N. Sun, M. Rahman, Y. Qin, M. L. Maxim, H. Rodríguez and R. D. Rogers, *Green Chem.*, 2009, **11**, 646–655.
- 273 O. V Surov, M. A. Krestianinov and M. I. Voronova, *Spectrochim. Acta Part A Mol. Biomol. Spectrosc.*, 2015, **134**, 121–126.
- 274 H. E. Gottlieb, V. Kotlyar and A. Nudelman, *J. Org. Chem.*, 1997, **62**, 7512–7515.
- 275 I. D. Cunningham and M. Woolfall, *J. Org. Chem.*, 2005, **70**, 9248–9256.

- 276 C. O. Haughton, *Chem. Eng. Sci.*, 1961, **15**, 145–146.
- 277 S. W. Keller, G. M. Schuster and F. L. Tobiason, *Polym. Mater. Sci. Eng.*, 1987, **57**, 906–910.
- 278 M.-C. Moreau-Descoings, F. Guillaume-Vilport, J.-P. Seguin, R. Uzan and J.-P. Doucet, *J. Mol. Struct.*, 1985, **127**, 297–303.
- 279 N. S. Golubev, S. N. Smirnov, V. A. Gindin, G. S. Denisov, H. Benedict and H.-H. Limbach, *J. Am. Chem. Soc.*, 1994, **116**, 12055–12056.
- 280 S. Hesse-Ertelt, T. Heinze, B. Kosan, K. Schwikal and F. Meister, *Macromol. Symp.*, 2010, **294**, 75–89.
- 281 P. V. Kortunov, L. S. Baugh, M. Siskin and D. C. Calabro, *Energy & Fuels*, 2015, **29**, 5967–5989.
- 282 L. Phan, D. Chiu, D. J. Heldebrant, H. Huttenhower, E. John, X. Li, P. Pollet, R. Wang, C. A. Eckert, C. L. Liotta and P. G. Jessop, *Ind. Eng. Chem. Res.*, 2008, **47**, 539–545.
- 283 V. M. Yurchenko, L. S. Abramova and L. S. Gal'braikh, *Fibre Chem.*, 1984, **15**, 233–234.
- 284 H. Xie, X. Yu, Y. Yang and Z. K. Zhao, *Green Chem.*, 2014, **16**, 2422–2427.
- 285 P. G. Jessop, *Nature*, 2005, **436**, 1102.
- 286 M. C. Ozturk, O. Yuksel Orhan and E. Alper, *Int. J. Greenh. Gas Control*, 2014, **26**, 76–82.
- 287 S. Shinkai, K. Araki, T. Tsubaki, T. Arimura and O. Manabe, *J. Chem. Soc. Perkin Trans. 1*, 1987, 2297–2299.
- 288 C. D. Gutsche, J. A. Levine and P. K. Sujeeth, *J. Org. Chem.*, 1985, **50**, 5802–5806.
- 289 P. Jose and S. Menon, *Bioinorg. Chem. Appl.*, 2007, **2007**, 1–16.
- 290 D. A. Fulton and J. F. Stoddart, *Bioconjug. Chem.*, 2001, **12**, 655–672.
- 291 S. K. Nayak and M. K. Choudhary, *Tetrahedron Lett.*, 2012, **53**, 141–144.
- 292 V. A. Burilov, R. I. Nugmanov, R. R. Ibragimova, S. E. Solovieva, I. S. Antipin and A. I. Konovalov, *Mendeleev Commun.*, 2013, **23**, 113–115.
- 293 S. Shang, D. V. Khasnis, J. M. Burton, C. J. Santini, M. Fan, A. C. Small and M. Lattman, *Organometallics*, 1994, **13**, 5157–5159.
- 294 V. Böhmer, E. Schade and W. Vogt, *Die Makromol. Chemie, Rapid Commun.*, 1984, **5**, 221–224.
- 295 M. Strobel, K. Kita-Tokarczyk, A. Taubert, C. Vebert, P. A. Heiney, M. Chami and W. Meier, *Adv. Funct. Mater.*, 2006, **16**, 252–259.
- 296 Y. I. Matvieiev, V. I. Boyko, A. A. Podoprigrorina and V. I. Kalchenko, *J. Incl. Phenom. Macrocycl. Chem.*, 2008, **61**, 89–92.

- 297 C. Jaime, J. De Mendoza, P. Prados, P. M. Nieto and C. Sanchez, *J. Org. Chem.*, 1991, **56**, 3372–3376.
- 298 G. Bifulco, L. Gomez-Paloma, R. Riccio, C. Gaeta, F. Troisi and P. Neri, *Org. Lett.*, 2005, **7**, 5757–5760.
- 299 A. J. Holding, M. Heikkilä, I. Kilpeläinen and A. W. T. King, *ChemSusChem*, 2014, **7**, 1422–1434.
- 300 H. Finkelstein, *Berichte der Dtsch. Chem. Gesellschaft*, 1910, **43**, 1528–1532.
- 301 R. A. Walton, *Q. Rev. Chem. Soc.*, 1965, **19**, 126.
- 302 A. I. Popov and F. B. Stute, *J. Am. Chem. Soc.*, 1956, **78**, 5737–5740.
- 303 M. Dalibart, M. Fouassier and M. T. Forel, *J. Mol. Struct.*, 1977, **36**, 7–23.
- 304 G. W. A. Fowles, D. A. Rice and N. Rolfe, *J. Inorg. Nucl. Chem.*, 1974, **36**, 31–34.
- 305 L. Legrand, A. Tranchant and R. Messina, *Electrochim. Acta*, 1996, **41**, 2715–2720.
- 306 F. H. Hurley and T. P. Wler, *J. Electrochem. Soc.*, 1951, **98**, 203.
- 307 1948.
- 308 J. Robinson and R. A. Osteryoung, *J. Am. Chem. Soc.*, 1979, **101**, 323–327.
- 309 J. S. Wilkes, J. A. Levisky, R. A. Wilson and C. L. Hussey, *Inorg. Chem.*, 1982, **21**, 1263–1264.
- 310 M. Lipsztajn and R. A. Osteryoung, *J. Electrochem. Soc.*, 1983, **130**, 1968.
- 311 M. Lipsztajn and R. A. Osteryoung, *Inorg. Chem.*, 1984, **23**, 1735–1739.
- 312 R. J. Gale, B. Gilbert and R. A. Osteryoung, *Inorg. Chem.*, 1978, **17**, 2728–2729.
- 313 S. Takahashi, N. Koura, M. Murase and H. Ohno, *J. Chem. Soc., Faraday Trans. 2*, 1986, **82**, 49–60.
- 314 A. K. Abdul-Sada, A. M. Greenway, P. B. Hitchcock, T. J. Mohammed, K. R. Seddon and J. A. Zora, *J. Chem. Soc. Chem. Commun.*, 1986, 1753.
- 315 A. K. Abdul-Sada, A. M. Greenway, K. R. Seddon and T. Welton, *Org. Mass Spectrom.*, 1989, **24**, 917–918.
- 316 A. K. Abdul-Sada, A. M. Greenway, K. R. Seddon and T. Welton, *Org. Mass Spectrom.*, 1993, **28**, 759–765.
- 317 H. A. Øye, M. Jagtoyen, T. Oksefjell and J. S. Wilkes, *Mater. Sci. Forum*, 1991, **73–75**, 183–190.
- 318 A. A. Fannin, D. A. Floreani, L. A. King, J. S. Landers, B. J. Piersma, D. J. Stech, R. L. Vaughn and J. S. Wilkes, *J. Phys. Chem.*, 1984, **88**, 2614–2621.
- 319 J. A. Boon, R. T. Carlin, A. M. Elias and J. S. Wilkes, *J. Chem. Crystallogr.*, 1995, **25**, 57–62.

- 320 R. Gale, B. Gilbert and R. Osteryoung, *Inorg. Chem.*, 1978, **17**, 2728–2729.
- 321 B. K. M. Chan, N. H. Chang and M. Ross Grimmett, *Aust. J. Chem.*, 1977, **30**, 2005–2013.
- 322 J. S. Wilkes and J. A. Levisky, *Air Force Syst. Command U. S. Air Force Acad. Color.* 80840.
- 323 A. A. Fannin, D. A. Floreani, L. A. King, J. S. Landers, B. J. Piersma, D. J. Stech, R. L. Vaughn, J. S. Wilkes and J. L. Williams, *J. Phys. Chem.*, 1984, **88**, 2614–2621.
- 324 J. S. Wilkes and M. J. Zaworotko, *J. Chem. Soc. Chem. Commun.*, 1992, 965.
- 325 J. Fuller, *J. Electrochem. Soc.*, 1997, **144**, 3881.
- 326 D. R. MacFarlane, S. A. Forsyth, J. Golding and G. B. Deacon, *Green Chem.*, 2002, **4**, 444–448.
- 327 J. J. Golding, D. R. MacFarlane, L. Spiccia, M. Forsyth, B. W. Skelton and A. H. White, *Chem. Commun.*, 1998, **456**, 1593–1594.
- 328 P. B. Hitchcock, T. J. Mohammed, K. R. Seddon, J. A. Zora, C. L. Hussey and E. Haynes Ward, *Inorganica Chim. Acta*, 1986, **113**, L25–L26.
- 329 T. B. Scheffler, C. L. Hussey, K. R. Seddon, C. M. Kear and P. D. Armitage, *Inorg. Chem.*, 1983, **22**, 2099–2100.
- 330 I. W. Sun, E. H. Ward, C. L. Hussey, K. R. Seddon and J. E. Turp, *Inorg. Chem.*, 1987, **26**, 2140–2143.
- 331 N. V. Plechkova and K. R. Seddon, in *Methods and Reagents for Green Chemistry*, John Wiley & Sons, Inc., Hoboken, NJ, USA, pp. 103–130.
- 332 M. Abai, M. P. Atkins, A. Hassan, J. D. Holbrey, Y. Kuah, P. Nockemann, A. A. Oliferenko, N. V. Plechkova, S. Rafeen, A. A. Rahman, R. Ramli, S. M. Shariff, K. R. Seddon, G. Srinivasan and Y. Zou, *Dalt. Trans.*, 2015, **44**, 8617–8624.
- 333 J. L. Atwood, D. C. Hrnčir and R. D. Rogers, *J. Incl. Phenom.*, 1983, **1**, 199–207.
- 334 J. G. Huddleston, H. D. Willauer, R. P. Swatloski, A. E. Visser and R. D. Rogers, *Chem. Commun.*, 1998, 1765–1766.
- 335 G. Gurau, H. Rodríguez, S. P. Kelley, P. Janiczek, R. S. Kalb and R. D. Rogers, *Angew. Chemie Int. Ed.*, 2011, **50**, 12024–12026.
- 336 A. E. Visser, R. P. Swatloski, W. M. Reichert, J. H. Davis Jr., R. D. Rogers, R. Mayton, S. Sheff and A. Wierzbicki, *Chem. Commun.*, 2001, 135–136.
- 337 C. A. Angell, *Chem. Rev.*, 1990, **90**, 523–542.
- 338 W. Xu, E. I. Cooper and C. A. Angell, *J. Phys. Chem. B*, 2003, **107**, 6170–

- 6178.
- 339 M. Angell, C.-J. Pan, Y. Rong, C. Yuan, M.-C. Lin, B.-J. Hwang and H. Dai, *Proc. Natl. Acad. Sci.*, 2017, **114**, 834–839.
  - 340 T. G. Tucker and C. A. Angell, *J. Electrochem. Soc.*, 2014, **161**, H796–H801.
  - 341 M. Gratzel, P. Wang, S. M. Zakeeruddin and P. Comte, *J. Am. Chem. Soc.*, 2003, **125**, 1166–1167.
  - 342 Z. Fei, D. Kuang, D. Zhao, C. Klein, H. A. Wee, S. M. Zakeeruddin, M. Grätzel and P. J. Dyson, *Inorg. Chem.*, 2006, **45**, 10407–10409.
  - 343 K. Ueno, H. Tokuda and M. Watanabe, *Phys. Chem. Chem. Phys.*, 2010, **12**, 1649–1658.
  - 344 K. Ueno, J. Murai, K. Ikeda, S. Tsuzuki, M. Tsuchiya, R. Tatara, T. Mandai, Y. Umebayashi, K. Dokko and M. Watanabe, *J. Phys. Chem. C*, 2016, **120**, 15792–15802.
  - 345 D. R. MacFarlane, M. Forsyth, P. C. Howlett, M. Kar, S. Passerini, J. M. Pringle, H. Ohno, M. Watanabe, F. Yan, W. Zheng, S. Zhang and J. Zhang, *Nat. Rev. Mater.*, 2016, **1**, 15005.
  - 346 F. Zhou, A. Izgorodin, R. K. Hocking, L. Spiccia and D. R. MacFarlane, *Adv. Energy Mater.*, 2012, **2**, 1013–1021.
  - 347 T. Welton, *Chem. Rev.*, 1999, **99**, 2071–2084.
  - 348 J. P. Hallett and T. Welton, *Chem. Rev.*, 2011, **111**, 3508–3576.
  - 349 P. Wasserscheid and W. Keim, *Angew. Chemie*, 2000, **39**, 3772–3789.
  - 350 G. W. Parshall, *J. Am. Chem. Soc.*, 1972, **94**, 8716–8719.
  - 351 S. P. Wicelinski, R. J. Gale and J. S. Wilkes, *J. Electrochem. Soc.*, 1987, **134**, 262.
  - 352 S. P. Wicelinski, R. J. Gale, S. D. Williams and G. Mamantov, *Spectrochim. Acta Part A Mol. Spectrosc.*, 1989, **45**, 759–762.
  - 353 S. P. Wicelinski, R. J. Gale, K. M. Pamidimukkala and R. A. Laine, *Anal. Chem.*, 1988, **60**, 2228–2232.
  - 354 C. Hardacre, R. W. Murphy, K. R. Seddon, G. Srinivasan and M. Swadźba-Kwaśny, *Aust. J. Chem.*, 2010, **63**, 845.
  - 355 J. Estager, A. A. Oliferenko, K. R. Seddon and M. Swadźba-Kwaśny, *Dalt. Trans.*, 2010, **39**, 11375.
  - 356 M. Markiton, A. Chrobok, K. Matuszek, K. R. Seddon and M. Swadźba-Kwaśny, *RSC Adv.*, 2016, **6**, 30460–30467.
  - 357 J. M. Hogg, F. Coleman, A. Ferrer-Ugalde, M. P. Atkins and M. Swadźba-Kwaśny, *Green Chem.*, 2015, **17**, 1831–1841.
  - 358 E. J. Angueira and M. G. White, *J. Mol. Catal. A Chem.*, 2007, **277**, 164–170.

- 359 X. Xing, G. Zhao and J. Cui, *Sci. China Chem.*, 2012, **55**, 1542–1547.
- 360 R. Kore, P. Berton, S. P. Kelley, P. Aduri, S. S. Katti and R. D. Rogers, *ACS Catal.*, 2017, **7**, 7014–7028.
- 361 S. P. Wicelinski, R. J. Gale, S. D. Williams and G. Mamantov, *Spectrochim. Acta Part A Mol. Spectrosc.*, 1989, **45**, 759–762.
- 362 R. Kore, P. Berton, S. P. Kelley, P. Aduri, S. S. Katti and R. D. Rogers, , DOI:10.1021/acscatal.7b01793.
- 363 K. R. Seddon, G. Srinivasan, M. Swadźba-Kwaśny and A. R. Wilson, *Phys. Chem. Chem. Phys.*, 2013, **15**, 4518.
- 364 L. H. S. Gasparotto, N. Borisenko, O. Höfft, R. Al-Salman, W. Maus-Friedrichs, N. Bocchi, S. Zein El Abedin and F. Endres, *Electrochim. Acta*, 2009, **55**, 218–226.
- 365 J. Zhang, M. An, Q. Chen, A. Liu, X. Jiang, S. Ji, Y. Lian and X. Wen, *Electrochim. Acta*, 2016, **190**, 1066–1077.
- 366 M. K. Carpenter and M. W. Verbrugge, *J. Mater. Res.*, 1994, **9**, 2584–2591.
- 367 M. J. Earle, U. Hakala, C. Hardacre, J. Karkkainen, B. J. McAuley, D. W. Rooney, K. R. Seddon, J. M. Thompson and K. Wähälä, *Chem. Commun.*, 2005, 903–905.
- 368 H. Q. N. Gunaratne, T. J. Lotz and K. R. Seddon, *New J. Chem.*, 2010, **34**, 1821.
- 369 J.-Z. Yang, P. Tian, L.-L. He and W.-G. Xu, *Fluid Phase Equilib.*, 2003, **204**, 295–302.
- 370 D. C. Apperley, C. Hardacre, P. Licence, R. W. Murphy, N. V. Plechkova, K. R. Seddon, G. Srinivasan, M. Swadźba-Kwaśny and I. J. Villar-Garcia, *Dalt. Trans.*, 2010, **39**, 8679.
- 371 Y. J. Kim and R. S. Varma, *Tetrahedron Lett.*, 2005, **46**, 7447–7449.
- 372 S.-L. Chen, S.-J. Ji and T.-P. Loh, *Tetrahedron Lett.*, 2003, **44**, 2405–2408.
- 373 J. Estager, P. Nockemann, K. R. Seddon, G. Srinivasan and M. Swadźba-Kwaśny, *ChemSusChem*, 2012, **5**, 117–124.
- 374 S. Tyrrell, M. Swadźba-Kwaśny and P. Nockemann, *J. Mater. Chem. A*, 2014, **2**, 2616.
- 375 J. M. Hogg, L. C. Brown, K. Matuszek, P. Latos, A. Chrobok and M. Swadźba-Kwaśny, *Dalt. Trans.*, 2017, **46**, 11561–11574.
- 376 H. M. A. Abood, A. P. Abbott, A. D. Ballantyne and K. S. Ryder, *Chem. Commun.*, 2011, **47**, 3523.
- 377 K. Matuszek, A. Chrobok, J. Hogg, F. Coleman and M. Swadźba-Kwaśny, *Green Chem.*, 2015, **17**, 4255–4262.

- 378 L. Legrand, M. Heintz, A. Tranchant and R. Messina, *Electrochim. Acta*, 1995, **40**, 1711–1716.
- 379 L. Legrand, *J. Electrochem. Soc.*, 1994, **141**, 378.
- 380 Y. Nakayama, Y. Senda, H. Kawasaki, N. Koshitani, S. Hosoi, Y. Kudo, H. Morioka and M. Nagamine, *Phys. Chem. Chem. Phys.*, 2015, **17**, 5758–5766.
- 381 X. Chen, X. Bao, J.-C. Zhao and S. G. Shore, *J. Am. Chem. Soc.*, 2011, **133**, 14172–14175.
- 382 J. M. Hogg, Queen's University Belfast, 2017.
- 383 J. Derouault and M. T. Forel, *Inorg. Chem.*, 1977, **16**, 3207–3213.
- 384 N. C. Means, C. M. Means, S. G. Bott and J. L. Atwood, *Inorg. Chem.*, 1987, **26**, 1466–1468.
- 385 A. H. Cowley, M. C. Cushner, R. E. Davis and P. E. Riley, *Inorg. Chem.*, 1981, **20**, 1179–1181.
- 386 A. El-Hellani, J. Monot, R. Guillot, C. Bour and V. Gandon, *Inorg. Chem.*, 2013, **52**, 506–514.
- 387 J. M. Hogg, L. C. Brown, K. Matuszek, P. Latos, A. Chrobok and M. Swadźba-Kwaśny, *Dalt. Trans.*, 2017, **46**, 11561–11574.
- 388 S. Calvin, *XAFS for Everyone*, CRC press, 2013.
- 389 S. S. Farvid, T. Sabergharesou, L. N. Hutfluss, M. Hegde, E. Prouzet and P. V. Radovanovic, *J. Am. Chem. Soc.*, 2014, **136**, 7669–7679.
- 390 V. E. A. V Ebsworth, D. W. H. Rankin and S. Cradock, *Structural methods in inorganic chemistry.*, Blackwell Scientific Publications, 1987, vol. 99.
- 391 S. S. Batsanov, *Bull. Acad. Sci. USSR Div. Chem. Sci.*, 1967, **16**, 1175–1180.
- 392 J. Rockenberger, U. zum Felde, M. Tischer, L. Tröger, M. Haase and H. Weller, *J. Chem. Phys.*, 2000, **112**, 4296–4304.
- 393 L. Dupont, E. Guillon, J. Bouanda, J. Dumonceau and M. Aplincourt, *Environ. Sci. Technol.*, 2002, **36**, 5062–5066.
- 394 L. Galois, G. Calas and M. . Arrio, *Chem. Geol.*, 2001, **174**, 307–319.
- 395 M. Newville, *J. Synchrotron Radiat.*, 2001, **8**, 322–324.
- 396 B. Ravel and M. Newville, *J. Synchrotron Radiat.*, 2005, **12**, 537–541.
- 397 J. Racine, *J. Appl. Econom.*, 2006, **21**, 133–141.
- 398 M. Newville, *J. Phys. Conf. Ser.*, 2013, **430**, 012007.
- 399 M. Blesic, M. Swadźba-Kwaśny, T. Belhocine, H. Q. N. Gunaratne, J. N. C. Lopes, M. F. C. Gomes, A. A. H. Pádua, K. R. Seddon and L. P. N. Rebelo, *Phys. Chem. Chem. Phys.*, 2009, **11**, 8939.
- 400 J. Jacquemin, P. Husson, A. A. H. Padua and V. Majer, *Green Chem.*, 2006, **8**, 172–180.



- 401 C. A. Tolman, *Chem. Rev.*, 1977, **77**, 313–348.
- 402 G. W. Scherer, *J. Am. Ceram. Soc.*, 1992, **75**, 1060–1062.
- 403 J. C. Mauro, Y. Yue, A. J. Ellison, P. K. Gupta and D. C. Allan, *Proc. Natl. Acad. Sci.*, 2009, **106**, 19780–19784.
- 404 C. A. Angell, *Science*, 1995, **267**, 1924–1935.
- 405 A. P. Abbott, K. Ryder, P. Licence and A. W. Taylor, in *Ionic Liquids Completely UnCOILed*, John Wiley & Sons, Inc, Hoboken, NJ, 2015, pp. 1–12.
- 406 T. H. U. of J. Institute of Chemistry, <sup>31</sup>P Phosphorus NMR, <http://chem.ch.huji.ac.il/nmr/techniques/1d/row3/p.html>, (accessed 12 April 2018).
- 407 N. Burford, B. W. Royan, R. E. v. H. Spence and R. D. Rogers, *J. Chem. Soc., Dalton Trans.*, 1990, 2111–2117.
- 408 S. Kobayashi, T. Busujima and S. Nagayama, *Chem. - A Eur. J.*, 2000, **6**, 3491–3494.
- 409 Z. Akdeniz, M. Çaliskana and M. P. Tosib, *Zeitschrift für Naturforsch. A*, DOI:10.1515/zna-2000-6-703.
- 410 J. Cui, J. de With, P. A. A. Klusener, X. Su, X. Meng, R. Zhang, Z. Liu, C. Xu and H. Liu, *J. Catal.*, 2014, **320**, 26–32.
- 411 M. Lijewski, J. M. Hogg, M. Swadźba-Kwaśny, P. Wasserscheid and M. Haumann, *RSC Adv.*, 2017, **7**, 27558–27563.
- 412 P. Hu, Y. Wang, X. Meng, R. Zhang, H. Liu, C. Xu and Z. Liu, *Fuel*, 2017, **189**, 203–209.
- 413 C. Gurnani, M. Jura, W. Levason, R. Ratnani, G. Reid and M. Webster, *Dalt. Trans.*, 2009, 1611.
- 414 B. A. M. Brodie and G. A. Rodley, 1968, 1968–1970.
- 415 L. C. Thomas and R. A. Chittenden, *Spectrochim. Acta*, 1964, **20**, 489–502.
- 416 J. A. T. I. Thof and D. W. Meek, .
- 417 F. N. Hooge and P. J. Christen, *Recl. Des Trav. Chim. Des Pays-Bas-Journal R. Netherlands Chem. Soc.*, 1958, **77**, 911–922.
- 418 R. A. Zingaro, *Inorg. Chem.*, 1963, **2**, 192–196.
- 419 F. Cheng, H. L. Codgbrook, A. L. Hector, W. Levason, G. Reid, M. Webster and W. Zhang, *Polyhedron*, 2007, **26**, 4147–4155.
- 420 A. J. Carty, H. A. Patel and P. M. Boorman, *Can. J. Chem.*, 1970, **48**, 492–500.
- 421 T. Timofte and A.-V. Mudring, *Zeitschrift für Anorg. und Allg. Chemie*, 2008, **634**, 624–625.

- 422 G. Garton and H. M. Powell, *J. Inorg. Nucl. Chem.*, 1957, **4**, 84–89.
- 423 D. R. MacFarlane, M. Forsyth, E. I. Izgorodina, A. P. Abbott, G. Annat and K. Fraser, *Phys. Chem. Chem. Phys.*, 2009, **11**, 4962.
- 424 K. Izutsu, in *Electrochemistry in Nonaqueous Solutions*, Wiley-VCH Verlag GmbH & Co. KGaA, Weinheim, FRG, pp. 313–330.
- 425 M. W. Verbrugge and M. K. Carpenter, *AIChE J.*, 1990, **36**, 1097–1106.
- 426 F. Endres, *ChemPhysChem*, 2002, **3**, 144–154.
- 427 M. K. Carpenter and M. W. Verbrugge, *J. Mater. Res.*, 2011, **9**, 2584–2591.
- 428 D. A. Atwood, *Coord. Chem. Rev.*, 1998, **176**, 407–430.
- 429 W. T. Robinson, C. J. Wilkins and Z. Zeying, *J. Chem. Soc., Dalt. Trans.*, 1990, 219–227.
- 430 A. J. Carty and D. G. Tuck, *J. Chem. Soc. A Inorganic, Phys. Theor.*, 1966, 1081.
- 431 L.-J. Baker, L. A. Kloo, C. E. F. Rickard and M. J. Taylor, *J. Organomet. Chem.*, 1997, **545–546**, 249–255.
- 432 M. Currie, J. Estager, P. Licence, S. Men, P. Nockemann, K. R. Seddon, M. Swadźba-Kwaśny and C. Terrade, *Inorg. Chem.*, 2013, **52**, 1710–1721.
- 433 C. P. J. M. van der Vorst, G. C. Verschoor and W. J. A. Maaskant, *Acta Crystallogr. Sect. B Struct. Crystallogr. Cryst. Chem.*, 1978, **34**, 3333–3335.
- 434 C. P. J. M. Van der Vorst and W. J. A. Maaskant, *J. Solid State Chem.*, 1980, **34**, 301–313.
- 435 G. Meyer, *Zeitschrift für Anorg. und Allg. Chemie*, 1981, **478**, 39–51.
- 436 G. Meyer and R. Blachnik, *Zeitschrift für Anorg. und Allg. Chemie*, 1983, **503**, 126–132.
- 437 J. M. van den Berg, *Acta Crystallogr.*, 1966, **20**, 905–910.
- 438 A. Bach, D. Fischer and M. Jansen, *Zeitschrift für Anorg. und Allg. Chemie*, 2013, **639**, 465–467.
- 439 A. J. Carty and D. G. Tuck, 1975, vol. 19, pp. 243–337.
- 440 R. L. Beddoes, D. Collison, F. E. Mabbs and J. Temperley, *Acta Crystallogr. Sect. C Cryst. Struct. Commun.*, 1991, **47**, 58–61.
- 441 S. Jin, V. McKee, M. Nieuwenhuyzen, W. T. Robinson and C. J. Wilkins, *J. Chem. Soc., Dalt. Trans.*, 1993, 3111–3116.
- 442 F. Fairbrother and N. Flitcroft, *J. Less Common Met.*, 1962, **4**, 504–511.
- 443 M. J. Taylor, D. G. Tuck and L. Victoriano, *Can. J. Chem.*, 1982, **60**, 690–694.
- 444 D. H. Brown and D. T. Stewart, *J. Inorg. Nucl. Chem.*, 1970, **32**, 3751–3755.
- 445 D. M. Adams, A. J. Carty, P. Carty and D. G. Tuck, *J. Chem. Soc. A*

- Inorganic, Phys. Theor.*, 1968, 162.
- 446 W. T. Robinson, C. J. Wilkins and Z. Zeying, *J. Chem. Soc. Dalt. Trans.*, 1988, 2187.
- 447 K. Darwin, L. M. Gilby, P. R. Hodge and B. Piggott, *Polyhedron*, 1999, **18**, 3729–3733.
- 448 O. Aschenbrenner, S. Supasitmongkol, M. Taylor and P. Styring, *Green Chem.*, 2009, **11**, 1217.
- 449 J. Zhang, Q. Yang, H. Cao, C. I. Ratcliffe, D. Kingston, Q. Y. Chen, J. Ouyang, X. Wu, D. M. Leek, F. S. Riehle and K. Yu, *Chem. Mater.*, 2016, **28**, 618–625.
- 450 S. Diaz-Moreno, S. Hayama, M. Amboage, A. Freeman, J. Sutter and G. Duller, *J. Phys. Conf. Ser.*, 2009, **190**, 012038.
- 451 S. Diaz-Moreno, M. Amboage, M. Basham, R. Boada, N. E. Bricknell, G. Cibir, T. M. Cobb, J. Filik, A. Freeman, K. Geraki, D. Gianolio, S. Hayama, K. Ignatyev, L. Keenan, I. Mikulska, J. F. W. Mosselmans, J. J. Mudd and S. A. Parry, *J. Synchrotron Radiat.*, 2018, **25**, 998–1009.
- 452 S. Diaz-Moreno, *J. Synchrotron Radiat.*, 2012, **19**, 863–868.
- 453 S. Hayama, G. Duller, J. Sutter, M. Amboage, R. Boada, A. Freeman, L. Keenan, B. Nutter, L. Cahill, P. Leicester, B. Kemp, N. Rubies and S. Diaz-Moreno, *J. synchrotron rad*, 2018, **TBC**, TBC.
- 454 B. Ravel and M. Newville, *Phys. Scr.*, 2005, 1007.
- 455 O. H. Ozutsumi K., Ishiguro S., *Bull. Chem. Soc. Jpn.*, 1988, 61, 945–951.
- 456 S. Ishiguro, B. G. Jeliakova and H. Ohtaki, *Bull. Chem. Soc. Jpn.*, 1985, 58, 1749–1754.
- 457 S. Ishiguro, H. Suzuki, B. G. Jelziakova and H. Ohtaki, *Bull. Chem. Soc. Jpn.*, 1986, **59**, 2407–2413.
- 458 M. Elleb, J. Meullemestre, M. J. Schwing-Weill and F. Vierling, *Inorg. Chem.*, 1980, **19**, 2699–2704.
- 459 M. Elleb, J. Meullemestre, M. J. Schwing-Weill and F. Vierling, *Inorg. Chem.*, 1980, **19**, 2699–2704.
- 460 C. F. and G. Moapurgo, *Theor. chim. Acta*, 1963, **1**, 102–105.
- 461 S. E. Manahan and R. T. Iwamoto, *Inorg. Chem.*, 1965, **4**, 1409–1413.
- 462 F. Garbassi, L. Sestili, A. Ciana and C. Furlani, *Electrochim. Acta*, 1970, **15**, 225–235.
- 463 D. N. Kharitonov and E. N. Golubeva, *Kinet. Catal.*, 2003, **44**, 513–517.
- 464 I. Černušák, M. Aranyosiová, O. Vollárová, D. Velič, O. Kirdajová and J. Benko, *Int. J. Quantum Chem.*, 2009, **109**, 2365–2372.

- 465 G. Vitale, A. B. Valina, H. Huang, R. Amunugama and M. T. Rodgers,  
*Society*, 2001, 11351–11364.
- 466 H. Morgan, Howard, *J. Chem. Soc. Trans.*, 1923, **123**, 2901–2907.
- 467 B. J. Hathaway, D. G. Holah and J. D. Postlethwaite, *J. Chem. Soc.*, 1961,  
3215.
- 468 J. Kubas, *Inorg. Synth.*, 1990, **28**, 68–70.
- 469 L. Le Clainche, M. Giorgi and O. Reinaud, *Eur. J. ...*, 2000, **6**, 1931–1933.
- 470 H. Okkersen, W. L. Groeneveld and J. Reedijk, *Recl. des Trav. Chim. des  
Pays-Bas*, 1973, **92**, 945–953.
- 471 T. N. Sorrell and D. L. Jameson, *J. Am. Chem. Soc.*, 1983, **105**, 6013–6018.
- 472 P. W. W. and Y. J. T., *Inorg. Compd. with Unusual Prop.*, 1976, **150**, 10–104.
- 473 J. A. Creighton and E. R. Lippincott, *J. Chem. Soc.*, 1963, 5134.
- 474 U. Geiser, R. D. Willett, M. Lindbeck and K. Emerson, *J. Am. Chem. Soc.*,  
1986, **108**, 1173–1179.
- 475 D. D. Axtel, Z. B. W. Good, W. P. William and J. T. Yoke, 1973, **29**, 4555–  
4559.
- 476 P. De Vreese, N. R. Brooks, K. Van Hecke, L. Van Meervelt, E. Mattheijs, K.  
Binnemans and R. Van Deun, *Inorg. Chem.*, 2012, **51**, 4972–4981.
- 477 R. Boada, G. Cibir, F. Coleman, S. Diaz-Moreno, D. Gianolio, C. Hardacre,  
S. Hayama, J. D. Holbrey, R. Ramli, K. R. Seddon, G. Srinivasan and M.  
Swadźba-Kwaśny, *Dalt. Trans.*, 2016, **45**, 18946–18953.
- 478 P. De Vreese, N. R. Brooks, K. Van Hecke, L. Van Meervelt, E. Mattheijs, K.  
Binnemans and R. Van Deun, *Inorg. Chem.*, 2012, **51**, 4972–4981.
- 479 P. Garra, F. Dumur, F. Morlet-Savary, C. Dietlin, J. P. Fouassier and J.  
Lalevée, *Macromolecules*, 2016, **49**, 6296–6309.
- 480 C. Nakayama, M. Harada and M. Iida, *Eur. J. Inorg. Chem.*, 2017, **2017**,  
3744–3754.
- 481 M. Watanabe, S. Takemura, S. Kawakami, E. Syouno, H. Kurosu, M. Harada  
and M. Iida, *J. Mol. Liq.*, 2013, **183**, 50–58.
- 482 G. Li, D. M. Camaioni, J. E. Amonette, Z. C. Zhang, T. J. Johnson and J. L.  
Fulton, *J. Phys. Chem. B*, 2010, **114**, 12614–12622.
- 483 F. Tisato, F. Refosco, G. Bandoli, G. Pilloni and B. Corain, *Inorg. Chem.*,  
2001, **40**, 1394–1396.
- 484 M. A. Tiedemann, C. L. Mandell, B. C. Chan and C. Nataro, *Inorganica Chim.  
Acta*, 2014, **422**, 193–201.
- 485 H. Lewin and U. Lepore, *J. Chem. Soc. D*, 1970, **0**, 1–2.
- 486 T. Kräuter and B. Neumüller, *Polyhedron*, 1996, **15**, 2851–2857.

- 487 F. H. Jardine, 1975, vol. 4, pp. 115–163.
- 488 W. T. Reichie, *Inorganica Chim. Acta*, 1971, **5**, 325–332.
- 489 M. Stricker, T. Linder, B. Oelkers and J. Sundermeyer, *Green Chem.*, 2010, **12**, 1589.
- 490 J. M. Hartley, C.-M. Ip, G. C. H. Forrest, K. Singh, S. J. Gurman, K. S. Ryder, A. P. Abbott and G. Frisch, *Inorg. Chem.*, 2014, **53**, 6280–6288.
- 491 M. J. Schneider, M. Haumann, M. Stricker, J. Sundermeyer and P. Wasserscheid, *J. Catal.*, 2014, **309**, 71–78.
- 492 S. M. Corcoran, W. Levason, R. Patel and G. Reid, *Inorganica Chim. Acta*, 2005, **358**, 1263–1268.
- 493 W. Ainscough, E and M. Brodie, A, *Coord. Chem. Rev.*, 1978, **27**, 59–86.
- 494 J. A. Tiethof, A. T. Hetey and D. W. Meek, *Inorg. Chem.*, 1974, **13**, 2505–2509.
- 495 D. Makanova, I. Kovacik, G. Ondrejovic and I. Chemistry, 1991, **4**, 389–396.
- 496 I. R. Beattie, T. R. Gilson and G. A. Ozin, *J. Chem. Soc. A Inorganic, Phys. Theor.*, 1968, 2772.
- 497 I. R. Beattie, K. Livingston and M. Webster, *J. Chem. Soc.*, 1965, 7421.
- 498 R. M. Denton, J. An, B. Adeniran, A. J. Blake, W. Lewis and A. M. Poulton, *J. Org. Chem.*, 2011, **76**, 6749–6767.
- 499 D. W. Meek and P. Nicpon, *J. Am. Chem. Soc.*, 1965, **87**, 4951–4952.
- 500 J. R. Black, W. Levason, M. D. Spicer and M. Webster, *J. Chem. Soc., Dalt. Trans.*, 1993, **4**, 3129.
- 501 N. R. Brooks, S. Schaltin, K. Van Hecke, L. Van Meervelt, K. Binnemans and J. Fransaer, *Chem. - A Eur. J.*, 2011, **17**, 5054–5059.
- 502 Y. Li, J. Sniekers, J. Malaquias, X. Li, S. Schaltin, L. Stappers, K. Binnemans, J. Fransaer and I. F. J. Vankelecom, *Electrochim. Acta*, 2017, **236**, 116–121.
- 503 V. Nadenau, D. Braunger, D. Hariskos, M. Kaiser, C. Köble, A. Oberacker, M. Ruckh, U. Rühle, R. Schäffler, D. Schmid, T. Walter, S. Zweigart and H. W. Schock, *Prog. Photovoltaics Res. Appl.*, 1995, **3**, 363–382.
- 504 L. Stolt, M. Bodegard, J. Kessler, M. Ruckh, K. O. Velthaus and H. W. Schock, in *Proc. 11th Euro. Photovoltaic Solar Energy Conf.*, 1993, p. 20.
- 505 M. A. Malik, P. O'Brien and N. Revaprasadu, *Adv. Mater.*, 1999, **11**, 1441–1444.
- 506 C.-H. Wu, F.-S. Chen, S.-H. Lin and C.-H. Lu, *J. Alloys Compd.*, 2011, **509**, 5783–5788.
- 507 V. Chikan and D. F. Kelley, *Nano Lett.*, 2002, **2**, 141–145.
- 508 S. Zhang, S. H. Wei, A. Zunger and H. Katayama-Yoshida, *Phys. Rev. B -*

- Condens. Matter Mater. Phys.*, 1998, **57**, 9642–9656.
- 509 S. Tyrrell, G. Behrendt and P. Nockemann, *Inorg. Chem.*, 2015, **54**, 4495–4503.
- 510 W. McFarlane and D. S. Rycroft, *J. Magn. Reson.*, 1976, **24**, 95–101.
- 511 F. Weller, Mark, Overton, Tina, Rourke, Jonathan, Armstrong, *Inorganic Chemistry*, 2014.
- 512 M. Swadźba-Kwaśny, L. Chancelier, S. Ng, H. G. Manyar, C. Hardacre and P. Nockemann, *Dalt. Trans.*, 2012, **41**, 219–227.
- 513 S. Bhattacharyya, S. B. Kumar, S. K. Dutta, E. R. T. Tiekink and M. Chaudhury, *Inorg. Chem.*, 1996, **35**, 1967–1973.
- 514 W. A. Anderson, A. J. Carty, G. J. Palenik and G. Schreiber, 1970, **49**, 761–766.
- 515 C. A. McAuliffe and W. Levason, *Transition metal complexes of phosphorus, arsenic and antimony ligands*, Halsted press, 1973.
- 516 D. D. Axtell and J. T. Yoke, *Inorg. Chem.*, 1973, **12**, 1265–1268.
- 517 G. Pilloni, G. Valle, C. Corvaja, B. Longato and B. Corain, *Inorg. Chem.*, 1995, **34**, 5910–5918.
- 518 H. G. M. Edwards, I. R. Lewis and P. H. Turner, *Inorganica Chim. Acta*, 1994, **216**, 191–199.
- 519 B. Carlsson and G. Wettermark, *Zeitschrift für Naturforsch. A*, 1976, **31**, 297–301.
- 520 F. A. Cotton, R. D. Barnes and E. Bannister, *J. Chem. Soc.*, 1960, 2199–2203.
- 521 R. A. Chittenden and L. C. Thomas, *Spectrochim. Acta*, 1964, **20**, 1679–1696.
- 522 B. G. Sukhov, N. K. Gusarova, N. I. Ivanova, M. V. Bogdanova, O. N. Kazheva, G. G. Aleksandrov, O. A. D'yachenko, L. M. Sinegovskaya, S. F. Malysheva and B. A. Trofimov, *J. Struct. Chem.*, 2005, **46**, 1066–1071.
- 523 B. R. James and R. J. P. Williams, *J. Chem. Soc.*, 1961, 2007–2019.
- 524 P. G. Eller and P. W. R. Corfield, *J. Chem. Soc. D Chem. Commun.*, 1971, 105.
- 525 S. J. Lippard and J. J. Mayerle, *Inorg. Chem.*, 1972, **11**, 753–759.
- 526 F. G. Moers and P. H. Op Het Veld, *J. Inorg. Nucl. Chem.*, 1970, **32**, 3225–3228.
- 527 K. Issleib and H.-R. Roloff, *Zeitschrift für Anorg. und Allg. Chemie*, 1963, **324**, 250–258.
- 528 K. Issleib and M. Haftendorn, *Zeitschrift für Anorg. und Allg. Chemie*, 1967,

- 351**, 9–17.
- 529 A. Siegler, M. A. L. Spek, E. Sperotto and R. J. M. Klein Gebbink, *CSD Commun.*
  - 530 G. A. Bowmaker, W. Jirong, R. D. Hart, A. H. White and P. C. Healy, *J. Chem. Soc. Dalt. Trans.*, 1992, 787.
  - 531 H. WANG, *chin.j.struct.chem.*, 1986, 94–96.
  - 532 L. shan Kau, D. J. Spira-Solomon, J. E. Penner-Hahn, K. O. Hodgson and E. I. Solomon, *J. Am. Chem. Soc.*, 1987, **109**, 6433–6442.
  - 533 I. Persson, J. E. Penner-Hahn and K. O. Hodgson, *Inorg. Chem.*, 1993, **32**, 2497–2501.
  - 534 L. S. Kau, K. O. Hodgson and E. I. Solomon, *J. Am. Chem. Soc.*, 1989, **111**, 7103–7109.
  - 535 T. L. Stemmler, T. M. Barnhart, J. E. Penner-Hahn, C. E. Tucker, P. Knochel, M. Boehme and G. Frenking, *J. Am. Chem. Soc.*, 1995, **117**, 12489–12497.
  - 536 K. Hämäläinen, D. P. Siddons, J. B. Hastings and L. E. Berman, *Phys. Rev. Lett.*, 1991, **67**, 2850–2853.
  - 537 A. Kotocova and G. Ondrejovic, *Chem. Pap.*, 1992, **46**, 94–98.
  - 538 O. P. Anderson, C. M. Perkins and K. K. Brito, *Inorg. Chem.*, 1983, **22**, 1267–1273.
  - 539 J. S. Thompson, T. J. Marks and J. a Ibers, *Proc. Natl. Acad. Sci. U. S. A.*, 1977, **74**, 3114–8.
  - 540 I. M. Wasser, S. de Vries, P. Moënné-Loccoz, I. Schröder and K. D. Karlin, *Chem. Rev.*, 2002, **102**, 1201–1234.
  - 541 G. N. Chremos and R. A. Zingaro, *J. Organomet. Chem.*, 1970, **22**, 637–646.
  - 542 Weller, Mark, T. Overton, R. Jonathan and F. Armstrong, *Inorganic Chemistry*, Oxford University Press, UK, 6 th., 2010.
  - 543 S. Mishra, E. Jeanneau and S. Daniele, *Polyhedron*, 2010, **29**, 500–506.
  - 544 L. A. Ba, M. Döring, V. Jamier and C. Jacob, *Org. Biomol. Chem.*, 2010, **8**, 4203.
  - 545 V. Gutmann, *Monatshefte für Chemie*, 1952, **83**, 159–163.
  - 546 G. Ghémard, S. Jaulmes, J. Etienne and J. Flahaut, *Acta Crystallogr. Sect. C Cryst. Struct. Commun.*, 1983, **39**, 968–971.
  - 547 A. Likforman, D. Carré and R. Hillel, *Acta Crystallogr. Sect. B*, 1978, **34**, 1–5.
  - 548 A. Politano, D. Campi, M. Cattelan, I. Ben Amara, S. Jaziri, A. Mazzotti, A. Barinov, B. Gürbulak, S. Duman, S. Agnoli, L. S. Caputi, G. Granozzi and A. Cupolillo, *Sci. Rep.*, 2017, **7**, 3445.
  - 549 X. Liu, X. Duan, P. Peng and W. Zheng, *Nanoscale*, 2011, **3**, 5090.

- 550 X. Duan, J. Ma, J. Lian and W. Zheng, *CrystEngComm*, 2014, **16**, 2550.
- 551 Q. Luo, M. Peng, X. Sun and A. M. Asiri, *RSC Adv.*, 2015, **5**, 87051–87054.
- 552 E. L. . Jadrowski, G. N. . Skomorokhov, A. N.; Asylguzhina, A. I. . Beskrovnyi and S. A. . Danilkin, *Selzvestya Akad. Nauk. Seriya Fiz.*, 2004, **68**, 604–606.
- 553 B. J. Stanbery, *Crit. Rev. Solid State Mater. Sci.*, 2002, **27**, 73–117.
- 554 M. Kemell, M. Ritala and M. Leskelä, *Crit. Rev. Solid State Mater. Sci.*, 2005, **30**, 1–31.
- 555 G. Zahn and P. Paufler, *Cryst. Res. Technol.*, 1988, **23**, 499–507.
- 556 M. Abai, M. P. Atkins, A. Hassan, J. D. Holbrey, Y. Kuah, P. Nockemann, A. A. Oliferenko, N. V. Plechkova, S. Rafeen, A. A. Rahman, R. Ramli, S. M. Shariff, K. R. Seddon, G. Srinivasan and Y. Zou, *Dalt. Trans.*, 2015, **44**, 8617–8624.
- 557 G. Zarca, I. Ortiz and A. Urtiaga, *J. Memb. Sci.*, 2013, **438**, 38–45.
- 558 X. Chen, S. Ming, X. Wu, C. Chen, C. Asumana and G. Yu, *Sep. Sci. Technol.*, 2013, **48**, 2317–2323.
- 559 S. Tyrrell, M. Swadźba-Kwaśny and P. Nockemann, *J. Mater. Chem. A*, 2014, **2**, 2616.
- 560 K. Klementiev and R. Chernikov, *J. Phys. Conf. Ser.*, 2016, **712**, 012008.
- 561 H. H. Johann, *Zeitschrift für Phys.*, 1931, **69**, 185–206.
- 562 R. Plackett, I. Horswell, E. N. Gimenez, J. Marchal, D. Omar and N. Tartoni, *J. Instrum.*, 2013, **8**, C01038–C01038.



## 8 Appendix

### 8.1 Table of Figures

Figure 1-1-Structures of some common cations and anions found in ionic liquids. _____	14
Figure 1-2-Formation of borenium ionic liquids. _____	17
Figure 1-3-TSIL for fragrance delivery by Gunaratne and co-workers. <sup>35</sup> _____	19
Figure 1-4-Figure by Dehnen and co-workers describing the general synthetic approach for the formation of crystalline chalcogen compounds in ionic liquids, outlining all the parameters that can be varied. The auxiliaries do not necessarily need to be part of the desired products; they instead help to trigger network formation or destruction. In most known cases known, E = Se. [Cat] <sup>+</sup> = cation, [An] <sup>-</sup> = anion. <sup>46</sup> _____	20
Figure 1-5-Boron cluster anions synthesised by Puga and co-workers. <sup>52</sup> _____	21
Figure 1-6-Carbon capture by amine functionalised imidazolium cations. <sup>56</sup> _____	22
Figure 1-7-Carbon capture by imazolate anions by Dai and co-workers. <sup>57</sup> _____	22
Figure 2-1-Reproduced from Mason et al. High-speed camera images of a Na/K alloy drop versus a water drop impacting on water. <sup>62</sup> _____	25
Figure 2-2-Predicted coordination within ammonia and metal salt solutions. _____	26
Figure 2-3- <sup>23</sup> Na NMR spectra achieved by Dye and co-workers of 2, 2, 2 crypt and sodium in ethylenediamine. <sup>79</sup> _____	29
Figure 2-4-Single crystal diffraction determined structure of [2, 2, 2-cryptandNa <sup>+</sup> ][Na <sup>-</sup> ] by Dye and co-workers. <sup>80</sup> _____	29
Figure 2-5- Solvation of sodium in liquid ammonia. _____	31
Figure 2-6-Birch reduction of benzene. _____	32
Figure 2-7-Lithium bistriflamide chelate ionic liquids by Li and co-workers. <sup>95</sup> _____	35
Figure 2-8- HOMOs and LUMOs of cations and anions in four ILs. LA/LC and HA/HC denote anion and cation energy levels. <sup>101,102</sup> _____	37
Figure 2-9- Single electron reduction of U(VI) to U(V) via lanthanide coordination Ln= Sm(II) or Y(III). <sup>118</sup> _____	39
Figure 2-10- Reduction of [LNiBr] by KC <sub>8</sub> in a nitrogen atmosphere. (L=[HC(CRNC <sub>6</sub> H <sub>3</sub> -(iPr) <sub>2</sub> ) <sub>2</sub> ]) <sup>119</sup> _____	40
Figure 2-11- Anionic structure of [Na-(crypt)] <sub>3</sub> [Sb <sub>7</sub> ] synthesised and determined by Corbett and co-workers. <sup>125</sup> _____	41
Figure 2-12- Structure of 4-aminopyridine and 1-alkyl-4-aminopyridinium ionic liquid cation. _____	42
Figure 2-13-Resonance within amino substituted pyridine molecules. _____	43
Figure 2-14-Synthesis of 4-aminopyridinium ionic liquids. _____	44
Figure 2-15- Single crystal diffraction determined structure of 1-pentyl-4-aminopyridinium bistriflamide. _____	45

Figure 2-16- Single crystal diffraction determined structure and packing of 1-pentyl-4-aminopyridinium bistriflamide.	45
Figure 2-17-Structure of 1-butyl-4-aminopyridinium bromide as determined by single crystal diffraction.	46
Figure 2-18- Formation of solvated electrons in 1-butyl-4-aminopyridinium bistriflamide.	46
Figure 2-19- Image of 1mm UV quartz cells containing sodium dissolved in 1-pentyl-4-aminopyridinium bistriflamide (left) and the neat ionic liquid (right).	47
Figure 2-20- UV/Vis-NIR Spectra of 1-pentyl-4-aminopyridinium bistriflamide with sodium (blue) and the neat IL (dashed).	48
Figure 2-21-UV/Vis-NIR Spectra of 1-pentyl-4-aminopyridinium bistriflamide with sodium (blue) and the neat IL (dashed).	49
Figure 2-22- <sup>1</sup> H NMR spectra of 1-pentyl-4-aminopyridinium bistriflamide before (red) and after (blue) sodium solvation and quenching.	51
Figure 2-23- <sup>19</sup> F NMR spectra of 1-pentyl-4-aminopyridinium bistriflamide before (red) and after (blue) sodium solvation and quenching.	51
Figure 2-24- <sup>13</sup> CNMR spectra of 1-pentyl-4-aminopyridinium bistriflamide before (red) and after (blue) sodium solvation and quenching.	52
Figure 2-25- <sup>23</sup> Na NMR spectrum of 1-pentyl-4-aminopyridinium bistriflamide.	53
Figure 2-26-Suspected coordination of sodium as a [Na(NTf <sub>2</sub> ) <sub>3</sub> ] <sup>2-</sup> anion in 1-pentyl-4-aminopyridinium bistriflamide.	54
Figure 2-27- Evan's method of 'low concentration' sodium in 1-pentyl-4-aminopyridinium bistriflamide. <sup>1</sup> H NMR spectra before (red) and after solvation of sodium (blue).	56
Figure 2-28- Evan's method of 'high concentration' sodium in 1-pentyl-4-aminopyridinium bistriflamide. <sup>1</sup> H NMR spectra before (red) and after solvation of sodium (blue).	56
Figure 2-29- Evan's method of 'low concentration' sodium in 1-pentyl-4-aminopyridinium bistriflamide. <sup>19</sup> F NMR spectra before (red) and after solvation of sodium (blue).	57
Figure 2-30- EPR spectra of elemental sodium dissolved in 1-pentyl-4-aminopyridinium bistriflamide.	59
Figure 2-31- EPR spectra of elemental sodium dissolved in 1-pentyl-4-aminopyridinium bistriflamide.	59
Figure 2-32-Except from the Treatises of Sound and Light, Encyclopaedia Metropolitana, 1848 by Sir, J. F. W. Herschel. <sup>141</sup>	60
Figure 2-33-The species which are present in lithium–ammonia solutions, as derived from a combination of the theoretical work done by Zurek et al. and experimental information. <sup>143</sup>	61
Figure 2-34-1-Butyl-4-(dimethyl)aminopyridinium cation.	62
Figure 2-35- 1-Butylpyridinium cation	62

Figure 2-36- 1-pentyl-4-aminopyridine cation with an excess electron at the PBE level. The left image presents a top-down view, while the right is a side-on view. Positive spin density is denoted in yellow, while negative spin is blue. Isosurfaces are drawn at $0.02 \text{ e}/\text{\AA}^3$ .	64
Figure 2-37- 1-pentyl-4-aminopyridine cation with a sodium atom present at the PBE level. The left image presents a top-down view, while the right is a side-on view. Positive spin density is denoted in yellow, while negative spin is blue. Isosurfaces are drawn at $0.02 \text{ e}/\text{\AA}^3$ .	64
Figure 2-38-1-pentyl-4-aminopyridine cation with an excess electron at the PBE0 level. The left image presents a top-down view, while the right is a side-on view. Positive spin density is denoted in yellow, while negative spin is blue. Isosurfaces are drawn at $0.02 \text{ e}/\text{\AA}^3$ .	65
Figure 2-39-1-pentyl-4-aminopyridine cation with a sodium atom present at the PBE0 level. The left image presents a top-down view, while the right is a side-on view. Positive spin density is denoted in yellow, while negative spin is blue. Isosurfaces are drawn at $0.02 \text{ e}/\text{\AA}^3$ .	66
Figure 2-40-cation with an excess electron at the PBE0 level. The left image presents a top-down view, while the right is a side-on view. Positive spin density is denoted in yellow, while negative spin is blue. Isosurfaces are drawn at $0.005 \text{ e}/\text{\AA}^3$ .	66
Figure 2-41-PDOS of the neutral structure at the PBE level. The positive axis and negative x-axis denote the spin-up and spin-down channels respectively.	68
Figure 2-42-PDOS of IL containing an excess electron at the PBE0 level. The positive axis and negative x-axis denote the spin-up and spin-down channels respectively.	68
Figure 2-43-PDOS of IL containing a sodium atom at the PBE0 level. The positive axis and negative x-axis denote the spin-up and spin-down channels respectively.	69
Figure 2-44-Target aliphatic cation for alkali metal solvation.	69
Figure 2-45-Phthalic anhydride protection of N,N'-dimethylethylenediamine.	70
Figure 2-46- Single crystal diffraction determined structure of phthalic anhydride protected N,N'-dimethylpropylenediamine.	70
Figure 2-47-Alkylation of Phthalic anhydride protected N,N'-dimethylethylenediamine.	70
Figure 2-48-Deprotection of Alkylated Phthalic anhydride protected N,N'-dimethylethylenediamine.	70
Figure 2-49-Single crystal diffraction determined structure hydrated KNTf <sub>2</sub> ·18-crown-6 complex.	74
Figure 2-50-Addition combinations of 1-pentyl-4-aminopyridinium bistriflamide and potassium-18-crown-6 solutions.	75
Figure 2-51- Single crystal diffraction determined structure of 1-butyl-4-aminopyridinium bistriflamide and 18-crown-6.	76
Figure 2-52- Single crystal diffraction determined structure of 1-butyl-4-aminopyridinium bistriflamide and 18-crown-6.	76
Figure 2-53-Single crystal determined structure of 2-aminopyridine and 18-crown-6.	77
Figure 2-54- Single crystal determined structure of 4-aminopyridine and 18-crown-6.	78
Figure 2-55- Single crystal determined structure of 4-aminopyridine and 18-crown-6.	78

Figure 2-56- Single crystal determined structure of 18-crown-6 of bromopropylamine hydrobromide.	79
Figure 2-57- Single crystal determined structure of 18-crown-6 of 4-bromopropylamine hydrobromide.	79
Figure 2-58-Apparatus used in sodium-IL and lead reduction experiments. Right apparatus before sodium and lead addition and left sealed ampoule after reaction.	81
Figure 2-59-Previously reported structure for sodium bistriflamide by Matsumoto and co-workers <sup>145</sup>	81
Figure 2-60-Radical formation in Birch reductions of benzene.	82
Figure 2-61-Reduction products of 1-alkyl-4-aminopyridinium bistriflamide.	83
Figure 2-62- <sup>1</sup> H NMR of 1-pentyl-4-aminopyridinium bistriflamide after undergoing a conventional NaBH <sub>4</sub> reduction reaction in methanol for 3 days. (d <sub>3</sub> -acetonitrile).	84
Figure 2-63- <sup>1</sup> H NMR of 1-butylpyridinium bistriflamide after undergoing a conventional NaBH <sub>4</sub> reduction reaction in methanol for 3 days. (d-chloroform).	85
Figure 2-64- Synthesis of simple diamine based ionic liquids.	92
Figure 3-1-Structure of tert-butylcalix-[4]-arene and a Krater calyx <sup>159</sup>	103
Figure 3-2- Condensation reaction of p-tert-butylphenol and formaldehyde.	105
Figure 3-3-bipyridyl functionalised tert-butylcalix-[4]-arene by Grigg et al. <sup>186</sup>	107
Figure 3-4-Examples of TBC motifs for chromogenic studies used by Diamond et al. <sup>190</sup>	108
Figure 3-5-TBC functionalised by Liu et al. for alkali metal complexation. <sup>207</sup>	109
Figure 3-6- p-tert-butylcalix-[4]-arene-dialkylimidazolium cations by Shreeve and Jin. <sup>212</sup>	110
Figure 3-7-Synthetic precursors to gold nanoclusters from TBC-ILs.	111
Figure 3-8--Esterification of p-tert-butylcalix-[4]-arenes with acyl chloride via 4 different methodologies. <sup>220,222</sup>	112
Figure 3-9-Etherification of p-tert-butylcalix-[4]-arenes with simple alkyl halides via 6 different methodologies. <sup>226,228–231</sup>	113
Figure 3-10- Etherification of p-tert-butylcalix-[4]-arenes with functionalised alkyl halides. <sup>233–236</sup>	115
Figure 3-11-Formation of intramolecular bridges p-tert-butylcalix-[4]-arenes with glycols. <sup>238–240</sup>	115
Figure 3-12- Cone conformer of p-tert-butylcalix-[4]-arene highlighting -CH <sub>2</sub> - linker groups.	116
Figure 3-13-Conformers of p-tert-butylcalix-[4]-arene.	117
Figure 3-14- Carbonate Based Ionic Liquid Synthesis (CBILS <sup>®</sup> , which is a registered trademark of Proionic GmbH). <sup>2,3,270</sup>	120
Figure 3-15-p-tert-butylcalix-[4]-arene dissolved in trihexyltetradecylphosphonium acetate (L-R: 0, 2.5, 5, 7.5, 10, 12.5, 15, 20 mol %).	122
Figure 3-16-Single crystal X-ray diffraction spectroscopy determined structure of 1-methyl-3-ethylimidazolium p-tert-butylcalix-[4]-arate ionic salts.	124
Figure 3-17- Single crystal X-ray diffraction spectroscopy determined structure of 1-methyl-3-ethylimidazolium p-tert-butylcalix-[4]-arate ionic salts.	124

Figure 3-18- Representation of endo (green) and exo (blue) areas where acetate charge density may be located. _____	126
Figure 3-19- Partial $^{13}\text{C}$ NMR spectra of $[\text{P}_{66614}][\text{OAc}]$ and <i>p</i> -tert-butylcalix-[4]-arene. (top-bottom) 20, 15, 10, 5, 0 mol%. (37-13 ppm) _____	127
Figure 3-20- Partial $^{13}\text{C}$ NMR spectra of $[\text{P}_{66614}][\text{OAc}]$ and <i>p</i> -tert-butylcalix-[4]-arene. (top-bottom) 20, 15, 10, 5, 0 mol%. (176-122 ppm) _____	127
Figure 3-21-Partial $^{13}\text{C}$ NMR spectra of $[\text{P}_{66614}][\text{OAc}]$ solutions with phenol and <i>p</i> -tert-butylcalix-[4]-arene. (27-17 ppm)_____	128
Figure 3-22- Partial $^{13}\text{C}$ VT NMR study of 10 mol% TBC in $[\text{P}_{66614}][\text{OAc}]$ . Top to bottom: 75 °C, 50 °C, 25 °C. (35-10 ppm)_____	129
Figure 3-23-UV/Vis spectral change on addition of 1 equiv of DBU to tert-butylcalix-[4]-arene in MeCN by Woolfall and Cunningham. <sup>275</sup> _____	130
Figure 3-24-UV/Vis spectra of $[\text{P}_{66614}][\text{OAc}]$ and TBC 20 mol % (IL-Calix) in MeCN with varying concentrations of DBU added. _____	131
Figure 3-25-UV/Vis spectra of $[\text{P}_{66614}][\text{OAc}]$ and TBC in MeCN. _____	131
Figure 3-26- UV/Vis spectra of $[\text{P}_{66614}][\text{NTf}_2]$ and TBC in MeCN with varying concentrations of DBU added._____	132
Figure 3-27- UV/Vis spectra of $[\text{NH}_4][\text{OAc}]$ and TBC in MeCN/MeOH with excess triflic acid added (with varying concentrations of DBU added. _____	133
Figure 3-28-TGA of <i>p</i> -tert-butylcalix-[4]-arene (commercial sample). Rate of heating 1 °Cmin <sup>-1</sup> .____	134
Figure 3-29-TGA of $[\text{P}_{66614}][\text{OAc}]$ . Rate of heating 1 °C min <sup>-1</sup> . _____	135
Figure 3-30-TGA of $[\text{P}_{66614}][\text{OAc}]$ and <i>p</i> -tert-butylcalix-[4]-arene 20 mol%. Rate of heating 1 °C min <sup>-1</sup> . _____	135
Figure 3-31-Density as a variation of temperature of $[\text{P}_{66614}][\text{OAc}]$ (circles) and $[\text{P}_{66614}][\text{OAc}]$ 20 mol% <i>p</i> -tert-butylcalix-[4]-arene (triangles) _____	136
Figure 3-32- Partial IR Spectra of $[\text{P}_{66614}][\text{OAc}]$ and <i>p</i> -tert-butylcalix-[4]-arene solutions. (3500-1000 cm <sup>-1</sup> ) _____	137
Figure 3-33- Partial IR Spectra of $[\text{P}_{66614}][\text{OAc}]$ and <i>p</i> -tert-butylcalix-[4]-arene solutions. (1800-1200 cm <sup>-1</sup> ) _____	137
Figure 3-34- Partial IR Spectra of $[\text{P}_{66614}][\text{OAc}]$ and <i>p</i> -tert-butylcalix-[4]-arene solutions. (1800-1200 cm <sup>-1</sup> ) _____	138
Figure 3-35- Normalised analysis of peak height of IR spectra of $[\text{P}_{66614}][\text{OAc}]$ and <i>p</i> -tert-butylcalix-[4]-arene solutions. _____	138
Figure 3-36-Phenol and potassium acetate interactions. _____	140
Figure 3-37- Infrared spectra of phenol, 5-20 mol% K[OAc] in phenol. _____	141
Figure 3-38- Partial IR spectra of phenol, 5-20 mol% K[OAc] in phenol. (1800-1400 cm <sup>-1</sup> ). _____	142
Figure 3-39-Partial infrared spectra of phenol, K[OAc] and 20 mol% K[OAc] in phenol. (1800-1400 cm <sup>-1</sup> )._____	142

Figure 3-40-Infrared spectra of phenol, K[OAc] and 20 mol% K[OAc] in phenol.	143
Figure 3-41-Structure of 1-Ethyl-3-methylimidazolium acetate, [Emim][OAc].	144
Figure 3-42- IR analysis of [Emim][OAc] and phenol mixtures.	145
Figure 3-43-IR analysis of [Emim][OAc] and Phenol mixtures	145
Figure 3-44- $^1\text{H}$ NMR spectra of [Emim][OAc] and Phenol mixtures. Top to bottom: [Emim][OAc], 20 mol%, 25 mol%, 33 mol%, 50 mol%.	146
Figure 3-45- $^{13}\text{C}$ NMR spectra of [Emim][OAc] and Phenol mixtures. Top to bottom: [Emim][OAc], 20 mol%, 25 mol%, 33 mol%, 50 mol%.	148
Figure 3-46-Partial $^{13}\text{C}$ NMR spectra of [Emim][OAc] and phenol mixtures. Top to bottom: [Emim][OAc], 20 mol%, 25 mol%, 33 mol%, 50 mol%. (186-146 ppm)	148
Figure 3-47- Infrared analysis of phenol in acetic acid mixtures of varying molar ratios.	150
Figure 3-48- IR spectra of phenol in acetic acid mixtures of varying ratios. Acetic acid: Phenol.	150
Figure 3-49- $^1\text{H}$ NMR analysis of acetic acid and phenol mixtures. Top to bottom: acetic acid, 50 mol%, 33 mol%, 25 mol%, and 20 mol% (concentrations of acetic acid)	151
Figure 3-50- $^{13}\text{C}$ NMR analysis of phenol in acetic acid mixtures. Top to bottom: acetic acid, 50 mol%, 33 mol%, 25 mol%, and 20 mol%.	152
Figure 3-51-1,1,3,3-tetramethylguanidine reactions with alcohols and carbon dioxide. <sup>284</sup>	152
Figure 3-52-Predicted acid-base interactions of p-tert-butylcalix-[4]-arenes and 1, 1, 3, 3-tetramethylguanidine.	153
Figure 3-53- $^1\text{H}$ NMR spectra of p-tert-butylcalix-[4]-arene and 1, 1, 3, 3-tetramethylguanidine in d-acetonitrile. (top-bottom) 1,1,3,3-tetramethylguanidine in d <sub>3</sub> -acetonitrile, 4.7 mol%, 9 mol%, 16.6 mol%, 20 mol%, 25 mol%, 33 mol%, 50 mol%.	154
Figure 3-54- Delta shift from $^1\text{H}$ NMR studies of TMG-CH <sub>3</sub> with varying ratios of TBC. Solvent-d <sub>3</sub> -acetonitrile.	155
Figure 3-55- UV/Vis spectrum of p-tert-butylcalix-[4]-arene in MeCN with aliquots of 1, 1, 3, 3-tetramethylguanidine added.	156
Figure 3-56- Plot of ABS at 290 nm as a function of TMG: TBC. Numbers above each point indicating the number of equivalents of TMG bas per TBC molecule.	156
Figure 3-57-Single crystal diffraction determined structure of [TMG][TBC]and TMG interaction from a 2:1 mixture.	158
Figure 3-58-Single crystal diffraction determined structure of [TMG][TBC]and TMG interaction from a 2:1 mixture.	159
Figure 3-59-Synthesis of methyl carbonate anion ionic liquids.	159
Figure 3-60-Decomposition of the methyl carbonate anion in the presence of a Brønsted acid.	160
Figure 3-61- Synthesis of [N <sub>2,2,2,1</sub> ][TBC] using methyl carbonate ionic liquids.	161
Figure 3-62-Structure of tris (-2-methoxyethoxy) methylamine [Npeg] cation.	161
Figure 3-63- UV/Vis spectrum of [N <sub>2,2,2,1</sub> ][TBC] in MeCN (dashed) and with excess triflic acid added. (solid).	162

Figure 3-64- Single crystal diffraction determined structure of triethylmethylammonium p-tert-butylcalix-[4]-arate, [N <sub>2 2 2 1</sub> ][TBC].	163
Figure 3-65- Single crystal diffraction determined structure of triethylmethylammonium p-tert-butylcalix-[4]-arate, [N <sub>2 2 2 1</sub> ][TBC].	164
Figure 3-66- Single crystal diffraction determined structure of tributylmethylammonium p-tert-butylcalix-[4]-arate, [N <sub>4 4 4 1</sub> ][TBC].	165
Figure 3-67- Single crystal diffraction determined structure of tributylmethylammonium p-tert-butylcalix-[4]-arate, [N <sub>4 4 4 1</sub> ][TBC].	165
Figure 3-68- Reaction schematic for the alkylation of p-tert-butylcalix-[4]-arenes from organic p-tert-butylcalix-[4]-arate salts.	168
Figure 3-69- Products obtained with isolated yields for alkylations of [N <sub>2 2 2 1</sub> ][TBC] with dialkyl sulphates and alkyl halides.	170
Figure 3-70- Conformers of TBC (L-R) cone, partial cone, 1, 3-alternate and 1, 2-alternate.	170
Figure 3-71- <sup>1</sup> H NMR monitoring of [N <sub>2221</sub> ][TBC] and dimethyl sulphate in d <sub>3</sub> -chloroform.	171
Figure 3-72- Uncycled p-tert-butylphenol units and p-tert-butylcalix-[6]-arenes.	174
Figure 3-73- Sequential use of the methyl carbonate anion as a deprotonation method for tetra-functionalised p-tert-butylcalix-[4]-arene.	175
Figure 3-74- Attenuated Total Reflection Infrared spectroscopy technique.	178
Figure 4-1- Plot demonstrating chloroaluminate species present in chloroaluminate ionic liquids by Wilkes et al. <sup>317</sup>	188
Figure 4-2- Acetylation of benzaldehyde with chlorogallate and chloroindate ionic liquids.	193
Figure 4-3- Homolytic and heterolytic cleavage of ammonia diborane complexes. <sup>382</sup>	196
Figure 4-4- Pictorial representation of Ga <sup>1</sup> -Cl bond strength as a function of L donor strength in L-GaCl <sub>2</sub> -(μCl)-GaCl <sub>3</sub> bu Hogg. <sup>382</sup>	197
Figure 4-5- Diagram showing a typical EXAFS spectrum.	199
Figure 4-6- Generation of a photo-electron in EXAFS spectroscopy.	201
Figure 4-7- Reproduced and annotated EXAFS spectra of mixed oxidation state manganese oxide doped materials. <sup>389</sup>	202
Figure 4-8- EXAFS single scattering in condensed matter.	202
Figure 4-9- EXAFS sample holders (left) thin liquid samples sandwiched between Kapton tape with a 1mm polycarbomer spacer (right) solid pellet sealed with Kapton tape.	206
Figure 4-10- EXAFS fitting procedure using the Demeter software package.	208
Figure 4-11- Density of P <sub>888</sub> E-GaCl <sub>3</sub> χ <sub>GaCl<sub>3</sub></sub> = 0.50.	211
Figure 4-12- VFT plot of P <sub>888</sub> E-GaCl <sub>3</sub> LCCs χ <sub>GaCl<sub>3</sub></sub> = 0.60.	215
Figure 4-13- VFT plot of P <sub>888</sub> O-GaCl <sub>3</sub> LCCs.	215
Figure 4-14- VFT plot of P <sub>888</sub> S-GaCl <sub>3</sub> LCCs.	216
Figure 4-15- VFT plot of P <sub>888</sub> Se-GaCl <sub>3</sub> LCCs.	216

Figure 4-16- <sup>31</sup> P NMR spectra of P <sub>888</sub> O-GaCl <sub>3</sub> $\chi_{\text{GaCl}_3} = 0.50$ (top), P <sub>888</sub> S-GaCl <sub>3</sub> $\chi_{\text{GaCl}_3} = 0.50$ (middle) and P <sub>888</sub> Se-GaCl <sub>3</sub> $\chi_{\text{GaCl}_3} = 0.50$ (bottom).	219
Figure 4-17- <sup>31</sup> P NMR spectra of P <sub>888</sub> Se-GaCl <sub>3</sub> $\chi_{\text{GaCl}_3} = 0.75$ , $\chi_{\text{GaCl}_3} = 0.67$ , $\chi_{\text{GaCl}_3} = 0.60$ , $\chi_{\text{GaCl}_3} = 0.50$ .	219
Figure 4-18- <sup>77</sup> Se NMR spectra of P <sub>888</sub> Se-GaCl <sub>3</sub> $\chi_{\text{GaCl}_3} = 0.75$ , $\chi_{\text{GaCl}_3} = 0.67$ , $\chi_{\text{GaCl}_3} = 0.60$ , $\chi_{\text{GaCl}_3} = 0.50$ .	221
Figure 4-19- <sup>77</sup> Se NMR of P <sub>888</sub> Se-GaCl <sub>3</sub> $\chi_{\text{GaCl}_3} = 0.60$ in d-dichloromethane at 20, 10, 0, -10, -20 °C.	221
Figure 4-20- <sup>31</sup> P NMR spectra of P <sub>888</sub> S-GaCl <sub>3</sub> $\chi_{\text{GaCl}_3} = 0.60$ in d-dichloromethane at 20 °C, 0 °C, -20 °C, -40 °C, -60 °C.	223
Figure 4-21- <sup>31</sup> P NMR spectra of P <sub>888</sub> O-GaCl <sub>3</sub> mixtures (top-bottom) $\chi_{\text{GaCl}_3} = 0.75, 0.67, 0.60, 0.50$ .	225
Figure 4-22-Stacked plot of Raman spectra of P <sub>888</sub> S-GaCl <sub>3</sub> LCCs. (top-bottom) $\chi_{\text{GaCl}_3} = 0.75, 0.67, 0.60, 0.50$ .	227
Figure 4-23- Stacked plot of Raman spectra of P <sub>888</sub> E-GaCl <sub>3</sub> LCCs. $\chi_{\text{GaCl}_3} = 0.50$ .	229
Figure 4-24-Stacked plot of Raman spectra of P <sub>888</sub> Se-GaCl <sub>3</sub> LCCs. (top-bottom) $\chi_{\text{GaCl}_3} = 0.75, 0.67, 0.60, 0.50$ .	229
Figure 4-25-Expanded Infrared spectra of P <sub>888</sub> S-GaCl <sub>3</sub> LCCs.	230
Figure 4-26- Possible species within chlorogallate LCCs.	232
Figure 4-27- EXAFS fit for P <sub>888</sub> Se-GaCl <sub>3</sub> $\chi_{\text{GaCl}_3} = 0.50$ in k-space.	233
Figure 4-28-EXAFS fits for P <sub>888</sub> O-GaCl <sub>3</sub> (top-bottom) $\chi_{\text{GaCl}_3} = 0.50, 0.60, 0.67$ in k-space.	234
Figure 4-29- EXAFS fit for P <sub>888</sub> O-GaCl <sub>3</sub> (top-bottom) $\chi_{\text{GaCl}_3} = 0.50, 0.60, 0.67$ in R-space.	235
Figure 4-30- EXAFS fit for P <sub>888</sub> Se-GaCl <sub>3</sub> $\chi_{\text{GaCl}_3} = 0.50$ in R-space	236
Figure 4-31- Density plot of P <sub>888</sub> E-InCl <sub>3</sub> $\chi_{\text{InCl}_3} = 0.40$ .	242
Figure 4-32- VFT fit of P <sub>888</sub> O-InCl <sub>3</sub> LCCs $\chi_{\text{InCl}_3} = 0.25, 0.33, 0.40$ .	244
Figure 4-33- VFT fit of P <sub>888</sub> S-InCl <sub>3</sub> LCCs $\chi_{\text{InCl}_3} = 0.25, 0.33, 0.40$ .	244
Figure 4-34- VFT fit of P <sub>888</sub> Se-InCl <sub>3</sub> LCCs $\chi_{\text{InCl}_3} = 0.25, 0.33, 0.40$ .	245
Figure 4-35- VFT fit of P <sub>888</sub> E-InCl <sub>3</sub> LCCs $\chi_{\text{InCl}_3} = 0.25$ .	245
Figure 4-36- <sup>31</sup> P NMR spectra of P <sub>888</sub> O-InCl <sub>3</sub> $\chi_{\text{InCl}_3} = 0.50$ (top), P <sub>888</sub> S-InCl <sub>3</sub> $\chi_{\text{InCl}_3} = 0.50$ (middle) and P <sub>888</sub> Se-InCl <sub>3</sub> $\chi_{\text{InCl}_3} = 0.50$ . (Bottom)	247
Figure 4-37- <sup>31</sup> P NMR spectra of P <sub>888</sub> Se-InCl <sub>3</sub> LCCs (top-bottom) $\chi_{\text{InCl}_3} = 0.50, 0.40, 0.33$ & $0.25$ .	247
Figure 4-38- <sup>31</sup> P NMR spectra of P <sub>888</sub> O-InCl <sub>3</sub> $\chi_{\text{InCl}_3} = 0.50$ , $\chi_{\text{InCl}_3} = 0.40$ , $\chi_{\text{InCl}_3} = 0.33$ , $\chi_{\text{InCl}_3} = 0.25$ , $\chi_{\text{InCl}_3} = 0.10$ * *NMR spectra recorded at 70 °C. (Top-bottom)	248
Figure 4-39- Suggested structures present in P <sub>888</sub> E-InCl <sub>3</sub> LCCs.	249
Figure 4-40- <sup>77</sup> Se NMR spectra of P <sub>888</sub> Se-InCl <sub>3</sub> $\chi_{\text{InCl}_3} = 0.50$ , $\chi_{\text{InCl}_3} = 0.40$ , $\chi_{\text{InCl}_3} = 0.33$ , $\chi_{\text{InCl}_3} = 0.25$ . (Top-bottom)	250
Figure 4-41- Rescaled stacked plot of Raman spectra of P <sub>888</sub> S-InCl <sub>3</sub> LCCs. (top-bottom) $\chi_{\text{InCl}_3} = 0.33, 0.25$ .	252
Figure 4-42-Rescaled stacked plot of Raman spectra of P <sub>888</sub> Se-InCl <sub>3</sub> LCCs. (top-bottom) $\chi_{\text{GaCl}_3} = 0.33, 0.25$ .	253



Figure 4-43- Expanded Infrared spectra of $P_{888}S-InCl_3$ LCCs.	254
Figure 5-1- Speciation studies of Cu (II) by Ishiguro et al. in acetonitrile solvent.	264
Figure 5-2-Suspected auto complexation by Gutmann and Elleb-(adapted figure). <sup>459</sup>	265
Figure 5-3-Reproduced schematic of various cation-anion structures in ionic liquid-water mixture for various mole fractions of water as indicated by Fulton and co-workers. <sup>482</sup>	268
Figure 5-4- Part of the crystal structure of the polymeric $[CuCl-(Se_2Ph_2)_2]_n$ . Ellipsoids are shown at a 50% probability level. <sup>509</sup>	272
Figure 5-5-Variable temperature NMR $^{31}P-\{^1H\}$ and $^{63}Cu$ NMR spectra of $[Cu(PPhH_2)_4]^+$ . <sup>500</sup>	275
Figure 5-6- $^{31}P$ NMR spectra of $P_{888}-CuCl$ $\chi_{CuCl} = 0.50, 0.33, 0.25$ . (Top-bottom).	277
Figure 5-7- $^{31}P$ NMR of $P_{888}Se-CuCl$ $\chi_{CuCl} = 0.50, 0.33$ . $P_{888}Se$ . (Top to bottom)	277
Figure 5-8- $^{31}P$ NMR of $P_{888}S-CuCl$ $\chi_{CuCl} = 0.50, 0.33$ and $P_{888}S$ . (Top-bottom)	278
Figure 5-9- LCCs (L-R) $P_{888}S-CuCl_2$ $\chi_{CuCl_2}=0.50$ and $P_{888}Se-CuCl_2$ $\chi_{CuCl_2} = 0.50$ .	279
Figure 5-10- SEM analysis of $P_{888}Se-CuCl_2$ $\chi_{CuCl_2} = 0.50$ precipitate.	279
Figure 5-11- $^{31}P$ NMR of $P_{888}S-CuCl$ $\chi_{CuCl} = 0.50$ , $P_{888}S-CuCl$ $\chi_{CuCl} = 0.33$ , $P_{888}S-CuCl_2$ $\chi_{CuCl_2} = 0.50$ and $P_{888}-CuCl$ $\chi_{CuCl} = 0.50$ . (Top-bottom)	280
Figure 5-12- $^{31}P$ NMR of $P_{888}Se$ , $P_{888}Se-CuCl$ $\chi_{CuCl} = 0.50$ , $P_{888}Se-CuCl_2$ $\chi_{CuCl_2} = 0.50$ and $P_{888}-CuCl$ $\chi_{CuCl} = 0.50$ . (Top-bottom)	281
Figure 5-13- $^{31}P$ NMR of $P_{888}-CuCl$ $\chi_{CuCl} = 0.25$ , and fresh $P_{888}-CuCl_2$ $\chi_{CuCl_2} = 0.25$ .	282
Figure 5-14- $^{31}P$ NMR of $P_{888}-CuCl_2$ LCCs made fresh, after 3 weeks, 3months and 6 months.	284
Figure 5-15- Raman spectra of $P_{888}-CuCl$ $\chi_{CuCl} = 0.25, 0.33$ & $0.50$ .	285
Figure 5-16- UV/Vis spectra of $P_{888}-CuCl$ $\chi_{CuCl} = 0.25$ and $0.50$ .	286
Figure 5-17- UV/Vis spectra of $P_{888}-CuCl$ $\chi_{CuCl} = 0.25$ in a 0.50 mm UV/Vis and quartz thin plate (TP).	287
Figure 5-18- UV/Vis spectra of $P_{888}-CuCl$ $\chi_{CuCl} = 0.50$ in a 0.50 mm UV/Vis and quartz thin plate (TP).	287
Figure 5-19-Infrared spectra of $P_{888}-CuCl$ $\chi_{CuCl} = 0.50, 0.33, 0.25$ .	289
Figure 5-20- Infrared spectra of $P_{888}O-CuCl$ $\chi_{CuCl} = 0.50, 0.33, 0.25$ .	289
Figure 5-21- Infrared spectra of $P_{888}O-CuCl_2$ $\chi_{CuCl_2} = 0.50, 0.33, 0.25$ .	290
Figure 5-22- Infrared spectra of $P_{888}S-CuCl$ $\chi_{CuCl} = 0.50, 0.33, 0.25$ and $P_{888}S-CuCl_2$ $\chi_{CuCl_2} = 0.50$ liquor.	290
Figure 5-23- Infrared spectra of $P_{888}Se-CuCl$ $\chi_{CuCl} = 0.50, 0.33, 0.25$ and $P_{888}Se-CuCl_2$ $\chi_{CuCl_2} = 0.50$ liquor.	291
Figure 5-24- Figure by Eller and Corfield of $[Cu(SPMe_3)_3][ClO_4]$ salt as determined by single crystal diffraction. <sup>524</sup>	291
Figure 5-25-Equilibria predictions by Lippard and Mayerle <sup>525</sup>	292
Figure 5-26-Postulated structures of tricyclohexylphosphine and Cu(I) salts in solution. <sup>526,527</sup>	293
Figure 5-27- Normalized overlaid EXAFS spectra of $P_{888}-CuCl$ $\chi_{CuCl} = 0.25, 0.33$ & $0.50$ .	294

Figure 5-28- Normalized stacked EXAFS spectra of $P_{888}\text{-CuCl}$ $\chi_{\text{CuCl}} = 0.25, 0.33 \text{ \& } 0.50$ .	294
Figure 5-29. Normalized overlaid EXAFS spectra of $P_{888}\text{-CuCl}$ $\chi_{\text{CuCl}} = 0.25, 0.33 \text{ \& } 0.50$ in $k$ -space.	295
Figure 5-30. Normalized overlaid EXAFS spectra of $P_{888}\text{-CuCl}$ $\chi_{\text{CuCl}} = 0.25, 0.33 \text{ \& } 0.50$ in $R$ -space.	295
Figure 5-31- R-factor of EXAFS fits of $P_{888}\text{-CuCl}$ $\chi_{\text{CuCl}} = 0.50$ as a function of $N_{\text{Cu-Cl}}/N_{\text{total}}$ .	296
Figure 5-32- R-factor of EXAFS fits of $P_{888}\text{-CuCl}$ $\chi_{\text{CuCl}} = 0.50$ as a function of $N_{\text{Cu-Cl}}/N_{\text{total}}$ .	298
Figure 5-33- R-factor of EXAFS fits of $P_{888}\text{-CuCl}$ $\chi_{\text{CuCl}} = 0.25$ as a function of $N_{\text{Cu-Cl}}/N_{\text{total}}$ .	298
Figure 5-34- R-factor of EXAFS fits of $P_{888}\text{-CuCl}$ $\chi_{\text{CuCl}} = 0.25$ as a function of $N_{\text{Cu-Cl}}/N_{\text{total}}$ .	299
Figure 5-35- R-factor of EXAFS fits of $P_{888}\text{-CuCl}$ $\chi_{\text{CuCl}} = 0.33$ as a function of $N_{\text{Cu-Cl}}/N_{\text{total}}$ .	299
Figure 5-36- R-factor of EXAFS fits of $P_{888}\text{-CuCl}$ $\chi_{\text{CuCl}} = 0.33$ as a function of $N_{\text{Cu-Cl}}/N_{\text{total}}$ .	300
Figure 5-37- EXAFS fits for $P_{888}\text{-CuCl}$ $\chi_{\text{CuCl}} = 0.25, 0.33$ and $0.50$ . $P_{888}\text{-CuCl}$ $\chi_{\text{CuCl}} = 0.25$ $N_{\text{total}} = 4$ $N_{\text{Cu-P}} = 3.18$ $N_{\text{Cu-Cl}} = 0.82$ ; $\chi_{\text{CuCl}} = 0.33$ $N_{\text{total}} = 3.33$ $\text{Cu-Cl} = 0.476$ $\text{Cu-P} = 2.854$ ; $P_{888}\text{-CuCl}$ $\chi_{\text{CuCl}} = 0.50$ $N_{\text{total}} = 2.67$ $N_{\text{Cu-P}} = 1.49$ $N_{\text{Cu-Cl}} = 1.18$ .	302
Figure 5-38- Triphenylphosphine copper(I) chloride complex from which EXAFS fits were modelled. CCDC- TPCUCL12.	303
Figure 5-39. Figure reproduced from Hodgson and co-workers highlighting the 4p orbital splitting that occurs in in Cu(I) complexes. <sup>533</sup>	306
Figure 5-40- Pictorial representation of the sources of the numerical analysis in Table 5-10.	307
Figure 5-41. Overlaid plot of high resolution XANES of $P_{888}\text{-CuCl}$ $\chi_{\text{CuCl}} = 0.10, 0.25, 0.33, 0.50$ .	308
Figure 5-42. Stacked plot of high resolution XANES of $P_{888}\text{-CuCl}$ $\chi_{\text{CuCl}} = 0.10, 0.25, 0.33, 0.50$ .	308
Figure 5-43- Visible sample degradation in $P_{888}\text{-CuCl}_2$ samples upon exposure to X-ray beam.	309
Figure 5-44- $P_{888}\text{-CuCl}_2$ LCCs (L-R) $\chi_{\text{CuCl}_2} = 0.60, 0.50, 0.33, 0.25$ and the two-phase solution that forms after 3 months.	311
Figure 5-45-(top -bottom) $^{31}\text{P}$ NMR of $P_{888}\text{-CuCl}$ $\chi_{\text{CuCl}} = 0.50$ + elemental sulphur, $P_{888}\text{-CuCl}$ $\chi_{\text{CuCl}} = 0.50$ + elemental selenium, $P_{888}\text{-CuCl}$ $\chi_{\text{CuCl}} = 0.50$ + elemental tellurium.	313
Figure 5-46-(top -bottom) $^{31}\text{P}$ NMR of $P_{888}\text{-CuCl}$ $\chi_{\text{CuCl}} = 0.50$ , $P_{888}\text{Se-CuCl}$ $\chi_{\text{CuCl}} = 0.50$ , $P_{888}\text{-CuCl}$ $\chi_{\text{CuCl}} = 0.50$ + elemental selenium.	313
Figure 5-47--(top -bottom) $^{31}\text{P}$ NMR of $P_{888}\text{-CuCl}$ $\chi_{\text{CuCl}} = 0.50$ , $P_{888}\text{S-CuCl}$ $\chi_{\text{CuCl}} = 0.50$ , and $P_{888}\text{-CuCl}$ , $\chi_{\text{CuCl}} = 0.50$ and elemental sulphur.	314
Figure 5-48- Infrared spectra of $P_{888}\text{-CuCl}$ $\chi_{\text{CuCl}} = 0.50$ with elemental sulphur, selenium and tellurium.	315
Figure 5-49- Infrared spectra of $P_{888}\text{-CuCl}$ $\chi_{\text{CuCl}} = 0.50$ with elemental sulphur, selenium and tellurium.	315
Figure 5-50-(top-bottom) $^{31}\text{P}$ NMR of $P_{888}\text{-CuCl}$ $\chi_{\text{CuCl}} = 0.50$ , $P_{888}\text{-CuCl}_2$ $\chi_{\text{CuCl}_2} = 0.50$ + elemental sulphur, $P_{888}\text{-CuCl}_2$ $\chi_{\text{CuCl}_2} = 0.50$ + elemental selenium, $P_{888}\text{-CuCl}_2$ $\chi_{\text{CuCl}_2} = 0.50$ + elemental tellurium.	319
Figure 5-51- $^{31}\text{P}$ NMR of $P_{888}\text{-CuCl}_2$ $\chi_{\text{CuCl}_2} = 0.33$ and $0.50$ + elemental selenium.	319
Figure 5-52- $^{77}\text{Se}$ NMR of $P_{888}\text{-CuCl}_2$ $\chi_{\text{CuCl}_2} = 0.50$ + elemental selenium.	320

Figure 5-53-Infrared spectra of $P_{888}\text{-CuCl}_2$ $\chi_{\text{CuCl}_2} = 0.50$ with elemental sulphur, selenium and tellurium.	320
Figure 5-54- Summary of chlorocuprate liquid coordination complexes and chalcogenide interactions.	323
Figure 5-55- $P_{888}\text{Se-GaCl}_3$ $\chi_{\text{GaCl}_3} = 0.50$ (a) LCC, (b) after microwave irradiation $80^\circ\text{C}$ for 30 s (c) isolated product	324
Figure 5-56-SEM image of microwave irradiated product of $P_{888}\text{Se-GaCl}_3$ $\chi_{\text{GaCl}_3} = 0.50$ .	325
Figure 5-57-EDX analysis of microwave irradiated $P_{888}\text{Se-GaCl}_3$ $\chi_{\text{GaCl}_3} = 0.50$ .	325
Figure 5-58-pXRD diffraction pattern of microwave irradiated $P_{888}\text{Se-GaCl}_3$ $\chi_{\text{GaCl}_3} = 0.50$ and ICSD PXRD pattern by Flahaut et al. <sup>546</sup>	325
Figure 5-59-(a) product formed with $P_{888}\text{Se-GaCl}_3$ $\chi_{\text{GaCl}_3} = 0.67$ (b) product after 96 hours exposure to air.	327
Figure 5-60-SEM analysis of ionothermal $P_{888}\text{Se-GaCl}_3$ $\chi_{\text{GaCl}_3} = 0.67$ reaction products.	327
Figure 5-61-EDX analysis of ionothermal $P_{888}\text{Se-GaCl}_3$ $\chi_{\text{GaCl}_3} = 0.67$ reaction product.	328
Figure 5-62-SEM analysis of ionothermal $P_{888}\text{Se-InCl}_3$ $\chi_{\text{InCl}_3} = 0.25$ reaction product.	329
Figure 5-63-EDX analysis of ionothermal $P_{888}\text{Se-InCl}_3$ $\chi_{\text{InCl}_3} = 0.25$ reaction product.	329
Figure 5-64-PXRD analysis of ionothermal $P_{888}\text{Se-InCl}_3$ $\chi_{\text{InCl}_3} = 0.25$ reaction product and ICSD PXRD pattern by D. Carre et al. <sup>547</sup>	330
Figure 5-65-SEM analysis of $P_{888}\text{Se-CuCl}$ $\chi_{\text{CuCl}} = 0.33$ reaction product.	331
Figure 5-66- Elemental distribution of $P_{888}\text{Se-CuCl}$ $\chi_{\text{CuCl}} = 0.33$ reaction product.	331
Figure 5-67-pXRD analysis of $P_{888}\text{Se-CuCl}$ $\chi_{\text{CuCl}} = 0.33$ reaction product (black) and ICSD reported $\text{Cu}_1.75\text{Se}$ reported structure (red). <sup>552</sup>	332
Figure 5-68- SEM analysis of $P_{888}\text{S-CuCl}$ $\chi_{\text{CuCl}} = 0.33$ isolated reaction product.	333
Figure 5-69-EDX mapping analysis of $P_{888}\text{S-CuCl}$ $\chi_{\text{CuCl}} = 0.33$ isolated reaction product.	334
Figure 5-70-SEM analysis of $P_{888}\text{Se-CuCl}$ $\chi_{\text{CuCl}} = 0.50$ , $P_{888}\text{Se-GaCl}_3$ $\chi_{\text{GaCl}_3} = 0.50$ and $P_{888}\text{-InCl}_3$ $\chi_{\text{InCl}_3} = 0.50$ in a 1:1:1 molar ratio isolated reaction product.	336
Figure 5-71- EDX analysis of $P_{888}\text{Se-CuCl}$ $\chi_{\text{CuCl}} = 0.50$ , $P_{888}\text{Se-GaCl}_3$ $\chi_{\text{GaCl}_3} = 0.50$ and $P_{888}\text{-InCl}_3$ $\chi_{\text{InCl}_3} = 0.50$ in a 1:1:1 molar ratio isolated reaction product.	336
Figure 5-72- EDX mapping of $P_{888}\text{Se-CuCl}$ $\chi_{\text{CuCl}} = 0.50$ , $P_{888}\text{Se-GaCl}_3$ $\chi_{\text{GaCl}_3} = 0.50$ and $P_{888}\text{-InCl}_3$ $\chi_{\text{InCl}_3} = 0.50$ in a 1:1:1 molar ratio isolated reaction product.	337
Figure 5-73-pXRD analysis of $P_{888}\text{Se-CuCl}$ $\chi_{\text{CuCl}} = 0.50$ , $P_{888}\text{Se-GaCl}_3$ $\chi_{\text{GaCl}_3} = 0.50$ and $P_{888}\text{-InCl}_3$ $\chi_{\text{InCl}_3} = 0.50$ in a 1:1:1 molar ratio isolated reaction product.	337
Figure 5-74-SEM analysis of $P_{888}\text{Se-CuCl}$ $\chi_{\text{CuCl}} = 0.50$ , $P_{888}\text{Se-GaCl}_3$ $\chi_{\text{GaCl}_3} = 0.50$ and $P_{888}\text{-InCl}_3$ $\chi_{\text{InCl}_3} = 0.50$ in a 1:1:1 molar ratio and elemental gallium isolated reaction product.	338
Figure 5-75-EDX analysis of $P_{888}\text{Se-CuCl}$ $\chi_{\text{CuCl}} = 0.50$ , $P_{888}\text{Se-GaCl}_3$ $\chi_{\text{GaCl}_3} = 0.50$ and $P_{888}\text{-InCl}_3$ $\chi_{\text{InCl}_3} = 0.50$ in a 1:1:1 molar ratio and elemental gallium isolated reaction product.	339

Figure 5-76-PXRD analysis of $P_{888}Se-CuCl$ $\chi_{CuCl} = 0.50$ , $P_{888}Se-GaCl_3$ $\chi_{GaCl_3} = 0.50$ and $P_{888}-InCl_3$ $\chi_{InCl_3} = 0.50$ in a 1:1:1 molar ratio and elemental gallium isolated reaction product.	339
Figure 5-77-SEM analysis of $P_{888}Se-CuCl$ $\chi_{CuCl} = 0.50$ , and $P_{888}Se-GaCl_3$ $\chi_{GaCl_3} = 0.50$ in a 1:1 molar ratio isolated reaction product.	340
Figure 5-78-EDX analysis of $P_{888}Se-CuCl$ $\chi_{CuCl} = 0.50$ , and $P_{888}Se-GaCl_3$ $\chi_{GaCl_3} = 0.50$ in a 1:1 molar ratio isolated reaction product.	341
Figure 5-79-Pictorial representation of LCC 'printing' of semiconductors.	343
Figure 8-1- $^1H$ NMR (300 MHz, $D_2O$ ) spectra of 1-Butyl-4-aminopyridinium bromide.	398
Figure 8-2- $^1H$ NMR (300 MHz, $D_2O$ ) spectra of 1-ethyl-4-aminopyridinium bromide.	398
Figure 8-3- $^1H$ NMR (300 MHz, $D_2O$ ) spectra of 1-pentyl-4-aminopyridinium bromide.	399
Figure 8-4- $^1H$ NMR (300 MHz, $D_2O$ ) spectra of 1-hexyl-4-aminopyridinium bromide.	399
Figure 8-5- $^1H$ NMR (300 MHz, $CDCl_3$ ) spectra of 1-Hexyl-N, N-dimethyl-pyridin-1-ium-4-amine iodide.	400
Figure 8-6- $^{13}C$ NMR ( $CD_3CN$ ) spectra of 1-Butyl-4-aminopyridinium bistriflamide.	400
Figure 8-7- $^{19}F$ NMR ( $CD_3CN$ ) spectra of 1-Butyl-4-aminopyridinium bistriflamide.	401
Figure 8-8- $^1H$ NMR spectra ( $CDCl_3$ ) of phthalic anhydride protected 2-aminopropuldimethylamine.	401
Figure 8-9- $^1H$ NMR spectra ( $CD_6CO$ ) of phthalic anhydride protected-2-Aminopropyl (dimethyl)pentylammonium iodide	402
Figure 8-10- $^1H$ NMR spectra ( $CDCl_3$ ) of 2-Aminopropyl(dimethyl)pentylammonium iodide.	402
Figure 8-11- $^1H$ NMR spectra ( $CO(CD_3)_2$ ) of 2-Aminopropyl(dimethyl)pentylammonium bistriflamide.	403
Figure 8-12- $^{19}F$ NMR spectra ( $CO(CD_3)_2$ ) of 2-Aminopropyl(dimethyl)pentylammonium bistriflamide.	403
Figure 8-13- $^1H$ NMR spectrum of a commercial sample of p-tert-butylcalix-[4]-arene	404
Figure 8-14- $^1H$ NMR spectrum of Tributylmethylammonium tert-butylcalix-[4]-arate salt.	404
Figure 8-15- $^1H$ NMR spectrum of Triethylmethylammonium tert-butylcalix-[4]-arate salt.	405
Figure 8-16- $^{13}C$ NMR spectrum of Triethylmethylammonium tert-butylcalix-[4]-arate salt.	405
Figure 8-17- $^1H$ NMR of methylated p-tert-butylcalix-[4]arene via dimethyl sulphate.	406
Figure 8-18-HSQC of methylated p-tert-butylcalix-[4]-arene via dimethyl sulphate.	406
Figure 8-19- $^{13}C$ NMR of methylated p-tert-butylcalix-[4]-arene via dimethyl sulphate.	407
<b>Figure 8-20-<math>^1H</math> NMR of methylated p-tert-butylcalix-[4]-arene via dimethyl sulphate with a drop of <math>D_2O</math>.</b>	407
Figure 8-21- $^1H$ NMR of ethylated p-tert-butylcalix-[4]-arene via diethyl sulphate.	408
Figure 8-22- $^{13}C$ NMR ethylated p-tert-butylcalix-[4]-arene via diethyl sulphate.	408
Figure 8-23-HSQC of ethylated p-tert-butylcalix-[4]-arene via diethyl sulphate.	409
Figure 8-24- $^1H$ NMR of ethylated p-tert-butylcalix-[4]-arene via diethyl sulphate with a $D_2O$ shake.	409
Figure 8-25- $^1H$ NMR of propylated p-tert-butylcalix-[4]-arene via dipropyl sulphate.	410

Figure 8-26- $^1\text{H}$ NMR of propylated <i>p</i> -tert-butylcalix-[4]-arene via dipropyl sulphate with $\text{D}_2\text{O}$ shake.	410
Figure 8-27- $^{13}\text{C}$ NMR of propylated <i>p</i> -tert-butylcalix-[4]-arene via dipropyl sulphate with $\text{D}_2\text{O}$ shake.	411
Figure 8-28-HSQC of propylated <i>p</i> -tert-butylcalix-[4]-arene via dipropyl sulphate.	411
Figure 8-29- $^1\text{H}$ NMR of butylated <i>p</i> -tert-butylcalix-[4]-arene via dibutyl sulphate.	412
Figure 8-30- $^{13}\text{C}$ NMR of butylated <i>p</i> -tert-butylcalix-[4]-arene via dibutyl sulphate.	412
Figure 8-31-HSQC of butylated <i>p</i> -tert-butylcalix-[4]-arene via dibutyl sulphate.	413
Figure 8-32- $^1\text{H}$ NMR of butylated <i>p</i> -tert-butylcalix-[4]-arene via dibutyl sulphate with $\text{D}_2\text{O}$ shake.	413
Figure 8-33- $^1\text{H}$ NMR of methylated <i>p</i> -tert-butylcalix-[4]-arene via methyl iodide.	414
Figure 8-34- $^{13}\text{C}$ NMR of methylated <i>p</i> -tert-butylcalix-[4]-arene via methyl iodide.	414
Figure 8-35-HSQC of methylated <i>p</i> -tert-butylcalix-[4]-arene via methyl iodide.	415
Figure 8-36- $^1\text{H}$ NMR of methylated <i>p</i> -tert-butylcalix-[4]-arene via methyl iodide with $\text{D}_2\text{O}$ shake.	415
Figure 8-37- $^1\text{H}$ NMR of ethylated <i>p</i> -tert-butylcalix-[4]-arene via ethyl iodide.	416
Figure 8-38- $^{13}\text{C}$ NMR of ethylated <i>p</i> -tert-butylcalix-[4]-arene via ethyl iodide.	416
Figure 8-39- $^1\text{H}$ NMR of ethylated <i>p</i> -tert-butylcalix-[4]-arene via ethyl iodide with a $\text{D}_2\text{O}$ shake.	417
Figure 8-40-HSQC of ethylated <i>p</i> -tert-butylcalix-[4]-arene via ethyl iodide.	417
Figure 8-41- $^1\text{H}$ NMR of ethylated <i>p</i> -tert-butylcalix-[4]-arene via ethyl iodide with $\text{D}_2\text{O}$ .	418
Figure 8-42- $^1\text{H}$ NMR of propylated <i>p</i> -tert-butylcalix-[4]-arene via propyl iodide.	418
Figure 8-43- $^{13}\text{C}$ NMR of propylated <i>p</i> -tert-butylcalix-[4]-arene via propyl iodide.	419
Figure 8-44-HSQC of propylated <i>p</i> -tert-butylcalix-[4]-arene via propyl iodide.	419
Figure 8-45- $^1\text{H}$ NMR of propylated <i>p</i> -tert-butylcalix-[4]-arene via propyl iodide with $\text{D}_2\text{O}$ shake.	420
Figure 8-46- $^1\text{H}$ NMR of butylated <i>p</i> -tert-butylcalix-[4]-arene via butyl iodide.	420
Figure 8-47- $^{13}\text{C}$ NMR of butylated <i>p</i> -tert-butylcalix-4-arene via butyl iodide.	421
Figure 8-48-TGA analysis of <i>p</i> -tert-butylcalix-[4]-arene.	421
Figure 8-49-TGA of trihexyltertrdecylphosphonium acetate, $[\text{P}_{66614}][\text{OAc}]$ .	422
Figure 8-50-TGA analysis of $[\text{P}_{66614}][\text{OAc}]$ and <i>p</i> -tert-butylcalix-[4]-arene 20 mol%.	422
Figure 8-51- TGA analysis of tributylmethylammonium <i>p</i> -tert-butylcalix-[4]-arate, $[\text{N}_{4441}][\text{TBC}]$ .	422
Figure 8-52-TGA analysis of triethylmethylammonium <i>p</i> -tert-butylcalix-[4]-arate, $[\text{N}_{2221}][\text{TBC}]$ .	423
Figure 8-53- Density plot of $\text{P}_{888}\text{O}-\text{GaCl}_3$ .	427
Figure 8-54- Density plot of $\text{P}_{888}\text{S}-\text{GaCl}_3$ .	427
Figure 8-55- Density plot of $\text{P}_{888}\text{Se}-\text{GaCl}_3$ .	428
Figure 8-56- Density plot of $\text{P}_{888}\text{O}-\text{InCl}_3$ .	428
Figure 8-57- Density plot of $\text{P}_{888}\text{S}-\text{InCl}_3$ .	429
Figure 8-58- Density plot of $\text{P}_{888}\text{Se}-\text{InCl}_3$ .	429
Figure 8-59- $^{31}\text{P}$ NMR spectra of $\text{P}_{888}\text{O}$ , $\text{P}_{888}\text{S}$ and $\text{P}_{888}\text{Se}$ . (Top-bottom)	432
Figure 8-60- $^{77}\text{Se}$ NMR spectra of $\text{P}_{888}\text{Se}$ .	432
Figure 8-61- $^{31}\text{P}$ NMR spectra of $\text{P}_{888}\text{O}-\text{GaCl}_3$ mixtures (top-bottom) $\chi_{\text{GaCl}_3} = 0.75, 0.67, 0.60, 0.50$ .	433

Figure 8-62- <sup>31</sup> P NMR spectra of P <sub>888</sub> S-GaCl <sub>3</sub> LCCs (top-bottom) $\chi_{\text{GaCl}_3} = 0.75, 0.67, 0.60 \text{ \& } 0.50$	433
Figure 8-63- <sup>31</sup> P NMR spectra of P <sub>888</sub> O-InCl <sub>3</sub> LCCs (top-bottom) $\chi_{\text{InCl}_3} = 0.50, 0.40, 0.33 \text{ \& } 0.25$	434
Figure 8-64- <sup>31</sup> P NMR spectra of P <sub>888</sub> S-InCl <sub>3</sub> LCCs (top-bottom) $\chi_{\text{InCl}_3} = 0.50, 0.40, 0.33 \text{ \& } 0.25$	434
Figure 8-65- <sup>31</sup> P NMR spectra of P <sub>888</sub> Se-InCl <sub>3</sub> LCCs (top-bottom) $\chi_{\text{InCl}_3} = 0.50, 0.40, 0.33 \text{ \& } 0.25$	435
Figure 8-66- <sup>77</sup> Se NMR spectra of P <sub>888</sub> Se-InCl <sub>3</sub> LCCs (top-bottom) $\chi_{\text{InCl}_3} = 0.50, 0.40, 0.33 \text{ \& } 0.25$	435
Figure 8-67-Infrared spectra of P <sub>888</sub> S-GaCl <sub>3</sub> LCCs.	439
Figure 8-68-Expanded Infrared spectra of P <sub>888</sub> S-GaCl <sub>3</sub> LCCs.	440
Figure 8-69- Infrared spectra of P <sub>888</sub> S-InCl <sub>3</sub> LCCs.	440
Figure 8-70- Expanded Infrared spectra of P <sub>888</sub> S-InCl <sub>3</sub> LCCs.	441
Figure 8-71- Infrared spectra of P <sub>888</sub> Se-GaCl <sub>3</sub> LCCs.	441
Figure 8-72-Expanded Infrared spectra of P <sub>888</sub> Se-GaCl <sub>3</sub> LCCs.	442
Figure 8-73-- Infrared spectra of P <sub>888</sub> Se-InCl <sub>3</sub> LCCs.	442
Figure 8-74- Expanded Infrared spectra of P <sub>888</sub> Se-InCl <sub>3</sub> LCCs.	443
Figure 8-75- EXAFS fit for ACA-GaCl <sub>3</sub> $\chi_{\text{GaCl}_3}=0.67$ in <i>k</i> -space.	446
Figure 8-76- EXAFS fit for ACA-GaCl <sub>3</sub> $\chi_{\text{GaCl}_3}=0.67$ in <i>R</i> -space.	447
Figure 8-77 EXAFS fit for DMA-GaCl <sub>3</sub> $\chi_{\text{GaCl}_3}=0.67$ in <i>k</i> -space.	447
Figure 8-78- EXAFS fit for DMA-GaCl <sub>3</sub> $\chi_{\text{GaCl}_3}=0.67$ in <i>R</i> -space.	447
Figure 8-79- EXAFS fit for Ur-GaCl <sub>3</sub> $\chi_{\text{GaCl}_3}=0.67$ in <i>k</i> -space.	448
Figure 8-80- EXAFS fit for Ur-GaCl <sub>3</sub> $\chi_{\text{GaCl}_3}=0.67$ in <i>R</i> -space.	448
Figure 8-81- EXAFS fit for SUR-GaCl <sub>3</sub> $\chi_{\text{GaCl}_3}=0.67$ in <i>k</i> -space.	448
Figure 8-82- EXAFS fit for SUR-GaCl <sub>3</sub> $\chi_{\text{GaCl}_3}=0.67$ in <i>R</i> -space.	449
Figure 8-83- EXAFS fit for P <sub>888</sub> -GaCl <sub>3</sub> $\chi_{\text{GaCl}_3}=0.50$ in <i>k</i> -space.	449
Figure 8-84- EXAFS fit for P <sub>888</sub> -GaCl <sub>3</sub> $\chi_{\text{GaCl}_3}=0.50$ in <i>R</i> -space.	449
Figure 8-85- EXAFS fit for P <sub>888</sub> -GaCl <sub>3</sub> $\chi_{\text{GaCl}_3}=0.60$ in <i>k</i> -space.	450
Figure 8-86- EXAFS fit for P <sub>888</sub> -GaCl <sub>3</sub> $\chi_{\text{GaCl}_3}=0.60$ in <i>R</i> -space.	450
Figure 8-87- EXAFS fit for P <sub>888</sub> -GaCl <sub>3</sub> $\chi_{\text{GaCl}_3}=0.67$ in <i>k</i> -space.	450
Figure 8-88- EXAFS fit for P <sub>888</sub> -GaCl <sub>3</sub> $\chi_{\text{GaCl}_3}=0.67$ in <i>R</i> -space.	451
Figure 8-89- EXAFS fit for P <sub>888</sub> Se-GaCl <sub>3</sub> $\chi_{\text{GaCl}_3}=0.50$ in <i>K</i> -space.	451
Figure 8-90- <sup>31</sup> P VT NMR spectra of P <sub>888</sub> -CuCl $\chi_{\text{CuCl}} = 0.25$ in 10 K increments from 223 K (top) to 323 K (bottom).	454
Figure 8-91-pXRD analysis of ionothermal P <sub>888</sub> Se-GaCl <sub>3</sub> $\chi_{\text{GaCl}_3} = 0.67$ reaction product.	454

## 8.2 Table of Tables

Table 2-1- Solvent dependent absorption spectrum of solvated electrons <sup>97–100</sup>	36
Table 2-2-Reduction screening experiments with 18-crown-6 and elemental potassium	72
Table 2-3- Hydrogen bonding distance in the amine-18-crown-6 interaction study.	80
Table 2-4- Summary of the frequency of measurements used for each spectrometer	87
Table 2-5- Single crystal data for amine and 18-crown-6 interactions	99

Table 2-6-Single crystal data for amine and 18-crown-6 interactions.....	100
Table 2-7-Single crystal data for 1-alkyl-4-aminopyridinium ionic liquids.....	101
Table 2-8- Single crystal data for 2-[3-(Dimethylamino)propyl]isoindoline-1,3-dione .....	102
Table 3-1- Etherification of <i>p</i> -tert-butylcalix-[4]-arenes with simple alkyl halides via 6 different methodologies. <sup>226,228–231</sup> .....	114
Table 3-2-p <i>K</i> <sub>a</sub> s of <i>p</i> -functionalisedcalix-[4]-arenes with <i>R</i> dictating the functional group para to the phenolic proton.....	118
Table 3-3- Comparison of <i>p</i> -tert-butylcalix-[4]-arene samples via <sup>1</sup> H NMR spectroscopy. ....	122
Table 3-4- <i>p</i> -tert-butylcalix-[4]-arene, TBC dissolved in trihexyltetradecylphosphonium acetate, [P <sub>66614</sub> ][OAc] .....	123
Table 3-5- UV/Vis investigation [P <sub>66614</sub> ][OAc] 20 mol% TBC vs DBU in acetonitrile. ....	130
Table 3-6-Phenol and potassium acetate solutions formed. (Solvent less) .....	140
Table 3-7- Phenol and [Emim][OAc] solutions formed .....	144
Table 3-8-Acetic acid in phenol solutions prepared .....	149
Table 3-9-Solutions of 1, 1, 3, 3-tetramethylguanidine, TMG and <i>p</i> -tert-butylcalix-[4]-arene, TBC....	153
Table 3-10- of <i>p</i> -tert-butylcalix-[4]-arene and 1,1,3,3-tetramethylguanidine <sup>1</sup> H NMR shifts.....	155
Table 3-11- UV/Vis study of <i>p</i> -tert-butylcalix-[4]-arene vs 1, 1, 3, 3 – tetramethylguanidine .....	157
Table 3-12-Single crystal data for triethylmethylammonium <i>p</i> -tert-butyl-calix-[4]-arate, [N <sub>2221</sub> ][TBC]. .....	164
Table 3-13- Single crystal data for triethylmethylammonium <i>p</i> -tert-butyl-calix-[4]-arate, [N <sub>2221</sub> ][TBC] .....	166
Table 3-14- Mass spectroscopic analysis of products from mono-alkylations of mono-anion <i>p</i> -tert-butylcalix-[4]-arate salts. ....	172
Table 3-15- Yields obtained from mono-alkylations of mono-anion <i>p</i> -tert-butylcalix-[4]-arate salts. ....	179
Table 3-16- Single crystal data for [N <sub>2221</sub> ][TBC] and [TMG][TBC] .....	184
Table 3-17- Single crystal data for [N <sub>4441</sub> ][TBC] and [Emim][TBC] .....	185
Table 4-1-Speciation observed in chlorogallate ionic liquids. <sup>351,352,354,360,361</sup> .....	191
Table 4-2- The dynamic equilibrium exhibited by LCCs in comparison to ILs as deduced by spectroscopic studies. <sup>22</sup> .....	194
Table 4-3- Combinations of GaCl <sub>3</sub> and P <sub>888</sub> E (E=O, S, Se) ligands that formed LCCs at given $\chi_{\text{MClx}}$ values.....	210
Table 4-4-Table of density fit data for chlorogallate LCCs.....	212
Table 4-5.- VFT fit parameters for P <sub>888</sub> E-GaCl <sub>3</sub> .....	214
Table 4-6-Integration of ionic vs. neutral peak in <sup>31</sup> P NMR spectra of chloroaluminate LCCs at $\chi_{\text{GaCl}_3}$ = 0.50 by Hogg and chlorogallate in this work. <sup>382</sup> .....	218
Table 4-7- <sup>31</sup> P and <sup>77</sup> Se shift and coupling in P <sub>888</sub> Se-GaCl <sub>3</sub> LCCs.....	222
Table 4-8- <sup>31</sup> P integration analysis of ionic vs. neutral species in P <sub>888</sub> S-GaCl <sub>3</sub> cooled LCCs.....	224
Table 4-9-Raman stretching frequencies of P <sub>888</sub> E-GaCl <sub>3</sub> LCCs .....	227

Table 4-10- Characteristic Raman shifts of gallium chloride molecular adducts and ionic species. ..	228
Table 4-11- Infrared stretching frequencies of $P_{888}S-GaCl_3$ .....	230
Table 4-12- EXAFS fitting statistics for $P_{888}O-GaCl_3$ LCCs.....	237
Table 4-13-Table of conductivity of LCC species.....	238
Table 4-14-Predicted speciation of chlorogallate liquid coordination complexes .....	240
Table 4-15- Combinations of $InCl_3$ and $P_{888}E$ ( $E=O, S, Se$ ) ligands that formed LCCs at given $\chi_{MClx}$ values.....	241
Table 4-16-VFT fit parameters for $P_{888}E-InCl_3$ .....	243
Table 4-17-Suggested speciation of $P_{888}E-InCl_3$ LCCs.....	249
Table 4-18- Characterising Raman shifts of indium chloride molecular adducts and ionic species. ....	251
Table 4-19- Raman shifts of Indium chloride LCCs .....	252
Table 4-20- Infrared stretching frequencies of $P_{888}S-GaCl_3$ .....	253
Table 4-21- Summary of the frequency of measurements used for each spectrometer .....	259
Table 5-1-UV/Vis spectroscopic studies absorption maxima of copper (II) chloride complexes in acetonitrile and dimethylformide. <sup>455-457</sup> .....	264
Table 5-2-Near IR assignments of copper (II) chloride species in DMF. ....	265
Table 5-3-Summary of chlorocuprate liquid coordination complexes prepared.....	274
Table 5-4- <sup>31</sup> P NMR signals of neat $P_{888}$ and liquid coordination complexes of $CuCl$ and $P_{888}$ .....	276
Table 5-5- <sup>31</sup> P NMR signals of neat $P_{888}S$ and $P_{888}Se$ liquid coordination complexes of $CuCl$ and $P_{888}$ . ....	278
Table 5-6- <sup>31</sup> P NMR signals of $P_{888}$ , $P_{888}S$ and $P_{888}Se$ liquid coordination complexes of $CuCl_2$ .....	284
Table 5-7-Infrared stretching frequencies of $P_{888}E-CuCl$ LCC systems.....	288
Table 5-8- Predicted speciation of $P_{888}-CuCl$ systems. ( $L=P_{888}$ ) .....	300
Table 5-9- EXAFS fitting parameters for $P_{888}-CuCl$ LCCs, at the compositions: $\chi_{CuCl} = 0.25, 0.33$ and $0.50$ .....	303
Table 5-10- Numerical analysis of pre-peak and edge intensities of $P_{888}-CuCl$ LCCs HRXANES spectra. ....	307
Table 5-11- Final best fit coordination numbers for $P_{888}-CuCl$ $\chi_{CuCl} = 0.25, 0.33$ and $0.50$ .....	310
Table 5-12- Copper (I) chloride- trioctylphosphine liquid coordination complexes $P_{888}-CuCl$ and elemental chalcogens .....	312
Table 5-13- <sup>31</sup> P NMR signals of $P_{888}-CuCl$ $\chi_{CuCl} = 0.50$ with the addition of elemental chalcogenide ....	312
Table 5-14- Infrared spectra of $P_{888}-CuCl$ $\chi_{CuCl} = 0.50$ with elemental sulphur, selenium and tellurium. ....	314
Table 5-15- Copper (II) chloride- trioctylphosphine liquid coordination complexes $P_{888}-CuCl_2$ and elemental chalcogens .....	317
Table 5-16-Elemental distribution of isolated product of $P_{888}Se-GaCl_3$ $\chi_{GaCl_3} = 0.50$ microwave reaction. ....	326
Table 5-17-Elemental distribution of $P_{888}Se-InCl_3$ $\chi_{InCl_3} = 0.25$ reaction product.....	329
Table 5-18- Elemental distribution of $P_{888}Se-CuCl$ $\chi_{CuCl} = 0.33$ reaction product.....	332



Table 5-19- EDX analysis of $P_{888}S-CuCl$ $\chi_{CuCl} = 0.33$ isolated reaction product. ....	333
Table 5-20-EDX elemental distribution of $P_{888}Se-CuCl$ $\chi_{CuCl} = 0.50$ , $P_{888}Se-GaCl_3$ $\chi_{GaCl_3} = 0.50$ and $P_{888}-InCl_3$ $\chi_{InCl_3} = 0.50$ in a 1:1:1 molar ratio isolated reaction product. ....	336
Table 5-21- Elemental distribution of $P_{888}Se-CuCl$ $\chi_{CuCl} = 0.50$ , $P_{888}Se-GaCl_3$ $\chi_{GaCl_3} = 0.50$ and $P_{888}-InCl_3$ $\chi_{InCl_3} = 0.50$ in a 1:1:1 molar ratio and elemental gallium isolated reaction product. ....	339
Table 5-22-Elemental distribution of $P_{888}Se-CuCl$ $\chi_{CuCl} = 0.50$ , and $P_{888}Se-GaCl_3$ $\chi_{GaCl_3} = 0.50$ in a 1:1 molar ratio isolated reaction product. ....	341
Table 5-23- Summary of the frequency of measurements used for each spectrometer .....	346
Table 8-1- Table of acronyms.....	424
Table 8-2- Density data for $P_{888}E-GaCl_3$ LCCs ( $E=O$ ) .....	424
Table 8-3- Density data for $P_{888}E-GaCl_3$ LCCs ( $E=S, Se$ ) .....	425
Table 8-4- Density data for $P_{888}E-InCl_3$ LCCs ( $E=O, S, Se$ ) .....	426
Table 8-5- Viscosity data for $P_{888}E-GaCl_3$ and VFT fit data ( $E=O$ ).....	430
Table 8-6- Viscosity data for $P_{888}E-GaCl_3$ and VFT fit data ( $E=O, S, Se$ ). ....	431
Table 8-7- Summary of $^{31}P$ NMR spectra of LCCs synthesised .....	436
Table 8-8- Correlation between viscosity, width at half peak height and $\chi_{GaCl_3}$ .....	437
Table 8-9- Correlation between viscosity, width at half peak height and $\chi_{InCl_3}$ .....	438
Table 8-10- $^{31}P$ and $^{77}Se$ shift and coupling in $P_{888}Se-GaCl_3$ LCCs.....	438
Table 8-11- $^{31}P$ and $^{77}Se$ shift and coupling in $P_{888}Se-InCl_3$ LCCs .....	439
Table 8-12- EXAFS fitting statistics for $P_{888}O-GaCl_3$ LCCs.....	444
Table 8-13- Fitting details for $P_{888}O-GaCl_3$ LCCs .....	444
Table 8-14- EXAFS guess parameters for $P_{888}O-GaCl_3$ $\chi_{GaCl_3}=0.50$ . ....	444
Table 8-15- EXAFS bond fits for $P_{888}O-GaCl_3$ $\chi_{GaCl_3} = 0.50$ . ....	445
Table 8-16- EXAFS guess parameters for $P_{888}O-GaCl_3$ $\chi_{GaCl_3}=0.60$ . ....	445
Table 8-17- EXAFS bond fits for $P_{888}O-GaCl_3$ $\chi_{GaCl_3}=0.60$ .....	445
Table 8-18- EXAFS guess parameters for $P_{888}O-GaCl_3$ $\chi_{GaCl_3}=0.67$ . ....	446
Table 8-19- EXAFS bond fits for $P_{888}O-GaCl_3$ $\chi_{GaCl_3}=0.67$ .....	446
Table 8-20- Fitting details for $P_{888}-CuCl$ LCC fits .....	452
Table 8-21- EXAFS fit parameters for $P_{888}-CuCl$ LCCs.....	452
Table 8-22-EXAFS fit bond parameters for $P_{888}-CuCl$ LCCs.....	453

## 8.3 Alkali metal solvation in ionic liquids

### 8.3.1 Nuclear Magnetic resonance spectroscopy

#### 8.3.1.1 Aminopyridinium ionic Liquids

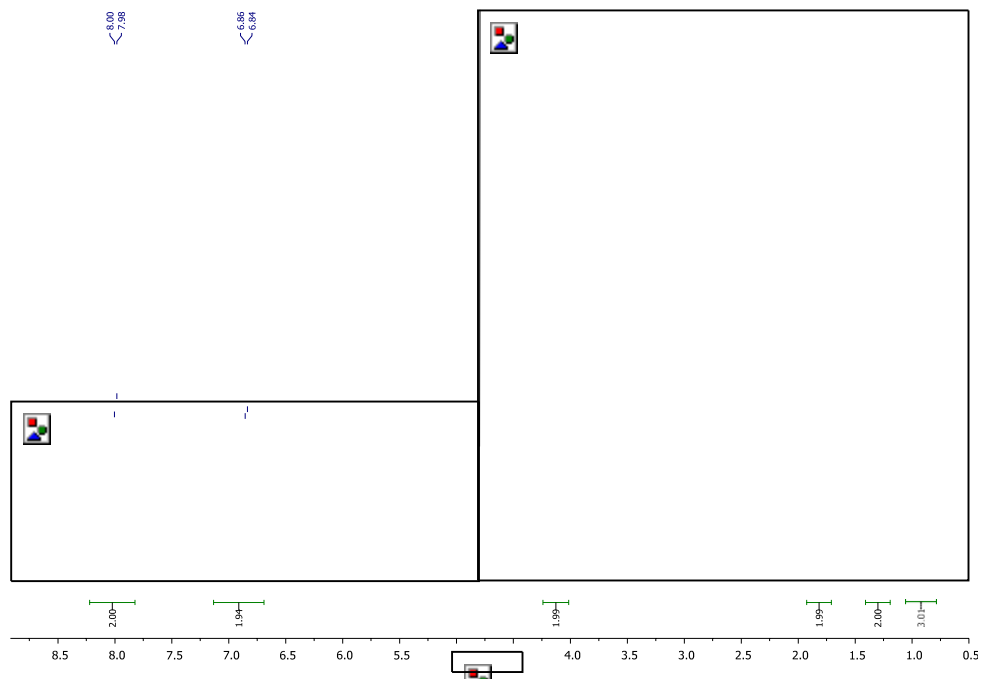


Figure 8-1-<sup>1</sup>H NMR (300 MHz, D<sub>2</sub>O) spectra of 1-Butyl-4-aminopyridinium bromide.

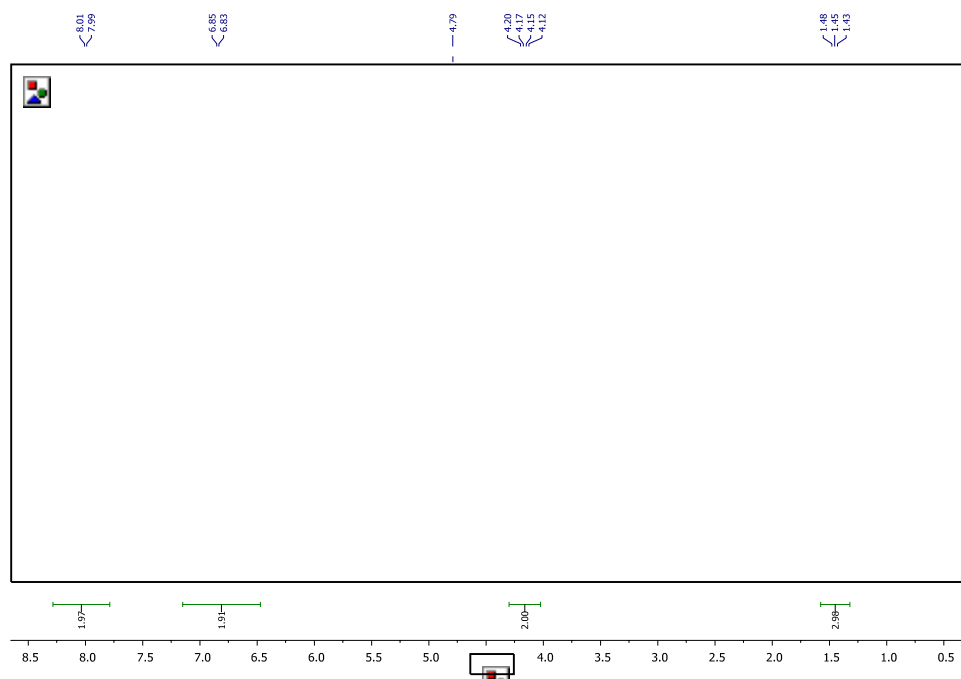
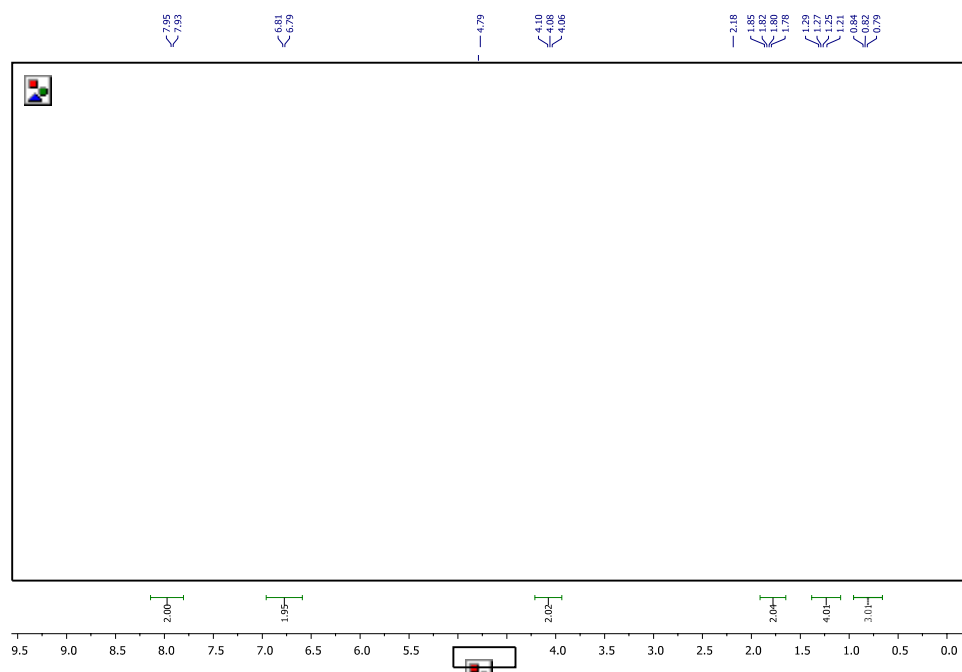
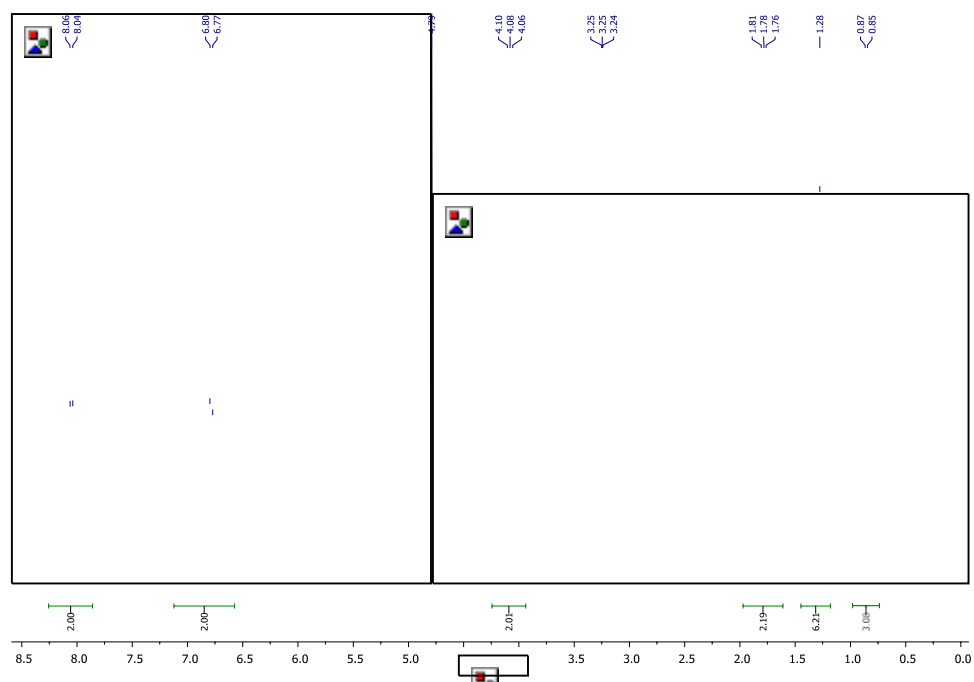


Figure 8-2-<sup>1</sup>H NMR (300 MHz, D<sub>2</sub>O) spectra of 1-ethyl-4-aminopyridinium bromide.



**Figure 8-3**  $^1\text{H}$  NMR (300 MHz,  $\text{D}_2\text{O}$ ) spectra of 1-pentyl-4-aminopyridinium bromide.



**Figure 8-4**  $^1\text{H}$  NMR (300 MHz,  $\text{D}_2\text{O}$ ) spectra of 1-hexyl-4-aminopyridinium bromide.

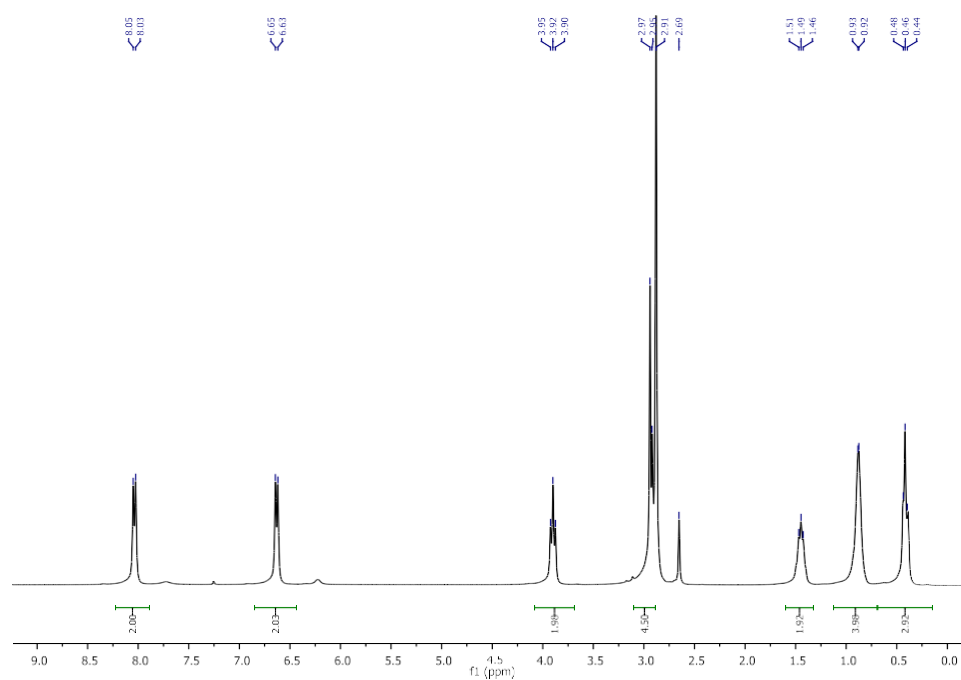


**Figure 8-5**  $^1\text{H}$  NMR (300 MHz,  $\text{CDCl}_3$ ) spectra of 1-Hexyl-N, N-dimethyl-pyridin-1-ium-4-amine iodide.

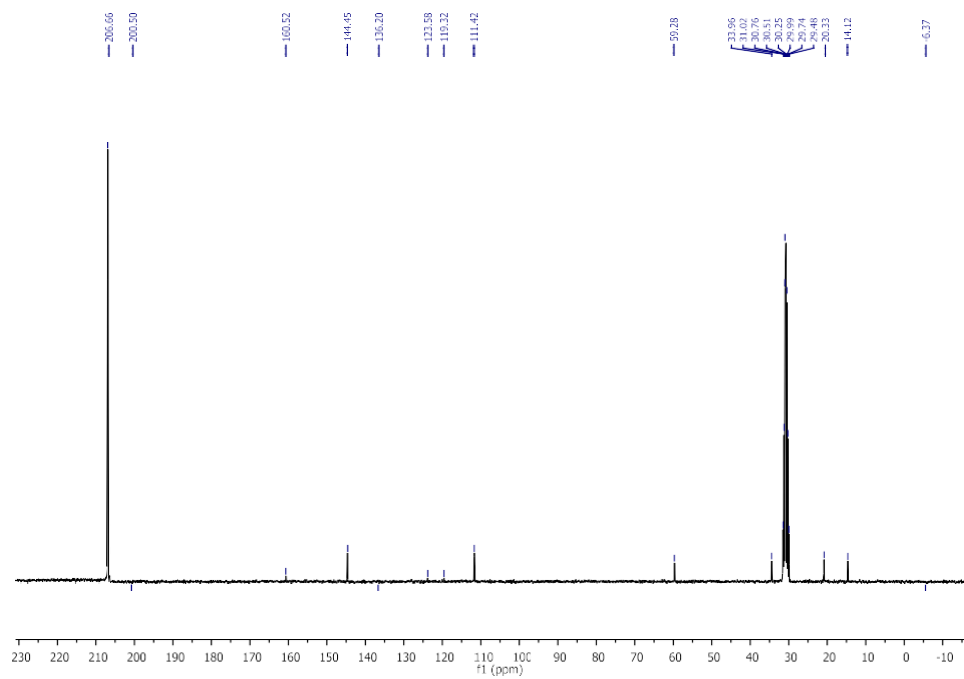


**Figure 8-6**  $^{13}\text{C}$  NMR ( $\text{CD}_3\text{CN}$ ) spectra of 1-Butyl-4-aminopyridinium bistriflamide.

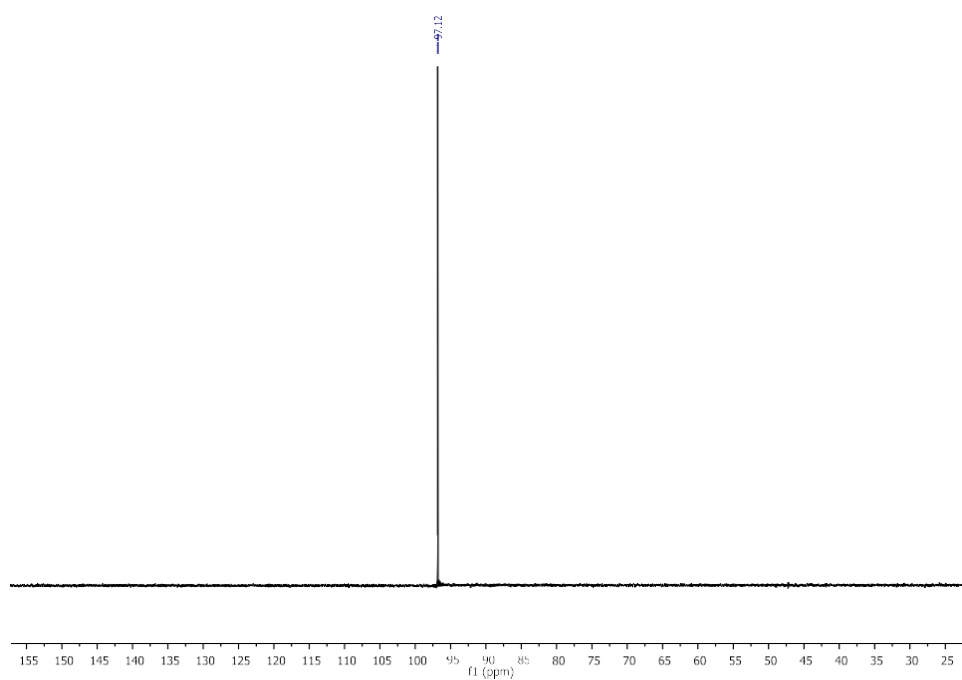


Figure 8-7- $^{19}\text{F}$  NMR ( $\text{CD}_3\text{CN}$ ) spectra of 1-Butyl-4-aminopyridinium bistriflamide.

### 8.3.1.2 Aliphatic amine functionalised ionic liquids

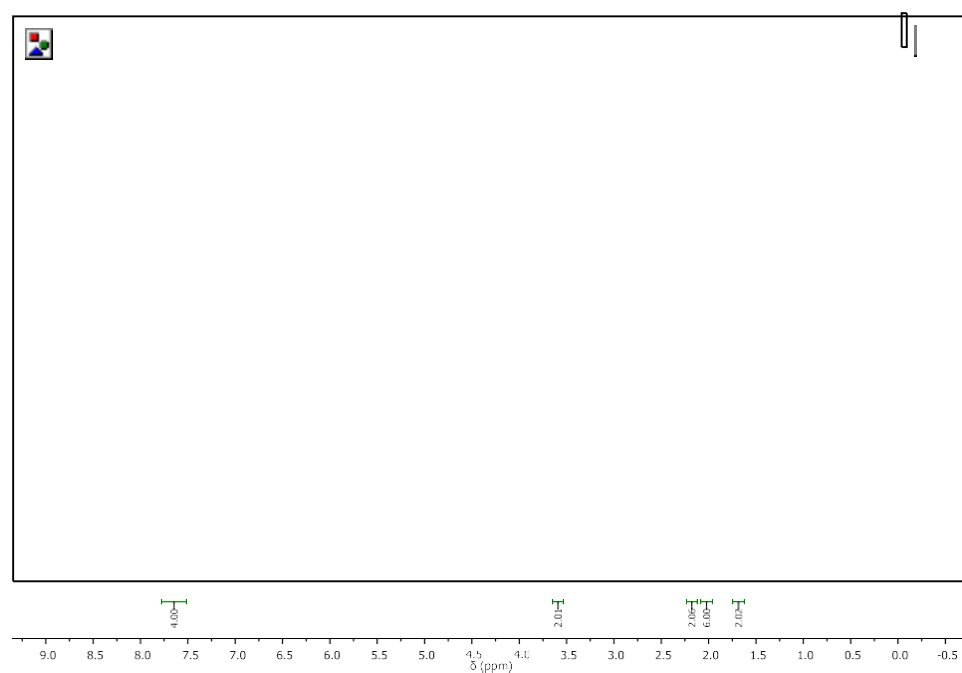
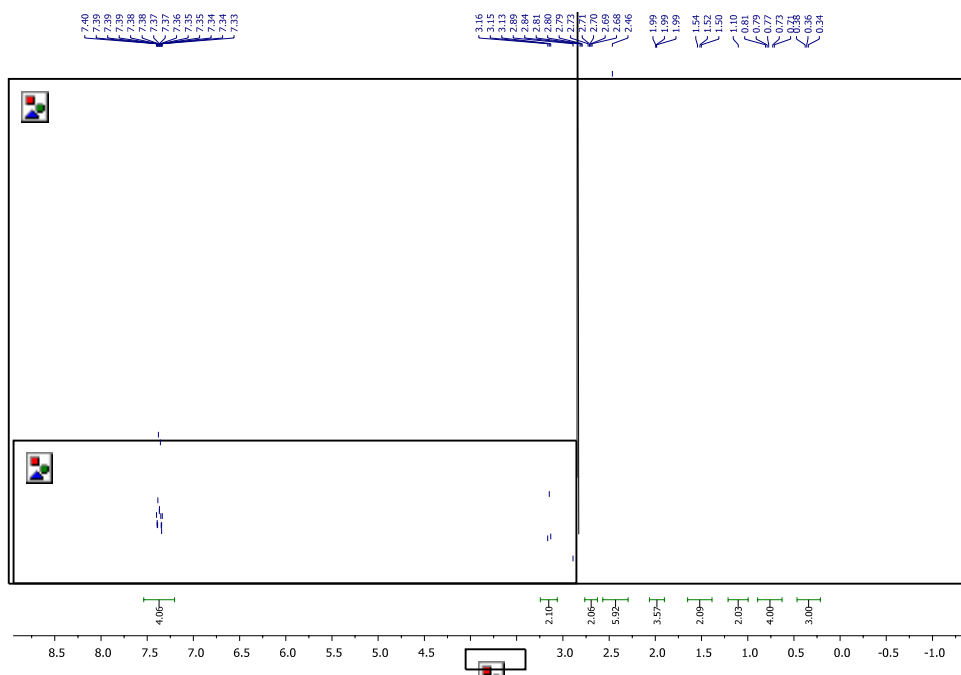
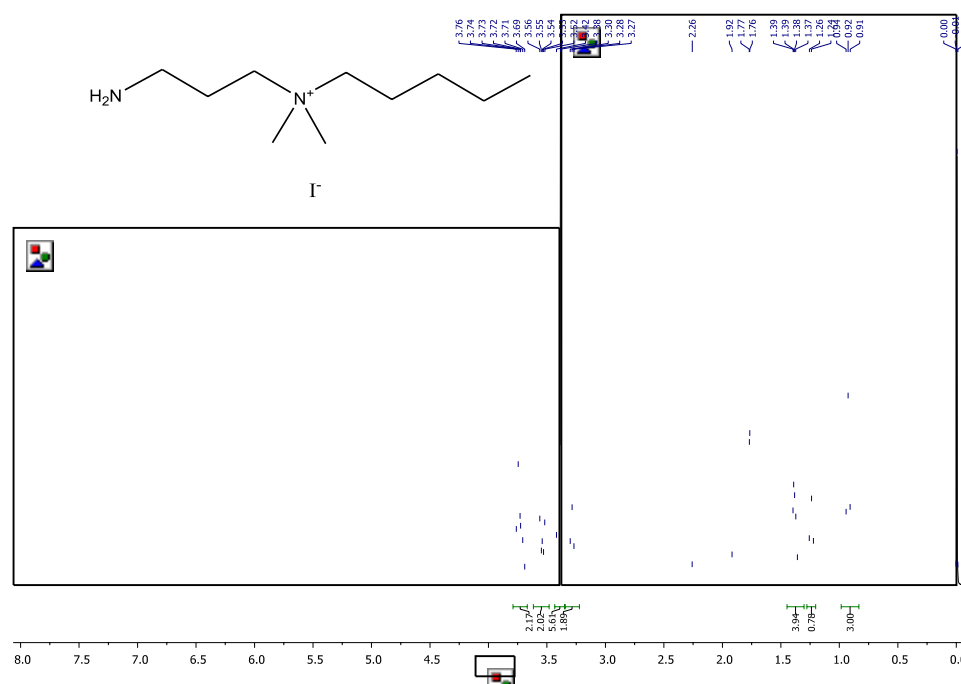


Figure 8-8- $^1\text{H}$  NMR spectra ( $\text{CDCl}_3$ ) of phthalic anhydride protected 2-aminopropuldimethylamine.



**Figure 8-9** <sup>1</sup>H NMR spectra (CD<sub>6</sub>CO) of phthalic anhydride protected-2-Aminopropyl (dimethyl)pentylammonium iodide



**Figure 8-10** <sup>1</sup>H NMR spectra (CDCl<sub>3</sub>) of 2-Aminopropyl(dimethyl)pentylammonium iodide.

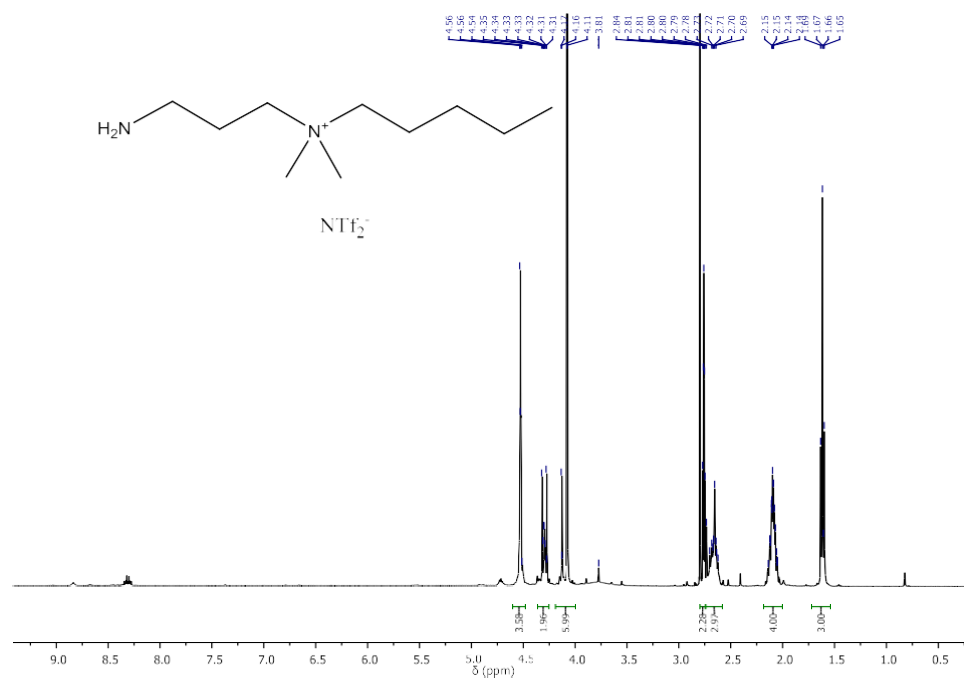


**Figure 8-11**- $^1\text{H}$  NMR spectra ( $\text{CO}(\text{CD}_3)_2$ ) of 2-Aminopropyl(dimethyl)pentylammonium bistrifluoromethanesulfonate.

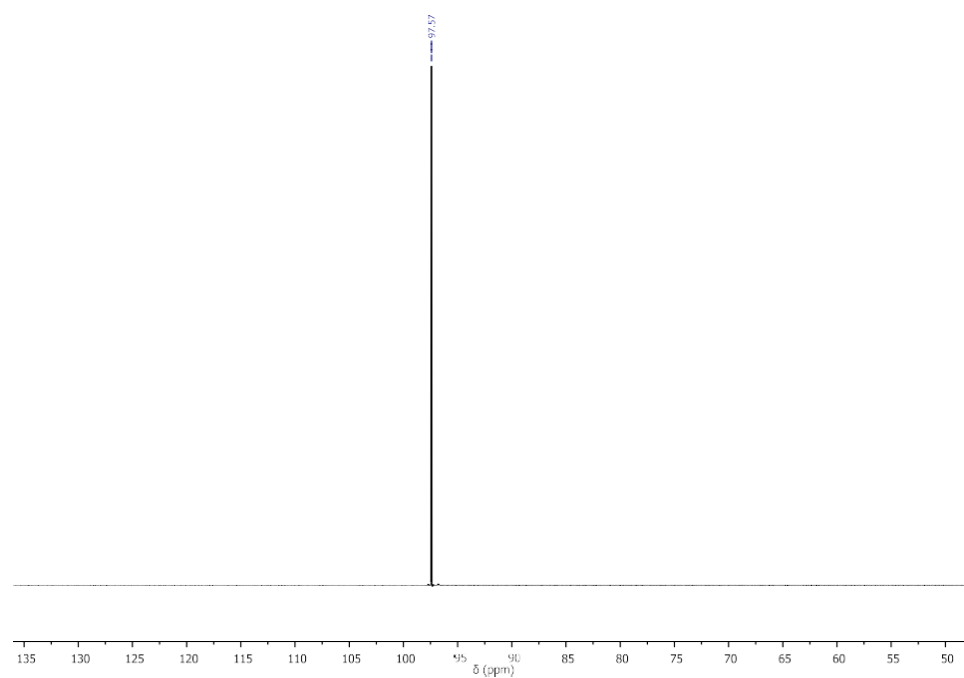


**Figure 8-12**- $^{19}\text{F}$  NMR spectra ( $\text{CO}(\text{CD}_3)_2$ ) of 2-Aminopropyl(dimethyl)pentylammonium bistrifluoromethanesulfonate.

## 8.4 *p-tert*-Butylcalix-[4]-arene solvation in basic ionic liquids

### 8.4.1 Nuclear magnetic resonance spectroscopic data

#### 8.4.1.1 *p-tert*-Butylcalix-[4]-arene-commercial sample

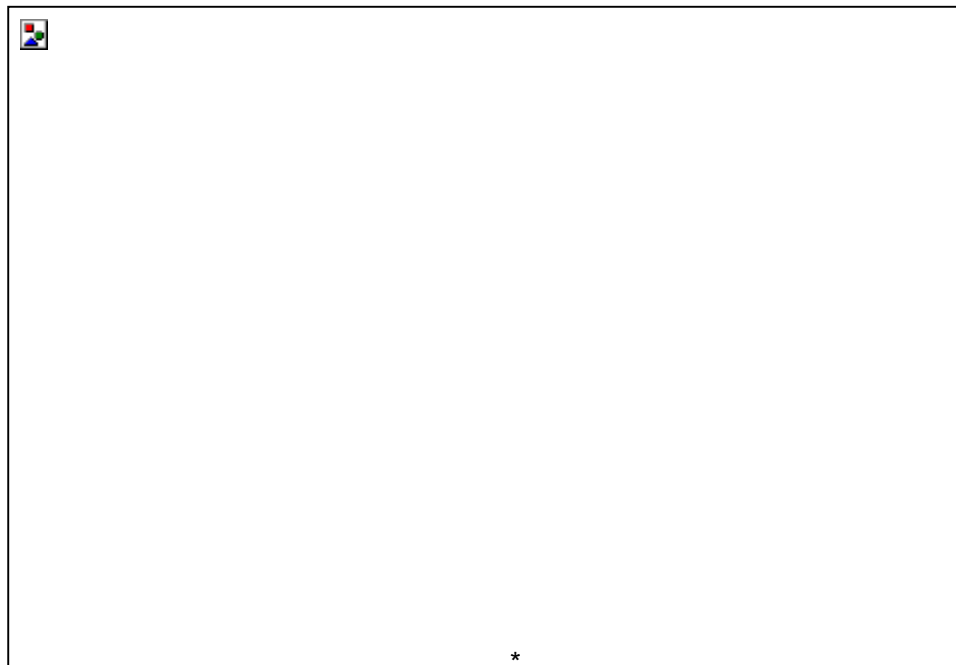


Figure 8-13-<sup>1</sup>H NMR spectrum of a commercial sample of *p-tert*-butylcalix-[4]-arene

Mono-anion calixarate salts

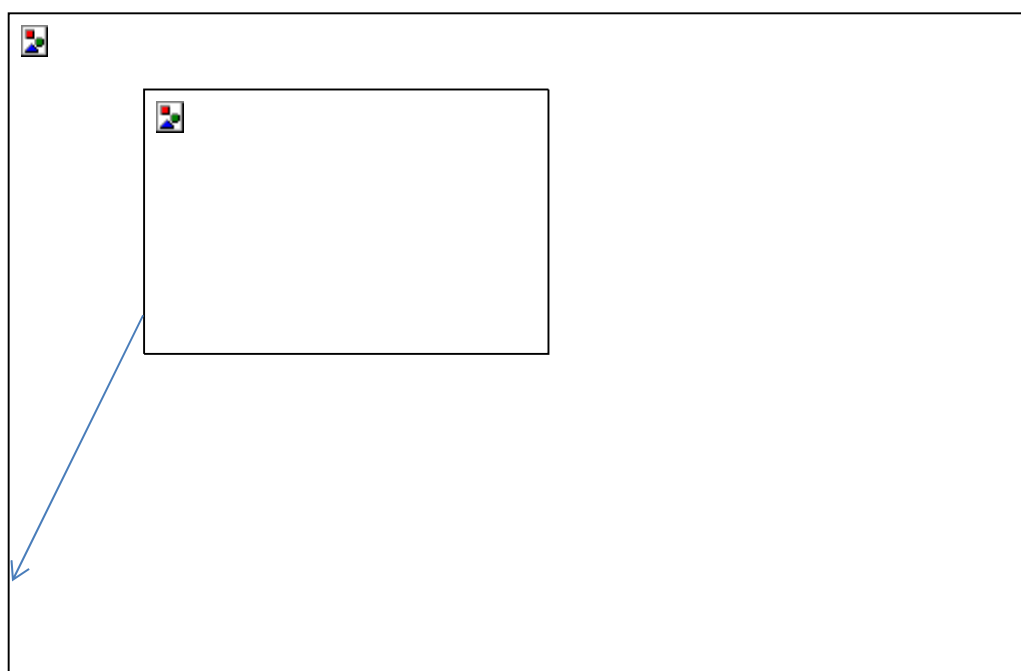
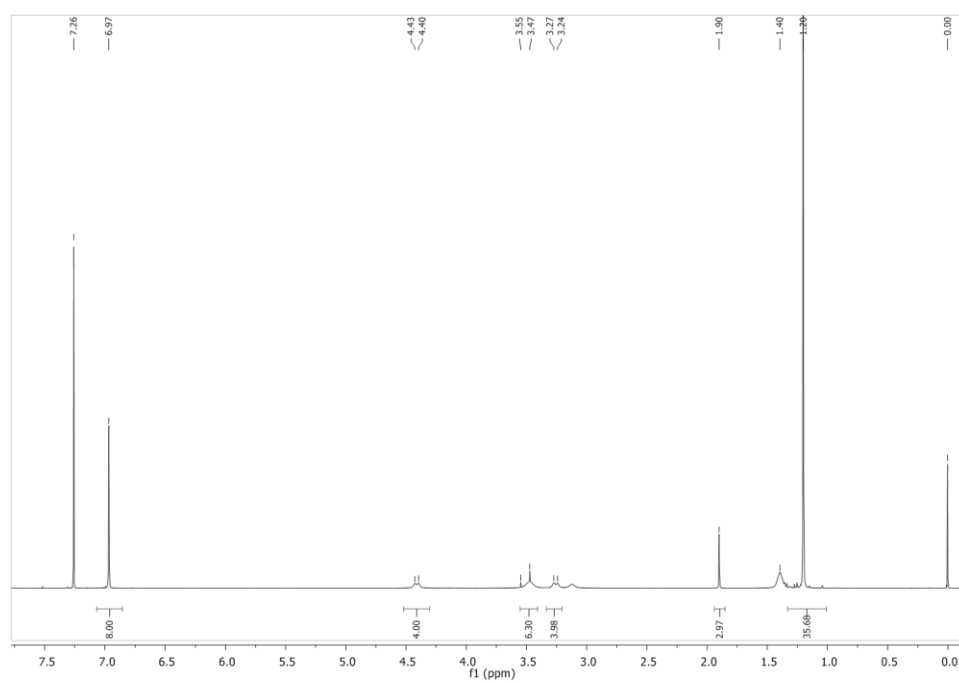
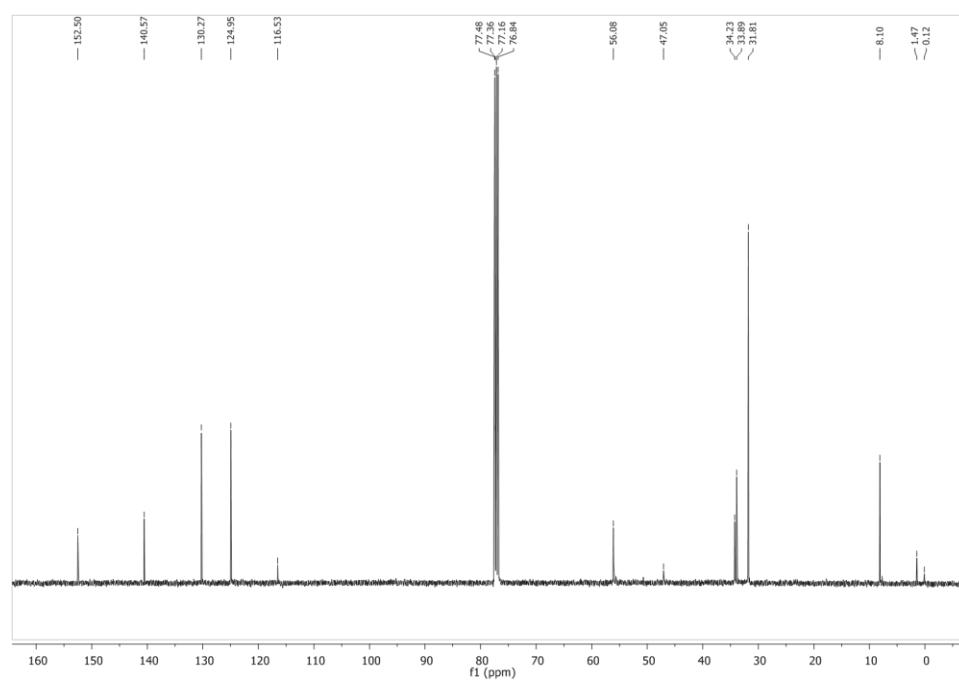


Figure 8-14-<sup>1</sup>H NMR spectrum of Tributylmethylammonium *tert*-butylcalix-[4]-arate salt.





**Figure 8-15-**<sup>1</sup>H NMR spectrum of Triethylmethylammonium *tert*-butylcalix-[4]-arate salt.



**Figure 8-16-**<sup>13</sup>C NMR spectrum of Triethylmethylammonium *tert*-butylcalix-[4]-arate salt.

#### 8.4.1.2 Mono-alkylations *via* dialkyl sulphates

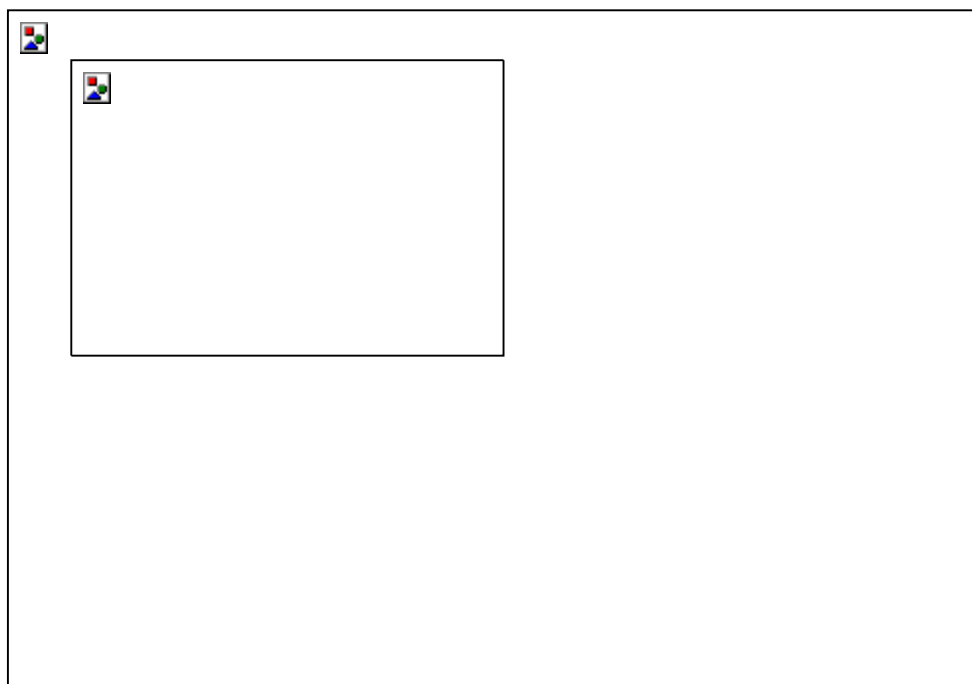


Figure 8-17-<sup>1</sup>H NMR of methylated *p-tert*-butylcalix-[4]arene *via* dimethyl sulphate.

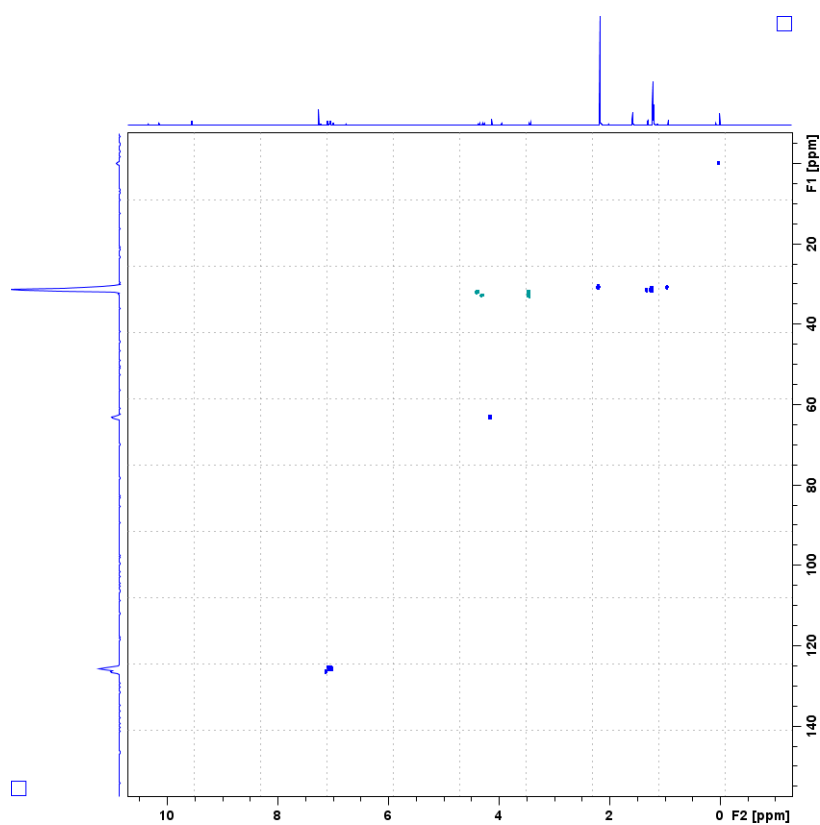
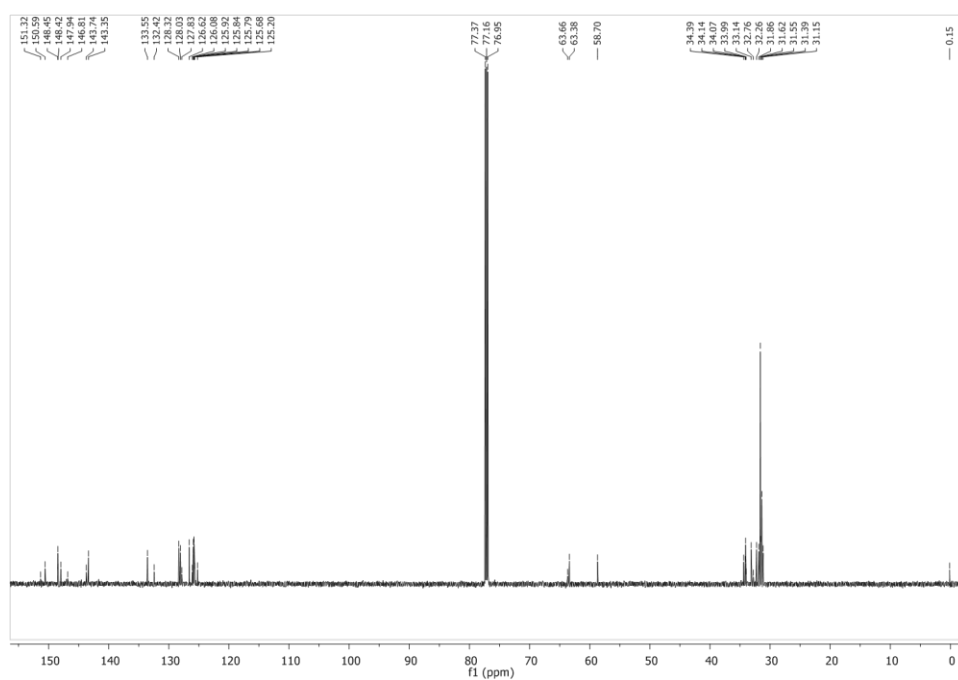
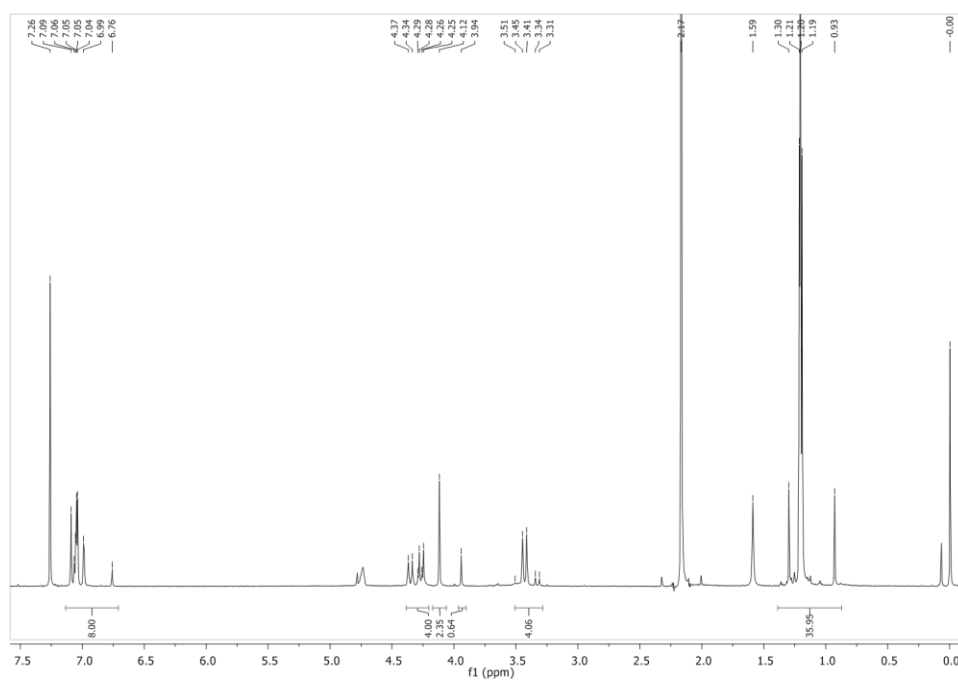


Figure 8-18-HSQC of methylated *p-tert*-butylcalix-[4]arene *via* dimethyl sulphate.



**Figure 8-19-**<sup>13</sup>C NMR of methylated *p-tert*-butylcalix-[4]-arene *via* dimethyl sulphate.



**Figure 8-20-**<sup>1</sup>H NMR of methylated *p-tert*-butylcalix-[4]-arene *via* dimethyl sulphate with a drop of D<sub>2</sub>O.

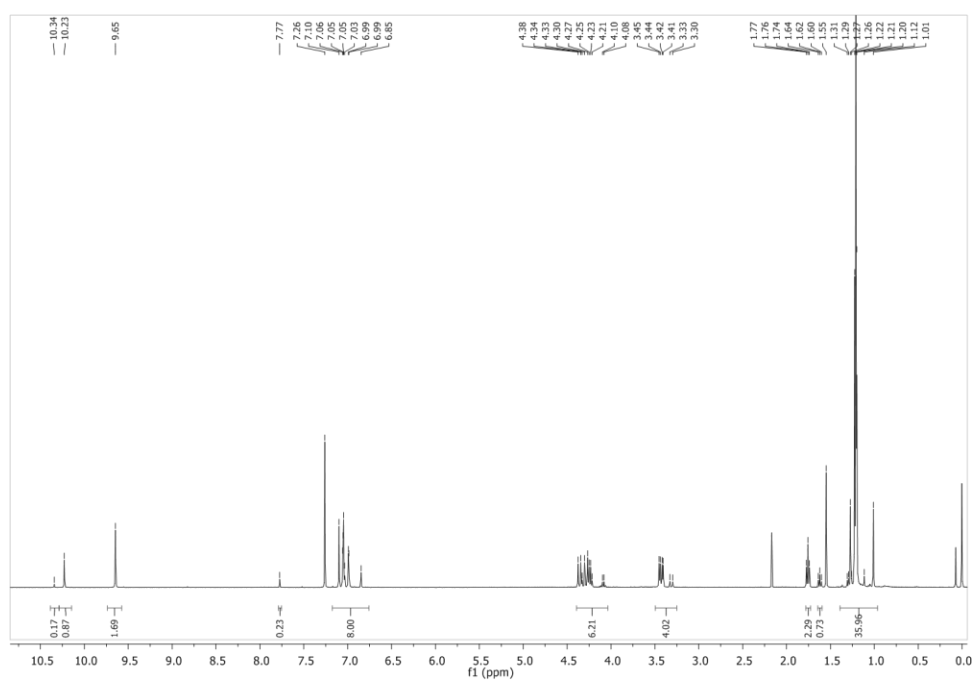


Figure 8-21- $^1\text{H}$  NMR of ethylated *p*-*tert*-butylcalix-[4]-arene via diethyl sulphate.

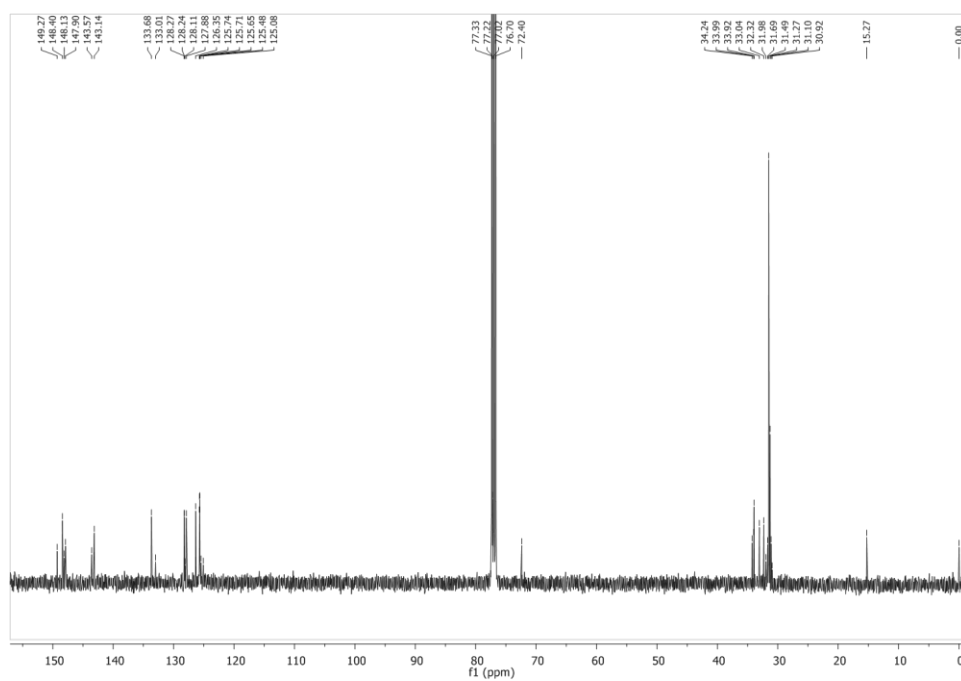


Figure 8-22- $^{13}\text{C}$  NMR ethylated *p*-*tert*-butylcalix-[4]-arene via diethyl sulphate.

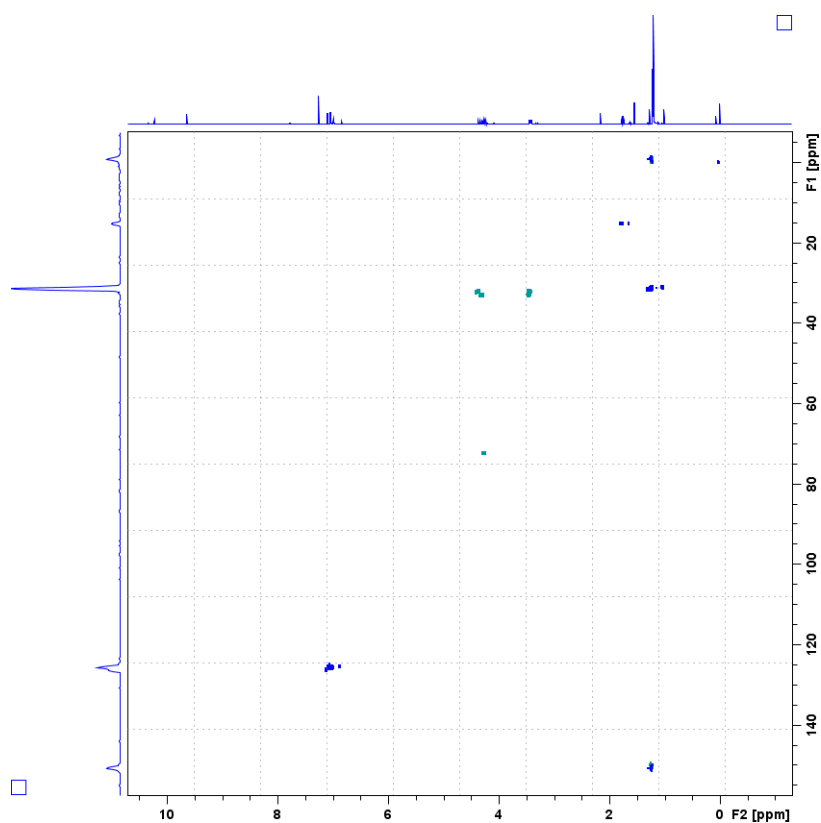


Figure 8-23-HSQC of ethylated *p*-*tert*-butylcalix-[4]-arene *via* diethyl sulphate.

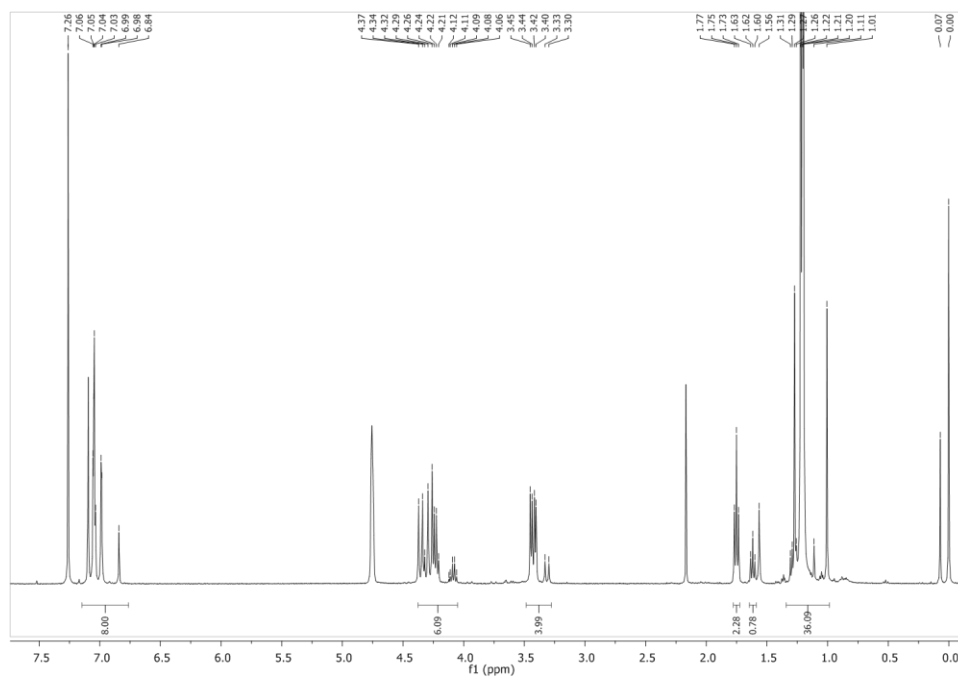
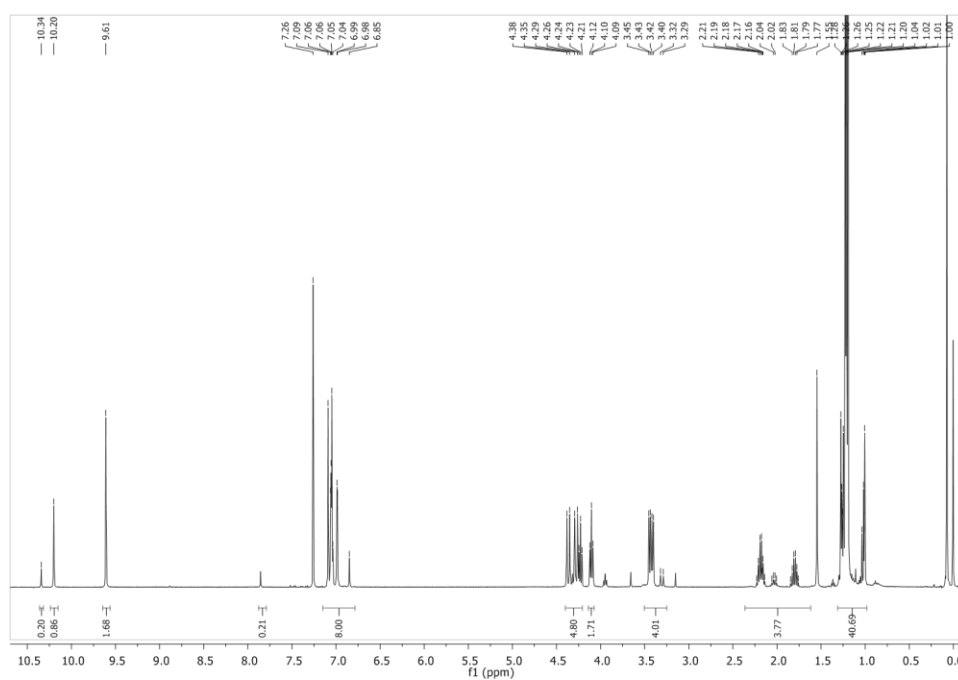
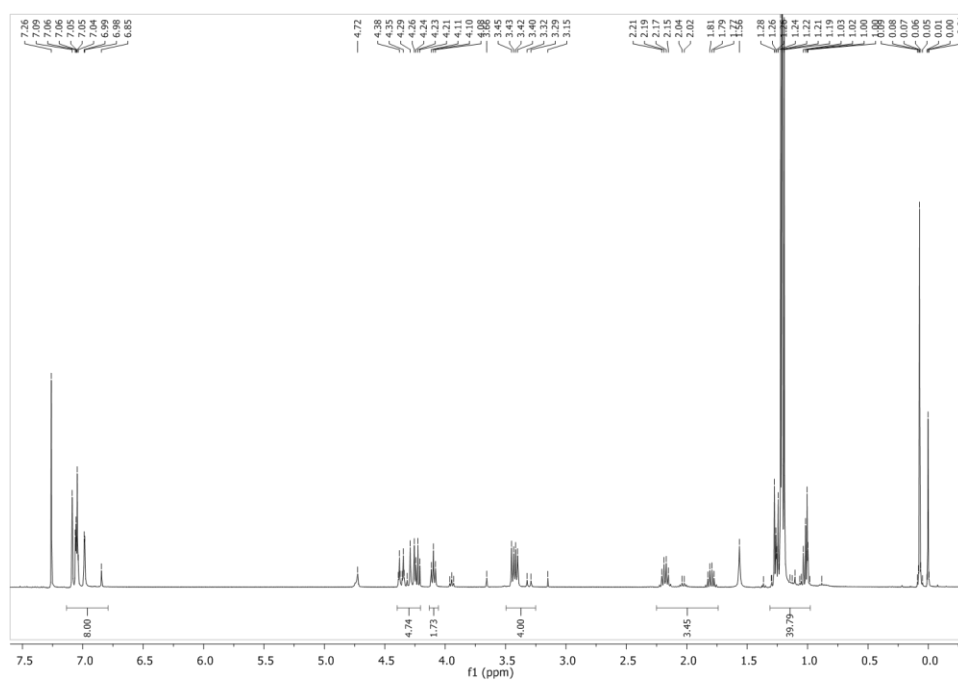


Figure 8-24- $^1\text{H}$  NMR of ethylated *p*-*tert*-butylcalix-[4]-arene *via* diethyl sulphate with a  $\text{D}_2\text{O}$  shake.



**Figure 8-25-** $^1\text{H}$  NMR of propylated *p*-*tert*-butylcalix-[4]-arene *via* dipropyl sulphate.



**Figure 8-26-** $^1\text{H}$  NMR of propylated *p*-*tert*-butylcalix-[4]-arene *via* dipropyl sulphate with  $\text{D}_2\text{O}$  shake.

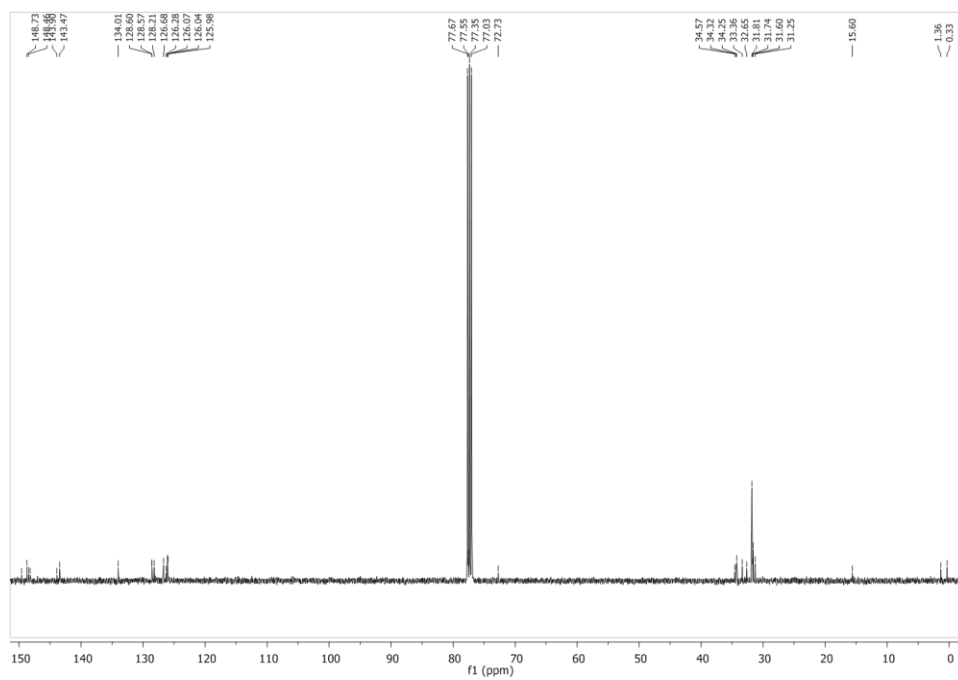


Figure 8-27-<sup>13</sup>C NMR of propylated p-tert-butylcalix-[4]-arene *via* dipropyl sulphate with D<sub>2</sub>O shake.

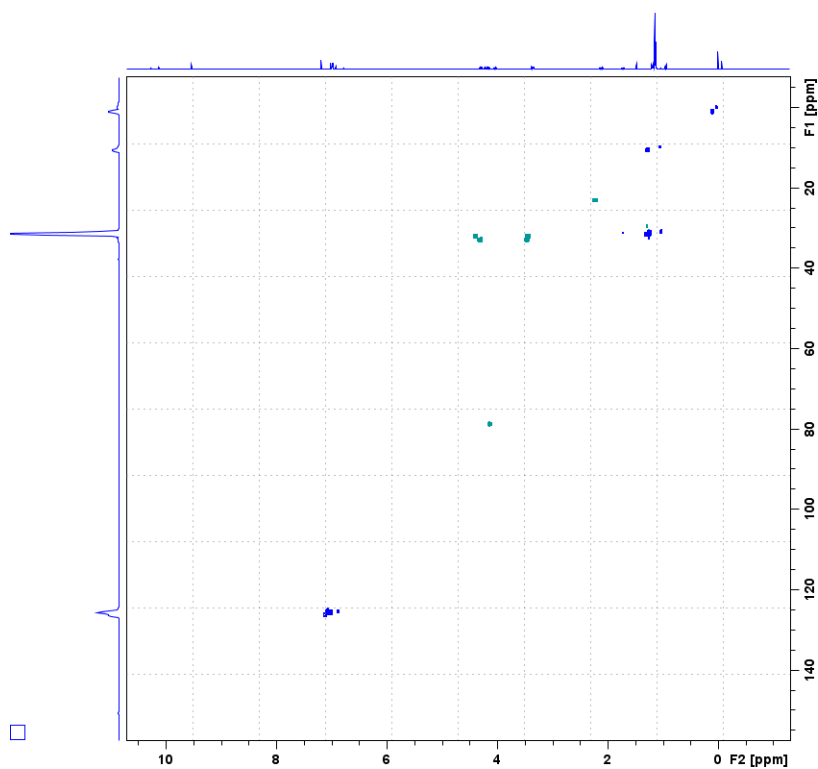


Figure 8-28-HSQC of propylated p-tert-butylcalix-[4]-arene *via* dipropyl sulphate.

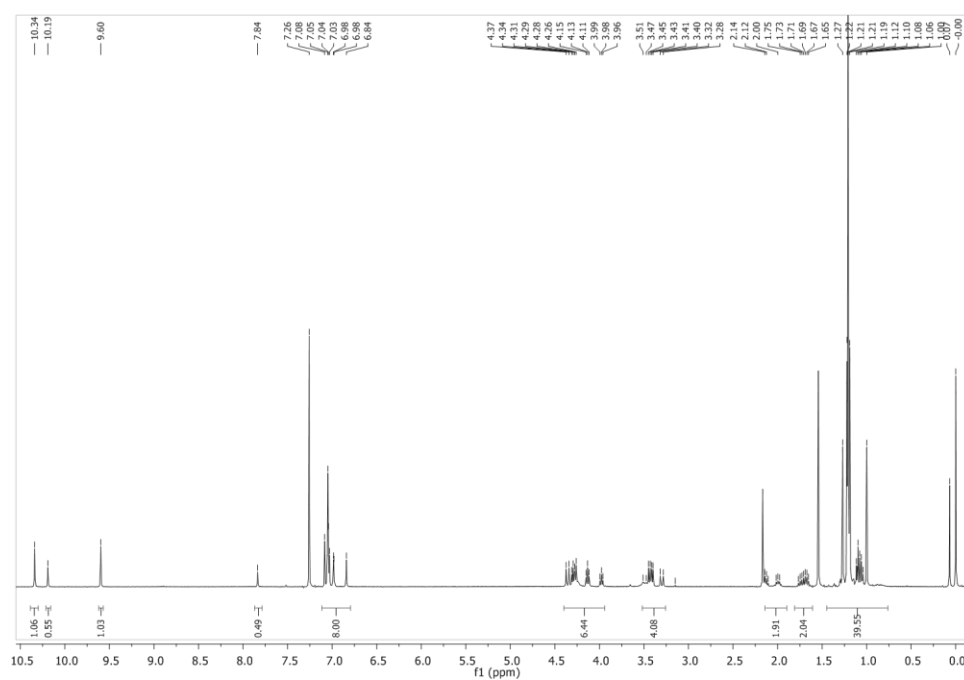


Figure 8-29-<sup>1</sup>H NMR of butylated *p*-*tert*-butylcalix-[4]-arene via dibutyl sulphate.

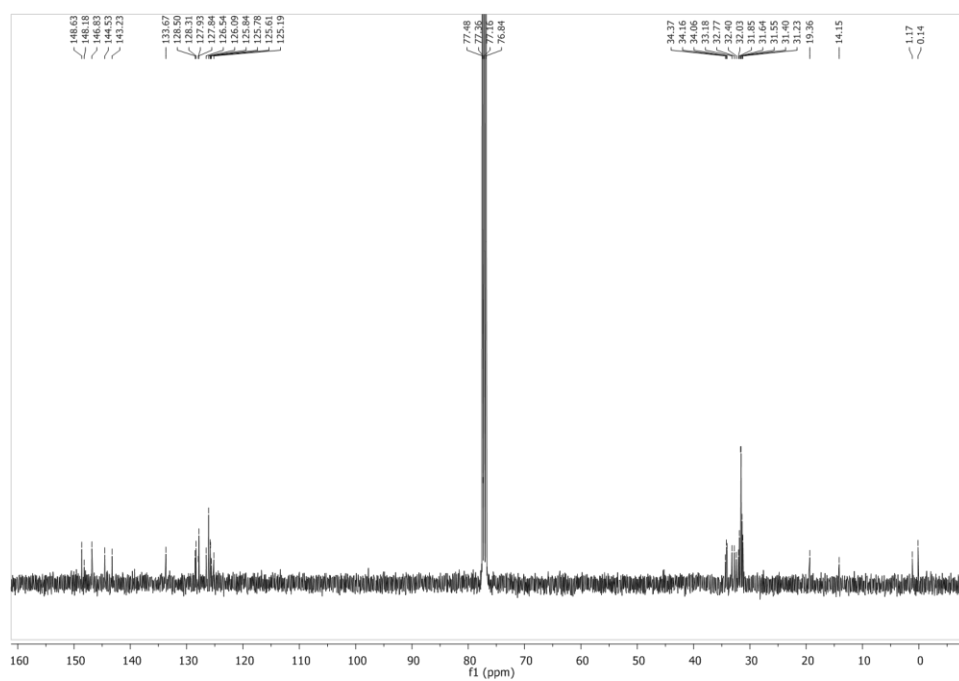


Figure 8-30-<sup>13</sup>C NMR of butylated *p*-*tert*-butylcalix-[4]-arene via dibutyl sulphate.



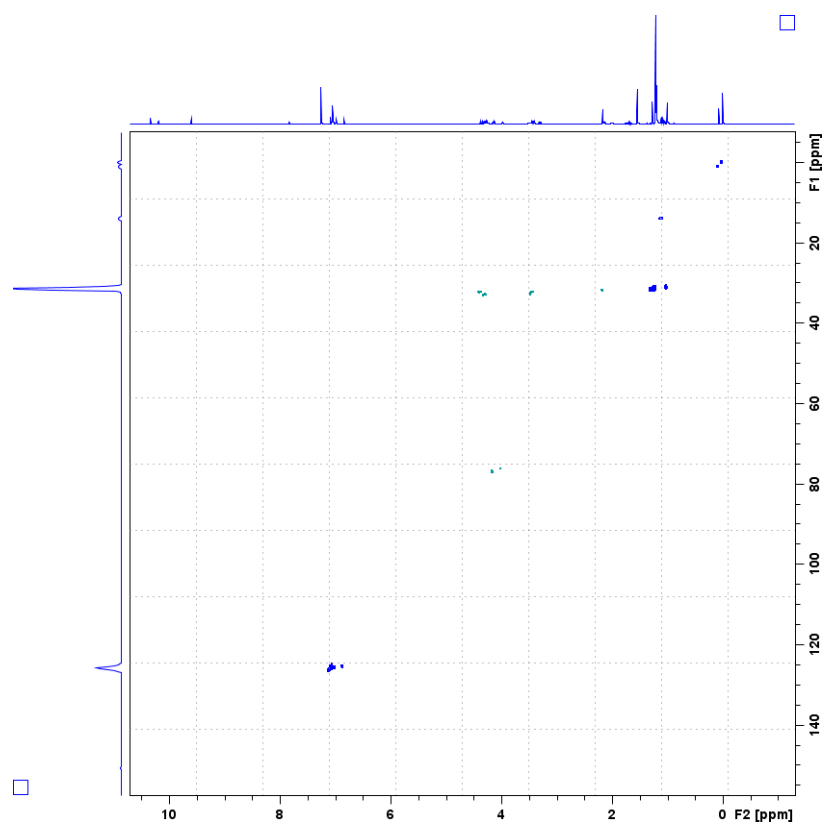


Figure 8-31-HSQC of butylated *p-tert*-butylcalix-[4]-arene *via* dibutyl sulphate.

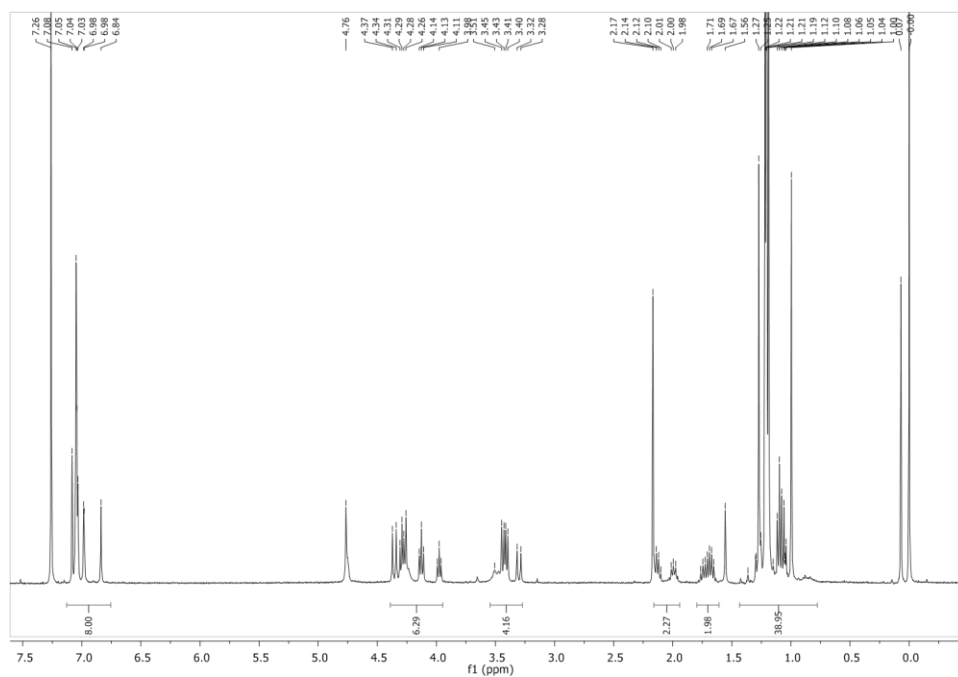


Figure 8-32- $^1\text{H}$  NMR of butylated *p-tert*-butylcalix-[4]-arene *via* dibutyl sulphate with  $\text{D}_2\text{O}$  shake.

### 8.4.1.3 Mono-alkylations *via* alkyl iodides

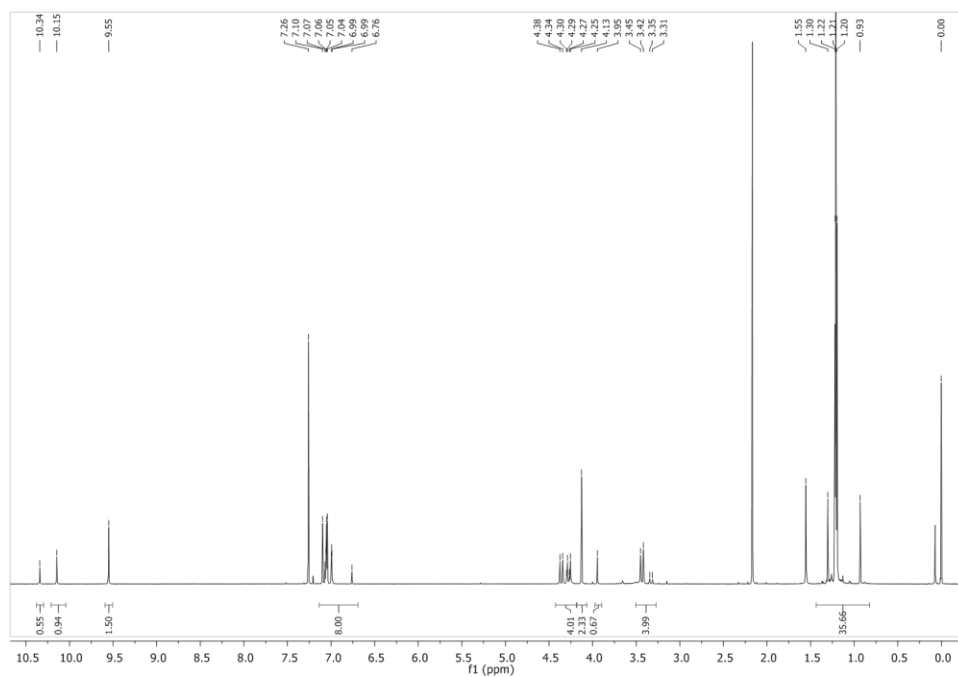


Figure 8-33-<sup>1</sup>H NMR of methylated *p*-*tert*-butylcalix-[4]-arene *via* methyl iodide.

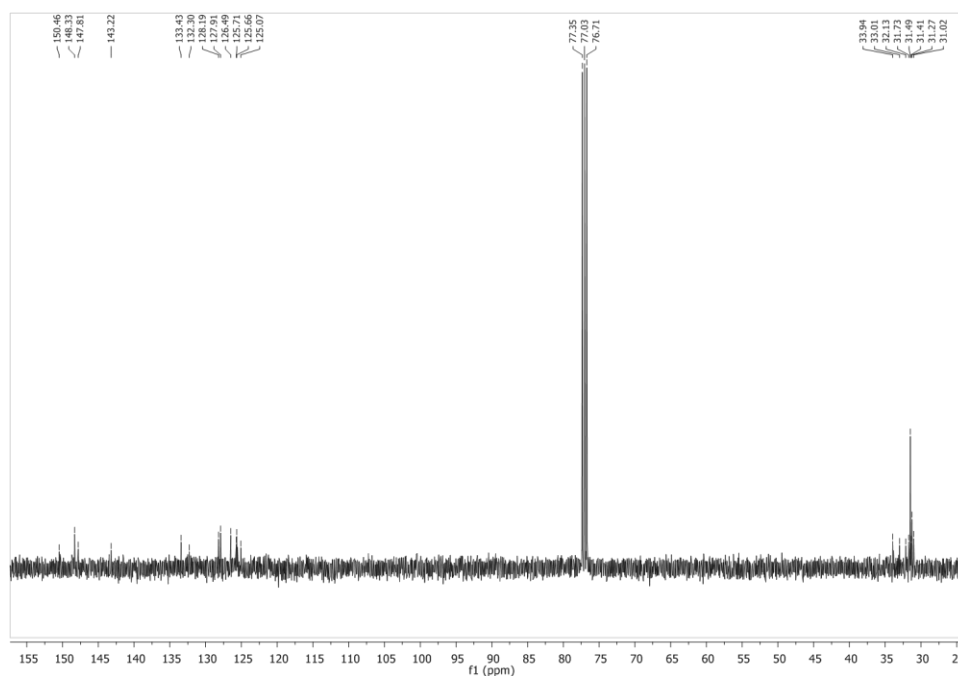


Figure 8-34-<sup>13</sup>C NMR of methylated *p*-*tert*-butylcalix-[4]-arene *via* methyl iodide.

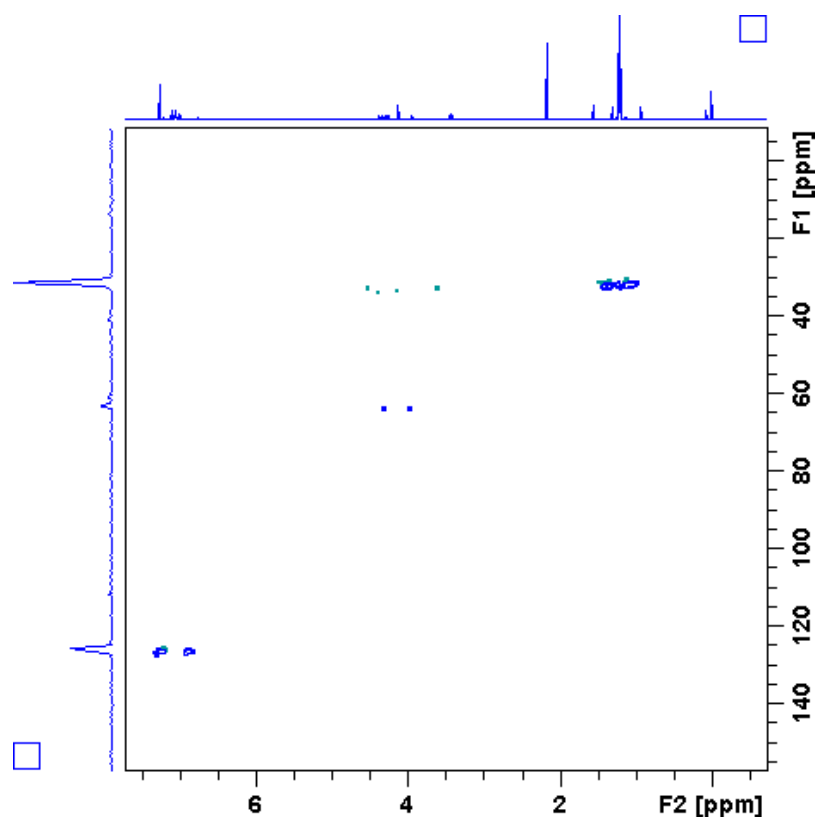


Figure 8-35-HSQC of methylated *p-tert*-butylcalix-[4]-arene *via* methyl iodide.

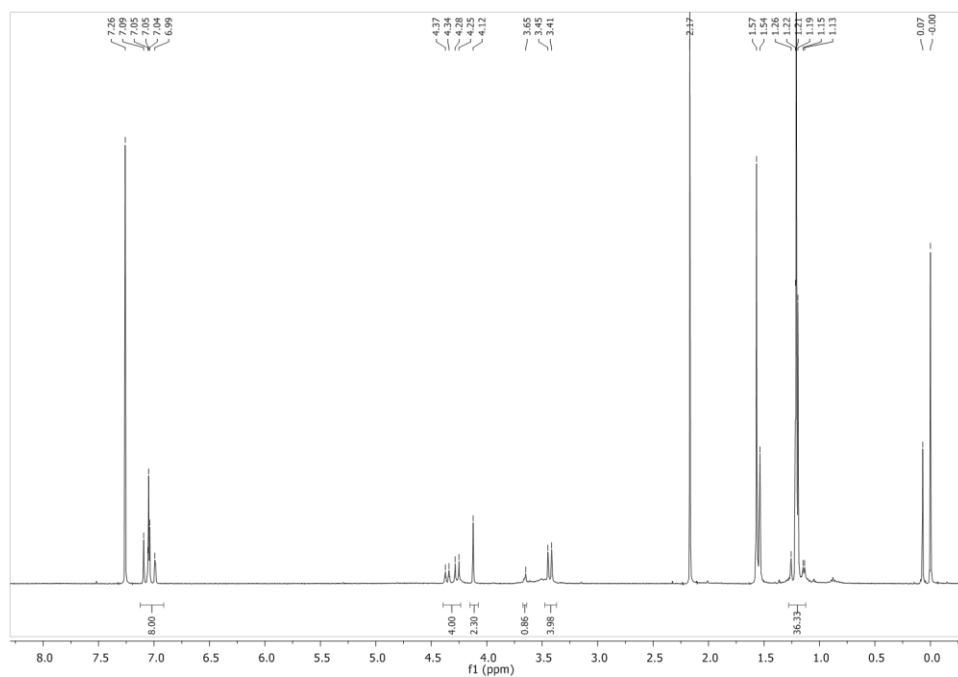


Figure 8-36- $^1\text{H}$  NMR of methylated *p-tert*-butylcalix-[4]-arene *via* methyl iodide with  $\text{D}_2\text{O}$  shake.

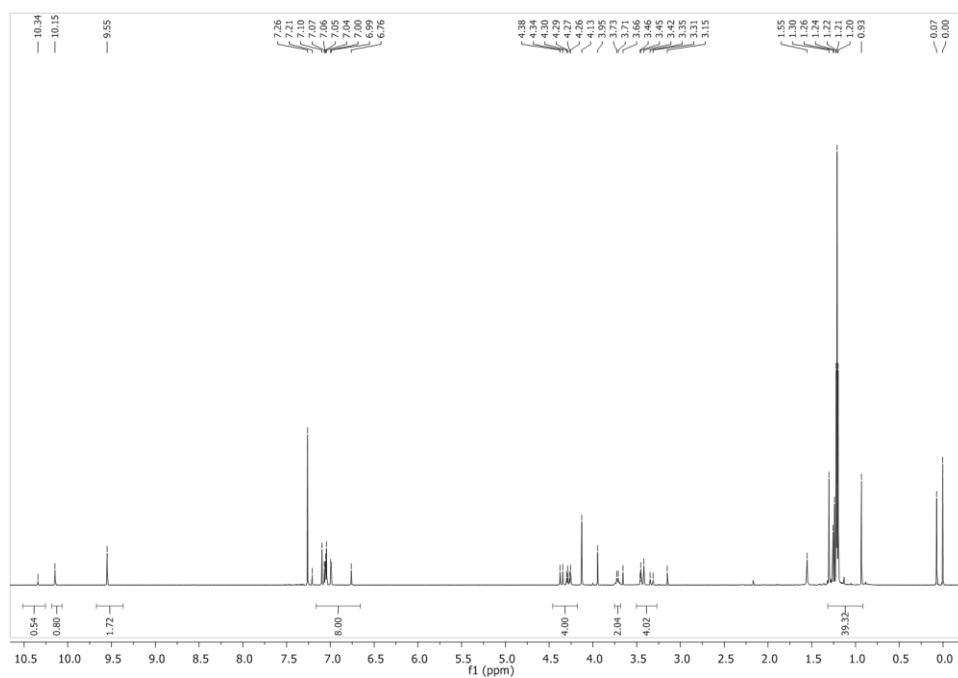


Figure 8-37-<sup>1</sup>H NMR of ethylated *p*-*tert*-butylcalix-[4]-arene *via* ethyl iodide.

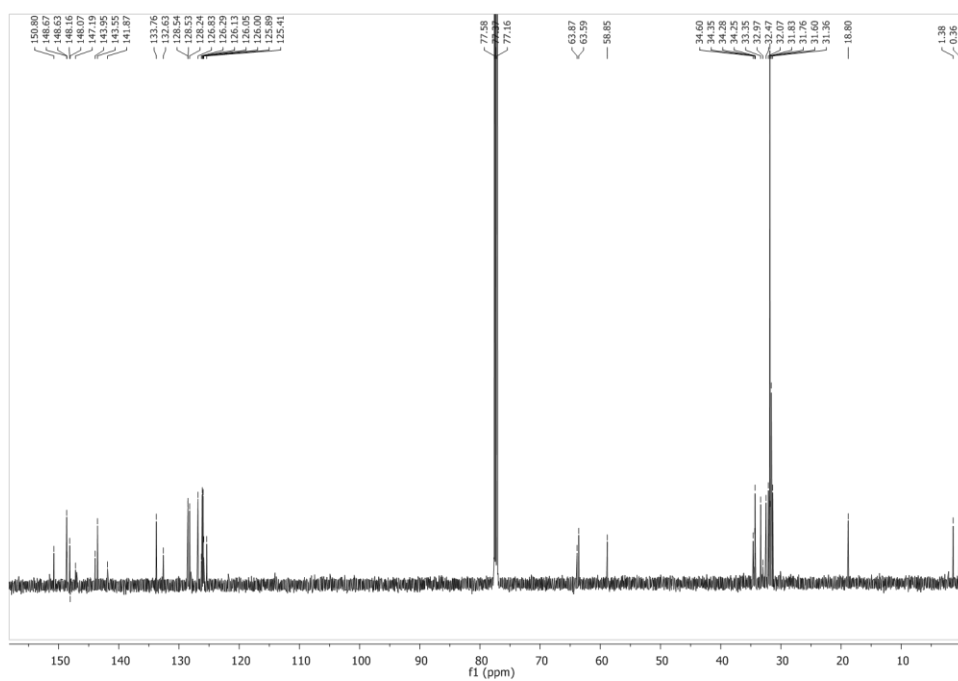
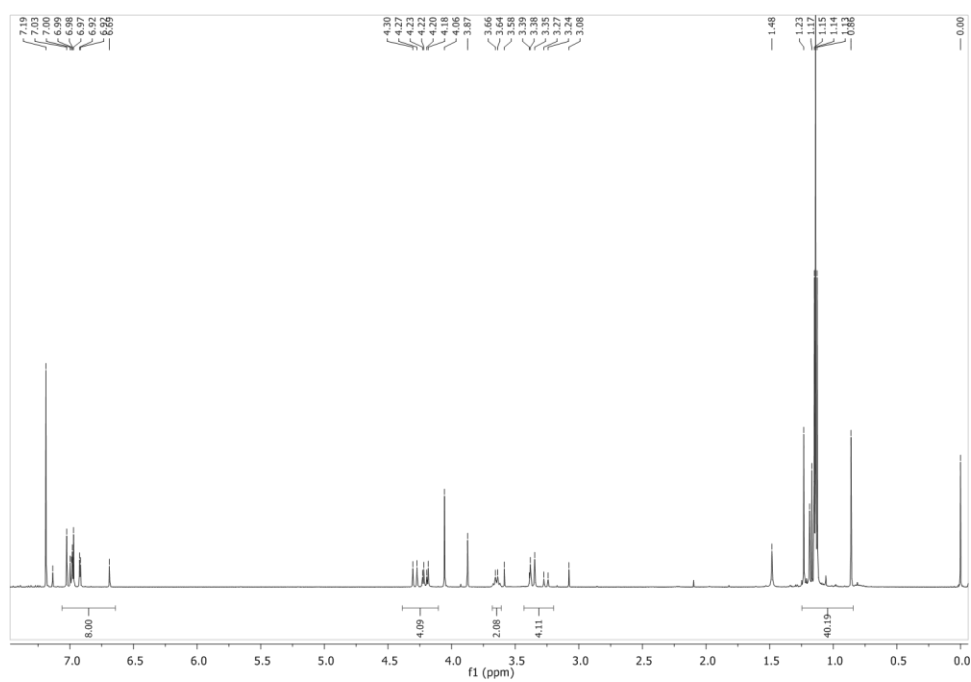
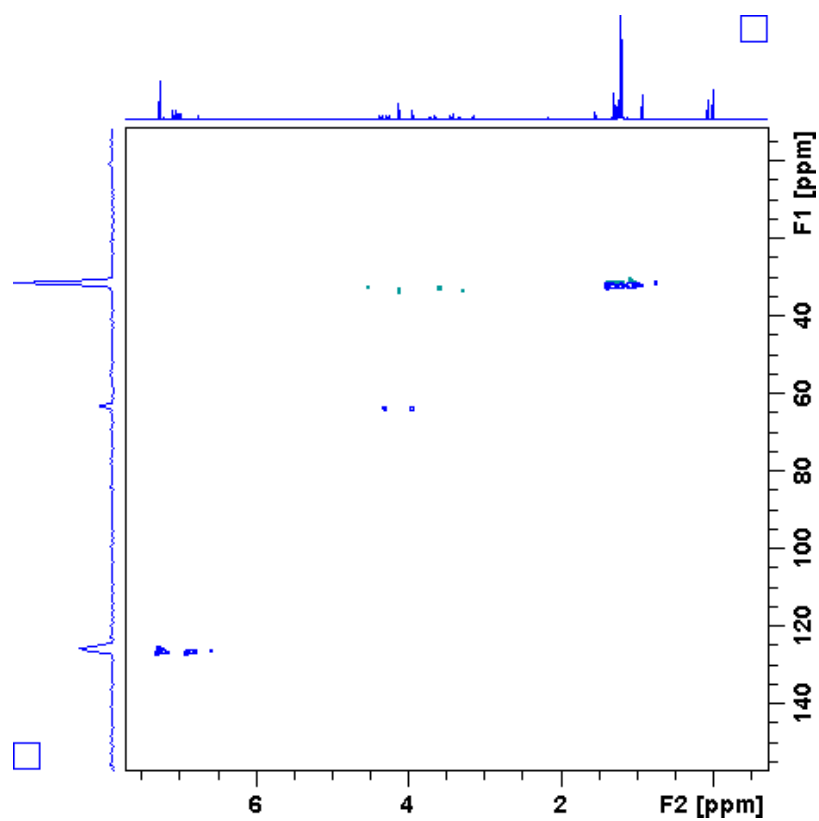


Figure 8-38-<sup>13</sup>C NMR of ethylated *p*-*tert*-butylcalix-[4]-arene *via* ethyl iodide.



**Figure 8-39-** $^1\text{H}$  NMR of ethylated p-*tert*-butylcalix-[4]-arene *via* ethyl iodide with a  $\text{D}_2\text{O}$  shake.



**Figure 8-40-**HSQC of ethylated p-*tert*-butylcalix-[4]-arene *via* ethyl iodide.

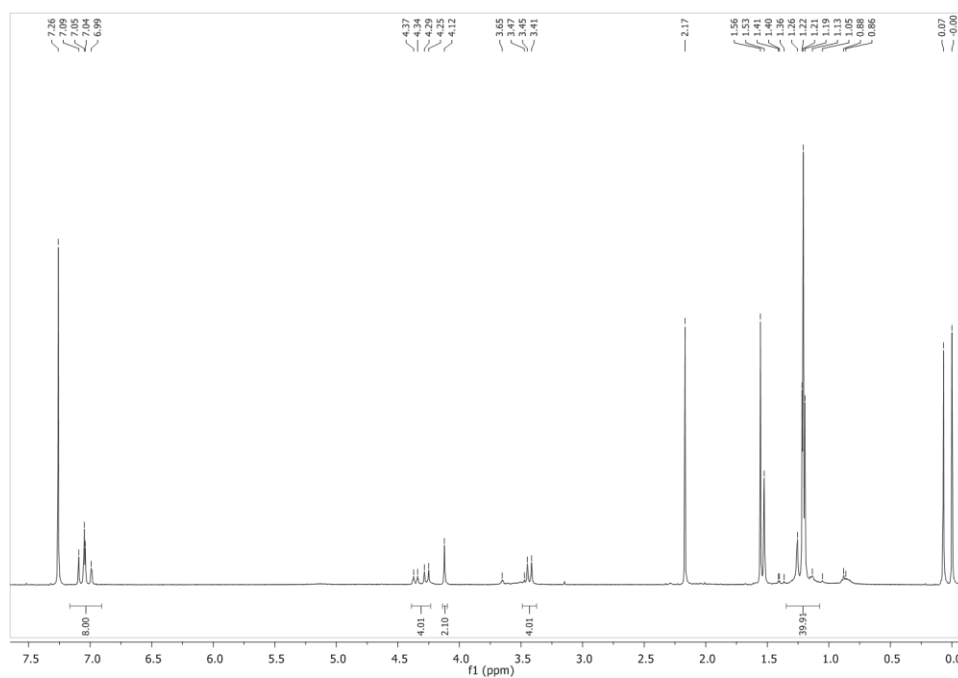


Figure 8-41- $^1\text{H}$  NMR of ethylated *p*-*tert*-butylcalix-[4]-arene via ethyl iodide with  $\text{D}_2\text{O}$ .

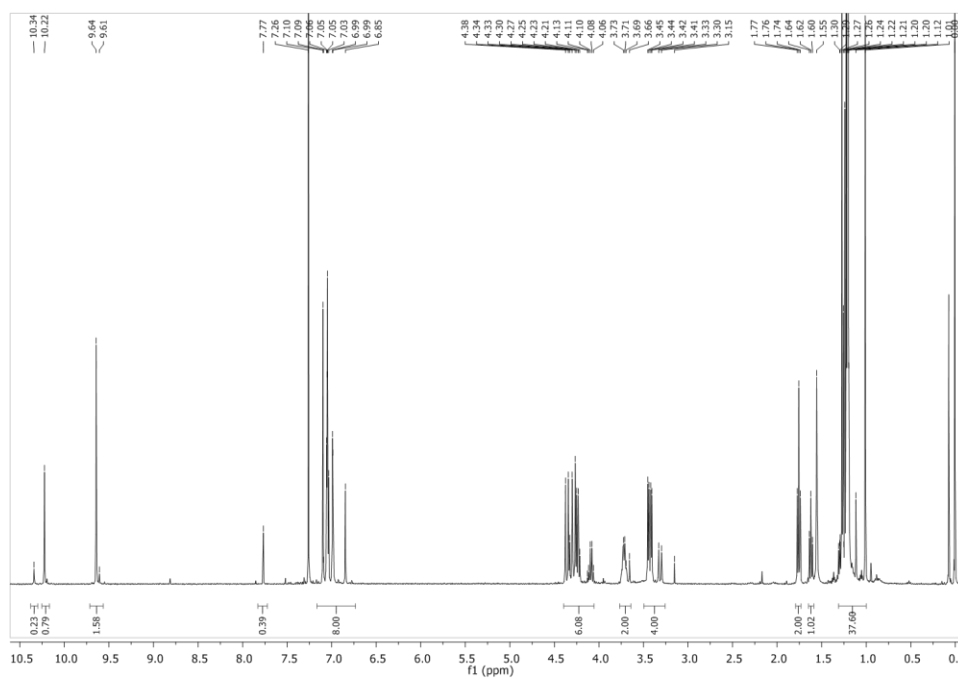


Figure 8-42-  $^1\text{H}$  NMR of propylated *p*-*tert*-butylcalix-[4]-arene via propyl iodide.

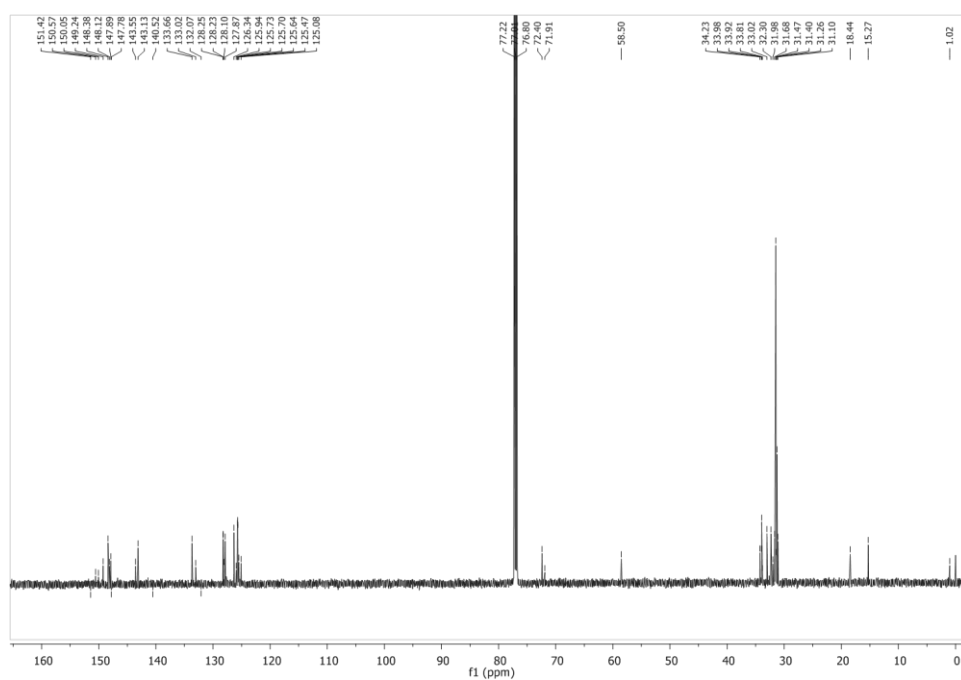


Figure 8-43- $^{13}\text{C}$  NMR of propylated *p*-*tert*-butylcalix-[4]-arene *via* propyl iodide.

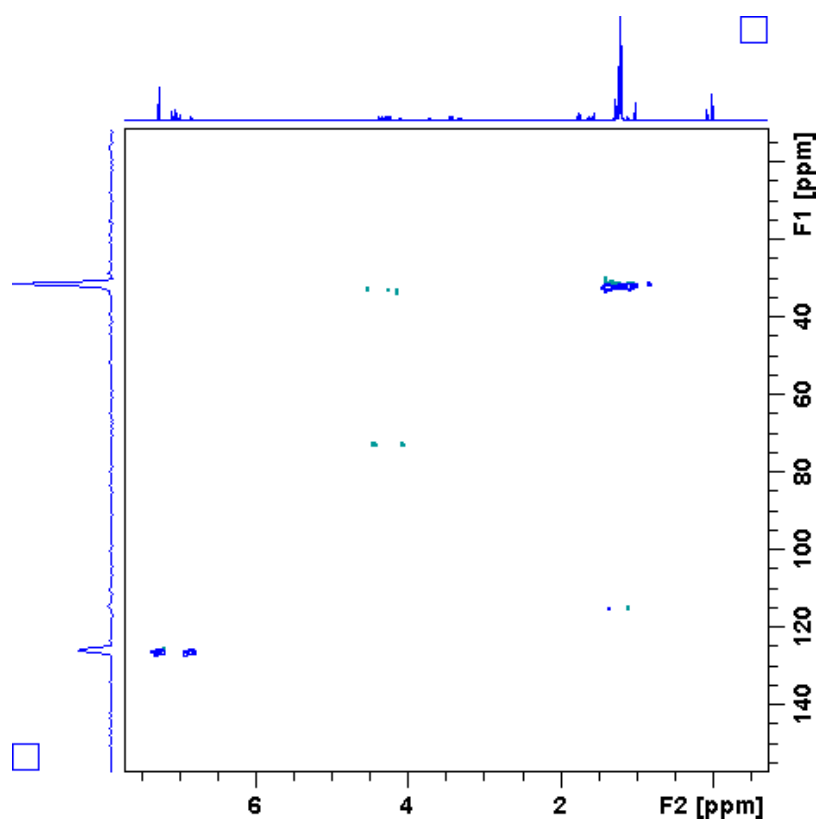


Figure 8-44-HSQC of propylated *tert*-butylcalix-[4]-arene *via* propyl iodide.

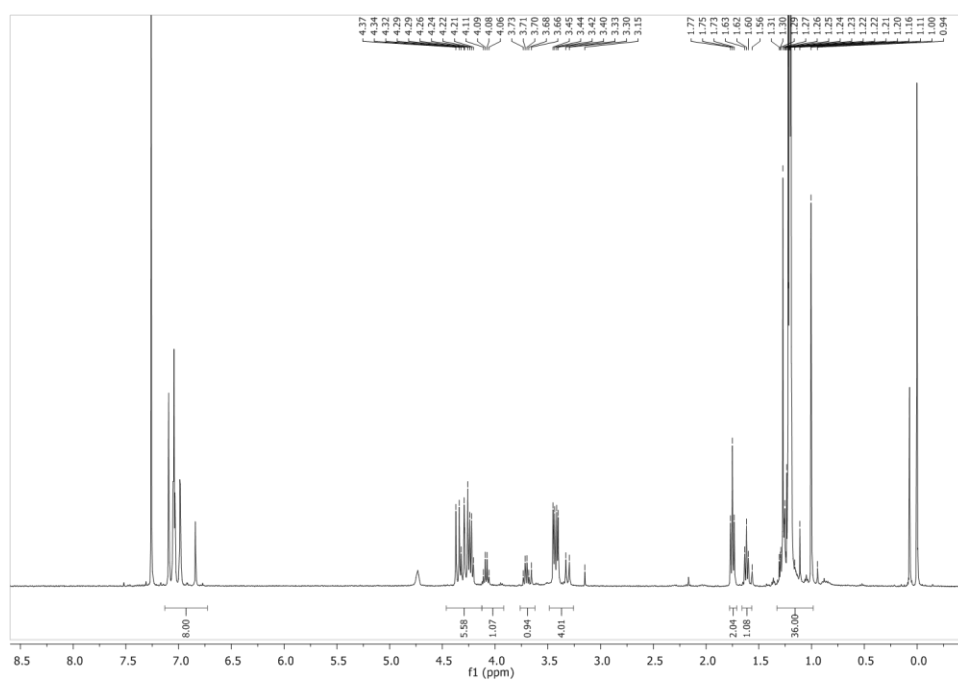


Figure 8-45-<sup>1</sup>H NMR of propylated *p*-*tert*-butylcalix-[4]-arene via propyl iodide with D<sub>2</sub>O shake.

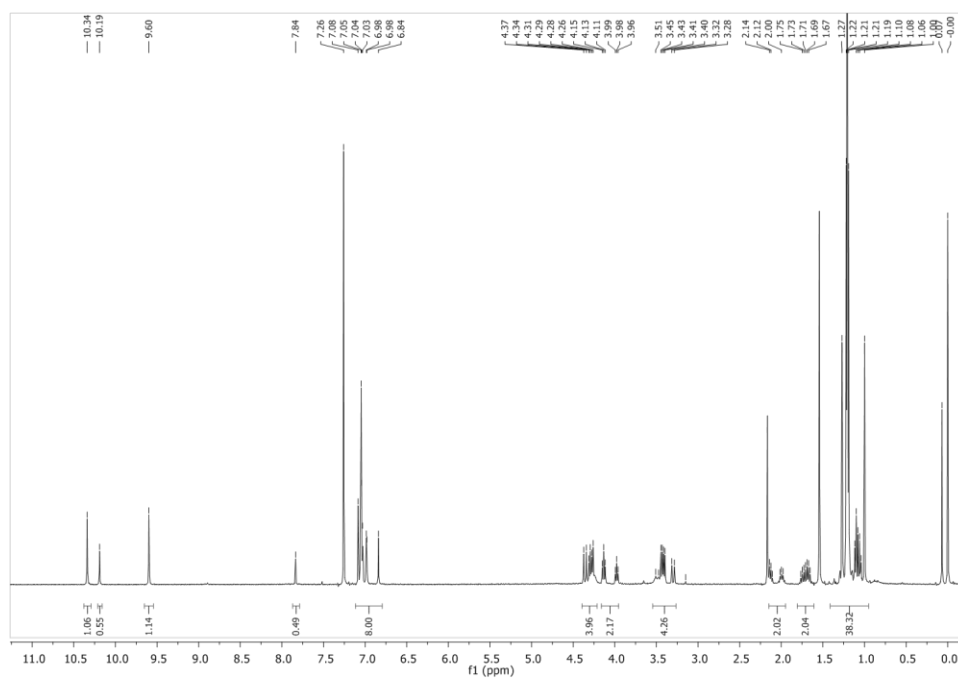


Figure 8-46-<sup>1</sup>H NMR of butylated *p*-*tert*-butylcalix-[4]-arene via butyl iodide.



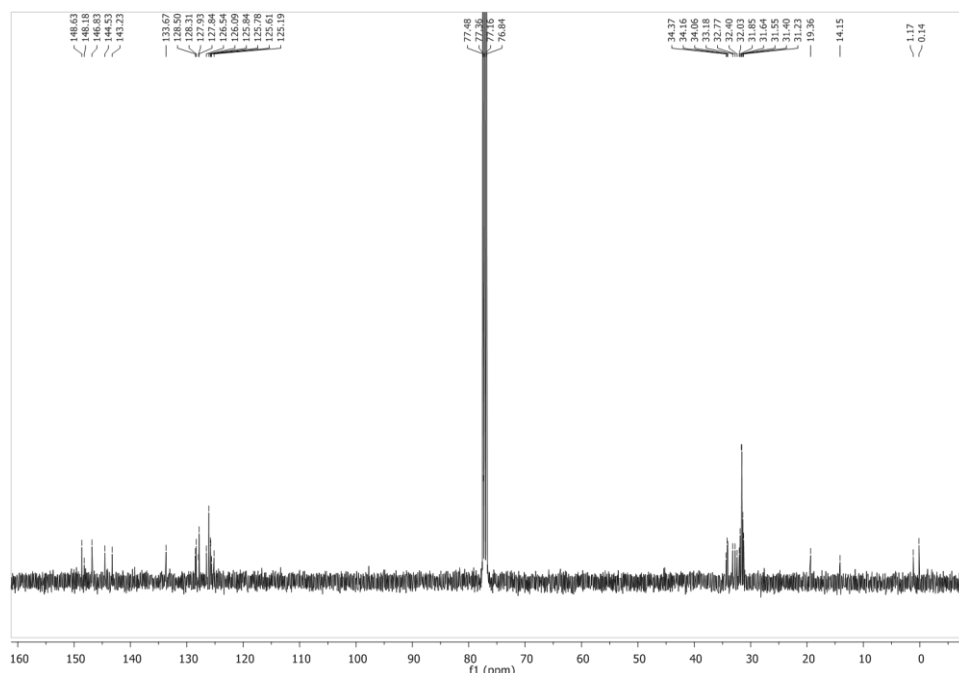


Figure 8-47- $^{13}\text{C}$  NMR of butylated *p*-*tert*-butylcalix-4-arene *via* butyl iodide.

## 8.4.2 Thermogravimetric analysis

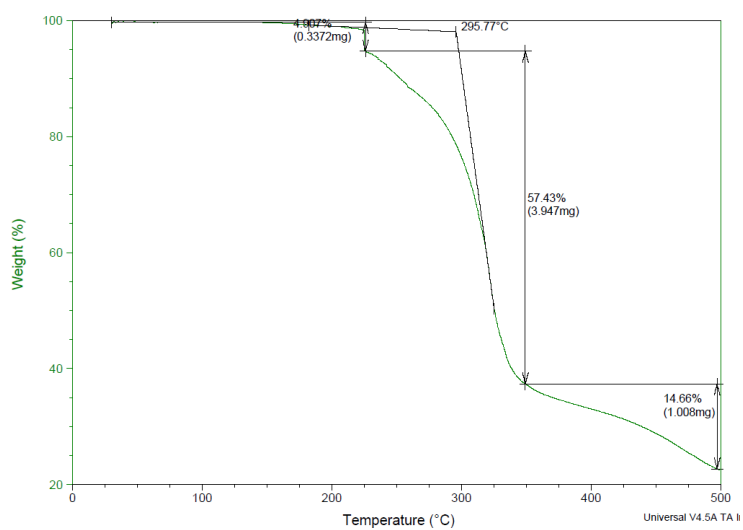
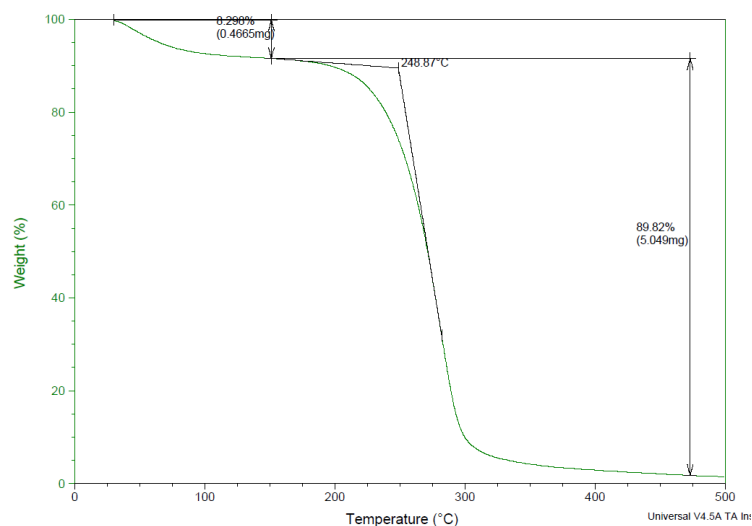
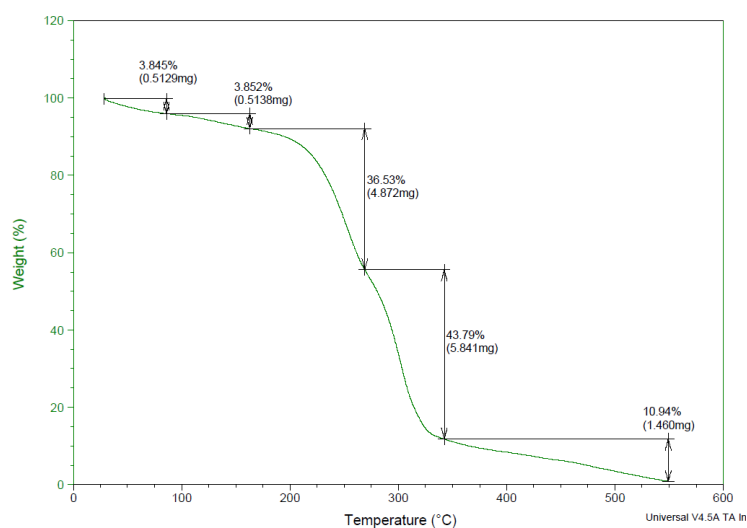


Figure 8-48-TGA analysis of *p*-*tert*-butylcalix-[4]-arene.



**Figure 8-49**-TGA of trihexylterradecylphosphonium acetate, [P<sub>66614</sub>][OAc].



**Figure 8-50**-TGA analysis of [P<sub>66614</sub>][OAc] and *p*-*tert*-butylcalix-[4]-arene 20 mol%.

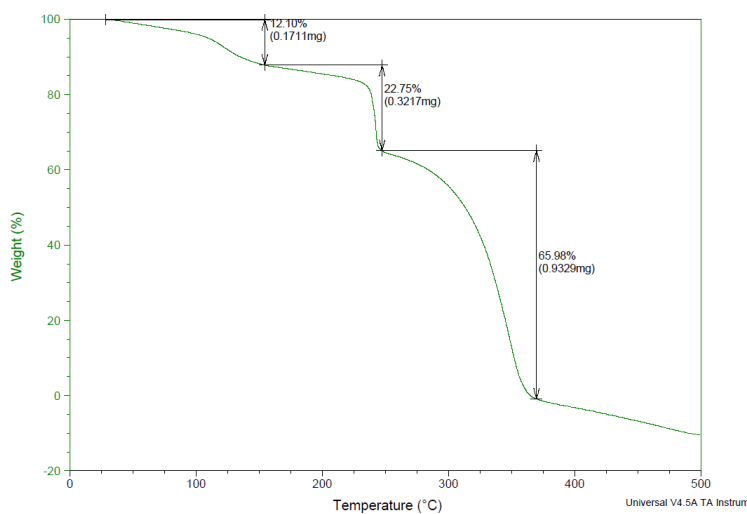


**Figure 8-51**- TGA analysis of tributylmethylammonium *p*-*tert*-butylcalix-[4]-arate, [N<sub>4441</sub>][TBC].

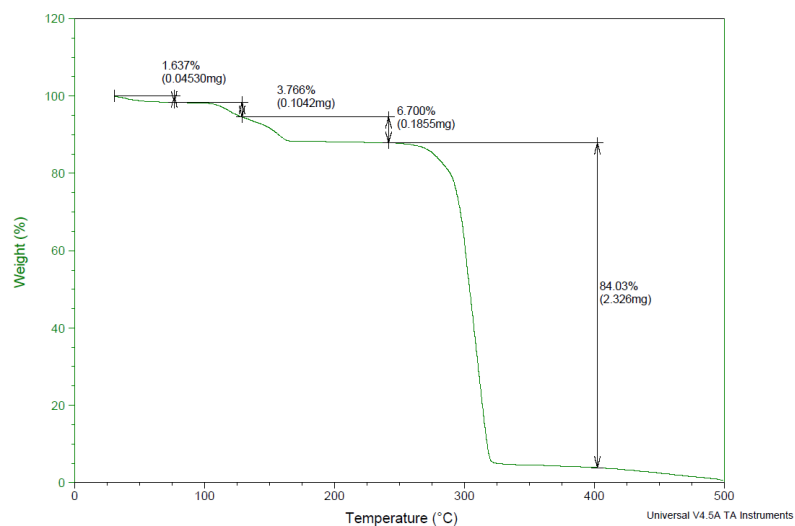


**Figure 8-52**-TGA analysis of triethylmethylammonium *p*-*tert*-butylcalix-[4]-arate, [N<sub>2221</sub>][TBC].

## 8.5 Liquid coordination complexes of chlorometallates and donor ligands

### 8.5.1 Acronyms

Table 8-1- Table of acronyms.

Acronym	Definition
ACA	Acetamide
DMA	Dimethylacetamide
Ur	Urea
SUr	Thiourea
P <sub>888</sub>	Trioctylphosphine
P <sub>888</sub> E	Trioctylphosphine chalcogenide
P <sub>888</sub> O	Trioctylphosphine oxide
P <sub>888</sub> S	Trioctylphosphine sulfide
P <sub>888</sub> Se	Trioctylphosphine selenide
LCC	Liquid coordination complex
IL	Ionic liquid

### 8.5.2 Density Data for chlorogallate and chloroindate liquid coordination complexes

Table 8-2- Density data for P<sub>888</sub>E-GaCl<sub>3</sub> LCCs (E=O)

		Temperature/ K						Linear fit		
Ligand		298	308	318	328	338	343	M	C	R <sup>2</sup>
		GaCl <sub>3</sub>								
Density g/cm <sup>3</sup>	$\chi_{\text{GaCl}_3}=0.5$									
	P <sub>888</sub> O	1.0796	1.0715	1.0638	1.0563	1.0492	1.0458	-0.0008	1.3027	0.9993
	$\chi_{\text{GaCl}_3}=0.60$									
	P <sub>888</sub> O	1.1544	1.1466	1.1387	1.1308	1.123	1.1191	-0.0008	1.3884	1
	$\chi_{\text{GaCl}_3}=0.67$									
	P <sub>888</sub> O	1.235	1.2265	1.2181	1.2098	1.2015	1.1973	-0.0008	1.4842	1
	$\chi_{\text{GaCl}_3}=0.75$									
	P <sub>888</sub> O	1.361	1.3518	1.3429	1.3334	1.3242	1.3195	-0.0009	1.6359	0.9999

**Table 8-3-** Density data for P<sub>888</sub>E-GaCl<sub>3</sub> LCCs (E=S, Se)

	Ligand	Temperature/kelvin								Linear fit		
		293	303	313	323	333	343	353	363	M	C	R <sup>2</sup>
Density g/cm <sup>3</sup>		GaCl <sub>3</sub>										
		$\chi_{\text{GaCl}_3}=0.5$										
	P <sub>888</sub> S	1.1068	1.0997	1.0963	1.0853	1.0782	1.071	1.0638	1.0567	-0.00073	1.3195	0.994
	P <sub>888</sub> Se	1.1881	1.1804	1.1769	1.1652	1.1577	1.1502	1.1427	1.1351	-0.00077	1.4124	0.994
		$\chi_{\text{GaCl}_3}=0.60$										
	P <sub>888</sub> S	1.1887	1.181	1.1773	1.1655	1.1578	1.1502	1.1424	1.1348	-0.00078	0.4173	0.9941
	P <sub>888</sub> Se	1.262	1.2539	1.25	1.2374	1.2293	1.2211	1.213	1.2049	-0.00083	1.5044	0.9939
		$\chi_{\text{GaCl}_3}=0.67$										
	P <sub>888</sub> S	1.2615	1.2534	1.2494	1.2368	1.2286	1.2206	1.2124	1.2043	-0.00083	1.5042	0.9941
	P <sub>888</sub> Se	1.3297	1.3209	1.3168	1.3035	1.2949	1.2863	1.2776	1.2691	-0.00088	1.5865	0.9942
		$\chi_{\text{GaCl}_3}=0.75$										
	P <sub>888</sub> S	1.3717	1.3627	1.3581	1.3442	1.3351	1.3261	1.3171	1.3081	-0.00092	1.6415	0.9944
	P <sub>888</sub> Se	1.4318	1.4222	1.4175	1.4031	1.3937	1.3845	1.3753	1.3661	-0.00095	1.7099	0.9945

**Table 8-4-** Density data for P<sub>888</sub>E-InCl<sub>3</sub> LCCs (E=O, S, Se)

	Ligand	Temperature/kelvin								Linear fit		
		293	303	313	323	333	343	353	363	M	C	R <sup>2</sup>
Density g/cm <sup>3</sup>	InCl <sub>3</sub>											
	$\chi_{\text{InCl}_3}=0.25$											
	P <sub>888</sub> O	1.0023	0.9948	0.9905	0.9795	0.972	0.9645	0.9569	0.9491	-0.00077	1.018589	0.9963
	P <sub>888</sub> S	1.0034	0.9954	0.991	0.9801	0.9727	0.9653	0.9579	0.9506	-0.00076	1.01906	0.996762
	P <sub>888</sub> Se	1.0932	1.0849	1.0803	1.0682	1.0601	1.0521	1.0442	1.0364	-0.00082	1.1104	0.9964
	$\chi_{\text{InCl}_3}=0.33$											
	P <sub>888</sub> O	1.0517	1.0446	1.041	1.0303	1.0231	1.0157	1.0082	1.0003	-0.00074	1.067779	0.9951
	P <sub>888</sub> S	1.0525	1.044	1.0394	1.0277	1.0198	1.0121	1.0043	0.9966	-0.00081	1.069048	0.996507
	P <sub>888</sub> Se	1.1401	1.1307	1.1258	1.1135	1.1053	1.0974	1.0893	1.0812	-0.00084	1.1571	0.9965
	$\chi_{\text{InCl}_3}=0.40$											
	P <sub>888</sub> O	1.0936	1.0851	1.0805	1.0687	1.0608	1.0528	1.0445	1.035	-0.00084	1.1112	0.9964
	P <sub>888</sub> S	1.0972	1.0886	1.0839	1.0718	1.0633	1.0547	1.0455	1.0352	-0.00089	1.116344	0.995646
	P <sub>888</sub> Se	1.186	1.1773	1.1727	1.1601	1.1516	1.1432	1.1348	1.1266	-0.00086	1.2049	0.9959

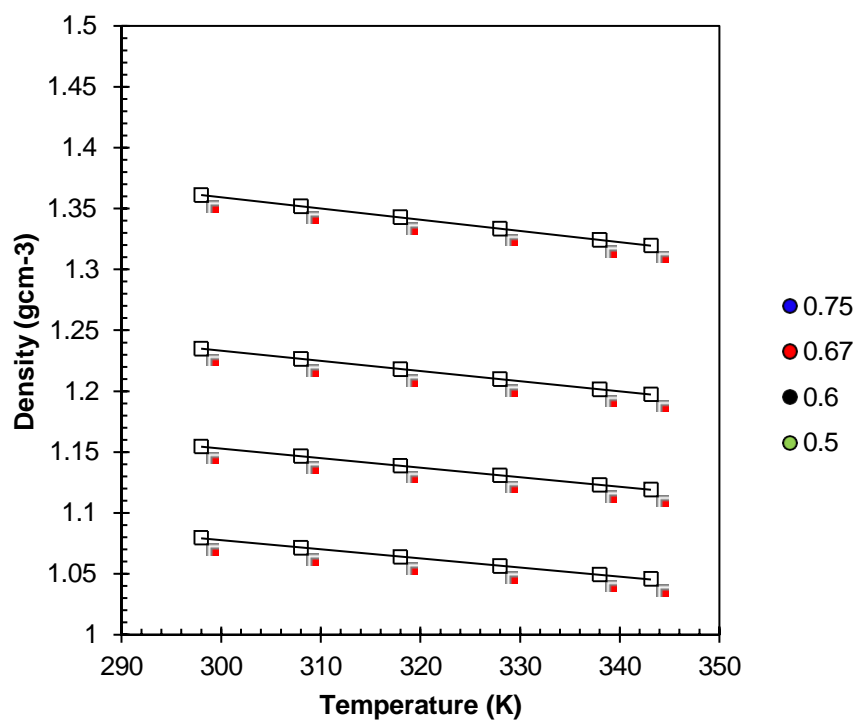


Figure 8-53- Density plot of P<sub>888</sub>O-GaCl<sub>3</sub>.

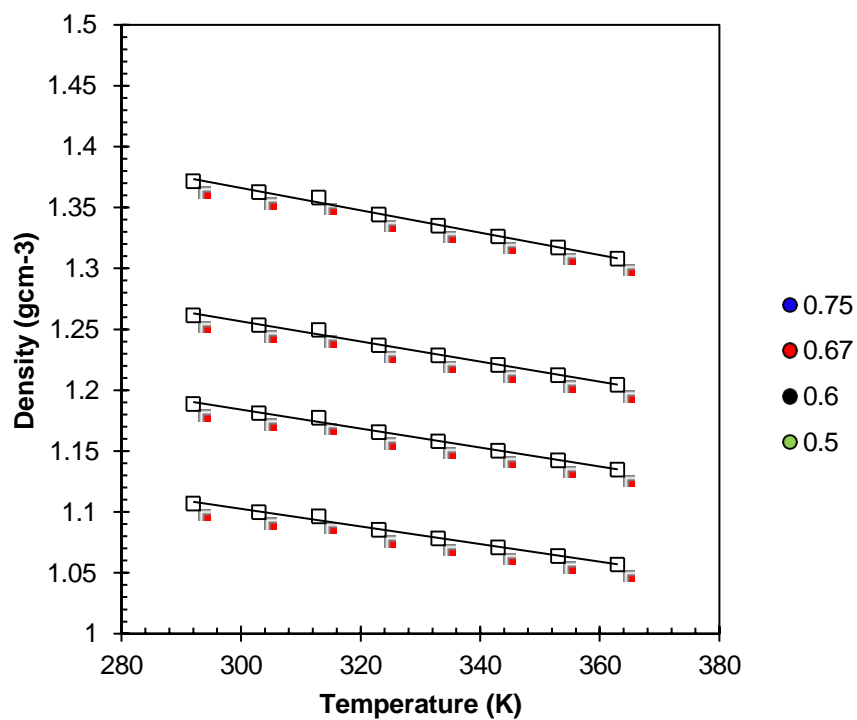


Figure 8-54- Density plot of P<sub>888</sub>S-GaCl<sub>3</sub>.

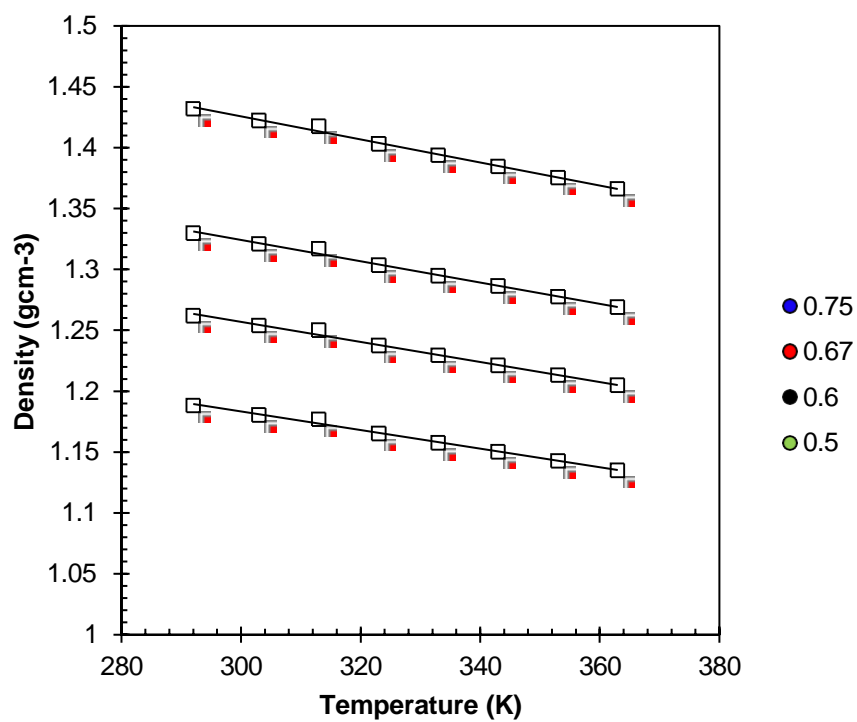


Figure 8-55- Density plot of P<sub>88</sub>Se-GaCl<sub>3</sub>.

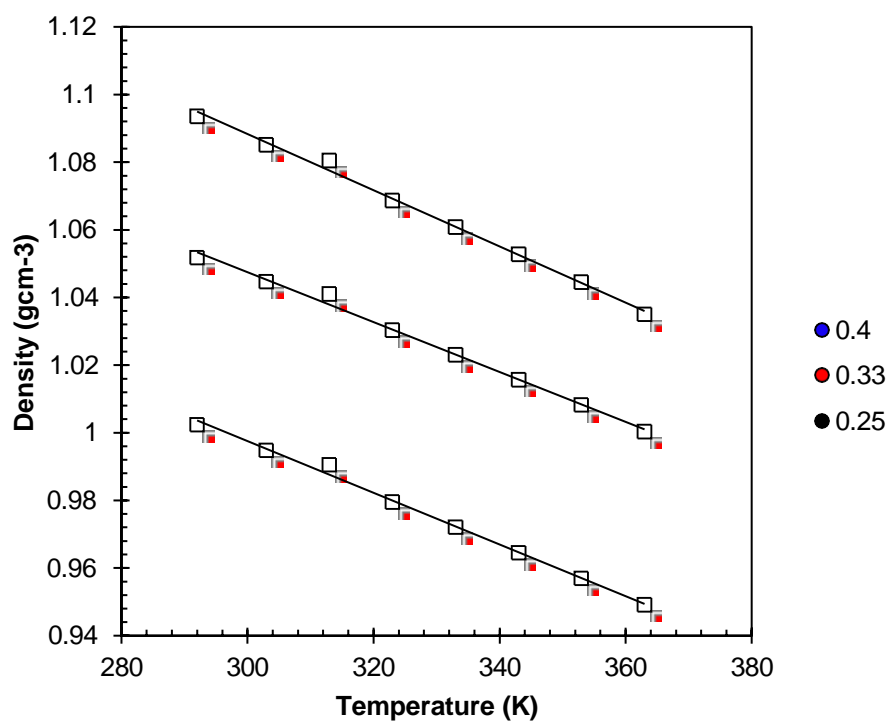


Figure 8-56- Density plot of P<sub>88</sub>O-InCl<sub>3</sub>.



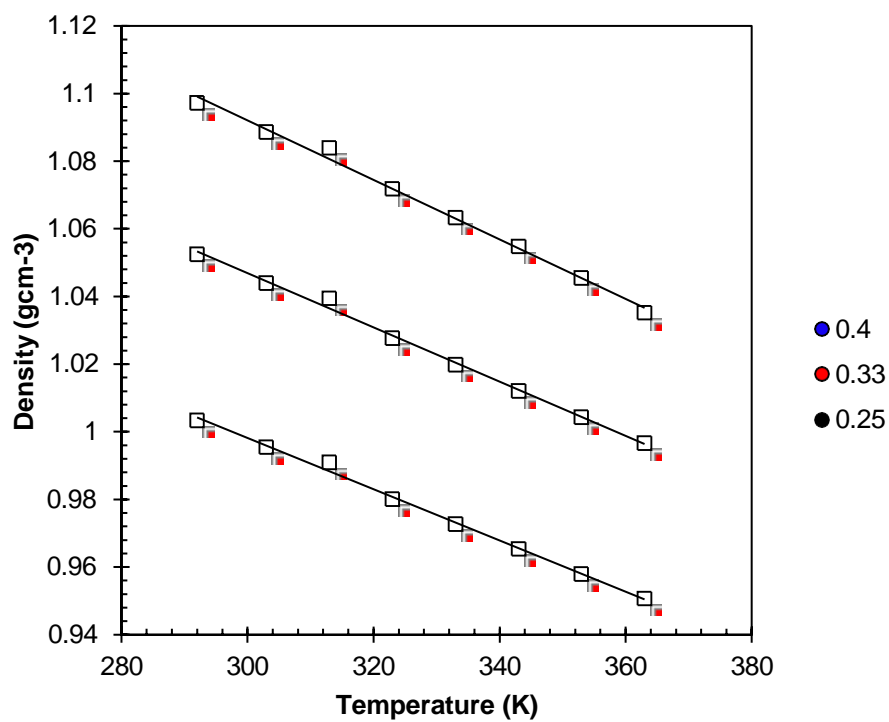


Figure 8-57- Density plot of  $P_{88}S-InCl_3$ .

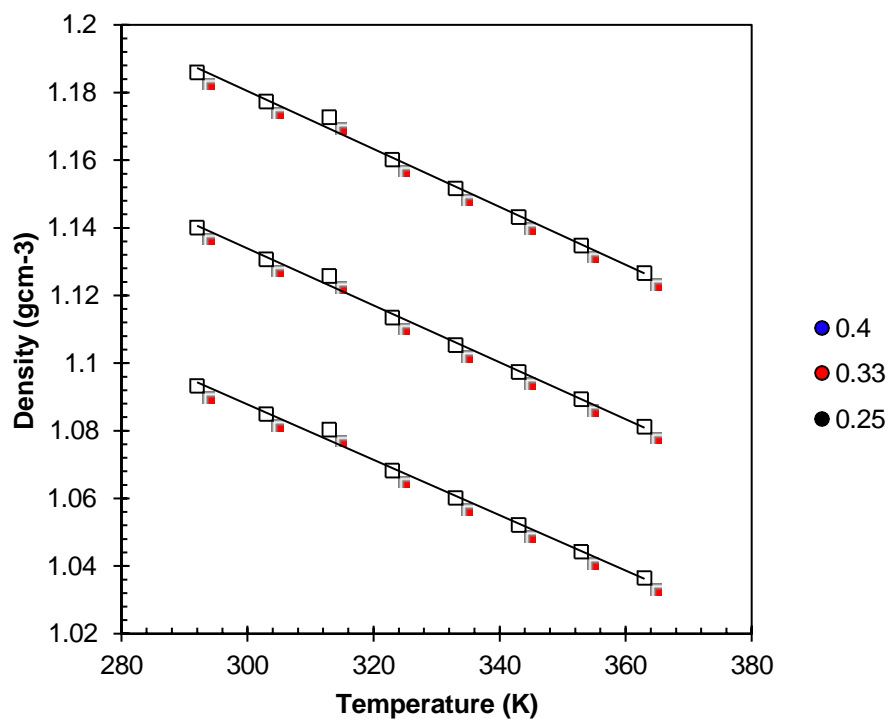


Figure 8-58- Density plot of  $P_{88}Se-InCl_3$ .

### 8.5.3 Viscosity data for chlorogallate and chloroindate liquid coordination complexes

**Table 8-5-** Viscosity data for P<sub>888</sub>E-GaCl<sub>3</sub> and VFT fit data (E=O).

VFT fit according to $Y=10^{A+(B/(T-T_0))}$	Ligand	P <sub>888</sub> O			
	$\chi_{\text{GaCl}_3}$	0.5	0.6	0.67	0.75
	A	-1.35376	-1.2295	-1.0655	-0.8688
	B	547.23872	526.88893	485.68992	410.41956
	T <sub>0</sub>	144.52966	143.54344	146.91057	160.9753
	Temperature/ Kelvin	Viscosity/ cP			
	298.15	161.6407	150.8096	139.9288	132.7722
	308.15	97.8352	93.6373	88.4397	83.1947
	318.15	62.9762	61.3622	59.0417	55.2462
	328.15	42.21	42.1623	41.1081	38.4889
	338.15	29.6738	30.0302	29.7741	28.0602
	343.15	25.2357	25.7262	25.7065	24.2536

**Table 8-6-** Viscosity data for P<sub>888</sub>E-GaCl<sub>3</sub> and VFT fit data (E=O, S, Se).

	Ligand	P <sub>888</sub> Se				P <sub>888</sub> S			
	$\chi_{\text{GaCl}_3}$	0.5	0.6	0.67	0.75	0.5	0.6	0.67	0.75
VFT fit according to $Y=10^{A+(B/(T-T_0))}$	A	-1.96571	-1.32219	-1.22159	-0.98005	-1.65659	-1.39853	-1.12849	-0.9176
	B	828.32222	620.21036	591.38062	498.89627	703.3058	634.39945	552.5303	464.34631
	T <sub>0</sub>	127.31288	145.86717	148.60426	158.6625	139.10436	141.98603	151.61204	163.32539
	Temperature/ Kelvin	Viscosity/ cP							
	293.15	1069.19237	774.12608	740.80658	536.48153	810.84681	628.34543	596.07229	456.16824
	303.15	556.19379	417.99416	402.71608	297.04335	427.69956	345.21413	329.12486	253.03583
	313.15	310.13935	242.84028	235.86566	177.68908	241.53935	203.07227	196.2501	152.13817
	323.15	182.87856	149.81689	146.35341	112.62915	146.34223	126.35476	123.60485	97.00253
	333.15	114.96109	97.80548	96.39957	75.93114	93.08425	83.65222	82.17315	65.64348

#### 8.5.4 Nuclear magnetic resonance spectroscopic data for chlorogallate and chloroindate liquid coordination complexes

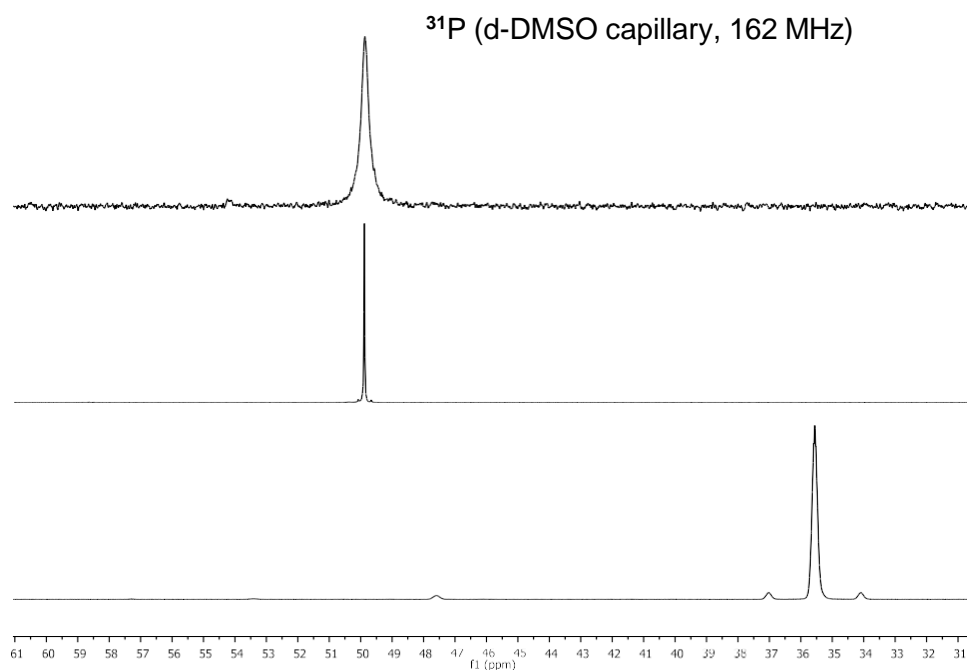


Figure 8-59- $^{31}\text{P}$  NMR spectra of  $\text{P}_{888}\text{O}$ ,  $\text{P}_{888}\text{S}$  and  $\text{P}_{888}\text{Se}$ . (Top-bottom)

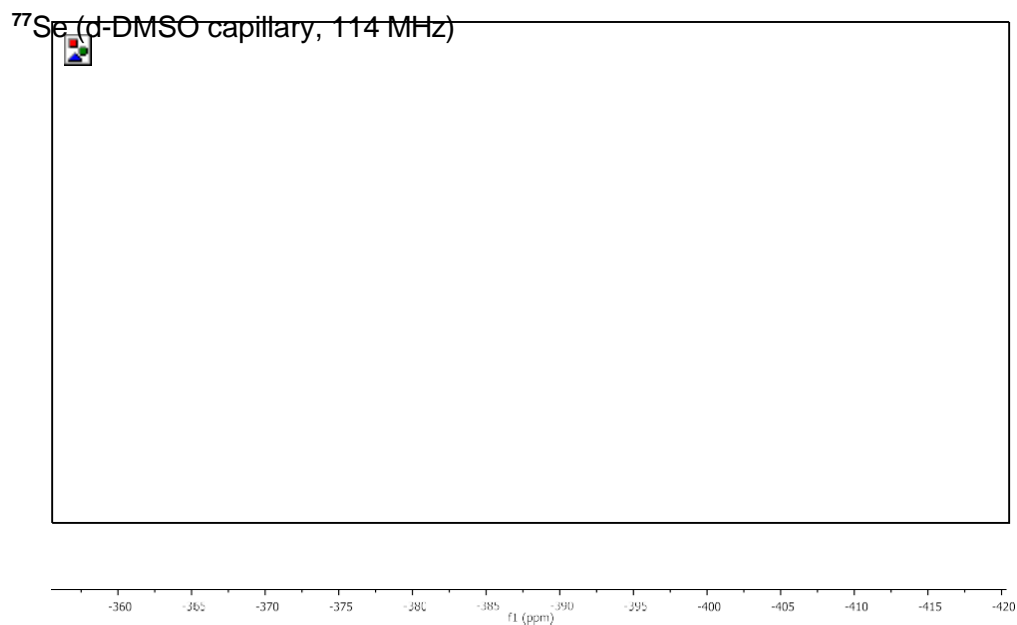
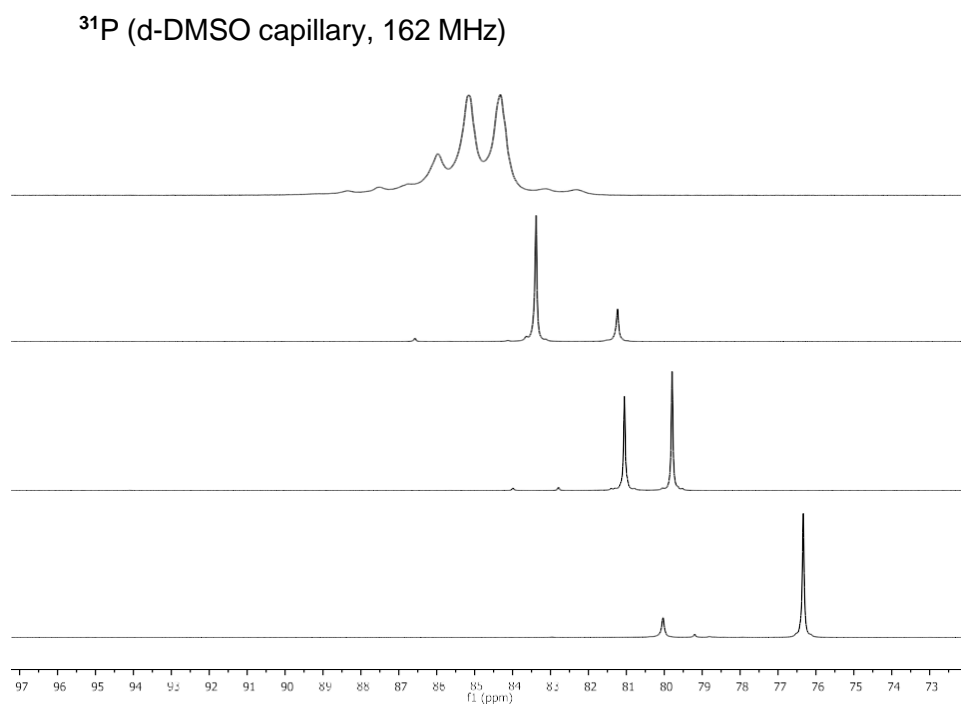
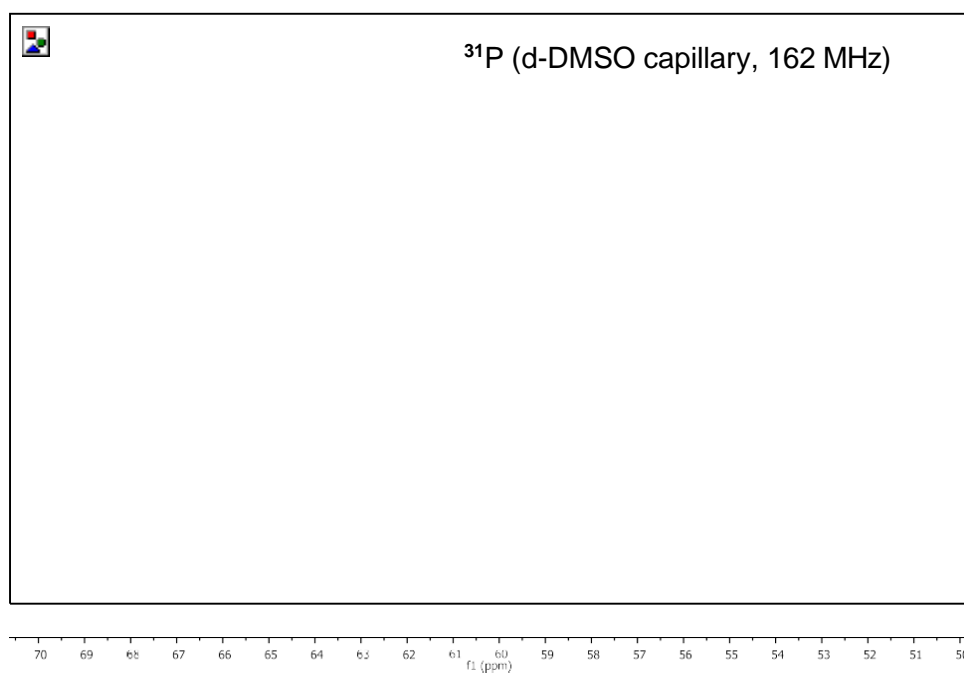


Figure 8-60- $^{77}\text{Se}$  NMR spectra of  $\text{P}_{888}\text{Se}$ .



**Figure 8-61**- $^{31}\text{P}$  NMR spectra of  $\text{P}_{88}\text{O-GaCl}_3$  mixtures (top-bottom)  $\chi_{\text{GaCl}_3} = 0.75, 0.67, 0.60, 0.50$ .



**Figure 8-62**- $^{31}\text{P}$  NMR spectra of  $\text{P}_{88}\text{S-GaCl}_3$  LCCs (top-bottom)  $\chi_{\text{GaCl}_3} = 0.75, 0.67, 0.60 \text{ \& } 0.50$

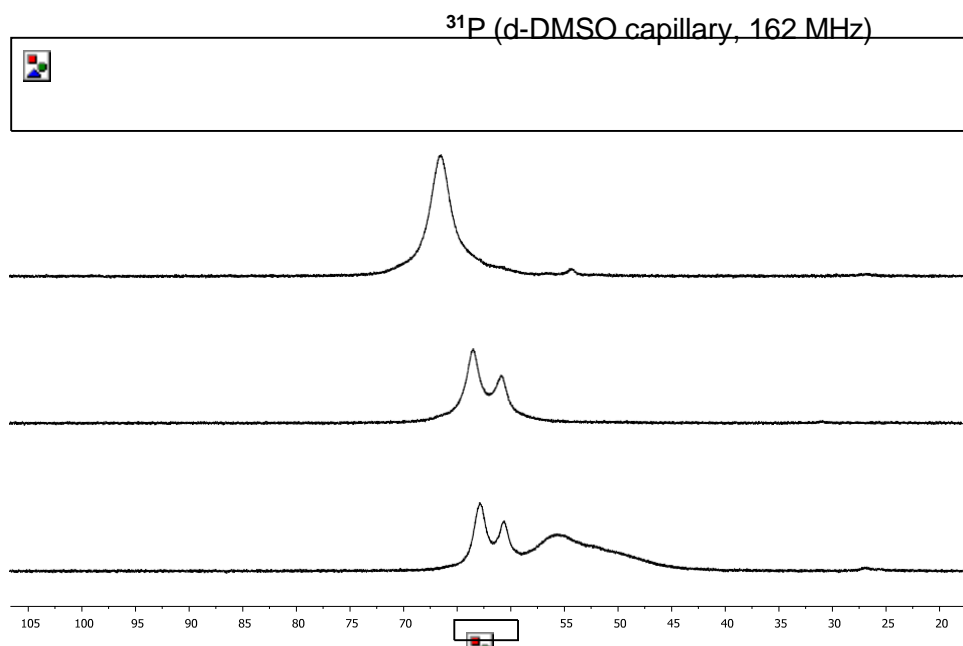


**Figure 8-63-**<sup>31</sup>P NMR spectra of P<sub>888</sub>O-InCl<sub>3</sub> LCCs (top-bottom)  $\chi_{\text{InCl}_3}$  = 0.50, 0.40, 0.33 & 0.25.

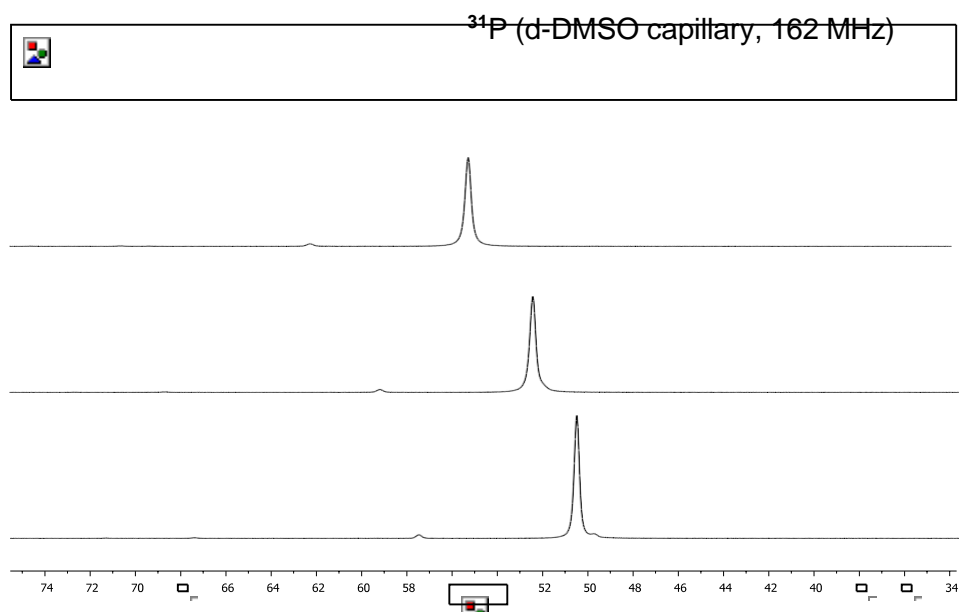


**Figure 8-64-**<sup>31</sup>P NMR spectra of P<sub>888</sub>S-InCl<sub>3</sub> LCCs (top-bottom)  $\chi_{\text{InCl}_3}$  = 0.50, 0.40, 0.33 & 0.25.

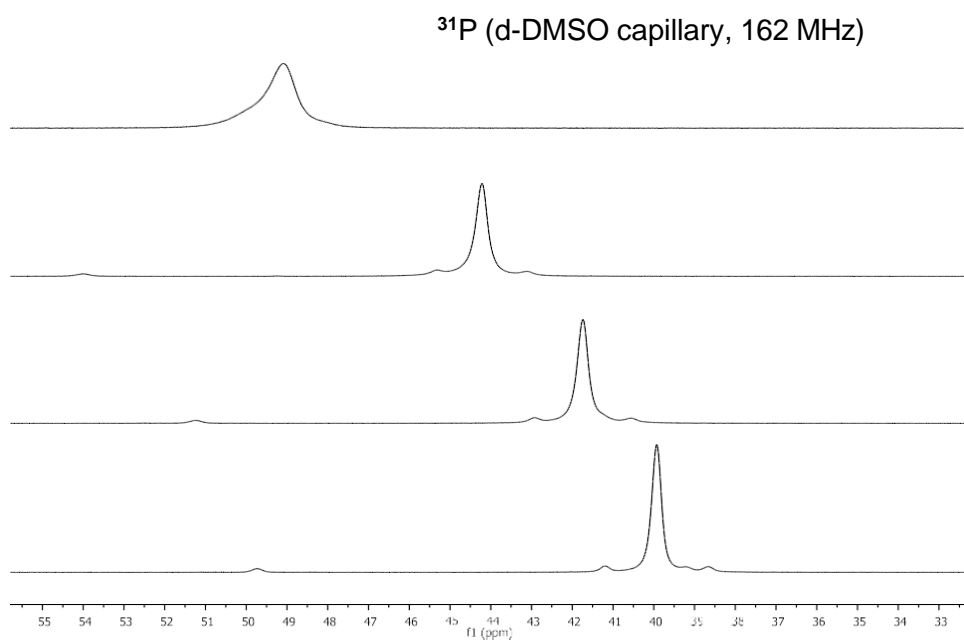


**Figure 8-65**-<sup>31</sup>P NMR spectra of P<sub>888</sub>Se-InCl<sub>3</sub> LCCs (top-bottom)  $\chi_{\text{InCl}_3}$  = 0.50, 0.40, 0.33 & 0.25.

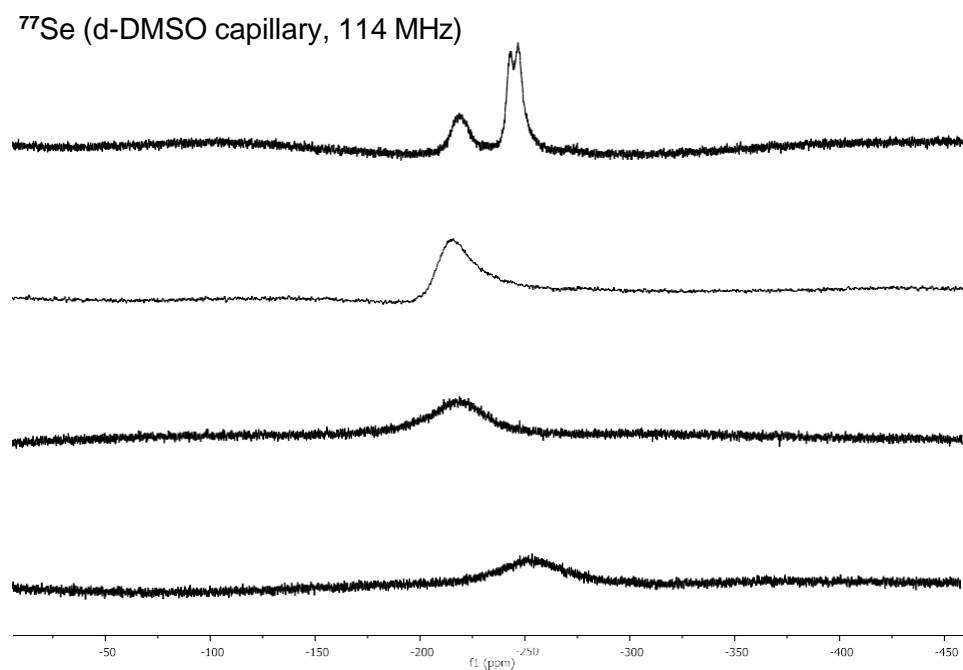


**Figure 8-66**-<sup>77</sup>Se NMR spectra of P<sub>888</sub>Se-InCl<sub>3</sub> LCCs (top-bottom)  $\chi_{\text{InCl}_3}$  = 0.50, 0.40, 0.33 & 0.25.

**Table 8-7-** Summary of  $^{31}\text{P}$  NMR spectra of LCCs synthesised.

		$\text{P}_{888}\text{O}$		$\text{P}_{888}\text{S}$		$\text{P}_{888}\text{Se}$	
		$\delta^{31}\text{P}$	$\Delta\delta^{31}\text{P}$	$\delta^{31}\text{P}$	$\Delta\delta^{31}\text{P}$	$\delta^{31}\text{P}$	$\Delta\delta^{31}\text{P}$
	$\chi_{\text{MClx}}$	ppm					
$\text{MCl}_3$	0	49.91	-	49.49	-	36.41	-
$\text{GaCl}_3$	0.5	76.5	26.59	57.93	8.44	47.51	11.1
		80.15	30.24	60.15	10.66	50.33	13.92
				64.66	15.17	57.03	20.62
	0.6	79.97	30.06	59.54	10.05	49.53	13.12
		81.23	31.32	61.12	11.63	59.36	22.95
				66.35	16.86		
	0.67	81.31	31.4	60.42	10.93	51.13	14.72
		83.41	33.5	62.33	12.84	61.06	24.65
				67.35	17.86		
	0.75	84.37	34.46	60.85	11.36	51.98	15.57
		85.21	35.3	61.42	11.93	62.1	25.69
		86.02	36.11	68.43	18.94		
$\text{InCl}_3$	0.25	55.92	6.01	49.9	0.41	40.1	3.69
		60.90	10.99	50.66	1.17	49.83	13.42
		63.11	13.20	57.6	8.11		
	0.33	60.56	10.65	52.49	3	41.79	5.38
		63.16	13.25	59.22	9.73	51.26	14.85
	0.4	54.52	4.61	55.16	5.67	44.36	7.95
		66.63	16.39	62.16	12.67	54.01	17.6
	0.5	71.76	21.85	59.68	10.19	49.09	12.68
				66.68	17.19	59.05	22.64



**Table 8-8-** Correlation between viscosity, width at half peak height and  $\chi_{\text{GaCl}_3}$ .

$\text{P}_{888}\text{S-GaCl}_3^{31}\text{P}$ NMR			
$\chi_{\text{GaCl}_3}$	Peak	Width at half peak height/ ppm	Viscosity at 30 °C/cP
0.5	57.9301	0.2001	427.6995614
	60.1495	0.21223	
0.6	59.5787	0.2911	345.2141327
0.67	60.7536	0.211	329.1248648
0.75	61.4246	0.1895	253.0358284
$\text{P}_{888}\text{Se-GaCl}_3^{31}\text{P}$ NMR			
$\chi_{\text{GaCl}_3}$	Peak	Width at half peak height/ ppm	Viscosity at 30 °C/cP
0.5	47.5121	0.1968	556.1937937
	50.3358	0.2088	
0.6	49.4976	0.2678	417.9941627
0.67	51.1436	0.1954	402.7160801
0.75	51.9643	0.1887	297.0433532

**Table 8-9-** Correlation between viscosity, width at half peak height and  $\chi_{\text{InCl}_3}$ .

$\text{P}_{888}\text{O-InCl}_3$ $^{31}\text{P}$ NMR			
$\chi_{\text{InCl}_3}$	Peak	Width at half peak height/ ppm	Viscosity at 30 °C/cP
0.1	46.0017	1.0269	-
0.25	63.1125	8.8961	947.1123568
0.33	63.1581	3.792	1448.46713617557
0.4	66.6324	2.2264	1273.41203307635
0.5	71.7619	2.5968	-
$\text{P}_{888}\text{S-InCl}_3$ $^{31}\text{P}$ NMR			
$\chi_{\text{InCl}_3}$	Peak	Width at half peak height/ ppm	Viscosity at 30 °C/cP
0.25	50.6504	0.2559	202.1331049
0.33	52.5141	0.3183	355.4689525
0.4	54.7696	0.3362	513.0057816
$\text{P}_{888}\text{Se-InCl}_3$ $^{31}\text{P}$ NMR			
$\chi_{\text{InCl}_3}$	Peak	Width at half peak height/ ppm	Viscosity at 30 °C/cP
0.25	39.698	0.26	276.5043816
0.33	41.716	0.323	532.2886262
0.4	42.24	0.3525	801.7340099

**Table 8-10-**  $^{31}\text{P}$  and  $^{77}\text{Se}$  shift and coupling in  $\text{P}_{888}\text{Se-GaCl}_3$  LCCs.

LCCs	$\delta$ $^{31}\text{P}$ (ppm)	$^1\text{J}$ ( $^{31}\text{P} - ^{77}\text{Se}$ ) (Hz)	$\delta$ $^{77}\text{Se}$ (ppm)	$^1\text{J}$ ( $^{31}\text{P} - ^{77}\text{Se}$ ) (Hz)
$\text{P}_{888}\text{Se}$	36.41	678.25	-388.57	709.68
$\text{P}_{888}\text{Se-GaCl}_3$ $\chi_{\text{GaCl}_3} = 0.50$	47.51	471.42	-161.245	463.98
	50.33	466.56	-183.585	468.54
$\text{P}_{888}\text{Se-GaCl}_3$ $\chi_{\text{GaCl}_3} = 0.60$	49.53	456.84	-167.25*	467.4*
	50.37*	N/A	-182.535*	459.42*
$\text{P}_{888}\text{Se-GaCl}_3$ $\chi_{\text{GaCl}_3} = 0.67$	51.13	442.26	-147.27	444.6
$\text{P}_{888}\text{Se-GaCl}_3$ $\chi_{\text{GaCl}_3} = 0.75$	51.98	447.12	-135.23	434.34

**Table 8-11-** $^{31}\text{P}$  and  $^{77}\text{Se}$  shift and coupling in  $\text{P}_{888}\text{Se-InCl}_3$  LCCs.

LCCs	$\delta ^{31}\text{P}$ (ppm)	$^1\text{J} (^{31}\text{P} - ^{77}\text{Se})$ (Hz)	$\delta ^{77}\text{Se}$ (ppm)	$^1\text{J} (^{31}\text{P} - ^{77}\text{Se})$ (Hz)
$\text{P}_{888}\text{Se}$	36.41	678.25	-388.57	709.68
$\text{P}_{888}\text{Se-InCl}_3$ $\chi_{\text{InCl}_3} = 0.25$	40.1	305.1	-254.99	-
$\text{P}_{888}\text{Se-InCl}_3$ $\chi_{\text{InCl}_3} = 0.33$	41.79	288.88	-219,75	-
$\text{P}_{888}\text{Se-InCl}_3$ $\chi_{\text{InCl}_3} = 0.40$	44.36	261.11	-210.07	-
$\text{P}_{888}\text{Se-InCl}_3$ $\chi_{\text{InCl}_3} = 0.50$	49.09	-	-218.68	486.44
	-	-	-244.95	-

### 8.5.5 Infrared spectroscopic data for chlorogallate and chloroindate liquid coordination complexes

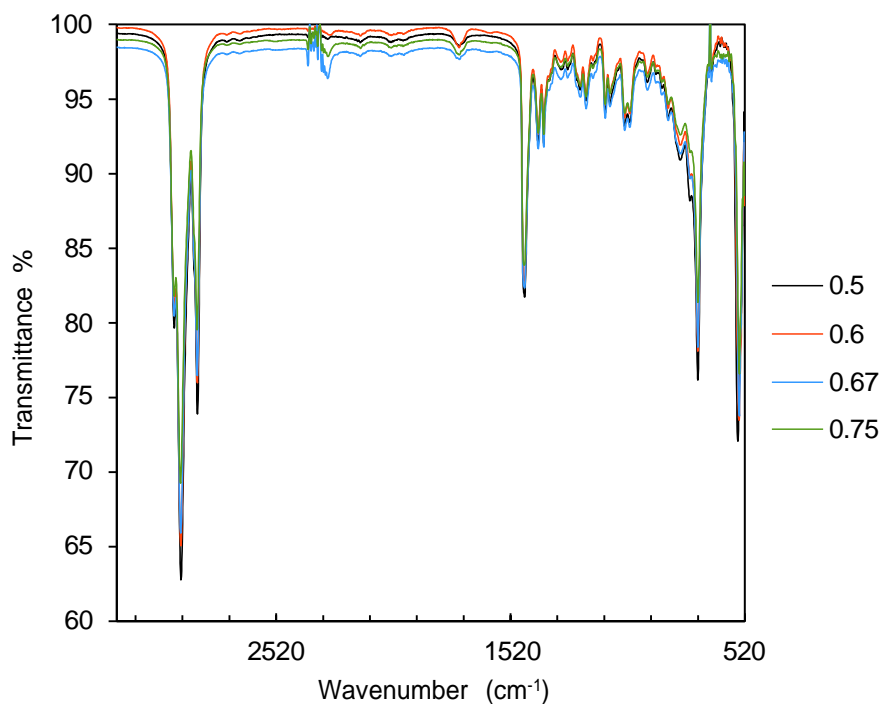


**Figure 8-67-**Infrared spectra of  $\text{P}_{888}\text{S-GaCl}_3$  LCCs.

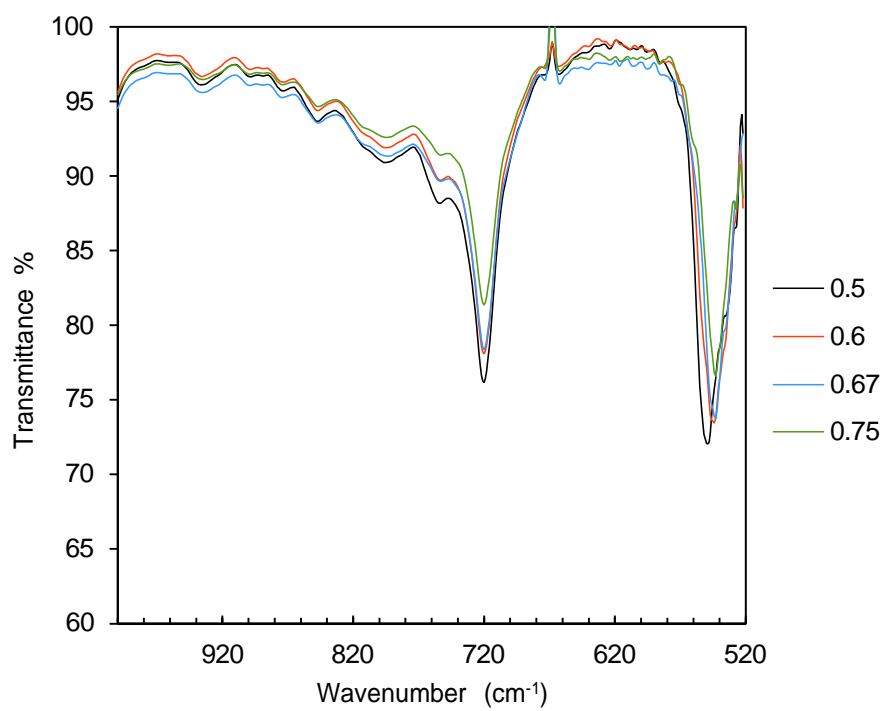


**Figure 8-68-**Expanded Infrared spectra of  $P_{88}S-GaCl_3$  LCCs.

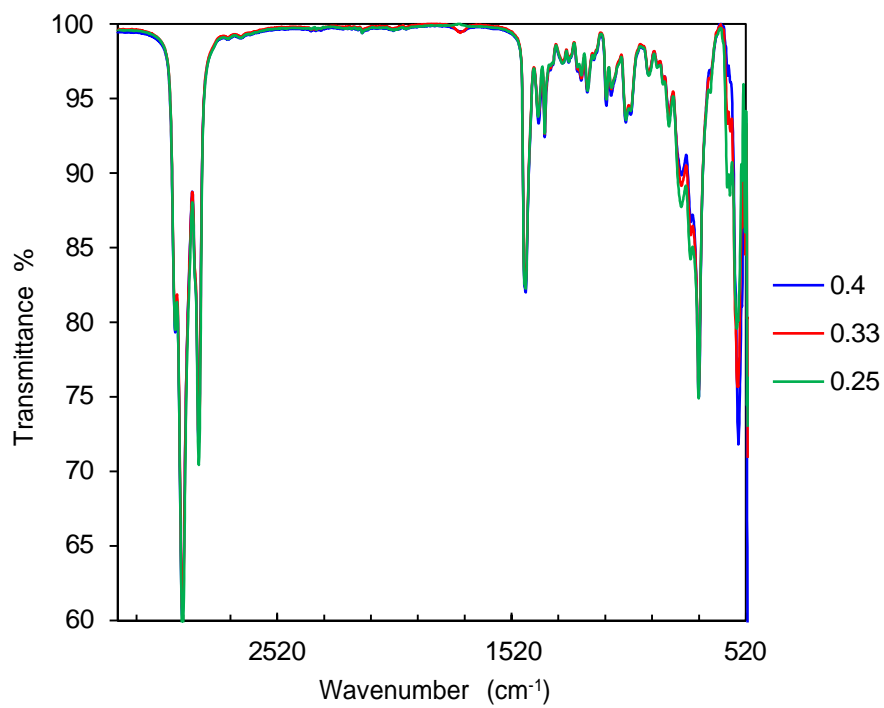


**Figure 8-69-** Infrared spectra of  $P_{88}S-InCl_3$  LCCs.

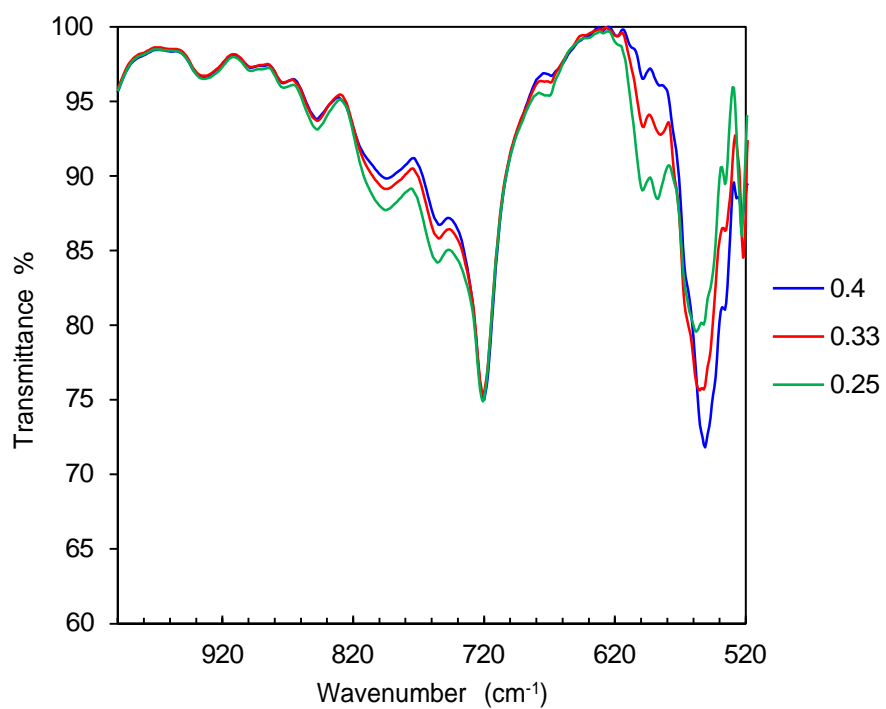


**Figure 8-70-** Expanded Infrared spectra of  $P_{888}S-InCl_3$  LCCs.

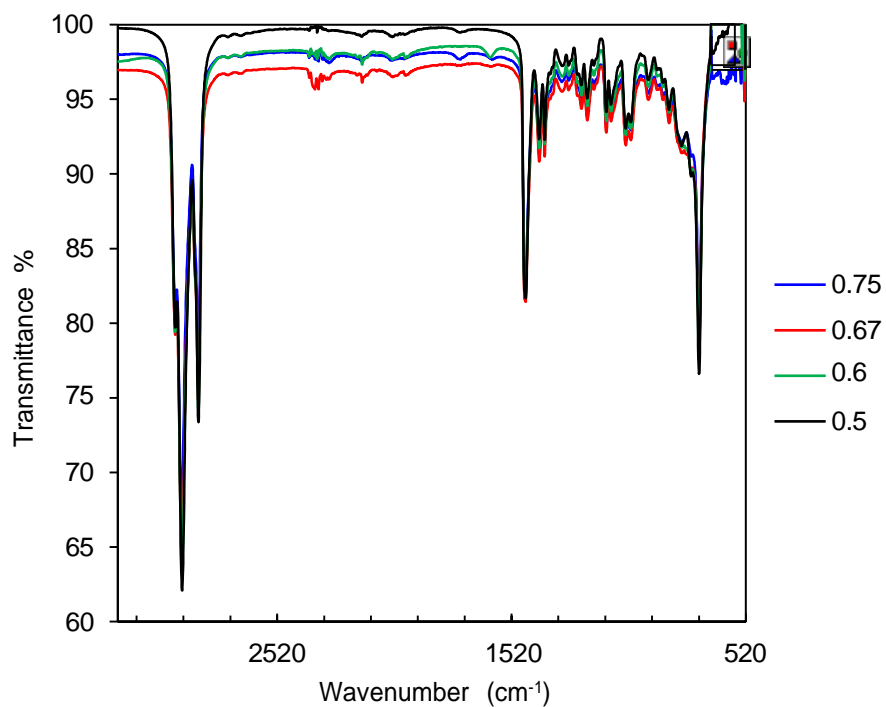


**Figure 8-71-** Infrared spectra of  $P_{888}Se-GaCl_3$  LCCs.

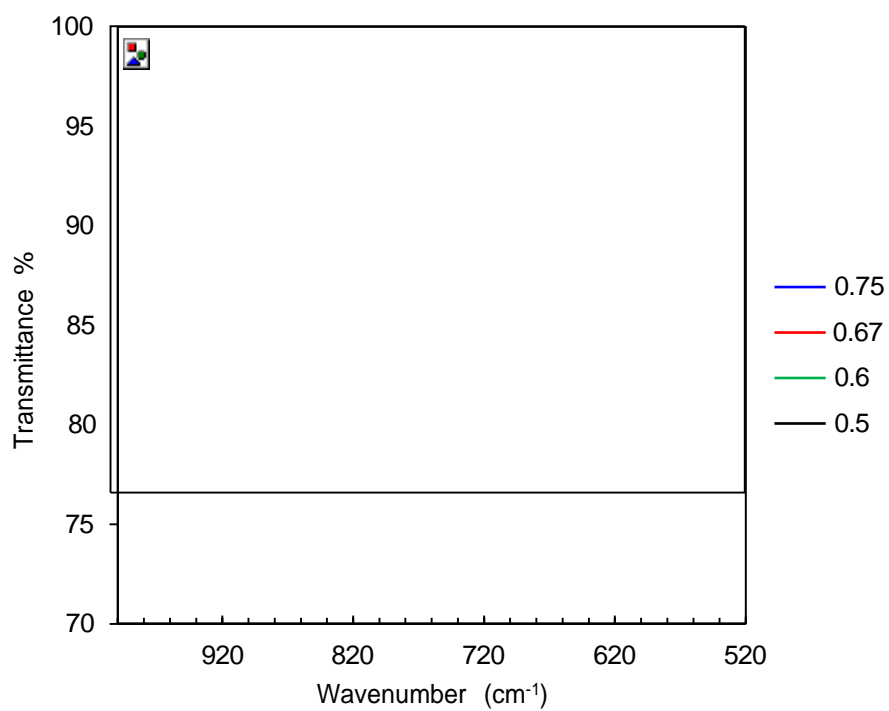


**Figure 8-72**-Expanded Infrared spectra of  $P_{888}Se-GaCl_3$  LCCs.

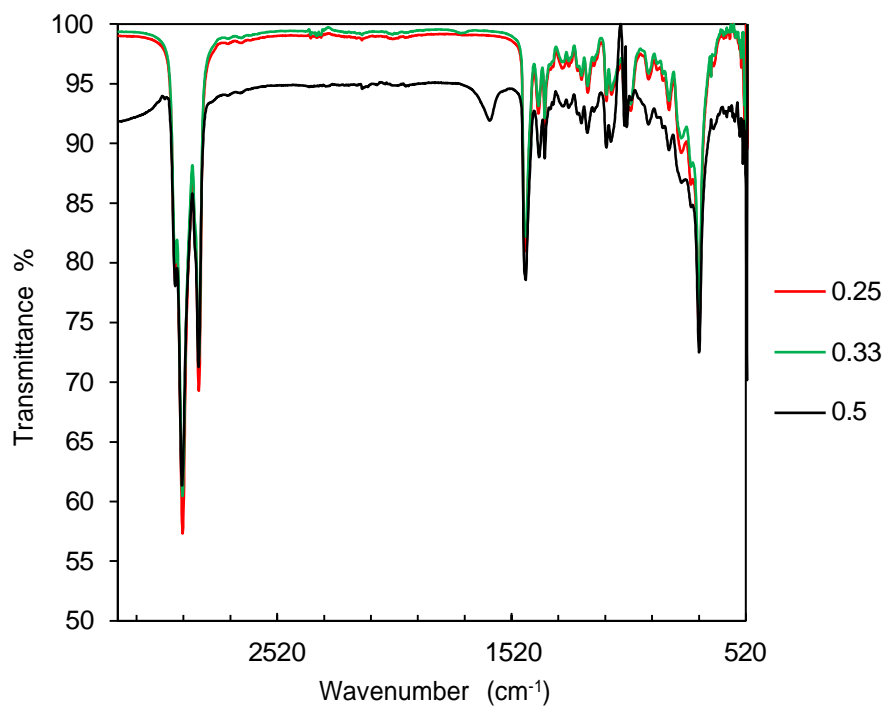


**Figure 8-73**-- Infrared spectra of  $P_{888}Se-InCl_3$  LCCs.

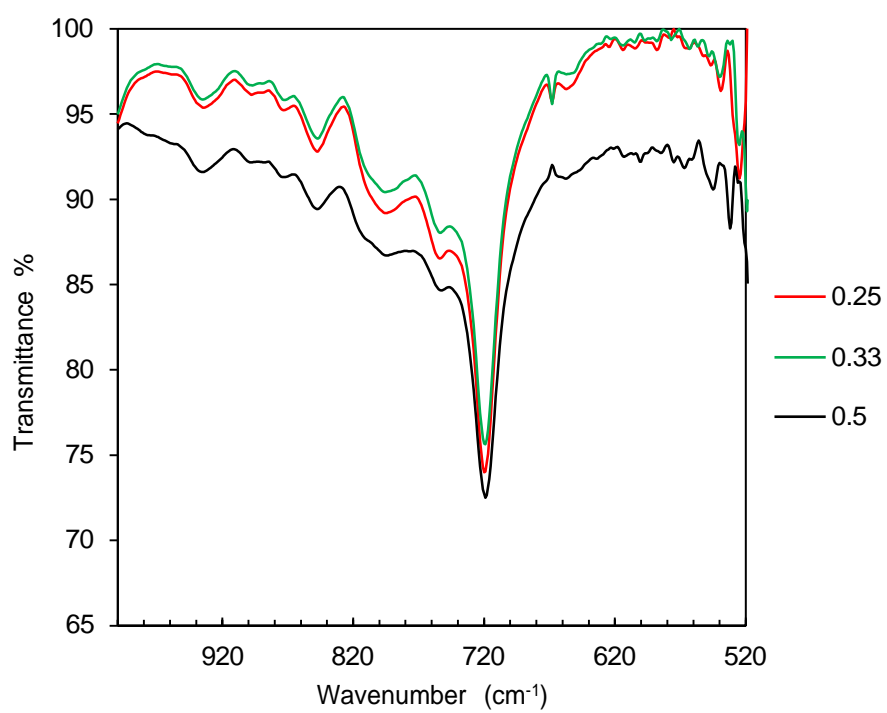


**Figure 8-74-** Expanded Infrared spectra of  $P_{888}Se-InCl_3$  LCCs.

## 8.5.6 Extended X-ray fine structure spectroscopy-Chlorogallate systems

**Table 8-12-** EXAFS fitting statistics for  $P_{888}O-GaCl_3$  LCCs.

$P_{888}O-GaCl_3$	$\chi_{GaCl_3}=0.50$	$\chi_{GaCl_3}=0.60$	$\chi_{GaCl_3}=0.67$
Independent points	9.3515625	29.6376953	21.5800781
Number of variables	6	12	10
Chi-square	401926114.2528110	2610159962.5667877	832933333.8034178
Reduced chi-square	119922010.7793935	132915798.9789840	7192812.7689914
R-factor	0.0237798	0.0176012	0.0535626

**Table 8-13-** Fitting details for  $P_{888}O-GaCl_3$  LCCs.

Fit	$P_{888}O-GaCl_3$ $\chi_{GaCl_3}=0.50$	$P_{888}O-GaCl_3$ $\chi_{GaCl_3}=0.60$	$P_{888}O-GaCl_3$ $\chi_{GaCl_3}=0.67$
k-range	2.76-19.9	2.833 - 19.9	2.79 - 15.5
k-window	Hanning	Hanning	Hanning
k-weight	1,2,3	1,2,3	1,2,3
R-range	1.2-2.1	1.0-3.75	1.3-4.0
R-window	Hanning	Hanning	Hanning
Fitting space	K	K	K
Rbkg	1	1	1

**Table 8-14-** EXAFS guess parameters for  $P_{888}O-GaCl_3$   $\chi_{GaCl_3}=0.50$ .

$P_{888}O-GaCl_3$ $\chi_{GaCl_3}=0.50$	Fit	Error
amp	0.93512062	+/- 0.31624515
enot	3.25809490	+/- 2.07603917
drCl <sub>t</sub>	0.00922793	+/- 0.00831592
ssCl <sub>t</sub>	0.00358211	+/- 0.00074378
drO <sub>t</sub>	0.03347872	+/- 0.03525333
ssO <sub>t</sub>	0.00411846	+/- 0.00314044



**Table 8-15-** EXAFS bond fits for  $P_{888}O-GaCl_3$   $\chi_{GaCl_3} = 0.50$ .

Bond	N	S02	Sigma^2	E0	delr	Reff	R
Ga-Ot	1	1.119	0.00412	3.258	0.03348	1.82760	1.86108
Ga-Clt	3	1.119	0.00358	3.258	0.00923	2.16030	2.16953

**Table 8-16-** EXAFS guess parameters for  $P_{888}O-GaCl_3$   $\chi_{GaCl_3}=0.60$ .

$P_{888}O-GaCl_3$ $\chi_{GaCl_3}=0.60$	Fit	Error
amp	0.92618343	+/- 0.07018642
enot	2.94602711	+/- 0.91122459
drClt	0.00533922	+/- 0.00420110
ssClt	0.00286827	+/- 0.00033349
drClb	-0.06604282	+/- 0.03495110
ssClb	0.00575490	+/- 0.00327591
drOt	0.02993082	+/- 0.01515961
ssOt	0.00309219	+/- 0.00125248
drGa	0.06048608	+/- 0.06402655
ssGa	0.01098445	+/- 0.00717803

**Table 8-17-** EXAFS bond fits for  $P_{888}O-GaCl_3$   $\chi_{GaCl_3}=0.60$ .

Bond	N	S02	Sigma^2	E0	delr	Reff	R
Ga-Clt	2.66	0.926	0.00287	2.946	0.00534	2.14350	2.14884
Ga-Clb	0.66	0.926	0.00575	2.946	-0.06604	2.31760	2.25156
Ga-Ot	0.66	0.926	0.00309	2.946	0.02993	1.82760	1.85753
Ga-Ga	0.66	0.926	0.01098	2.946	0.06049	3.75470	3.81519

**Table 8-18-** EXAFS guess parameters for  $P_{888}O-GaCl_3$   $\chi_{GaCl_3}=0.67$ .

$P_{888}O-GaCl_3$ $\chi_{GaCl_3}=0.67$	Fit	Error
amp	0.84764356	+/- 0.21131867
enot	0.93197384	+/- 3.52810758
drClt	-0.03810872	+/- 0.01993611
ssClt	0.00139172	+/- 0.00261540
drClb	-0.0380172	+/- 0.04479768
ssClb	0.00071738	+/- 0.00480686
drOt	-0.00903572	+/- 0.02530201
ssOt	-0.00267870	+/- 0.00166561
drGa	0.066025742	+/- 0.09229240
ssGa	0.00730584	+/- 0.00911909

**Table 8-19-** EXAFS bond fits for  $P_{888}O-GaCl_3$   $\chi_{GaCl_3}=0.67$ .

Bond	N	S02	Sigma^2	E0	delr	Reff	R
Ga-Clt	2.50	0.848	0.00139	0.932	-0.03811	2.16030	2.12219
Ga-Clb	1	0.848	0.00072	0.932	-0.03016	2.25930	2.22914
Ga-Ot	0.50	0.848	-0.00268	0.932	-0.00904	1.82760	1.81856
Ga-Ga	1	0.848	0.00751	0.932	0.06603	3.73070	3.79673

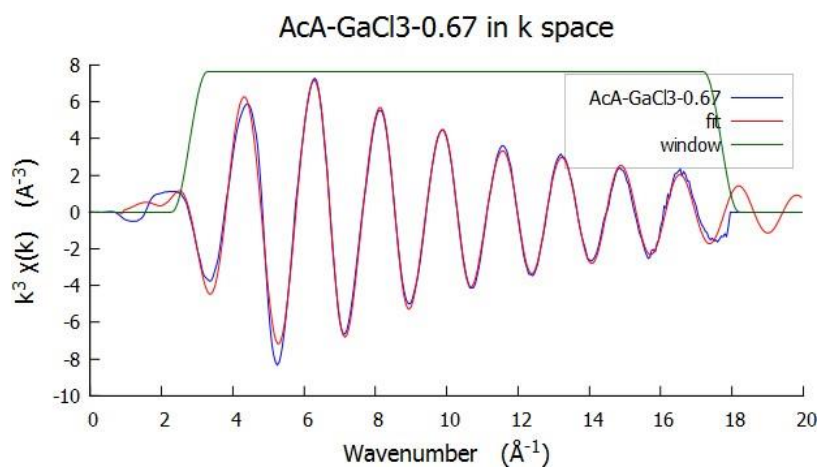


**Figure 8-75-** EXAFS fit for ACA-GaCl<sub>3</sub>  $\chi_{GaCl_3}=0.67$  in k-space.

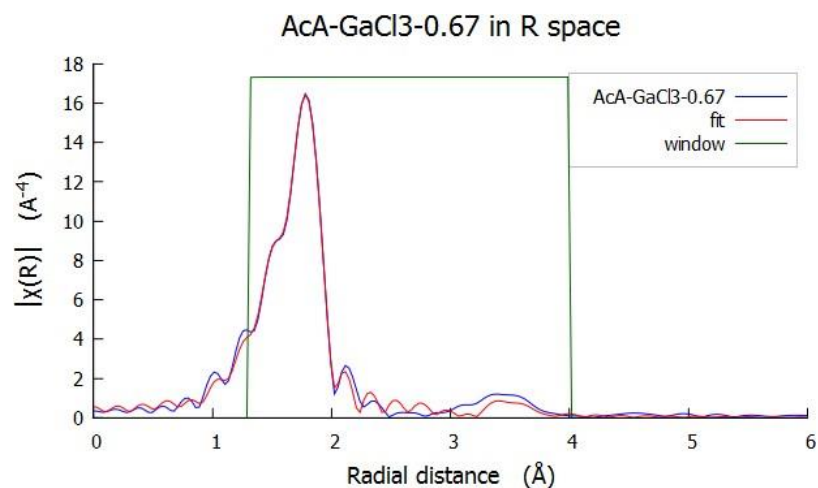


Figure 8-76- EXAFS fit for ACA-GaCl<sub>3</sub>  $\chi_{\text{GaCl}_3}=0.67$  in R-space.

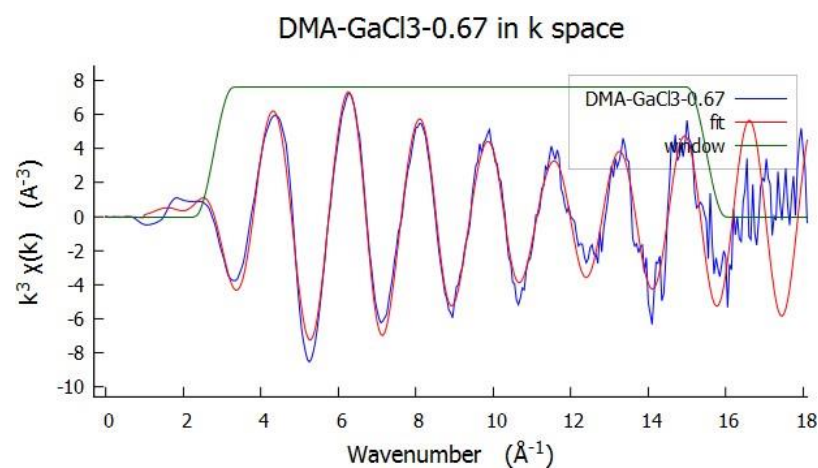


Figure 8-77 EXAFS fit for DMA-GaCl<sub>3</sub>  $\chi_{\text{GaCl}_3}=0.67$  in k-space.

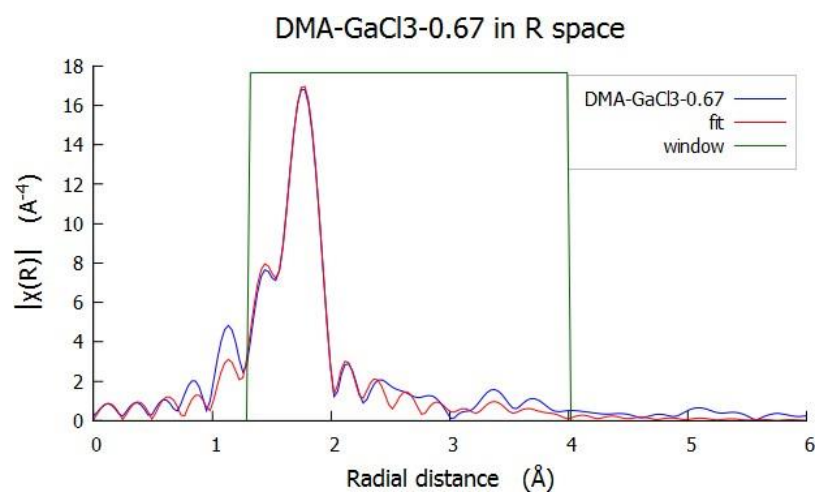


Figure 8-78- EXAFS fit for DMA-GaCl<sub>3</sub>  $\chi_{\text{GaCl}_3}=0.67$  in R-space.

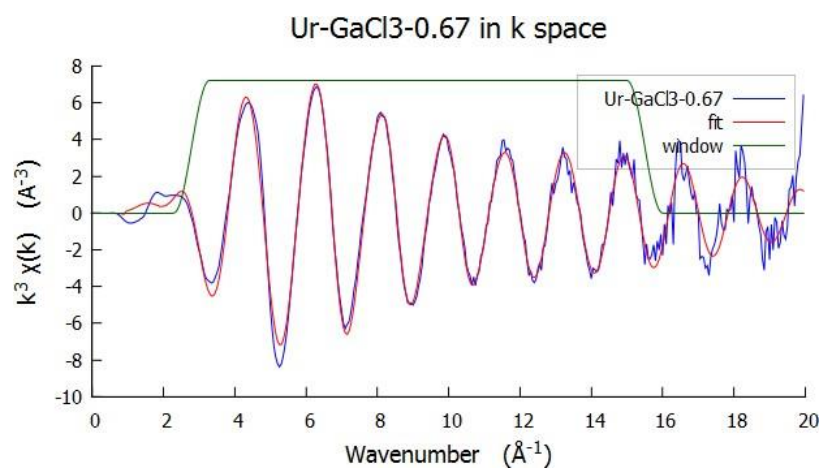


Figure 8-79- EXAFS fit for Ur-GaCl<sub>3</sub>  $\chi_{\text{GaCl}_3}=0.67$  in k-space.

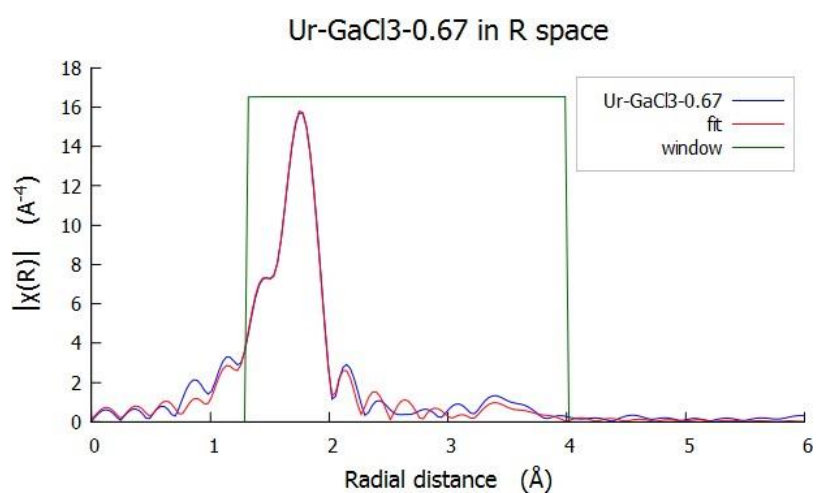


Figure 8-80- EXAFS fit for Ur-GaCl<sub>3</sub>  $\chi_{\text{GaCl}_3}=0.67$  in R-space.

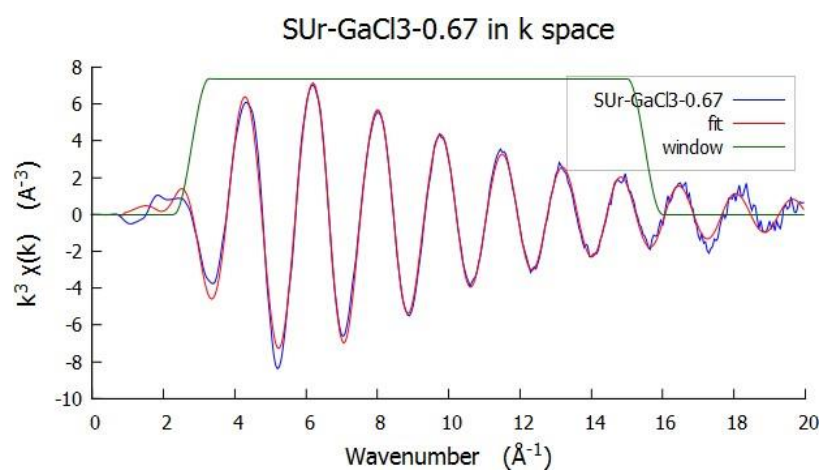
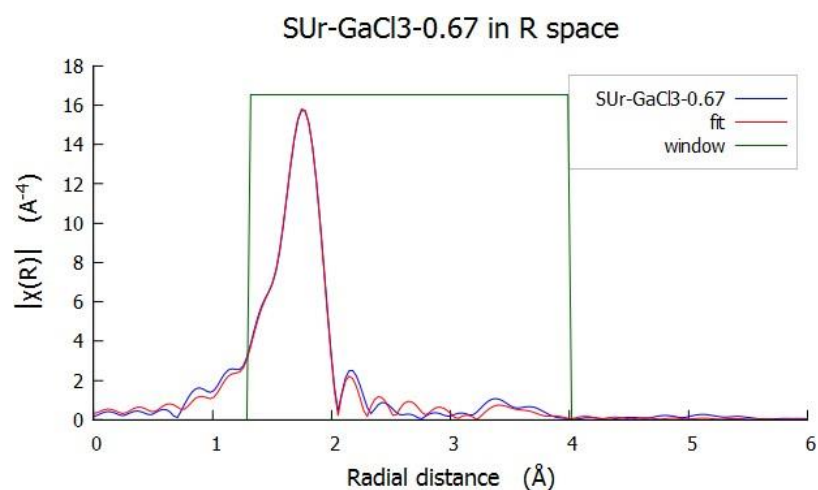
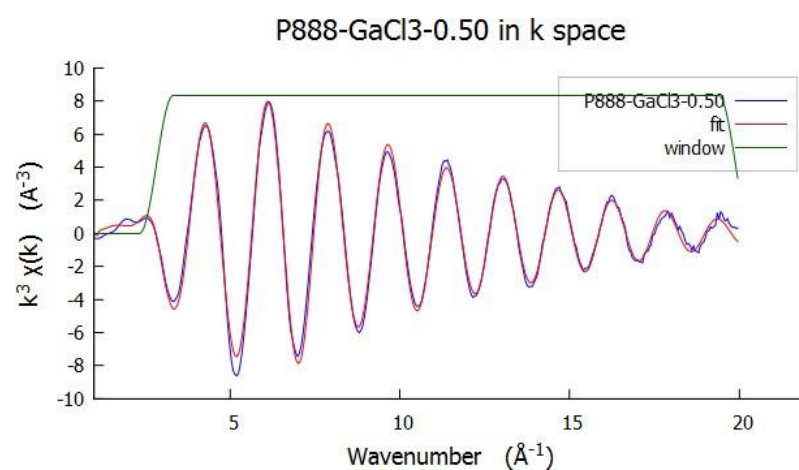


Figure 8-81- EXAFS fit for SUR-GaCl<sub>3</sub>  $\chi_{\text{GaCl}_3}=0.67$  in k-space.



**Figure 8-82-** EXAFS fit for SUR-GaCl<sub>3</sub>  $\chi_{\text{GaCl}_3}=0.67$  in R-space.



**Figure 8-83-** EXAFS fit for P<sub>888</sub>-GaCl<sub>3</sub>  $\chi_{\text{GaCl}_3}=0.50$  in k-space.

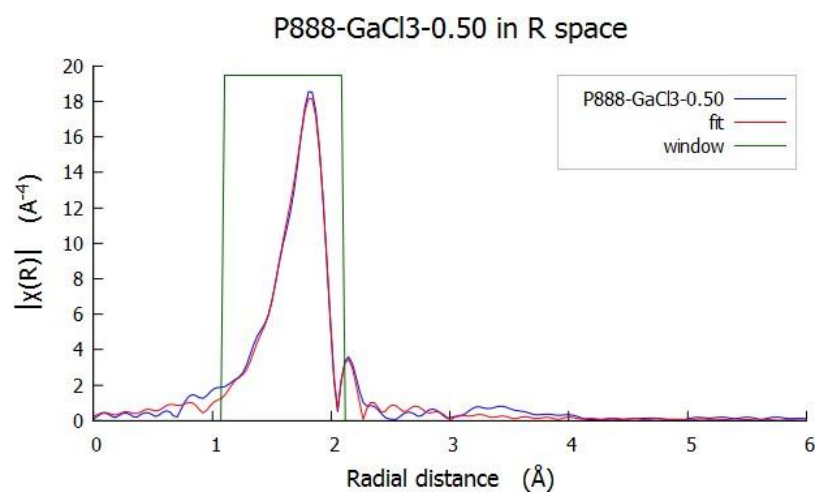


**Figure 8-84-** EXAFS fit for P<sub>888</sub>-GaCl<sub>3</sub>  $\chi_{\text{GaCl}_3}=0.50$  in R-space.

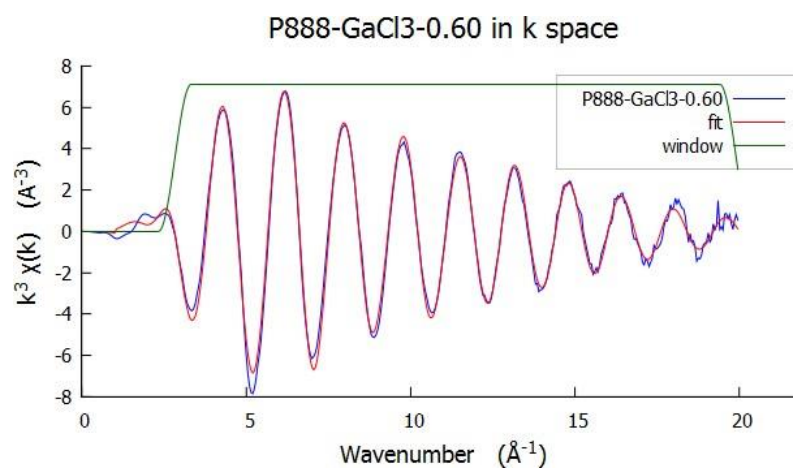


Figure 8-85- EXAFS fit for  $P_{888}\text{-GaCl}_3$   $\chi_{\text{GaCl}_3}=0.60$  in k-space.

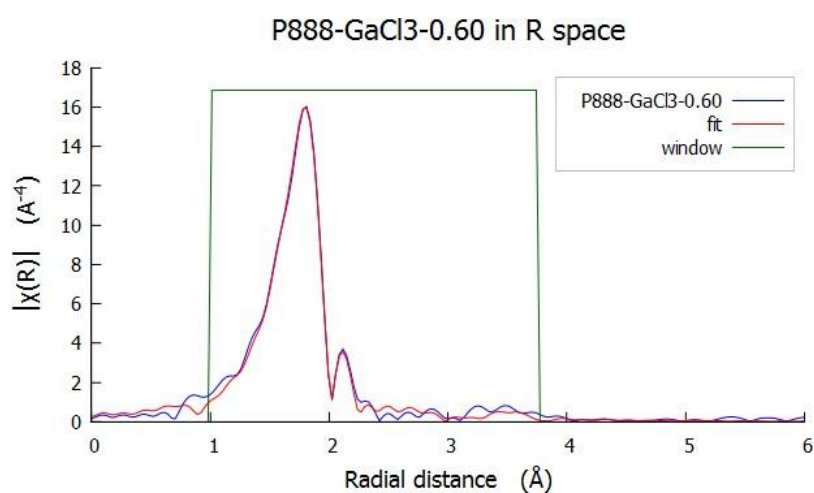


Figure 8-86- EXAFS fit for  $P_{888}\text{-GaCl}_3$   $\chi_{\text{GaCl}_3}=0.60$  in R-space.

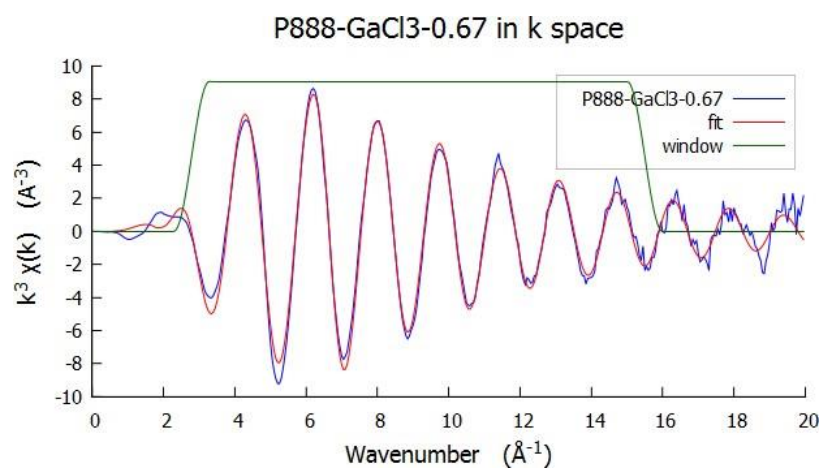
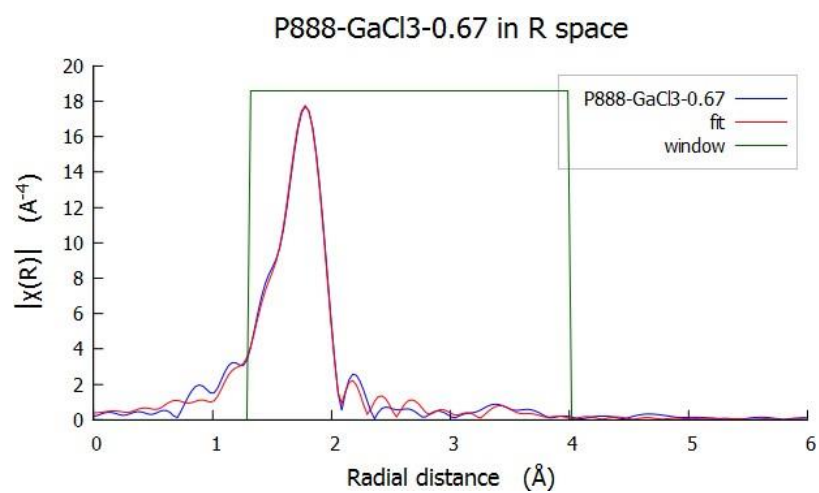
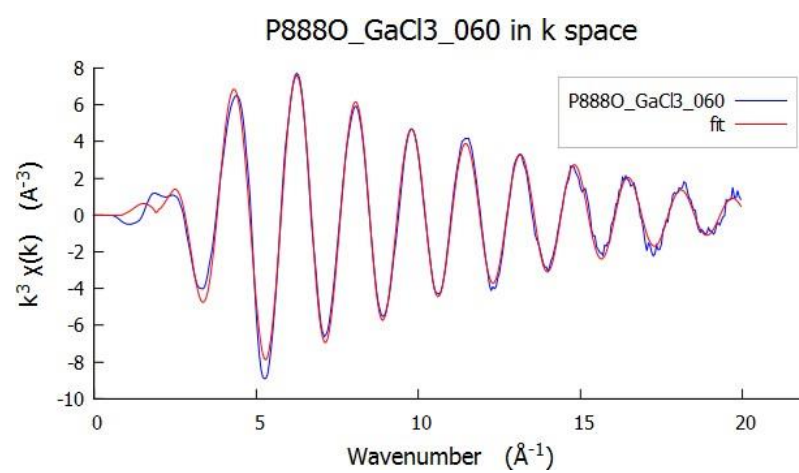


Figure 8-87- EXAFS fit for  $P_{888}\text{-GaCl}_3$   $\chi_{\text{GaCl}_3}=0.67$  in k-space.



**Figure 8-88-** EXAFS fit for P<sub>888</sub>-GaCl<sub>3</sub>  $\chi_{\text{GaCl}_3}$ =0.67 in R-space.



**Figure 8-89-** EXAFS fit for P<sub>888</sub>Se-GaCl<sub>3</sub>  $\chi_{\text{GaCl}_3}$ =0.50 in K-space.

### 8.5.7 Extended X-ray fine structure spectroscopy-Chlorocuprate systems

**Table 8-20-** Fitting details for P<sub>888</sub>-CuCl LCC fits.

Fit	P <sub>888</sub> -CuCl $\chi_{\text{CuCl}} = 0.25$	P <sub>888</sub> -CuCl $\chi_{\text{CuCl}} = 0.33$	P <sub>888</sub> -CuCl $\chi_{\text{CuCl}} = 0.50$
k-range	3.09 - 13.46	3.07 - 13.72	3.07 - 13.72
k-window	Hanning	Hanning	Hanning
k-weight	1, 2, 3	1, 2, 3	1, 2, 3
R-range	1.2 - 2.7	1.1 - 2.47	1.1 - 2.247
R-window	Hanning	Hanning	Hanning
Fitting space	K	K	K
Rbkg	1	1	1

**Table 8-21-** EXAFS fit parameters for P<sub>888</sub>-CuCl LCCs.

P <sub>888</sub> -CuCl $\chi_{\text{CuCl}} = 0.50$	Fit	Error
amp	2.79600	+/- 1.36269168
enot	3.17691	+/- 4.65101021
drCl	-0.05935	+/- 0.03299654
ssCl	0.00995	+/- 0.00387074
drP	0.22293	+/- 0.07665715
ssP	0.01634	+/- 0.00765009
P <sub>888</sub> -CuCl $\chi_{\text{CuCl}} = 0.33$	Fit	Error
amp	1.589176	+/- 0.33991732
enot	4.499790	+/- 2.08222635
drCl	0.181535	+/- 0.05036390
ssCl	0.005749	+/- 0.00331122
drP	0.091931	+/- 0.01810364
ssP	0.008865	+/- 0.00197099
P <sub>888</sub> -CuCl $\chi_{\text{CuCl}} = 0.25$	Fit	Error
amp	1.400936	+/- 0.04513426
enot	5.761056	+/- 1.81581278
drCl	0.162585	+/- 0.04513426
ssCl	0.007159	+/- 0.00482698
drP	0.110255	+/- 0.01646670
ssP	0.00782097	+/- 0.00192206



**Table 8-22**-EXAFS fit bond parameters for P<sub>888</sub>-CuCl LCCs.

P <sub>888</sub> -CuCl $\chi_{\text{CuCl}} = 0.50$							
Bond	N	S02	Sigma^2	E0	delr	Reff	R
Cu-Cl	1.18	2.496	0.00995	3.177	-0.05936	2.247	2.18764
Cu-P	1.49	2.796	0.01634	3.177	0.22293	2.177	2.39993
P <sub>888</sub> -CuCl $\chi_{\text{CuCl}} = 0.33$							
Bond	N	S02	Sigma^2	E0	delr	Reff	R
Cu-Cl	0.476	1.589	0.00575	4.5	0.18154	2.247	2.42854
Cu-P	2.854	1.589	0.00886	4.5	0.0919	2.177	2.26893
P <sub>888</sub> -CuCl $\chi_{\text{CuCl}} = 0.25$							
Bond	N	S02	Sigma^2	E0	delr	Reff	R
Cu-Cl	0.82	1.401	0.00716	5.761	0.16259	2.247	2.40958
Cu-P	3.18	1.401	0.00782	5.761	0.11026	2.177	2.28726

### 8.5.8 Nuclear magnetic resonance spectroscopic data for chlorocuprate systems

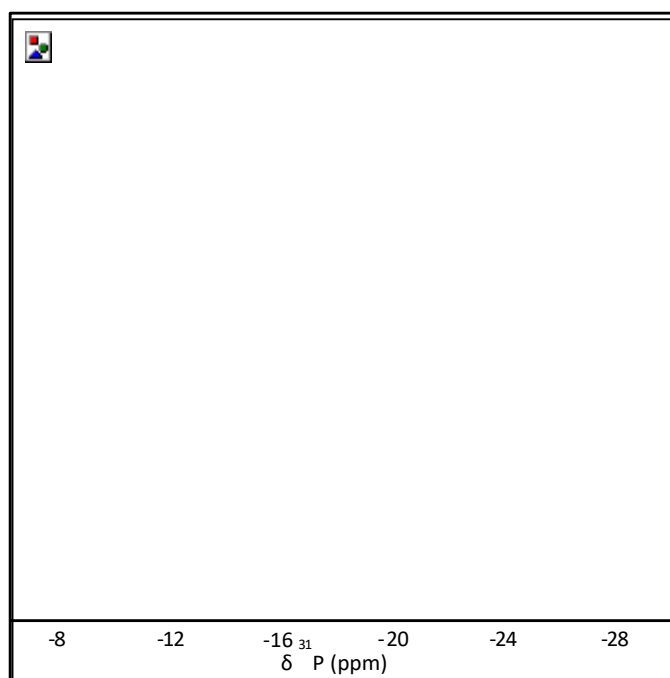


**Figure 8-90**  $^{31}\text{P}$  VT NMR spectra of  $\text{P}_{888}\text{-CuCl}$   $\chi_{\text{CuCl}} = 0.25$  in 10 K increments from 223 K (top) to 323 K (bottom).

### 8.5.9 Powder X-ray diffraction data

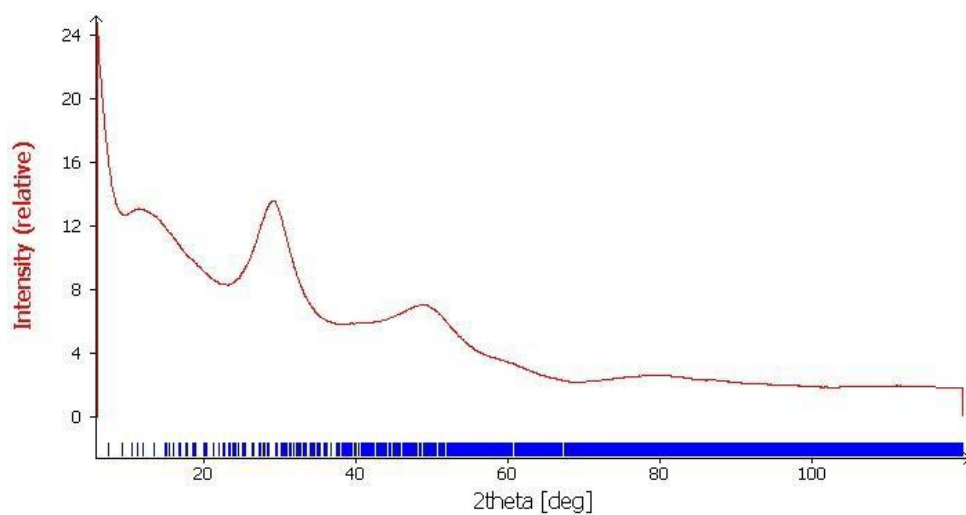


**Figure 8-91** pXRD analysis of ionothermal  $\text{P}_{888}\text{Se-GaCl}_3$   $\chi_{\text{GaCl}_3} = 0.67$  reaction product.